Create a Consortium and Develop Premium Carbon Products from Coal

ANNUAL TECHNICAL REPORT

For Reporting Period Ending May 31, 2004

Principal Authors:
Frank Rusinko, Consortium Director, June 1998-December 2002
John Andresen, Consortium Director, January 2003-November 2004

Report Prepared By: Jennifer E. Hill, Harold H. Schobert, and Bruce G. Miller

Date of Submission: *January 2006*

Work Performed Under Cooperative Agreement No. DE-FC26-98FT40350

Submitting Organization: *The Energy Institute*
The Pennsylvania State University
405 Academic Activities Building
University Park, PA 16802-2398
Phone: (814) 863 8265
Fax: (814) 863 8892

DISCLAIMER

ABSTRACT

The objective of these projects was to investigate alternative technologies for non-fuel uses of coal. Special emphasis was placed on developing premium carbon products from coal-derived feedstocks. A total of 14 projects, which are the 2003 Research Projects, are reported herein. These projects were categorized into three overall objectives. They are:

(1) To explore new applications for the use of anthracite in order to improve its marketability;
(2) To effectively minimize environmental damage caused by mercury emissions, CO_2 emissions, and coal impounds; and
(3) To continue to increase our understanding of coal properties and establish coal usage in non-fuel industries.

Research was completed in laboratories throughout the United States. Most research was performed on a bench-scale level with the intent of scaling up if preliminary tests proved successful.

These projects resulted in many potential applications for coal-derived feedstocks. These include:

- Use of anthracite as a sorbent to capture CO_2 emissions
- Use of anthracite-based carbon as a catalyst
- Use of processed anthracite in carbon electrodes and carbon black
- Use of raw coal refuse for producing activated carbon
- Reusable PACs to recycle captured mercury
- Use of combustion and gasification chars to capture mercury from coal-fired power plants
- Development of a synthetic coal tar enamel
- Use of alternative binder pitches in aluminum anodes
- Use of Solvent Extracted Carbon Ore (SECO) to fuel a carbon fuel cell
- Production of a low cost coal-derived turbostratic carbon powder for structural applications
- Production of high-value carbon fibers and foams via the co-processing of a low-cost coal extract pitch with well-dispersed carbon nanotubes
- Use of carbon from fly ash as metallurgical carbon
- Production of bulk carbon fiber for concrete reinforcement
- Characterizing coal solvent extraction processes

Although some of the projects funded did not meet their original goals, the overall objectives of the CPCPC were completed as many new applications for coal-derived feedstocks have been researched. Future research in many of these areas is necessary before implementation into industry.

TABLE OF CONTENTS

EXECUTIVE SUMMARY

The objective of these projects was to investigate alternative technologies for non-fuel uses of coal. Special emphasis was placed on developing premium carbon products from coal-derived feedstocks. A total of 14 projects, which are the 2003 Research Projects, are reported herein. These projects were categorized into three overall objectives. They are:

(1) To explore new applications for the use of anthracite in order to improve its marketability;
(2) To effectively minimize environmental damage caused by mercury emissions, CO_2 emissions, and coal impounds; and
(3) To continue to increase our understanding of coal properties and establish coal usage in non-fuel industries.

Each of these topics had a broad range of subtopics that was the result of individual research projects. These subtopics are project-specific and include developing high-value carbon fibers and foam via processing of a low-cost extract pitch with well dispersed nanotubes, determining the feasibility of recyclable PACs, and exploring the mechanisms of carbon-catalyzed reactions to design carbon catalysts for additional reactions. Many other subtopics were also explored in this research, and are discussed in the individual final reports for the 2003 projects.

Research was completed in laboratories throughout the United States. Most research was performed on a bench-scale level with the intent of scaling up if preliminary tests proved successful.

The overall success of the projects initiated by the CPCPC was astounding. Most projects successfully met their objectives and those that did not still documented and provided information useful for the growth of the carbon industry outside of fuel-related applications. Many applications for carbon were determined such as:

a. Use of anthracite as a sorbent to capture CO_2 emissions
b. Use of anthracite-based carbon as a catalyst
c. Use of processed anthracite in carbon electrodes and carbon black
d. Use of raw coal refuse for producing activated carbon
e. Reusable PACs to recycle captured mercury
f. Use of combustion and gasification chars to capture mercury from coal-fired power plants
g. Development of a synthetic coal tar enamel
h. Use of alternative binder pitches in aluminum anodes
i. Use of Solvent Extracted Carbon Ore (SECO) to fuel a carbon fuel cell
j. Production of a low cost coal-derived turbostratic carbon powder for structural applications
k. Production of high-value carbon fibers and foams via the co-processing of a low-cost coal extract pitch with well-dispersed carbon nanotubes
l. Use of carbon from fly ash as metallurgical carbon
m. Production of bulk carbon fiber for concrete reinforcement
n. Characterizing coal solvent extraction processes

These applications and many others enable the coal industry to diversify and find moneymaking opportunities outside of the fuel industry. In addition, many of the above mentioned applications use low marketed or waste coals as the feedstock. Also of importance are the environmental benefits these solutions provide. By minimizing coal waste streams and more effectively controlling emissions, the coal industry becomes much more environmentally responsible.

Additional research is needed for these projects as they were only done on a small scale. This research would be beneficial in determining the extent to which these applications can be commercialized and as a basis for an economical analysis. Indeed, these results are most promising.

INTRODUCTION

The overall purpose of the Consortium for Premium Carbon Products from Coal (CPCPC) is to explore new methods and uses for coal outside its traditional use as a fuel. In order to achieve this, three main objectives were the focus of the 2003 projects. They are:

1. To explore new applications for the use of anthracite in order to improve its marketability;
2. To effectively minimize environmental damage caused by mercury emissions, CO_2 emissions, and coal impounds; and
3. To continue to increase our understanding of coal properties and establish coal usage in non-fuel industries.

Using these objectives as guidelines, research was conducted in many different areas and ranged from the possible uses of coal impound ponds to producing high-value carbon fibers and foam using low-cost pitch feed stock.

Within each of the three overall objectives there are many individual goals. These individual goals are summarized below

For **Objective 1**: *To explore new applications for the use of anthracite in order to improve its marketability*, the goals are:

- To explore the mechanisms of two carbon-catalyzed reactions in order to develop the knowledge needed to design a carbon catalyst for existing commercial reactions,
- To develop a method for anthracite exfoliation that is safer than using perchloric acid and to test the exfoliated anthracite as an electrode material,
- To improve the properties of coal-based electrodes and cathodes to maintain and expand the usage of anthracite coal in carbon products, and
- To synthesize high-surface-area powdered anthracites, impregnate them with amine compounds, and determine the feasibility of using these materials for CO_2 capture.

For **Objective 2**: *To effectively minimize environmental damage caused by mercury emissions, CO_2 emissions, and coal impounds*, the goals are:

- Determine the feasibility of using high-surface-area powdered anthracites impregnated with amine compounds for CO_2 capture,
- To determine the feasibility of the removal and recovery of mercury that is sorbed to powered activated carbon (PAC) from coal combustion power plant flue gas streams,
- To develop activated carbon sorbents from coal chars to determine their mercury capacity and compare them to commercially activated carbons, and
- To develop activation techniques for coal recovered from coal slurry water and treatment of coal slurry water to National Pollutant Discharge Elimination System (NPDES) standards.

And finally, for **Objective 3**: To *continue to increase our understanding of coal properties and establish coal usage in non-fuel industries*, the goals are:

- To determine if cyclone-fired boilers can produce fly ash with sorptive potential, activated carbon potential, or metallurgical carbon potential,
- To assess performance improvements associated with the addition of fiber reinforcement in concrete,
- To produce high-value carbon fibers and foam from low-cost extract pitch with well-dispersed carbon nanotubes,
- To use solvent-extracted carbon ore (SECO) to fuel a fuel cell,
- To determine the performance of additional binder pitches, the physical and chemical properties of anode butts, and the interaction between the pitch and different parts of the anode butt,
- To determine what petrographic, physical, and chemical characteristics of bituminous coal lead to the production of maximum yield in N-methylpyrrolidone (NMP),
- To produce a coal extract surrogate for conventional coal pitch, and
- To develop a synthetic coal tar enamel that closely matches commercial products.

The objective of this report is to summarize the findings and conclusions produced as a result of the 2003 projects and to show how each of the projects undertaken meets the objectives of the overall consortium. This will be accomplished in the following format: experimental work will briefly be summarized and referenced to specific projects, overall results will be discussed, and conclusions will be drawn from those results.

EXPERIMENTAL

Experimental work was completed in university and industrial facilities across the country. In each setting, experimental work was completely documented such that additional work could be completed based on the initial work being done. Some experiments were designed and completed in only one facility whereas others were sent to multiple facilities for work. Each experiment followed standard procedures found in literature or common in industry. All equipment used was either thoroughly documented or the standard used in the given application. Accidents and injuries were kept to a minimum by following the required safety guidelines. Most experimental work was done on a bench-scale level with the intent on continuing research if initial tests were deemed successful. For further information on the experimental set-up of individual projects, reference can be made to the project's final report. (See Appendix A for the final reports of the 2003 projects).

RESULTS AND DISCUSSION

This section discusses the results found under each of the three overall objectives and explains their significance to the coal/carbon industry.

Objective 1: To explore new applications for the use of anthracite in order to improve its marketability

Testing done to fulfill this objective shows promising results. Through these tests, it has been found that there are many possibilities for additional uses of anthracite. These opportunities include: use as a sorbent to capture CO_2 emissions, use of anthracite as a carbon catalyst, and use of processed anthracite in carbon electrodes and carbon black. These findings will be explained in more detail below. In addition, exploratory experiments were done to determine the ability to exfoliate anthracite, but were inconclusive, leaving room for additional studies in that area.

Anthracite Sorbents for CO_2 Capture

Because the costs of CO_2 separation and capture are so significant in the fossil fuel industry, there is a demand for more revolutionary capture technologies. Currently, new solid-based sorbents are being investigated; however, the supports used so far (including commercial molecular sieves and activated carbons) are very expensive, making the process uneconomical. This results in a need for low-cost precursors that can compete with expensive commercial supports, and to develop effective solid sorbents that can easily be regenerated. Due to the inherent chemical properties, fine porosity, and relative low price, anthracites would be ideal as sorbent precursors for activated carbon.

Three Pennsylvania anthracites were used in this study. They were activated with steam in a fluidized-bed reactor. The activated anthracites had a highly developed micropore structure (based on nitrogen adsorption isotherms at 77 K), with some mesoporosity. The optimum activation time was three hours, and it was possible to obtain surface areas approaching 800 m^2/g for activation at 800°C, and exceeding 900 m^2/g at 850°C. Interestingly, longer activation times actually reduced surface area as did increasing the activation temperature to 890°C. Surface area alone, however, is not the only part of the story. The anthracite with the highest CO_2 adsorption capacity (66 mg CO_2/g anthracite) was one with a surface area of only 540 m^2/g. Very likely, the crucial relationship is not the absolute pore volume or surface area, but rather that between microporosity and the CO_2 physisorption process. This is further substantiated by the fact that CO_2 adsorption results are not a linear function of surface area. Both ammonia treatment and polyethylenimine impregnation can increase CO_2 capacity, presumably due to the introduction of basic nitrogen-containing functional groups on the anthracite surface. The impact of these reagents on surface area is different, with ammonia treatment increasing surface area, but polyethylenimine causing a drastic decrease (likely by simple physical blocking or occlusion of pores). Again it can be seen that surface area alone is not a reliable indicator of the performance of activated anthracite in CO_2 adsorption.

These results are significant, in that anthracite is a fairly inexpensive feed source for activated carbon and shows potential in the CO_2 capture process.

Development of Anthracite-Based Catalyst

Being able to use anthracite or other forms of carbon as catalysts in place of metal has many benefits. Specifically, anthracite is a low cost material, has reasonably low chemical and electrochemical reactivity, and has an easily reproducible and controllable surface chemistry. The preliminary results show promise in the area of carbon catalysts.

The principal goal of this work was to obtain additional information on the catalytic mechanisms of the reduction of nitrobenzene to aniline by hydrazine and the decomposition of hydrazine. Understanding how these reactions are catalyzed by carbons then opens up the possibility of using anthracites (or other coals or coal-derived products) as catalysts for these reactions. Further, the possibility of carbon catalysis, or even catalysis by coals, could then be extended to other reactions.

The catalytic activity of various commercial carbons (activated carbons, carbon blacks, charcoals, and graphite) was investigated for both reactions, in refluxing *iso*-propanol. The specific reactions of nitrobenzene reduction and hydrazine decomposition are easy to study, by measuring the production of gases as a function of time in a simple gas burette. All of the carbons tested catalyzed both reactions. Reaction rates were proportional to the catalyst concentration and increased with surface area, but were independent of stirring conditions. These observations suggest that the reactions may be surface-controlled. For the specific case of nitrobenzene, an effect of pore diffusion cannot be ruled out, because of a near-linear relationship between initial reaction rates and external surface area and pore volume of the carbons.

For both reactions, the activity of the carbon catalysts varied linearly with the surface area and with the bulk oxygen content (at low oxygen contents). The dependence of activity on surface area actually plots as two straight lines, depending on whether the carbons are acidic or basic. This is an indication that the adsorption of hydrazine and nitrobenzene is affected by two different types (i.e., acidic or basic) of oxygen functional groups.

Hydrazine decomposition is first order at low concentrations of hydrazine, but changes to zero-th order at higher concentrations. The kinetics of nitrobenzene reduction also show a change in order, from a fractional positive value of low nitrobenzene concentrations to a fractional negative one at higher concentrations. The kinetics of the nitrobenzene reaction are complicated by the fact that hydrazine is simultaneously undergoing decomposition on its own and is involved in the reduction of the nitrobenzene. Presumably the hydrazine decomposition begins with a Langmuir adsorption (the slow step) of hydrazine non-dissociatively onto the carbon surface. Subsequently, these adsorbed hydrazine molecules react with other hydrazine molecules still in the solution phase. The rate-determining step in the nitrobenzene reduction is a reaction between an adsorbed nitrobenzene molecule and an adsorbed hydrazine, following the well-known Langmuir-Hinshelwood model.

Processing of Anthracite Coals for Carbon Products

In order to increase productivity, both aluminum and silicon smelters are significantly raising the power input into the smelting furnaces. For this reason, the property requirements for carbon electrode and carbon blacks are becoming more stringent. Without improvement, current anthracite markets will not be able to meet these standards.

Testing in this area showed that heat treatment of anthracite coals is effective at upgrading the coal quality. In addition, testing showed that the optimum temperature range for anthracite use in carbon electrodes and carbon blacks is between 2300º and 2700ºC.

The optimal heat-treatment temperature is in the range of 2300–2700°C. Little additional improvement is obtained by pushing to 3000°C. Heat treatment of electrically calcined anthracite (ECA) has two effects. One is a "true graphitization" that improves the crystallinity of regions essentially free of mineral constituents; the other is a catalytic graphitization effected by the minerals (or vaporized ash-derived species). The amount of "catalytic graphite" increases with increasing heat treatment temperature. X-ray diffraction, electron microscopy, "real" and helium densities, and optical microscopy studies are all consistent with this.

For aluminum smelters, cathodes made from anthracite treated at higher temperatures have lower ash content, lower with-grain CTE, lower sodium uptake, and higher thermal conductivity. They also have more resistance to electrolytic attack. For silicon smelters, electrodes made from the anthracites having higher heat treatment temperatures have better thermal shock resistance. Fracture toughness tests were inconclusive.

If existing ECA furnaces were operated at higher temperatures and with more uniform temperature distribution internally, the results of this work could possibly be implemented. Of course, a detailed economic assessment of the cost would be essential.

Overall

Overall, these tests show possibilities for anthracite usage in commercial areas where anthracite has not traditionally been used. Additional research on a larger scale is needed in these areas along with economic analysis to determine the feasibility of implementation.

The significance of these tests should not be overlooked as there is the potential of both saving industry money and opening up new markets in the anthracite industry. Both parties are benefited by these findings.

More additional information on these findings can be found in the final project reports in Appendix A:

"Anthracite Coal for Cathode/Electrode Applications in Aluminum/Silicon Smelters"
"Development of Anthracite-Based Carbon Catalysts"
"Novel Anthracite Sorbents for CO_2 Capture"
"Potential Applications for Exfoliated Anthracite: Filler in Cathodes"

Objective 2: To effectively minimize environmental damage caused by mercury emissions, CO_2 emissions, and coal impounds

The testing associated with this objective was generally successful. Many aspects of these experiments have significant results for helping the coal industry to meet environmental regulations. Specifically, it was found that anthracite can be used as a sorbent to capture CO_2 emissions, slurry water is treatable through the use of TiO_2, raw coal refuse can be used as activated carbon, reusable PACs are a distinct possibility, and there are possibilities for the use of activated carbon to capture mercury from coal fired power plants. Each of these results is further explained below.

Sorbents for CO_2 Capture

Anthracites have inherent chemical properties, fine pore structure and relatively low price that makes them excellent raw materials for the production of premium carbon products, such as for the synthesis of CO_2 sorbents. The President's Global Climate Change Initiative commits to reduce greenhouse gas intensity by 18% over the next ten years. However, the costs of current CO_2 separation and capture technologies are estimated to be about 75% of the total cost of ocean or geological sequestration. Furthermore, the demand to develop revolutionary direct capture technologies has also been identified by the U.S. DOE. The use of anthracite in this role has been discussed in Objective 1, above.

Metal Treatment in Slurry Water

Coal slurry impoundments hold the effluents from washing processes that coal producers perform on raw coal once it is brought to the surface. The result is usually a large amount of highly acidic water combined with solid particulate matter, contained by dams. Unfortunately, the containment dams are sometimes designed, causing overflows during storms and leakage. These problems are dangerous and costly. Consequently, research was done to determine the feasibility of remediation of the coal slurry water through various means.

It was found that the use of activated carbon was unsuccessful in removing the metals from the slurry water. Also, pretreatment of the water by exposure to UV radiation proved unsuccessful. However, treatment with TiO_2 photocatalyst, with or without UV exposure, was successful under some experimental conditions. Specifically, the pH of the water was an important factor in metal removal. Increasing the pH from 2 to 6–7 precipitated most of the iron and aluminum from solution. Manganese remained in solution because it is soluble to pH 10. Therefore, an additional treatment step would be needed to remove manganese.

Further research is underway to continue to find a cost-effective way to treat coal slurry water. This work shows promising results in impound remediation. In addition, this research is significant to all coal-fired power plants with coal slurry water impoundments. By finding a method to treat this waste, and possibly market some of it, the coal industry will spend less money cleaning up dangerous impoundment overflows, benefiting both industry and the environment.

Raw Coal Refuse for use as Activated Carbon

In addition to the project explained directly above, raw coal refuse was tested to determine the feasibility of its use for activated carbon production. Raw coal received from impoundment had exceptionally low surface areas, on the order of 1 m^2/g. Steam activation at 840–950°C for 2–3 hours resulted in surface areas of 69–137 m^2/g, well below the values of $\geq$600 m^2/g characteristic of commercial coal-derived activated carbons. Chemical activation, using phosphoric acid or sodium hydroxide, produced carbons with surface areas of 260 and 324 m^2/g, respectively, an improvement but still well below values for commercial carbons.

Use of a proprietary third-party treatment with hydrofluoric acid, followed by steam activation at 850–950°C for 2–5 hours produced carbons with surface areas in the range of 382–850 m^2/g. Interestingly, analogous CO_2 activation experiments failed to develop significant porosity in these carbons. The HF chemical pretreatment costs an estimated $0.01/lb. The raw material normally

used for activated carbon production is ≈$0.04/lb. Since the raw coal refuse is nominally of no cost, or even of negative value, this work suggests that the HF-treated coal could potentially serve as a raw material for activated carbon production.

Reusable PACs for Mercury Capture

Due to the new EPA regulations regarding mercury emissions and the negative effects of mercury on water supplies in the world it has become necessary to find ways to control mercury emissions in a cost effective manner. One possibility that is being explored is the use of PACs; however, the current production capacity for PACs is only 10% of the capacity that is necessary to meet these regulations. Therefore, it is desirable to design a PAC system that can be recycled.

Results from this testing show that a recyclable PAC system is indeed feasible. The thermal desorption process involves heating for 30 minutes at 550^{o} C in inert atmosphere. This system will save operating costs by allowing the same PAC to be used over and over instead of being discarded. In addition, mercury was removed from the PAC during the recycling stage of the process. This mercury can then be purified and sold for other applications. Therefore, this system not only saves in operating costs, but allows a potentially hazardous material to be sold instead of disposed.

This work is important to coal-fired power plants because it allows an economical method of mercury control. Additional testing is needed on a larger level and determine what must be done before this process is marketable.

Activated Carbon for Mercury Capture

For the same reasons explained above, research is being done to determine feasible methods for mercury capture. In this work, it was found that fly ash carbons from coal-fired power plants have the potential to capture mercury if they have mesoporous structure (about 50% mesoporousity on a surface basis or 75% on a volume basis) and oxygen and halogen functional groups. Although the chars used in this work had varying levels of mercury capture, values of 1.85 mg/g were obtained, not far off the value of 2.77 mg/g for a commercial activated carbon. They are a potentially low-cost sorbent and addition testing should be done. If additional testing proves successful, fly ash could be a potential new source of material for mercury capture. This would also benefit coal fired power plants and the economy.

Overall

Overall, these projects show potential for mercury capture, CO_2 emissions treatment, and coal water slurry treatment. These treatments would be beneficial to the environment and to the coal industry. Each of these projects focused on either cost-effective treatments or treatments that could actually save the power plant money.

Additional research is necessary to determine the feasibility of these findings in industry as most of these tests were run on a bench-scale level. For more information on these tests, see the final project reports listed below.

"Novel Anthracite Sorbents for CO_2 Capture"

"Remediation of Coal Impounds: Efficacy of Coal for Activated Carbon"

"Processing and Reuse of Activated Carbon Used to Adsorb Mercury from Power Plant Flue Gases"
"Use of Coal Gasification and Combustion Chars for Mercury Capture"

Objective 3: To continue to increase our understanding of coal properties and establish coal usage in non-fuel industries

The testing done to fulfill this objective was much more varied that the testing done for the previous two objectives. Many different types and forms of coal were tested for use in an equally many new ways. These tests explore many aspects of coal and coal byproducts being used for new applications. Specifically, these tests focused on: development of a synthetic coal tar enamel, the study of alternative binder pitches in aluminum anodes, the use of SECO to fuel a carbon fuel cell, the production of a low-cost coal-derived turbostratic carbon powder for structural applications, development of nanotube-enhanced coal extract pitches, investigation of new fly ash sources for metallurgical carbon, and characterizing coal solvent extraction processes. In addition, research into the benefits of using pitch-derived fibers to reinforce concrete concluded that there were no real benefits associated with the addition of these fibers. These results are discussed in further detail below.

Development of Synthetic Coal Tar Enamel

Coal tar enamel is used as coatings for pipelines and other objects that require protection from environmental conditions. Currently the pitch component of coal tar enamel is obtained from the high-temperature carbonization of coal during the production of metallurgical coke and as such is similar to coal tar binder pitch. Because domestic coke production is predicted to decline there is a need for alternate sourcing.

A synthetic coal tar enamel was prepared using solvent-extracted pitch and a commercial "heavy oil." The pitch was prepared by extracting a West Virginia bituminous coal with tetralin, followed by de-ashing with N-methylpyrrolidone. It was blended with a commercial coal tar distillate called "heavy oil." Most of the properties of the synthetic enamel are within the specifications of commercial products. The synthetic enamel is more volatile than the commercial product, but not so much so that it would not be usable. Penetration values were lower than for commercial enamels, but not out of specification range. The synthetic enamel can serve as an adhesive for carbon foam–steel composites. Cathodic disbonding tests were not as good as for the commercial enamel. On the whole, however, the overall good results show great promise for this synthetic material.

This research provides additional uses for coal-derived heavy oils and partially solves the problem of declining coke production for coal tar enamels. In addition, this research shows the possibility of synthetic coal tar enamel being used in multiple applications, adding to its appeal as a marketable resource.

Binder Pitches in Aluminum Anodes

Traditionally, coal tar binder pitches were obtained from coal tars that come as a byproduct of bituminous coal coking processes. With this supply declining, it was proposed to find alternate binder pitches.

Research in this area concluded that petroleum pitch offers potential to be used as an additive to the standard coal tar pitches for use as binders in aluminum anode production. Three anode butts were also studied in this project. X-ray CT scanning, pore volume, and density measurements showed a decrease in apparent density but increase in absolute density and specific pore volume from the center of the butt to the surface. Experimental laboratory-scale anodes made from the top and bottom of the butt materials gave lower apparent green densities than anodes made from the middle part of the butt. These results correlate with the high porosity of the top and bottom of the butt materials, which inhibited pitch penetration into the pores. Anodes made from a pitch mixture that contained 20% petroleum pitch and 20% gasification pitch (with standard coal tar pitch) gave comparable baked densities to those made using 100% coal tar pitch.

This research provides possibilities for alternate binder pitches to replace a diminishing supply. Additionally, this research finds alternate uses for petroleum pitch, coal-extracted pitch, and gasification pitch.

Use of SECO in Carbon Fuel Cells

Research was focused on producing a low cost coal-derived turbostratic carbon power and testing it in a carbon fuel cell. The carbon fuel cell produces electrical power through the combustion of carbon with oxygen from ambient air. The products are carbon dioxide and electricity. Turbostratic carbon with microscopic domain size of 30nm or smaller and an ash value less than 0.5% is ideal for the carbon feed of the fuel cell. Research was done to determine the feasibility of a low-cost coal-derived feedstock.

The results showed that a significant reduction in the volatile matter to less than 10% was necessary before the created samples were usable. Heat treatment at 800º C was found desirable as carbon that is more conductive was obtained at higher heat treatments. SECO heat-treated at 800º C has a volatile matter content of 4%, carbon content of 89%, ash yield of 0.3%, and resistivity of 29 ohm-cm. After heat treatment, the SECO showed favorable performance in the carbon fuel cell. It was determined that the low ash characteristic (<0.3%) apparent in these SECO samples makes them very attractive for this application. Additional research in this area will further determine the success of using turbostratic carbon power in fuel cells.

Development of Turbostratic Carbon Powder for Structural Purposes

Again, it was determined that development of low cost coal-derived turbostratic carbon powder had potential as a use in structural processes. Carbon foams consisting of oxidized SECO samples and coal tar pitch were made and their properties were assessed. A crush test was conducted on the sample and resulted in a value of 12.3 MPa. The foam had a density of $0.87 g/cm^3$. These results were comparable to other carbon foams produced from a variety of feedstocks.

This research is significant in demonstrating yet another application of coal-derived turbostratic carbon. If this product can be produced at a lower cost than the other foams then substantial savings could be made. An economic analysis to this extent should be performed. In addition, further research should be done to optimize the combination of SECO and coal tar pitch for this application.

Nanotube Enhancement of Coal Extract Pitches

High-performance pitch-based carbons are typically made from mesophase pitch; however, the high processing costs and low yields associated with the production of mesophase pitch makes the pitch expensive to produce. Therefore, research was conducted to determine the feasibility of producing high-value carbon fibers and foams via the co-processing of a low-cost coal extract pitch with well-dispersed carbon nanotubes. The testing results on nanotube-doped materials were mixed. For epoxy-coated pitch and pitch/nanotube composite fibers, in one case addition of nanotubes enhanced tensile strength and had no effect (within experimental error) on elastic modulus. However, for a different fiber, tensile strength decreased. A 2% loading of nanotubes increased the thermal diffusivity by about 30% in the range 25–700°C. At 25°C, for example, thermal diffusivity increased from 1.335 mm^2/s to 1.483 with the nanotubes added. For carbon foams derived from pitches, the effect of nanotube addition on bulk density, porosity, and open-cell volume was strongly dependent on the nature of the original pitch. As an example, the addition of nanotubes to Ashland A-240 pitch increased bulk density of the resulting carbon foam from 0.34 to 0.41 g/cc, but, using a coal-based synthetic pitch, the respective values showed a decrease in bulk density, from 0.42 to 0.34 g/cc. Nanotube addition to pitch seemed to have little effect on the compressive yield strengths of carbon foams. For example, with a foam derived from a synthetic pitch, the compressive yield strength was 2.5 MPa without nanotube addition to the pitch, and 2.7 MPa with addition.

If further research proves successful, then the ability to produce higher value materials with a small addition of nanotubes could result in materials of high commercial and military interest. Some examples may include: structures, thermal management, and electromagnetic shielding. This research shows the potential for exceptional cost savings in this application.

New Fly Ash Sources for Metallurgical Carbon

Carbon with an LOI higher than 80% has the potential to be used in electric arc furnaces (EAF). Carbon added to the EAF makes it more energy efficient, increases its refractory life, and minimizes nitrogen and hydrogen in steel. Fly ash from Reliant Energy's Niles cyclone boiler (CB) is currently being marketed as metallurgical carbon for the above explained use. However, increasing demand of this carbon has initiated research to find other CBs that have fly ash similar to Niles. In all, 36 plants were contacted. Of these 14% make marketable carbon material, 14% make marginal carbon material, 29% have fly ash unsuitable for carbon marketing, 14% currently already market their fly ash, 19% were geographically undesirable, and 10% did not cooperate. These findings show there is a potential for the market of fly ash from CB power plants. This would enable a current waste stream to be recycled into a useful application with the potential for significant cost savings.

Characterization of Coal Solvent Extraction Processes

It was desirable to determine what petrographic, physical, and chemical characteristics of bituminous coals leads to the production of maximum extraction yield in NMP. It was found that coals with mean maximum vitrinite reflectance below 1.0 were difficult to process by filtration because they were colloidal in nature. In addition, those above 1.2 processed well by produced only moderate extraction efficiencies. Those most suitable for NMP extraction exhibited vitrinite reflectance of about 1.10. Yields of extract were nearly 75% in this case. Additional testing showed that low ranking bituminous coals were most affected by NMP in terms of physical

alteration. Finally it was found that the coals most suitable to NMP extraction exhibited Gieseler plasticity of about 30,000 dial divisions per minute, produce free-swelling indexes up to 9, and exhibited Audibert-Arnu dilatation of about 300%. Coals with these characteristic usually fall in the hvA bituminous rank. These findings are significant in understanding NMP extraction processes more fully.

Overall

Overall, these research projects show great potential for alternate uses of coal. There are many applications for coal and coal-derived products made available through this research. Additional research should be done in these areas as they were conducted on a small scale and must be scaled up to determine the full potential. For further information on these projects, refer to the final reports listed below.

"Synthetic Coal Tar Enamel Using Solvent Extraction"
"Binding Efficiency of Coal-Derived Binders Towards Anode Butts"
"Turbostratic Carbon Powder"
"Nanotube Enhancement of Coal Extract Pitches: Fibers and Foams"
"Expanding Supply for Fly Ash Derived Carbons"
"Characterization of Coal Solvent Extraction Processes using Petrographic, Chemical, and Physical Methods"
"Pitch Derived Fiber Reinforced Fly Ash Concrete"

CONCLUSION

Research performed under the direction of the CPCPC (i.e., the 2003 research projects) led to the completion of 14 research projects. These were performed in order to expand the use of coal outside the traditional fuel industry. From these projects significant results were found, which have the possibility to open new markets to the coal industry, develop new methods for helping the coal industry to be more environmentally friendly, and to understand coal properties and characteristics at a new level. Future research in these areas based on this initial research could result in a much more diversified coal industry.

APPENDIX A: *List of Final Reports for 2003 Projects*

POTENTIAL APPLICATION FOR EXFOLIATED ANTHRACITE: FILLER IN CATHODES
Final Report

Start Date: March 1, 2003
End Date: June 30, 2004

Principle Investigator: Dr. Caroline E. Burgess Clifford
Report Issue: July 15, 2004

Internal Agreement No. 2486-TPSU-DOE-0350,
For Award No.: DE-FC26-98FT40350

The Energy Institute
Penn State University
209 Academic Projects Bldg.
University Park PA 16802

DISCLAIMER

ABSTRACT

Anthracite has some unique properties as a carbon, but it also has similar properties to graphite as well. Graphite is known to exfoliate, and exfoliation of graphite improves its electrical properties. Therefore, it was thought that exfoliation of anthracite may improve its electrical properties. Exfoliation of anthracite can be accomplished by intercalating perchloric/nitric acids and exfoliating at temperatures of 700-800°C.

However, three factors inhibit the use of exfoliated anthracite as an electrode material. First, with perchloric acid having such explosive properties, scaling the process up to an industrial scale is not feasible. The second factor is there is no basis for choice of a particular anthracite coal because it is not known which properties make anthracite able to be exfoliated. Finally, the only application that exfoliated anthracite has been tested for is as an activated carbon; we anticipate that exfoliated anthracite would be useful in many applications.

The main goal of the current project was to develop a method for anthracite exfoliation that would be safer than with using perchloric acid. Once a method was established, we expected to apply exfoliation to different anthracite coals, and to test the exfoliated anthracite as electrode material.

Several methods of exfoliation were tested, all methods that are known to be successful on graphite. Details of the methods tested are included in the report. The methods could be classified into three types: graphite oxidation, graphite reduction, and methods that required no oxidation or reduction. Exfoliation using acid intercalation was considered an oxidation method, and exfoliation using alkali metals was considered a reduction method.

We successfully exfoliated coal using oxidative methods, particularly the perchloric/nitric acid method in order to determine coals amenable to exfoliation. We successfully exfoliated Summit and Hongay coals using this method, both semi-anthracites. Several coals were obtained from FB Leopold; however, no more coals were tested using this method because of the explosive nature of perchloric acid.

Marginal success was obtained in exfoliating Summit coal using two methods: intercalation using sulfuric/nitric acids with exfoliation at 700-800°C and intercalation by electrochemical oxidation and sulfuric acid with exfoliation at 700-800°C. More data was needed to determine the extent of exfoliation (surface area characterization), but data was not obtained by publication date of this report. Information from the surface area data would be useful in determining the best conditions for anthracite exfoliation.

Graphite reduction exfoliation methods were tested, but were not successful. We were not successful exfoliating anthracite using alkali metals. While it is possible modification of these methods could induce exfoliation, we did not have time to explore further.

Materials were sent to Carbone to make test electrodes, but data was not available by the publication date of this report. Therefore, we could not determine if exfoliated anthracite would make a good electrode material.

TABLE OF CONTENTS:

INTRODUCTION

Anthracite is an abundant and inexpensive natural resource that has not been fully exploited as a useful material. Historically, anthracite coal has been used as a slow-burning, high heating value fuel. It had a use for domestic heating and cooking, as well as industrial applications in iron smelting.[1] Production peaked at 100 million tons per year in 1917 and 1918[2], but now appears to have stabilized at about 3.2 million tons in 1999.[3] More recently, it has found a market as a water filter medium, but only anthracite obtained as-mined is used because of the difficulty (and expense) in grinding.

Anthracite is an intriguing feedstock for premium carbon materials. Most anthracites contain 92–98% carbon, virtually all of which is present as aromatic carbon in large polycyclic sheets.[4] These sheets may contain thirty or more fused aromatic rings,[5,6] resulting in extraordinary properties such as highly ordered carbon that also exhibits a high ultra-microporosity pore volume. Exploiting one or more of these properties of anthracite to produce value-added products offers the potential for developing new markets for this resource.

Typically, anthracites have been most important in amorphous based cathodes, as these cathodes have a moderate thermal conductivity and electrical conductivity, while having high abrasion resistance and crushing strength.[7] Amorphous cathodes can also be made of mixtures of anthracites and graphite, which seems to improve on the properties of anthracite alone. Semi-graphitic carbon blocks have been accepted as replacements for anthracite blocks because they have some improved properties similar to graphitized blocks but are not as costly. If there were a way to increase the thermal conductivity and reduce the electrical conductivity of anthracite without increasing the cost significantly, the material would indeed be desirable to the aluminum and steel industries.[7]

Recently, we have been exploring the exfoliation of anthracite[8-11], a method to cause "flaking" or "breaking apart" of the anthracite, in order to react or structurally reform the original material. We anticipate that by either breaking apart or even opening up the pore structure of the anthracite, that with application of heat, the structure can become more ordered and hence improve the electrical properties while hopefully maintaining the strength of the material compared to graphites. Research has shown that exfoliated graphite had improved electrical properties compared to the original graphite.[12] Anthracites and carbons have been shown to intercalate several compounds. As mentioned, anthracite is an intriguing carbon because structurally, it is not quite a graphite, a crystalline carbon, or an amorphous carbon; and, at the same time, it is an extremely hard, yet microporous material. Intercalation may be restricted in some anthracite coals due to the geometry in the coal.

The key to being able to exfoliate a material is to intercalate ions/compounds/elements that, when rapidly thermally shocked or reacted, will expand inside the structure rather than vaporize out. Intercalation is different from physical adsorption. For physical adsorption, the compound goes into the pores and may have some interaction with the pore surface, but does not become a part of the structure. To accomplish intercalation, two factors must be considered. The first factor is the coal structure must be amenable to intercalating a compound, which means the structure must allow access to the intercalate.[13] The second factor is the intercalating compound/element must be small enough to fit into the structure, but also interact with the structure so it will not vaporize out upon activation. The intercalate must be able to overcome the intermolecular forces between the planes of graphitic carbon planes.[14] The binding energy between carbon layers is estimated to be 1.5 kcal/mol, so this energy must be overcome for a

compound to intercalate into carbon.[14] Bartlett and McQuillan[14] suggest mainly two types of intercalation that take place in graphite: intercalation with graphite reduction and intercalation with graphite oxidation. For graphite oxidation, mineral acids have been the intercalate of choice, and for graphite reduction, metal alkalis have been the most studied.

Carbons and anthracites have been shown to intercalate alkalis such as sodium, lithium, and potassium when using organic solvent,[13,15-17] so there is evidence of intercalation by carbon reduction. Carbons and anthracites can also be intercalated by carbon oxidation, using acids such as perchloric and sulfuric acids, but only when used in combination with nitric acid (i.e., chemical oxidation).[8-11,14,18] Anodic electrochemical oxidation can also be used to intercalate acid salts, such as HSO_4^-.[14,18-22] For anthracite in particular, perchloric/nitric acid mixtures have been intercalated into the anthracite; the resulting intercalated carbons were thermally shocked in order to exfoliate it for use as a precursor for activated carbons.[8-11]

The following is the final report for the work done over the year of funding for CPCPC. The main goal was to develop a method for anthracite exfoliation, and with success and if time permitted, determine the best exfoliating coals and the use of exfoliated anthracite as an electrode material. Several methods were employed to attempt intercalation/exfoliation of acids and alkalis, and all methods will be described in detail. All samples were screened using SEM to detect if exfoliation occurred. We expected to have BET surface area characterization done on those samples that were thought to have exfoliated, but we were not able to acquire this data before publication of this report. While it was anticipated that several coals would be tested, only a few were tested, with focus mainly on Summit coal. The following discussion details the methods that accomplished exfoliation and the implications for future work.

EXPERIMENTAL

Choice of Coals

Several coals have been chosen to test in this application. Initial experiments were conducted on Hongay, Summit, and Jeddo coals, with most of the success occurring on Summit coal. FB Leopold provided some additional samples. Proximate analysis information is provided in Table 1. Summit and Jeddo coals were tested in previous work,[23] and Hongay analysis comes from the literature.[8-11] FB Leopold obtained proximate analyses on their coals. These coals are of both anthracite and semi-anthracite rank. It is expected that semi-anthracite coals may exfoliate better, as some anthracite coals may be structurally unable to intercalate alkali metals or acids.

Intercalation and Exfoliation Using Acids

In the literature, only one method of exfoliation has been shown to exfoliate coals.[8-11] This involves the use of a 50/50 mixture of perchloric acid and nitric acid. Previous work was done using this method. Table 2 summarizes the various materials and methods of intercalation and exfoliation using acids.

Perchloric/Nitric Acid Methods

Method 1

Previous work in our lab has been done to attempt exfoliation. We attempted exfoliation using two anthracites. Two -20 mesh samples of Pennsylvania anthracites, one from the Mammoth vein of the Eastern middle seam (Jeddo) and the other unprocessed anthracite from

the Tracey vein (Summit), were chosen for exfoliation in this experiment. Each anthracite sample was dried at 105°C under vacuum for one hour to remove moisture from the sample before exposure to the acid treatment.

The coals were intercalated according to the following procedure. To introduce intercalate compounds into the pore structures, the anthracites were treated with varying mixtures of Sigma Aldrich fuming nitric acid and 70% perchloric acid. Each sample of anthracite was placed in excess acid on the order of 10 ml of the acid mixture per gram of sample; perchloric acid concentrations varying from 25 to 75 volume percent, nitric acid making up the rest of the acid mixture.[8]

Each acid mixture was preheated to 120°C before the addition of the anthracite sample. During the acid treatment, the temperature of the mixture was raised 10°C each hour and allowed to stabilize until the mixture reached a maximum temperature of 150°C; once the treatment reached the temperature maximum, it was held there for one hour.[8] After the acid treatment, each sample was filtered and dried under vacuum. The dried samples were placed in a tube furnace under an argon atmosphere and subjected to heat treatment (slow heat-up) on the order of 700 and 800°C for three hours at the peak temperature.

As will be reported in the results section, this method of intercalation and exfoliation did not appear to exfoliate the coals, so acid intercalation and exfoliation was attempted using slightly different conditions, on Hongay semi-anthracite and Summit semi-anthracite.

Method 2

Again, Hongay coal was heated in acid as discussed previously. On the first attempt, only 0.5 g was recovered from the addition of 5 g of coal. The intercalated sample was dried, then later mixed with water to form a paste and heated to 700°C, using a fast heating rate, in a volatile matter furnace, exposed to the atmosphere.

On a second attempt to intercalate Hongay semi-anthracite, an explosion occurred and most of the sample was lost. It also resulted in injury (second degree burns and cuts), so it was decided to modify the procedure to just mix the coal with acids without heating. More than one method of intercalation was used in the literature, one with heat and the other without heat.[8-11]

Method 3

Hongay coal and Summit coal were mixed with 50/50 mixtures of perchloric/nitric acids for 2 hours at room temperature.[8-11] The mixture was filtered and the resulting paste was loaded into crucibles. Crucibles were heated to 700°C in a volatile matter furnace. For the Summit coal, exfoliation was achieved, but for the Hongay coal, sample spontaneously combusted and most of the sample was lost. If this method is attempted in the future, we will heat in a furnace in an inert atmosphere. However, we are still exploring other methods of intercalation and exfoliation to reduce the safety hazards associated with the explosive nature of perchloric acid, using other acid treatments.

Sulfuric Acid Procedure

Method 1

Graphite is commonly exfoliated by intercalating a mixture of sulfuric and nitric acids and thermally shocking the resulting material to 700-800°C for ~1-2 minutes.[12,17] We first tested this method on graphite to determine if indeed exfoliation occurred with this method. Approximately 5 g of Summit coal was mixed with 41 mL of a 3/1 ratio of sulfuric acid and

nitric acids for two hours. The mixture was filtered and rinsed with a small amount of water. The resulting material was loaded into crucibles and heated to 700°C. One portion of the sample was heated 45 seconds, and another portion was heated to 700°C for 2 minutes.

Method 2

While the previous method is known to intercalate and exfoliate graphite, several researchers have explored the use of introducing the acid intercalate electrochemically.[14,18-22] Exfoliation occurred in graphites using acids other than sulfuric acid.[18,20] Adding the acid electrochemically provides a driving force to introduce the acid between the layers of the graphite similar to using nitric acid.[14] Doing this electrochemically may either reduce the contact time of the acid, allowing the use of an acid that is weaker and less environmentally hazardous than sulfuric acid, or provide a method to introduce intercalate into carbons that may be more resistant to intercalation.

Figure 1 is a schematic of the method to intercalate anthracite. Coal was added to a polypropylene bag (5 μm pore size), with a stainless steel metal piece (2" x 0.5") inserted into the middle of it (anode). The cathode was another piece of stainless of the same size. The electrolyte in this case was sulfuric acid (98 %). A power supply was connected using 9.6 V, with a resulting current of 0.05 A and a power consumption of 2.2 Ah/kg. The voltage was applied for ~2 h. Vigorous bubbling took place, with the stainless steel electrode turning grey. The voltage was then turned off, the bag with sample removed and dipped into water to remove excess acid. The sample was then loaded into a crucible and heated to 800°C for 50 seconds in a volatile matter furnace.

Intercalation and Exfoliation Using Alkali Metals

Previous reports have shown that lithium will intercalate into crystal structures by soaking the substrate in a solution of *n*-butyllithium and hexanes.[24] *n*-Butyllithium is a strong reducing agent.[25] The Li^+ ion is then a good oxidizing agent and upon intercalation reduction takes place (Eq. 1). Once the lithium is intercalated into the substrate, the substrate is reacted with water to cause exfoliation. The extremely exothermic reaction of lithium and water causes small "explosions" within the substrate, which increases the porosity of the substance (Eq. 2).

$$\text{Sub} + n\text{-BuLi} \rightarrow \text{Sub}^- + \text{Bu}\cdot + \text{Li}^+ \rightarrow \text{LiSub} + \text{octane} \qquad \text{Eq. 1}$$

$$\text{LiSub} + H_2O \rightarrow \text{Sub(exfoliated)} + \text{LiOH} + 1/2H_2 \qquad \text{Eq. 2}$$

Method 1

Preliminary tests were conducted by mixing 1.6 M *n*-butyllithium (in hexane) with Hongay anthracite coal (under inert atmosphere). This was done using a beaker and stir bar within a glove box with an argon atmosphere. The first reaction was done for ~1 h, at which time the solvent hexane evaporated completely. One gram of coal was used with ~7.8 mL of 1.6 M of *n*-butyllithium. After mixing, the sample was reacted in water, using ultrasonication in order to improve the coal/water interaction. Reaction 2 was similar, except ~17 mL of 1.6 M *n*-butyllithium was added and mixing continued for 2 hours. Little activity occurred under these conditions, so the following was implemented to allow for much longer reactions times.

All glassware was dried in an oven overnight prior to the reaction at a temperature above 110°C. The lithium intercalation reaction was done using a two-neck round bottom flask and condenser with a steady stream of nitrogen flowing in through the round bottom and out through the top of the condenser. One neck of the round bottom was connected to the condenser and the other had a septum attached with a needle for the nitrogen flow and also to inject the *n*-butyllithium. The nitrogen output then went through a nitrogen bubbler to maintain an inert atmosphere within the reaction vessel (Figure 2).

The dried glassware was assembled under an inert atmosphere. One gram of the anthracite was added to the round bottom and then the reaction vessel was sealed for the remainder of the reaction. *n*-Butyllithium (10 mL) was then added using the Sure/Seal technique to avoid exposure to air. The reaction was then stirred with water flowing through the condenser to minimize hexane evaporation, for up to 5 days.[24,25] More *n*-butyllithium or hexane can be added if evaporation occurred.

After intercalation, the round bottom was removed from the condenser, but with nitrogen still flowing through the side-arm while the flask was stoppered. In a glove box, the sample was washed with hexane to remove any excess lithium present in solution. Standard gravity filtration was used.

The "intercalated anthracite" was then placed in water. At this point, hydrogen gas forms. Several reports mention the use of sonication to promote lithium intercalation and then lithium reaction with water.[25,26] Therefore, sonication was used to promote the interaction of the water with the intercalated alkali. The anthracite can be dried on a high vacuum line or the house vacuum in a dessicator and then analyzed. Additionally, it was hoped that increasing the reaction temperature would increase the interaction.[27] Because a condenser was used, loss of solvent was not a problem and temperature was added to the reaction.

Method 2

We tried a second method of lithium intercalation, to see what differences would take place.[28] This method uses lithium borohydride ($LiBH_4$), which has similar chemical properties to *n*-butyllthium.[28] The reaction for intercalation (Eq. 3) and exfoliation (Eq. 4) are similar to those using *n*-butyllithium.

$$LiBH_4 + Sub \rightarrow LiSub + 1/2B_2H_2 + 1/2H_2 \qquad \text{Eq. 3}$$

$$LiSub + H_2O \rightarrow Sub + LiOH + 1/2H_2 \qquad \text{Eq. 4}$$

This reaction was first tried using solvated $LiBH_4$ and $NaBH_4$. $LiBH_4$ (2.0 M in THF) and $NaBH_4$ are available and a procedure similar to the procedure used with *n*-butyllithium was followed to intercalate lithium and then exfoliate the anthracite. The reaction temperature would have to remain below 50°C for safety and evaporation reasons. Additionally, KBH_4 is also very a good reducing agent (better than $LiBH_4$); however, it is significantly less stable in air and recommended use would be only with dilute solutions (preferably used in the glove box). The literature suggests that strong reducing agents and larger atomic radii will increase exfoliation, so $NaBH_4$ and KBH_4 may work better than lithium.[25,29]

Several reactions were done with these two lithium intercalation procedures, using a condenser and reacting the sample for 4 days with a lithium or sodium compound dissolved in a solvent, followed by reaction in water. Table 3 summarizes the different conditions tested used

on the Hongay anthracite. Each sample was intercalated with the alkali metal, then reacted in water before doing any analytical tests on the material.

Other potential methods of alkali intercalation/exfoliation have been described in the literature.[14,30-34] Most of these methods involve the heating of the alkali metal to a liquid or vaporization temperature. As Na and K are much more reactive in moisture and air, it would be necessary to do experiments in a glove box. Therefore, we decided to postpone further investigation, as having to keep everything in an inert atmosphere would add expense to a process.

Method 3

A method was tried that was based on a method to introduce function groups to exfoliated graphite.[35-37] Exfoliated graphites have been chemically modified by reaction with quinones, with the added quinone functionality improving on the electrical properties of the exfoliated graphite.[35-37]

Other Methods of Exfoliation

Supercritical CO_2 Intercalation/Exfoliation

Supercritical CO_2 intercalation/exfoliation of graphite has been shown in the patent literature; however, details of the method are sketchy at best.[38,39] We developed our own method based on the patent literature and conditions for supercritical CO_2 extraction.[38-41] A horizontal tubing reactor was loaded with 7 g of Summit anthracite coal, and filled to 1500 psi of CO_2 cold. The reactor was heated using heat tape. The sample was heated to 120°C, with a pressure of 4000 psi, and held under those conditions for 15 minutes. While the reactor was still hot, the pressure was released to cause destructive depressurization.

Liquid N_2 Intercalation/Exfoliation

Bartlett and McQuillan suggest that intercalation can take place without apparent oxidation or reduction of the substrate, noting that noble gas fluorides can intercalate into graphite.[14] We tried one method of intercalation using very cold liquid N_2 and thermal shocking using boiling water, as this method could be a way to see how thermal shocking might affect the anthracite. The –20 mesh Summit sample (5 g) was placed in a wire mesh bag (-200 mesh) in order to access the cooling and heating mediums as quickly as possible. The filled bag was dipped into liquid N_2 for several minutes. The sample was then removed and immediately placed into boiling water. The resulting material was then dried for further evaluation.

Characterization of Samples

Scanning electron microscopy (SEM) has been used to characterize the coals before and after reaction. SEM is a useful qualitative method to detect exfoliation and was the method used to screen reacted materials to test for exfoliation.[8-11] SEM was done on two different instruments: one instrument a Philips XL20 with a filament gun, the magnification range for the instrument 20 to 50000X, and the other a Hitachi S-3500N with a similar magnification range.

We expected to determine the BET surface area using a Quantchrome Autosorb 1 instrument, using 5 data points to determine the surface area value. This technique was only to be used on samples that we identified from SEM as materials that may have exfoliated. However, the instrument was still under repair at the time of publication of this report.

RESULTS AND DISCUSSION

Results of Acid Intercalation and Exfoliation

Results Perchloric/Nitric Acid Procedure

Method 1

Figure 3 shows the SEM micrographs of untreated Jeddo anthracite, and Jeddo after acid treatment with 50:50 nitric/perchloric acid followed by heat treatment at 700°C. The heat treatment does not appear to have had much effect on the surface of the coal, but the acid treatment followed by heating at 700°C appears to have affected the surface of the coal significantly. Figure 4 shows the SEM micrographs of untreated Summit anthracite, Summit after heat treatment at 700°C, and Summit after acid treatment with 50:50 nitric/perchloric acid followed by heat treatment at 800°C. Acid treatments (followed by heating at 700°C and 800°C) appear to have had significant effect on the anthracite surface as well as possibly affecting the porosity. The treated anthracites appear to be both flaking and expanding, similarly to what would be expected for natural graphite exfoliation. However, it appears that most of the reaction occurred on the surface, so exfoliation does not appear to have been achieved. It was decided to use a faster heating method to achieve exfoliation.

Method 2

Figure 5 shows the SEM micrographs of untreated Hongay coal and the slightly exfoliated Hongay coal. While it appears slight exfoliation occurred, as will be seen later, this procedure did not fully exfoliate the coal. It is thought that drying the coal prior to the heating step could have prevented exfoliation.

Method 3

Figure 6 shows SEM micrographs of untreated Summit coal and the exfoliated Summit coal. Exfoliation appears to have taken place. As mentioned in the previous section, Hongay coal spontaneously combusted during heating and could not be analyzed effectively. For samples that appear to exfoliate, we will collect surface area data to determine the change in surface area of the whole sample. Surface area data will be used to determine extent of exfoliation and be a more definitive method to determine the best exfoliation method. However, the instrument is in the process of being repaired and data will not be able to be collected before submission of this report.

Results from Sulfuric Acid Intercalation and Exfoliation

Method 1

Figure 7 shows SEM micrographs of Summit coal after treatment with acid/heating (a) 700°C for 45 seconds and (b) 700°C for 2 minutes (the SEM photo of untreated Summit is in Figure 6). For both sets of samples, there are definitely smaller particles and the surface of the material appears to have changed. More changes seemed to occur with the 2 minute heating of the acid intercalated coal at 700 °C. There does seem to be some flaking of the coal particles as well, an indication that exfoliation may have occurred. A control experiment was performed on graphite, raw graphite in Figure 7(c) and exfoliated graphite in Figure 7(d). However, because of

the orientation of the exfoliated anthracite particle, it is difficult to detect expansion that looks exactly like the exfoliated graphite particle. There is also the possibility that some of the smaller particles could be silica based, and future experiments using energy dispersive X-ray spectroscopy (EDS) will confirm if there is a significant amount of silica on the sample. It is possible that the acid etched some of the silica from the glass beaker used for stirring the sample. More will be explained in the alkali intercalation/exfoliation section, as silica may also have contaminated the sample. For samples that appear to exfoliate, we will collect surface area data to determine the change in surface area of the whole sample. Surface area data will be used to determine extent of exfoliation and be a more definitive method to determine the best exfoliation method. However, the instrument is in the process of being repaired and data will not be able to be collected before submission of this report.

Method 2

Figure 8 shows SEM micrographs of Summit coal after treatment with electrochemical acid intercalation (a) before heat treatment and (b) after heat treatment at 800°C for 50 seconds. It appears that some expansion may have occurred before heating the sample. Exfoliation appears to have taken place after heating. For samples that appear to exfoliate, we will collect surface area data to determine the change in surface area of the whole sample. Surface area data will be used to determine extent of exfoliation and be a more definitive method to determine the best exfoliation method. However, the instrument is in the process of being repaired and data will not be able to be collected before submission of this report.

Results of Alkali Intercalation

SEM micrographs were taken of the anthracite that was reacted. SEM has been shown to be a useful method to detect exfoliation.[8-11] This was the method used to detect any obvious visual changes. Figure 9 shows the SEM micrographs for reactions BG 1-7 (methods 1-3 for exfoliation). In all cases, the main visual change seemed to be to the surface of the anthracite. There appeared to be striations on the surface, probably due to the reaction of lithium with water, forming a strong base that may have etched the anthracite surface. In a few reactions, particularly BG 2, there appeared to be "fuzzy" particles on the surface, clumps of "puffy" particles, and some porous areas on some of the particles. Initially, we thought we had achieved some sort of exfoliation, but preliminary elemental examination by SEM and EDS indicated the "fuzzy" and "puffy" particles might be silica based. For BG-4 (reacted with method 3), the main feature seems to be cracks in the coal. However, exfoliation did not take place.

In the future, we will continue to analyze to see if BG-2 does indeed contain silica based particles and determine the source of the silica. Coals can contain silica based mineral matter; when enough coal is available, we will test the mineral matter content of Hongay coal. Another source of silica could be the reaction vessels, which were glass. In this case, we would use a different type of reaction vessel, either alumina or Nalgene based, as these materials are not affected by strong acid or base. At this point, we also want to know if lithium is being intercalated under the conditions used. This can be determined by XRD.[30,31] Alkali intercalation of anthracite can be achieved under certain conditions.[30-34] Carbon exfoliation has been achieved by potassium intercalation and exfoliation.[32] However, potassium is the most reactive of the alkali metals, and could also be a source of explosion if not carefully handled. Time was also limited, therefore, we could not complete testing other methods of alkali exfoliation. For samples that appear to exfoliate, we will collect surface area data to determine the change in surface area

of the whole sample. Surface area data will be used to determine extent of exfoliation and be a more definitive method to determine the best exfoliation method. However, the instrument is in the process of being repaired and data will not be able to be collected before submission of this report.

Results of Other Methods of Intercalation/Exfoliation

Other methods of Intercalation/Exfoliation were done on coal. As discussed in the introduction, several criteria must be met in order to intercalate and exfoliate a substance. The intercalate must be small enough to go into the pores of the substrate, as well has some kind of driving force to overcome the energy between the layers of carbon sheets.[14] It has been reported recently that graphite can be intercalated using supercritical CO_2 and exfoliated by explosive/destructive depressurization.[38,39] However, this has been reported in patents, which contain little detail on how to accomplish intercalation/exfoliation. We also thought to try using liquid nitrogen as the intercalate, then using a thermal shock with boiling water to cause exfoliation. We continue to have ideas, but will not have time to complete additional ideas during the time of the project.

CO_2 Intercalation/Exfoliation

Figure 10 shows SEM micrographs of Summit treated with supercritical CO_2 destructive depressurization, with (a) at 20 μm, and (b) at 50 μm. Some particles appear to have some surface changes, but many of the particles remain unchanged. While there appear to be changes, it does not appear that exfoliation has taken place. However, the CO_2 intercalation at 120°C and 4000 psi was only done for 15 minutes, and actual diffusion of CO_2 into an anthracite particle may need to take place for a significantly longer period of time. Because there are surface changes on some of the particles, exfoliation may occur if the CO_2 is allowed to diffuse into the particle.

Liquid Nitrogen Intercalation/Thermal Shock

Figure 11 shows SEM micrographs of Summit treated with liquid N_2/thermal shocking (a) at 200 μm and (b) at 20 μm. It does not appear that any type of particle expansion took place, although the process may have fragmented the coal to some extent. This was expected, as nitrogen does not have the ability to oxidize or reduce chemically. It also indicates that some chemical interaction does need to take place in order to cause exfoliation.

Testing of Materials as Electrodes

Three raw coals were sent to Carbone to make test electrodes, but data from those electrodes will not be available before the final report must be submitted. While it does appear that exfoliation was successful with Summit coal, not enough material was generated to date in order to make a test electrode.

CONCLUSIONS

Research has shown that exfoliated graphite improves upon the electrical properties of graphite before pretreatment.[12] It was hypothesized that if anthracite coal could be exfoliated, the electrical properties could be improved.

Graphite can be exfoliated using several methods: (1) perchloric/nitric acid intercalation followed by exfoliation at 700°C for ~2 minutes, (2) bromine intercalation/reversible exfoliation,

(3) supercritical CO_2 destructive depressurization, (4) alkali intercalation followed exfoliation in water or ethanol, and (5) intercalation with sulfuric/nitric acids or by electrochemical oxidation of sulfuric acid and exfoliating at 700-1000°C for a few seconds to a couple of minutes. Several methods of exfoliation were tested on anthracite. One method was completely successful: perchloric/nitric acid intercalation followed by exfoliation at 700°C for ~2 minutes. Literature reports this to be a successful method,[8-11] however, due to safety concerns, the goal of the project was to determine other successful methods of exfoliation that would be useful in an industrial setting. Marginal success was achieved with (5), intercalation with sulfuric/nitric acids or by electrochemical oxidation of sulfuric acid and exfoliating at 700-1000°C for a few seconds to a couple of minutes. Some particles appeared to have exfoliated, but some particles did not exfoliate and there may have been some contamination by silica from the beaker used. Conclusive evidence of extent of exfoliation and of silica contamination could not be confirmed by the time the report had to be completed. To determine the best conditions for full exfoliation of anthracite, these issues must be solved.

Alkali intercalation/exfoliation was not achieved on anthracite using the Li/Na metal methods. It is expected that alkali intercalation can be achieved by other methods. Older methods for alkali metal intercalation use the pure metal (preferably as powders or fine particles) in conjunction with solvents such as THF and DMSO.[32,33] This method is particularly dangerous because the solvent must be dried thoroughly either through distillation or using a solvent system that is closed off to air. Exposure to traces of water should be absolutely avoided for Li, Na and K metals.

While electrode fabrication and testing of raw anthracites is currently underway, completion will not be achieved by the time the report will be submitted. It was also difficult to obtain enough exfoliated material for fabrication an electrode (1 kg needed for electrode), therefore this task was unable to be completed.

REFERENCES

1. Wallace, A.F.C., *St. Clair: A Nineteenth Century Town's Experience with a Disaster Prone Industry.* Alfred Knopf, New York, 1987.
2. Hower, J., Levine, J., Skehan, J., Danial, E., Lewis, S., Davis, A., Gray, R., Altaner,. S., *Org. Geochem.* **70** (1993) 519.
3. *Keystone Coal Industry Manual.* Intertec Publishing, Chicago, 2001.
4. Pappano, P.J., Mathews, J.P., Schobert, H.H., *Preprints, Amer. Chem. Soc. Div. Fuel Chem.* **44** (1999) 567.
5. Gerstein, B.C., Murphy, P.D., Ryan, L.M., In: *Coal Structure.* Academic Press, New York, 1982, Chapter 4.
6. van Krevelen, D.W., *Coal: Typology–Chemistry–Physics–Constitution.* Elsevier, Amsterdam, 1981.
7. Sørlie, M. and Øye, H.A., *Cathodes in aluminum electrolysis,* Aluminum-Verlag GmbH: Dusseldorf, 1994, pp. 1-20.
8. Pettijean, D., Klatt, M., Furdin, G., and Hérold, A., *Carbon*, 1994, **32** (3), 461.
9. Albiniak, A., Furdin, G., Begin, D., Mareche, J.F., Kaczmarczyk, J., and Broniek, E., *Carbon*, 1996, **34** (11),1329.
10. Furdin, G., *Fuel*, 1998, **77** (6) 479.
11. Daulan, C, Lyubchik, S.B., Rouzaud, J-N., and Béguin, F., *Fuel*, 1998, **77** (6), 495.

12. Chung, D.D.L., *J. Mat. Sci,* 1987, **22** (12), 4190 and reference therein.
13. Inagaki, M., *Solid State Ionics*, 1996, **86-88**, 833-839.
14. Bartlett, N., McQuillan, B.W., "Graphite Chemistry," in *Intercalation Chemistry*, Ed. M. Stanley Whittingham and Allan J. Jacobson, Academic Press:London, 1982, pp. 19-53.
15. Inagaki, M. and Tanaike, O, *Carbon,* 2001, **39**, 1083-1090.
16. Narita, N., Nagai, S., and Shugo, S., *Phys. Rev. B.,* 2001, **64**, 245408.
17. McKay, S.F., *J. Appl. Phys.,* 1964, **35**, 1992-1993.
18. Toyoda, M., Katoh, H., and Inagaki, M., *Carbon*, 2001, **39**, 2231-2237.
19. Ubbelode, A.R., *Proc. R. Soc. London, Ser. A,* 1969, **309**, 297.
20. Ubbelode, A.R., *Proc. R. Soc. London, Ser. A,* 1971, **321**, 445.
21. Toyoda, M., Sedlacik, J., Inagaki, M., *Synthetic Metals,* 2002, **130**, 39-43.
22. Kang, F., Zheng, Y-P., Wang, H-N., Nishi, Y, Inagaki, M., *Carbon*, 2002, **40**, 1575-1581.
23. Pappano, P.J., *M.S. Thesis.* The Pennsylvania State University, University Park, PA, 2001.
24. Murphy, D.W., Di Salvo, F.J., Hull, G.W., and Waszczak, J.V., *Inorg. Chem.,* 1976, **15** (1),17.
25. Heising, J.; Kanatzidis, M. G. *J. Am. Chem. Soc.,* 1999, **121,** 11720-11732.
26. Miremadi, B. K.; Morrison, S. R. *J. Appl. Phys,* 1988, **63**, 4970-4974.
27. Yang, D.; Frindt, R. F. *J. Phys. Chem. Solid,* 1996, **57**, 1113-1116.
28. Tsai, H. L.; Heising, J.; Schindler, J. L.; Kannewurf, C. R.; Kanatzidis, M. G. *Chem. Mater,* 1997, **9**, 879-882.
29. Hérold, C; Marêché, J. F.; Lagrange, P. *Carbon*, 1996, **34**, 517-521.
30. Berger, D., Carton, B., Metrot, A., and Herold, A. in *"Chemistry and Physics of Carbon,"* 1975, **Vol**. **12**, Ed. P.L. Walker and P.A. Thrower, pp. 1-37.
31. Anderson, S.H., and Chung, D.D.L., *Carbon*, 1984, **22** (3), 253-263.
32. Viculis, L.M., Mack, J.J., and Kaner, R.B., *Science*, 2003, **299** (5611), 1361-1361.
33. (a) Vadla, J.J., Quandt, H.C., Rich, D.J., Metall., 1980, **34** (12) 1102-1105. (b) Diez, M-A., Marsh, H., Light Metals, 2001, 739-746, (c) Marsh, H., Murdie, N., Edwards, I.A.S. and Boehm, H.P., "Interactions of Carbons, Cokes, and Graphites with Potassium and Sodium," in Chemistry and Physics of Carbon, 1987, **Vol. 20**.
34. Dresselhaus, M. S.; Dresselhaus, G. *Adv. Phys.,* 1981, **30**, 139.
35. Agarwal, R.K., Noh, J.S., and Schwarz, J.A. *Carbon* (1987), **25**, 219.
36. Ramesh, P. and Sampath, S., *Chem. Commun.* (1999), 2221.
37. Ramesh, P. and Sampath, S., *Analyst* (2001), **126**, 1872.
38. Manke, C.W., Gulari, E, Mielewski, D.F., Lee, E.C., U.S. Patent No. 6,469,073, Oct. 22, 2002.
39. Kaschak, D.M., Reynolds III, R.A., Krassowski, D.W., Ford, B.M., U.S. Patent Application, No. 20040033189, Feb. 19, 2004.
40. Li, w., Lazar, I.M., Wan, Y.J., Butala, S.J., Shen, Y., Malik, A., Lee, M.L., *Energy Fuels,* 1997, **11**, 945-950.
41. Williams, D.F., *Chem. Engr. Sci.,* 1981, **36** (11), 1769-1788.

TABLES AND FIGURES

Table 1. Characteristics of Jeddo and Summit Anthracite

Anthracites	Rank	Moisture (wt %)	Ash (wt %)	Volatiles (wt %)	Fixed Carbon (wt %)
Hongay[a]	Semi-anthracite	3.0	2.7	5.6	91.7
Jeddo[b]	Anthracite	4.7	8.1	6.1	85.9
Summit[b]	Semi-anthracite	2.6	17.6	11.1	71.2
AFM-700[c]	Anthracite	4.6	12.22	5.77	82.0
AFM-1400[c]	Anthracite	3.8	14.9	6.7	78.4
AFM-2300[c]	Anthracite	3.6	19.6	5.9	74.5

a Data obtained from literature references 8-11.
b Data obtained from literature references 4 and 23.
c Coals and data obtained from FB Leopold

Table 2: Summary of reaction conditions for acid intercalation exfoliation.

Sample ID	Material Intercalated	Acid Mixture (volume/volume)	Intercal[a] Time (h)	Temp (°C)	Exfoliation Time	Exfoliation Condition (°C)
HT1	Jeddo coal	50/50 Nitric/Perchloric	1	150	3 hours (slow)	700/800
HT2	Summit coal	50/50 Nitric/Perchloric	1	150	3 hours (slow)	700/800
HT3	Jeddo coal	25/75 Nitric/Perchloric	1	150	3 hours (slow)	700/800
HT4	Summit coal	25/75 Nitric/Perchloric	1	150	3 hours (slow)	700/800
HT5	Summit coal	75/25 Nitric/Perchloric	1	150	3 hours (slow)	700/800
ABCB 1	Hongay coal	50/50 Nitric/Perchloric	1	150	1-2 minutes	700
ABCB 2	Hongay coal	50/50 Nitric/Perchloric	1	150	1-2 minutes	700
ABCB 3	Hongay coal	50/50 Nitric/Perchloric	2	25	1-2 minutes	700
ABCB 4	Summit coal	50/50 Nitric/Perchloric	2	25	1-2 minutes	700
SUM 1	Summit coal	75/25 Sulfuric/Nitric	2	25	45 seconds	700
SUM 2	Summit coal	75/25 Sulfuric/Nitric	2	25	2 minutes	700
SUM 4, 6	Summit coal	75/25 Sulfuric/Electro[b]	2	25	50 seconds	800

a – intercalation

b – electrochemical oxidation instead of using nitric acid

Table 3: Reaction conditions for alkali intercalation; for each reaction, the alkali was intercalated and then sonicated in water for several hours.

Sample ID	Method No.	Reaction Time	Alkali Substrate	Solvent	Type of Mixing	Temperature (°C)
BG-1	1	4 days	*n*-butyllithium	Hexane	Stirring	25
BG-2	1	4 days	*n*-butyllithium	Hexane	Stirring	70
BG-3	1	4 days	*n*-butyllithium	Hexane	Sonication	40
BG-5	1	4 days	*n*-butyllithium	Hexane	Sonication	25
BG-6	2	4 days	$NaBH_4$	THF	Stirring	25
BG-7	2	4 days	$LiBH_4$	THF	Stirring	25

Figure 1: Schematic of experimental setup for electrochemical intercalation of sulfuric acid into Summit coal.

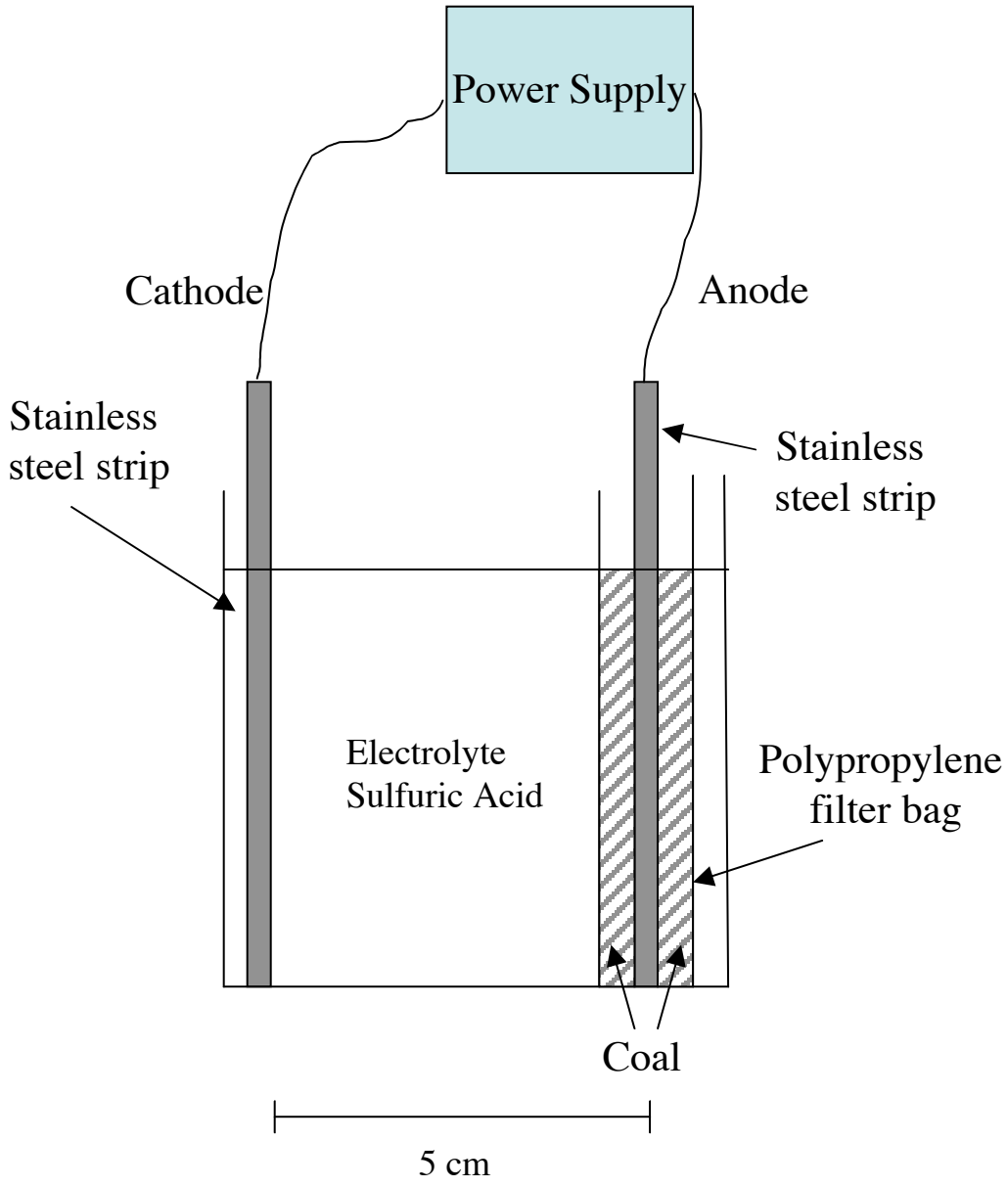

Figure 2: Reaction Setup for alkali intercalation, to prevent air and moisture from sample.

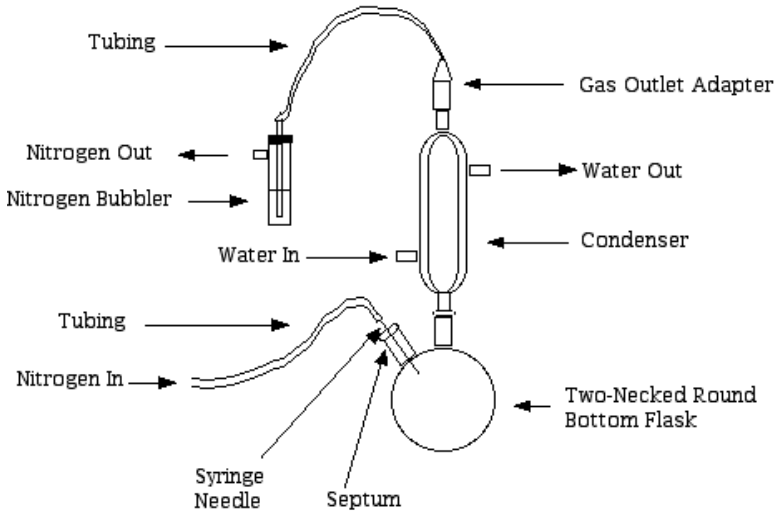

Figure 3: SEM micrographs of untreated Jeddo anthracite and products of various treatments. SEM micrographs of (a) raw Jeddo anthracite and (b) Jeddo anthracite acid treated in 50:50 nitric/perchloric acid with heat treatment at 700°C.

(a) (b)

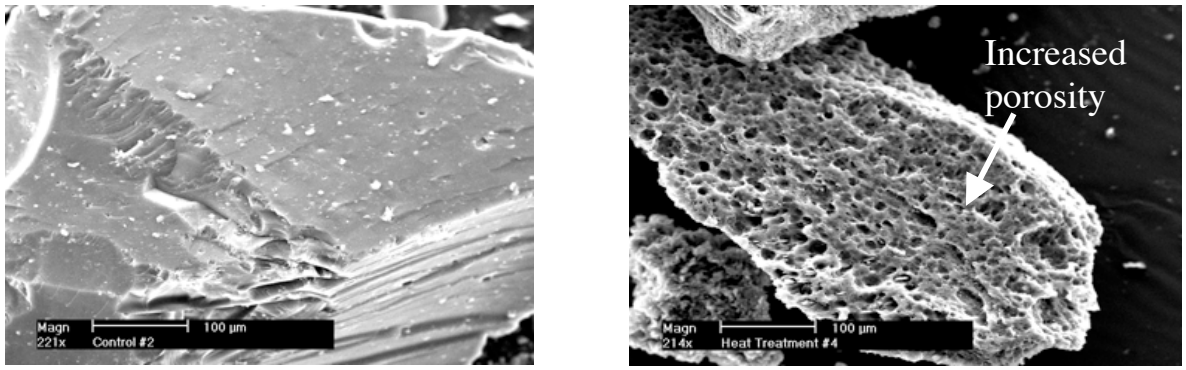

Figure 4. SEM micrographs of untreated Summit anthracite and products of various treatments. SEM micrographs of (a) raw Summit anthracite, (b) Summit anthracite treated at 700°C, (c) Summit anthracite acid treated in 50:50 nitric/perchloric acid with heat treatment at 800°C.

(a) (b)

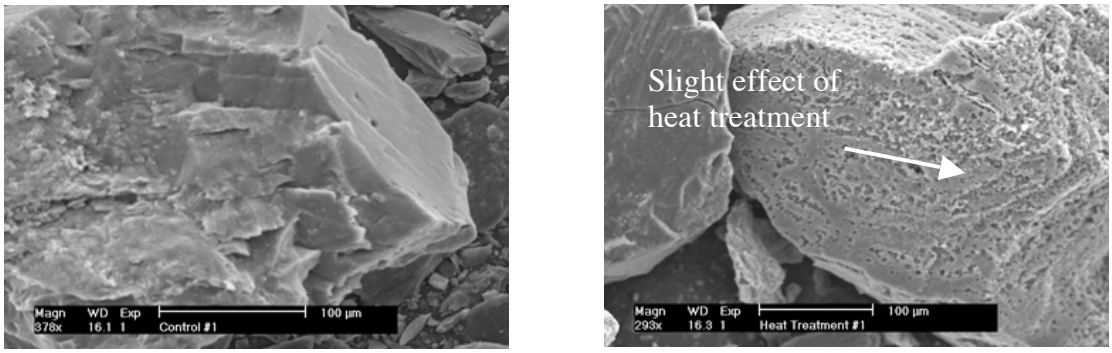

(c)

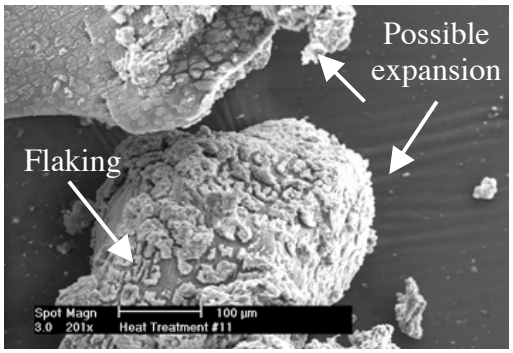

Figure 5: SEM micrographs of (a) untreated Hongay coal and (b) slightly exfoliated Hongay coal.

(a)

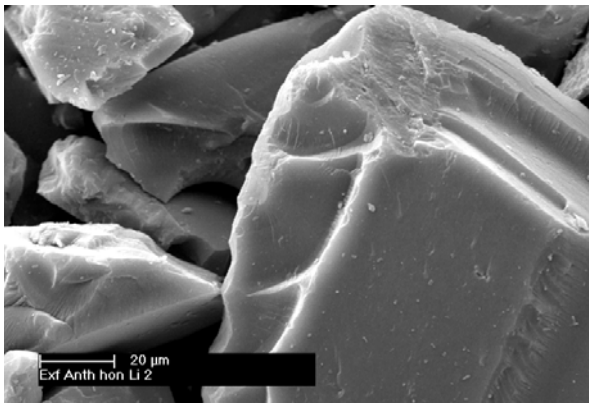

(b)

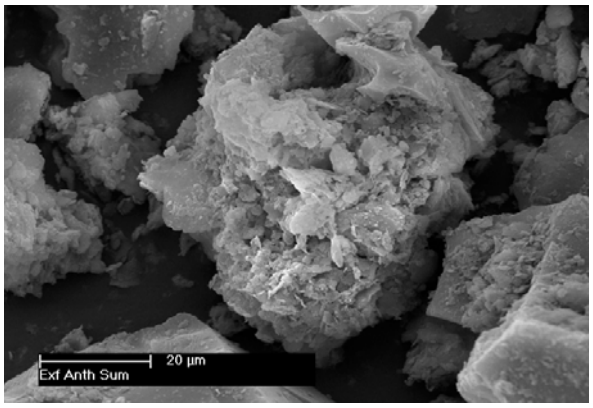

Figure 6: SEM micrographs of (a) untreated Summit coal and (b) acid/heat-treated Summit coal from perchloric/nitric acid treatment.

(a)

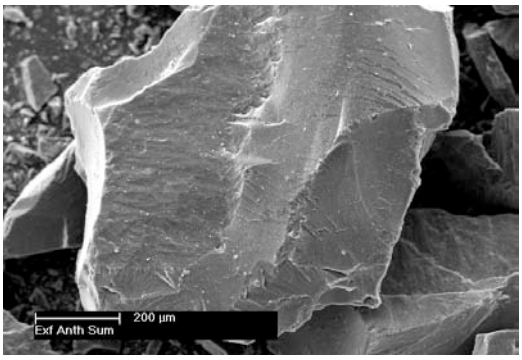

(b)

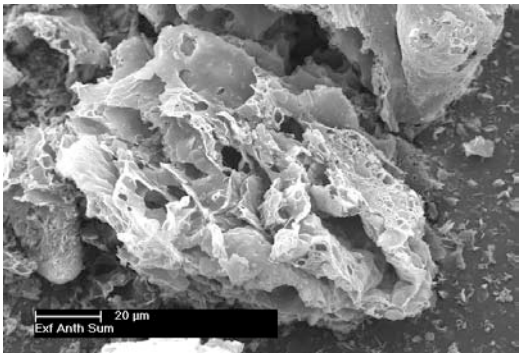

Figure 7: SEM micrographs of treated Summit coal from sulfuric/nitric acid treatment (a) 45 second heat treatment and (b) 2 minute heat treatment and of (c) graphite and (d) treated graphite.

(a)

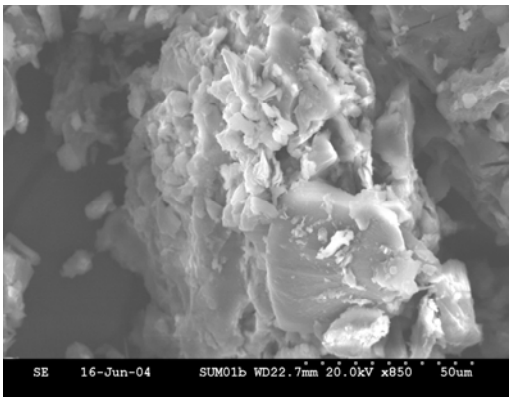

(b)

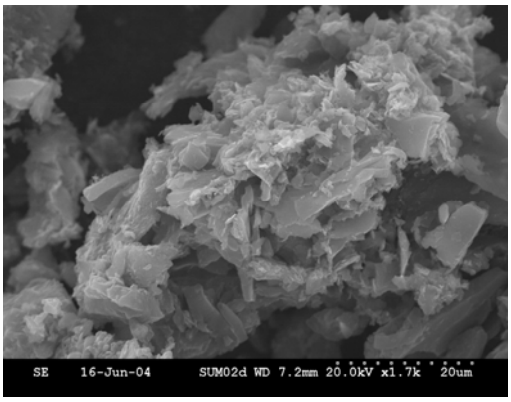

(c)

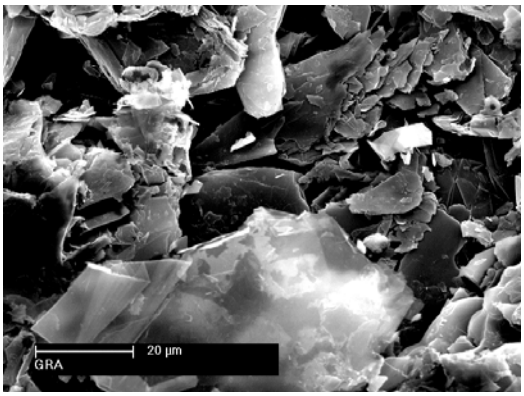

(d)

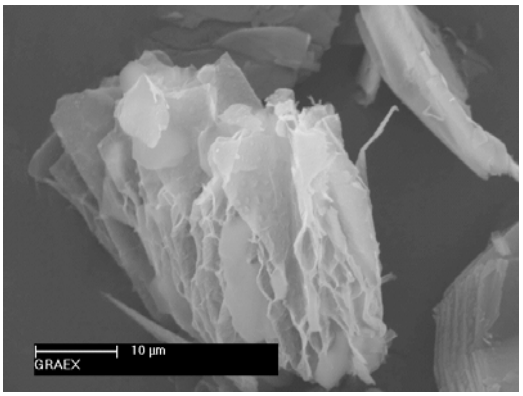

Figure 8: SEM micrographs of treated Summit coal from electrochemical sulfuric acid treatment (a) before heat treatment and (b) after 50 second heat treatment.

(a)

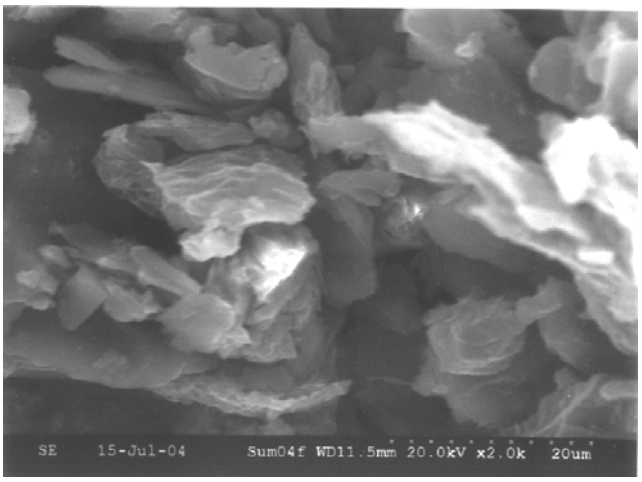

(b)

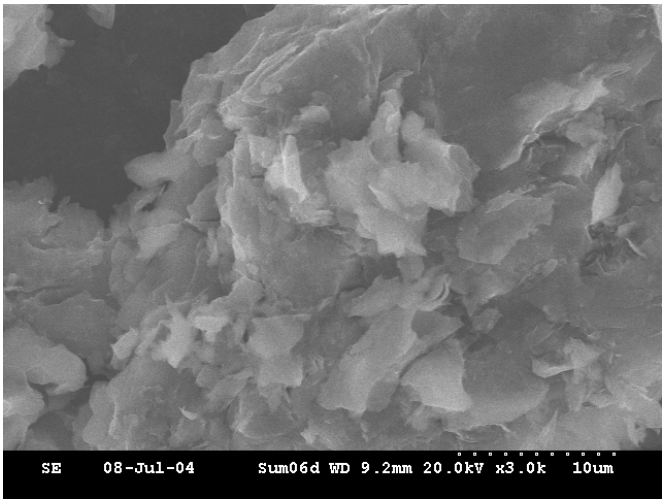

Figure 9: SEM micrographs of Hongay coal after intercalation with lithium and reaction in water (a) BG-1, (b) BG-2, (c) BG-3, (d) BG-5, (e) BG-6, (f) BG-7, and (g) BG-4.

(a)

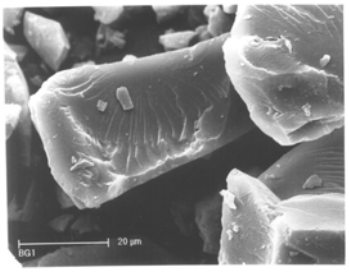

(b)

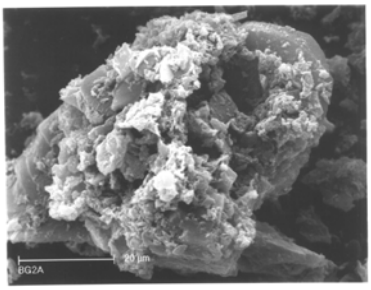

(c)

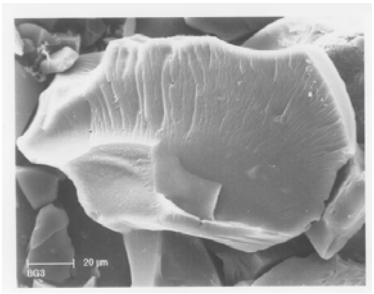

(d)

(e)

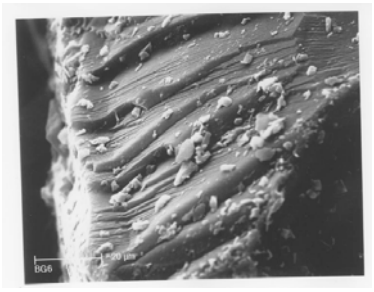

(f)

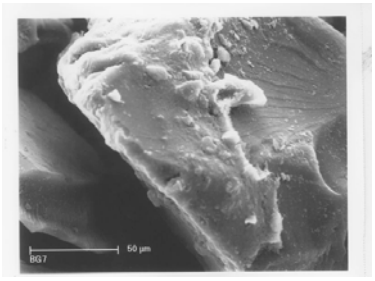

(g)

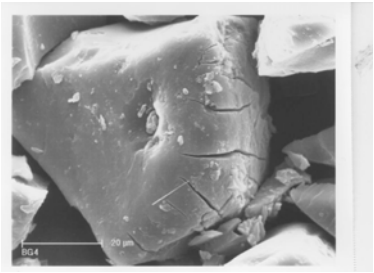

Figure 10: SEM micrographs of Summit treated with supercritical CO_2 destructive degradation (a) at 20 µm and (b) 50 µm

(a) (b)

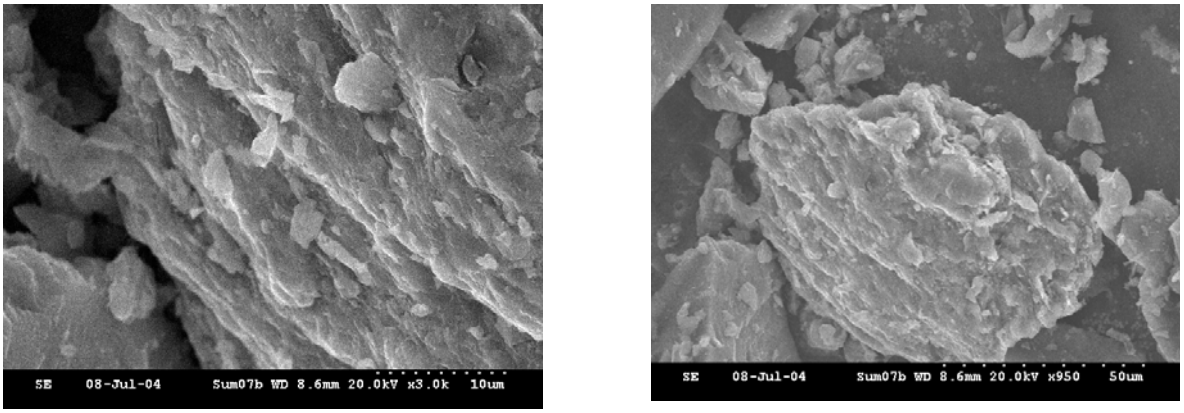

Figure 11: SEM micrographs of Summit treated with liquid N_2 thermal shocking (a) at 200 µm and (b) at 20 µm.

(a) (b)

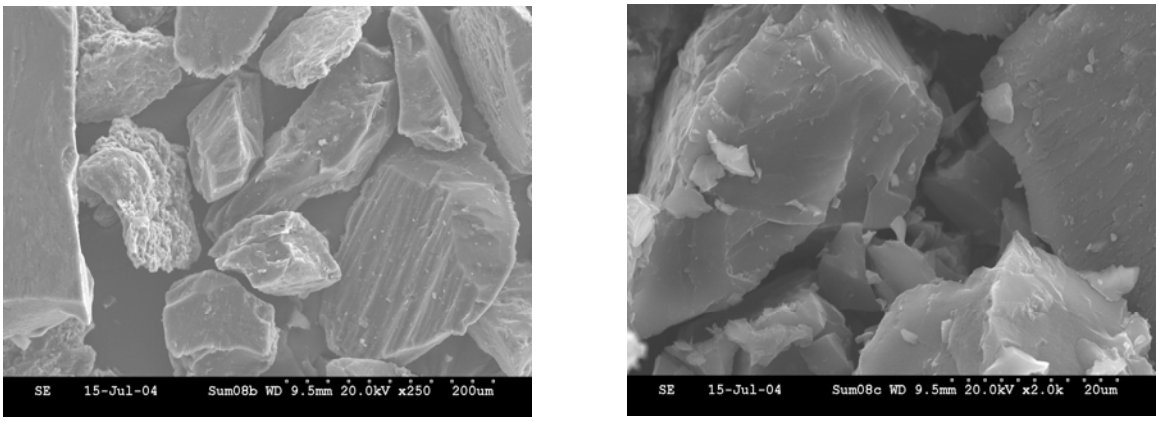

FINAL TECHNICAL PROGRESS REPORT
SUBMITTED TO

CONSORTIUM FOR PREMIUM CARBON PRODUCTS FROM COAL
The Pennsylvania State University
C211 Coal Utilization Laboratory
University Park, PA 16802-2398

USE OF COAL GASIFICATION AND COMBUSTION CHARS FOR MERCURY CAPTURE

Reporting Period Start Date: *March 1, 2003*

Reporting Period End Date: *June 30, 2004*

Submission Date: *September 1, 2004*

Principal Authors: *Dr. M. Mercedes Maroto-Valer, PI*
Mr. Bruce Miller, Co-PI
Dr. Yinzhi Zhang

DOE Award number: *DE-FC26-98FT40350*

Submitting Organization: The Energy Institute
The Pennsylvania State University
405 Academic Activities Building
University Park, PA 16802-2398
Phone: (814) 863 8265

Disclaimer

Abstract

Due to the increasing restricted use of landfill, the coal industry needs to find uses for high carbon chars from coal-fired combustors or gasifiers instead of their current disposal practice. Following this demand, a one-step activation protocol was developed by the proposers to produce activated carbons from coal chars. Compared to the conventional two-step process that includes a devolatilization of the raw materials, followed by an activation step, chars only require a one-step activation process, since they have already gone through a devolatilization process while in the combustor or gasifier. The produced activated carbons with a fine particle size are not only rich in micropores, but they also present a high content of mesopores, which leads to good mass transfer properties during the adsorption process, and therefore, activated coal chars could be a superior mercury sorbent candidate. Accordingly, the overall objective of the proposed research program is to develop activated carbon sorbents from coal chars to determine their mercury capacity and compare them to commercial activated carbons.

In this work, under Task 1 “Procurement and characterization of coal gasification and combustion chars” eleven char samples, including six samples from boiler systems and five samples from gasifiers were collected and analyzed. These samples consisted of 4 biomass-based samples and 7 coal-based samples. In addition, two commercial activated carbons, which have been widely adopted as a baseline for mercury sorbent studies, were also analyzed. Of the samples collected, the wood-based samples have higher loss-on-ignition (LOI) than the coal-based samples. Compared to the coal-based samples, all wood-based samples have a lower starting point for weight loss (180-300^{o}C vs. 200-400^{o}C), and their thermal reaction is more complex. Under Task 2 “Preparation and characterization of coal char sorbents”, selected samples were activated using the protocol previously developed by the authors. In addition, a cleanability study of one char was conducted to generate an enriched carbon sample that can be used to produce mercury sorbents and to study the effect of the carbon content in its mercury capture capacity. The enriched carbon sample has an ash content of around 3.6% and its surface area and pore volume are 53 m^2/g and 0.04 ml/g, respectively. This suggests that the some porosity was generated while in the pulverized coal (PC) combustor. Compared to the parent sample, the one-step steam activation process successfully increased the surface area and pore volume (53 vs. 863m^2/g and 0.040 vs. 0.490ml/g, respectively). Furthermore, two selected samples, one biomass-based sample from a gasifier and one coal-based sample from a boiler, were activated by steam and the porous textures of the resultant samples were analyzed. Under Task 3, "Mercury capture by the prepared char sorbents", the mercury content in selected raw char samples was tested using CVAA. The mercury contents were very low, mainly below 0.1 ppm. Selected char and activated char samples were tested with mercury capacity using a fix-bed protocol. Interestingly, the activated sample has lower mercury capacity (0.23mg/g) than its precursor fly ash carbon, although its surface area is around 15 times larger than its precursor, 863m^2/g vs. 53m^2/g. The pore size of the sorbent seems to play a role in the mercury capacity of the sorbents. However, the very different mercury capacity of the samples studied here cannot only be ascribed to differences in their porous structures. Other properties, especially surface functionality, are also important to determine their mercury capacity.

FINAL TECHNICAL PROGRESS REPORT

March 1, 2003 – June 30, 2004

Table of contents

1. Introduction

1.1. Rationale

On December 15, 2003 the U.S. Environmental Protection Agency (EPA) proposed for the first time to permanently cap and reduce mercury emissions from power plants. EPA is proposing two alternatives for controlling emissions of mercury from utilities. One alternative proposes to require utilities to install controls known as "maximum achievable control technologies" (MACT), which would reduce nationwide emissions of mercury by 14 tons (29%) by the end of 2007. The second alternative proposes to establish "standards of performance" limiting mercury emissions for new and existing utilities. If implemented, the nationwide utility emissions of mercury would be reduced in two distinct phases. In the first phase, due by 2010, emissions will be reduced by taking advantage "co-benefit" controls – that is mercury reductions achieved by reducing SO_2, and NO_x emissions. When fully implemented in 2018, mercury emissions will be reduced by 33 tons (69%).

Mercury is a naturally occurring element that can accumulate in the water and especially in the larger fish and pose the greatest risk to people who eat them regularly. According to a report of the U.S. Environmental Protection Agency (EPA), coal-fired utility boilers are the largest source of anthropogenic mercury, accounting for 33% of the total (EPA, 2002). Therefore, mercury emissions from coal-fired utility boilers have been identified as a hazardous air pollutant of greatest potential public health concern by EPA. Accordingly, there is a growing interest to develop technologies for mercury capture (EPA, 2002). The injection of commercial activated

carbons is a promising technology to control mercury emissions from coal-fired combustion systems. However, due to the very low concentration of mercury in the flue gas (1 ppb vol), the complexity of the flue gas composition, the very short residence time (~6s) of the carbon sorbent in flue gas, and the poor selectivity of the carbon sorbent towards mercury, excess carbon adsorbent needs to be injected into the flue gas, resulting in carbon-to-mercury ratios around 1000:1 to 100,000:1 for commercially available activated carbons. Therefore, novel sorbents are being sought for mercury capture (Brown et al., 2000). Previous studies have shown that the reaction of mercury with the carbon sorbent is mass-transfer limited and, therefore, activated carbons with high mesopore and macropore volume, as well as high mercury selectivity and low particle size, will be superior candidates for mercury sobents (Sjostrom et al., 2002).

Due to the increasing restricted use of landfills, the coal industry needs to find uses for high carbon chars from coal-fired combustors or gasifiers instead of their current disposal practice. Following this demand, a one-step activation protocol was developed by the proposers to produce activated carbons from coal chars. Compared to the conventional two-step process that includes devolatilization of the raw materials followed by an activation step, chars only require a one-step activation process (Maroto-Valer et al., 2000, 2001; Zhang et al., 2003a) since they have already undergone devolatilization process while in the combustor or gasifier. The char-produced activated carbons have a fine particle size, are rich in micropores, and also present a high content of mesopores, which leads to good mass transfer properties during the adsorption process. Activated coal chars, therefore, can be a superior mercury sorbent candidate. Accordingly, the overall objective of the proposed research program is to develop activated

carbon sorbents from coal chars for mercury capture and to determine their mercury capacity and compare them to commercial carbons.

1.2. Program objective

The objective of this research program was to develop activated carbon sorbents from coal chars for mercury capture. This research program included the selection and characterization of a suite of coal combustion and gasification chars provided by Southern Company and Penn State University. The characterization of the suite of samples collected was conducted at Penn State University using a battery of tests developed previously by the proposers. These samples were then activated following the protocols developed in previous CPCPC projects (See Section 1.3). Finally, the mercury capacity of the activated samples were tested and compared to commercial carbons.

1.3. Research design and tasks

This research program can be divided into the following three tasks described below.

- Task 1 “Procurement and characterization of coal gasification and combustion chars”. This task included the procurement and characterization of coal chars from different combustor and gasification units, and it was conducted in collaboration with Southern Company and Penn State University. The samples were characterized using a battery of tests, previously developed by the

proposers, that includes thermogravimetric profiles, particle size distribution studies, and proximate and elemental analyses. Furthermore, the properties of these chars towards their use as precursors for activated carbons were also investigated, particularly their porous structure.

- Task 2 "Preparation and characterization of coal char sorbents". The selected samples were activated using the protocol previously developed by the proposers (Maroto-Valer et al, 2001). The samples were heated under nitrogen flow to the desired temperature, and then steam was introduced in the reactor, while the reactor was kept isothermally for 0.5-2 hours. The properties of the activated carbons that have been synthesized under controlled conditions were systematically characterized. This study included a detailed description of the porous structure (micro-, meso- and macroporous) using conventional adsorption techniques, like N_2 adsorption isotherms at 77K. Finally, a cleanability study of the selected chars was conducted to generate enriched carbon samples that can be used for the produce mercury sorbents and to study the effect of the carbon content in their mercury capture capacity.

- Task 3 "Mercury capture by the prepared char sorbents". This task investigated the ability of the prepared activated chars to capture mercury using a reactor developed by the proposers. The observed mercury sorption capacities were compared to those of commercial activated carbons.

2. Experimental

2.1. Task 1: Procurement and characterization of coal gasification and combustion chars

2.1.1. Study samples

Eleven char samples together with two commercial activated carbon samples, which are used typically as the benchmark for mercury capture study and field tests, were collected. Five char

samples were provided by Southern Company, including three samples collected from a boiler at Plant Miller (Georgia) burning PRB coal (DarkAsh 99, DarkAsh00, and F9830) and two samples collected from a gasifier feeding lignite (Gasif-1 and Gasif-2). CPC-Filter and CPC-Knockout were collected from a gasifier fed with wood and provided by Community Power Corporation. GTI-Woodchar was also a wood-based sample and wasprovided by Gas Technologies Institute. The final sample, Tra-Woodchar, was provided by Tractebel Electricity & Gas International cogeneration facility in Northumberland, Pennsylvania, which is burning wood. Two lignite-based commercial activated carbon samples, Darco FGD and FGL, were provided by Norit Americas Inc.

2.1.2. LOI of the samples

The loss-on-ignition (LOI) contents of the char samples were determined according to the ASTM C311 procedure. Around 1 g of sample was oxidized in air for 3 hours at 800^{o}C to constant weight in a muffle furnace. The LOI content was then calculated from the weight loss of the sample after oxidation. The LOI analyses were conducted in duplicate.

2.1.3. Porosity studies

The porous texture of the char samples was characterized by conducting N_2 adsorption isotherms at 77K using a Quantachrome adsorption apparatus, Autosorb-1 Model ASIT. The pore volume was calculated as the volume measured in the nitrogen adsorption isotherm at a relative pressure of 0.95 ($V_{0.95}$). The total specific surface area, S_t, was calculated using the multi-point BET

equation in the relative pressure range 0.05-0.35. From the desorption branch, the micropore volume, V_{mi}, and external surface area, S_{ext}, were calculated using the α_S-method , where non-graphitized non-porous carbon black Cabot BP 280 (S_{BET}=40.2m^2/g) was used as a reference adsorbent. The mesopore volume (V_{me}) was calculated by subtracting the volume of V_{mi} from $V_{0.95}$. The micropore surface area, S_{mi}, was determined by subtracting the external surface area from the S_t. The pore sizes, 2nm and 50nm, were used as the limits between micro- and mesopores, and meso- and macropores, respectively, following the IUPAC nomenclature. The Barrett-Joyner-Halenda (BJH) method was used to calculate the mesopore size distributions. The desorption branch of the hysteresis loop in the isotherm was used for the mesopore size analysis.

2.1.4. TGA profiles

The thermogravimetric analyses were conducted on a Perkin Elmer TGA7. Typically around 10 mg of sample was heated under air flow (100ml/min) from room temperature to 100^{o}C then held for 10 minutes to remove moisture. The sample was heated to 900^{o}C at a heating rate of 10^{o}C/min.

2.2. Task 2: Preparation and characterization of coal char sorbents

The activation of the samples was performed in a horizontal activation reactor. The samples were heated under a nitrogen flow to the desired temperature, and then steam was introduced into the reactor for 1-3 hours, while the reactor was kept under isothermal conditions, as described elsewhere (Maroto-Valer et al., 2000, 2001; Zhang et al., 2003). In addition, the char sample

FA1 was subjected to physical separation by a sink/flotation technique using a liquid medium with density 1.6-2.5 g/ml and then followed by an acid digestion step of $HCl/HNO_3/HF$ at 65°C to produce a carbon rich sample (FA1-Dem) that was used for the subsequent mercury capture studies. The FA1-Dem sample was steam activated at 850°C for 60 minutes using a horizontal furnace, under the conditions described above. The porous structure of the activated chars was characterized by N_2-77K isotherms, as described in Section 2.1.3.

2.3. Task 3: Mercury capture by the prepared char sorbents

2.3.1. Mercury capacity studies

The samples prior to the mercury adsorption tests were analyzed by a cold vapor atomic absorption spectrophotometer (CVAA) according to EPA 7470 method for inherent mercury content. A char sample and its activated counterpart, together with a commercial activated carbon, Darco Insul, were tested for mercury adsorption using a fixed-bed with a simulated flue gas at 138°C. A detailed description of the mercury capacity test protocol used in this work can be found elsewhere (Granite et al., 2000). The simulated flue gas used in the study contains 16% CO_2, 5% O_2, 2,000ppm SO_2, 270ppm Hg and balance nitrogen, and the length of exposure is 350 minutes.

2.3.2. XPS studies

The surface chemistry of the samples was investigated by X-ray photoelectron spectroscopy (XPS) using a Kratos Analytical Axis Ultra instrument and a monochromatic aluminum (1486.6eV) X-ray source. All data were charge corrected as C-C in carbon 1 s at 284.4 eV. The samples were mounted on double-sided adhesive tape and analyzed as received. XPS quantification was performed by applying the appropriate relative sensitivity factors (RSFs) of the Kratos instrument to the integrated peak areas. These RSFs take into consideration of the X-ray across section and the transmission function of the spectrometer. The approximate sampling depth under these conditions was 25 Å.

3. Results and Discussion

3.1. Task 1: Procurement and characterization of coal gasification and combustion chars

3.1.1. LOI of the samples

Eleven char samples and 2 commercial activated carbons, which are typically used as benchmarks for mercury capture studies, were collected. Among the char samples, 4 are biomass (wood) based and 7 are coal based (3 from PRB, 2 from subbituminous coal and 2 from lignite). Five samples were generated from gasifiers and 6 were generated from boilers, as listed in Table 1.

The LOI of the collected samples are widely distributed. Some samples contain more than 50% LOI. For instance, CPC-Knockout, which is a biomass-based sample collected from a gasifier, has a LOI as high as 89.6%, and contains only 10.4% ash. The other sample collected from the

same facility, CPC-Filter, also has a high LOI, 70.6%. Another wood-based char sample, collected from the GTI gasifier, contains very small aluminum beads; however, they were separated from the char sample by sieving. The separated char sample, GTI-Woodchar, also has a high LOI (85.4%), as presented in Table 1. The other wood-based sample Tra-WoodFA, has a relatively low LOI, 22%, compared to the other wood-based samples.

Table 1. Summary of the samples collected in the present report.

Sample	Feed used	System	LOI, wt%	Ash,%
Gasif-1	Lignite	Gasifier	9.30	91.7
Gasif-2	Lignite	Gasifier	43.1	57.1
CPC-Filter	Wood	Gasifier	70.6	29.4
CPC-Knockout	Wood	Gasifier	89.6	10.4
GTI-Woodchar	Wood	Gasifier	85.4	14.6
Tra-WoodFA	Wood	Boiler	22	78
FA1	Subbit.	Boiler	62.7	37.3
FA2	Subbit.	Boiler	28.0	72.0
F9830	Subbit. (PRB)	Boiler	1.03	98.9
DarkAsh99	Subbit. (PRB)	Boiler	0.66	99.3
DarkAsh00	Subbit. (PRB)	Boiler	0.83	99.2
FGD	Lignite	Activation	63.8	36.2
FGL	Lignite	Activation	68.3	31.7

Some of the coal-based samples also have high LOI, such as FA1 and Gasif-2 (62.7% and 43.1%, respectively). The two Gasif-1 and Gasif-2 samples were collected from the same Southern Company's gasifier. Gasif-1 has an LOI of 9.3%, while Gasif-2 has a higher LOI of 43.1%. Gasif-2 is not a typical fly ash sample because it was collected from a vessel at the end of the run, and not collected during a steady-state operation conditions. However, there are some coal-based samples that have very low LOI, such as the samples collected from Southern Company boiler, DarkAsh99, DarkAsh00 and F9830, that have a LOI value as low as ~1%. The sample DarkAsh99 has the lowest LOI, 0.66%. Generally, the biomass-based samples collected have higher LOI than the coal-based samples.

Darco FGD and FGL are commercial activated carbons, which have been widely adopted as a baseline for mercury sorbent studies. Therefore, during this reporting period, they have been intensively characterized, including their LOI and detailed porous structure analysis. Darco FGD is a lignite-based commercial activated carbon, with very small particle size (less than 325 mesh), and is claimed as a free flowing powdered carbon. Its LOI value is 65% as listed in Table 1 (i.e., it contains 35% ash).

3.1.2. Porosity studies

3.1.2.1 Isotherms of coal-based char samples

The N_2-77K isotherms of seven coal-based samples are shown in Figure 1. The isotherms of two lignite-based samples (Gasif-1 and Gasif-2) are obviously different from those of subbituminous

coal (FA1, FA2, F9830, DarkAsh99 and DarkAsh00). The former has a little increment in the range of micropore filling at low relative pressure, which keeps increasing with the relative pressure until the saturation pressure is reached. Additionally, there is a large hystersis loop in the isotherms, which suggests that there are many mesopores in the samples. Additionally, Gasif-1 and Gasif-2, collected from a gasifier fed with lignite, have isotherms with similar shape, which suggests that although they have different carbon content, the pore volume distributions of the two samples are similar. In contrast, the isotherms of the subbituminous coal-based samples, especially FA1 and FA2, indicate that there are many micropores and macropores in the samples.

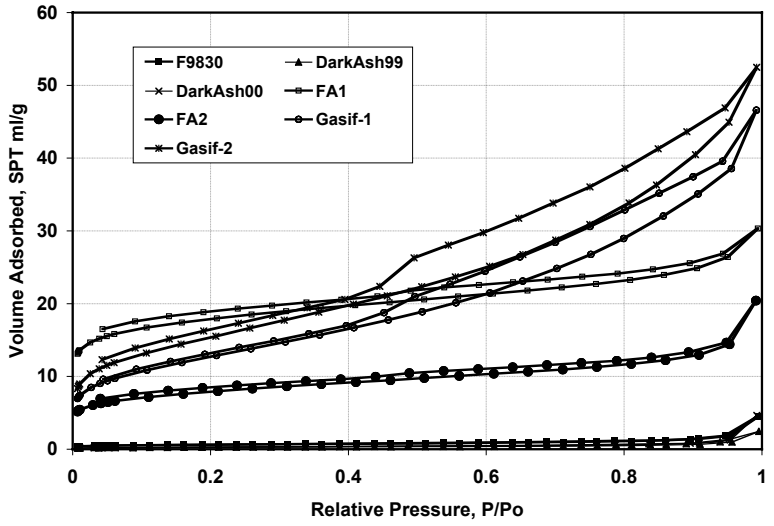

Figure 1. N_2-77K isotherms of coal-based char samples.

3.1.2.2. Isotherms of biomass-based char samples

The N_2-77K isotherms of the biomass-based samples are shown in Figure 2. Corresponding to its high carbon content of 89.6%, CPC-Knockout has the greatest adsorption, while Tra-WoodFA has the lowest adsorption among the wood-based samples. Two isotherms of samples from CPC gasifier, CPC-Knockout and CPC-Filter, exhibit an adsorption increasing trend in the entire relative pressure range, especially for CPC-Filter, which has a large increase when the pressure approaches saturation. Therefore, these two samples may have many mesopores and macropores, especially the CPC-Filter sample. In contrast, for the Tra-WoodFA sample collected from a boiler, its adsorption increases much less with increasing relative pressure, which suggests that the sample is dominated by micropores.

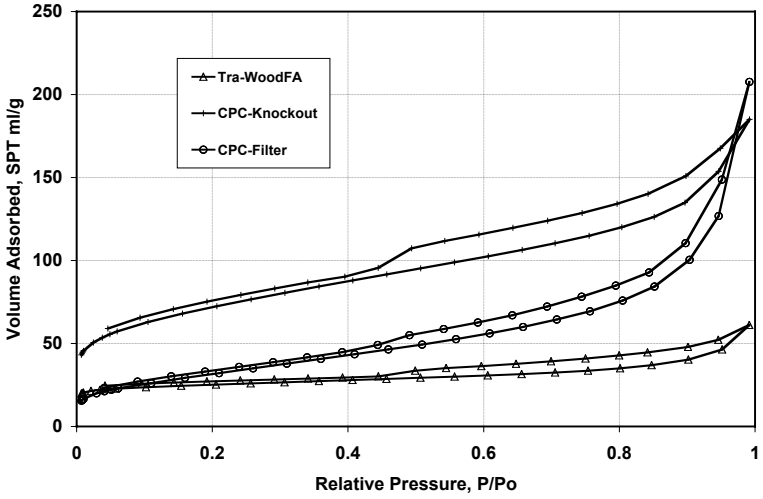

Figure 2. N_2-77K Isotherms of wood-based char samples.

3.1.2.3 Surface area and pore volume of the samples

Based on the isotherms shown in Figures 1 and 2, the surface area and pore volume of the char samples were calculated and are listed in Table 2. Corresponding to its high LOI and adsorption capability, CPC-Knockout has the highest surface area and pore volume, 243.2 m^2/g and 0.238 ml/g, respectively. It confirms our previous observation that the remaining carbon in fly ash has generated a certain porosity during the combustion/gasification process. The sample CPC-Knockout can be expected to have sorbent properties prior to any further treatment. Another sample collected from the sample facility, CPC-Filter, also has a high surface area and pore volume, 119.6 m^2/g and 0.196 ml/g, respectively.

Table 2. Porosity analysis results of the char samples.

Sample	S_{BET}, m^2/g	V_t, ml/g
Gasif-1	45.4	0.060
Gasif-2	54.5	0.070
CPC filter	120	0.196
CPC Knockout	243	0.238
Tra-WoodFA	77.4	0.072
FA1	53.1	0.040
FA2	25.5	0.020
F9830	2.10	0.003
DarkAsh99	0.90	0.002
DarkAsh00	1.10	0.002
FGD	526	0.473
FGL	476	0.411

The two samples collected from Southern Company's gasifier, Gasif-1 and Gasif-2, have similar surface areas of 45.4 and 54.5 m^2/g, respectively, although they have quite different LOI, 8.3 and 42.9%, respectively. Three low LOI samples collected from the Southern Company boiler, F9830, DarkAsh99 and DarkAsh00, as expected from their low LOI, have surface areas as low as 1~2 m^2/g. As expected, the commercial activated carbons have the highest surface areas and pore volumes of the studied samples.

3.1.3. TGA profiles

3.3.3.1. Coal-based char samples

The TGA curves of four samples from subbituminous coal are shown in Figure 3. All the samples began to loss weight at around 450^{o}C and continue to lose weight at a constant rate until 650^{o}C with one step change, except for sample Gasif-2, which began to lose weight as early as 200^{o}C until it reached 480^{o}C and it exhibited two step changes in weight loss. This suggests that the sample Gasif-2 may have a different reactivity rate during the activation process compared to other other samples, especially Gasif-1, although both Gasifi-1 and Gasif-2 were collected from the same facility and have similar surface area.

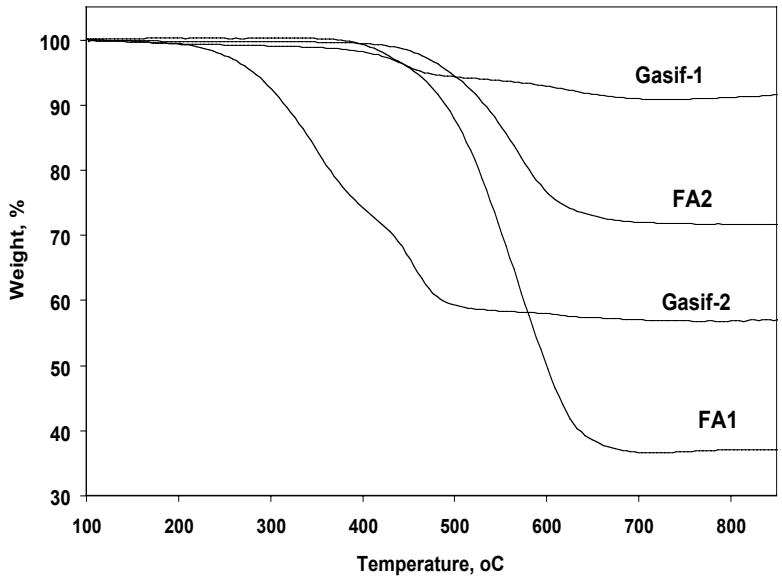

Figure 3. TGA curves of coal-based char samples.

3.1.3.2 Biomass-based char samples

The weight changes of wood-based char samples, when heated up to 850^{o}C in air, are recorded and shown in Figure 4. Compared to the samples from coal, all wood-based samples have a lower starting point for the initiation of weight loss (180-300^{o}C), and their thermal reaction is much more complex in the view of the TGA data, which have more than one weight loss step during a broader temperature range. For example, GTI-Woodchar lost around 80% of its weight in the temperature range 180 to 350^{o}C, then lost another 2% weight at 550 to 700^{o}C. While CPC-Knockout sample lost around 90% weight within 350-520^{o}C with 7 different rates.

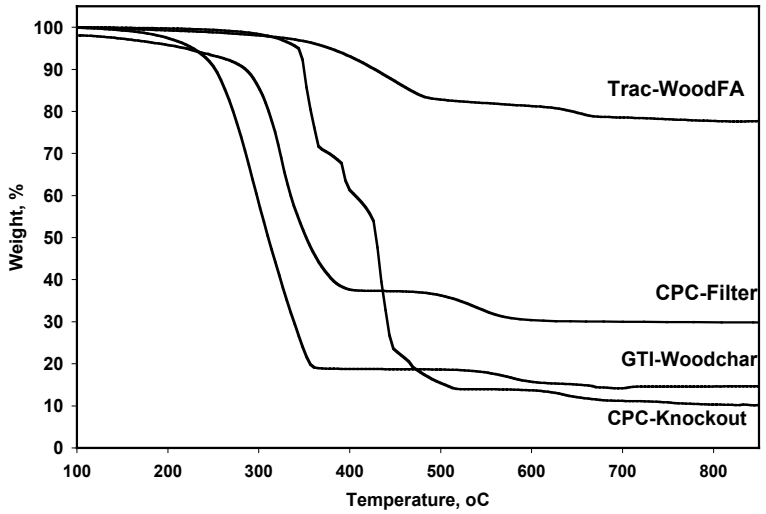

Figure 4. TGA curves of wood-based char samples.

3.2. Task 2: Preparation and characterization of coal char sorbents

3.2.1. Isotherms of activated chars

The char samples, GTI and FA1, were activated with steam at 850^{o}C for 30 minutes. These two samples were selected for the activation studies because of their high LOI contents. The isotherms of the resultant activated carbons, FA1-30 and GTI-30, are shown in Figure 5. It should be noted that the isotherms of the activated chars shown in Figure 5 are on a carbon basis, while the isotherms of the parent chars (Figures 1 and 2) were presented on a total weight basis. The isotherms of the commercial activated carbons, FGD and FGL are also shown in Figure 5. It is obvious that the activated GTI char has a similar isotherm to that of the commercial activated

carbon. All isotherms contain a hysteresis loop, which is usually associated with the filling and emptying of mesopores by capillary condensation. Besides the steep rise at the low relative pressure, which corresponds to micropore filling, the isotherm keeps increasing with the relative pressure, even near saturation pressure, which suggests there are mesopores and macropores in the sample. In contrast, activated coal-based char, FA1-30, has a type 1 isotherm, which features a steep increase at low relative pressure and levels off at higher relative pressure. However, compared to the raw char (FA1 and GTI-Woodchar, Figure 1), both activated char samples (FA1-30 and GTI-30) have much more developed porosity after the 30 minutes one-step activation process.

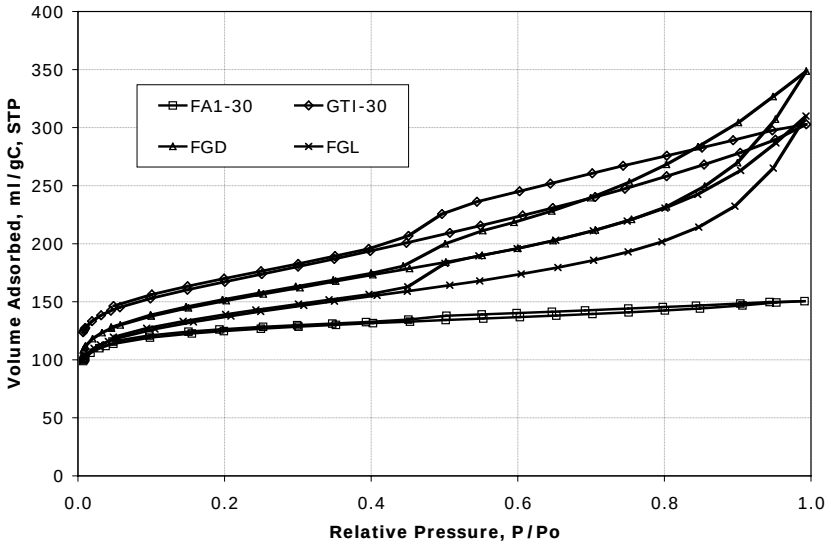

Figure 5. Isotherms of activated chars (FA1-30 and GTI-30) and commercial activated carbons (FGD and FGL).

3.2.2. Surface area and pore volume distribution of activated chars

The surface area and pore volume distribution of the samples were calculated from the isotherms in Figure 5 using the alpha-s method and the results are presented in Figures 6 and 7. The surface area and pore volume distribution of the activated chars are presented on a carbon basis.

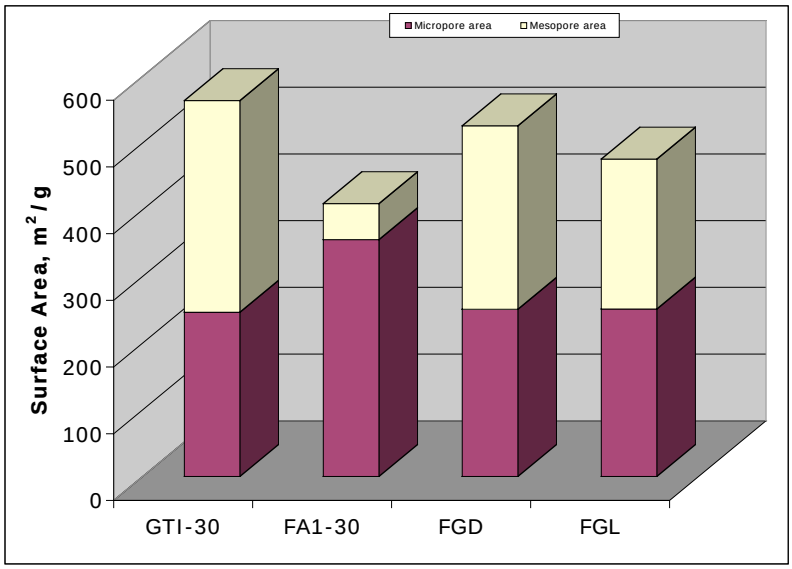

Figure 6. Surface area distribution of the activated chars (GTI-30 and FA-30) and commercial activated carbons (FGD and FGL).

The activated GTI sample has the greatest surface area (564m^2/g) on a carbon basis, and there is 317m^2/g contributed from mesopores, which accounts for ≈56% of the total. The commercial activated carbon FGD has a surface area of 526m^2/g, and ≈53% (275m^2/g) is from mesopores. Corresponding to its different isotherm shape, activated FA1 has only 13% surface area that is contributed from mesopores (54 vs. 409m^2/g).

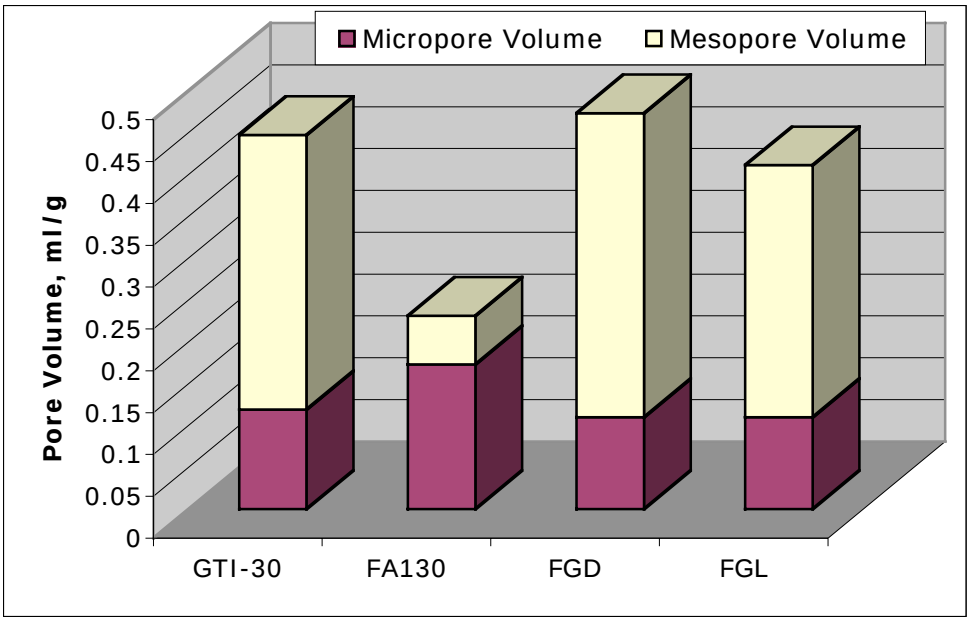

Figure 7. Pore volume distribution of the activated chars (GTI-30 and FA-30) and commercial activated carbons (FGD and FGL).

FGD has a total pore volume of 0.473 ml/g and 77% of the pore volume is from mesopores. GTI-30 has a similar pore volume distribution, with a total pore volume of 0.447ml/g of which ≈73% is from mesopores. Activated FA1 has more micropores and a larger mesopore volume, but the mesopores only account for 25% of the total pore volume.

Due to the small size of the micropores and overlapping of the fields of opposite walls of the micropores, the micropores are the major active site for most adsorbates. The mesopores act as adsorption sites for larger molecules and as transportation routes for small adsorbates. In certain cases, the transportation function of the mesopores are much more important than their adsorption function. For instance, for the carbon sorbent injection technology to control mercury emissions from coal-fired flue gas, the retention time of carbon in the flue gas is very short, on

the order of several seconds; consequently, the reaction of the mercury and the carbon is mass transfer-limited (Sjostrom et al., 2002). Therefore, carbon sorbents for the mercury capture market should be those sorbents with good mass transfer properties. Darco FGD is a commercial activated carbon, which has been widely adopted as a baseline for mercury sorbent studies, and as expected, it presents a large amount of mesopores. The activated char sample, GTI-30, has a large quantity of mesopores and its surface area is comparable to the commercial activated carbon FGD (564 vs. 526m^2/g).

3.2.3. Cleanability and sample porosity

The sample FA1 was collected from a pulverized coal unit and has a carbon content around 58%, which is higher than those reported in previous studies that are typically ~15%. However, this work focuses on the utilization of high carbon fly ashes, and therefore, this high carbon content sample was intentionally selected. It is known that the mercury capacity of the inorganic fraction is very low compared to the carbon present in ash (Serre et al., 2000; Hassett et al, 1999). Therefore, the sample was subjected to physical separation by a sink/flotation technique using a liquid medium with density 1.6-2.5 g/ml and then followed by an acid digestion step of $HCl/HNO_3/HF$ at 65^oC to produce a carbon rich sample (FA1-Dem) that was used for the mercury capture studies. The ash content and porosity of the samples were characterized by TGA and nitrogen 77K isotherms, respectively. The ash content and porous structure, including total surface area, pore volume and average pore size (based on the cylinder pore model), for DEM-PCC1 are presented in Table 3.

Table 3. Porosity of the de-ashed char sample FA1-Dem, activated char AC-FA1 and Darco Insul.

Sample	Ash Content	S_{BET}	$V_{0.95}$	D_a
	%	m^2/g	ml/g	nm
FA1-Dem	3.6	53	0.040	3.0
AC-FA1	11.2	863	0.490	2.3
Darco Insul.	-	700	-	-

Note: Darco Insul is a byproduct of Darco FGD.

The cleanability process adopted in the present study can effectively remove the ash from the char sample, ash content 3.6% vs. 37.3% for FA1-Dem and FA1, respectively. The sample, FA1-Dem, has surface area and pore volume of 53 m^2/g and 0.04 ml/g, respectively. This suggests that the fly ash carbon has already generated certain porosity while in the PC combustor prior to the activation process, and the pores generated are mainly in the mesopore range with an average pore size about 3nm.

The porosity of the activated sample, AC-FA1, is also listed in Table 3. Compared to the parent char sample, the one-step steam activation process has successfully increased the surface area and pore volume of the char sample by creating new micropores or small mesopores. After activation the sample has a surface area of $863m^2/g$, which is even higher than that of Darco Insul ($700m^2/g$, Table 4), that is a commercial activated carbon. Furthermore, the average pore size narrowed to 2.3nm compared to 3.0nm for the precursor char sample.

The mesopore size distribution curves of the de-ashed sample and the activated sample are shown in Figure 8. For the char sample, FA1-Dem, most of the mesopores are around 4.0nm, similar to other activated fly ash carbons and activated carbon fibers (Zhang et al, 1997). However, for the activated char, AC-FA1, besides the main peak at around 4.0 nm, another peak around 2.nm is observed, indicating some small mesopores have been generated during the activation process.

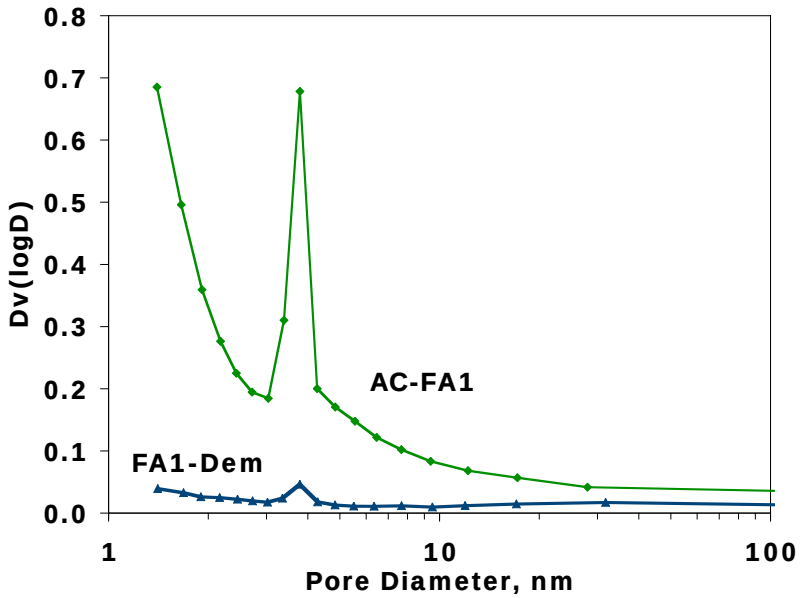

Figure 8. Mesopore size distribution of the demineralized fly ash carbon (FA1-Dem) and the activated fly ash carbon (AC-FA1).

3.3. Task 3: Mercury capture by the prepared char sorbents

3.3.1. Inherent mercury content of the char samples

The inherent mercury content of the char samples was analyzed by CVAA and the data is presented in Table 4. The mercury contents are very low, mainly below 0.1 ppm, and for two samples (FGD and Gasif-2), the mercury concentrations are below the instrument detection level (<0.01ppm). The sample from the GTI gasifier using wood as feedstock, GTI-Woodchar, has the highest mercury content (2.84 ppm). Darco FGD is a lignite-based commercial activated carbon, which has been widely adopted as a baseline for mercury sorbent studies. The FGD sample has a very small particle size (less than 325 mesh), and is claimed as a free flowing powdered carbon. Its mercury content is around 0.01ppm as listed in Table 4.

Table 4. Mercury content of selected samples collected in this study.

Sample	Coal Used	System	LOI, wt%	Mercury, ppm
Gasif-2	Lignite	Gasifier	43.1	0.11
CPC-Filter	Wood	Gasifier	70.6	0.03
CPC-Knockout	Wood	Gasifier	89.6	0.02
GTI-Woodchar	Wood	Gasifier	85.4	2.84
FA1	Subbit.	Boiler	62.7	0.20
FGD	Lignite	Activation	63.8	<0.01 [1]

[1] Below instrument detection level

3.3.3. Mercury capacity studies

Mercury adsorption test results are listed in Table 5, where the data obtained under the same conditions for the commercial activated carbon Darco Insul are also presented. The de-ashed char sample FA1-Dem has a mercury capacity as high as 1.85mg/g, which is somewhat comparable to the commercial activated carbon Darco Insul, whose mercury capacity is 2.77mg/g. Surprisingly, the activated char sample AC-FA1 has lower mercury capacity than its precursor fly ash carbon FA1-Dem, although its surface area is around 15 times larger than its precursor, 863m^2/g vs. 53m^2/g. However it should be noted that the precursor fly ash carbon has larger pore size than the activated sample (Table 4 and Figure 8), which suggests that the parent fly ash carbon has better mass transfer properties than its activated counterpart.

Table 5. Mercury capacity of selected samples.

Sample	Mercury Capacity, mg/g *
FA1-Dem	1.85
AC-FA1	0.23
Darco	2.77

Note: Tested using a fixed bed at 138°C and the simulated flue gas (Section 2.3.1).

Previous studies on a Thief sorbent, which is a semi-combusted coal extracted from a combustion chamber, have also shown that sorbents with modest surface areas yet exhibit good

capacities for mercury from flue gas (Granite et al., 2000). Micropores (< 2nm) are the major active sites for most adsorbates, while mesopores (2-50nm) act as adsorption sites especially for larger molecules, and also as transportation routes for small adsorbates. In certain cases, the transportation function is more important than the adsorption site function. For instance, in the carbon sorbent injection technology to control mercury emissions, the retention time of carbon in flue gas is very short, and therefore, at most conditions, mass transfer rate is the determining factor and the adsorption of the mercury onto the carbon surface is mass-transfer-limited (Sjostrom et al, 2002). Therefore, a carbon sorbent selected for mercury capture should have good mass transfer properties. This is consistent with the date reported here, where in addition to the total surface area, the pore size also seems to play a role in the mercury capacity of the sorbents. However, the very different mercury capacity of the samples studied here cannot only be ascribed to differences in their porous structures. Other properties, especially surface functionality, are also important to determine their mercury capacity, as described in the Section below.

3.3.4. XPS studies

In order to investigate the surface properties of the samples, FA1-Dem and AC-FA1, XPS analyses were conducted using a Kratos Analytical Axis Ultra instrument, and the resultant survey spectra are shown in Figure 9. For FA1-Dem, in addition to the two major peaks C1s and O1s, there are also two small peaks at 690 KeV and 200 KeV, which are ascribed to F1s and Cl 2p, respectively. The presence of fluorine and chlorine in the FA1-Dem sample is probably a

result of the acid digestion step, where HCl and HF acids were used. Furthermore, the comparison of the spectra for the two samples also shows that the O 1s peak for FA1-Dem is larger than that for AC-FA1. This indicates that the activation process may have caused the loss of certain oxygen functional groups. In addition, the activation process also removed almost all of F and Cl species from the surface of the sample, as shown by the lack of peaks at 690 Kev and 200 KeV for F 1s and Cl 2p, respectively, for AC-FA1 (Figure 9).

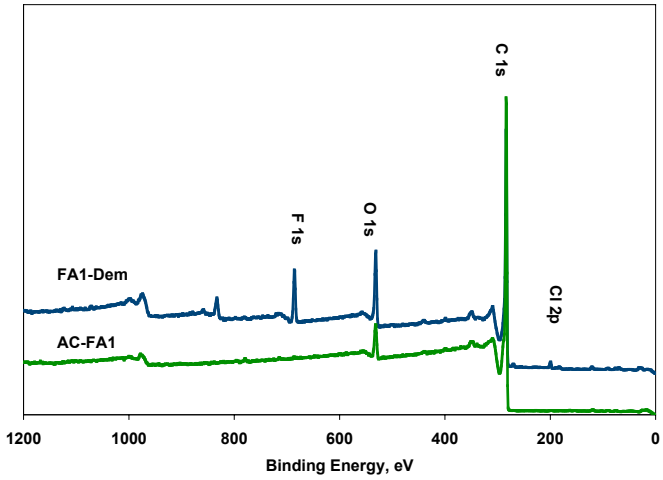

Figure 9. XPS survey spectra of the demineralized fly ash carbon (FA1-Dem) and the activated fly ash carbon (AC-FA1).

The high resolution scan data of O1s and C1s peaks for these two samples are shown in Figure 10 and 11, respectively. In Figure 10, the C 1s curve of DEM-PCC1 shows a shoulder at higher binding energy besides the main peak at 284 KeV, which is ascribed to oxidized carbon. This corresponds to the O 1s spectrum in Figure 11, which splits into two peaks at around 532 KeV and 531.5KeV that are assigned to single bond C-O and double bond C=O, respectively (Wang et al., 2000).

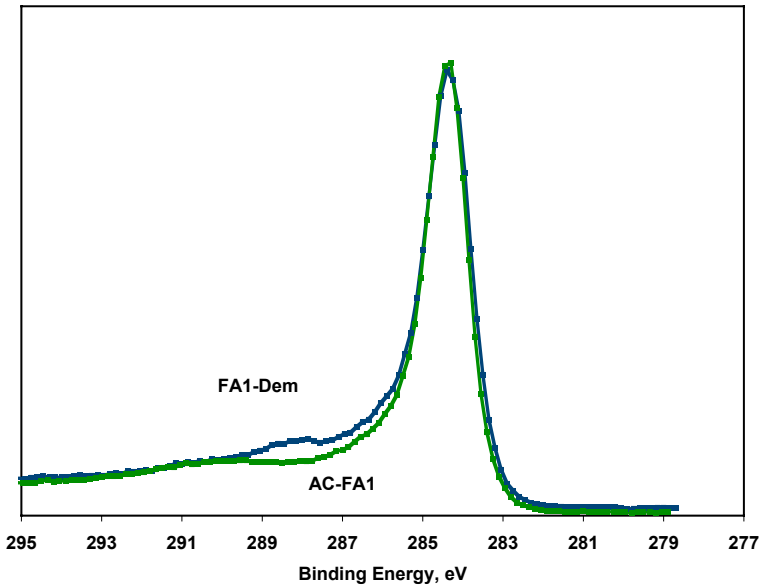

Figure 10. C 1s spectra of the demineralized fly ash carbon (FA1-Dem) and the activated fly ash carbon (AC-FA1).

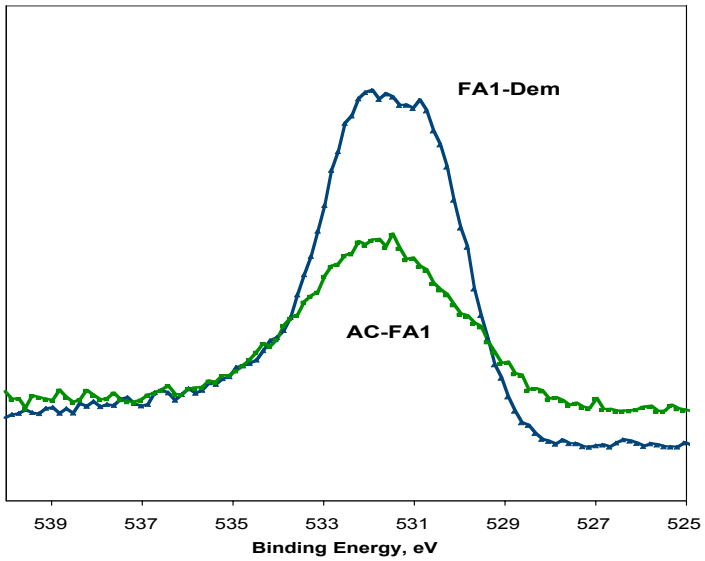

Figure 11. O 1s spectra of the demineralized fly ash carbon (FA1-Dem) and the activated fly ash carbon (AC-FA1).

Previous studies have focused on different adsorbents for mercury, including activated carbon, and also investigated the effect of several elements including F, Cl, I, S and O on mercury adsorption (Granite et al., 2000). EPA studies on the effect of activated carbon surface moisture on low temperature mercury adsorption indicated that surface oxygen complexes provide the active sites for mercury bonding (Li et al., 2002), where possibly lacton and carbonyl groups, are the active sites for Hg^0 capture (Li et al., 2003). However, other published work on the impact of surface heterogeneity on mercury uptake by carbonaceous sorbents under ultra high vacuum and atmospheric pressure concluded that in physisorption regime, oxygen functional groups decrease mercury adsorption due to their blocking of access for mercury to micropores, while in chemisorption regime, no significant impact of oxygen functionalities was observed (Won et al., 2002). The data discussed here supports the claim that the oxygen functionality and the presence of halogen species on the surface of fly ash carbons may promote mercury adsorption, while the surface area does not seem to have a significant impact on its mercury capacity (Table 5). Moreover, it has previously been reported that pre-treating activated carbon with HCl leads to higher capacity for Hg^0 adsorption in fixed bed capture tests (Ghorishi et al., 2002). Based on the above data, fly ash carbons from coal-fired power plant have the potential to capture mercury if they have mesoporous structure, and oxygen and halogen functional groups. It has been postulated that carbon sorbents have independent reaction sites that comprise at least an oxidation site and also a binding site for the oxidized Hg (Olson et al., 2000). Although this work cannot differentiate between the effect of oxygen functional groups, halogen species, and carbon sites, further studies on the modification of the surface properties of fly ash carbons and

their mercury adsorption properties are underway to ascertain the effect of oxygen functionalities, halogen species and carbon sites.

4. Conclusions

Following the demand for mercury emission control and utilization of chars, this work focuses on developing sorbents from coal chars for mercury capture and to determine their mercury capacity under typical flue gas compositions. During this project, eleven char samples, including six samples from boiler systems (DarkAsh 99, DarkAsh00, F9830, Tra-WoodFA, FA1 and FA2) and five samples from gasifiers (Gasif-1, Gasif-2, CPC-Filter, CPC-Knockout and GTI-Woodchar) were collected and analyzed. These samples consisted of 4 biomass-based samples (CPC-Filter, CPC-Knockout, Tra-WoodFA and GTI-Woodchar) and 7 coal-based samples (including lignite- and sub-bituminous-based, Gasif-1, Gasif-2, FA1, FA2, DarkAsh 99, DarkAsh00 and F9830). In addition, two commercial activated carbons (Darco-FGD and FGL), which have been widely adopted as a baseline for mercury sorbent studies, were also analyzed. Furthermore, two selected samples, one biomass-based sample (GTI-Woodchar) from a gasifier and one coal-based sample (FA1) from a boiler, were activated by steam and the porous textures of the resultant samples were analyzed.

Of the samples collected, the wood-based samples have higher LOI than the coal-based samples. For example, wood-based sample CPC-Knockout has a LOI as high as 89.6%, although some coal-based samples also have high LOI, such as FA1 and Gasif-2 (62.7 and 43.1%, respectively).

The lignite-based commercial activated carbon, Darco FGD, contains 35% ash. Corresponding to its high LOI and adsorption amount, CPC-Knockout has the highest surface area and pore volume, 243.2 m^2/g and 0.238 ml/g, respectively. The sample CPC-Knockout can be expected to be a good sorbent prior to any further treatment. Compared to the coal-based samples, all wood-based samples have a lower starting point for weight loss (180-300^oC vs. 200-400^oC), and their thermal reaction is more complex.

Compared to the raw char (FA1 and GTI-Woodchar), both activated char samples (FA1-30 and GTI-30) have much more developed porosity after the 30 minutes one-step activation process. The activated GTI sample has surface area as high as 564m^2/g on a carbon basis, which is comparable to the commercial activated carbon FGD of 526m^2/g. The mesoporosity of activated GTI char is 56% on surface basis or 73% on volume basis. This is comparable to the commercial activated carbon FGD, which is 53% is on surface basis or 77% on volume basis. Both samples have a porous structure containing a large amount of mesopores, suggesting that they will have good mass transfer properties. A high mass transfer rate is a key factor in determining the mercury capture properties for mercury control in coal-combustion flue gas.

This work has studied the mercury capture capacity of fly ash carbon, and the effect of the properties of fly ash carbon and its activated product, including nano-pore structure and surface functionality. The fly ash carbon sample FA1-Dem has a mercury capacity as high as 1.85mg/g, which is comparable to the commercial activated carbon Darco Insul, whose mercury capacity is 2.77mg/g. Surprisingly, the activated fly ash carbon sample AC-FA1 has lower mercury capacity (0.23mg/g) than its precursor fly ash carbon FA1-Dem, although its surface area is around 15

times larger than its precursor, 863m^2/g vs. 53m^2/g. However, XPS data indicates that the demineralization using HCl/HNO_3/HF not only removed most of ash from the sample, but it also changed the surface chemistry of the sample, leaving F, Cl elements and oxygen functional group on the surface of fly ash carbon. On the other hand, the activation process at 850^{o}C for 60 minutes may cause the loss of certain oxygen functional groups and almost all of F and Cl elements from the surface of the sample. The data in the present paper suggests that the oxygen functionality and the presence of halogen species on the surface of fly ash carbons may promote mercury adsorption, while the surface area does not seem to have a significant impact on its mercury capacity

Based on this work, fly ash carbons from coal-fired power plant have the potential to capture mercury if they have mesoporous structure, and oxygen and halogen functional groups. The studies presented here have shown that the chars investigated showed different mercury capacities. Although mercury capture technologies will be site specific, this work indicated that chars are a potential low-cost sorbent. Further studies on the modification of the surface properties of fly ash carbons and their mercury adsorption properties are underway to ascertain the effect of oxygen functionalities, halogen species and carbon sites.

5. Publications resulting of this project

1. M. M. Maroto-Valer, Y. Zhang, Z. Lu, E. Granite, and H. Pennline, Development of activated carbons from unburned carbon for mercury capture, *Proceedings International Ash Utilization Symposium*, CAER-University of Kentucky and U.S. DOE National Energy Technology Laboratory, Lexington, KY, October 20-22, 2003, Paper 90 (CD-ROM publication).
2. Y. Zhang, M. M. Maroto-Valer, E. Granite, Z. Tang, and H. Pennline, Understanding the properties of unburned carbon in fly ash towards its mercury capture capacity, *Proceedings of 20th Annual International Pittsburgh Coal Conference*, University of Pittsburgh, Pittsburgh, PA, September 15-18, 2003, Paper 240.pdf (CD-ROM publication).
3. Y. Zhang, E.J. Granite, M. M. Maroto-Valer, and Z. Tang, Activated carbons produced from unburned carbon in fly ash and their application for mercury capture *Prepr. Am. Chem. Soc. Div. Fuel Chem*., 2003, 48(1), 32-33.
4. M.M. Maroto-Valer, Y. Zhang, B.G. Miller, E. Granite, Z. Tang and H. Pennline, Mercury oxidation and capture by coal chars, *Proceedings Carbon 2004*, American Carbon Society, Providence, RI, July 11-16, 2004, Paper L035.pdf (CD-ROM publication).
5. M.M. Maroto-Valer, Y. Zhang, and B.G. Miller, Development of activated carbons from coal and biomass combustion and gasification chars, *Prepr. Am. Chem. Soc. Div. Fuel Chem.*, 2004, 49(2), 690-691.
6. M.M. Maroto-Valer, Y. Zhang, E. J. Granite, Z. Tang, H. W. Penline, Effect of porous structure and surface functionality on the mercury capacity of a fly ash carbon and its activated sample, *Fuel*, In Press.

6. Acknowledgements

The authors would like to acknowledge the Consortium for Premium Carbon Products from Coal (CPCPC) for support and Southern Company, Norit Americas Inc, Community Power Corporation, Tractebel Electricity & Gas International and Gas Technology Institute for providing the study samples. The authors would also like to thank DOE National Energy Technology Laboratory for the mercury capacity studies.

7. References

Brown, T.D., Smith, D.N., O'Dow, W.J., and Hargis, R.A., 2000, Fuel Proc. Tech, 65, 311.

EPA mercury web site, 2002, http:// www.epa.gov/mercury/information.htm#fact_sheets.

Ghorishi SB, Keeney RM, Serre SD, Gullett BK, Jozewicz WS. Environmental Sc. & Tech. 2002; 36(20):4454

Granite, E.J., Pennline, H.W. and Hargis, R. A. Ind. Eng. Chem. Res. 2000*, 39*, 1020.

Hassett D.J. and Eylands K.E. Fuel 1999:78:243.

Kwon S., Borguet, E. and Vidic, R.D., Environ. Sci. Technol., 2002, 36, 4162-4169

Li, Y.H., Lee, C.W. and Gullet, B.K., Carbon 40(2002)

Li, Y.H., Lee, C.W. and Gullet, B.K., Carbon 40(2002) 65-72

Maroto-Valer, M.M, Andrésen, J., and Morrison, J., 2000, DOE Conf. on Unburned Carbon, 21.

Maroto-Valer, M.M., Zhang, Y., Lu, Z., Andrésen, J. M., and Schobert, H.H., 2001, Proc. 18th Intern. Pittsburgh Coal Conf., CD publication, 52-01.pdf.

Olson, E.S., Dunham, G.E., Sharma, R.K., Miller, S.J. Prepr. Pap.—Am. Chem. Soc., Div. Fuel Chem. 2000; 45 (4): 886.

Serre S.D., and Silcox G.D. Ind. Eng. Chem. Res. 2000;39:1723

Sjostrom, S., Ebner, T., Ley, T., Slye, R., Richardson, C., Machalek, T., Richardson, M., and Chang, R., 2002, J. Air & Waste Manage. Assoc., 52, 902.

Wang Y., Viswanathan H., Audi A.A., Sherwood P.M.A. Chem Mater. 2000;12:1100

Zhang, Y.; Wang, M.; He, F. and Zhang, B. J. Mater. Sci. *1997, 32*, 6009

Zhang, Y., Lu Z., Maroto-Valer, M.M, Andrésen, J.M. and Schobert H.H., Energy and Fuel, 2003a, 17, 369-377.

Zhang, Y., Maroto-Valer, M.M, Granite, E., Tang, Z., Pennline, H., Proceedings of 20th annual international Pittsburgh coal conference, 2003b, CD-Rom, paper 240.pdf.

BINDING EFFICIENCY OF COAL-DERIVED BINDERS TOWARDS ANODE BUTTS

Final Technical Progress Report

Start Date: June 1, 2003
End Date: June 30, 2004

Principle Investigator: Dr. John M. Andresen
Report Issue: June 2004

Internal Agreement No. 2485-TPSU-DOE-0350,
For Award No.: DE-FC26-98FT40350

The Energy Institute
Penn State University
C-211 Coal Utilization Lab
University Park PA 16802

DISCLAIMER

ABSTRACT

This work can be divided into three parts: the study of the performance of alternative binder pitches, the physical and chemical properties of the butt materials, and the interaction of different pitches on different parts of the butt materials. There are four binder pitches used in this work: standard coal tar pitch (SCTP), petroleum pitch (PP), coal-extracted pitch (WVU), and gasification pitch (GP). The results of this study show that the petroleum pitch offers a potential to be used as additives to the standard coal-tar pitches for use as binders in the aluminum anode production, while the addition of coal-extracted pitch and gasification pitch give comparable anode properties when the ratio of standard coal tar pitch to the alternative pitch is greater than 50:50. Further work should be conducted to study the causes of improvement of adding alternative pitches to better understanding the roles of the binders from various types of pitches.

Three industrial anode butts, with and without recycled butt material, were studied. Non-destructive X-Ray imaging was used to quantify the spatial distribution of density and porosity in the sample. Apparent and absolute densities were measured and the specific pore volumes were calculated as a function of the distance from the airburn side. The results from the X-Ray CT and the densities and pore volume measurement showed a decrease in apparent density, and an increase in absolute density and specific pore volume from the center of the core to the surfaces. The anode butt that did not contain recycled butt material in the original formulation showed a higher reactivity with air at the airburn side while it had lower reactivity with CO_2 at the electrolytic side. It can be confirmed from this work that the main factors that derived the change in air and CO_2 reactivities of the anodes along the electrolytic surface to the airburn surface were the concentration of the inorganic contents, e.g. sodium, calcium, etc., and the porosity of the carbon material.

The experimental-scale anodes made from the top and bottom of the butt materials gave quite lower green apparent densities than the anodes made from the

middle part of the butt materials. These results were linked with high porosity of the top and bottom of the butt materials that inhibited the pitch to penetrate well into the pores. However the effect of porosity was weakened in the baked apparent density. Anodes that made from the pitch mixture that contained 20% PP and 20%GP gave comparable baked density to the anodes made from SCTP only. Whereas the anodes that were made from the pitch mixture that contained 20% WVU gave somewhat lower baked densities than the SCTP only and these results were caused by a high pitch loss of this pitch after baking.

TABLE OF CONTENTS

LIST OF TABLES

LIST OF FIGURES

1. Introduction

Carbon anodes are manufactured from calcined petroleum coke, butt fillers and coal tar pitch. Since the demand of the coal tar pitch in the aluminum industry accounts for about 75% of the pitch market [1] and the production of coal tars is rapidly decreasing in the United States as well as throughout the world [2], the development of alternative binders were considered in this work. Coal tar binder pitches are traditionally obtained from coal tars that are the by-product of bituminous coal coking process used to make coke for blast furnaces in iron production. During the manufacturing of carbon anodes coal tar pitch is mixed with calcined petroleum coke, where petroleum coke is the by-product from the delayed coker in a refinery. Remaining parts of spent anodes from the aluminum production, namely butts, are also crushed and used as filler [3].

The alternative binder pitches considered in this work are petroleum pitch (PP), coal-extracted pitch (WVU), and gasification pitch (GP). Petroleum pitch is a residue produced from heat-treatment and distillation of petroleum fractions. A production of coal-extracted pitch involves a prehydrogenation of coal followed by extraction using a dipolar solvent. Gasification pitches are distilled by-product tars produced from the coal gasification process. The mix of binder, filler and some additives are heated to about 50°C above the softening point of the pitch, typically 160°C. This temperature is sufficient to enable the pitch to wet the carbon particles [4]. The mix is then either extruded, vibrated or pressed to form a green anode. The wetting of coke by pitch is very important to the anode property. The pitch has to flow over the coke surface and has to enter into the surface porosity to generate a cohesive paste. Quinoline insolubles or QI play an important role in filling the spaces between petroleum and recycled anode coke particles on which the pitch is supported and prevent the pitch from fully penetrating the pores of the coke particle [4]. It is generally accepted that pitches with up to 15 %wt QI yield better anodes [5]. The only pitch studied in this work that contains QI is the SCTP, whereas the others contain about 0.1 wt% or less of QI. Mixing of the SCTP and the alternative pitch creates a various content of QI to the mixture.

The Hall-Héroult process, where alumina is reduced by carbon to produce aluminum, is currently the largest user of premium carbon products worldwide consuming over 11 million tons in form of carbon anodes annually [1]. To improve the economics of the process, anode butts, the unused parts of the anode remaining from operation in the reducing pot, are crushed and used as filler in the production of new anodes. About 20% of the anode is recycled butt material that accounts for over 300,000 tons annually [2]. The lower part has been in contact with the hot electrolyte experiencing temperatures in the range of 930 to 980°C. The lower part of the anode may also have been consumed by CO_2 burn, where typically the binder coke is attacked selectively. CO_2 burn may also affect the side of the anode. Further, the top part of the anode may reach temperatures of 350 to 600°C depending on the protective cover of electrolyte material, and air burn may also take place. Hence, the butt chemistry may differ significantly from that of petroleum coke, where the lower part of the butt may be altered due to the interaction with the cryolite as well as the modification of the surface chemistry due to the burn-off from CO_2. The top part of the butt could be highly oxidized during the air burning, while the middle part of the butt may not be affected by any of the above.

The objectives of this work were to determine:

1. the performance of each alternative binder pitch from various sources of pitches
2. the physical and chemical properties of the butt materials from different conditions in the reducing pots
3. the interaction of different pitches on different parts of the butt materials

To fulfill the first objective, each alternative pitch was mixed with a standard coal tar pitch (SCTP) at various mixtures and laboratory-scale test anodes were formed and studied. The ratio of pitch:coke:butt remained constant for the whole study. Mixing of the SCTP and the alternative pitch creates a various content of QI to the mixture. This may provide a suitable level of QI that gives a good laboratory-scale anode property.

A range of tests were performed to study the physical and chemical properties of the butt materials. This work examined the spatial distribution of physical properties such as densities and porosities of anode butts as a function of their position in the reducing pot. X-Ray Computed Tomography (X-Ray CT) was used to non-destructively study the overall structure of an anode butt. Other physical properties such as apparent density, and absolute density were directly measured. The thermal gravimetric analyzer (TGA) was used to examine the air and CO_2 reacitivities at different conditions. Alcoa Co., Ltd. provided the Inductively Coupled Plasma (ICP) analyses of different inorganic contents, e.g. sodium, fluoride, aluminum, etc. to different parts of the anode butts. Finally, attempts were made to determine the relationships among these physical and chemical properties.

The last part of this study was to examine how different pitches interact with different parts of the butt material, i.e. bath side, middle, and electrolytic side. Since these different parts of the anode butts have experienced different conditions such as different temperatures, chemical exposure, etc. These effects may cause different properties throughout the anode butt. Since a certain amount of butt materials were crushed and recycled to make a new anode, the output of this study may be used to improve the property of the anode and, hence, improve the economy of the pre-baked anode production.

2. Experimental

The experimental can be divided into three different parts: the binder pitch study, the anode butt study, and the pitch/butt study.

2.1 Binder Pitches Study

2.1.1 Materials

Four types of pitch were used in this study: two standard coal tar binder pitches (SCTP-1), a petroleum pitch (PP-1), a coal-extracted pitch (WVU-5), and a gasification pitch (GP-1). The properties of each pitch are summarized in Table 1. Petroleum coke

and recycled anode butts were crushed and aggregated into three different sizes: (i) Fines: >200 mesh size; (ii) Intermediate: 60-200 mesh size; and (iii) Coarse: <60 mesh size

Table 1 Properties of pitches.

Property	SCTP-1	SCTP-2[1]	GP-1	GP-2	PP-1[1]	WVU-4[2]	WVU-5[2]
Softening Point (°C)	112.5	111.9	115	130	111.9	127.1	112.2
Quinoline Insolubles (wt%)	13.6	15.9	<0.1	<0.1	0.1	<0.1	<0.1
Toluene Insolubles (wt%)	27.8	30.9	N.A.	N.A.	3.2	N.A.	N.A.
Coking Value (wt%)	N.A.	57.9	N.A.	N.A.	47	43.9	50.3
Ash Content (wt%)	N.A.	0.29	N.A.	N.A.	0.08	0.1	0.2
Specific Gravity @ 25°C	N.A.	1.34	N.A.	N.A.	1.246	1.2	1.25
Sulfur Content (wt%)	N.A.	0.56	N.A.	N.A.	1.21	N.A.	N.A.
Metal							
Calcium (ppm)	N.A.	49	N.A.	N.A.	5	N.A.	N.A.
Chlorine (ppm)	N.A.	18	N.A.	N.A.	15	N.A.	N.A.
Iron (ppm)	N.A.	269	N.A.	N.A.	19	N.A.	N.A.
Lead (ppm)	N.A.	38	N.A.	N.A.	N.D.	N.A.	N.A.
Nickel (ppm)	N.A.	4	N.A.	N.A.	4	N.A.	N.A.
Phosphorous (ppm)	N.A.	N.D.	N.A.	N.A.	N.D.	N.A.	N.A.
Potassium (ppm)	N.A.	39	N.A.	N.A.	2	N.A.	N.A.
Silicon (ppm)	N.A.	439	N.A.	N.A.	377	N.A.	N.A.
Sodium (ppm)	N.A.	N.D.	N.A.	N.A.	54	N.A.	N.A.
Vanadium (ppm)	N.A.	3	N.A.	N.A.	8	N.A.	N.A.
Zinc (ppm)	N.A.	80	N.A.	N.A.	0	N.A.	N.A.

N.A. = Not Available
N.D. = Not Detectable
[1] Data provided by Koppers Co., Ltd
[2] Data provided by the West Virginia University

2.1.2 Compositions of Experimental-Scale Anodes

All experimental-scale anodes in this work were made using the following compositions:

Pitch:Butt:Coke = 22:29:49

Fine:Intermediate:Coarse = 40:35:25

2.1.3 Mixing and Forming

The aggregate fillers and binders, which weighed about 15 grams in total, were mixed at about 50°C above the softening point of the pitch mixture. The CARVER cylindrical mold with an inside diameter of 28.58 mm was preheated to about 10°C above

the softening point of the pitch mixture. The hot mix was placed into the mold and rapidly pressed at 9,000 psi for 2.5 minutes. The final green anode was cylindrical in shape with typically 28.60 mm. in diameter and 13.00-14.00 mm in height.

2.1.4 Baking

The green anodes were baked with a low heating rate to about 1075°C over a period of 5-6 days prior to cooling. The temperature profile was 25°C/hr from 25°C to 125°C; 3.5°C/hr from 125 to 600°C; 100°C/hr from 600 to 1075°C; hold at the temperatures between 950 and 1075°C for 6 hours; and cool down in the furnace to room temperature.

2.1.5 Properties Measurement

The green and baked anodes were weighed to the nearest 0.001 gram and their dimensions were measured by a caliper to the nearest 0.01 millimeter. The apparent densities of both green and baked anodes were calculated by a ratio of mass and volume. The amount of pitch loss after baking was calculated by assuming that all the weight loss was resulting from the pyrolysis of pitch. Finally, the volume change of the baked anodes relative to the green ones was calculated.

2.2 Anode Butts Study

The experiments conducted using industrial anode butts, BUTT-1, BUTT-2, and BUTT-4 collected from different plants. The bath temperature was about 960°C and the pots were operated at 4.6 volts and 100,000 to 350,000 amps. The height of a new anode was 58 centimeters prior to setting in the pot and this height reduced to 18 centimeters when the butt was removed after approximately 24 days of service. Butt-2 contained recycled anode butts in the formulation of the original anode and had experienced standard operating conditions in the pot as well as a preparation for recycling. Butt-4 was

a butt from an anode that originally did not contain any recycled anode-butt material. Table 2 summarizes the conditions of these two anode butts.

Table 2 Characteristics of selected anode butts.

Anode butt code	Characteristics
Butt-1	-About 24 days of operation in the pot. -Formulation of original anode included recycled butts.
Butt-2	-About 24 days of operation in the pot. -Formulation of original anode included recycled butts.
Butt-4	-About 24 days of operation in the pot. -Formulation of original anode did not included recycled butts.

The samples used in this study were cored from the center of the butts (core #5) and had approximately 51 millimeters O.D. These samples were first scanned with the X-Ray CT scanner using a large focal spot source at 200 kV. X-Ray Tomography (CT) is a non-destructive method for obtaining three-dimensional attenuations of an object. The attenuation maps depend on bulk density and apparent atomic number of the material. With proper calibration the distribution of parameters such as density, porosity, and composition can be acquired. Samples shorter than 150 millimeters were scanned parallel to the axial axis of the sample with a resolution of about 400 microns. Samples longer than 150 millimeters were scanned perpendicular to the axial axis with a resolution of about 300 microns.

The middle core of each anode butt (see Figure 1), namely Core #5, was sliced perpendicular to the axial axis into sections approximately 5 millimeters thick. Different names were given to call each slice of the core, i.e. T1, T2, T3, …, M1, M2, M3,…, B4, B3, B2, B1, as shown in Figure 2. T1 represents the most top and B1 represents the most bottom of the core. The diameter and thickness of each slice were measured to the nearest 0.01-millimeter by a Caliper. The weight of each slice was measured to the nearest 0.0001 gram. The apparent density (ρ_{app}) was calculated by the ratio of mass and volume. Each slice was later cracked into smaller pieces approximately 1-3 grams. About 5-6 grams of sample were weighed to the nearest 0.0001-gram and the absolute volume was performed by a Helium substitution using the Quantachrome

Multipcynometer. The absolute density (ρ_{abs}) was calculated by the ratio of mass and volume. The specific pore volume (v_P) was calculated by

$$v_P = \frac{1}{\rho_{App}} - \frac{1}{\rho_{abs}} \qquad \text{Equation (1)}$$

Parts of each slice of the anode butt Core #5 were sent to Alcoa Co., Ltd to perform the ICP analyses to measure the concentrations of inorganic materials, e.g. sodium, fluoride, aluminum, etc. of each section of the butt core. Only Butt-2 was used in the thermal analyses. The leftover materials from the ICP analyses of each slice were crushed to pass a 200-mesh size screen. About 9-11 mg of the +200 mesh size of each slice was used in a thermal gravimetric study. Separate tests were done to ensure that the particle size and the amount of the sample for a TGA run were appropriate to eliminate the effect of mass transfer throughout the sample bed. Three TG analyses were performed: (1) non-isothermal air reactivity from the room temperature to 800°C at 10°C/min; (2) isothermal air reactivity at approximately 500°C; and (3) isothermal CO_2 reactivity at approximately 960°C. The experimental procedures of this part of the study were schematically summarized in Figure 3

A simple and systematic reactivity test was developed by Jenkins et al. [6]. In this work, about 9-11 mg of sample was placed in a TGA apparatus and heated the sample up at 50°C/min to the target temperature with dry nitrogen at a rate of 100 cm^3/min. After the temperature was stabilized at the target temperature, dry air or CO_2 was introduced isothermally at a rate of 100 cm^3/min. The weight loss of the sample was continuously recorded. Typically, the burn-off (versus time) curve exhibited a rectilinear part over a period of about 40% of the char that was gasified [6] (see Figure 24), and followed by a decrease in slope. A maximum reactivity was observed in this rectilinear region and was calculated by

$$R_{\max} = -\frac{1}{m_C}\frac{dm_C}{dt} \qquad \text{Equation (2)}$$

where R_{max} is a maximum reactivity at a desired temperature (mg h^{-1} mg^{-1}), m_C is the initial mass of char on an ash-free basis (mg). dm_C/dt is the maximum weight loss rate (mg h^{-1}) or the slope of the burn-off versus time. The reactivity (Equation (2)) also can be written in term of the conversion, $X_C = \frac{m_{c0} - m_c}{m_{c0}}$, as follows:

$$R = \frac{1}{1 - X_C}\frac{dX_C}{dt} = kC_C \qquad \text{Equation (3)}$$

The burn-off versus time plot can be normalized using a dimensionless time scale, i.e. $t/\tau_{0.5}$, where $\tau_{0.5}$ is the time at a fractional burn-off of 0.5 [7]. The typical shape for most chars derived from coals of a wide range of ranks exhibit similar shapes of the burn-off versus $t/\tau_{0.5}$. However, this normalized burn-off curve is not sufficient to offer the 'characteristic' shape for all type of cokes because of the complexity of the char gasification reactions. The initial slow increase in the slope of the TGA plot is due to the opening of closed pores and enlarging of existing pores to increase the accessibility of reactant gas during the induction period. The slope increases as burn-off increases until a maximum is reached. Then the slope starts to decline, slowly decreasing to complete burn-off. The decrease in slope results from decreases of amount of gasifiable material and from lower reactive area due to the coalescence of pores as burn-off proceeds.

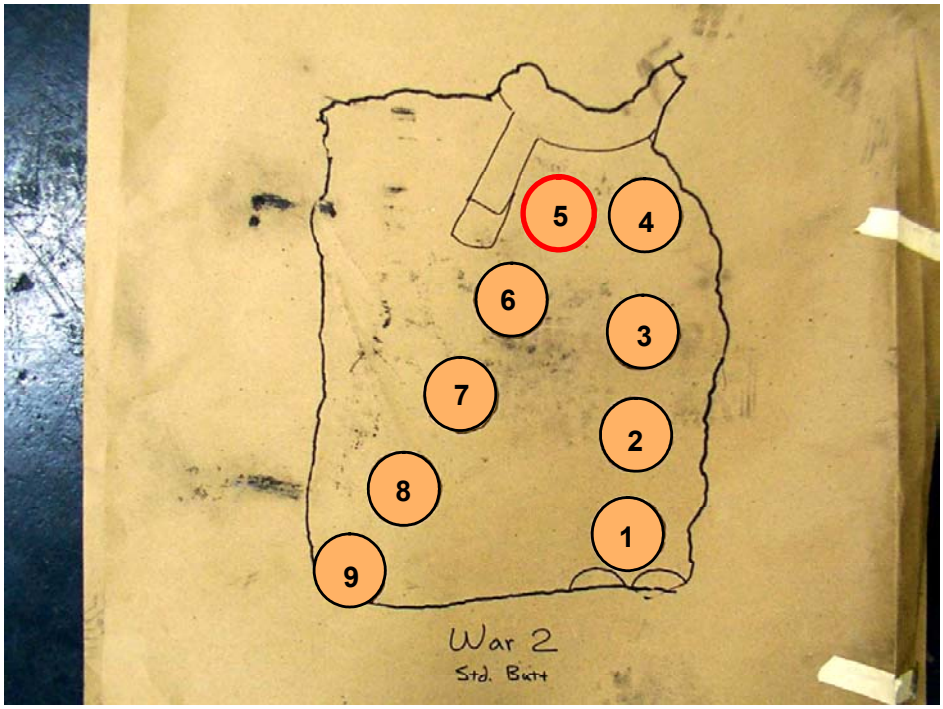

Figure 1 Position of the Core #5 in the anode butt.

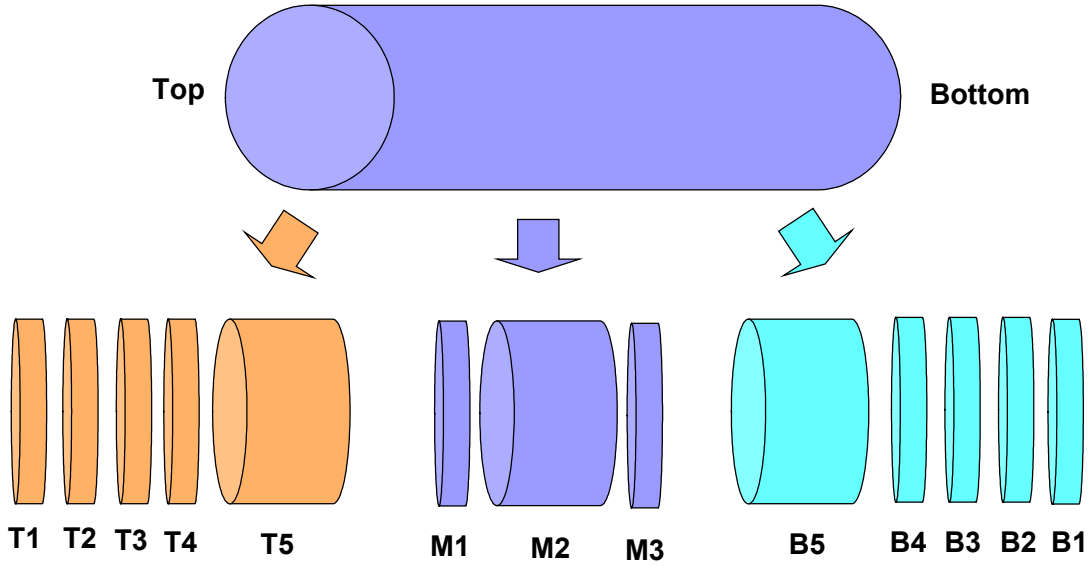

Figure 2 Names of different slices of the cut anode butt.

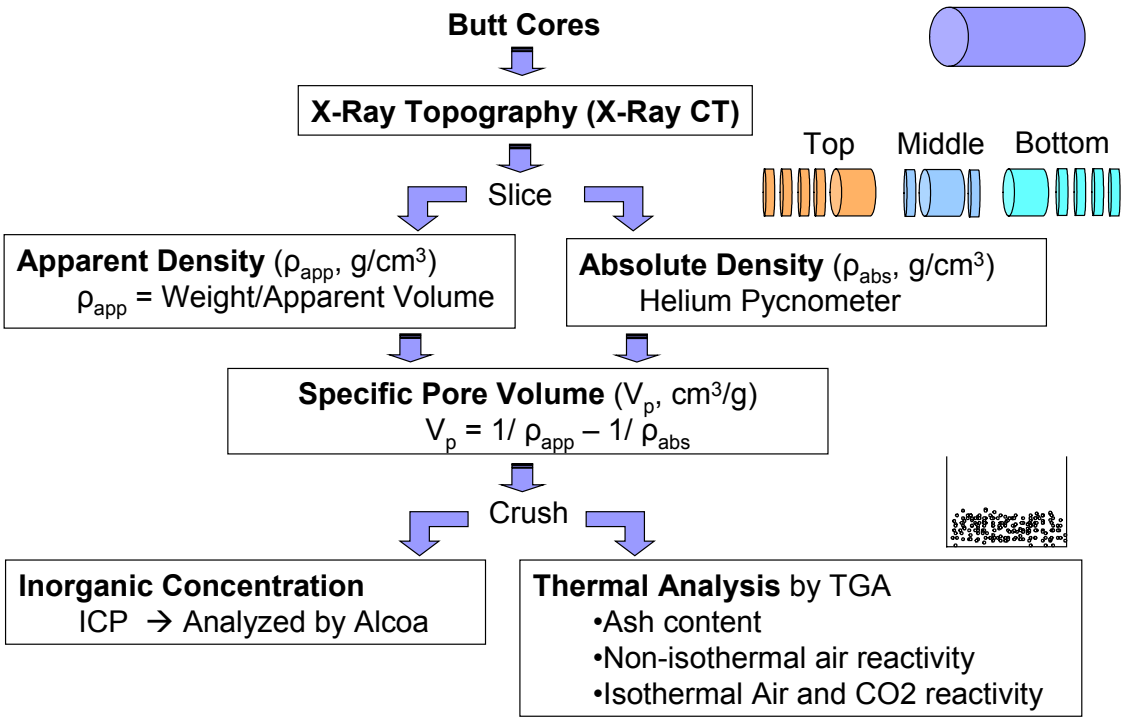

Figure 3 Experimental procedure.

2.3 Pitches/Butts Study

In this part of the study, the procedures of making a laboratory-scale anode and the property measurement of the anode were the same as described in Section 2.1. The pitch:coke:butt ratio remained the same, i.e. 22:49:29. However, there were some minor changes in the material used in the compositions of the anode as follows:

2.3.1 Pitch

Since the limited amount of the SCTP-1, which was used in the study of pitches in Section 2.1, the SCTP-2 was used instead and its property is shown in Table 1. Four different compositions of pitch mixture were used to make the laboratory-scale anodes: (1) 100% SCTP-2; (2) 20% PP-1 and 80% SCTP-2; (3) 20% WVU-5 and 80% SCTP-2; and (4) 20% GP-1 and 80% SCTP-2. All percentages are in weight basis. 20% of the

alternative pitches were used because it was shown in the pitches study (see Section 3.1) that up to 50% of the alternative pitch may be added to balance the SCTP to give comparable properties of the laboratory-scale anode made by only SCTP.

2.3.2 Coke

The same ratio and coke materials were used as those laboratory-scale anodes made in Section 2.1.1 and 2.1.2.

2.3.3 Butt materials

Because of the limited amount of butt material obtained from the Butt-2 Core #5 from the anode butts study in Section 2.2, Butt-2 Core #3 was employed in this study. Core #3 was sliced into different sections as shown in Figure 2. Only the most top (T1), middle (M1), and the most bottom (B1) were crushed to fine, intermediate and coarse sizes. Each part of the butt materials, i.e. T1, M1, and B1, was mixed with coke and pitch mixture. Hence four experimental anodes were made from each of T1, M1, or B1, i.e. (1) 100% SCTP-2; (2) 20% PP-1 and 80% SCTP-2; (3) 20% GP-1 and 80% SCTP-2; and (4) 20% WVU-5 and 80% SCTP-2.

3. Results and Discussion

3.1 Binder Pitches Study

In this study, three different alternative pitch sources were investigated, namely gasification pitch (GP-1 and –2), petroleum pitch (PP-1), and coal-extracted pitch (WVU 4 and –5). Each type of pitch was mixed with the standard coal tar pitch (SCTP) at various percentages while maintaining the total pitch content of 22 wt%. Because of a limited amount of SCTP, two samples of SCTP, namely, SCTP-1 and –2, were used. Both SCTPs have a comparable softening point; however, the SCTP-2 has a slightly higher QI and TI than the SCTP-1 as shown in Table 1. Figure 4 to Figure 8 show the apparent and baked densities of the green and baked anodes, %pitch loss and %volume

change of the experimental-scale anodes of the SCTP-1 + GP-1, SCTP-1 + GP-2, SCTP-2 + PP-1, SCTP-2 + WVU-4, and SCTP-2 + WVU-5 mixtures, respectively.

The experimental-scale anodes made from SCTP-1 and -2 gave slightly different green and baked densities, however, the SCTP-1 gave quite lower pitch loss and volume change after baking than the SCTP-2. The higher in pitch loss and volume change after baking of the SCTP-2 might cause by a higher QI in this pitch than the SCTP-1. The higher QI fraction could give rise to the alpha resin fraction in pitch. The alpha resins consist of two subdivisions: the fine spherical materials (typically below 2 μm in diameter) and the mesophase generated by the alpha-resins. The former has favorable properties and gives a better anode because it has a higher carbon to hydrogen ratio (between 3.5 and 4) which causes the pitch not to undergo excessive swelling and the fine particles could fill up the pores. On the other hand, the mesophase is large in the particle size (up to 80 μm) and has a carbon to hydrogen ration between 3.5 to 4. These characteristics inhibit the pitch to fill in the finer pores and also cause a higher swelling. Consequently, a pitch that contains more proportion of the mesophase gives more swelling and a lower apparent density in a baked anode [5]. However, the chemistry of pitches is not in the scope of this study. A further investigation will be needed to understand the causes of these results.

Table 3 A comparison of the properties of green and baked experimental-scale anodes made from SCTP-1 and SCTP-2.

Properties	Experimental Anodes Made from	
	SCTP-1 (QI =13.6%)	SCTP-2 (QI = 15.9%)
Green Apparent Density (g/cm^3)	1.695±0.03	1.719±0.0002
Baked Apparent Density (g/cm^3)	1.589±0.03	1.542±0.003
% Pitch Loss	28.14±4.38	33.8±0.1
% Volume Change	0.03±2.89	3.2±0.2

The results of this section can be divided into two parts: the discussion of the softening point effect and the effect of adding alternative pitches. Since GP and WVU

studied here have two different softening points, i.e. the softening point of GP-1 and WVU-5 is about 110-115°C and it is about 126-130°C for GP-2 and WVU-4 (See Table 1). It is worth discussing the effect of higher softening point pitches here. A comparison between GP-1 and GP-2 and between WVU-4 and WVU-5 shows that the higher softening point pitches give poorer properties to the anodes, i.e. slightly lower green apparent density, significant lower baked apparent density, significant higher pitch loss and higher volume change after baking. Factors that affect the anode properties from different softening point pitches are the mixing temperature and the chemistry of pitch itself. The mixing temperature directly affects the wettability between pitch and coke. However, a comparison between the green apparent densities between Figure 4(a) and Figure 5(a) for GP and between Figure 7(a) and Figure 8(a) for WVU pitches shows that the mixing temperature is only a minor effect to the anode quality. Pitches with higher softening point only gave slightly lower green apparent density anodes than those made from the lower softening point pitches. Both higher softening point GP and WVU pitches gave a significant reduction in baked apparent density as compared to the pitches with lower softening point. These results are due to the higher in pitch loss after baking of these higher softening point pitches. This effect may cause by the chemistry of pitches. The effect of QI is not the reason here since both low and high softening point GP and WVU pitches did not contain a significant amount of QI. Other chemistry of pitches drove these results. Again, it is worth in the future studying the pitch chemistry to develop knowledge of this field.

The effect of adding alternative pitches to the apparent densities of the green and baked laboratory-scale anodes is shown in Figures 4(a), 5(a), 6(a), 7(a), and 8(a) for GP-1, GP-2, PP-1, WVU-4, and WVU-5, respectively. The apparent densities of the green anodes made from a mixture of SCTP and the alternative pitch are quite similar to those when the SCTP was used only. However, this trend does not keep up for the apparent baked densities. The more ratio of the alternative pitch to the SCTP, the more decrease in the apparent densities for all alternative pitches except PP-1. The addition of PP-1 gives an improvement in apparent densities for both green and baked anodes (Figure 6(a)). The main factor for the reduction in baked density is due to the increase in loss of binder

during baking as shown in Figures 4(b), 5(b), 6(b), 7(b) and 8(b). The pitch loss is defined as a reduction in anode weights before and after baking over the initial pitch content (22%) since the weight loss of the coke material can be neglected. The addition of GP and WVU to the SCTP tends to give higher pitch loss than the PP. Also, for all SCTP + alternative pitch studied here, the addition of the alternative pitch more likely gives a lower volume change of the baked anodes as compared to the baked anodes with SCTP only as shown in Figures 4(c), 5(c), 6(c), 7(c), and 8(c).

The reason of the high loss of pitch content in the anodes with higher alternative pitch concentration may result from the lack of QI as well as the difference in molecular composition. The QI plays a very important role in how pitches perform excellent binder functions, i.e. wetting and penetrating petroleum coke particles during mixing and forming, and bridging between pitch-coke particles during baking [4]. Although the importance of QI is well established, the optimum amount of QI in binder pitch is still not clear [4]. Because pure alternative pitches give comparable or higher green apparent density, it can be hypothesized that these pitches wet and penetrate petroleum coke well but they lack of a capability to prevent pitch from escaping the inter- and intra-pores. However, these alternative pitches need to be optimized in terms of pitch loss prior to commercial interest.

Of all pitch mixtures studied here, the addition of an alternative pitch shows quite similar trends, i.e. SCTP gives a lower pitch loss and higher volume change compared to the pure alternative pitches. Among all three alternative pitches, the addition of WVU and GP shows poorer properties of the anodes among all three mixtures, i.e. high pitch loss and low baked densities, while the addition of PP-1 shows little impact on the properties of the anodes for most SCTP-PP-1 compositions. The addition of GP and WVU also gives comparable anode properties when the SCTP:WVU/GP ratio is greater than 50:50. The comparison of the properties of the anode made from 20-25% and 50% alternative pitches and those made from 100% SCTP-1 and –2 is shown in Figure 9 and Figure 10 for the apparent density, Figure 11 for the pitch loss and Figure 12 for the volume change after baking.

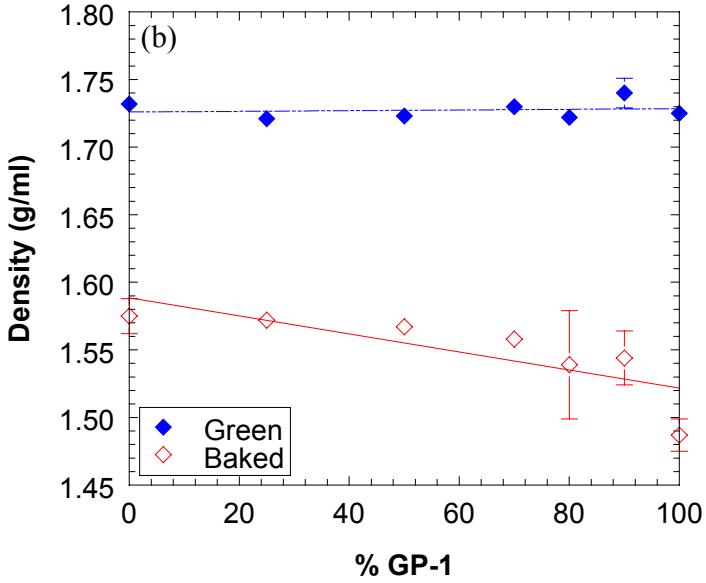

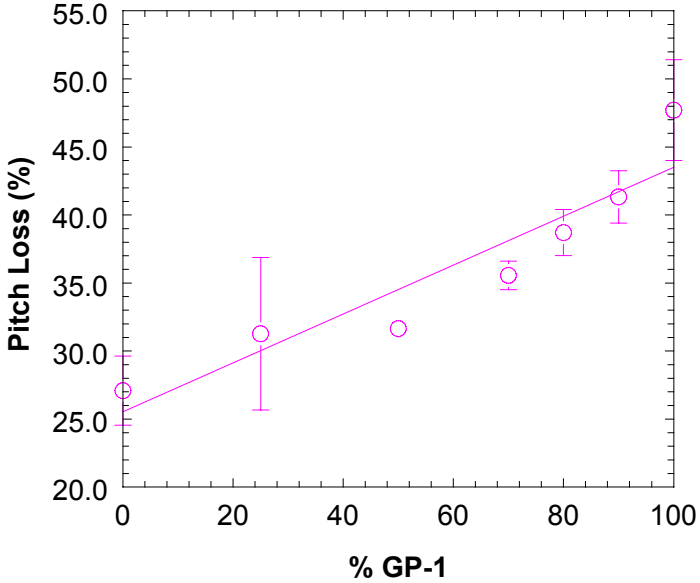

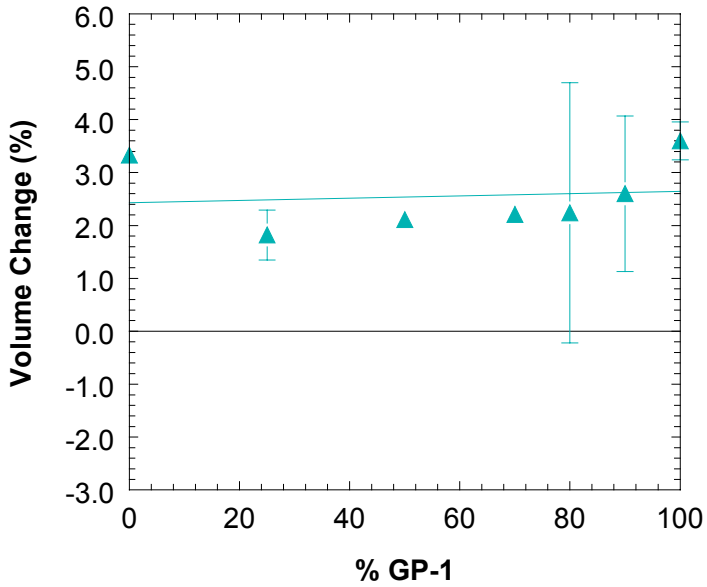

Figure 4 Properties of green and baked anodes prepared by using different pitches compositions varying from 0% GP-1 (or 100% SCTP-1) to 100% GP-1 (or 0% SCTP-1): (a) Apparent densities of green and baked anodes; (b) Percentages of pitch loss after baked; (c) Percentages of volume change after baked. The error bars show the standard deviations of each experimental set. The dashed lines show the linear relationship of the mixtures

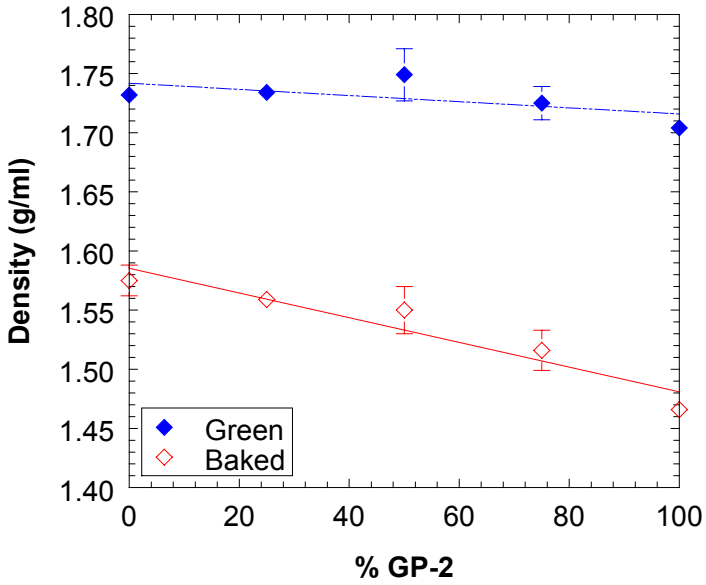

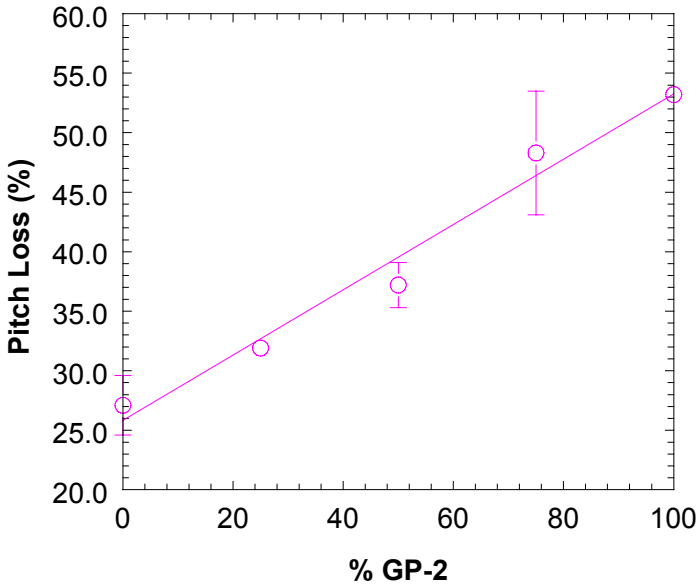

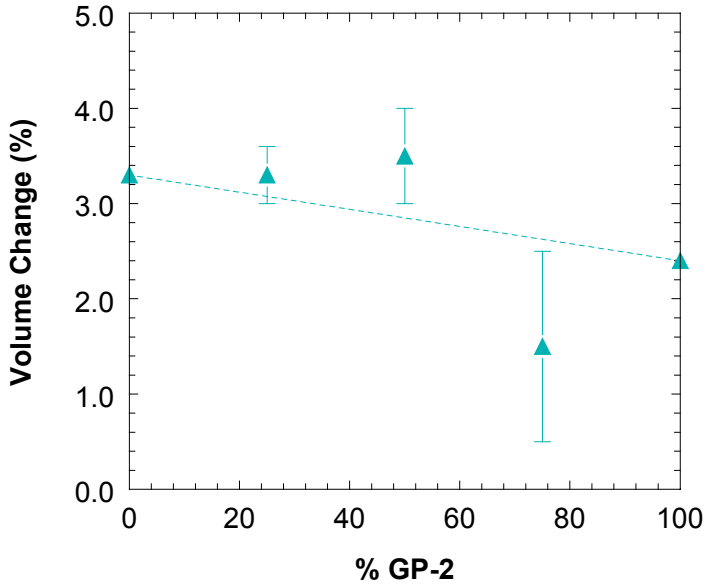

Figure 5 Properties of green and baked anodes prepared by using different pitches compositions varying from 0% GP-2 (or 100% SCTP-1) to 100% GP-2 (or 0% SCTP-1): (a) Apparent densities of green and baked anodes; (b) Percentages of pitch loss after baked; (c) Percentages of volume change after baked. The error bars show the standard deviations of each experimental set. The dashed lines show the linear relationship of the mixtures

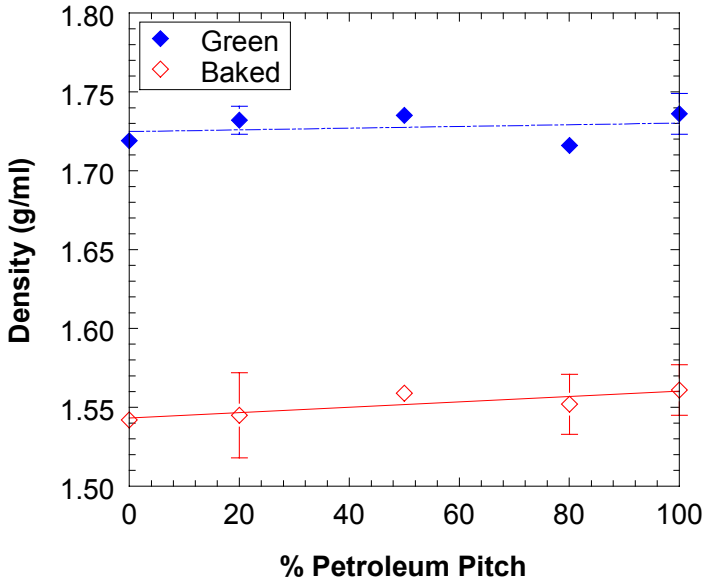

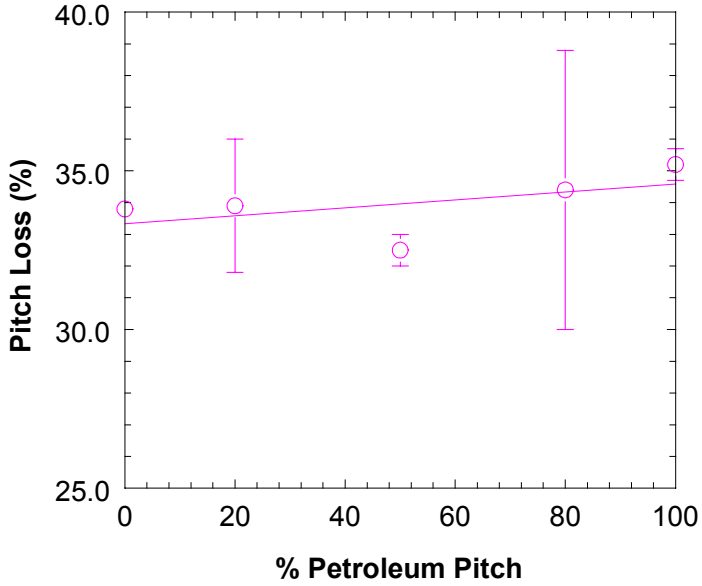

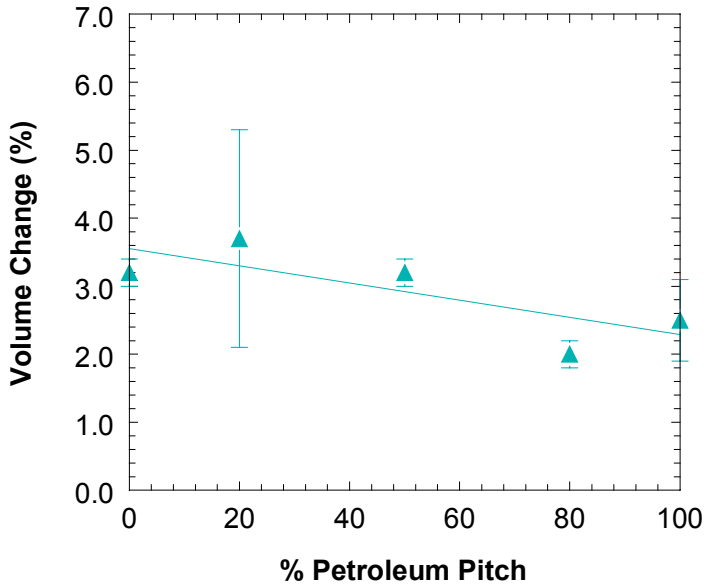

Figure 6 Properties of green and baked anodes prepared by using different pitches compositions varying from 0% PP-1 (or 100% SCTP-2) to 100% PP-1 (or 0% SCTP-2): (a) Apparent densities of green and baked anodes; (b) Percentages of pitch loss after baked; (c) Percentages of volume change after baked. The error bars show the standard deviations of each experimental set. The dashed lines show the linear relationship of the mixtures.

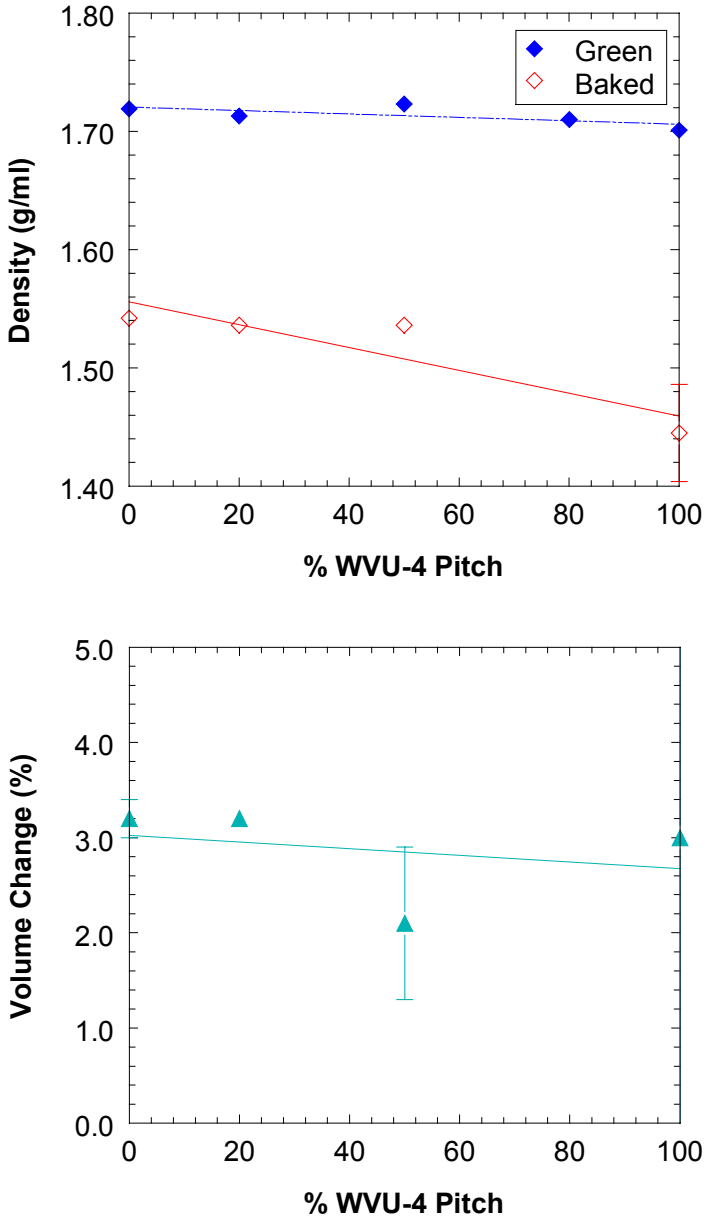

Figure 7 Properties of green and baked anodes prepared by using different pitches compositions varying from 0% WVU-4 (or 100% SCTP-2) to 100% WVU-4 (or 0% SCTP-2): (a) Apparent densities of green and baked anodes; (b) Percentages of pitch loss after baked; (c) Percentages of volume change after baked. The error bars show the standard deviations of each experimental set. The dashed lines show the linear relationship of the mixtures.

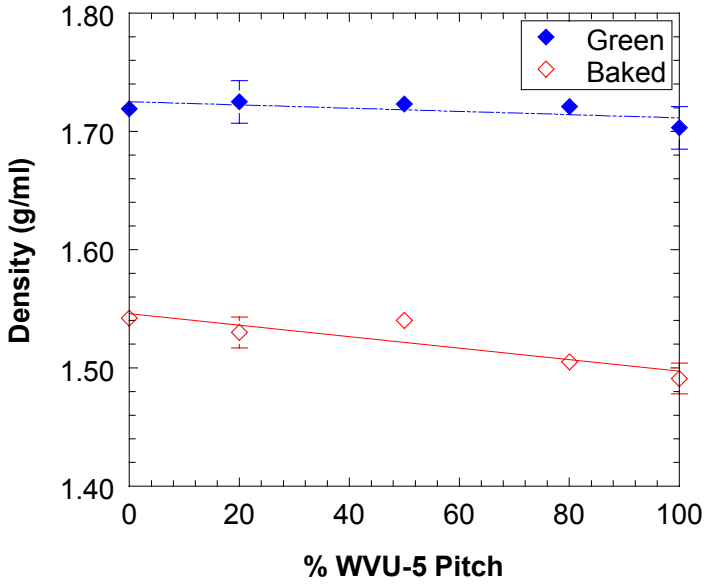

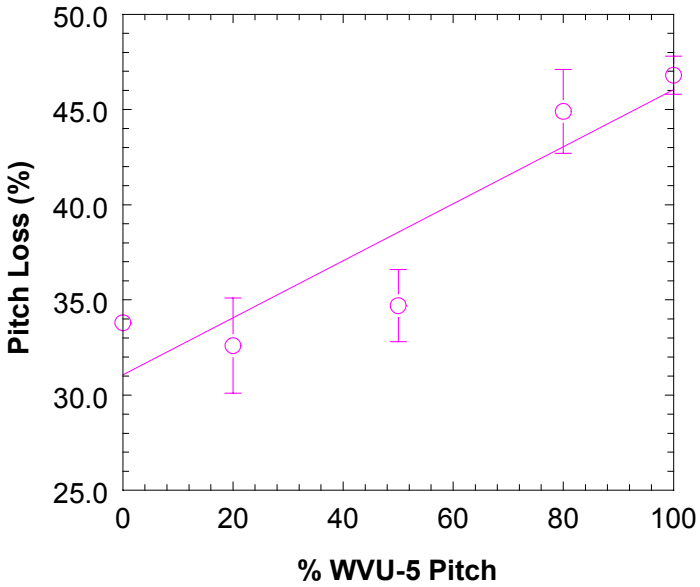

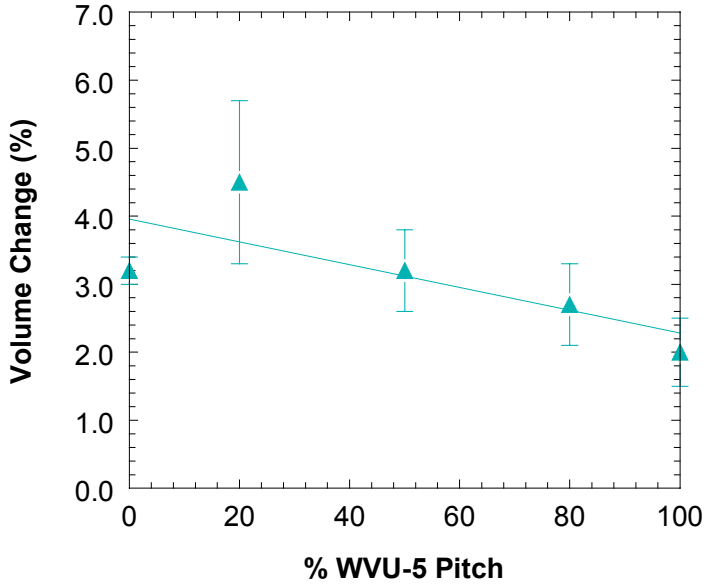

Figure 8 Properties of green and baked anodes prepared by using different pitches compositions varying from 0% WVU-5 (or 100% SCTP-1) to 100% WVU-5 (or 0% SCTP-1): (a) Apparent densities of green and baked anodes; (b) Percentages of pitch loss after baked; (c) Percentages of volume change after baked. The error bars show the standard deviations of each experimental set. The dashed lines show the linear relationship of the mixtures.

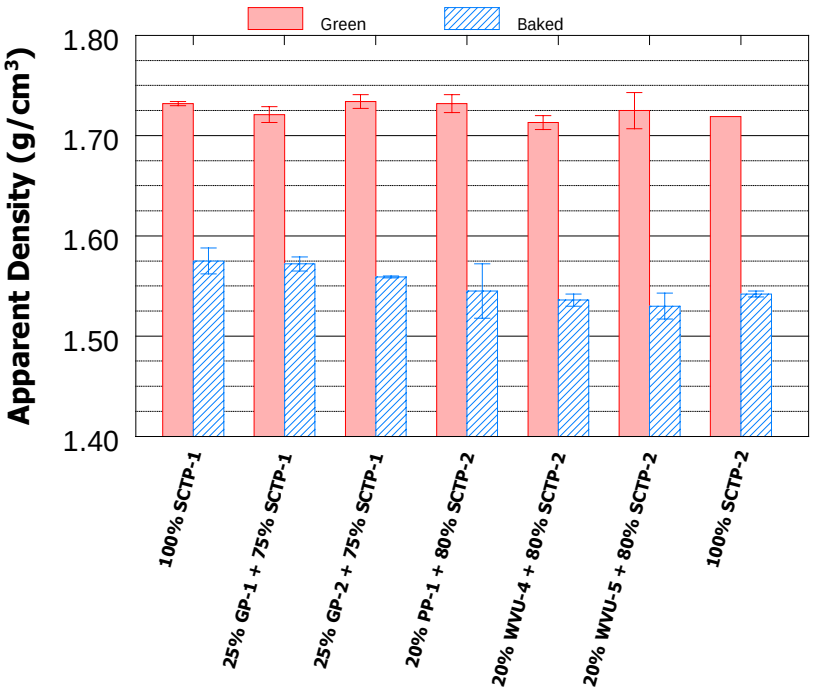

Figure 9 Green and baked apparent densities of the experimental-scale anodes made from 20-25 %wt alternative pitch (GP-1, -2, PP-1, WVU-4, and –5) as compared to the anodes made from 100% SCTP-1 and –2.

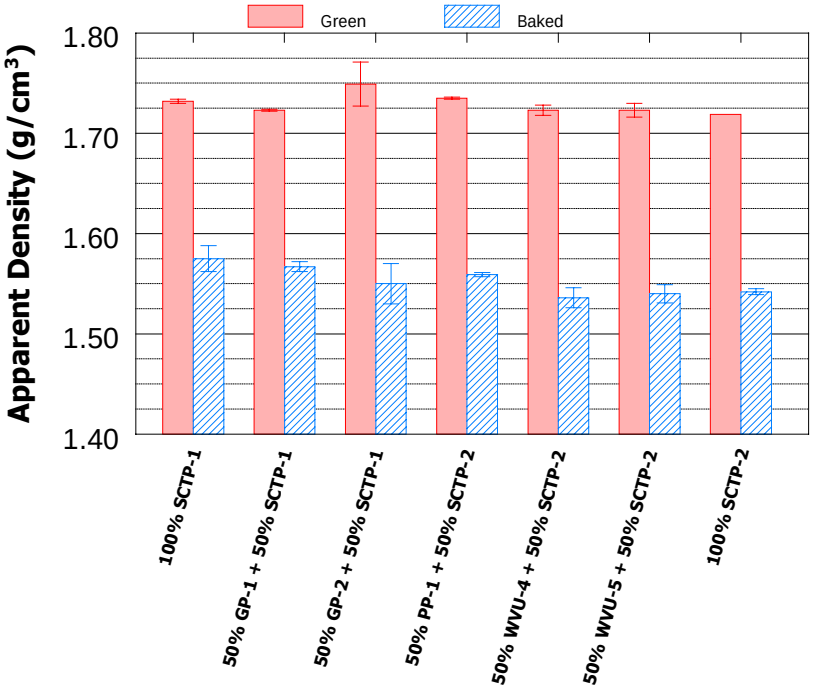

Figure 10 Green and baked apparent densities of the experimental-scale anodes made from 50 %wt alternative pitch (GP-1, -2, PP-1, WVU-4, and –5) as compared to the anodes made from 100% SCTP-1 and –2.

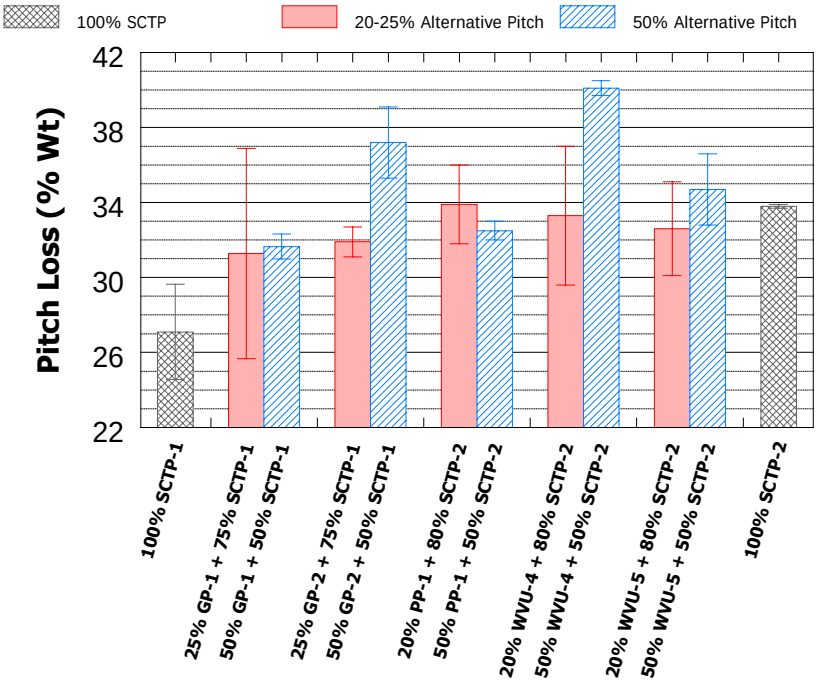

Figure 11 Percentages of pitch loss of the experimental-scale anodes made from 20-25 %wt and 50 %wt alternative pitch (GP-1, -2, PP-1, WVU-4, and –5) as compared to the anodes made from 100% SCTP-1 and –2.

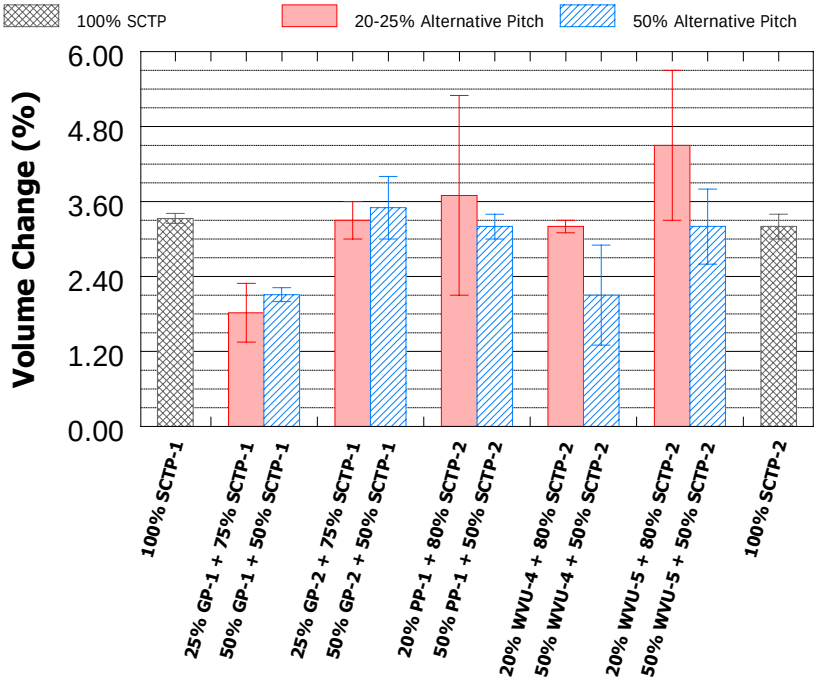

Figure 12 Volume changes of the experimental-scale anodes made from 20-25 %wt and 50 %wt alternative pitch (GP-1, -2, PP-1, WVU-4, and –5) as compared to the anodes made from 100% SCTP-1 and –2.

3.2 Anode Butts Study

3.2.1 X-Ray CT and Physical Properties Results

The X-Ray CT of all the anode butt samples received from the Alcoa Co., Ltd. was shown in our previous report [8]. In this final report, we focus on the physical and chemical properties of the anode butts as a function of distance from the airburn side. Only the Core #5 of Butt-1, -2, and -4 were studied. The tested properties are apparent density, absolute density, specific pore volume, chemical analyses, ash content, and air and CO_2 reactivities. The chemical analyses were performed by the Alcoa Co., Ltd using the ICP technique. The other tests were performed by the Energy Institute, PSU.

Three radial CT slices—the airburn end, middle, and electrolytic end—of Butt-1, and Butt-4 samples, and an axial slice of Butt-2 sample are shown in Figure 13(a), Figure 14(a), and Figure 15(a), respectively. The variation in density and rough heterogeneities are seen throughout the sample. A brighter color at the electrolytic end shows a higher density of the carbon material compared to a darker color at the rest of the core. This indicates a densification of the structure of the carbon that has been in contact with the electrolytic bath. A slightly lighter color at the airburn end of the anode butt shows a higher density of the carbon material that has experienced the air burn-off. The black spots indicate that various sizes of pores are distributed throughout the butt samples.

The results from the CT scanning agree quite well with the absolute density as shown as a function of distance from the airburn side for all three butts (Figure 13 (b) for Butt-1, Figure 14(b) for Butt-2, and Figure 15(b) for Butt-4). All anode butts tend to follow the same patterns in terms of physical properties. The absolute densities are higher at both ends and are quite uniform at the middle, while the apparent densities are quite lower at both ends and perform uniformly at the center. As a result, the calculated specific pore volumes, as calculated by Equation (1), are higher at both ends and quite uniform at the middle of the anode butt. From these results, the CT observation is an effective tool to non-destructively analyze the physical properties of an object. However, the axial axis scanning shown here does not properly relate the pore distribution to the

apparent density and the specific pore volume. This relationship is clearly explained in Figure 13(a) and Figure 15(a) where Butt-1 and –4, respectively, were scanned perpendicular to the axial axis. Three CT slices are shown: airburn side, middle, and electrolytic side. The airburn side (left) shows high porosity (dark spots) which the electrolytic end (right) shows high density and low porosity. The CT observation are confirmed by the apparent and absolute densities measurements and the calculation of the specific pore volumes as shown in Figures (b), (c), and (d), respectively, of Figure 13 for Butt-1 and Figure 15 for Butt-4.

All Butt-1, -2 and -4 gave similar results in terms of physical properties throughout the cores, where both anode butts exhibited a major change in densities and pore volume at a distance about 20 millimeters from both airburn and electrolytic ends. The apparent density is quite uniform at the center and decreases toward both airburn and electrolytic ends. The absolute density also exhibits quite uniformly at the center, and increases toward both ends, however. This contradiction between the apparent and absolute densities is seen by an increase in specific pore volume from uniform values at the center to higher values at both ends. The results obtained in this study were similar to those obtained by Cutshall and Bullough [9] who observed a decrease in apparent density and an increase in porosity from the center of the core to the electrolytic surface. The high density sites associated with the large porosity at both ends indicates the connection of these properties to the reactions occurred at the airburn and the electrolytic ends.

Butt-4 shows slightly lower apparent and absolute densities than Butt-1 and -2 since Butt-4 did not contain recycled butt material. Butt-4 also shows a significantly higher specific pore volume at the airburn side and a lower specific pore volume at the electrolytic side, indicating a high reactivity with air from the anode butt. These results indicate that Butt-4 has a higher reactivity with CO_2 than the anode butt which originally contained recycled butt material. The observation discussed here confirmed previous results that sodium content greatly promotes CO_2 reactivity and may be assigned to variations in anode consumption rates [10, 11].

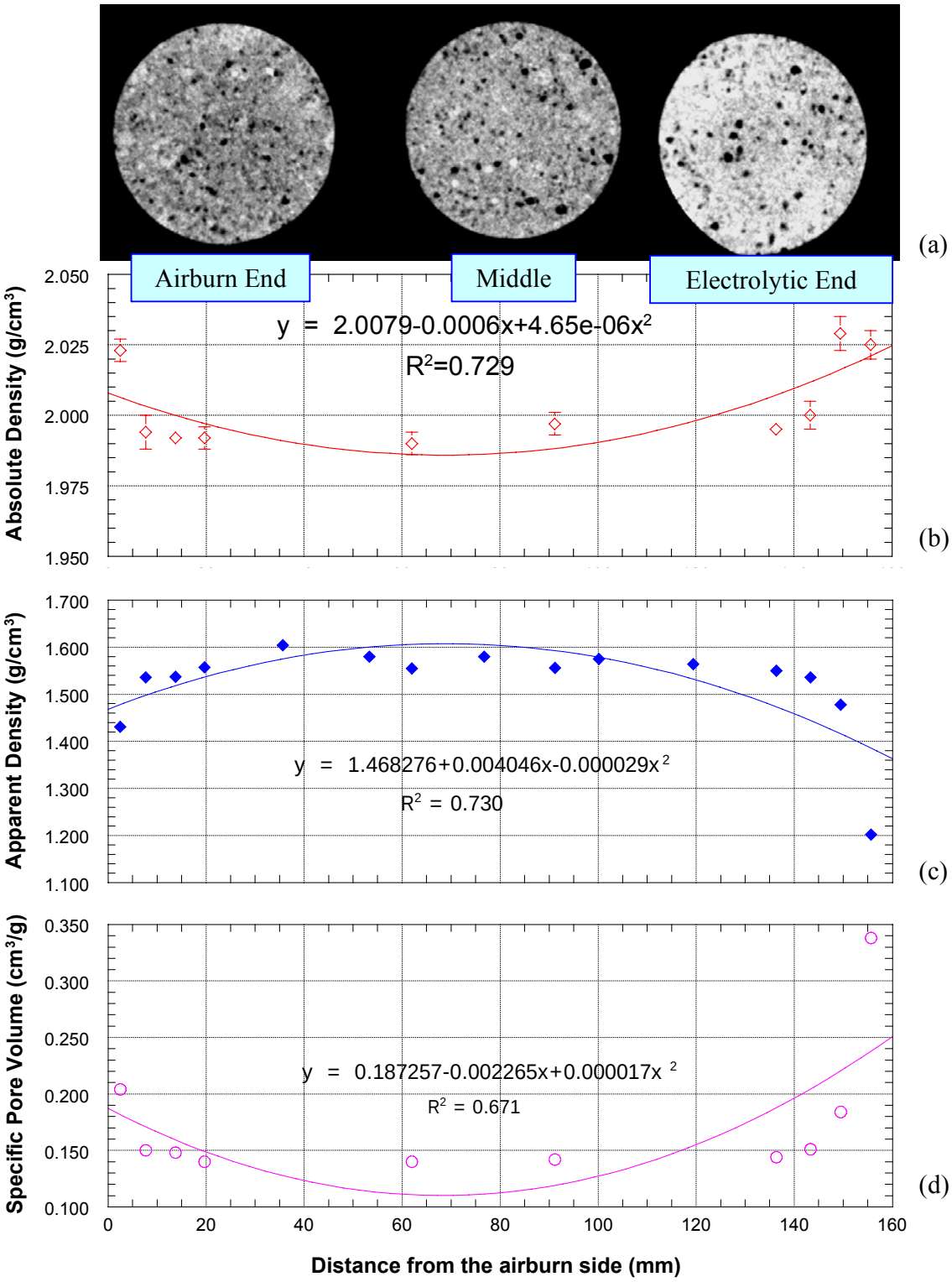

Figure 13 (a) Radial scanning of the X-Ray CT with the same intensity color maps, (b) absolute density (◇), (c) apparent density (◆), and (d) specific pore volume (○) of the Butt-1 Core #5 at different distance from the airburn side. The solid lines show the polynomial relationship of these properties with the distance from the airburn side.

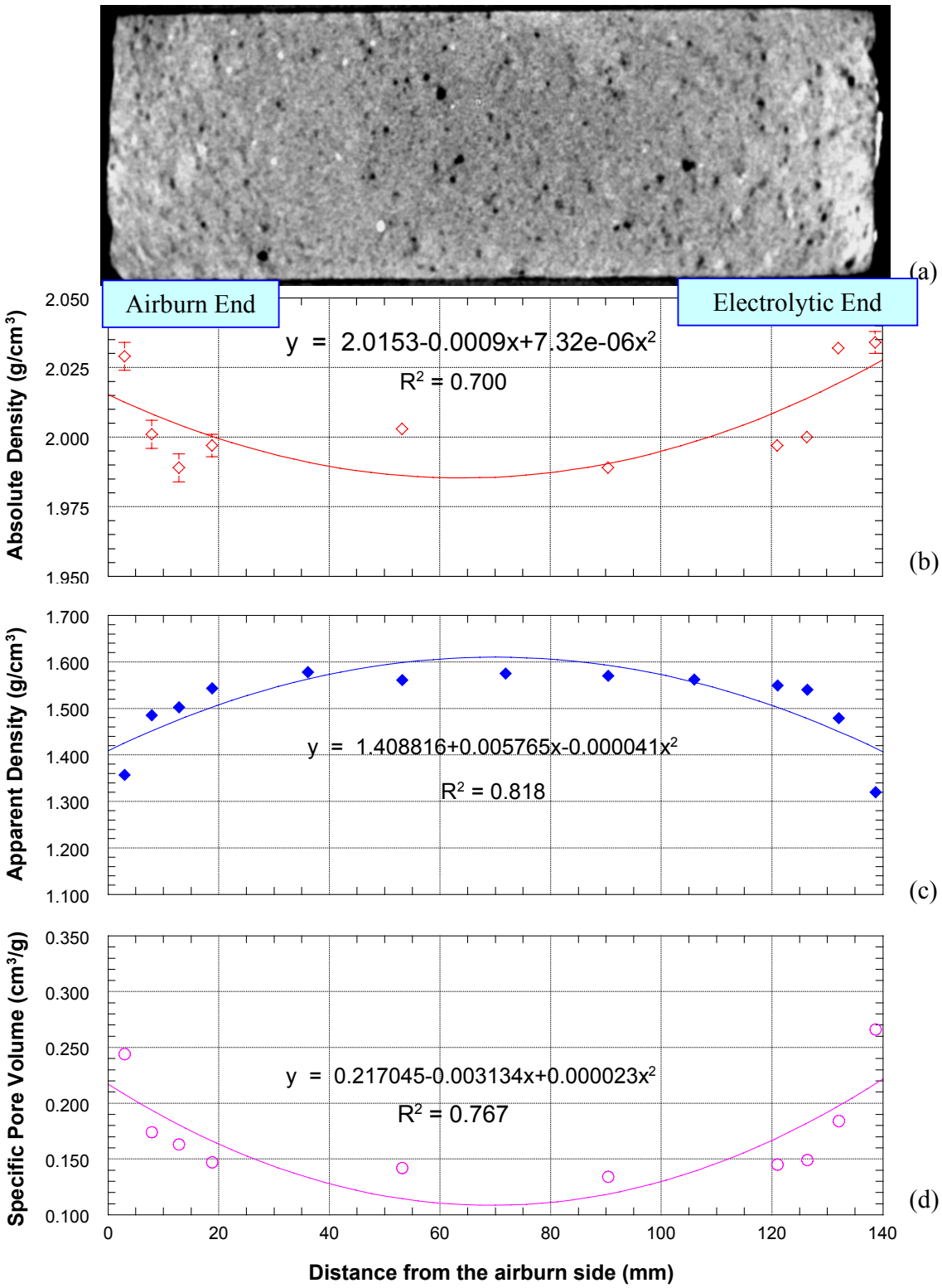

Figure 14 (a) Axial scanning of the X-Ray CT with the same intensity color maps, (b) absolute density (◇), (c) apparent density (◆), and (d) specific pore volume (○) of the Butt-2 Core #5 at different distance from the airburn side. The solid lines show the polynomial relationship of these properties with the distance from the airburn side.

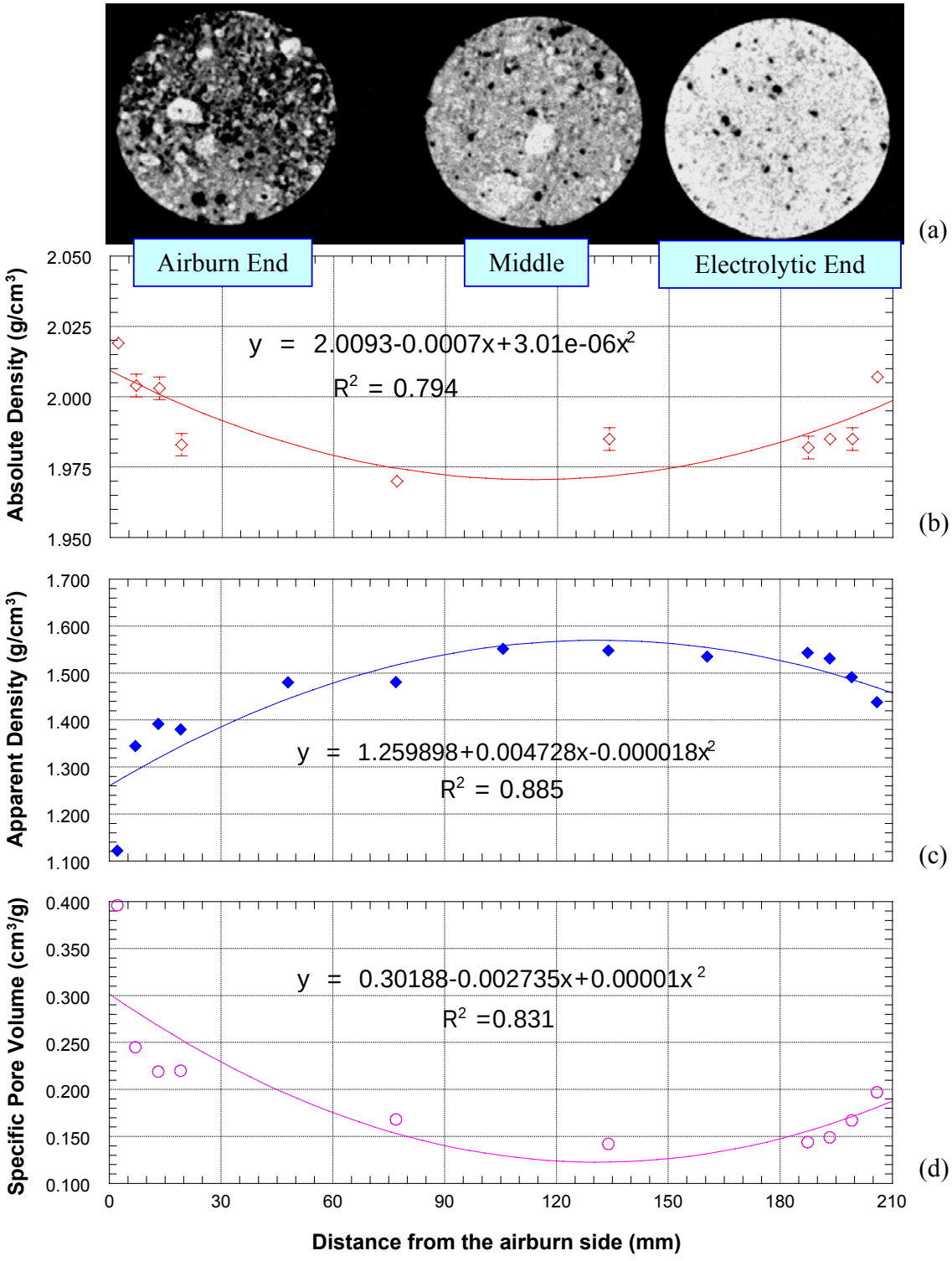

Figure 15 (a) Radial scanning of the X-Ray CT with the same intensity color maps, (b) absolute density (◇), (c) apparent density (◆), and (d) specific pore volume (○) of the Butt-4 Core #5 at different distance from the airburn side. The solid lines show the polynomial relationship of these properties with the distance from the airburn side.

3.2.2 Chemical Analyses

The chemical analyses of Butt-1 and -2 were performed using ICP technique and Butt-4 by the ICP/MS technique by Alcoa Co., Ltd. Figure 16, Figure 17(a), and Figure 18 show the ICP results of Butt-1, -2, and -4, respectively. All anode butts exhibit similar results. As shown by a comparison Figure 19, the most top butt material (T1) contains more inorganic contents than the butt material from the middle and the most bottom (B1). Only aluminum, sodium and fluoride were analyzed in Butt-1, and -2. Fluoride content appears to be the highest concentration and follows by sodium and aluminum, respectively, for both anode butts. Various types of inorganic matters except fluoride were analyzed in Butt-4 as shown in Figure 18. Among T1, M3 and B1 samples, T1 contains the highest concentration for most inorganic contents presented here. Iron content in this sample is very high especially in the T1 sample, i.e. 2700 ppm. B1 and M3 also contain rather high iron content, i.e. 420 and 340 ppm, respectively. Other major inorganic contents are sulfur, sodium, aluminum and calcium. It has been shown that the presence of inorganic contents can enhance the reactivity of chars under oxidation [12]. Walker et al. [12] summarized that the reactivity of chars (or cokes) made from lignites in CO_2 and air followed same order as followed: Na > K > Ca. Iron appeared to be less reactive than the raw chars. Since T1 contains rather higher sodium and calcium than M3 and B1, it can be presumed that T1 would exhibit a fairly higher reactivity in both CO_2 and air than the rest of the butt samples. Although the GC/MS was not performed in Butts -1 and -2, the amount of inorganic contents in these two butts should not be very different than what have been shown in Butt-4.

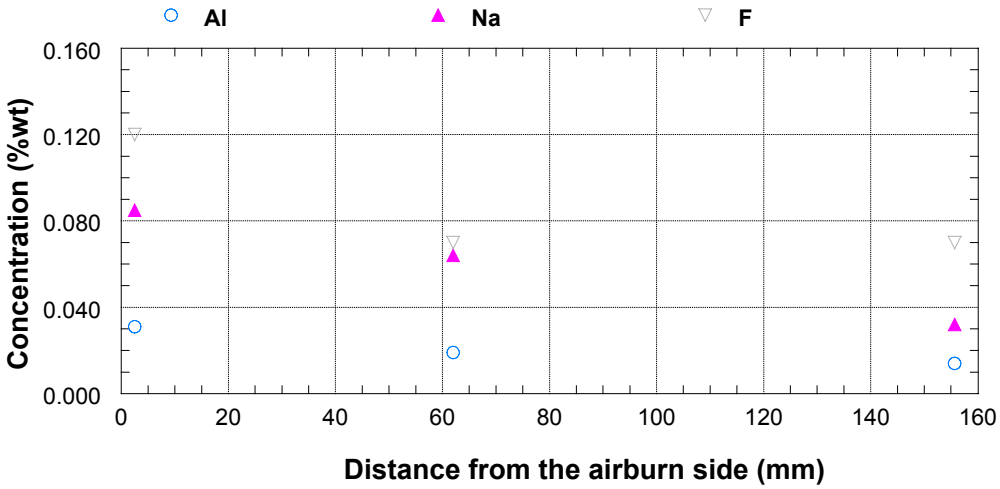

Figure 16 Concentration of aluminum, sodium and fluoride at different positions from the airburn side of Butt-1 Core #5.

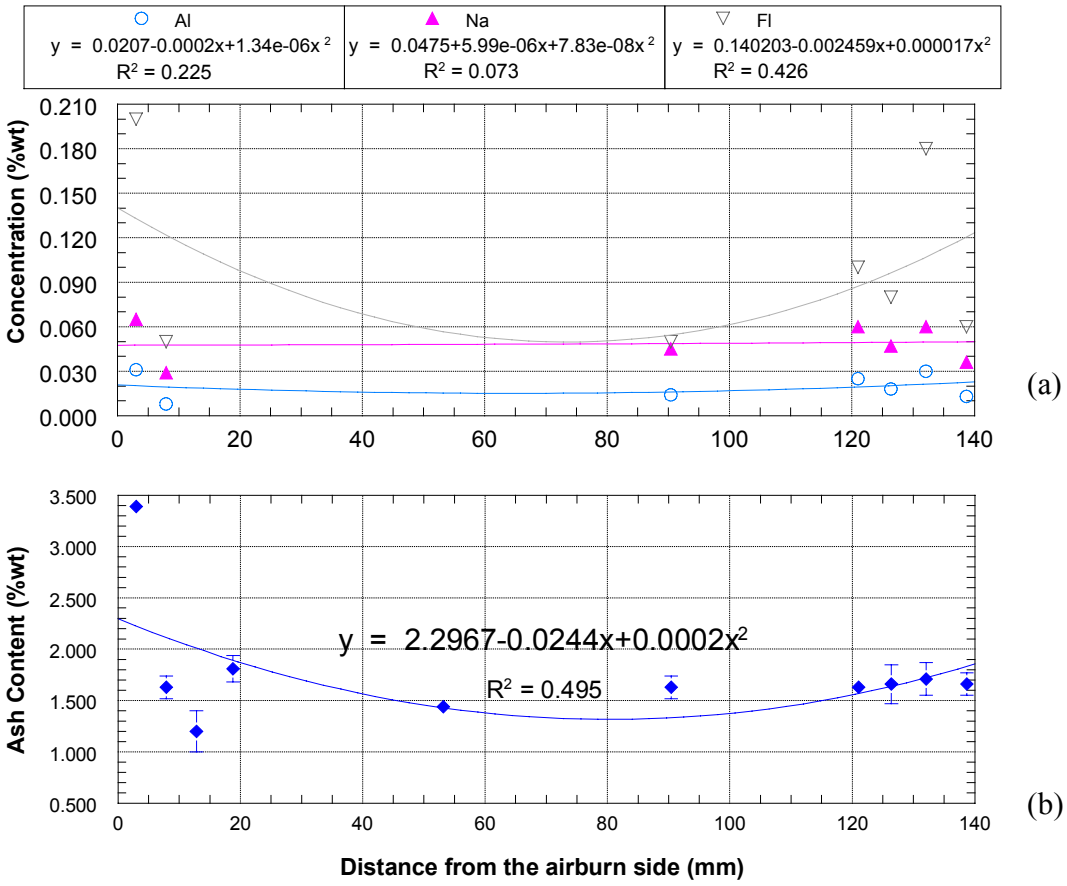

Figure 17 Properties of the Butt-2 Core #5 as a funcition of the airburn side: (a) Concentration of aluminum, sodium and fluoride. (b) Ash content. The solid lines show the polynomial relationship of these properties with the distance from the airburn side.

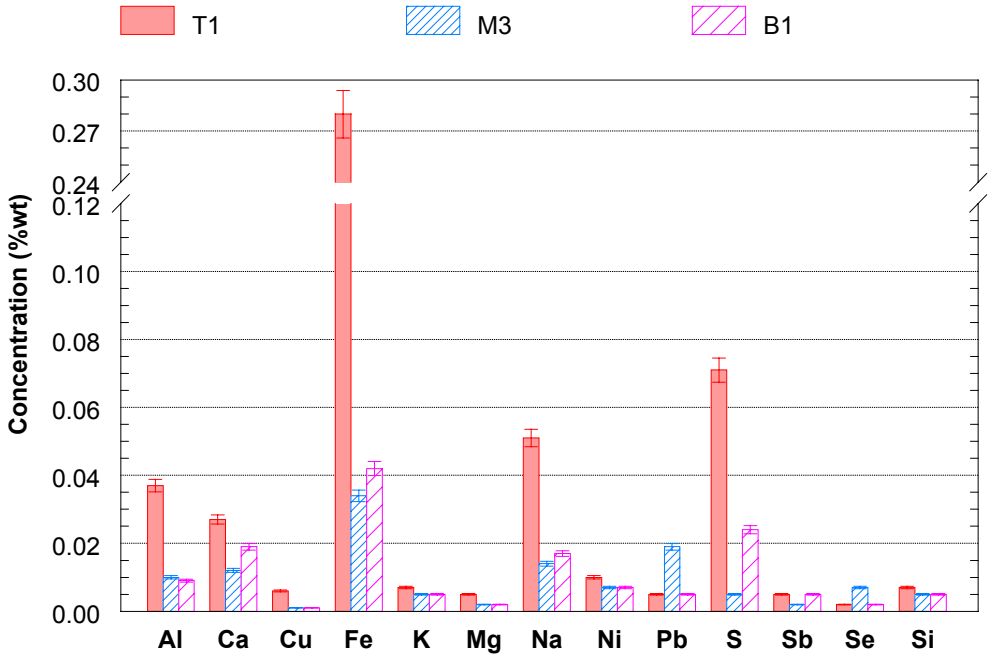

Figure 18 ICP/MS analyses of Butt-4

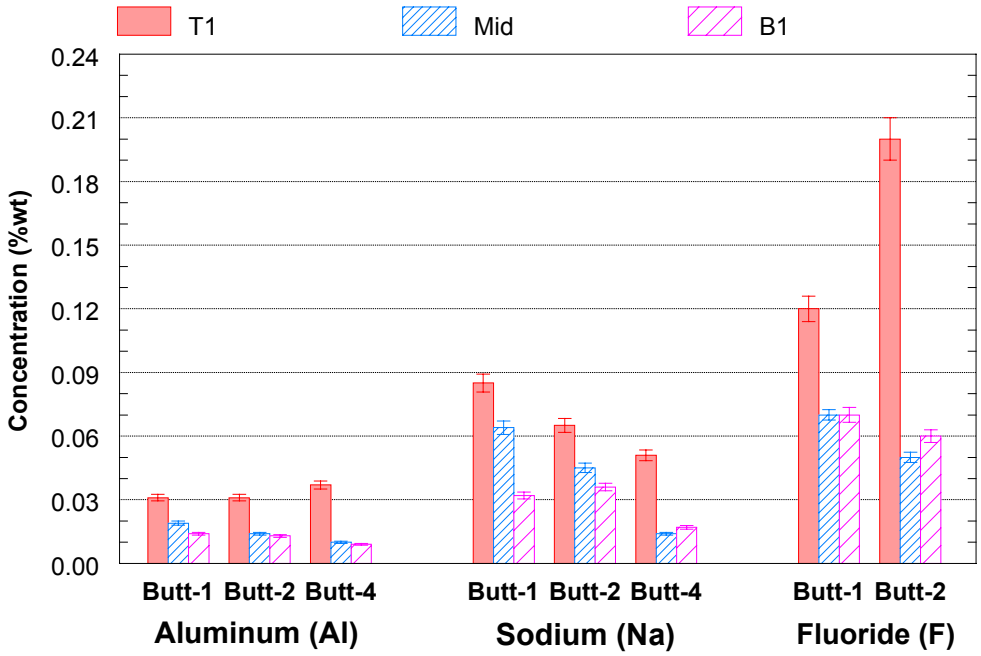

Figure 19 Comparison of aluminum, sodium and fluoride concentrations of the top, middle, and bottom part of Butt-1, -2, and -4.

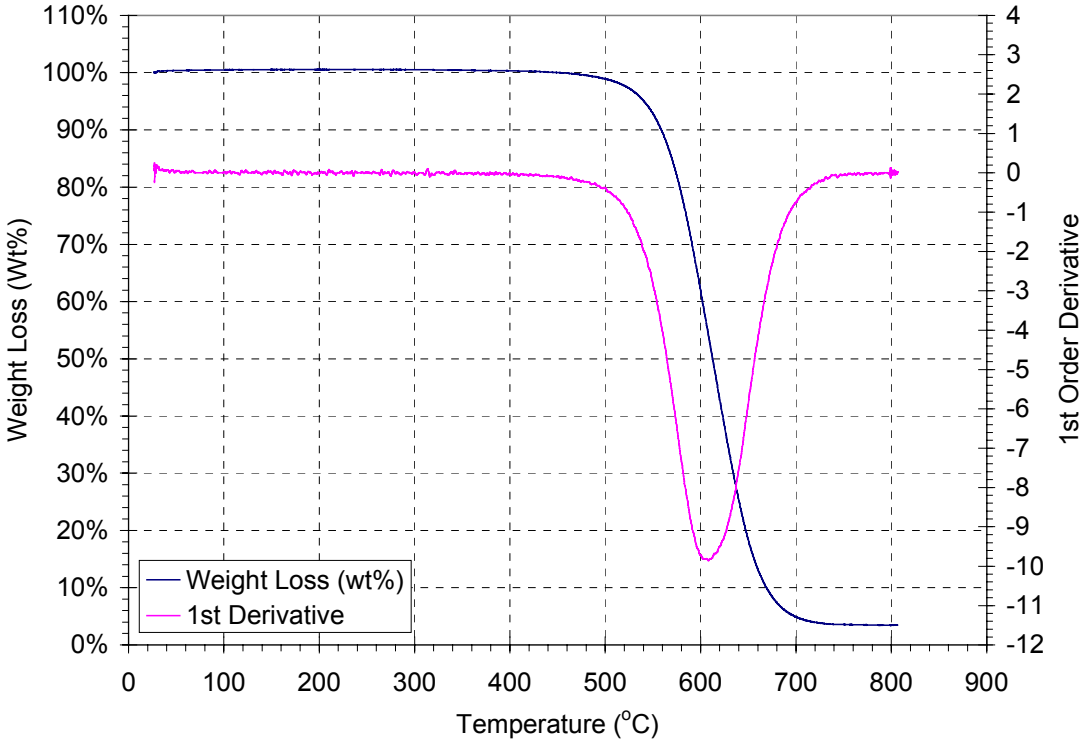

Figure 20 Typical TGA plots.

3.2.3 Thermal Analyses: Non-Isothermal Air Reactivity

Typical TGA plots are shown in Figure 20. The weight loss plot shows a slight weight gain at the temperature close to 100°C due to the oxygen adsorption to the carbon surface. At the temperature about 350°C the carbon material starts oxidizing with oxygen and the material weight starts to decrease. The rate of weight loss decreases as the temperature increases until it reaches a maximum rate of weight loss which is shown by the minimum value of the derivative weight loss plot. The rate of weight loss then decreases and diminishes at about 800°C.

The weigh loss and the derivative weight loss plots of samples from Butt-2 Core #5 from the airburn end to the electrolytic end are shown in Figure 21 and Figure 22, respectively. Both weight loss and derivative weight loss indicate a high air reactivity of the most top sample (T1), and a fairly lower reactivity of the samples from the middle

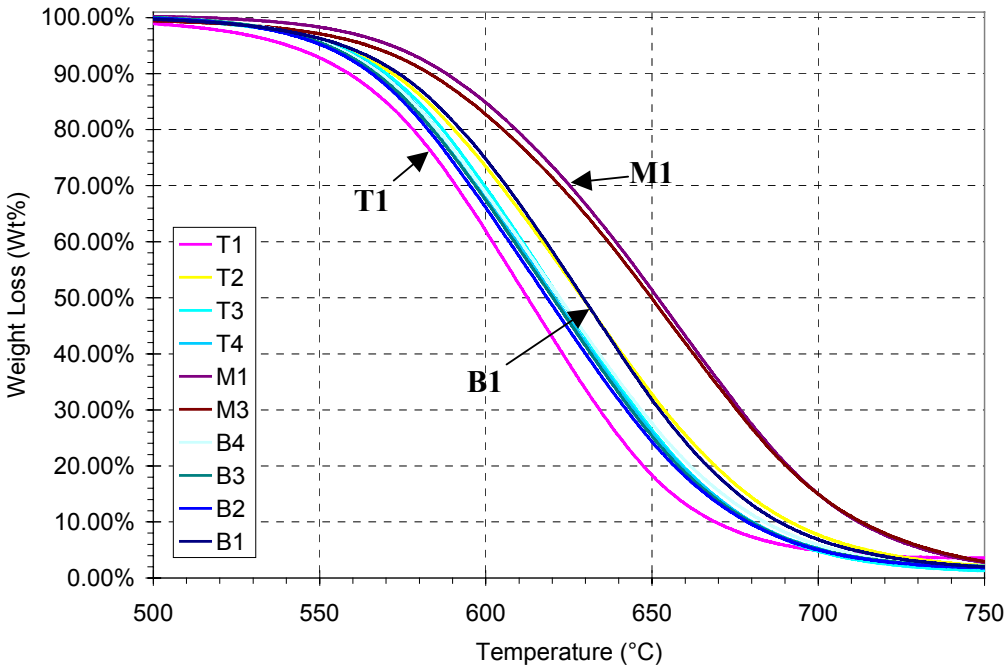

Figure 21 TGA weight loss v.s. temperatures of BUTT-2 Core #5 from top to bottom of the anode butt.

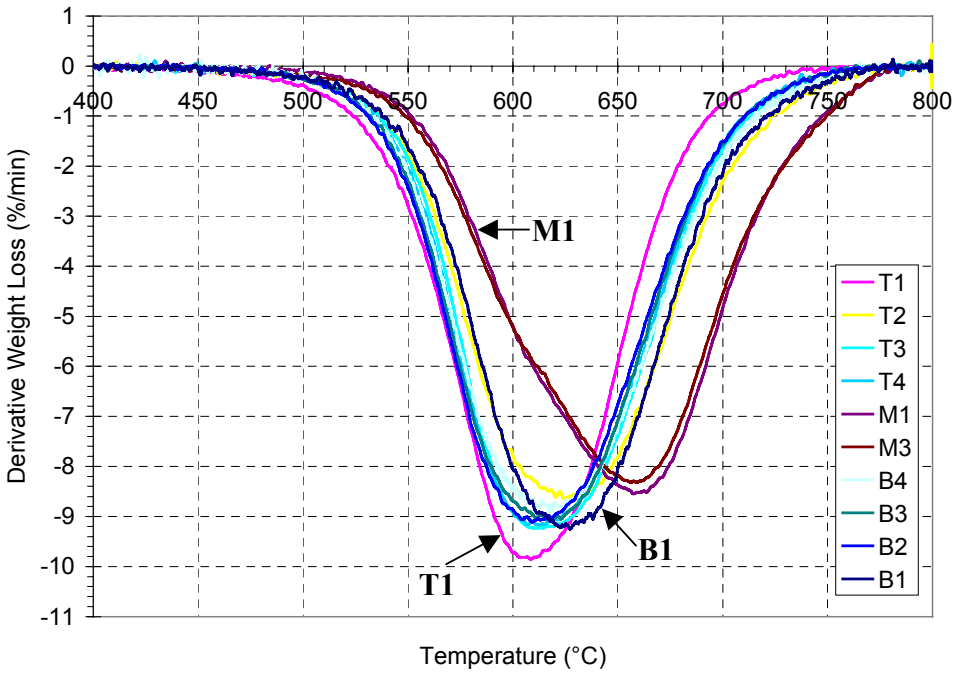

Figure 22 First derivative of weight loss v.s. temperatures of BUTT-2 Core #5 from top to bottom of the anode butt.

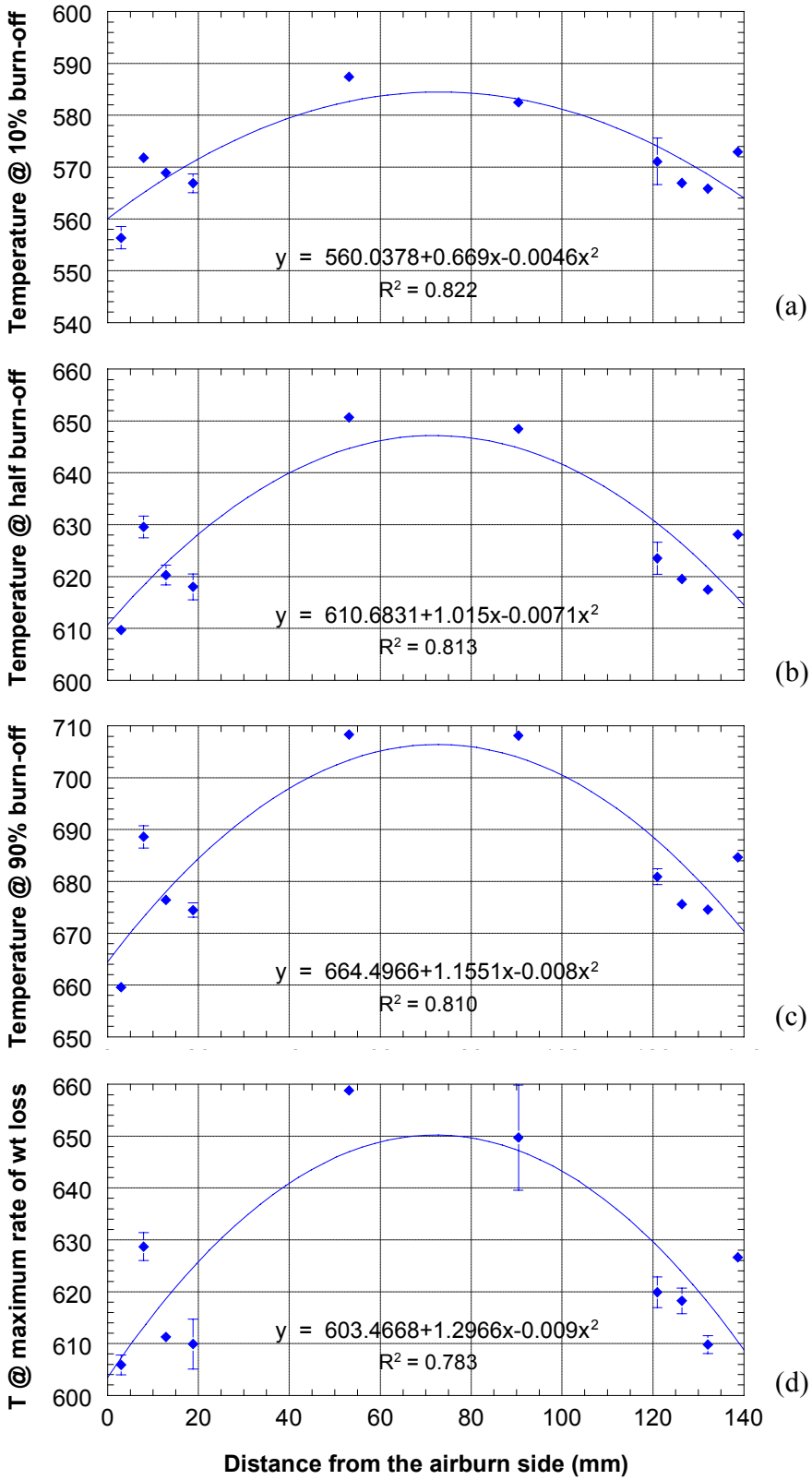

Figure 23 Non-isothermal air reactivity of BUTT-2 Core #5 at different distance from the airburn side: (a) Temperature @ 10% burn-off; (b) Temperature @ 50% burn-off; (c) Temperature @ 90% burn-off; and (d) Temperature @ maximum rate of weight loss. The solid lines show the polynomial relationship of the plots.

part (M1 and M3), whereas the rest are in between. The plots of temperatures at different burn-off (Figure 23) indicate that all samples show the same order of air reactivity for the whole range of air burn-off. These results are in agreement with the chemical analyses. T1 which exhibits the highest air reactivity also contains the highest concentration of inorganic contents. It is of interest to see that B2 (about 7.5 mm from the electrolytic end) shows higher air reactivity than B1, which was in contact with the cryolite in the bath (see Figure 23). This result also coincides with the chemical analyses shown in Figure 17(a) where the concentrations of fluoride, sodium, and aluminum in B2 are higher than those components in B1. Although B1 contains higher pore volume than B2 as shown in Figure 14(d), the porosity effect in this reactivity study can be neglected since the particle sizes in this TGA analysis were controlled, i.e. less than 75 μm (+200 mesh) and most pores were broken apart from the crushing process. Since there are two main factors that affect the air reactivity: the chemical compositions that act as catalysts and the porosity of the anode. As a result, this reactivity study eliminated the mass transfer effect and only the inorganic contents mainly influence the air reactivity.

It came up with a question why B1, which was in contact with the cryolite, contains such lower concentrations of inorganic matters as shown in Figure 17(a), i.e. B1 contains lower concentration of inorganic contents than B2, B3, and B4. This could possibly explained by the concept of carrying over of material from the bottom to the top. During the reactions in the bath, carbon was consumed and CO_2 was produced. As a result, when CO_2 rose up to the top of the anode, the molten inorganic matters would have been carried over from the bottom to a higher level. Since the porosity of the anode close to the working surface is higher, i.e. B1, than the inner part, these inorganic contents were not accumulated here and, instead, passed through the next layer. In contrast, B2, B3 and B4, which contain a fairly lower porosity than B1, had a potential to accumulate these inorganic matters and, hence, resulted in higher reactivity than B1.

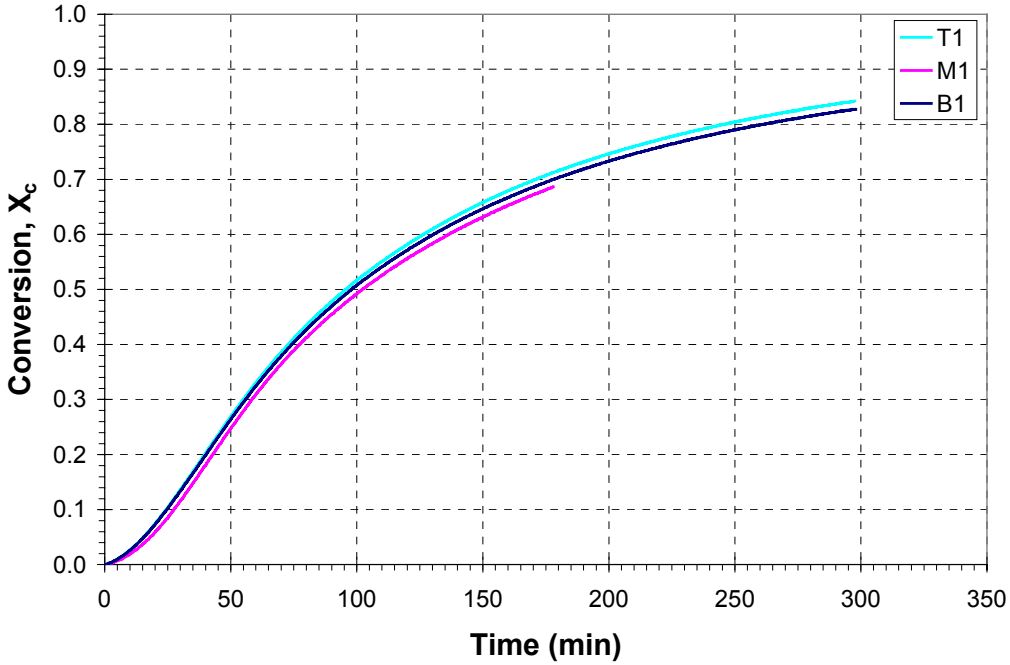

Figure 24 Conversion (daf) v.s. time curves for T1, M1, and B1 of BUTT-2 Core#5 in 1 atm air at 504±1°C.

3.2.4 Thermal Analyses: Isothermal Air Reactivity

There were three samples studied in the isothermal air reactivity at 504±1°C: T1, M1, and B1. These three samples represent the most top, the middle and the most bottom of the anode butt. From Figure 24 T1, M1, and B1 exhibit the same shape of the conversion versus time curves. Since the results of the isothermal air reactivity are not very different for all three samples, other samples were not studied. At the same conversion, T1 was oxidized faster than B1 and M1, respectively. This indicates that T1 is the most reactive and M1 is the least reactive to air. These results are in agreement with the non-isothermal air reactivity discussed in the previous part. Figure 25 and Figure 26 show the rate of conversion versus conversion and the normalized time ($t/t_{X_C=0.5}$), respectively. All three samples exhibit the same trends and magnitudes for the whole range of the x-axes. Hence, at about 500°C it can be said that all anode material has fairly uniform air reactivity throughout the core from the electrolytic to the airburn ends.

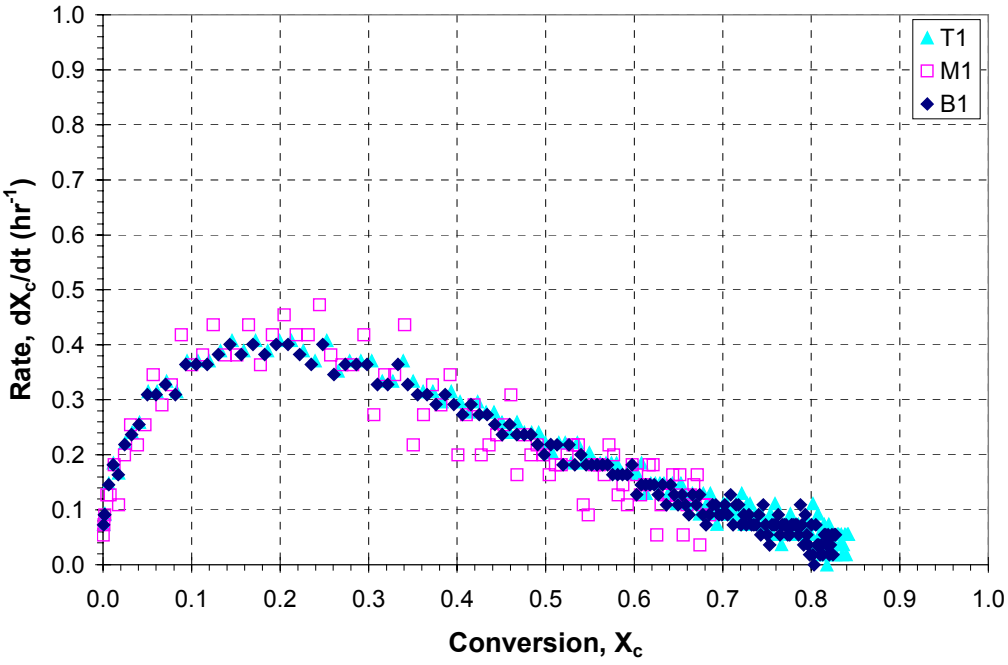

Figure 25 Rate v.s. conversion (daf) curves for T1, M1, and B1 of BUTT-2 Core#5 in 1 atm air at 504±1°C.

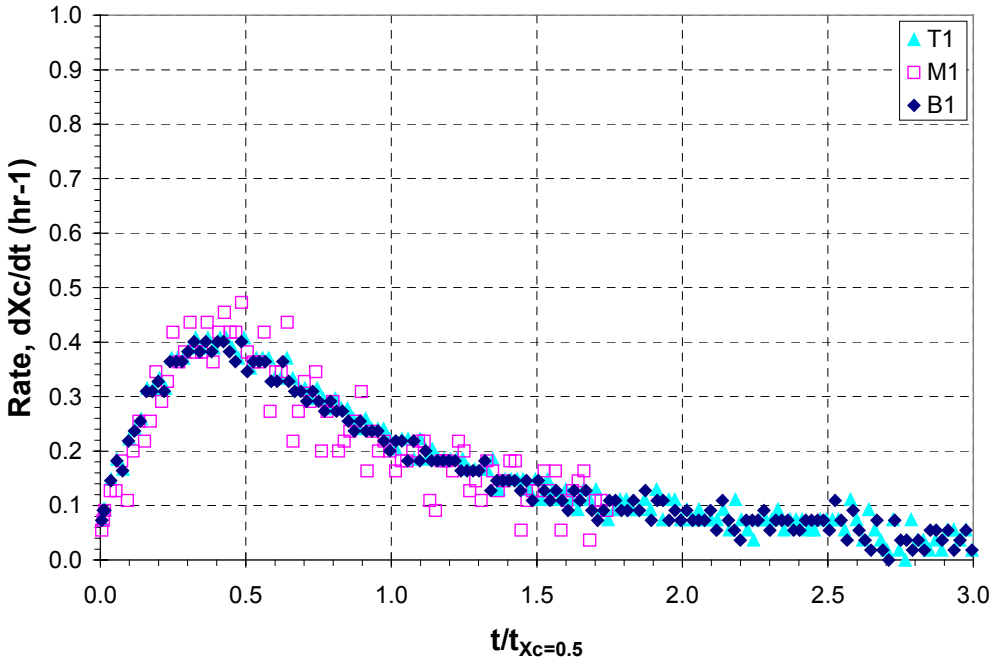

Figure 26 Rate v.s. normalized time curves for T1, M1, and B1 of BUTT-2 Core#5 in 1 atm air at 504±1°C.

3.2.5 Thermal Analyses: Isothermal CO_2 Reactivity

In the CO_2 isothermal reactivity experiment at 976±1°C, five samples were studied: T1, T2, M1, B2 and B1. The variation in CO_2 reactivity is shown in Figure 27. The reactivity of these samples is in the following order: T1 > B2 > T2 > B1 ≈ M1. The order of CO_2 reactivity at 976±1°C shows a very similar result to the non-isothermal air reactivity (see Figure 23 and Figure 27). Since the CO2 reactivity of the inner parts of the butt core approached the results obtained from the middle one (M1), other samples, e.g. B3, B4, T3, T4, etc., were presumably exhibited similar to those of M1 and were not included in this test.

Figure 28 and Figure 29 show the plots of rate versus conversion and normalized time, respectively. It can be seen that the reaction rate of CO_2 oxidation is very high at the initial stage. Especially, T1 is about twice more reactive than the butt material from the middle of the core. The reaction rate later decreases as the conversion increases (or time increases) and the reaction rates of all samples approach toward the middle of the core sample.

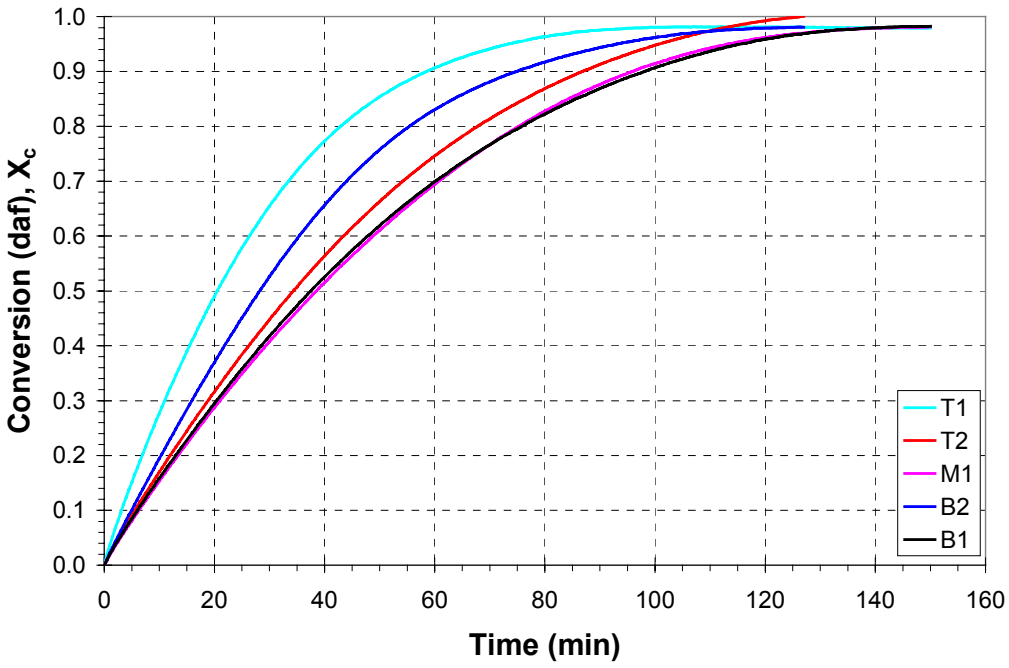

Figure 27 Conversion (daf) v.s. time curves for T1, T2, M1, B2, and B1 of BUTT-2 Core#5 in 1 atm CO_2 at 976±1°C.

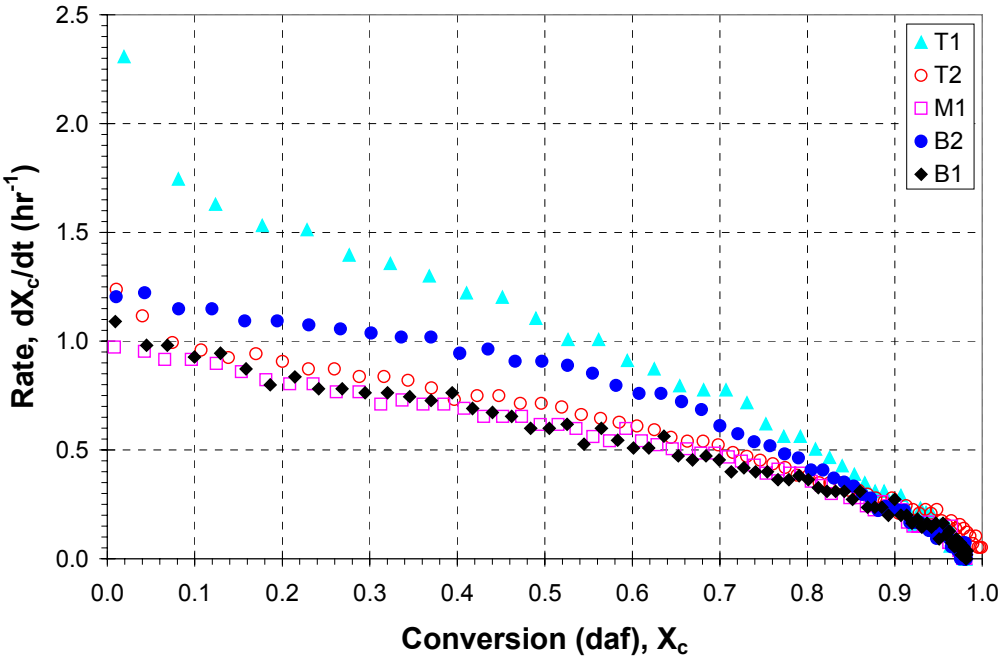

Figure 28 Rate v.s. conversion (daf) curves for T1, T2, M1, B2, and B1 of BUTT-2 Core#5 in 1 atm CO2 at 976±1°C.

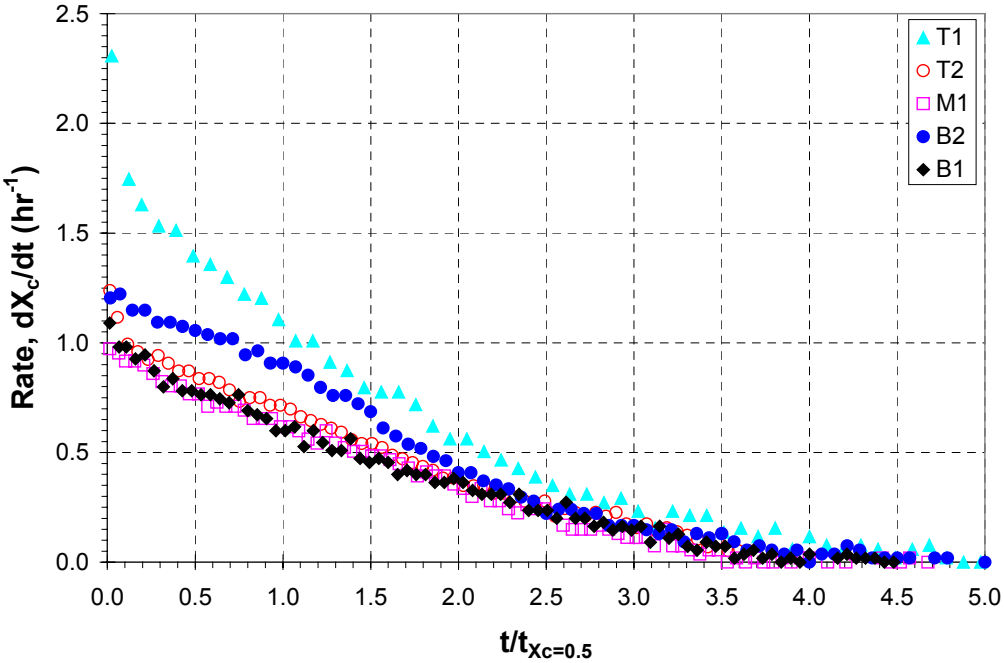

Figure 29 Rate v.s. normalized time curves for T1, T2, M1, B2, and B1 of BUTT-2 Core#5 in 1 atm CO_2 at 976±1°C.

3.2.6 Discussion of Anode Butt Chemistry

Since a lot of anode butts properties were measured, it is of interest to figure out if there is any relationship among them. Figure 30 show plots of inorganic contents (Al, Na and F) versus the apparent and absolute densities, specific pore volume and the ash content. It appears that the apparent and absolute densities and the specific pore volume are related to the inorganic contents as shown in Figures 30(a), (b), and (c), respectively. The ash content appears to have a slight relationship with the inorganic content as shown in Figure 30(d).

The air reactivities as represented by the temperatures at half burn-off were plotted with the Al, Na and F contents as shown in Figures 31(a), (b) and (c), respectively. The differences in the positions of the butt sample, i.e. top, middle and bottom, are also distinguished in these plots. The lower the temperature at half burn-off, the higher the air reactivity the butt material is exhibited. Higher inorganic contents are shown to have higher air reactivities. Hence, these inorganic matters performed as catalysts in the air oxidation. The effect of porosity is also important to the reactivity of a carbon material. The active surfaces, found primarily in micropores in the carbon material, must be well connected to the exterior surface of the particles by the feeder pores (transitional and macropores) [12]. Hence, reactant gas, e.g. air or CO_2, can rapidly diffuse otherwise these active surfaces will not be consumed. The effect of pore volume was added to the inorganic contents as shown in Figures 31(d), (e), and (f) by multiplying the inorganic concentration by the specific pore volume. The reason why the butt materials from the middle of the butt core exhibit significant lower air reactivity than the top and the bottom is clearer here. Not only the inorganic content of the butt materials from the middle butt core is relatively lower than the top and the bottom of the butt core, but the specific pore volume is also lower. These two effects help the air to react with the carbon materials slower in the middle butt core than the airburn and catalytic ends.

The temperature at half burn-ff were also plotted with the ash content, specific pore volume and the absolute density as shown in Figures 32(a), (b) and (c), respectively.

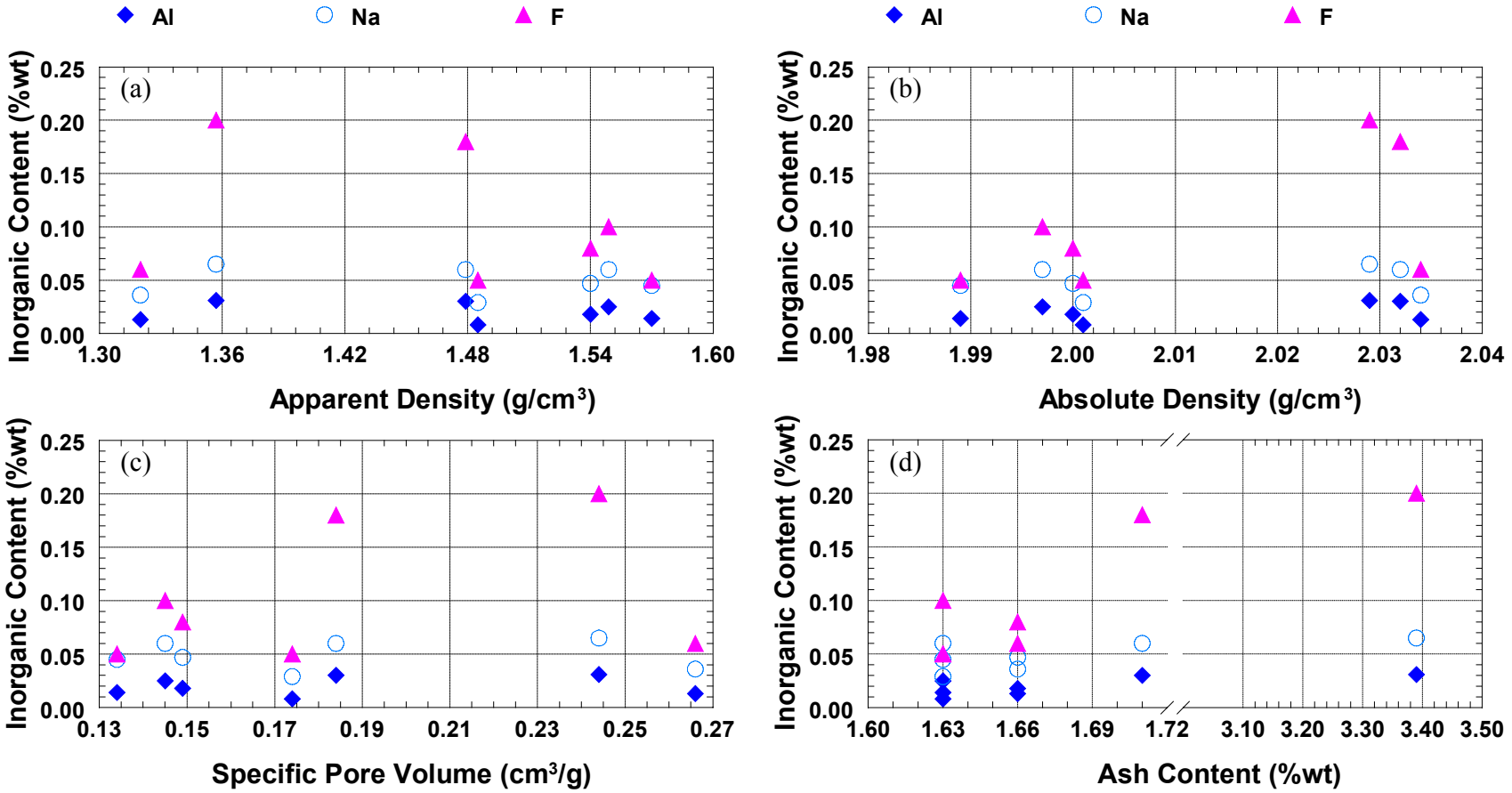

Figure 30 Inorganic contents v.s. (a) Apparent density; (b) Absolute density; (c) Specific pore volume; and (d) Ash content plots of BUTT-2 Core#5.

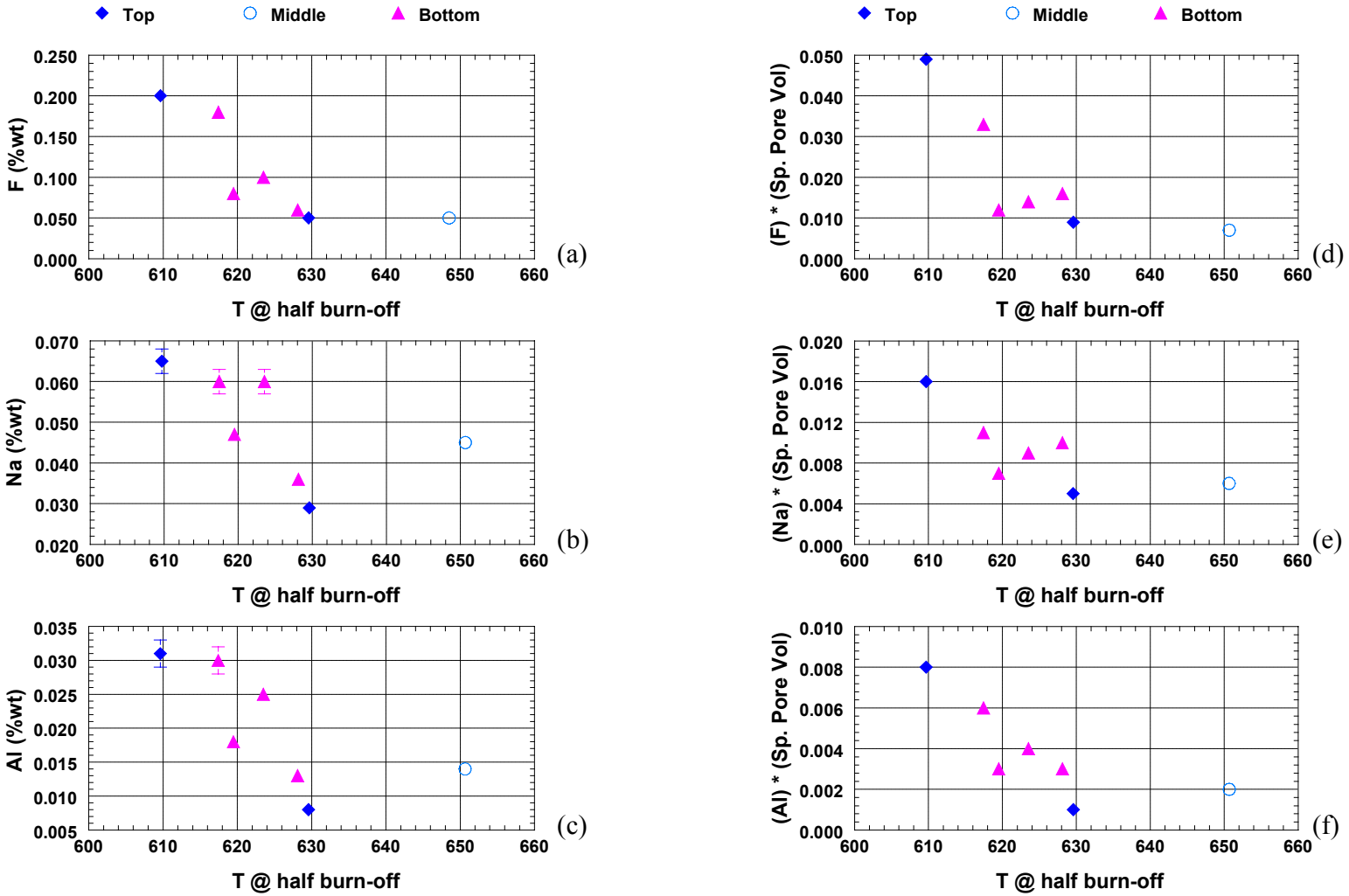

Figure 31 The effects of inorganic contents and (inorganic content ✕ specific pore volume) on air reactivities (represented by the temperature at half burn-off) of BUTT-2 Core#5.

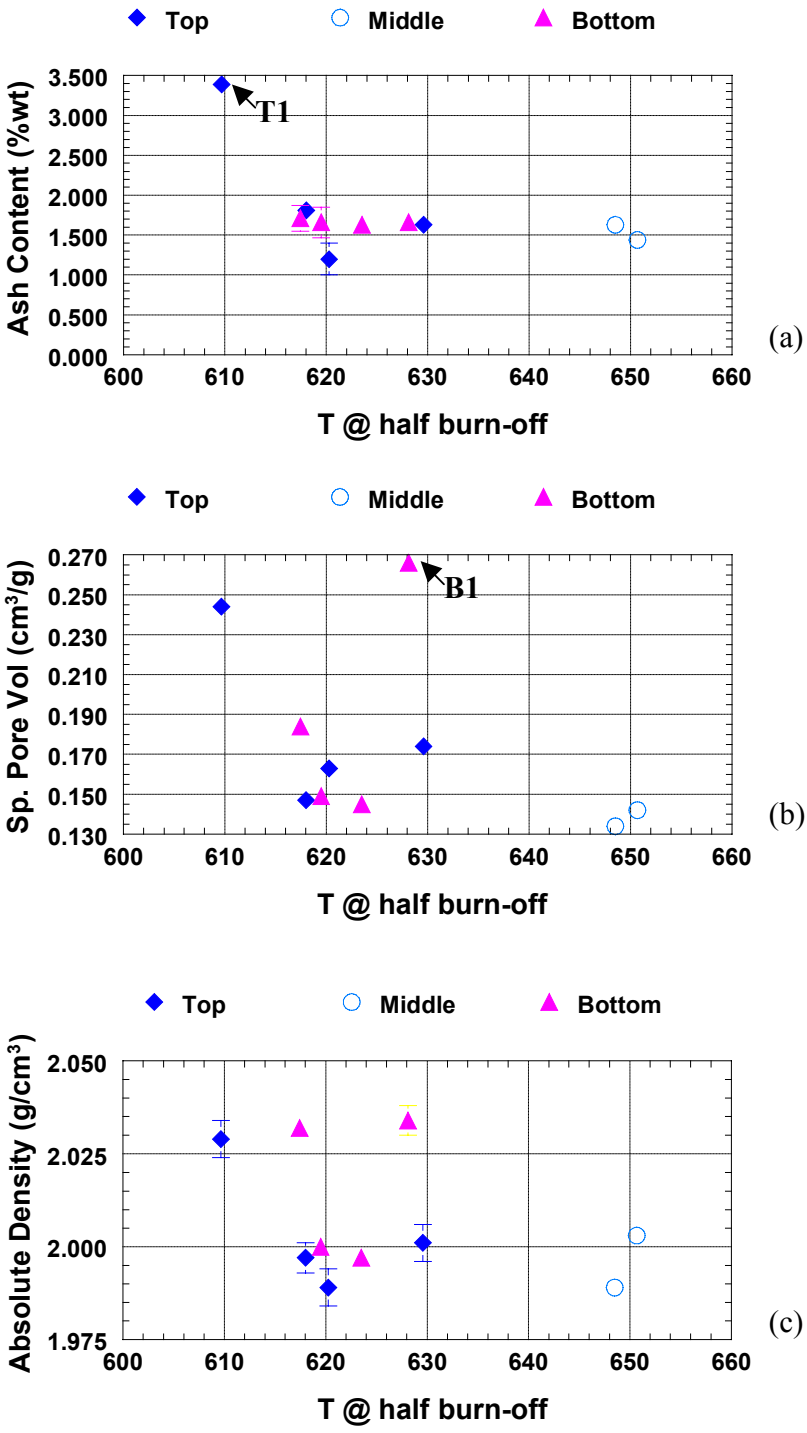

Figure 32 Effects of (a) Ash content, (b) specific pore volume, and (c) absolute density on the air reactivity (represented by the temperature at half burn-off) of BUTT-2 Core#5.

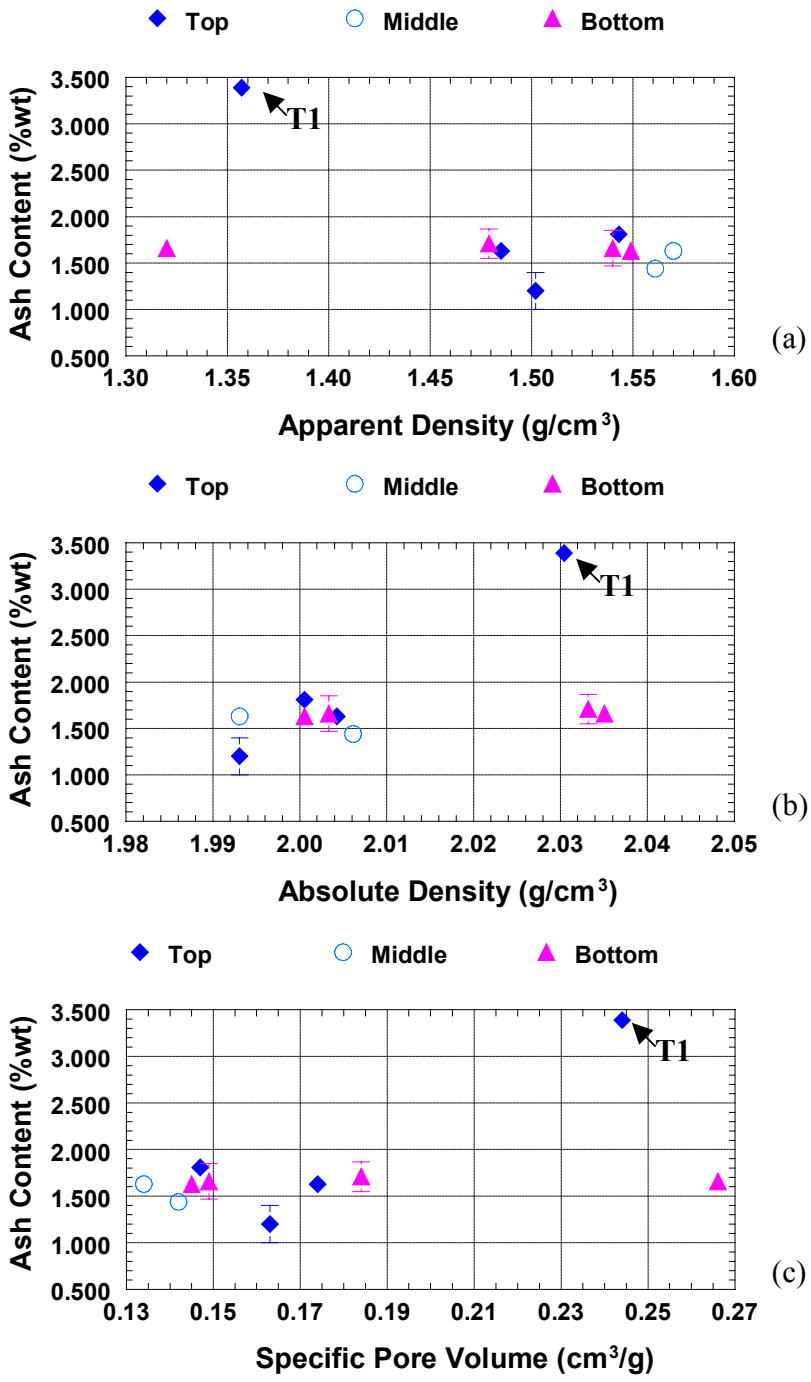

Figure 33 Relationship between physical properties and ash content of BUTT-2 Core#5: (a) Ash content v.s. apparent density; (b) Ash content v.s. absolute density; and (c) Ash content v.s. specific pore volume.

Figure 32 (a) shows no relationship between the air reactivity and the ash content. All samples contain about equal amount of ash except T1, which has about double amount of ash content than others. As mentioned earlier, the specific pore volume is very important to the reactivity of the carbon material. The air reactivity tends to have some relationship with the specific pore volume as shown in Figure 32(b). B1 seems not to follow this trend. This can be explained that B1 contains a lower concentration of reactive components, such as sodium, than the rest of the samples, as shown in Figure 19. A combined effect of inorganic contents and the specific pore volume was already explained previously. Figure 32(c) shows no relationship between the absolute density and the air reactivity.

Figures 33(a), (b) and (c) show the plots of the ash contents versus the apparent density, absolute density, and the specific pore volume, respectively. T1 contains fairly higher ash content than the other samples, which have comparable amount of ash. Apart from T1, the other samples do not have any relationship between the ash content and physical properties.

Figure 34 shows a plot of CO_2 reactivity versus distance from the airburn side. $(dX_c/dt)_{max}$ or R_{max}, which is the initial slope of the conversion versus time plot (Figure 28), is used to represent the isothermal reactivity of a material under a certain gas environment. All samples show a comparable value of reactivity except T1, which is about double as reactive as others. Hence, it can be concluded that no relationship was found between the CO_2 reactivity and the position of the butt material in the butt core. The relationship between the CO_2 reactivity and the ash content is not quite clear as shown in Figure 35(a). Although the ash content tends to slightly increase with the increase in CO_2 reactivity, these values are pretty similar and only T1 sample shows a significant higher in both reactivity and the ash content. Hence, it is presumed that there is no relationship between these two parameters. Figure 35(b) clearly shows that there is no relationship between the CO_2 reactivity and the absolute density. Similar to the air reactivity, CO_2 reactivity exhibits a relationship with the specific pore volume as shown in Figure 35(c). Although B1 which contains a high porosity has such a low reactivity as

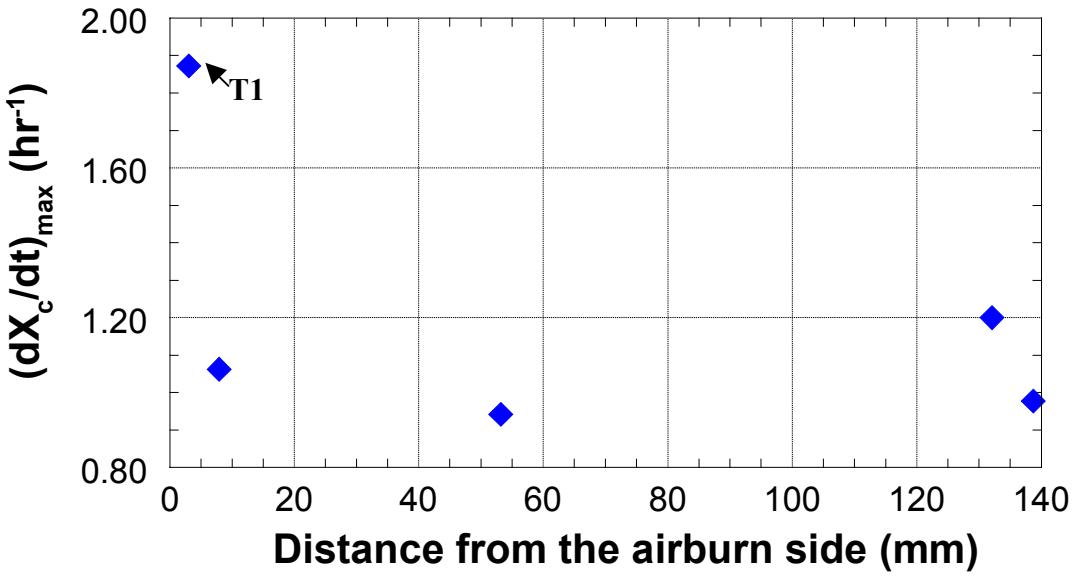

Figure 34 Reactivity (represented by $(dX_c/dt)_{max}$ or R_{max}) of Butt-2 Core #5 in 1 atm CO_2 at 976±1°C v.s. distance from the airbrun side.

compared as other butt materials from other positions, this result was derived from a low concentration of inorganic material in this specific sample. The inorganic contents and the combined effect between the inorganic content and the specific pore volume have similar effects to the CO_2 reactivity as previously shown in the air reactivity (see Figure 36(a) to (f) compared to Figure 31(a) to (f)). Either the specific pore volume or the inorganic content alone shows some relationships with the CO_2 reactivity and the combined effect between these two is even pronounced. Hence, among all parameters tested in this study, it can be concluded that only the specific pore volume and the inorganic contents are the most important factors that affect the reactivity of the anode butt materials.

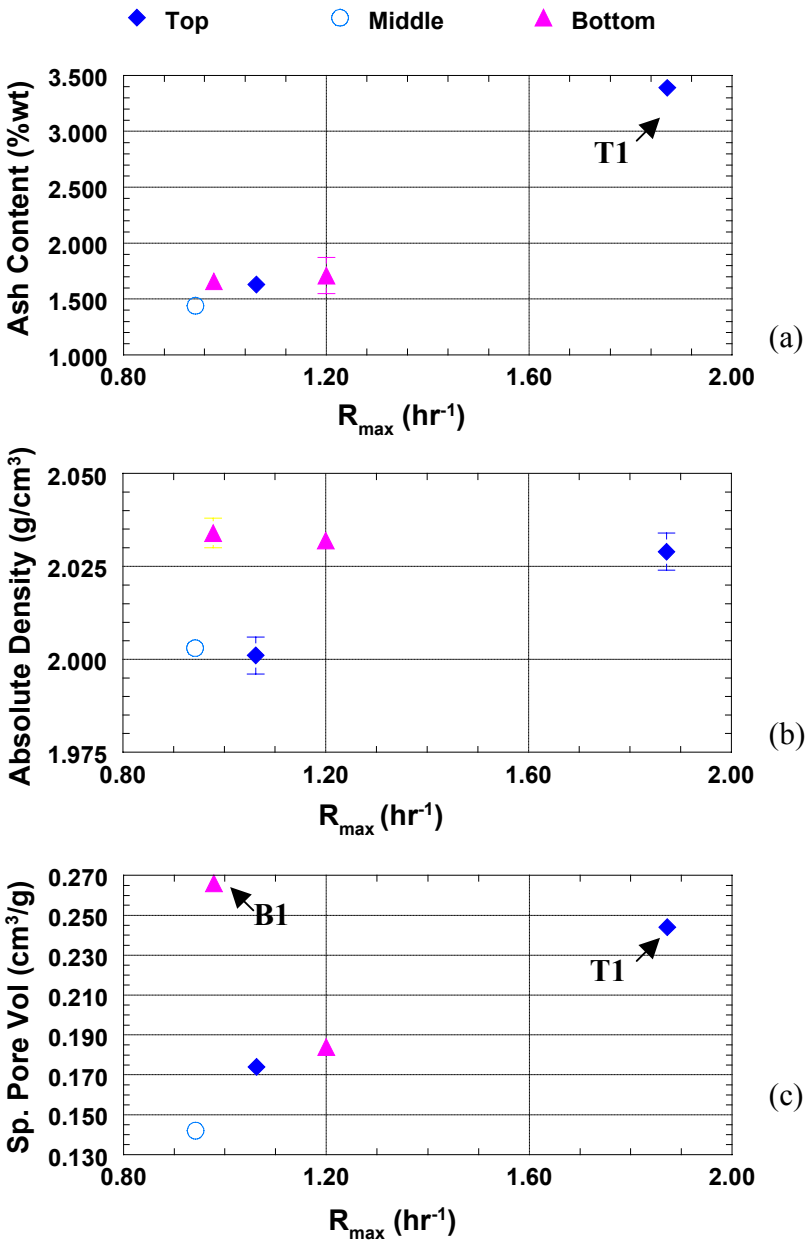

Figure 35 Effects of (a) Ash content, (b) Absolute density, and (c) Specific pore volume on the CO_2 reactivity (represented by (dXc/dt)max or Rmax) in 1 atm CO_2 at 976±1°C of BUTT-2 Core#5.

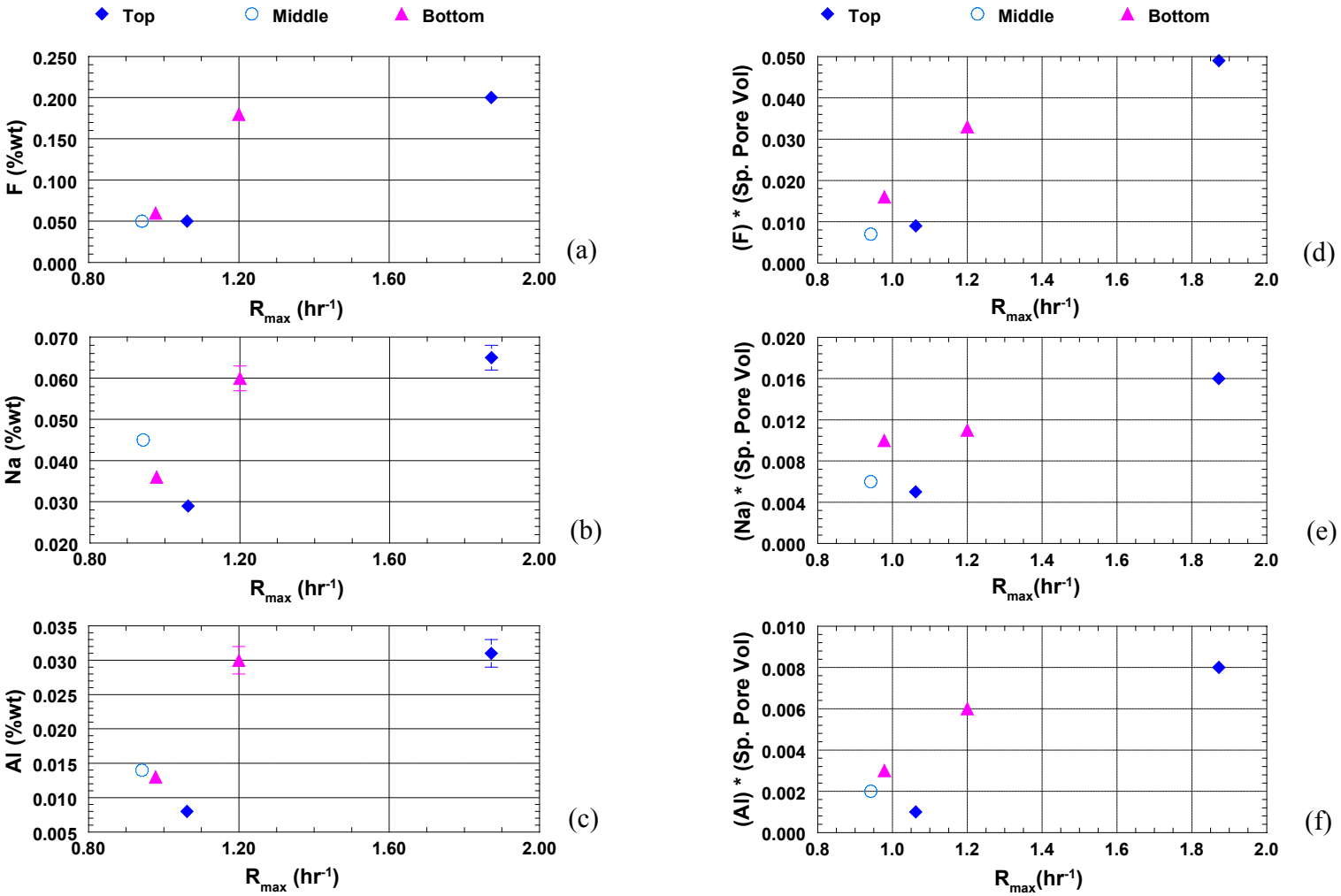

Figure 36 The effects of inorganic contents and (inorganic content ✕ specific pore volume) on the CO_2 reactivity (represented by $(dX_c/dt)_{max}$ or R_{max}) in 1 atm CO_2 at 976±1°C of BUTT-2 Core#5.

3.3 Pitches/Butts Study

In this part of the study, only the alternative pitches which have the softening point around 110-115°C were used to mix with the SCTP-2. The ratio of the alternative pitch to SCTP-2 was fixed to 20:80 and the properties of these pitch mixtures were compared to the experimental-scale anodes made from 100% SCTP-2. Three types of butt materials from the most top, middle, and the most bottom were used to study how different parts of the butt interact with each pitch. All results from this section were also compared to the results obtained in Section 3.1 where the mixed butt materials were used.

Different parts of the butt materials gave a significant difference in the green apparent density. Figure 37 shows the green apparent densities of the experimental-scale anodes made from the most top, middle, and the most bottom parts of the butt core. The middle part butt material gave a significant higher green apparent density than the top and the bottom parts for each pitch mixture. These results are directly due to the higher porosity of the top and bottom part than the middle one. It is of interest to observe that the experimental-scale anodes made from the Top + SCTP-2 and the Bottom + SCTP-2 gave lower green apparent densities than the Top + alternative pitch and the Bottom + alternative pitch. This may cause by the effect of QI in the SCTP-2, i.e. a lower QI pitch could penetrate into pores better than a higher QI pitch. The green apparent densities of the anodes made from the Top, Middle and Bottom parts are also compared with those made from the mixed butt materials. Only the anodes made from the middle part gave comparable results to the mixed anode butts while the anodes made from the top and bottom gave significantly lower green apparent densities.

Figure 38 shows the baked apparent densities of the experimental-scale anodes made from the Top, Middle, and the Bottom parts of the butt core. The SCTP-2 only gave slightly lower baked apparent densities of the anode made from the top and bottom parts than those made from the middle part. All other anodes made from the alternative pitch + SCTP-2 mixture gave slightly lower baked apparent densities of the anodes made from the top part, while the apparent densities of those made from the bottom and middle

are comparable. A comparison of the baked apparent densities of the anodes made from the Top, Middle, or Bottom to the anodes made from the mixed butt materials suggests that the SCTP-2 only (Figure 38(a)) and the pitch mixture of PP-1 + SCTP-2 (Figure 38(b)) gave comparable results to the anodes made from the mixed butt materials, while the pitch mixtures of WVU-5 + SCTP-2 (Figure 38(d)) gave quite lower results. In the case of GP-1 + SCTP-2, although the baked apparent densities are only slightly lower than those of the SCTP-2 only (Figure 38(c)) for all Top, Middle, and Bottom, these baked apparent densities are quite lower than the anodes made from the mixed butt materials. These results can be explained as follows. When the Top, Middle, or Bottom of the butt materials mixed with the GP-1 + SCTP-2 pitch mixture gave similar pitch loss to the anodes made from the mixed butt materials (Figure 39(c)). The lower baked apparent densities in this case were derived from the higher change in volume after baking as compared to the mixed butt materials (Figure 40(c)).

On the other hand, the low baked apparent densities of the WVU-5 + SCTP-2 pitch mixture mixed with the Top, Middle, or Bottom part of the anode butts were directly derived from a fairly high pitch loss as shown in Figure 39(d). Nevertheless, the pitch loss and the volume change of the Top, Middle or Bottom butt materials mixed with the SCTP-2 only or the PP-1 + SCTP-2 are similar to those of the mixed butt materials (Figure 39(a), (b) and Figure 40(a), (b)). However, the Middle butt material + SCTP-2 only gives a rather high in volume change than other samples of the same pitch mixture. This high volume change may derive from the low pitch loss of this anode (see Figure 39 (a)) and, hence, pitch was trapped inside the anode and underwent volume expansion during baking.

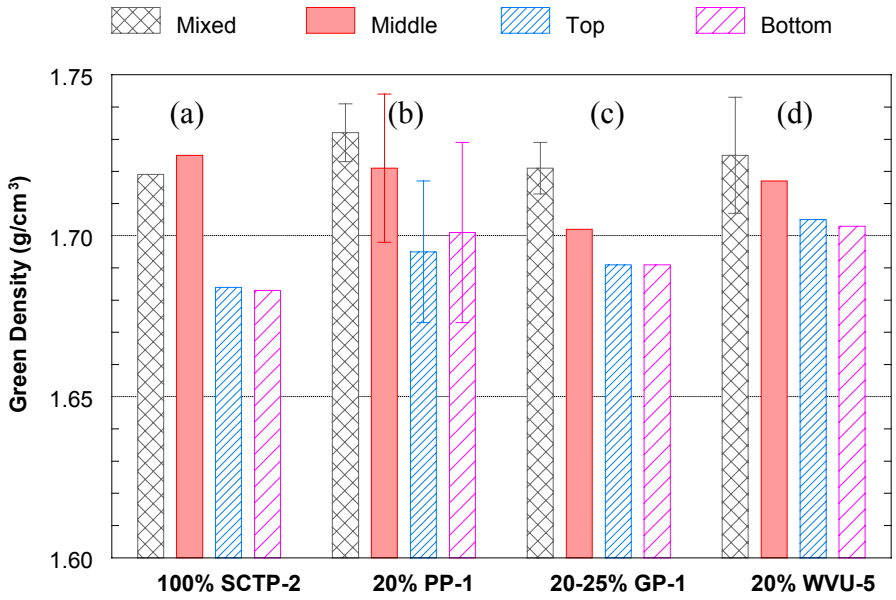

Figure 37 Green apparent densities of the anodes made from 49% petroleum coke, 29% butt materials (mixed, top, middle, or bottom parts), and 22% pitch mixture(s). (a) 100% SCTP-2; (b) 20% PP-1 and 80% SCTP-2; (c) 20% GP-1 and 80% SCTP-2; and (d) 20% WVU-5 and 80% SCTP-2.

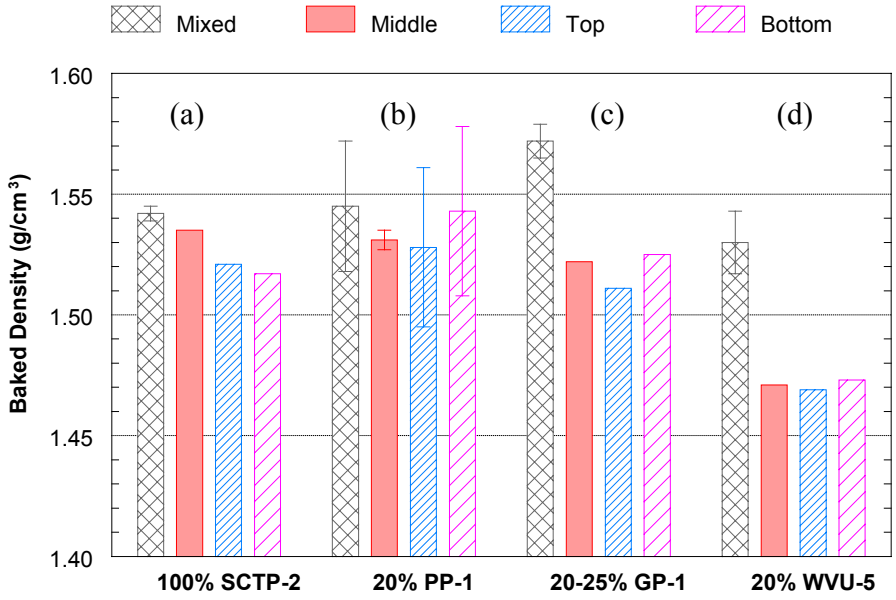

Figure 38 Baked apparent densities of the anodes made from 49% petroleum coke, 29% butt materials (mixed, top, middle, or bottom parts), and 22% pitch mixture(s). (a) 100% SCTP-2; (b) 20% PP-1 and 80% SCTP-2; (c) 20% GP-1 and 80% SCTP-2; and (d) 20% WVU-5 and 80% SCTP-2.

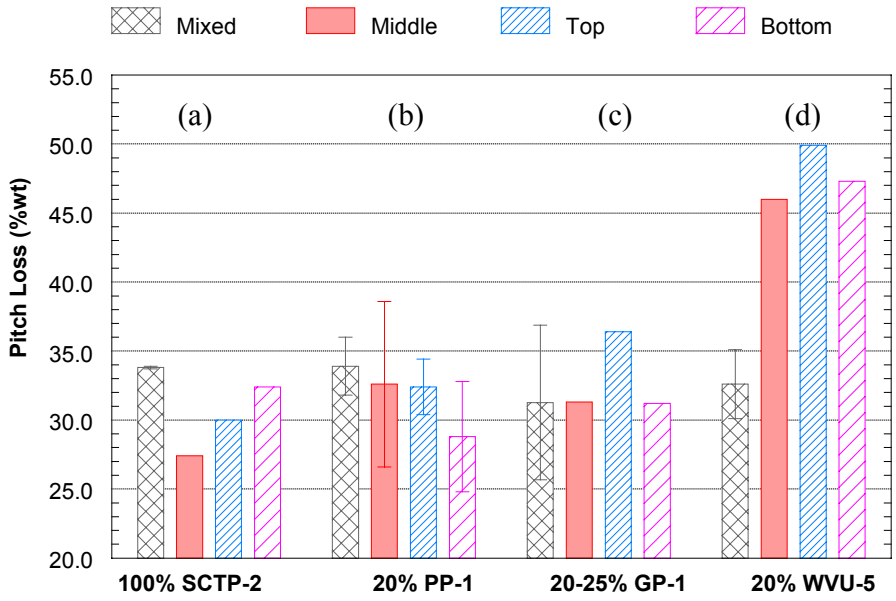

Figure 39 Percentages of pitch loss after baked of the anodes made from 49% petroleum coke, 29% butt materials (mixed, top, middle, or bottom parts), and 22% pitch mixture(s). (a) 100% SCTP-2; (b) 20% PP-1 and 80% SCTP-2; (c) 20% GP-1 and 80% SCTP-2; and (d) 20% WVU-5 and 80% SCTP-2.

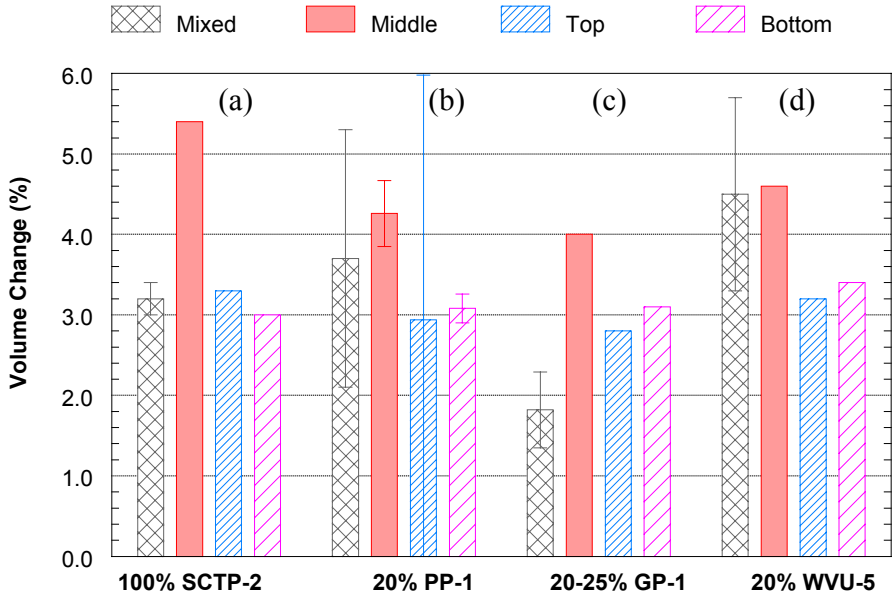

Figure 40 Percentages of volume change after baked of the anodes made from 49% petroleum coke, 29% butt materials (mixed, top, middle, or bottom parts), and 22% pitch mixture(s). (a) 100% SCTP-2; (b) 20% PP-1 and 80% SCTP-2; (c) 20% GP-1 and 80% SCTP-2; and (d) 20% WVU-5 and 80% SCTP-2.

4. Conclusion

4.1 Binder Pitches Study

The results of this study show that the petroleum pitch offers a potential to be used as additives to the standard coal-tar pitches for use as binders in the aluminum anode production, while the addition of coal-extracted pitch and gasification pitch give comparable anode properties when the ratio of standard coal tar pitch to the alternative pitch is greater than 50:50. Further work should be conducted to study the causes of improvement of adding alternative pitches to better understanding the roles of the binders from various types of pitches.

4.2 Anode Butts Study

Three industrial anode butts, with and without recycled butt material, were studied. Non-destructive X-Ray imaging was used to quantify the spatial distribution of density and porosity in the sample. Apparent and absolute densities were measured and the specific pore volumes were calculated as a function of the distance from the airburn side. The results from the X-Ray CT and the densities and pore volume measurement showed a decrease in apparent density, and an increase in absolute density and specific pore volume from the center of the core to the surfaces. The anode butt that did not contain recycled butt material in the original formulation showed a higher reactivity with air at the airburn side while it had lower reactivity with CO_2 at the electrolytic side. It can be confirmed from this work that the main factors that derived the change in air and CO_2 reactivities of the anodes along the electrolytic surface to the airburn surface were the concentration of the inorganic contents, e.g. sodium, calcium, etc., and the porosity of the carbon material.

4.3 Pitches/Butts Study

The experimental-scale anodes made from the top and bottom of the butt materials gave quite lower green apparent densities than the anodes made from the

middle part of the butt materials. These results were linked with high porosity of the top and bottom of the butt materials that inhibited the pitch to penetrate well into the pores. However the effect of porosity was weakened in the baked apparent density. Anodes that made from the pitch mixture that contained 20% PP and 20%GP gave comparable baked density to the anodes made from SCTP only. Whereas the anodes that were made from the pitch mixture that contained 20% WVU gave somewhat lower baked densities than the SCTP only and these results were caused by a high pitch loss of this pitch after baking.

5. References

[1] CRU International, Carbon Products – Aluminum Raw Materials, London, U.K., May 2002.

[2] Rusinko, F., Andresen, J. M., Adams, A., Chapter 13 in Great Lakes Carbon Corp. 6th Carbon Conference (Houston. USA), 2000.

[3] Schmidt-Hatting, W., Kooijman, A. A., Perruchoud, R., Investigation of the Quality of Recycled Anode Butts, Light Metals, 705-720, 1991.

[4] Gray, R. J.., and Krupinski, K. C., In Introduction to Carbon Technologies; Marsh H, Heintz EA., and Rodriguez-Reinoso F, Ed.; Secretariado de Publicaciones, 1997, pp 329-424.

[5] Grjotheim, K. and Welch, B. J., In Aluminum Smelter Technology; 2nd ed.; Aluminum-Verlag: Dusseldorf, 1988, pp 75-118.

[6] Jenkins, R.G., Nandi, S. P., and Walker, P. L. Jr., Reactivity of Heat-Treated Coals in Air at 500 [Deg]C, Fuel, 52, 288-93, 1973.

[7] Mahajan, O. P., and Walker, P. L., Jr. "Porosity of Coals and Coal Products." In Analytical Methods for Coal and Coal Products, edited by C. Karr, Jr., 125-62. New York: Academic Press, 1978.

[8] The Energy Institute Penn State University, Binding Efficiency of Coal-Derived Binders Towards Anode Butts: 1st Quarterly Technical Progress Report, June 2003.

[9] Cutshall, E. R., and Bullough, V. L., Influence of baking temperature and anode effects upon carbon sloughing, Light Metals,1039-1076, 1985.

[10] Perruchoud, R. C., Meier, M. W. and Fischer, W. K. Bath impregnation of carbon anodes. Light Metals, 543-549, 1996.

[11] Sadler, B. A. and Salisbury, C. Impact of recycled anode waste materials on anode quality. Light Metals, 609-614, 1994.

[12] Walker, P. L. Jr., Matsumoto, S., et al., Catalysis of gasification of coal-derived cokes and chars, Fuel, 62(2), 140-149, 1983

"Processing and Reuse of Activated Carbon Used to Adsorb Mercury from Power Plant Flue Gases"

Final Report

Dale L. Nickels
Dr. Thomas Weyand

Contract #: 2477-PMET-DOE-0350

Pittsburgh Mineral & Environmental Technology
700 Fifth Ave.
New Brighton, PA 15066

June 24, 2004

ABSTRACT

The Environmental Protection Agency (EPA) has decided to regulate mercury emissions from coal fired power plants. The regulations will be developed and finalized, with full compliance anticipated by 2007. Test work performed by others has identified a system by which the mercury in flue gases can be captured onto Powdered Activated Carbon (PAC) to control mercury emissions. However, the existing production capacity for PAC is only 10% of the capacity required for full implementation.

The process envisioned and defined in this project enables the reuse of PAC after its injection and collection from a flue gas stream in which the PAC injection point is after the electrostatic precipitators but prior to a baghouse. Once collected, the PAC is thermally treated in an inert atmosphere to desorb the contained mercury allowing the PAC to be returned to the injection system for reuse. The desorbed mercury is sequestered and concentrated for recovery into saleable product.

Compared to single-pass PAC that is injected once, collected and disposed of; this process offers significant operating cost savings, reduced PAC consumption to stretch the existing supply, and mercury emissions that are recyclable.

A bid package was prepared for the construction of a demonstration plant suitable for processing mercury laden PAC (or other sorbents) for a 270MW power plant.

TABLE OF CONTENTS

TABLES, FIGURES AND DRAWINGS

TABLES

FIGURES

DRAWINGS

INTRODUCTION

This project addresses the removal and recovery of mercury that is sorbed to Powdered Activated Carbon (PAC) to remove mercury from coal combustion power plant flue gas streams.

Previous work performed by ADA ES and others for the US DOE has demonstrated the effectiveness of injecting PAC into flue gas streams for mercury removal. This approach has been highly successful in removing up to 80% of the mercury from the flue gas when the PAC is injected ahead of a COHPAC facility.

To date, the PAC with sorbed mercury is assumed to be disposed after use. This will result in a significant expense for the mercury removal, since the most effective PAC employed to date is DARCO FGD manufactured by Norit Americas is estimated to cost approximately $0.50/ pound delivered to the power plant. In addition to the purchase expense, the disposal of this material may potentially fall under regulations requiring its disposal in "special" or hazardous waste landfills.

The proposed approach dramatically reduces the need for ongoing PAC purchases and provides for a thousand fold concentration of mercury in a specially formulated carbon that can subsequently be treated for mercury recovery as a salable metal, thus avoiding any disposal of potentially toxic waste streams. The estimated operating cost for this process is ~$0.05/lb of treated PAC compared with a purchase price of $0.50/lb PAC and an unknown but potentially significant disposal cost.

The process is shown in schematic in Figure 1.

FIGURE 1
Mercury Control System

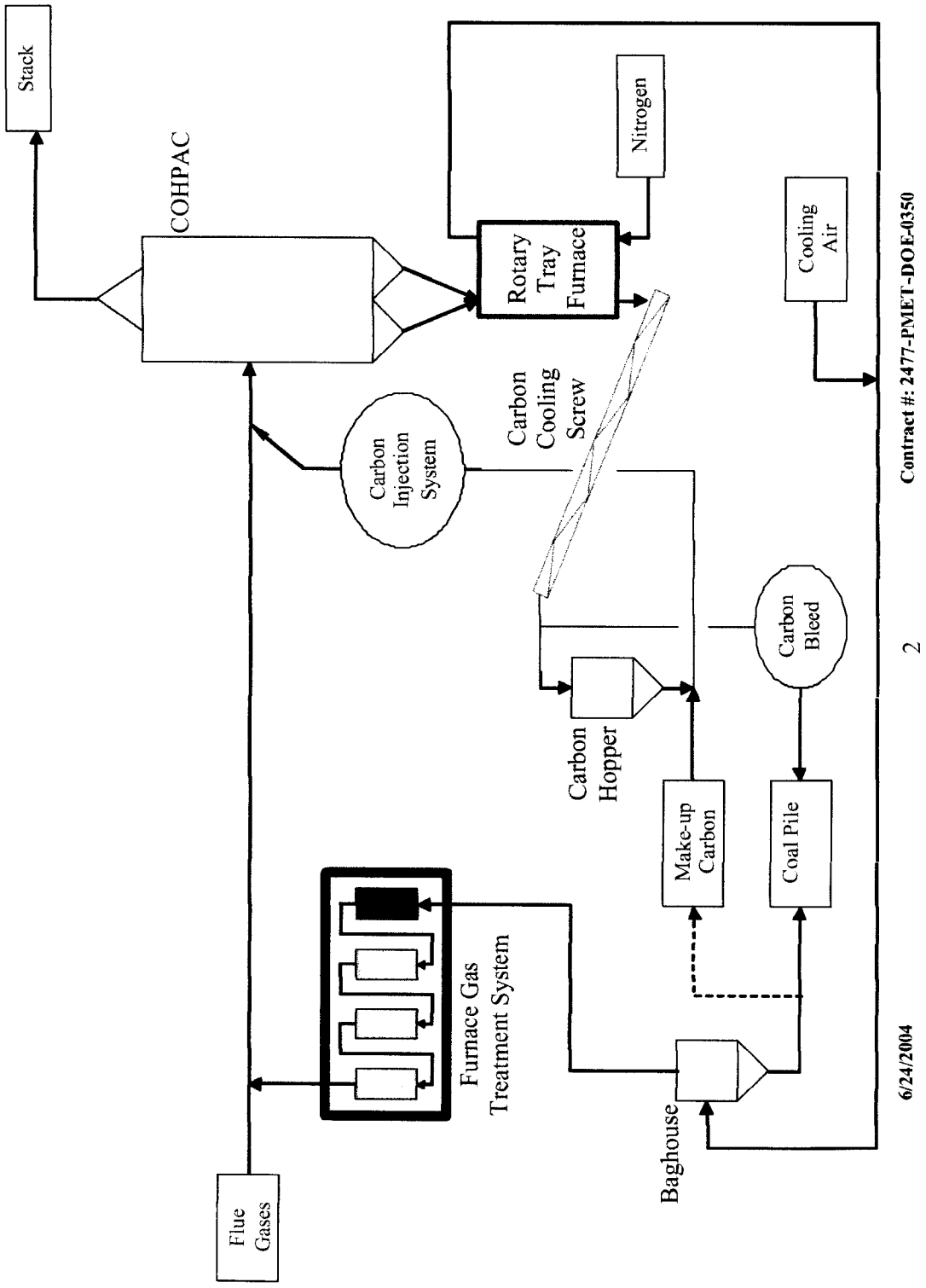

PAC is injected into the flue gas stream ahead of the COHPAC bag filter. Mercury contained in the flue gas is removed from the gas stream as gas passes thru the carbon layer on the COHPAC bags and exits the facility via the plant stack. PAC in the COHPAC is periodically removed from the filter bags and fed to a rotary tray furnace for mercury removal from the PAC. This furnace is sealed and operates under an inert counter flowing nitrogen atmosphere. Mercury vapor exits the rotary tray furnace with the nitrogen process gas and is directed to a multiple column gas treatment system which utilizes packed beds of sulfur impregnated carbon to remove the gaseous mercury from the cooled process gas stream. After passing thru the sulfur impregnated carbon columns, the carrier gas is injected into the flue gas stream ahead of the carbon injection site.

Carbon exits from the rotary tray furnace via an air lock to a water-cooled screw conveyor. The cooled carbon is returned to the carbon hopper supplying the PAC injection system. Depending upon the amount of ash recovered in the COHPAC, a bleed stream of carbon will be required to maintain a material balance in the system. The bleed stream will take a portion of the desorbed carbon from the screw discharge. This material can be combusted in the coal-fired boiler.

The focus of this project is two fold:

1. Perform bench scale feasibility testing is to determine if the process envisioned in Figure 1 is technically viable.

2. Prepare a bid package for the construction of a demonstration plant based upon the process in Figure 1 that is suitable for processing mercury laden PAC (or other sorbents) for a 270MW power plant.

EXECUTIVE SUMMARY

The Environmental Protection Agency (EPA) has decided to regulate mercury emissions from coal fired power plants. The regulations will be developed and finalized, with full compliance anticipated by 2007. Test work performed by others has identified a system by which the mercury in flue gases can be captured onto Powdered Activated Carbon (PAC) to control mercury emissions. However, the existing production capacity for PAC is only 10% of the capacity required for full implementation.

The process envisioned and defined in this project enables the reuse of PAC after its injection and collection from a flue gas stream in which the PAC injection point is after the electrostatic precipitators but prior to a baghouse. Once collected, the PAC is thermally treated in an inert atmosphere to desorb the contained mercury allowing the PAC to be returned to the injection system for reuse. The desorbed mercury is sequestered and concentrated for recovery into saleable product.

Based upon the results from the bench-scale feasibility testing in this report, the envisioned process is technically viable when the thermal desorption operation occurs under the following parameters:

- Inert atmosphere during elevated temperature processing;
- 550°C desorption temperature; and
- 30 minutes of retention at temperature

Using this process, PAC can be recycled at least 10 times without any degradation of the sorption characteristics.

Based upon the operating parameters established above, a bid package was prepared for the construction of a demonstration plant suitable for processing mercury laden PAC (or other sorbents) for a 270MW power plant.

Use of the PAC desorption/recycling system will decrease the yearly operating costs by at least $216,200 resulting in a return-on-investment (uninstalled capital basis) of 28.14%.

Compared to single-pass PAC that is injected once, collected and disposed of; this process offers:

- Significant yearly operating cost savings,
- Reduced PAC consumption to stretch the existing supply,
- Mercury emissions that are recyclable, and
- Eliminated environmental liability from landfilled mercury laden PAC.

SECTION 1
BENCH SCALE FEASIBILITY TESTING

PURPOSE AND SCOPE

The purpose of bench scale feasibility testing is to determine if the process envisioned in Figure 1 is technically viable. The criteria for this determination are:

- Will the PAC physically degrade when exposed to air at elevated temperatures?
- Will the PAC retain its sorptive properties when exposed to several desorption cycles?
- Can mercury be desorbed from the loaded PAC?

In order to answer these questions the following scope of work was carried out:

- Acquisition of a virgin PAC from Norit Americas (DARCO FGD).
- Acquisition of a mercury laden PAC that was produced from an operating mercury control system. The virgin PAC used in this control system was also Norit's DARCO FGD.
- Generate a synthetically mercury loaded PAC for testing.
- Generate temperature versus loss in mass data for PAC in air.
- Produce thermally cycled model PAC for sorptive properties testing.
- Perform mercury desorption on the synthetically loaded sample.
- Perform mercury desorption on the field sample of mercury loaded PAC.
- Perform sorption characteristic testing on the starting and thermally cycled PAC for comparison.

SAMPLE ACQUISITION

Two PAC samples (supplied by ADA-ES) were acquired from a coal fired power plant operating a mercury control system in which the PAC is injected into the flue gas down stream of the ESP's and prior to a baghouse. Referred to as SITE hereinafter.

- PMET RFA# 4444-1
  - 10 gallon sample: Received on 9/23/03
- PMET RFA# 4444-3
  - 5 gallon sample: Received on 12/29/03

GENERATION OF SYNTHETICALLY LOADED PAC

Prior to the arrival of the SITE sample material, a synthetically loaded PAC (DARCO FGD, the same grade of PAC used at SITE) was generated.

One gram of $HgCl_2$ and Hg were blended into coarse sand. This material and PAC were introduced into an apparatus to transfer the mercury compounds from the sand to the PAC. One 24 hour transfer test generated 250g of PAC that contained 6.4 ppm of total mercury, which is similar to what is expected at the SITE. The transfer apparatus is depicted in Figure 2.

FIGURE 2

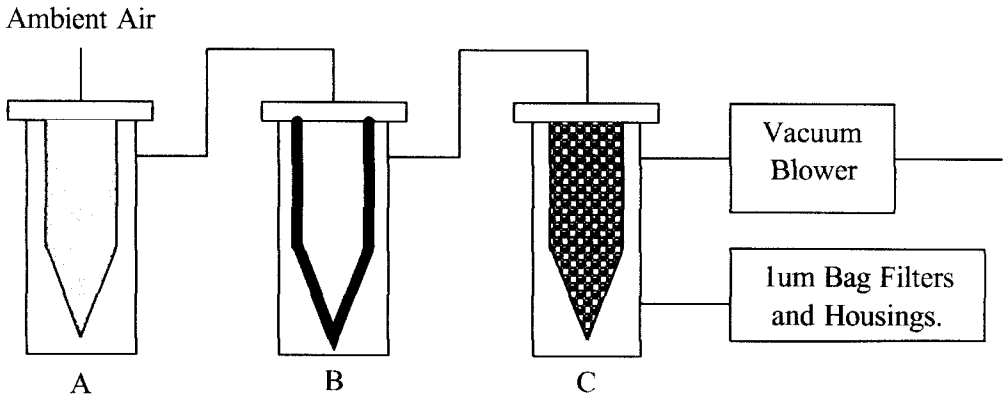

A: Mercury laden sand.
B: PAC ¼" thick.
C: Sulfur impregnated carbon for mercury exhaust control.

TESTING OF THE MODEL PAC

Two series of thermal treatments of the model PAC were performed. Both of these treatments were performed in air rather than nitrogen to study the reactivity of the carbon at various temperatures. The oxidation of the carbon was tracked by the loss in weight of the sample when the material was subjected to air at temperature for 60 minutes. The results of these tests are shown in Figure 3.

FIGURE 3

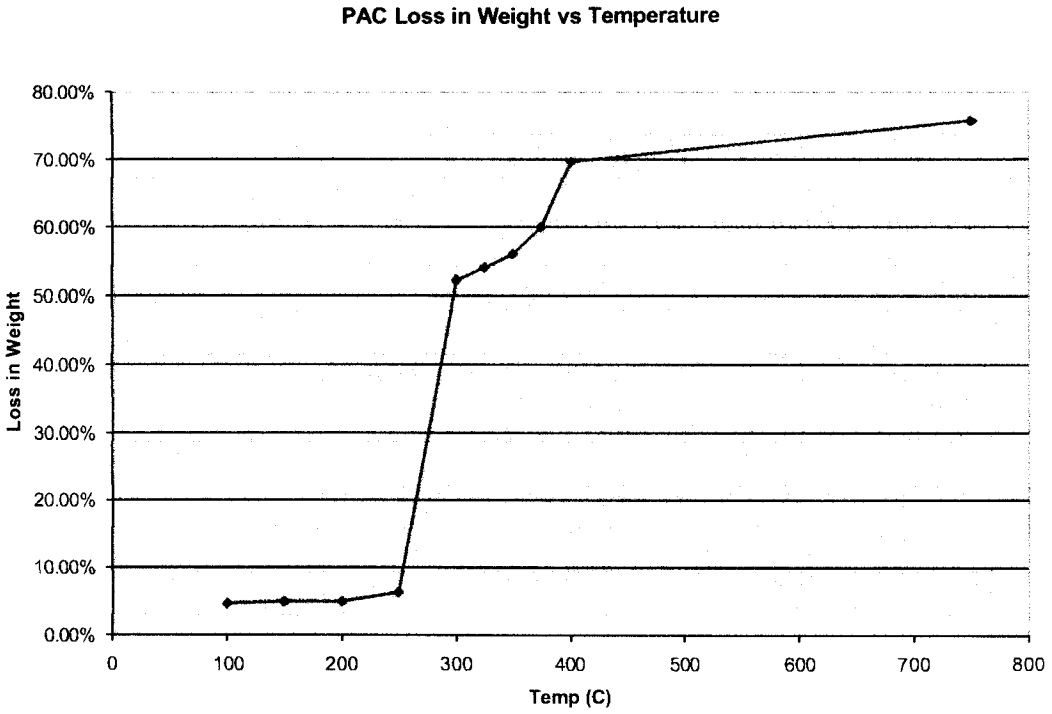

Some loss in weight (~5%) occurs at temperatures up to 200°C, and above 250°C the carbon reacts vigorously with essentially all of the available carbon being oxidized. This particular PAC sample (DARCO FGD) has an ash content of approximately 25%.

Figure 4 shows the loss in weight for a PAC sample exposed to air at 250°C.

FIGURE 4

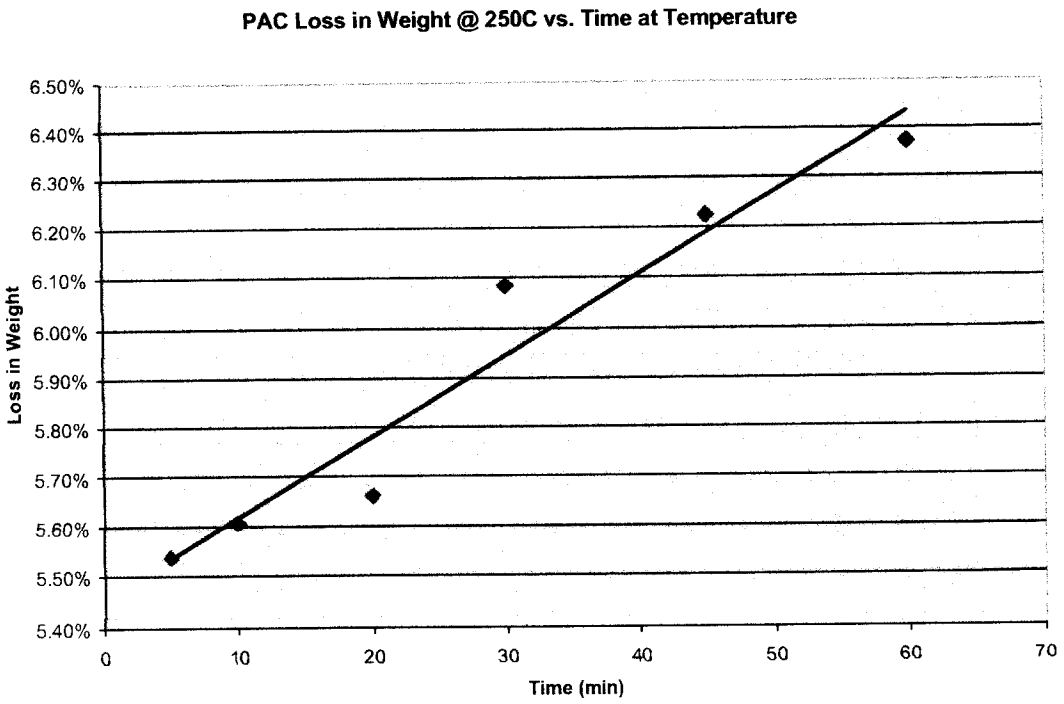

Figure 4 shows that even at a modest temperature of 250°C; the sample material undergoes oxidation of the carbon at a fairly constant rate of 0.016% Loss in Weight per minute exposed.

Clearly this testing indicates that an inert atmosphere is required for the tray desorption furnace to avoid significant losses of the PAC material during mercury desorption.

One thermal desorption test was performed using an inert atmosphere (nitrogen) in which the model PAC was cycled from ambient to 450°C ten times to simulate multiple recycles in the commercial system.

Figure 5 shows the change in carbon sorption capacity and surface area over the ten cycles.

FIGURE 5

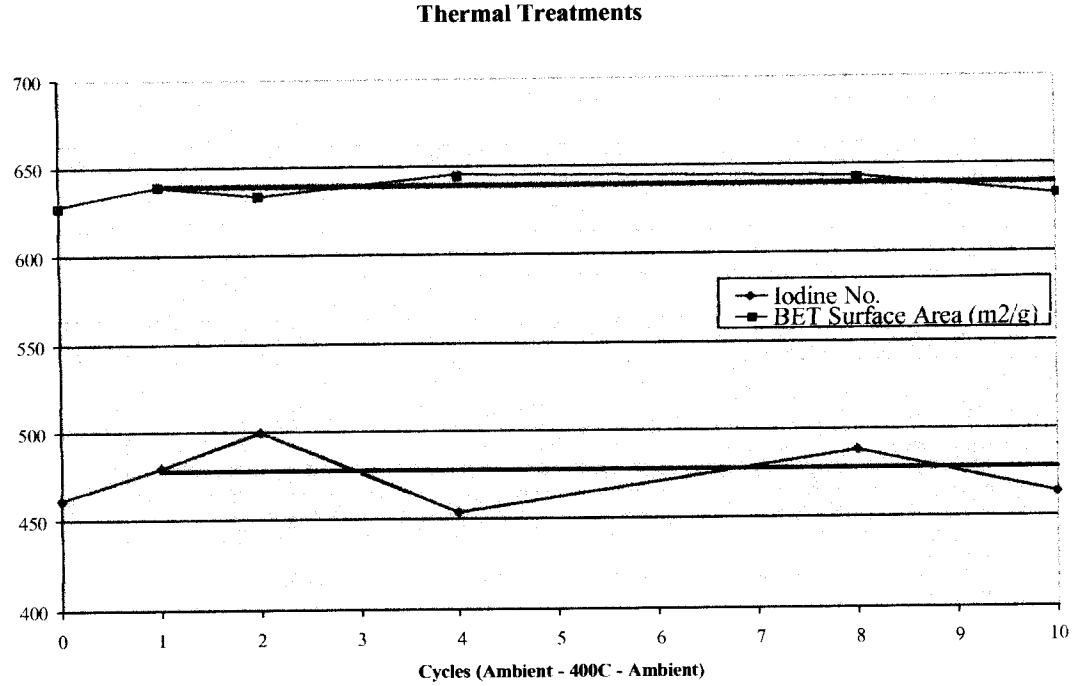

The weight loss of the model PAC over the ten cycles was less than 0.1%.

Figure 6 shows the nitrogen isotherm comparison of the model PAC and cycled PAC (10 thermal desorption cycles).

FIGURE 6

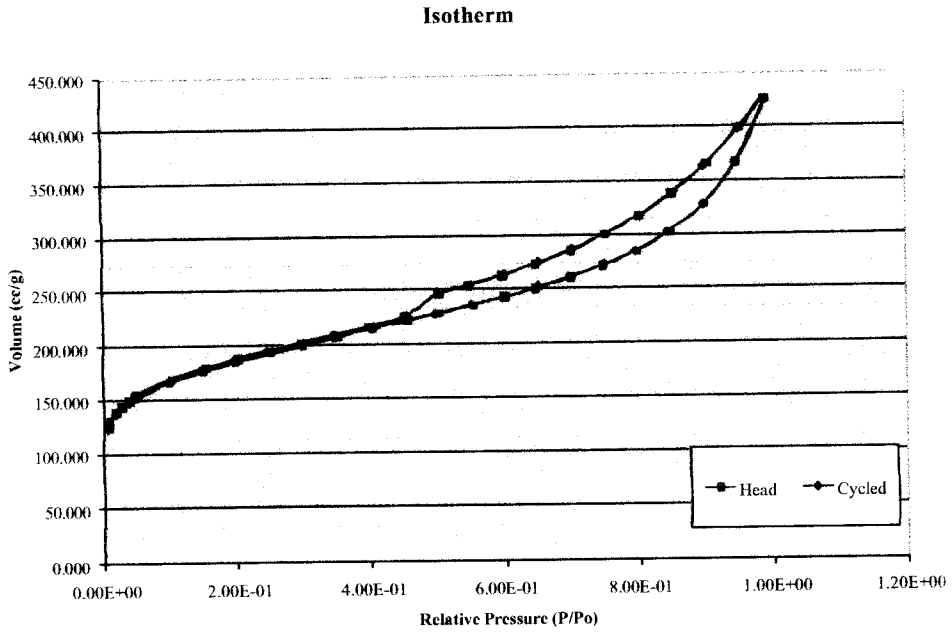

Figure 7 shows the pore size distribution comparison of the model PAC and cycled PAC (10 thermal desorption cycles).

FIGURE 7

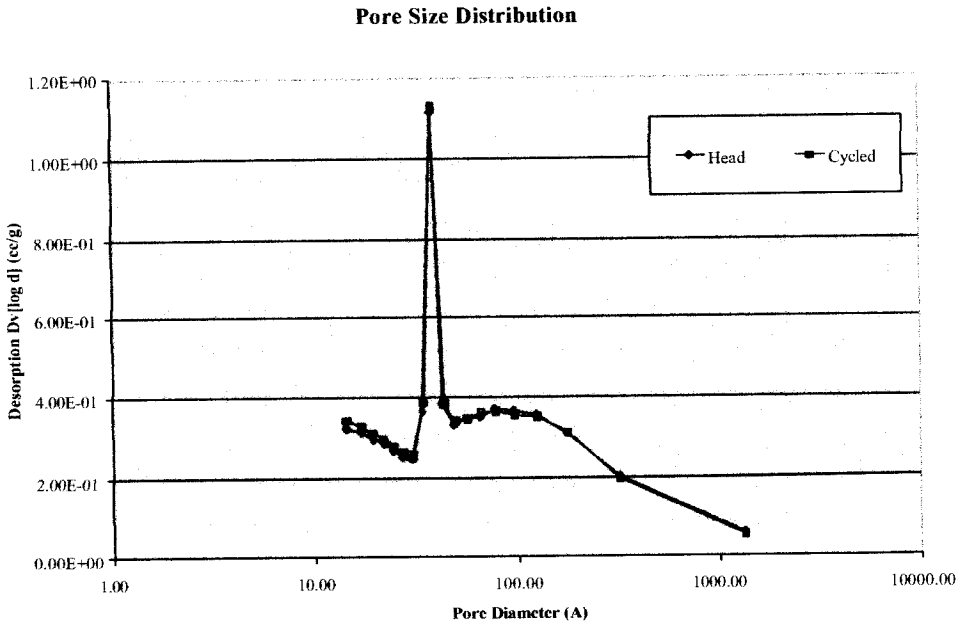

Comparison of the "Area-Volume-Pore Size" Data

Analysis	Head PAC	Recycled PAC
Multipoint BET	605.9 m^2/g	603.7 m^2/g
Single Point BET	616.3 m^2/g	613.6 m^2/g
t-Method External Surface Area	257.9 m^2/g	257.9 m^2/g
t-Method Micro Pore Surface Area	348.0 m^2/g	345.8 m^2/g
Total Pore Volume for pores with dia. < 390Å @ P/Po = 0.9475	0.5689 cc/g	0.5676 cc/g
t-Method Micro Pore Volume	0.1750 cc/g	0.1734 cc/g
Average Pore Diameter	37.56 Å	37.61 Å

Another thermal desorption test was run, in which the synthetically loaded PAC was subjected to conditions that would mimic a commercial rotary tray furnace.

- The loaded model PAC was placed into a tray to a depth of ½".
- This tray was placed into a retort oven and the nitrogen purge was started.
- The sample was ramped to 400°C in 15 minutes and held at temperature for 15 minutes.
- The sample was allowed to cool to 200°C over 60 minutes.
- The sample was then removed and agitated.
- This thermal desorption cycle was repeated 4 times using the same PAC sample.

After 15 minutes thermal desorption the total mercury was reduced to 0.38 ppm, and after 30 minutes the total mercury was reduced to <0.1 ppm.

SITE SAMPLE TESTING

The as received PAC was assayed for mercury and LOI (Loss On Ignition).

Sample ID	Mercury Content (ppm)	LOI (%)
4444-1	37.9	24.5
4444-3	35.3	19.0
Virgin PAC	0.1	75.7

The SITE PAC is loaded with mercury; however it also contained a large amount of ash. This must be fine ash that was not collected by the ESPs and allowed to pass to the COHPAC where it is collected with the injected PAC. Fine ash escaping from the ESPs must be minimized in order for the PAC to be recycled.

The mercury laden PAC was thermally desorbed at 450°C, 550°C, 650°C and 750°C in an inert atmosphere to simulate a commercial furnace.

Sample 4444-1 Mercury Desorption Data

Elapsed Time in Furnace (min)	Mercury Concentration (ppm)			
	450°C	550°C	650°C	750°C
0	37.9	37.9	37.9	37.9
30	9.54	BDL	BDL	BDL
60	8.24	BDL	BDL	BDL

BDL < 0.01 ppm Hg

Sample 4444-3 Mercury Desorption Data

Elapsed Time in Furnace (min)	Mercury Concentration (ppm)			
	450°C	550°C	650°C	750°C
0	35.3	35.3	35.3	35.3
30	14.4	BDL	BDL	BDL
60	12.3	BDL	BDL	BDL

BDL < 0.01 ppm Hg

Mercury was successfully stripped from both samples at 550°C and higher. However, the mercury was not completely removed from the PAC at 450°C.

CONCLUSIONS

When PAC is exposed to air at elevated temperatures, it clearly starts to physically degrade. This degradation occurs by the partial oxidation of the carbon structure. In order for the proposed process to function properly, the mercury desorption operation must occur in an inert atmosphere such as nitrogen, argon or helium.

As evidenced by the testing performed on virgin PAC and PAC that was thermally cycled 10 times to simulate multiple passes through the mercury desorption operation, the sorption characteristics of the cycled PAC remained unchanged in comparison the virgin PAC.

Whether it was the synthetically loaded PAC or the SITE sample, the attached mercury is able to be desorbed from the PAC to levels less than 0.01ppm. The SITE sample required temperatures in excess of 500°C for 30 minutes during the desorption operation. Since the boiling points of mercury and mercury chloride are below 450°C, it can be surmised that an active binding agent exists in the SITE PAC. This could occur if other halogens (such as Fluorine) existed in the flue gas.

The envisioned process is technically viable when the thermal desorption operation occurs under the following parameters:

- Inert atmosphere during elevated temperature processing;
- 550°C desorption temperature; and
- 30 minutes of retention at temperature.

SECTION 2
BID PACKAGE

PURPOSE AND SCOPE

The purpose of this section is to generate a bid package that would enable a reputable engineering firm to cost out the procurement and installation of a pilot-plant within 20% of the actual cost.

The following items were produced as part of the bid package:

- Mass Balance
- Process Flow Diagram (PFD)
- Equipment List
- General Arrangement Drawing
- Elevation Drawing
- Process and Instrumentation Diagrams (P&IDs)

A budgetary economic evaluation was also produced to compare this process to single-pass injection, collection and disposal options.

MASS BALANCE

The mercury control system that is installed at Alabama Power E.C. Gaston[1] was used as the baseline case for the mass balance. Other criteria used as the basis for the mass balance include:

- 270 MW boiler
- 80% boiler capacity factor
- 1,000,000 acfm of flue gas to the COHPAC (baghouse)
- 80% mercury removal efficiency
- 1.5 lbs of PAC per MMacf of flue gas
- 6,700 operating hours per year
- $0.50 per pound of virgin PAC
- 20% PAC bleed rate
- 1.15 COHPAC loading factor

The mass balance and PFD was produced using the data produced in SECTION 1 along with the baseline case and basis points.

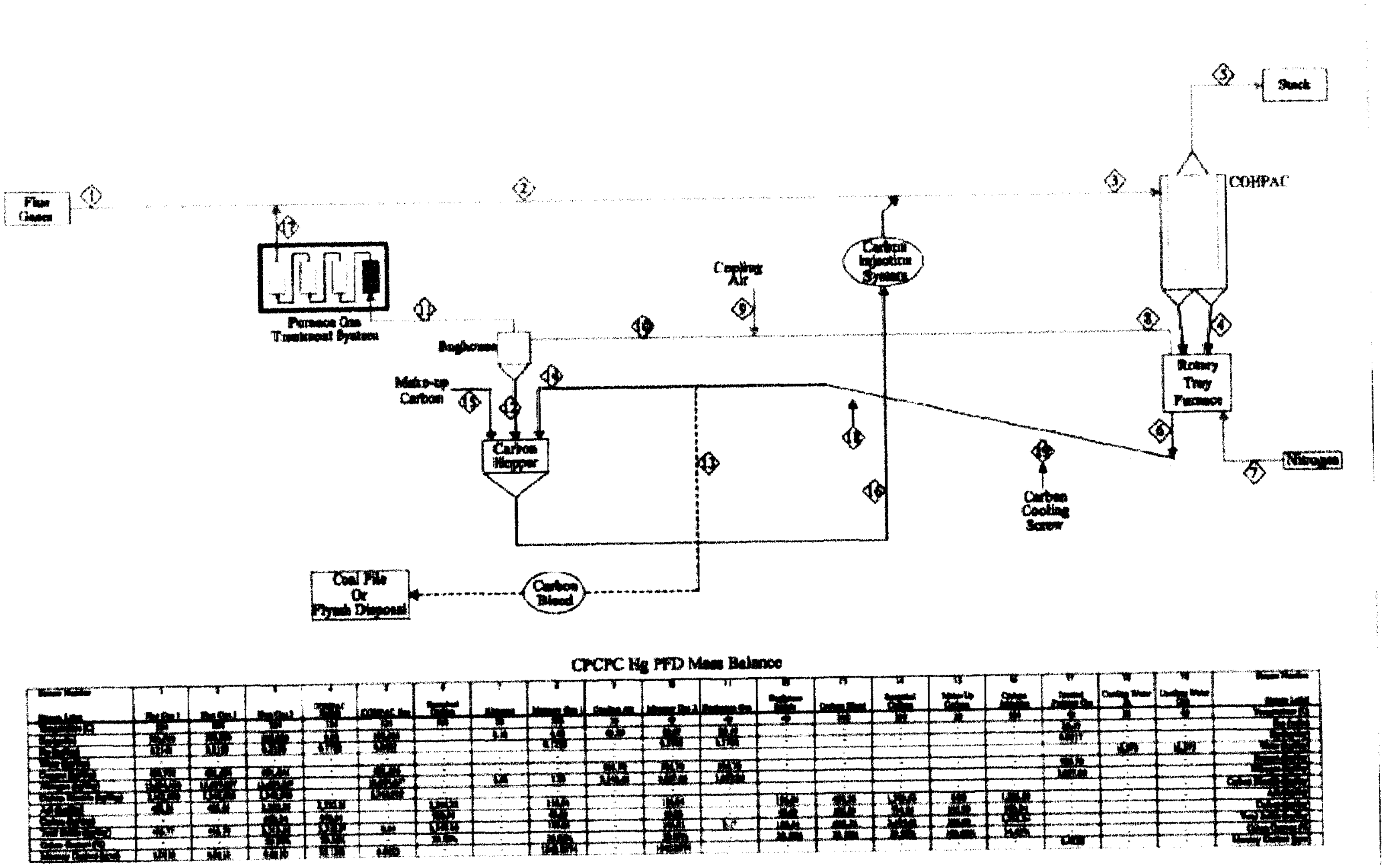

CPCPC Hg PFD Mass Balance

PITTSBURGH MINERAL AND ENVIRONMENTAL TECHNOLOGY	DWG NO.
PROJECT: CPCPC Hg PFD	05
DATE: MARCH 10, 2004 | REVISION: | DRAWN BY: MRP	

To aid in the viewing of this document, the following enlargement of the mass balance is included.

Stream Number Stream Label	1 Flue Gas 1	2 Flue Gas 2	3 Flue Gas 3	4 COHPAC Solids	5 COHPAC Gas	6 Desorbed Carbon
Temperature (C)	124	124	124	124	124	550
Gas (acfm)	500,000	500,089	500,089	0.00	500,089	-
Hg (kg/day)	0.2142	0.2160	0.2160	0.1728	0.0432	-
Water (kg/day)	-	-	-	-	-	-
Oxygen (kg/day)	600,730	601,656	601,656	-	601,656	-
Nitrogen (kg/day)	13,604,000	13,607,057	13,607,057	-	13,607,057	-
Carbon Dioxide (kg/day)	5,342,900	5,342,900	5,342,900	-	5,342,900	-
Ash (kg/day)	466.56	466.56	2,332.86	2,332.86	-	2,216.22
Carbon (kg/day)	-	-	979.94	979.94	-	930.94
Total Solids (kg/day)	466.77	466.78	3,313.02	3,312.97	0.04	3,147.16
Carbon Content (%)	-	-	29.58%	29.58%	-	29.58%
Mercury Content (ppm)	0.0110	0.0110	0.0110	52.1526	0.0022	-

Stream Number Stream Label	7 Nitrogen	8 Mercury Gas 1	9 Cooling Air	10 Mercury Gas 2	11 Baghouse Gas	12 Baghouse Solids
Temperature (C)	20	550	20	49	49	49
Gas (acfm)	0.18	0.18	89.29	89.47	89.47	-
Hg (kg/day)	-	0.1728	-	0.1728	0.1728	-
Water (kg/day)	-	-	-	-	-	-
Oxygen (kg/day)	-	-	925.70	925.70	925.70	-
Nitrogen (kg/day)	8.38	8.38	3,048.62	3,057.00	3,057.00	-
Carbon Dioxide (kg/day)	-	-	-	-	-	-
Ash (kg/day)	-	116.64	-	116.64	-	116.64
Carbon (kg/day)	-	49.00	-	49.00	-	49.00
Total Solids (kg/day)	-	165.81	-	165.81	0.17	165.64
Carbon Content (%)	-	29.55%	-	29.55%	-	29.58%
Mercury Content (ppm)	-	1042.0374	-	1042.0374	-	-

Stream Number Stream Label	13 Carbon Bleed	14 Recycled Carbon	15 Make-Up Carbon	16 Carbon Injection	17 Treated Furnace Gas	18 Cooling Water In	19 Cooling Water Out
Temperature (C)	200	200	20	184	49	20	40
Gas (acfm)	-	-	-	-	89.47	-	-
Hg (kg/day)	-	-	-	-	0.0017	-	-
Water (kg/day)	-	-	-	-	-	16,376	16,376
Oxygen (kg/day)	-	-	-	-	925.70	-	-
Nitrogen (kg/day)	-	-	-	-	3,057.00	-	-
Carbon Dioxide (kg/day)	-	-	-	-	-	-	-
Ash (kg/day)	466.56	1,749.66	0.00	1,866.30	-	-	-
Carbon (kg/day)	195.99	734.95	195.99	979.94	-	-	-
Total Solids (kg/day)	662.55	2,484.61	195.99	2,846.24	-	-	-
Carbon Content (%)	29.58%	29.58%	100.00%	34.43%	-	-	-
Mercury Content (ppm)	-	-	-	-	0.4338	-	-

EQUIPMENT LIST

Based upon the PFD and mass balance, the following equipment list was generated. It includes all the primary pieces of process equipment.

Description	Utility Requirements	Size	Cost
Rotary Tray Furnace	20 kW, 480V, 3Ø, 100A	Size L	$100,000
Nitrogen Supply System		4 Dewer Manifold	$2,000
Mercury Laden PAC Feeder – Furnace Inlet	2 HP, 480V, 3Ø		$5,000
Rotary Air Lock – Furnace Discharge	2 HP, 480V, 3Ø	6" dia.	$2,500
Desorbed Carbon Cooling Screw Conveyor	5 HP, 480V, 3Ø 3 gpm 20°C water	6" dia., 40 rpm	$5,000
Desorbed Carbon Hopper		300 ft^3	$4,000
Virgin PAC Feeder	2 HP, 480V, 3Ø	2 ft^3	$5,000
Pneumatic Conveying System	30 HP, 480V, 3Ø	3" w/ 250' max run 275 cfm @ 10 psi	$4,000
Blower	3 HP, 480V, 3Ø	2" w/ 300' max run 100 cfm @ 5 psi	$1,500
Baghouse	1 cfm Compressed Air @ 125 psi	50 ft^2	$3,000
Carbon Columns		15 ft3 8.5 sec. of contact time	$5,000
Sub-Total			**$137,000**
Instrumentation			$30,000
Utility Hookups			$20,000
Uninstalled Total			**$187,000**

Since this bid package envisions a pilot-plant with limited life, the equipment is priced based upon used/refurbished equipment. The pricing was obtained from several used equipment dealers across the US.

Pricing for a new rotary tray furnace was provided by Wyssmont (Appendix A). This was obtained to provide the unit specifications for the primary piece of equipment.

GENERAL ARRANGEMENT DRAWING

Once the equipment was specified, it was laid out as if the pilot-plant site had a large (40' x 40') and level plot for installation.

The original CAD drawing is to scale however, to make it fit within the 8.5" by 11" size format the drawing was compressed and is no longer to scale.

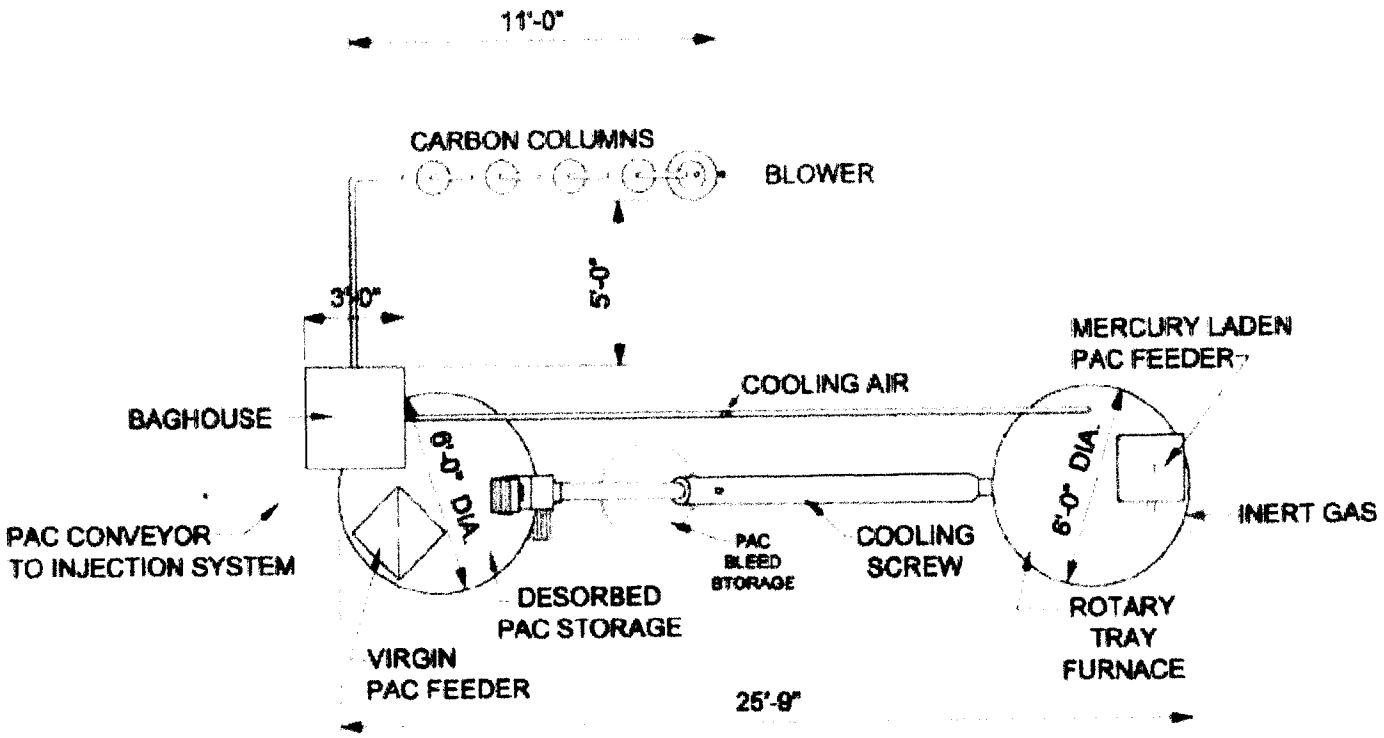

PLAN - PAC DESORPTION / RECYCLING PLANT

SCALE: 1/2" = 1'-0"

PITTSBURGH MINERAL AND ENVIRONMENTAL TECHNOLOGY

DWG NO. 02

PROJECT NO: 03V64

DATE: APRIL 22, 2004

REVISION:

DRAWN BY: MRP

ELEVATION DRAWING

In order to show the elevations of all the pieces of equipment, the elevation drawing arrangement does not match the general arrangement drawing.

The original CAD drawing is to scale however, to make it fit within the 8.5" by 11" size format the drawing was compressed and is no longer to scale.

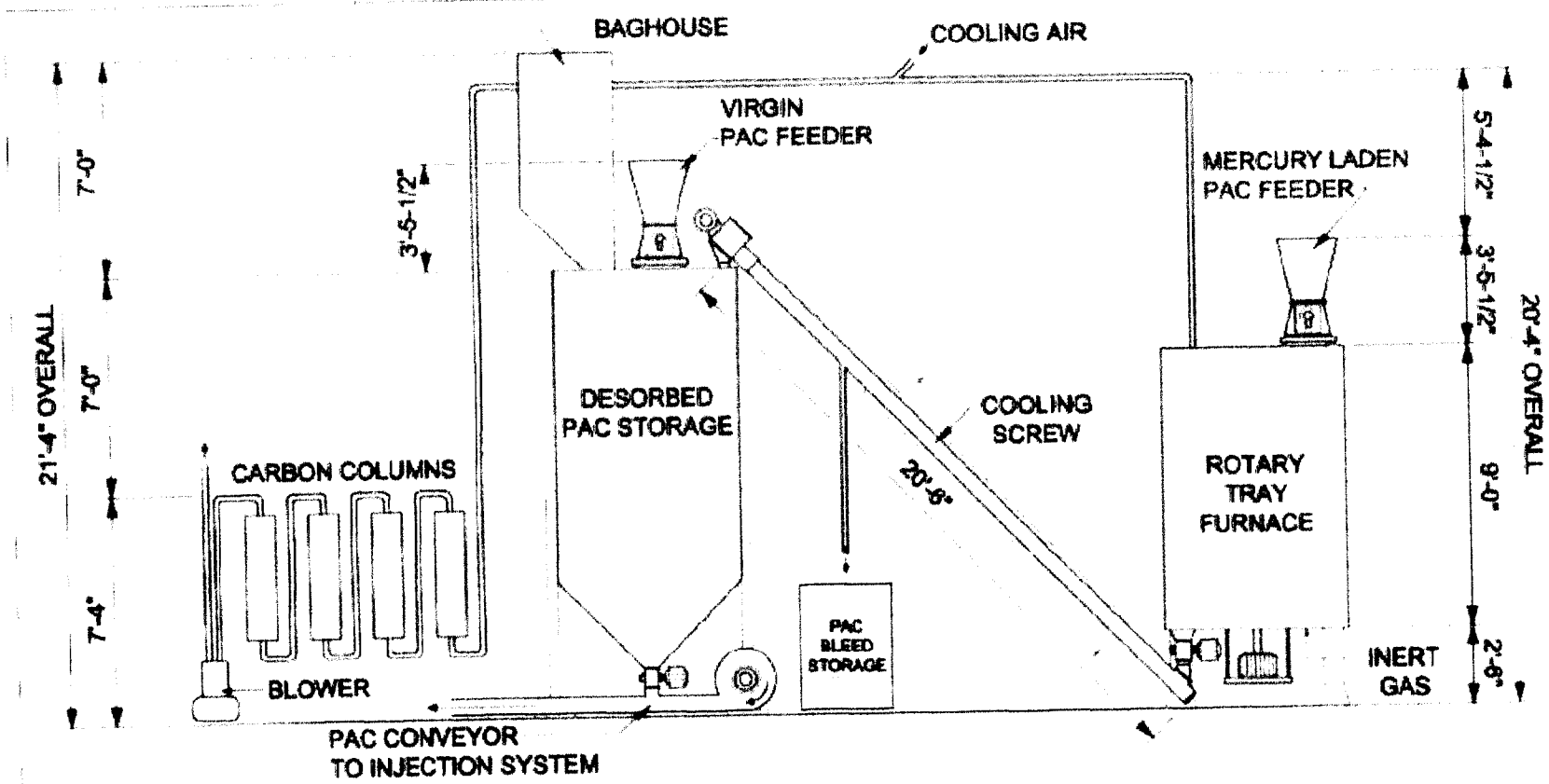

ELEVATION - PAC DESORPTION / RECYCLING PLANT

SCALE: 1/4" = 1'-0"

PITTSBURGH MINERAL AND ENVIRONMENTAL TECHNOLOGY

PROJECT NO: 03V64

DATE: APRIL 12, 2004

REVISION: APRIL 22, 2004 DRAWN BY: MRP

DWG NO. 01

PROCESS AND INSTRUMENTATION DIAGRAMS

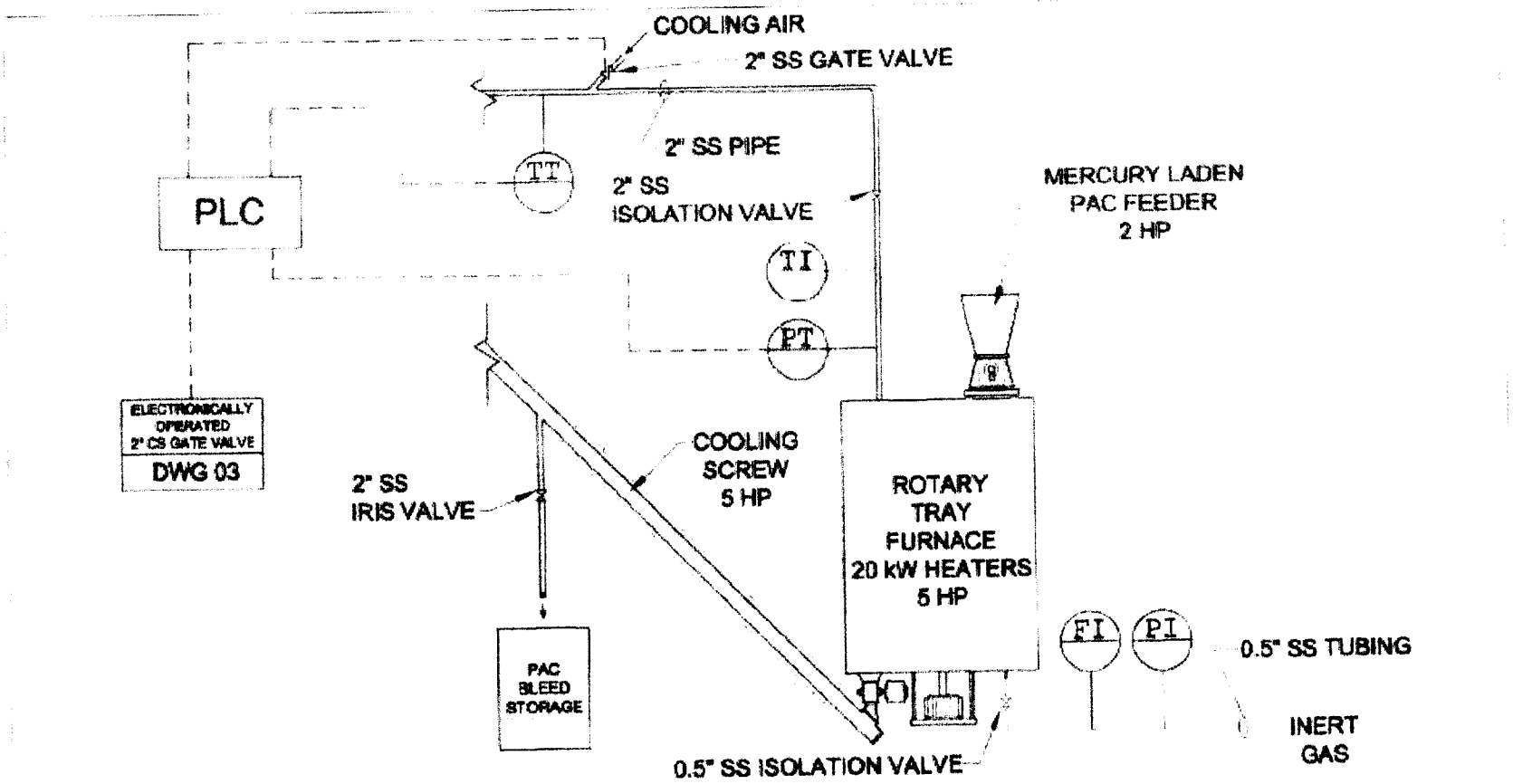

ELEVATION - PAC DESORPTION / RECYCLING PLANT

SCALE: N.T.S.

PITTSBURGH MINERAL AND ENVIRONMENTAL TECHNOLOGY

DWG NO. 04

PROJECT NO: 03V64

DATE: MAY 10, 2004

REVISION: MAY 12, 2004 DRAWN BY: MRP

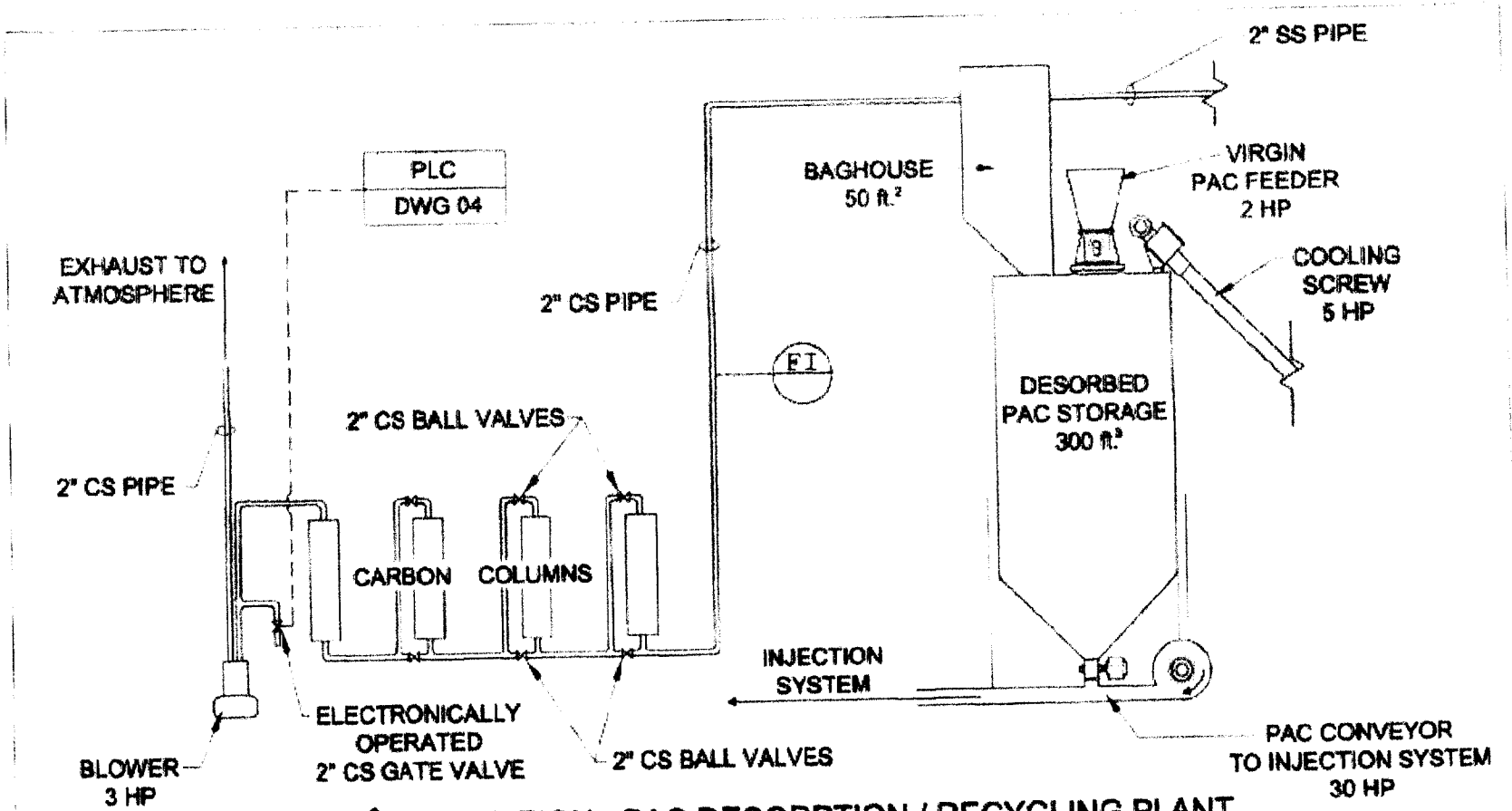

ELEVATION - PAC DESORPTION / RECYCLING PLANT

SCALE: N.T.S.

PITTSBURGH MINERAL AND ENVIRONMENTAL TECHNOLOGY

DWG NO. 03

PROJECT NO: 03V64

DATE: MAY 06, 2004

REVISION: MAY 12, 2004 DRAWN BY: MRP

Based upon the bid package presented in this section and data taken from the Gaston testing final report[1], the following yearly operating costs were derived.

	Dust Carry Over from ESP to COHPAC (gr/acf)	
	0.04	0.01
	Standard ADA System	ADA System With Recycling System
Capital Costs		
COHPAC	$1,000,000	$1,150,000
Injection System	$500,000	$575,000
Carbon Recycling System		$187,000
Sub-Total	$1,500,000	$1,912,000
Yearly Amortization (5 yrs @ 8%)	**$364,975**	**$465,222**
Operating Costs		
PAC	$301,500	$60,300
Labor	$100,500	$100,500
Utilities & Consumables	$25,000	*$50,000*
Consumed PAC Disposal	???	$0
Sub-Total	**$427,000**	**$210,800**
Total (Yearly Costs)	**$791,975**	**$676,022**
	ROI (uninstalled basis)	28.14%

The COHPAC capital cost was estimated utilizing engineering capital cost estimating data. The capital cost of the injection system was taken from the Gaston testing final report[1].

The 1.15 loading factor that was applied to COHPAC and injection system costs. This reflects a 1.15X increase in size of equipment due to the additional volume of carbon and ash that is carried into the COHPAC as a result of an 80% recycle stream.

In order to minimize the loading factor, the dust carry over value was deceased to the lowest value achieved during testing of the Gaston COHPAC (0.01 gr/acf). Normal operations require the dust carry over value to be <0.04 gr/acf.

It is assumed that with a sufficient level of automation, the same manpower could run both systems as easily as one.

Return On Investment (ROI) was calculated using the following method:

Savings in Yearly Operating Costs / Increase in Capital Required

This cost analysis does not include any installation costs, as the Gaston testing final report[1] did not include any installation costs for the injection or COHPAC systems.

It should be noted that this budgetary economic evaluation does not include any cost to dispose of the consumed PAC from the standard ADA mercury control system. This cost could range from $12/ton[2] (fly ash) to $1,200/ton[2] (mercury containing hazardous waste). This could result in an additional $360,000 in yearly operating costs. 181

In utilizing the PAC recycling system, the mercury is removed from the PAC prior to the bleed point which allows the spent PAC to be used for fuel value in the boiler avoiding all disposal costs.

CONCLUSIONS

The loading factor value is very sensitive to the fine ash carry over. It is extremely important that the ESP's are operating at maximum capacity so that the COHPAC, injection system and PAC desroption/recycling systems are not over loaded with material. Ultimately this will affect the process economics as the loading factor increases the size and cost of the systems.

Use of the PAC desorption/recycling system will decrease the yearly operating costs by $216,200. The capital required to install the PAC desorption/recycling system will be paid for in less than four years.

If mercury contaminated PAC is disposed of as hazardous waste, there is some future concern with regard to liability. There are numerous examples of instances when mercury containing materials were disposed of using the guidelines for that period of time; however as time passed the guidelines changed resulting in landfills that are now tagged as "Superfund" sites. Some of the parties responsible for the generation of the material that resides in those landfills are now liable for damages and/or cleanup costs. Use of the PAC desorption/recycling system removes all mercury liability from the spent PAC.

1. C. Bustard, S. Sjostrom, S. Renninger, L. Monroe Ph.D., R. Miller, R. Chang Ph.D. "Full-Scale Evaluation of Mercury Control with Sorbent Injection and COHPAC at Alabama Power E.C. Gaston". www.adaes.com/publications/Gaston Paper Final 2001-30-02.pdf, January 30, 2002.

2. L. Monroe, J. Cichaniwicz, G. Offen. "UARG Comments on Process Inputs for EPA's Planned IPM Modeling Runs". www.epa.gov/ttnatw01/combust/utiltox/uarg ipm comments.doc, April 19, 2002.

APPENDIX A

Wyssmont ™ Company, Inc.

Process Engineers: drying, sublimation, cooling, calcining, gas-solids reaction.

1470 Bergen Boulevard
Fort Lee, NJ 07024-2197

Phone: (201) 947-4600
Fax: (201) 947-0324
E-mail:sales@wyssmont.com
www.wyssmont.com

February 19, 2004

PMET
700 Fifth Avenue
New Brighton, PA 15066

Attention: Mr. Dale Nickels
e-mail: dale@pmet-inc.com

Reference: Heat-Treating Activated Carbon
in the Wyssmont System
Our Reference Number B02206

Dear Dale:

Thank you for your interest in our equipment.

This is and ideal application for our equipment. Our TURBO-HEAT-TREATER• can uniformly vaporize the Mercury in the feed material.

The Wyssmont TURBO-DRYER operates continuously and almost always gives the lowest operating cost per pound of product when all costs are considered. Please refer to the attached letter of additional benefits of the TURBO-DRYER.

The benefits of the TURBO-HEAT-TREATER for this application include:

- **Excellent product quality and uniformity**. The material bed is turned over gently after each transfer. This continuous mixing and levelling, along with the close temperature control and controlled residence time assure the highest product quality and uniformity.

- **Gentle handling and low exhaust velocities minimize particle attrition and dust carryover.** This is one of the many advantages of the TURBO-HEAT-TREATER compared to high air flow units such as flash, fluid or rotary units.

- **Flexibility.** The unit can handle materials with a wide range of handling characteristics – from sludges and pastes through filter and centrifuge cakes to pellets and powders. For even the wettest material, backfeed is seldom required. Easily adjustable drying parameters allow for handling different moisture levels. Upstream upsets that can cause heat transfer surfaces to foul, hot spots, and consequent process problems are eliminated with a TURBO-HEAT-TREATER.

- **Easy automatic operation.** It is self-compensating for variations in the feed rate. The system can be operated at 20-25% of capacity up to the maximum without requiring changes by the operator – the heat-treater automatically adjusts for this amount of change and produces the same product quality – unlike other dryers. Most users say they "turn it on and forget it."

Mechanically, the unit offers the following advantages:

1. **Reliable, continuous and automatic operation.** Our units are famous for extended periods of operation without shutdown for maintenance.

2. **Low Maintenance Costs**. Usually the annual maintenance costs are less than 1% of the initial capital cost.

3. **Low Horsepower Requirements**. The unit has low horsepower requirements. This further reduces operating costs.

We are pleased to submit our preliminary design based on the information you provided.

Product Rate	140 kg/hr
Mercury in Feed	0.004%
Retention Time, minutes	30

TURBO-HEAT TREATER Size L

Dimensions	
Diameter, ft.	6
Height, ft.	9
Horsepower Requirements	
TURBO-TURBO-Fans	½
Tray System	½
Approximate Price*	$275,000. - $300,000.

*Type 316 stainless steel for all interior parts, designed for operation at 550°C.

We have included an internal electrical heating system with a small (5-10cfm) of inert gas to remove the mercury vapor from the system. This small exhaust stream can then be processed in your mercury recovery system.

PMET
New Brighton, PA

February 19, 2004

Control instrumentation which includes two-station temperature control and local panelboard will cost approximately $25,000. We have not included a PLC in this control package. Generally our system does not require a separate PLC. If you can incorporate our system in another PLC most of the items in our control package can be eliminated. We can then provide temperature sensors, damper operators and SCR controller.

A Multiple Screw Feeder→ Model MSF-836 can be provided to meter the feed into the dryer and spread the feed across the top shelf. In type 316 Stainless Steel construction with variable speed drive the cost is approximately $18,000.

We can also recommend a discharge airlock to seal the product discharge. In type 316 Stainless Steel with drive the cost is approximately $8,000.

We are very proud of our excellent reputation throughout the industry. Over the last twenty (20) years in CHEMICAL ENGINEERING MAGAZINE Research Reports, in which thousands of chemical engineers were polled, Wyssmont was cited as the most preferred supplier of dryers by more than a 2:1 margin.

We look forward to working with you on this project. If you have any questions please do not hesitate to contact us or our local representative, Mr. Kirk Marker.

Very truly yours,

WYSSMONT COMPANY, INC.
Joseph Bevacqua

Joseph Bevacqua
Vice President – Sales

JB/jt
Enc: Process Letter

cc:Daco Technical Sales
P. O. Box 527
Morgan, PA 15064-0527
412-257-1810

FINAL TECHNICAL PROGRESS REPORT

SUBMITTED TO

CONSORTIUM FOR PREMIUM CARBON PRODUCTS FROM COAL

The Pennsylvania State University
407 Academic Activities building
University Park, PA 16802-2398

NOVEL ANTHRACITE SORBENTS FOR CO_2 CAPTURE

Reporting Period Start Date: *March 1, 2003*
Reporting Period End Date: *February 29, 2004*
Principal Authors: *Dr. M. Mercedes Maroto-Valer, PI*
Dr. Zhong Tang

Report Issued Date: *July 15, 2004*

DOE Award number: *DE-FC26-98FT40350*

Internal Agreement Number: *2484-TPSU-DOE-0350*

Submitting Organization: *The Energy Institute*
The Pennsylvania State University
405 Academic Activities Building
University Park, PA 16802-2398
Phone: (814) 863 8265

DISCLAIMER

FINAL TECHNICAL PROGRESS REPORT

March 1, 2003 – February 29, 2004

Table of contents

Abstract

Anthracites have inherent chemical properties, fine pore structure and relatively low price that makes them excellent raw materials for the production of premium carbon products, such as for the synthesis of CO_2 sorbents. The President's Global Climate Change Initiative commits to reduce greenhouse gas intensity by 18% over the next ten years. However, the costs of current CO_2 separation and capture technologies are estimated to be about 75% of the total cost of ocean or geological sequestration. Furthermore, the demand to develop revolutionary direct capture technologies has also been identified by the U.S. DOE. Accordingly, the objective of this project was to synthesize high-surface-area powdered anthracites and impregnate them with amine compounds. The feasibility of using these materials for CO_2 capture was investigated.

Three Pennsylvania anthracites (PSOC-1468, AFM 800 and AFM 2600) were selected for this work. PSOC-1468 was obtained from the Penn State Coal Bank, and AFM 800 and AFM 2600 were provided by FB Leopold. A parametric study was conducted to ascertain the effect of time and temperature on the porous structure of activated carbons produced from anthracite. A lab scale fluidized bed reactor was used for the activation. The N_2-77K isotherms show that the activated anthracites have highly developed microporosity and a small amount of mesopores. The surface area can get up to 792m^2/g with 3 hours activation time. However, extending the activation time beyond 3 hours decreases the surface area. Regarding the activation temperature effect, it has been shown here that the surface area and pore volume of the activated anthracite increased first going from 800 to 850°C, where the sample activated at 850°C has a surface area and volume of 927.9m^2/g and 0.442mL/g, respectively. However, when increasing the activation time to 890°C resulted in a decrease of both surface area and pore volume. Moreover, the anthracite activated at the lowest temperature (800°C0 has the largest CO_2 adsorption capacity, probably due to its narrow pore structure. The surface areas go through a maximum with increasing solid yields.

The adsorption capacity of the activated anthracites decreases rapidly with increasing adsorption temperature, probably due to the adsorption being a physisorption process. The anthracite with the highest CO_2 adsorption capacity was the sample activated at 800°C for 2 hours, whose surface area was only 540m^2/g, and the adsorbed amount of CO_2 was 65.7mg-CO_2/g-adsorbent. This is probably due to a relationship between microporosity and CO_2 physisorption processes. Several surface treatment methods, including NH_3 heat treatment, HNO_3 oxidization and polyethylenimine (PEI) impregnation, were used to modify the surface properties of the activated anthracites in an attempt to increase their CO_2 capture capacity at higher temperatures. The surface treatment methods investigated changed the porous structure and surface chemistry of the anthracites, and therefore, affected their CO_2 capacities. No significant difference was observed between the adsorption capacities of the three anthracites (PSOC-1468, AFM 800 and AFM 2600) investigated in this work.

List of tables

List of figures

1. INTRODUCTION

1.1. Rationale

Anthropogenic emissions have increased the CO_2 concentration on the atmosphere with over 30% compared to pre-industrial levels [1]. Most of these anthropogenic emissions are caused by fossil fuel utilization, where around one-third is due to electricity generation from fossil fuel combustion, mainly coal-fired units. Furthermore, fossil fuel electricity generation units rank as the first target to reduce anthropogenic emissions due to their stationary nature. However, the costs of current CO_2 separation and capture technologies are estimated to be about 75% of the total cost of ocean or geological sequestration, including the costs for compression to the required pressure for subsequent sequestration [2]. For instance, for a pulverized coal power plant, the estimated capture costs are \$35-\$264/ton of CO_2 with a power cost increase of 25-215 mills/kWh. Consequently, there is a demand to develop revolutionary "direct capture" technologies. New solid-based sorbents are being investigated, where the amine groups are bonded to a solid surface, resulting in an easier regeneration step [3, 4]. The supports used thus far, including commercial molecular sieves and activated carbons, are very expensive and hinder the economical viability of the process. Accordingly, there is a need to find low-cost precursors that can compete with the expensive commercial supports, and develop effective solid sorbents that can be easily regenerated, and therefore, have an overall lower cost over their lifetime performance.

Anthracites contain mostly carbon (92–98%) present in large polycyclic aromatic sheets, resulting in a highly ordered structures with a high ultra-microporosity [5]. Due to their

inherent chemical properties, fine porosity and relatively low price, significant opportunities exist for the non-fuel uses of anthracites, especially as sorbents precursors. Furthermore, previous studies have shown that being able to produce an activated carbon with high surface area and pore volume, while maintaining the pore volume in a narrow pore range, may prove to make the best activated carbons, as it is the case for anthracites.

Activated carbons are sorbents with a highly developed porosity, especially micro- and mesopores, that are used in a wide range of household, medical, industrial, military and scientific applications, including gas-phase and liquid-phase processes [6]. The activation process together with the intrinsic nature of the precursors strongly determines the characteristics of the resulting activated carbons. Activated carbons can be produced from different precursors, including coals of different rank, and lignocellulosic materials, by physical or chemical activation processes [7-12]. Recently, increasing attention has been focused on using anthracites as feedstock for activated carbons, due to their inherent chemical properties, fine structure and relatively low price that make them excellent raw materials for the production of activated carbons with highly developed microporosity [13-18].

The porous structure (surface area and pore size distribution) and surface chemistry control the adsorption properties of the activated carbons in traditional applications like water filtration and air purification [6]. Similarly, the CO_2 adsorption capacity of activated carbons is a function of their pore structure and surface chemistry properties. It has been reported that the CO_2 adsorption capacities of activated carbons decrease with increasing adsorption

temperature due to the physical nature of the adsorption process [4]. Therefore, different surface treatments have been developed to improve the CO_2 adsorption capacity of activated carbons. For example, it has been shown that the CO_2 capture capacity can be increased by introducing nitrogen functional groups on the surface either by NH_3 heat treatment or chemical impregnation [19, 20, 21]. Previous work has focused on applying these treatments to high surface area materials, like commercially available activated carbons and zeolites, and to a lesser extent fly ash carbons [19, 20, 21]. The authors have previously shown that high surface area activated carbons can be produced from anthracite by steam activation [15, 18]. Unfortunately, the use of anthracites as precursors for adsorbent materials is being under-exploited, probably due to the limited number of studies assessing the possible routes for their conversion into activated carbons.

1.2. Program objectives

The overall objective of this research program is to develop low-cost, high-surface- area, amine impregnated powdered anthracites and test their possible use for CO_2 capture. The sorbents developed here will satisfy the need to develop revolutionary "direct capture" technologies, as identified by the U.S. Department of Energy. The outlook for the activated carbon market is for continued growth, as increasing stringent environmental requirements drive both developed and developing regions to incorporate activated carbons into water and air treatment systems. One of the applications that could increase dramatically the market volume is for CO_2 capture, due to the large volumes that need to be adsorbed. Therefore, this project could open a huge market for the anthracite industry. It is anticipated that the proposed sorbents will have significant performance and cost savings benefits over other

solid sorbents used for CO_2 capture. Furthermore, the anthracite precursors selected for this study are lower cost materials than other proposed sorbent supports, like zeolites.

1.3. Research design and tasks

This research program can be divided into the following three tasks described below.

- Task 1: Procurement and characterization of anthracites. In this task, a series of Pennsylvania anthracites provided by F.B. Leopold Co. Inc., were procured. It is anticipated that around 4 samples from different Pennsylvania coal seams will be included in this study. The sample selection will be conducted on basis of the chemical properties, including ash and volatile matter. The samples were prepared by F.B. Leopold Co. Inc to different particle sizes. The anthracites were then characterized by Penn State University using a customary suite of coal analyses.

- Task 2: Development of anthracite based sorbents. The samples were activated using the protocol previously developed by the authors [15, 18]. This protocol includes a one-step activation process using a system that consists of a stainless steel tube reactor and a vertical tube furnace. The anthracite samples were activated under a wide range of controlled operating variables in order to establish the optimum route for the generation of activated anthracites with properties similar to commercial zeolites and activated carbons (i.e. surface area >1,000m^2/g). The porous structure (micro-, and mesopores) was characterized using N_2 adsorption isotherms. The activated anthracite samples were then amine impregnated using alcohol amines by immersing them in an amine solution.

- Task 3: Capture of CO_2 by anthracite-derived sorbents. The samples prepared under Task 2 were tested as possible sorbents for CO_2 capture. The sorbents performance was

determined for CO_2 adsorption and desorption using a TGA analyzer. The adsorption was reported as mg CO_2/g sorbent. The CO_2 sorption/desorption capacities of the prepared activated sorbents were compared to those of commercial sorbents.

2. EXPERIMENTAL

2.1. Task 1: Procurement and characterization of anthracites

F.B. Leopold and Penn State University initially identified eight Pennsylvania anthracite samples for this work. These samples were selected from a suite of seventeen Pennsylvania anthracite samples. The selection criteria included ash and volatile matter content and rank. The samples present ash contents between 7.45 to 16.27, and volatile matters (daf) between 4.0 to 10.1. Furthermore, the suite selected includes four anthracites (HS, JED, LCN, CC and COL) and three semi-anthracites (7300, MB and 8800). The characterization analyses included proximate and porous texture analysis (Section 2.2.3).

2.2. Task 2: Development of anthracite-based CO_2 sorbents

2.2.1. Steam activation

Three Pennsylvania anthracites (PSOC-1468, AFM 800 and AFM 2600) were selected for the activation studies. PSOC-1468 was obtained from the Penn State Coal Bank and AFM

800 and AFM 2600 were provided by FB Leopold. For the activation experiments, the anthracite was first grounded and screened, and the sample with particle size between 150-250μm was used for steam activation.

A fluidized bed reactor was used for the activation experiments, as shown in Figure 1. The activation temperature was between 700-850^{o}C, and the steam concentration was 65.8% in the feeding gas stream. The stainless steel reactor was the most important part of the system, which was heated by a vertical furnace that has a 3.5" inside diameter. The reactor was designed to withstand temperatures up to 1100ºC. The versatility of the design allowed the use of different particle size, activating agent, heat treatment, residence time, flow rate of activation agent and amount of sample.

2.2.2. CO_2 sorbent preparation

Several surface treatment methods, including NH_3 heat treatment, HNO_3 oxidization and PEI impregnating, were selected to modify the surface properties of the activated anthracite produced from PSOC-1468. The effect of the surface treatment on the CO_2 capture capacity of the activated anthracites was investigated. The activated anthracite samples used for this study include: AC-850-3 (PSOC-1468 activated at 850^{o}C for 3 hours), AC-850-2 (PSOC-1468 activated at 850^{o}C for 2 hours) and AC-890-3 (PSOC-1468 activated at 890^{o}C for 3 hours).

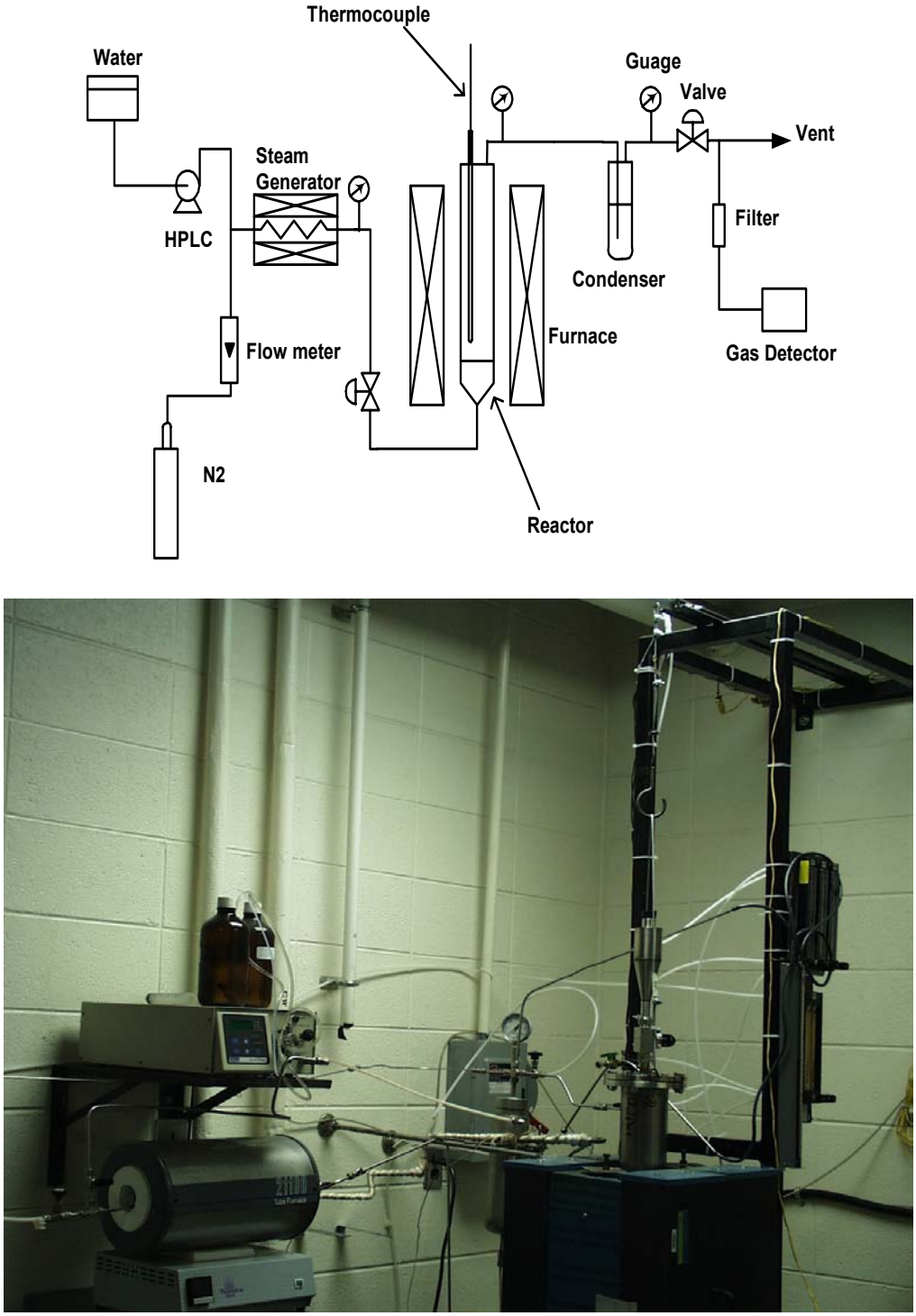

Figure 1. Diagram and picture of the activation system used for this work.

2.2.2.1 NH_3 treatment

AC-850-3 was used for this treatment. A known amount of AC-850-3 was put into a quartz boat that was placed in the middle of a horizontal tube furnace. NH_3 gas was then introduced, while the furnace was heated up to desired treatment temperature. After the furnace was held at the set temperature for 90 minutes, the NH_3 gas was switched to argon and the furnace was cooled down. The sample was removed from the reactor tube at room temperature. The produced samples were labeled as AC-850-3-NH_3-xxx, where the last three digits of the sample name indicate the treatment temperature.

2.2.2.2 HNO_3 treatment

For this treatment, 3 g of AC-850-2 was put into 100mL 5N HNO_3 solution. The sample was oxidized in boiling nitric acid for 5 hours, and then filtered and washed with de-ionized water till the pH of the filtrate was around 7. The treated sample was dried at 110^{o}C for overnight, and labeled as AC-850-2-HNO_3.

2.2.2.3 Amine impregnation

The AC-850-3 and AC-890-3 samples were impregnated with a PEI (polyethylenimine) in methanol solution (30wt%) and then dried in a vacuum oven at 75^{o}C overnight. The resultant samples were labeled as AC-850-3-PEI and AC-890-3-PEI.

2.2.3. Sorbent characterization

The porosity of the samples was characterized by conducting N_2 adsorption isotherms at 77K using a Quantachrome adsorption apparatus, Autosorb-1 Model ASIT (Figure 2). The total pore volume, V_t was calculated from the amount of vapor adsorbed at relative pressure of 0.95, and the total surface area S_t was calculated using multi-point BET equation in the relative pressure range 0.05-0.35. The pore sizes 2nm and 50nm were taken as the limits between micro- and mesopores and meso- and macropores, respectively, following the IUPAC nomenclature [22]. The mesopore size distribution was calculated by the Barrett-Joyner-Halenda (BJH) method. The micropore size distribution was calculated by density functional theory (DFT) method.

Figure 2. Quantachrome adsorption apparatus, Autosorb-1 Model ASIT.

A Kratos Analytical Axis Ultra XPS was used to study the surface chemistry of the modified activated anthracites. XPS quantification was performed by applying the appropriate relative sensitivity factors (RSFs) for the Kratos instrument to the integrated peak areas. These RSFs take into consideration the X-ray cross section and the transmission function of the spectrometer. The X-ray source is monochromatic aluminum (1486.6 eV) and the X-ray power is 280 Watts. The approximate sampling depth under these conditions is 25Å. The C-C in carbon 1s at 284.4eV was selected for the charge correction.

2.3. Capture of CO_2 by anthracite sorbents

The adsorption and desorption performance of the produced activated anthracites was conducted using a PE-TGA 7 thermogravimetric analyzer, shown in Figure 3. The weight change of the adsorbent was followed to determine the adsorption and the desorption performance of the activated anthracites. In a typical adsorption/desorption process, about 20-25mg of the sample was placed in a small platinum pan, heated to 100^{o}C in N_2 atmosphere at a flow rate of 100mL/min, and held at that temperature for 30 minutes. The temperature was then adjusted to the desired adsorption temperature and 99.8% bone-dry CO_2 adsorbate was introduced at a flow rate of 100mL/min. After adsorption, the gas was switched to 99.995% pure N_2 at a flow rate of 100mL/min to perform desorption at the same temperature. Adsorption capacity in mg-adsorbate/g-adsorbent and desorption capacity in

percentage were used to evaluate the adsorbent, where these values are calculated from the weight change of the sample in the TGA adsorption/desorption process.

Figure 3. Picture of the PE-7A TGA apparatus used for the CO_2 studies.

3. RESULTS AND DISCUSSION

3.1. Task 1: Procurement and characterization of anthracites

Table 1 shows the proximate analysis result of the three samples investigated. AS expected for anthracites, the volatile mater content is low (<5%). These samples were also selected due to their low ash content.

Table 1. Proximate analyses of the anthracite samples studied

Name	Moisture	Ash	Volatile	Fixed carbon daf*
PSOC-1468	4.51	6.83	3.65	96.9
AFM 800	5.04	6.43	3.36	97.0
AFM 2600	4.58	9.73	4.64	95.9

* Calculated based on ASTM D 388-99

3.2. Task 2: Development of anthracite-based CO_2 sorbents

It is known that the activation conditions, time and temperature, as well as the properties and structure of the precursor affect the porous structure of the resultant activated carbons [13, 23, 24]. Accordingly, a parametric study was conducted to ascertain the effect of time and temperature on the porous structure of activated carbons produced from anthracite.

3.2.1 Effect of activation time on the porosity of the activated anthracites

For this study, the anthracite PSOC-1468 was selected. The activation temperature was first selected at 850^{o}C according to previous studies conducted by the authors [15]. The typical isotherms of the resultant activated carbon with different activation time are shown in Figure 4. For comparison, the isotherm of the raw sample (PSOC-1468) is also presented in Figure 4.

Figure 4 shows that the activation dramatically increases the surface area and pore volume of the anthracite. All the isotherms of ACs are Type I according to the BDDT (Brunauer, Deming, Deming, Teller) Classification [25]. This indicates that the AC made from anthracite has many micropores and only a few mesopores. With increasing activation time, the isotherm shows a more open knee at lower relative pressure of the isotherm, indicating a broader pore size distribution with larger micropores and increasing mesoporosity.

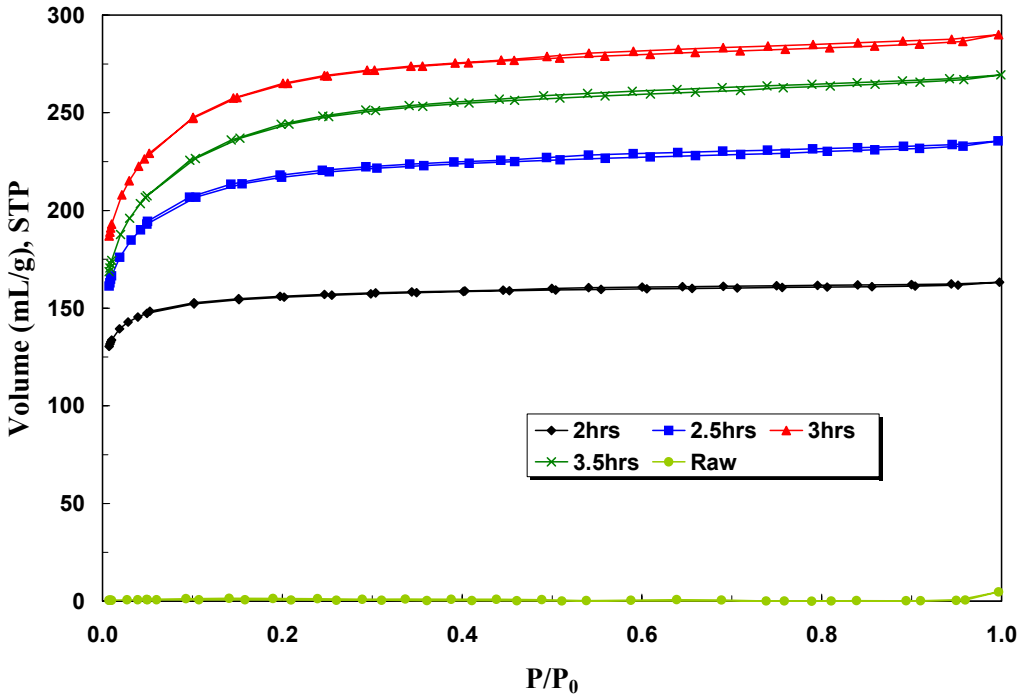

Figure 4. N_2-77K isotherms of the raw anthracite (PSOC-1468) and its steam activated carbons produced at 850°C

Figures 5 and 6 show the micropore and mesopore size distribution of the activated anthracites that were activated at 850°C with different activation time, respectively. It can be seen that there are no micropores and few mesopores for the raw anthracite. In contrast, after activation, there is a significant amount of mesopores in the activated anthracites (Figure 5 and Figure 6). For the activated anthracite after 2 hours activation time, there is a large peak between 0.4-1.0nm. For the anthracites produced after 2.5 and 3.0 hours activation time, the peak between 0.4-1.0nm is still there, and there are some additional peaks at 1.6 and 2.0 nm, and also a peak at 2.4nm for the anthracite sample produced after 3 hours steam activation. Furthermore, for the sample produced after 3 hours activation time, the largest peak moves to 1.2nm, and the height of the peaks at 1.6, 2.0 and 2.4nm increases. Due to technical

limitations of the instrument, it is not possible to get adsorption data at very low relative pressure, and therefore the pore size distribution < 0.4nm cannot be calculated by the DFT method. However, the results indicate that the pore development during activation includes pore opening followed by pore enlargement.

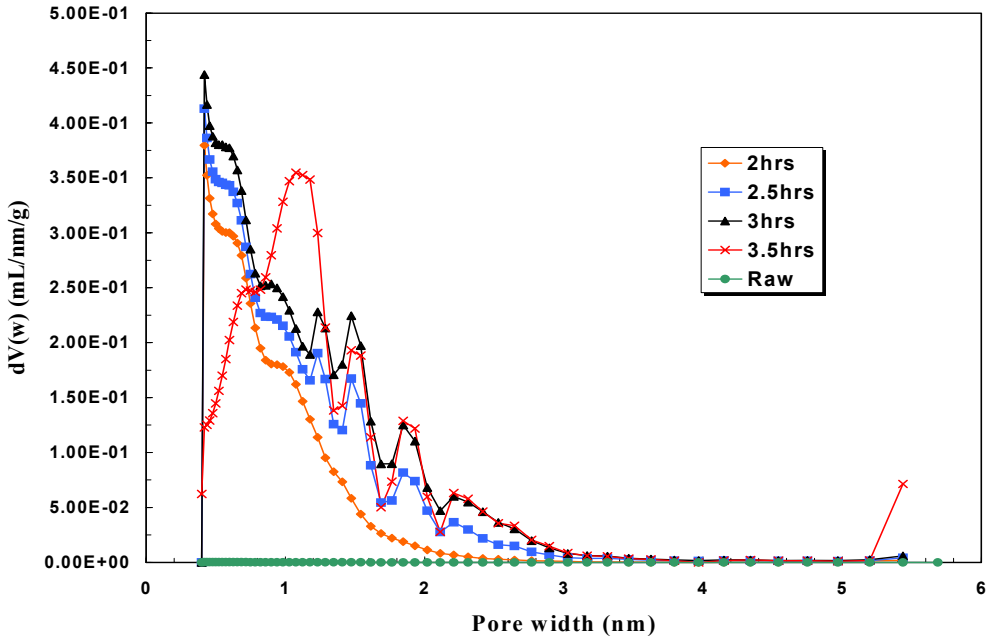

Figure 5. Micropore size distribution by DFT method of the raw anthracite (PSOC-1468) and its steam activated carbons produced at 850°C

Figure 6 shows that all the activated anthracites with different activation time have the same mesopore distribution profile. This indicates that the anthracites activated at 850°C have similar mesoporous structure.

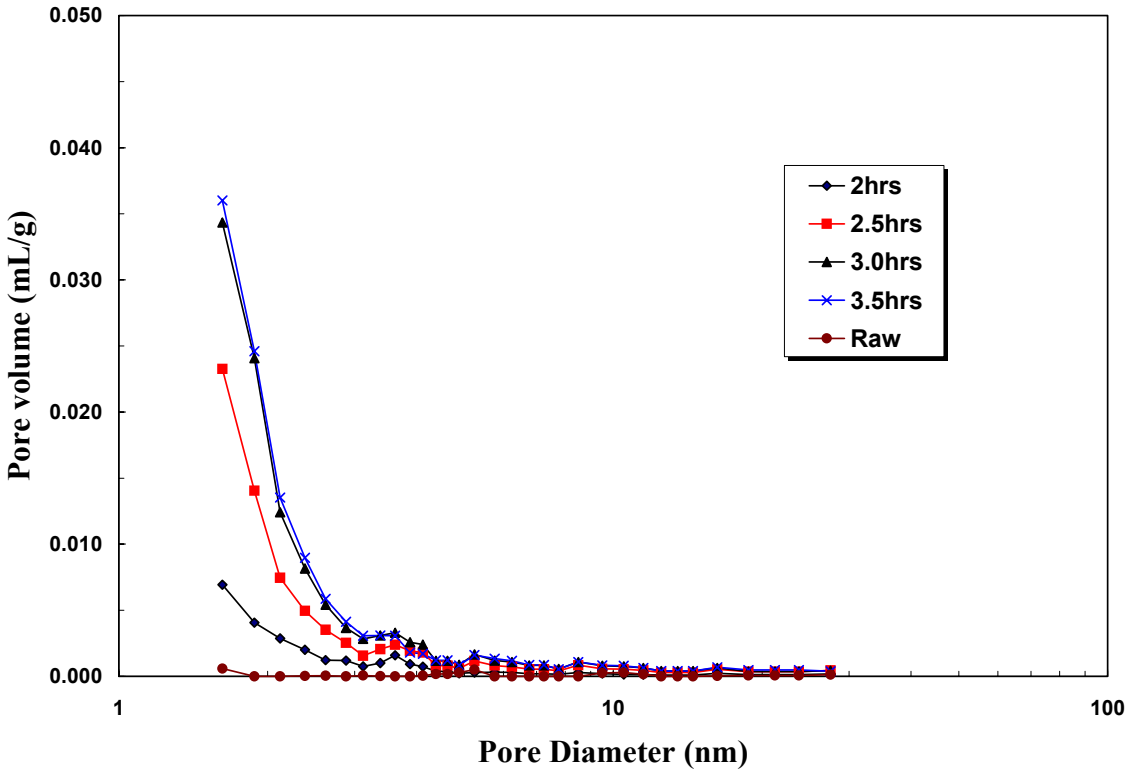

Figure 6. Mesopore size distribution by BJH method of the raw anthracite (PSOC-1468) and its steam activated carbons produced at 850^{o}C

The surface areas and pore volumes for the activated carbons produced by steam activation at 850^{o}C of the PSOC-1468 anthracite are presented in Table 2. The surface and pore volume first increase with increasing activation time and get to a maximum value after 3.0 hours activation (928m^2/g and 0.442mL/g), and then decrease with increasing activation time (855m^2/g and 0.412mL/g for AC for 3.5 hours activation time). However, the ratio of micropore surface area over total surface area and the ratio of micropore volume over total pore volume keep decreasing with increasing activation time. For instance, the ratio of micropore surface area decreases from 99% to 97%, when increasing the activation time from 2 to 3.5 hours. Similarly, the ratio of micropore volume to total pore volume decreases

from 92% to 84% when increasing the activation time from 2 to 3.5 hours. This indicates that larger pores were produced with increasing activation time.

Table 2. Surface areas and pore volumes of the raw anthracite (PSOC-1468) and its steam activated carbons produced at 850°C

Sample number	Activation time, hr	S_t m^2/g	S_m m^2/g	V_t mL/g	V_m mL/g
Raw		1.29			
1	2.0	452.4	437.6	0.2502	0.2314
2	2.5	636.6	600.2	0.3604	0.3128
3	3.0	793.0	742.0	0.4434	0.3774
4	3.5	732.0	681.1	0.4131	0.3460

S_t : Total surface area, S_m: Micropore surface area

V_t : Total surface area, V_m: Micropore surface area

3.2.2. Effect of activation temperature on the porous structure of the activated anthracites

In the previous section, the effect of the activation time on the porous structure of the PSOC-1468 anthracite activated at 850°C was investigated. The study showed that the surface area was as high as 928 m^2/g after 3 hours activation. However, extending the activation time beyond three hours decreases the surface area. Therefore, for this study three hours activation time was selected to investigate the effect of the activation temperature on the pore structure

of the produced activated anthracites. It should be noted that the optimum activation time may vary as a function of the activation temperature.

Figures 7 and 8 shows the surface area and pore volume (micropores and mesopores) of the the PSOC-1468 anthracite activated for 3 hours at 800, 850 and 890°C. It can be seen that the surface area and pore volume of the activated anthracite increased first going from 800 to 850°C, where the sample activated at 850°C has a surface area and volume of 928m^2/g and 0.442mL/g, respectively. However, increasing the activation time to 890°C resulted in a decrease of both surface area and pore volume.

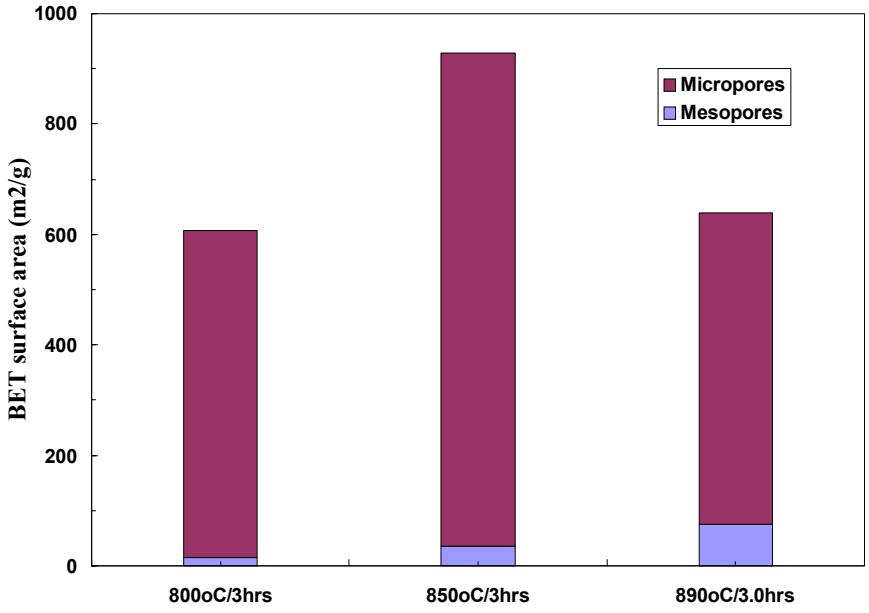

Figure 7. Surface area of the PSOC-1468 anthracite activated for 3 hours at 800, 850 and 890°C

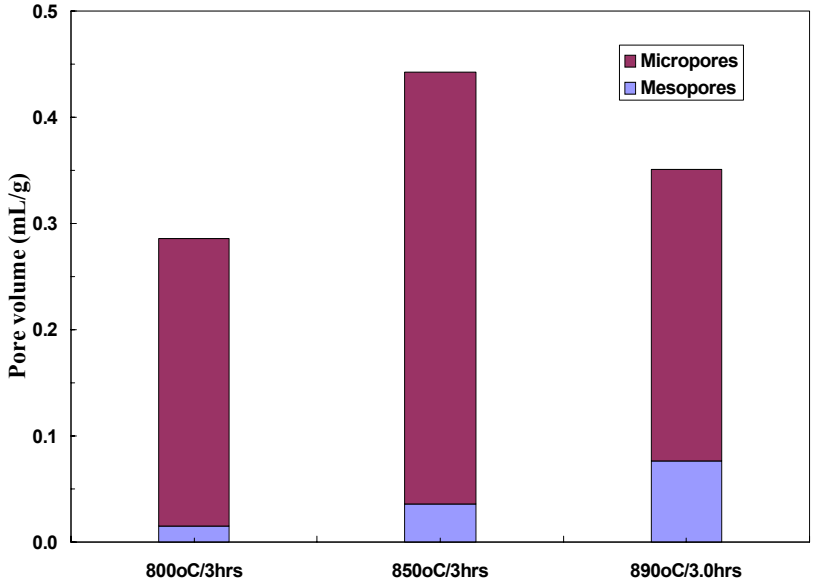

Figure 8. Pore volume of the PSOC-1468 anthracite activated for 3 hours at 800, 850 and 890°C.

On the other hand, the mesopore surface area and mesopore volume kept increasing with increasing activation temperature from 800 to 890°C, where the mesopore surface area was 15.6, 36.5 and 74.4m^2/g for the anthracites activated at 800, 850 and 890^{o}C, respectively (Figure 7). However, all the activated carbons produced are mainly microporous. This indicates that the lower activation temperature (800 and 850°C) helped to produce highly microporous activated carbon from anthracite, while higher temperatures (890°C) developed more mesopores in the activated carbon.

Figure 9 shows the mesopore size distribution, as determined by the BJH method, of the PSOC-1468 anthracite activated at different temperatures for 3 hours. It can be seen clearly that the mesopore size of the activated anthracites increased with increasing activated

temperature. This is consistent with the trends observed for the surface area and pore volumes (Figures 7 and 8).

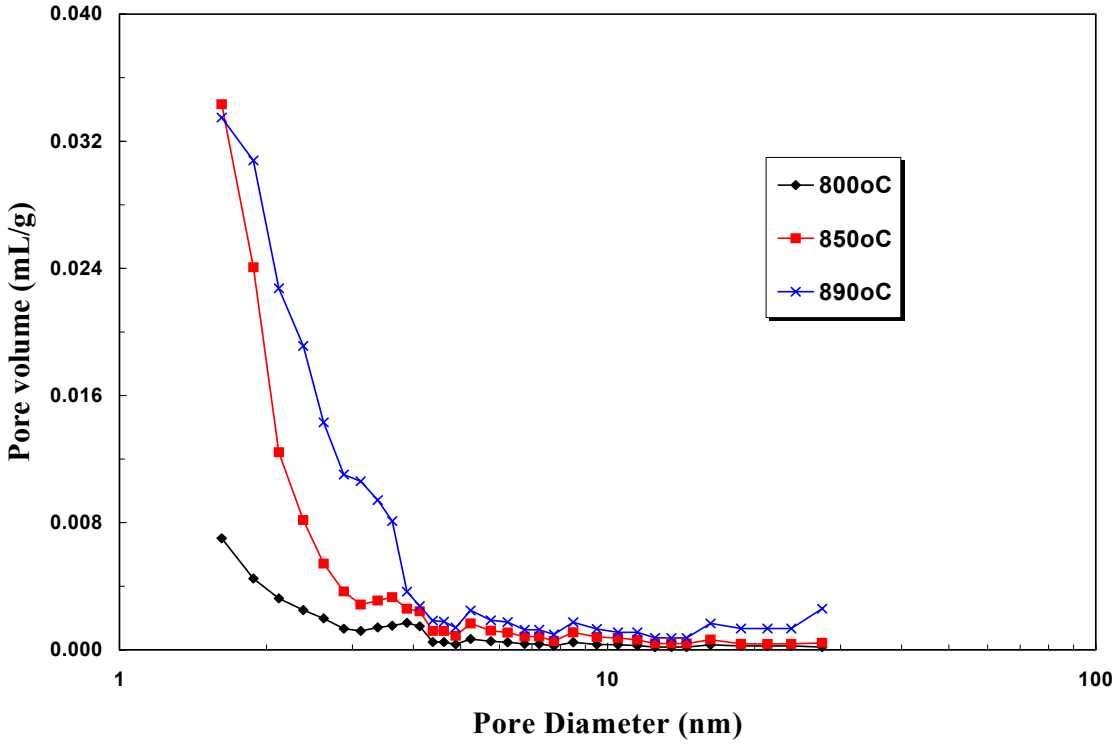

Figure 9. Mesopore size distribution by BJH method of the PSOC-1468 anthracite activated at different temperatures for 3 hours

In order to understand the effect of both the activation time and temperature on the porous structure of the activated anthracites, a series of activation experiments were conducted for different times (2.0 –3.5 hours) and temperatures (800 - 890^{o}C). In addition, a sample was activated at 700^{o}C for 2 hours. Figures 10 and 11 show the variation of the surface area and pore volume of the PSOC-1468 activated anthracites. The sample activated at 890^{o}C for 2

hours has the highest surface area and pore volume (1071m^2/g and 0.553mL/g, respectively). In contrast, the surface area and pore volume of the anthracite activated at 700^{o}C for 2 hours were only 22m^2/g and 0.015mL/g, respectively. Therefore, this low temperature activation (700^{o}C) did not develop significantly the pore structure of the anthracite. This is probably because of the low reactivity of the anthracite at this activation temperature that is not effective to even to open the closed porosity of the anthracite.

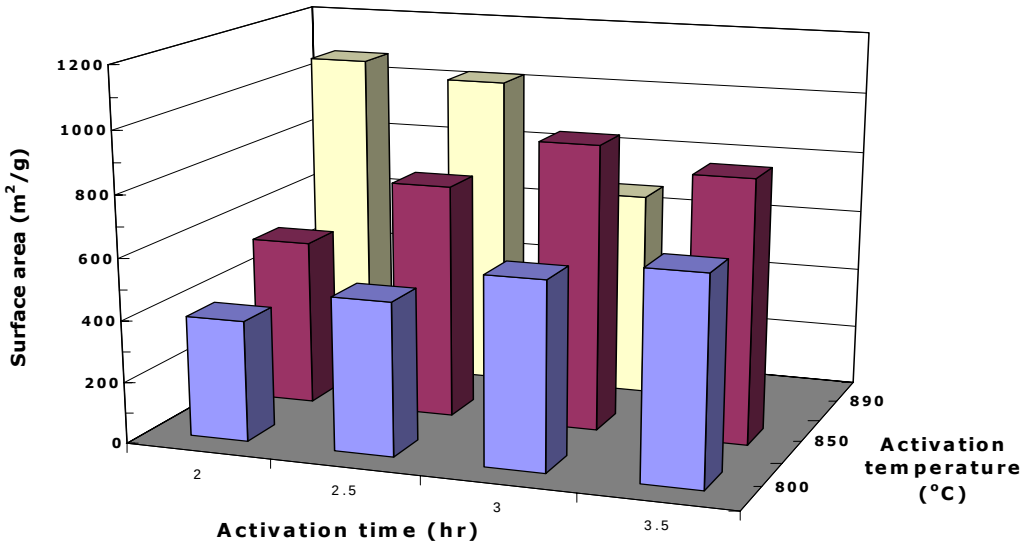

Figure 10. Surface area of the PSOC-1468 anthracite activated under different temperature and time conditions

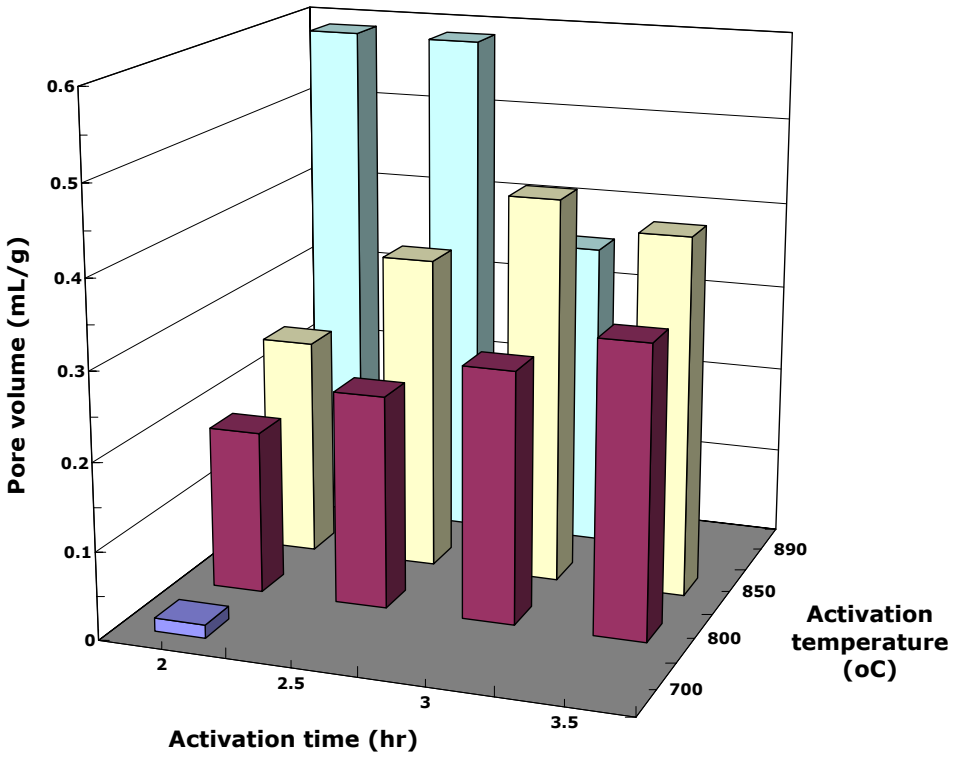

Figure 11. Pore volume of the PSOC-1468 anthracite activated under different temperature and time conditions

Table 3 lists the solid yield of the anthracite activated under different conditions (time and temperature). Figure 12 shows the relationship between surface area and the solid yield of the activated anthracites. As expected, the solid yields decrease with increasing activation time and temperature. For example, for the anthracite activated for 2 hours, the solid yield goes from 81% for the 800°C activation down to 24% at 890°C. Similarly, for a given activation temperature, the solid yield decreases with activation time. For example, for the anthracite activated at 850°C, the solid yields were 61 and 17% for the 2 and 3.5 hours activation, respectively. As described when increasing the activation time at a given temperature, the

surface area does not increase continuously with decreasing solid yields (or conversely, higher burn–off levels).

Table 3. Solid yield (wt.%) of anthracites activated under different conditions (time and temperature)

	2 hours	2.5 hours	3 hours	3.5 hours
800°C	81	78	68	56
850°C	61	47	36	17
890°C	24	20	5	n.d.

n.d.: not determined

Figure 12 shows that the surface areas go through a maximum with increasing solid yields. For example, for the activation at 850°C, the surface area first increases with decreasing solid yield and reaches a maximum value at around 40% solid yield, after which the surface area decreases. This behavior has been previously reported for anthracites activated using steam and CO_2 , although the solid yield value at which the surface area peaks varies within these studies, probably due to the different activation conditions used [13, 16]. The initial increase in surface area is probably due to opening of porosity and formation of micropores, while the decrease in surface area for lower solid yields (<40%) is due to the enlargement of micropores and and pore wall removal. This is also consistent with the variations reported for surface area and pore volume as a function of activation conditions (Figures 7-8 and 10-

11) that indicated a widening of the porosity with extended times and temperatures, and consequently, lower solid yields.

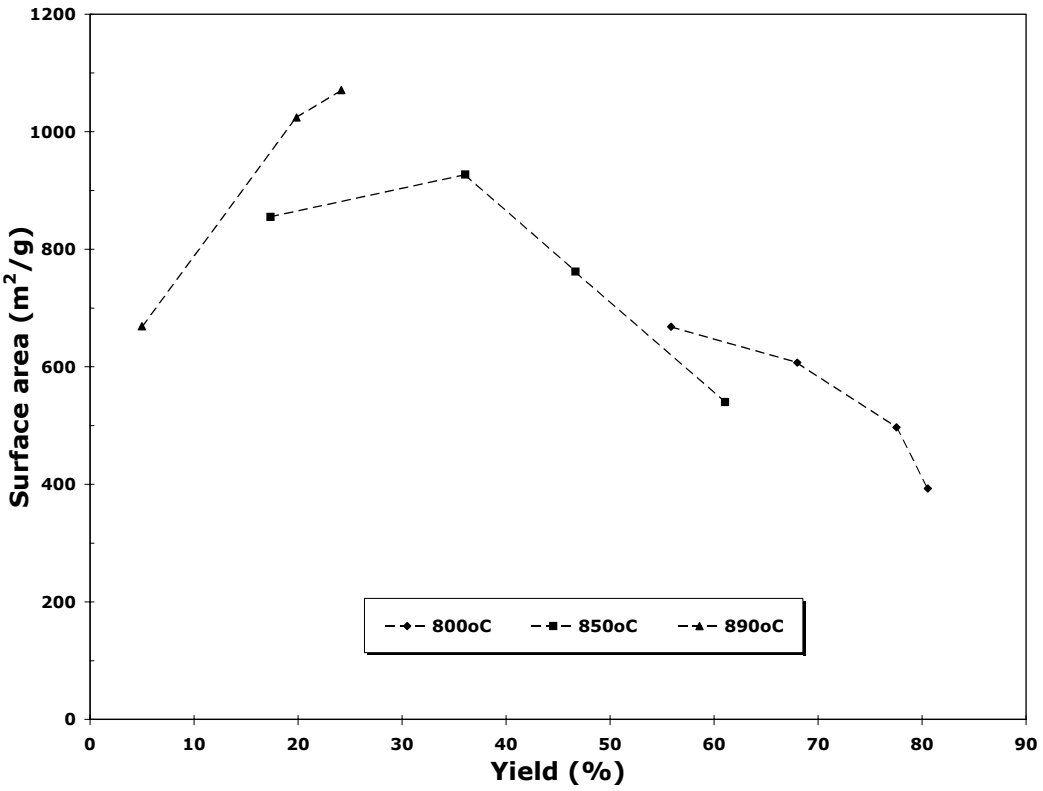

Figure 12. Variation of the surface area as a function of solid yield

3.2.3. Characterization of surface treated activated anthracites

The porous texture properties, as determined from the 77K N_2-isotherms, of the parent activated carbons and their counterparts treated with NH_3 and HNO_3 are shown in Table 4. The NH_3 treatment increased the surface area of the activated samples, especially at lower temperatures (650°C), while the HNO_3 treatment decreased the surface area of the activated

anthracites. For example, the surface area of the NH_3 treated activated anthracites increased from 928 to 1052 and 952 m^2/g at 650 and 800^oC, respectively.

Most of the pores of the activated anthracites AC-850-3 and AC-850-2, which were produced from anthracite by steam activation at 850°C using different activation times, are mainly micropores (>92%). The low temperature NH_3 treatment (650°C) can increase the surface area while keeping the sample microporosity (92%). In contrast, the high temperature NH_3 treatment (800°C) increases slightly the surface area of the anthracite, but increases significantly its pore diameter from 1.91 to 1.97 nm. The surface area of the activated anthracite decreased for the HNO_3 treatment, due the formation of mesopores, resulting in an increase of the average pore size from 1.85nm to 2.21nm.

Table 4. Porous texture of the parent activated anthracites and their counterparts treated with NH_3 and HNO_3

Sample	BET surface area m^2/g	Pore volume ml/g	Microporosity ratio, %	Average pore diameter, nm
AC-850-3	928	0.442	92	1.91
AC-850-3-NH_3-650	1052	0.523	92	1.91
AC-850-3-NH_3-800	952	0.469	88	1.97
AC-850-2	540	0.250	96	1.85
AC-850-2-HNO_3	195	0.108	86	2.21

Table 5 shows the porous structure varaitions of the activated anthracites that were impregnated with PEI. The chemical impregnation results in a dramatic decrease of the surface area of the activated anthracite, where the surface area and pore volume of the impregnated anthracites are very small ($1 m^2/g$ and 0.005ml/g). This is probably due to pore blockage and surface coverage by PEI, as previously reported for MCM-41 materials impregnated with PEI [20].

Table 5. Porous structure properties of the activated anthracites and their impregnated counterparts

	Before treatment		After treatment	
	S_{BET}, m^2/g	V_t, ml/g	S_{BET}, m^2/g	V_t, ml/g
AC-850-3	928	0.442	<1	<0.01
AC-890-3	636	0.351	<1	<0.01

3.2.4. Characterization of activated anthracites produced from different parent anthracites

Figure 13 shows the surface area and pore volume of the activated anthracite from different parent anthracites (PSOC-1468, AFM –800 and AFM-2600), which were activated at 800°C for 3 hours. The surface area and pore volume values of the activated PSOC-1468 sample

were higher than those reported for the activated AFM-800 and AFM-2600 samples. This may indicate that the reactivity of PSOC-1468 was higher than that of AFM-800 and AFM-2600.

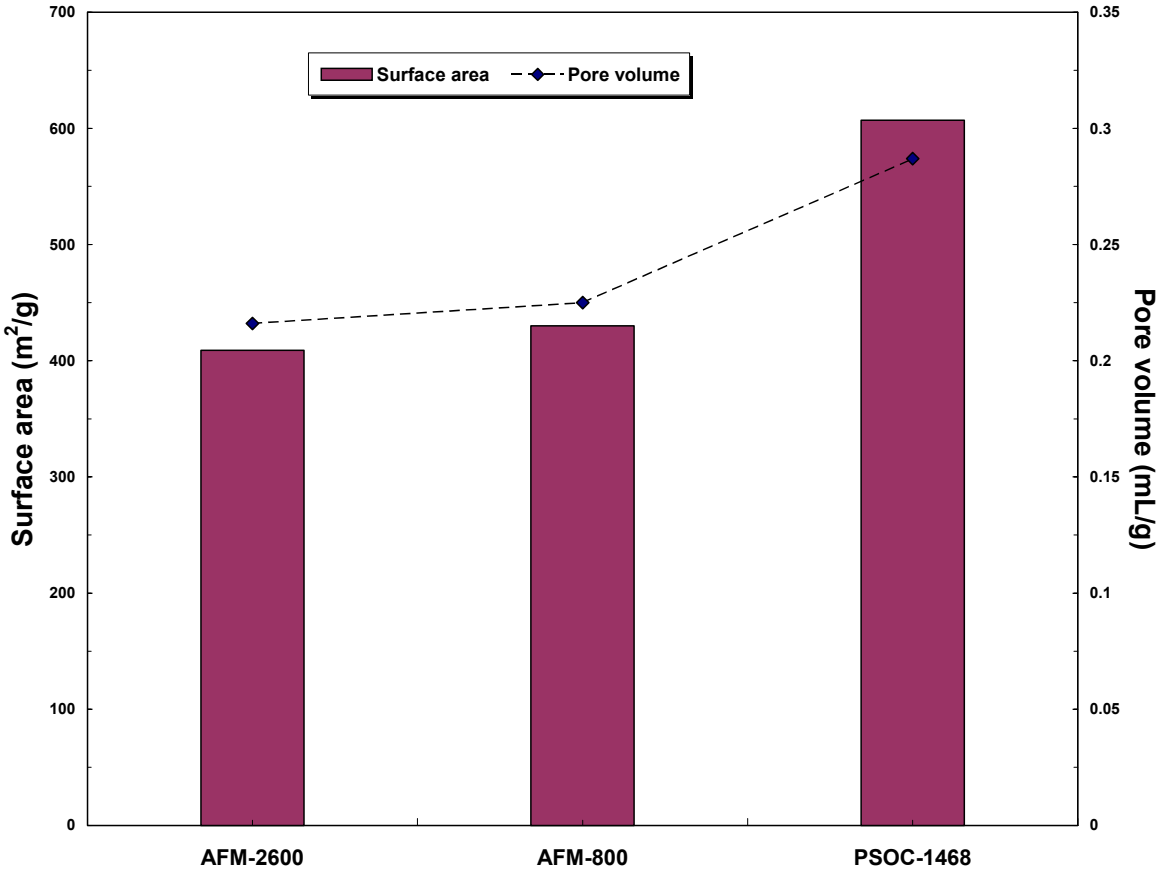

Figure 13. Surface area and pore volume of activated anthracites from different parent anthracites activated at 800°C for 3hours

3.3. Task 3: Capture of CO_2 by anthracite sorbents

Figure 14 shows a typical adsorption and desorption profiles of the activated samples made from anthracite using TGA. It can be seen that the adsorption process takes longer time than the desorption. For instance, at 30°C, for the sample after 2.0 hours activation time, it takes about 300 minutes for the sample to get saturated in CO_2, while it needs only about 100 minutes to complete the desorption. The small fluctuations observed at the beginning of the adsorption and desorption processes are due to the change of the gas environment from N_2 to CO_2 or from CO_2 to N_2.

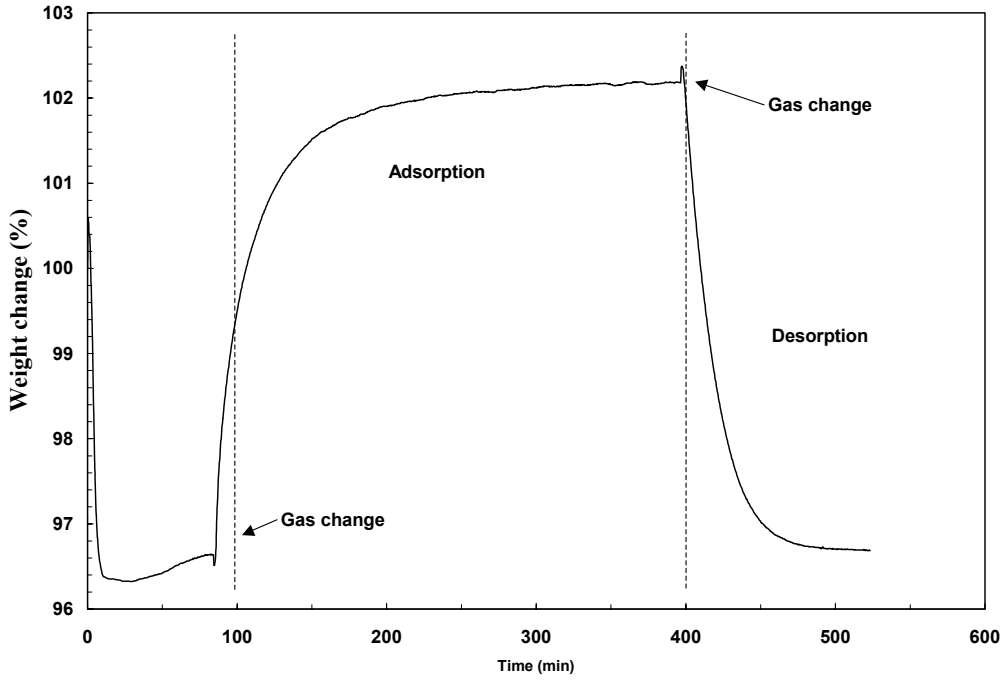

Figure 14. Typical adsorption/desorption profile at 30°C for the activated anthracite AC-850-3

3.3.1. Effect of adsorption temperature

Table 6 lists the CO_2 adsorption and desorption results at 30 and 75°C of the PSOC-1468 anthracite that was activated at 850°C. Because the CO_2 adsorption of activated anthracites is mainly a physical process, the adsorption capacity decreases with increasing adsorption temperature. For example, the CO_2 capture capacity of the activated anthracites at 75°C is about half to one-third to that at 30°C. At 75°C, the anthracite after 2.0 hours activation has the highest CO_2 capture value (26.3mg-CO_2/g-AC), and the CO_2 capture capacity decreased with increasing surface area or pore volume. In contrast, at 30°C, the anthracite after 3.5 hours activation has the highest CO_2 capture value (60.9mg-CO_2/g-AC). However, it was expected that the sample with the highest surface area would give the highest CO_2 capture value. Finally, Table 6 shows that for all the samples the desorption is higher than 97%, indicating that these samples can readily desorb the CO_2 and be reused.

Table 6. CO_2 capacities at 30 and 75°C for the anthracites activated at 850°C.

AC sample	30°C		75°C	
	Adsorption mg-CO_2/g-sorbent	Desorption %	Adsorption Mg-CO_2/g-sorbent	Desorption %
2.0hrs	58.5	97	26.3	97
2.5hrs	58.5	97	24.2	98
3.0hrs	60.6	99	21.6	99
3.5hrs	60.9	99	21.7	99

3.3.2. Effect of activation conditions on the CO_2 adsorption capacities

Figure 15 shows the CO_2 capacity values at 30°C for all the activated anthracites (PSOC-1468) produced under different conditions. For the purposes of comparison, the raw anthracite and one commercial activated carbon are also included. F-400.

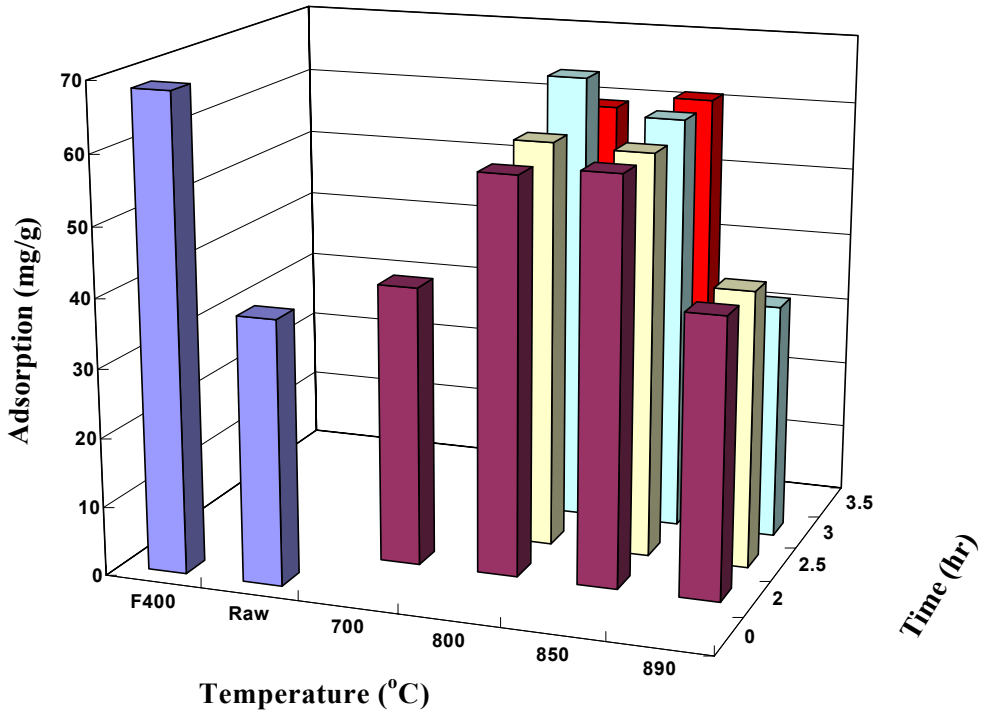

Figure 15. CO_2 adsorption capacities at 30°C of the activated samples produced from PSOC-1468 and the commercial F400 carbon

The CO_2 adsorption capacity decreased with increasing activation temperature for all the adsorption temperatures studied here, where the anthracite activated at 800°C for 3 hours has the highest CO_2 capacity (65.7mg-CO_2/g-adsorbent). Moreover, this value is very similar to

that of the commercial activated carbon F-400 (68.5mg-CO_2/g-adsorbent). The CO_2 capture capacity of the anthracite activated at 890°C for 2 hours is around 40mg-CO_2/g-adsorbent, although this sample has the highest surface area and pore volume. Figure 15 also shows that the raw anthracite together with the anthracites activated at lower temperatures (700°C) for 2 hours have surprisingly high CO_2 adsorption capacities (38 and 40mg-CO_2/g-adsorbent, respectively), despite of their low porosity. For example, the surface area of the activated anthracite at 700°C for 2 hours was only 22.4m^2/g. This is presumably due to the fine pore structure of the parent anthracite and the low temperature activated samples, which is discussed in more detail in section 3.3.3.

Since the CO_2 adsorption results show that the anthracite activated at 800°C has the largest CO_2 adsorption capacity, this temperature was selected to further investigate the effect of parent anthracite on the CO_2 adsorption, as shown in Figure 16.

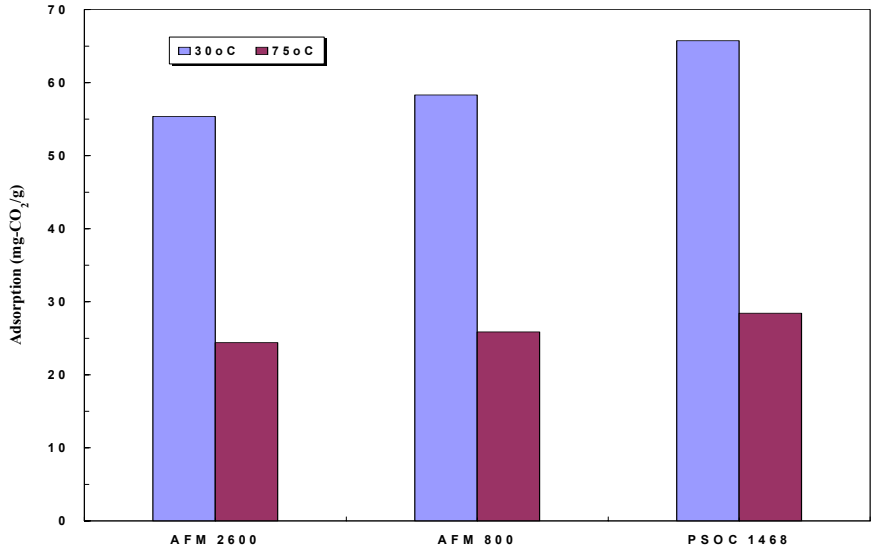

Figure 16. CO_2 adsorption capacities of activated samples generated from different parent anthracites

Figure 16 shows the CO_2 adsorption capacities of activated samples generated from different parent anthracites. It can be seen that the activated carbon made from PSOC-1468 has the highest CO_2 adsorption capacity (65.8mg-CO_2/g-adsobent. The CO_2 adsorption capacity of the activated carbons made from AFM 2600 and AFM 800 have similar value (55.4 and 58.3mg-CO_2/g-adsobent at 30^{o}C adsorption, respectively).

3.3.3. Effect of surface treatment on the CO_2 adsorption capacities

The CO_2 adsorption capacities of the activated anthracites and their NH_3 and HNO_3 treated counterparts were determined at 30, 50 and 75^{o}C, as shown in Figures 17 and 18.

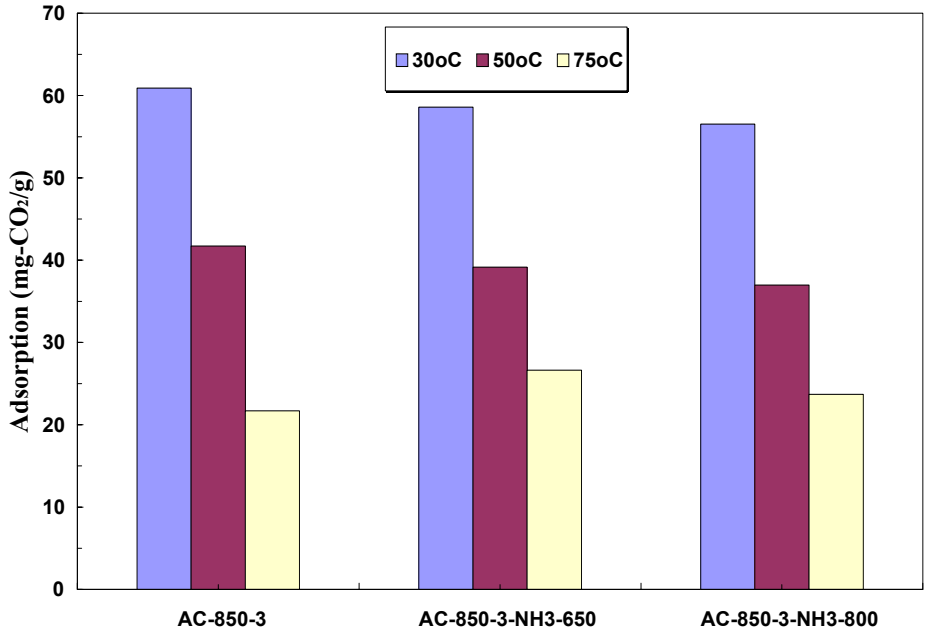

Figure 17. CO_2 adsorption capacities of AC-850-3 and its NH_3 treated samples, AC-850-3-NH_3-650 and AC-850-3-NH_3-800 at different adsorption temperature

It can be seen that there are significant changes in the CO_2 adsorption capacity of the parent and treated anthracites with temperature. At 30°C, the adsorption of the untreated activated anthracites was slightly higher than the treated samples. At higher adsorption temperatures (50°C and 75°C), the adsorption capacities of the treated samples was slightly higher than that of the parent activated anthracite. For instance, at 75°C, the CO_2 adsorption capacity was 21.7, 26.6 and 23.7 mg-CO_2/g-sorbent for AC-850-3, AC-850-3-NH_3-650 and AC-850-3-NH_3-800, respectively.

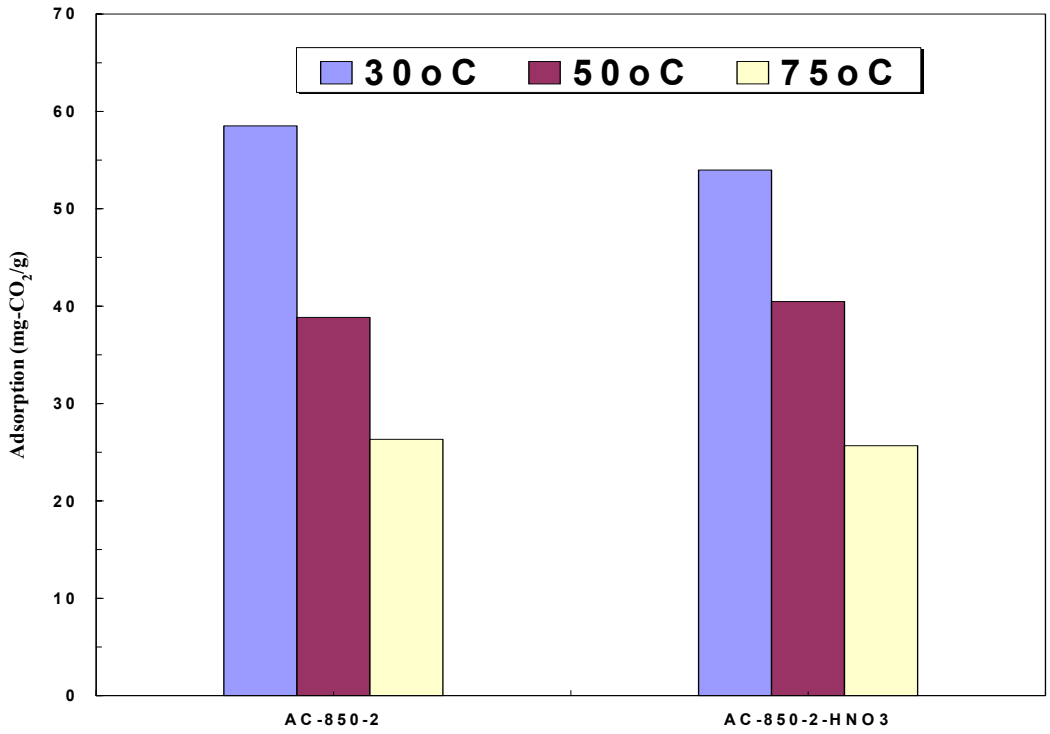

Figure 18. CO_2 adsorption capacities of AC-850-2 and its HNO_3 treated sample: AC-850-2-HNO_3 at different adsorption temperature

For the HNO_3 treatment, the CO_2 adsorption was 38.8 and 40.5 mg-CO_2/g-sorbent for AC850-2 and AC-850-2-HNO_3 at 50^oC, respectively. This indicates that the treatment process can improve the CO_2 adsorption of the anthracite, particularly at higher temperatures. This is probably due to the introduction of nitrogen groups. Further studies were conducted to assess the nitrogen functional groups that affect CO_2 adsorption (Section 3.3.3).

Figure 19 shows the CO_2 adsorption capacities of the AC-850-3 and AC-890-3 samples, and their PEI impregnated samples, AC-850-3-PEI and AC-890-3-PEI. It can be seen that impregnation with PEI increases significantly the CO_2 adsorption capacities, particularly for AC-890-3. For instance, the adsorption capacity increased from 21.6 to 26.3 mg-CO_2/g for AC-850-3 after impregnation. For the AC-890-3 sample, the PEI impregnation increased more significantly the CO_2 adsorption capacity from 16.9 to 37.5 mg-CO_2/g. This increase in the CO_2 adsorbed after amine impregnation is consistent with that reported for molecular sieve materials MCM-41 and fly ash carbons [7, 20]. The higher CO_2 adsorbed amount for AC-850-3 compared to AC-890-3 is probably due to the presence of more micropores (92% vs. 78%). Previous studies conducted on MCM-41 and fly ash carbons have shown that the CO_2 chemical adsorption for PEI impregnated materials is favored by the presence of mesopores that can promote mass transfer within the pores.

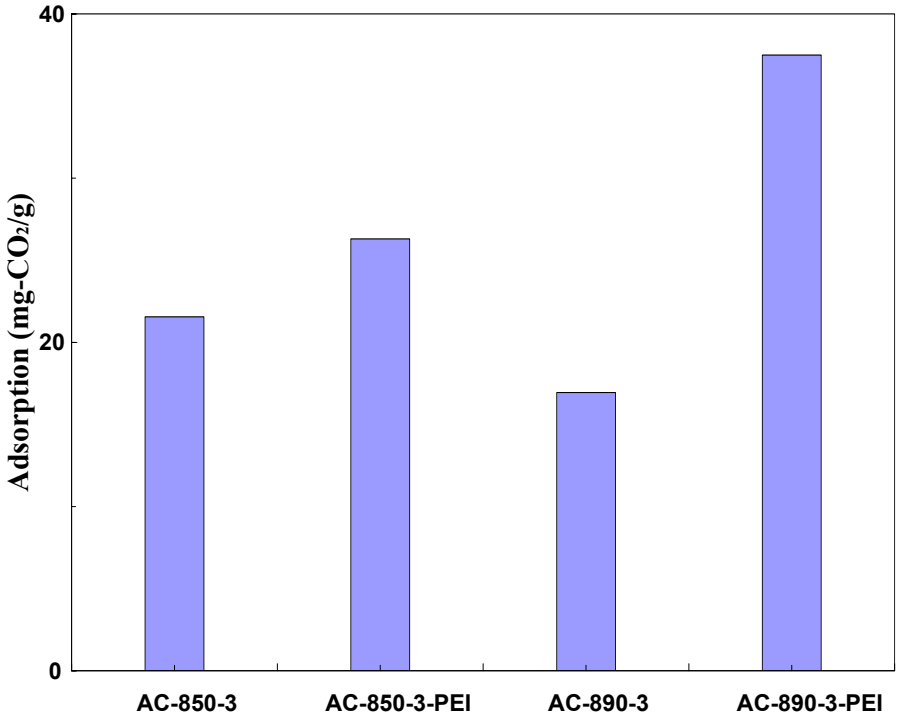

Figure 19. CO_2 adsorption capacities of AC-850-3 and AC-890-3 and their PEI impregnated samples, AC-850-3-PEI and AC-890-3-PEI at 75°C adsorption

3.3.4. Factors that influence the CO_2 adsorption of activated anthracites

From the CO_2 adsorption studies described above, the sample with the highest CO_2 adsorption capacity was the anthracite activated at 800°C for 2 hours, whose surface area was 540 m^2/g, and the adsorbed amount of CO_2 was 65.72mg-CO_2/g-adsorbent. However, the anthracite with the highest surface area and pore volume (1049m^2/g and 0.558ml/g, respectively) was that activated at 850°C for 3 hours and its CO_2 capacity was only 40.0mg-CO_2/g-adsorbent. It should be noted that the experimental adsorbed amount of CO_2 is much

lower than the theoretical amount that can be derived from the total pore volume and taking the liquid density of CO_2 is 0.93g/L (assuming that the adsorbed CO_2 changes to the liquid phase in the nanopores [26]). For example, the calculated theoretical CO_2 adsorption capacity of the anthracite activated at 800^oC for 2 hours and 850^oC for 3hrs are 232.7mg/g, and it is 412.4mg/g for AC, respectively. This indicates that not all the surface area or the pore volume of the activated anthracites contributes to the adsorption of the CO_2.

The relationship between CO_2 adsorption and the microporosity of the activated anthracites is presented in Figure 20. It seems like the samples with the highest microporosity have the highest CO_2 adsorption capacity. Previous studies have shown that only pore sizes less than 5 times that of the molecular size of the adsorbate are effective for gas adsorption at atmospheric pressure. This observation was confirmed empirically [27] as well as by mathematical simulation using grand canonical Monte Carlo (GCMC) and the nonlocal density functional theory (NLDFT) [28]. Since the molecular size of CO_2 is 0.209 nm, only pores less than 1.0nm are effective towards CO_2 capture at atmospheric pressure. Therefore, it is desirable to tailor the pore size distribution of the activated carbons, especially in order to maximize the pore less than 1.0nm, to optimize the physical adsorption of CO_2 onto the carbon surface.

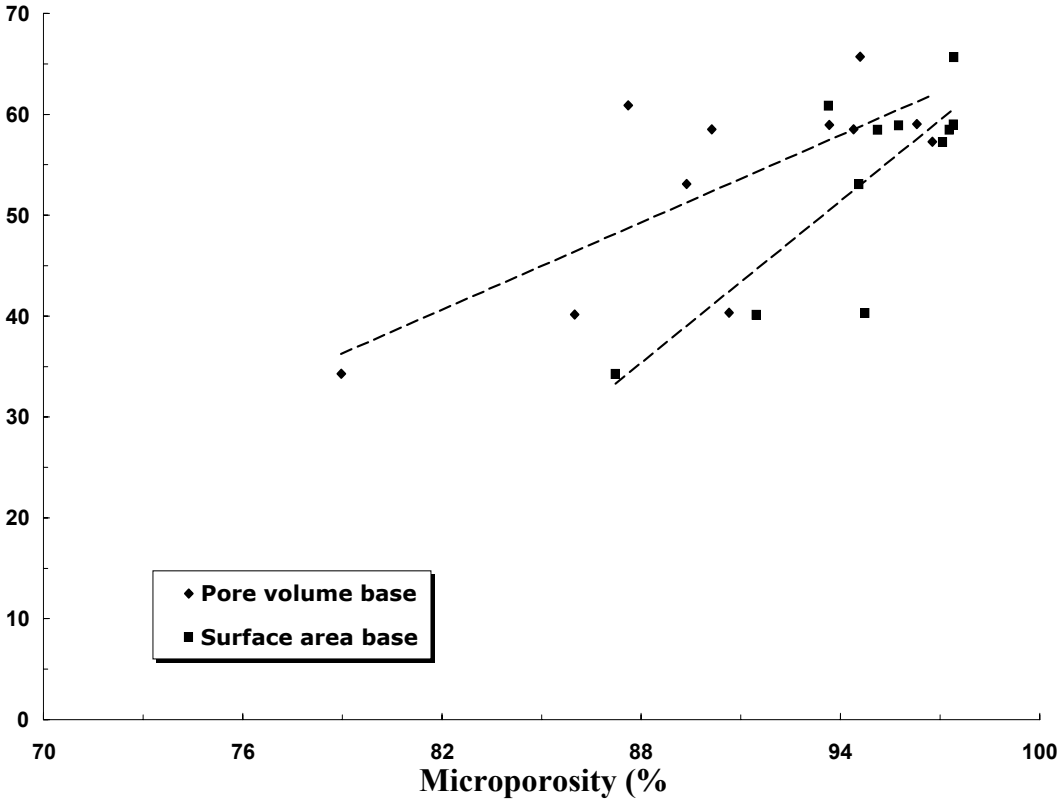

Figure 20. Variation of CO_2 adsorption capacities and microporosity of the activated anthracites

As shown in Figure 15, the raw anthracite can adsorb as much as 38.2mg-CO_2/g-sorbent at 30^{o}C, while its surface area and pore volume are very small (1.39m^2/g and less than 0.001mL/g respectively). There are two hypotheses that can explain this behavior, as described below. Firstly, the raw anthracite has very fine micropores that cannot be reached by N_2 at 77K, where the smallest pore size is 0.5nm using DFT method from N_2 isotherm [18]. However, as previously described, pores less than 0.5nm may also have the capability to adsorb CO_2. The second hypothesis is that there are some surface functional groups on the surface of raw anthracite that can contribute to the chemical adsorption of CO_2. This second

hypothesis is partially supported by the XPS data shown in Tables 7 and 8, as described below.

In order to understand the effect of the surface functional groups on the adsorption of CO_2, XPS analysis was conducted to characterize the functional groups of raw anthracite, activated anthracite (AC-850-3), NH_3 treated activated anthracites (AC-850-3-NH_3-800), HNO_3 oxidized activated anthracite (AC-850-3-HNO_3) and PEI impregnated activated anthracite (AC-850-3-PEI). Figure 21 shows the binding energy spectra of XPS analysis for AC-850-3, AC-850-3-NH_3-800 and AC-850-3-HNO_3, while Figure 22 shows the binding energy spectra of XPS analysis for AC-850-3 and AC-850-3-PEI. The major difference between the activated anthracite and the surface treated samples, is the presence of the peak at 400eV, which corresponds to the element N. This indicates that the surface treatment introduced N into the surface of the activated anthracites, and the amount introduced varied for the different methods.

Figures 23 and 24 show the C 1s and O 1s spectra of AC-850-3, AC-850-3-NH_3-800 and AC-850-3-HNO_3 respectively, and Figures 265 and 26 present the C1s and O 1s of AC-850-3 and AC-850-3-PEI, respectively.

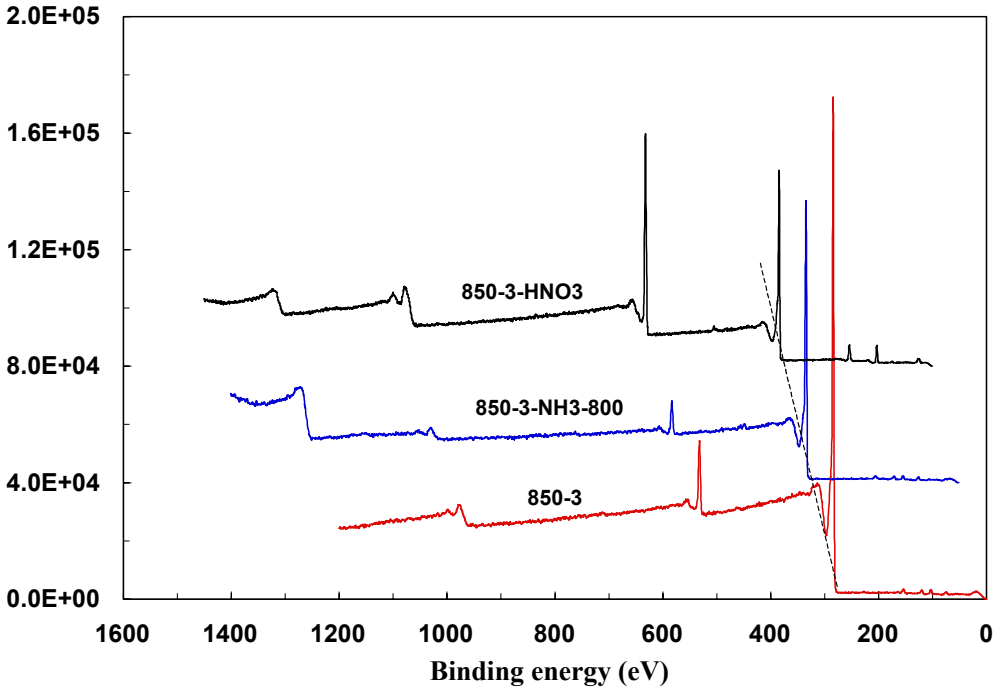

Figure 21. XPS spectra of the activated anthracite AC-850-3 and its HN_3 and HNO_3 treated samples

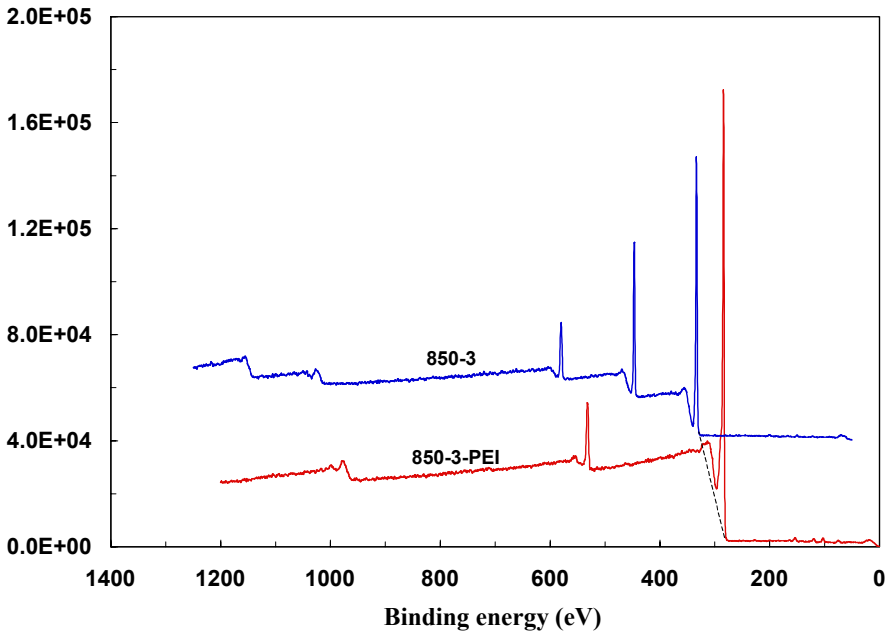

Figure 22. XPS spectra of the activated anthracite AC-850-3 and its PEI impregnated samples

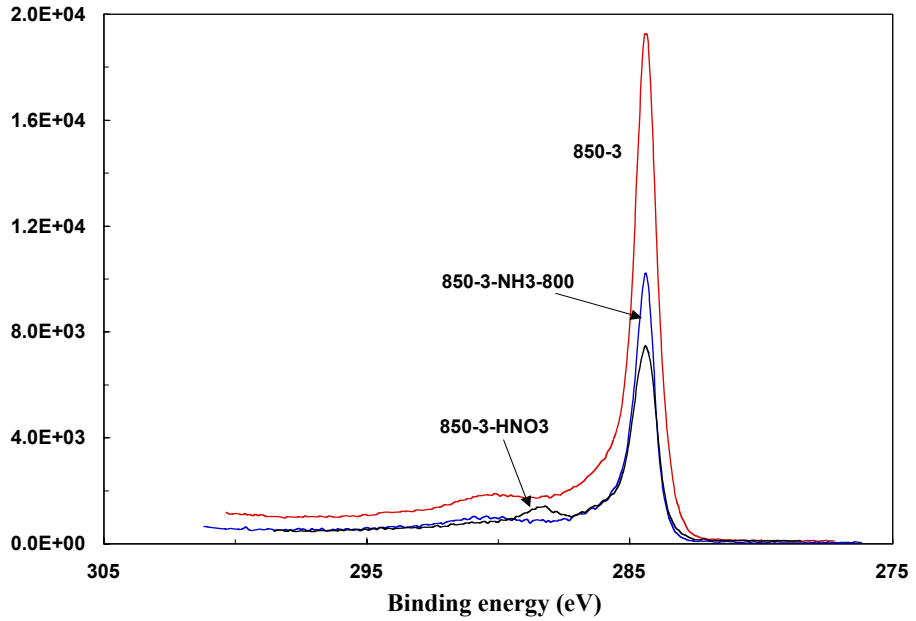

Figure 23. C 1s spectra of activated anthracite (AC-850-3) and its HN_3 and HNO_3 treated samples

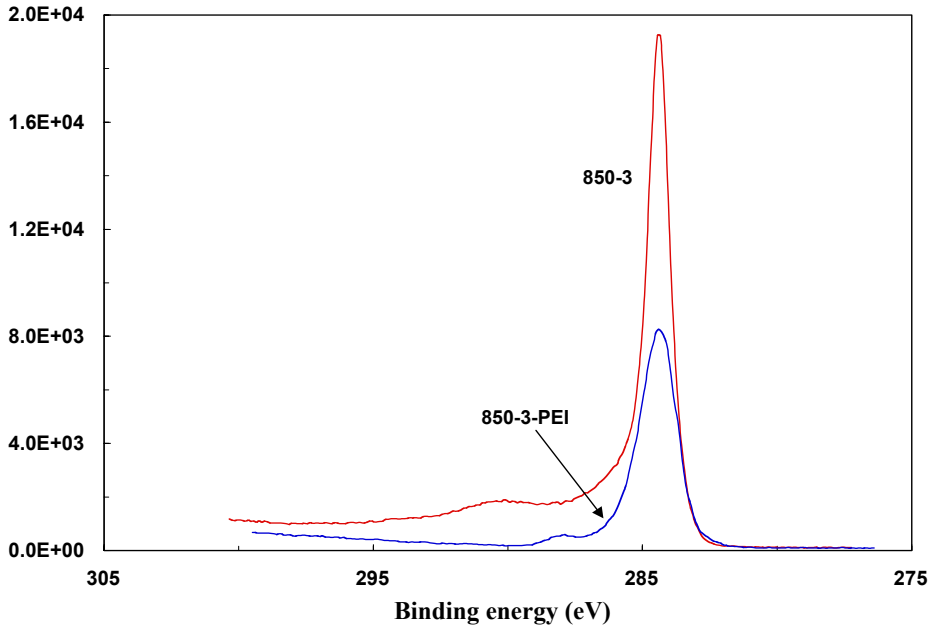

Figure 24. O 1s spectra of activated anthracite (AC-850-3) and its HN_3 and HNO_3 treated samples

For the AC-850-3 sample, there are bands that correspond to C-C, C-N and small quantities of organic oxygen species. Although not acquired in higher resolution mode on every sample, Si and Al (presumably from mineral contamination) were observed in AC-850-2-HNO_3 and AC-850-3-PEI. The Si and Al concentrations were roughly 1 atom%. Assuming the presence of SiO_2 and Al_2O_3, the Si and Al would then account for 3-4atom% of the oxygen observed.

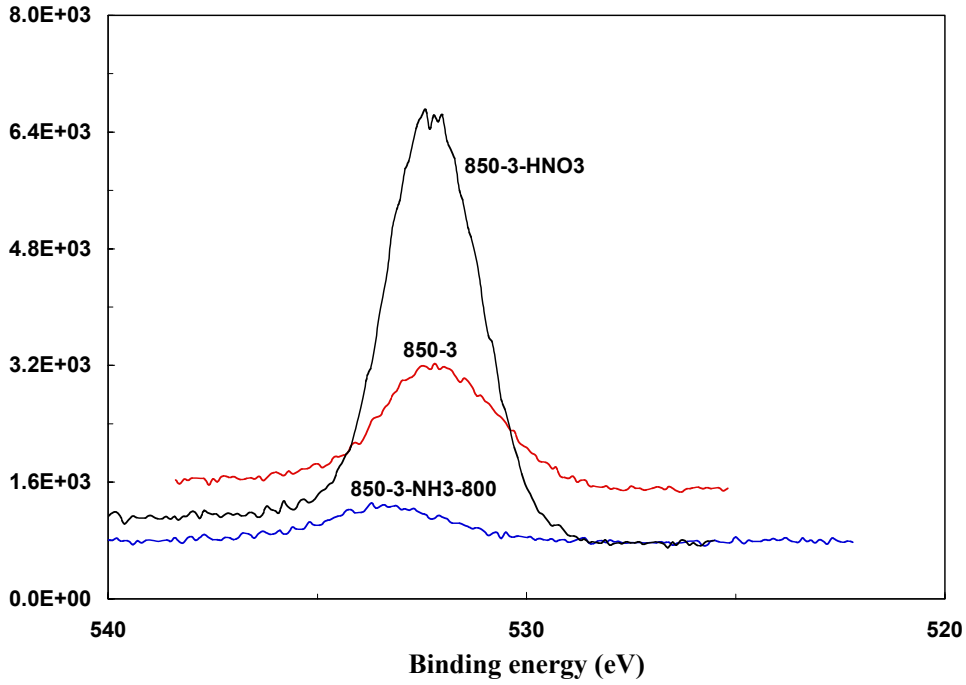

Figure 25. C 1s spectra of activated anthracite (AC-850-3) and its PEI impregnated sample

AC-850-2-HNO_3 contained a large quantity of oxygen (Figure 25). The C 1s spectrum contained a characteristic COO^- peak at 288.4 eV. Finally, two types of nitrogen were observed: C-N and a higher binding energy peak tentatively assigned as NO_2.

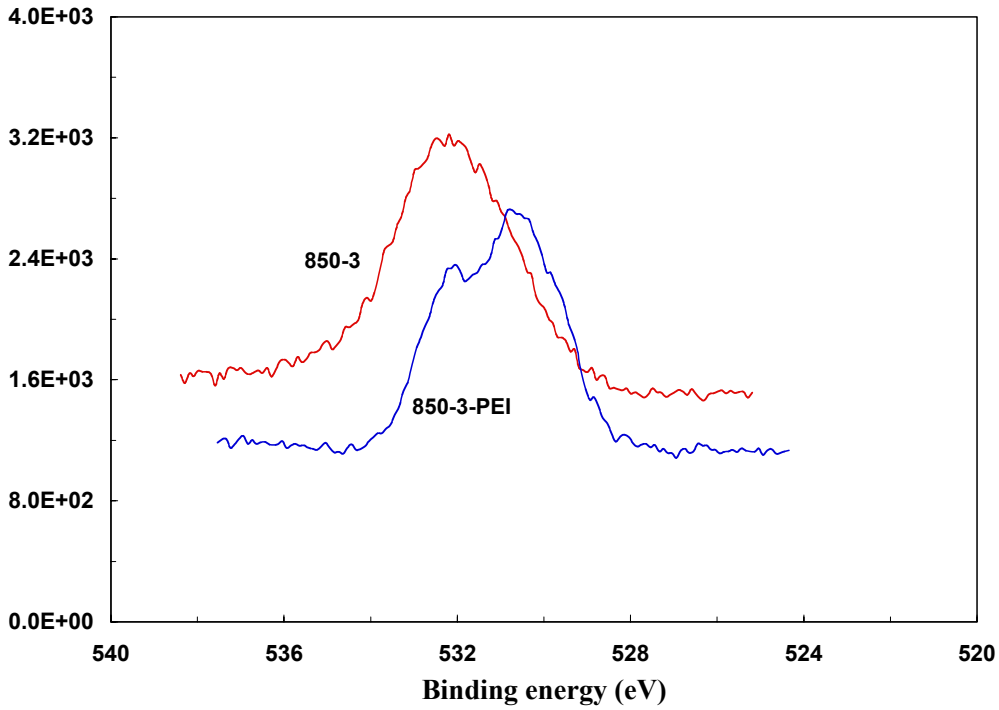

Figure 26. O1s spectra of activated anthracite (AC-850-3) and its PEI impregnated sample

AC-850-3-PEI contained significant quantities of nitrogen, as expected from the PEI impregnation. Assuming that all the nitrogen detected was from PEI, then 60-65% of the signal detected was from PEI. A small amount of COO^- (or possibly O=C-N) was detected on both samples.

The XPS results are summarized in Tables 7 and 8 below. The raw anthracite has 1.1% nitrogen atoms on the surface. After activation, the nitrogen content in the activated anthracite (AC-850-3) was lower than that in the raw anthracite since probably the nitrogen in the anthracite was lost during the activation process. As expected, the NH_3 treatment introduced nitrogen surface groups on the activated carbon, especially at high temperature.

The nitrogen content increased from 0.1% in the untreated activated carbon to 1.1% in the NH_3 treated activated carbon, as shown by the XPS data presented in Table 7.

Table 7. Summary of the elements detected by XPS (Rel. Atom%)

Sample	C	O	N
Raw	90.3	8.6	1.1
AC-850-3	93.6	6.3	0.1
AC-850-3-NH_3-800	94.0	4.9	1.1
AC-850-3-PEI	73.3	8.4	18.3

Since CO_2 is an acid gas, alkaline surface functional groups will favor chemisorption of CO_2. Among the surface functional groups studied on the activated carbon surface, only some nitrogen groups are alkaline. This is also why surface treatment methods are employed to improve the CO_2 adsorption capacity of sorbents by means of increasing the nitrogen content [21, 29]. Therefore, high resolution XPS analysis was conducted on the N 1s and the curve fitting results are presented in Table 8

In addition to the different nitrogen content on the surface of the studied samples (Table 7), the nitrogen functional groups are also different for these samples. The nitrogen groups on the raw anthracite, NH_3 treated activated anthracite and PEI impregnated activated anthracite that have alkaline character are amine groups (around 400.0eV) and imine groups (around 396eV). The presence of these groups also explains why these samples have higher CO_2 capacities, probably due to chemisorption processes. For the same token, the untreated

activated anthracite did not have any imine group and a lower concentration of pyridine groups, resulting in lower CO_2 adsorption capacities.

Table 8. Surface content of nitrogen species obtained by deconvolution of the N 1s XPS peak

	Content of nitrogen (at.%)					CO_2 absorbed at
	N-Imine	Pyridine / C-N	Nitriles	Pyrrolic / amine	Oxides	75°C (mg-CO_2/g)
Raw	-	50.91	-	45.28	3.81	16.05
AC-850-3	-	21.45	29.18	37.86	11.52	21.55
AC-850-3-NH_3-800	43.52	27.86	-	14.09	15.03	23.69
AC-850-3-PEI	33.92	66.08	-	-	-	26.30

4. CONCLUSIONS

Three anthracite samples (PSOC-1468, AFM-800, AFM-2600) were selected for this study to produce activated carbon for CO_2 capture. A lab scale fluidized bed was used for the activation and the activation temperature used was between 700-890°C. Three surface treatment methods (NH_3 heat treatment, HNO_3 oxidization and PEI impregnation) were conducted to modify the surface properties of the activated anthracites and to improve their CO_2 capture capacity. A TGA instrument was used to characterize the CO_2 capture capacity at 30 and 75°C. The N_2-77K isotherms were used to characterize the pore structure of the

activated anthracites. XPS analyses were used to characterize the surface functional groups of the activated anthracites and surface treated activated anthracites.

High surface area (over 1,000m^2/g) activated carbons were prepared from an anthracite sample (PSOC-1468) by steam activation using fluidized bed reactor. N_2-77K adsorption studies show that the activated anthracites are mainly microporous and the microporosity decreased with increasing activation time and temperature. The maximum surface area and pore volume are 1071m^2/g and 0.588mL/g for the anthracite activated at 890^{o}C for 2 hours. The surface areas go through a maximum with increasing solid yields. The initial increase in surface area is probably due to opening of porosity and formation of micropores, while the decrease in surface area for lower solid yields (<40%) is due to the enlargement of micropores and and pore wall removal.

The adsorption of CO_2 on the activated anthracite is mainly a physical adsorption process and the adsorbed amount decreased with increasing adsorption temperature. The CO_2 capture results do not show a linear relationship with the surface area. For example, the sample with the highest CO_2 adsorption capacity (65.7mg-CO_2/g-adsorbent) was the anthracite activated at 800^{o}C for 2 hours, whose surface area was only 540 m^2/g. This is probably due to only certain size pores being effective for CO_2 adsorption.

Two surface treatment methods, including NH_3 heat treatment and polyethylenimine (PEI) impregnation, were used to modify the surface properties of the activated anthracites to increase their CO_2 capture capacity at higher temperatures. The NH_3 treatment increases the

surface area of the activated samples, especially at lower temperatures (650°C). The chemical impregnation with PEI results in a dramatic decrease of the surface area of the activated anthracite, probably due to pore blockage and surface coverage by PEI. Both the NH_3 treatment and PEI impregnation can increase the CO_2 capture capacity of the activated antrhacites at higher adsorption temperature, due to the introduction of alkaline nitrogen groups on the surface.

5. Acknowledgments

This work was funded by the US Department of Energy (DOE) through a grant of the Consortium for Premium Carbon Products from Coal (CPCPC) at Penn State University (DOE Award number: *DE-FC26-98FT40350,* Internal Agreement Number: 2484-TPSU-DOE-0350). The authors would like to thank Dr. Yinzhi Zhang from the Energy Institute, Penn State University for her help to analyze the N_2 isotherms and discuss the analysis data; Dr. Xiaochun Xu from the Energy Institute, Penn State University for his help to provide the PEI sample and helpful suggestion; and Dr. Jeff Shallenberger from MRL (Materials Characterization Laboratory), Penn state University for his help to do the XPS analysis and data treatment. Finally, the authors also thank the Coal Bank at Penn State University and FB Leopold, PA for providing the anthracite samples.

6. Publications resulting of this project

1. Z. Tang, M. M. Maroto-Valer, Y. Zhang, CO_2 capture using anthracite based sorbents. Prepr. Am. Chem. Soc. Div. Fuel Chem., 2004, 49(1), 298-299.

2. Z. Tang, Y. Zhang, and M.M. Maroto-Valer, Study of CO_2 adsorption capacities of modified activated anthracites. Prepr. Am. Chem. Soc. Div. Fuel Chem., 2004, 49(1), 308-309.

3. M. M. Maroto-Valer, Z. Tang, and Y. Zhang, Use of activated anthracites for CO_2 capture, *Proceedings Carbon 2004*, American Carbon Society, Providence, RI, July 11-16, 2004, Paper J022.pdf (CD-ROM publication).

4. Z. Tang, M. M. Maroto-Valer, Y. Zhang, CO_2 capture of activated and impregnated anthracites, Fuel Processing Technology, To be submitted.

7. References

1. C.D., Keeling, T. Whorf. (1998). Trends: A Compendium of Data on Global Change, Oak Ridge.
2. H.J. Herzog, (1998) Proc. Stakeholders' Workshop on Carbon Sequestration, MIT EL 98-002.

3. P.J., Birbara, and T.A. Nalette (1996) US patent No: 4, 810, 266.
4. R.V. Siriwardane, M.S. Shen, E.P. Fisher, J.A. Poston. (2001) *Energy & Fuel*. 15, 279.
5. H.H. Schobert, J.P. Mathews, A.D. Jones, P.J. Pappano, R.H. Hurt (2001). Proc.11th International Conference on Coal Science, CD-ROM publication, Paper No. ICCS~220.PDF.
6. R.C. Bansal, J. Donnet, F. Stoeckl, Activated Carbon, Marcel Dekker, Inc. (1998).
7. T. Wigmans, Carbon 27(1) (1989) 13.
8. A.K. Dalai, A.I. Chowdhury, E.S. Hall, J. Zaman, E.L. Tollefson, Fuel 75 (1996) 384.
9. J.J. Pis, M. Mahamud, J.A. Pajares, J.B. Parra, R. C. Bansal, Fuel Processing Technology 57 (1998) 149.
10. J. A. Conesa, M. Sakurai, M.J. AntalJr, Carbon 38(6) (2000) 839.
11. J. Díaz-Terán, D.M. Nevskaia, J.L.G. Fierro, A.J. López-Peinado, A. Jerez, Microporous and Mesoporous Materials, 60(1-3) (2003) 173.
12. F. Rodríguez-Reinoso, M. Molina-Sabio, Carbon 30(7) (1992) 1111.
13. K. Gergova, S. Eser, H.H. Schobert, Energy & Fuel 7 (1993) 661.
14. J. Pis, J. Parra, G. Puente, F. Rubiera, J. Pajares, Fuel 77(6) (1998) 625.
15. M.M. Maroto-Valer, H.H. Schobert, In: B.Q. Li, Z.Y. Liu (Eds), Prospects for Coal science in the 21st Century, Shanxi Science and Technology Press., Taiyuan, China (1999) 909
16. M. Mittelmeijer-Hazeleger, J. Martin-Martinez, Carbon 30(4) (1992) 695.
17. D. Spencer, J. Wilson, Fuel 55 (1976) 291.

18. Z. Tang, M.M. Maroto-Valer, YZ Zhang, American Chemical Society Fuel Chemistry Division Preprints, 2004, 49(1), 298-299
19. Z. Tang, M.M. Maroto-Valer, YZ Zhang, American Chemical Society Fuel Chemistry Division Preprints, 2004, 49(1), 308-309
20. X. Xu, C.S. Song, J.M. Andresen, B.G. Miller, A.W. Scaroni, Energy & Fuel 16 (2002) 1463.
21. M.L. Gray, Y. Soong, K.J. Champagne, J. Baltrus, R.W. Stevens, Jr. P. Toochinda, S.S.C. Chuang, Separation and Purification Technology 35 (2004) 31.
22. K.S.W. Sing, D.H. Everett, R.A.W. Hual, and et al, Pure & Appl. Chem. 57(4) (1985) 603
23. Y.Z Zhang, Z. Lu, M.M. Maroto-Valer, J.M. Andrésen, H.H. Schobert, Energy & Fuel, 17 (2003) 369.
24. M. Turmuzi, W. R. W. Daud, S. M. Tasirin, M. S. Takriff and S. E. Iyuke, Carbon, 42 (2003) 453.
25. Duong D. Do, Adsorption Analysis: Equilibria and Kinetics (Series on Chemical Engineering, Series Editor: Ralph T. Yang), Imperial College Press, London 1998
26. D. Cazorla-Amorós, J. Alcañiz-Monge, A. Linares-Solano, Langmuir 12 (1996) 2820.
27. J.M. Martín-Martínez, R. Torregrosa-Maciá, M.C. Mittelmeijer-Hazeleger, Fuel 74 (1995) 111.
28. A. Vishnyakov, P.I. Ravikovitch, A.V. Neimark, Langmuir 15 (1999) 8736
29. J. Przepiórski, M. Skrodzewicz, A.W. Morawski, Applied Surface Science 225(1-4) (2004) 235.

CONSORTIUM FOR PREMIUM CARBON PRODUCTS FROM COAL

Nanotube Enhancement of Coal Extract Pitches: Fibers and Foams

SUBCONTRACT NO. 2480-UK-DOE-0350

FINAL REPORT

for Period 1 March through 30 June 2004

by

University of Kentucky

Center for Applied Energy Research

&

West Virginia University

Department of Chemical Engineering

August 2004

Disclaimer

ABSTRACT

The results of Laboratory and supporting technical assessments conducted under Subcontract No. 2480-UK-DOE-0350 are reported for the period March 1, 2002 to June 30, 2004. This contract is with the University of Kentucky Research Foundation, which supports work with the University of Kentucky Center for Applied Energy Research and West Virginia University. This work involves multiwall carbon nanotube enhancement of coal-derived pitches for carbon fiber and carbon foam applications.

TABLE OF CONTENTS

EXECUTIVE SUMMARY

High performance pitch based carbons are typically made from mesophase pitch. The mesophase pitch contains liquid crystal domains that tend to align in the axial direction of the fiber or ligaments of foam so that when carbonized and ultimately graphitized, a highly ordered graphitic lattice is formed, imparting excellent physical, electrical, and thermal properties to the resultant materials. However, the high processing costs and low yields associated with the production of mesophase pitch suitable for these applications makes the pitch expensive to produce, and adds significantly higher costs to the product. Hence, if viable methods of producing high performance carbon fibers and foams from low cost isotropic pitch feedstocks could be developed, a significant cost advantage could be gained. It is the aim of this project to produce high value carbon fibers and foams via the co-processing of a low cost coal extract pitch with well-dispersed carbon nanotubes.

The carbon nanotubes were dispersed in pitch and selected mixtures formed into filaments or foams. During fiber spinning, nanotubes aligned axially with the fiber. The second product was a lightweight high-strength porous carbon, usually referred to as carbon foam.

The presence of nanotubes in these fiber and foams improved strength, modulus, and thermal conductivity. The ability to generate higher value materials with a small addition of nanotubes to a coal extract pitch will result in materials of high commercial and military interest for structures, thermal management and electromagnetic shielding.

1. SECTION ONE

UNIVERSITY OF KENTUCKY

CENTER FOR APPLIED ENERGY RESEARCH

INTRODUCTION

Coal-derived carbon fibers and foams composites containing highly aligned nanotubes were shown to have enhanced physical properties compared to pitch derived foams and fibers. The component materials, coal extract pitches from WVU and UK and high purity multiwall carbon nanotubes from UK, were produced, blended and formed into fibers (UK) and foams (WVU). The materials were heat treated and tested for their physical, and thermal properties.

Multiwalled carbon nanotubes, which have graphene planes wrapped into a cylindrical configuration, have extremely high specific strengths (200x steel), elastic modulus (>1 TPa), and electrical and thermal conductivities. Typically, the nanotubes produced by UK have diameters less than 25 nanometers, and lengths of about 50 μm. Although nanotube-enhanced pitches can be used to form a suite of materials (including carbon pitch matrix composites, artificial graphite, carbon foams, carbon black and carbon fibers), this project focused on two main carbon products. The first is a lightweight high-strength porous carbon, usually referred to as carbon foam. Carbon foams pioneered by West Virginia University have, for a given density, resulted in higher strength and modulus than other known processes for carbon foam. The second product is pitch-derived continuously spun carbon fibers, which has been a major research focus at the University of Kentucky.

The starting point for both materials is the use of coal-derived extract pitches. These materials have a significant content of high molecular weight aromatic hydrocarbons, permitting a high degree of graphitization when heat treated. The tendency to form a graphitic lattice, as opposed to amorphous or turbostratic carbon, is significantly enhanced by the addition of carbon

nanomaterials, which might act to enhance the formation of highly oriented crystalline domains. Yet improved performance and reduced cost can result from the addition of small amounts of carbon nanomaterials, which can significantly enhance the graphitic character of the bulk material. As a result, when this material is converted to carbon, macroscopic domains are created with preferred crystal orientation, and enhanced index of graphitization.

In the case of carbon foam, coal is hydrogenated to about 2 weight percent hydrogen Mild hydrogenation increases the aromatic content of the coal, which is desirable from the point of view of forming carbon materials. The solvent extract is refined by distilling off low molecular weight components, resulting in an aromatic pitch. By carefully controlling the temperature and pressure in a nitrogen-pressurized autoclave, the outgassing volatiles create a porous structure.

In the case of carbon fibers, high modulus as well as high thermal conductivity requires the formation of well-ordered graphite domains, and fibers are usually derived from mesophase pitch or PAN. However, as pointed out previously, added carbon nanotubes not only act as reinforcing composite fibers, but also impose long-range order in the matrix pitch over many microns of interlocking domains, and hence may offer significant advantages compared to conventional mesophase pitch.

It should be also noted that the addition of nanotubes is not necessarily expensive, and can even reduce cost. UK has installed a pilot-scale continuous reactor for the production of 1 to 3 kg/day of high purity multiwalled carbon nanotubes. This unit was be operable in December 2002, and estimated costs of the nanotubes are less than $100/kg. In the future, much lower costs are

projected due to economies of scale and process improvements. In any case, the use of a few grams of nanotubes per kg of pitch will greatly enhance the product properties while having only incremental effect on the material costs. The proposed work offers one promising route to move low cost coal-extract pitches into medium- and high-performance structural, thermal management and electrical shielding applications (with an ensuing increase in value).

Task 1.0 Production of Coal Derived Pitches – UK CAER.

Anthracene oil was used to extract pitch from a Western Kentucky #9 coal (W.Ky), Table 1, using low severity extraction conditions. Extraction conditions produced a high softening point pitch suitable as a feedstock for carbon fibers and nanotube composite carbon fibers. Approximately 1 kg of Western Kentucky coal extract pitch was prepared. The extraction technique can be summarized as follows.

Table 1. Proximate and ultimate coal analysis.

	W.Ky
Moisture (%)	5.2
Ash (%)	19.0
Volatiles (%)	34.6
Fixed Carbon (%)	41.2
Carbon (% daf)	80.0
Hydrogen (% daf)	6.3
Nitrogen (% daf)	1.7
Total Sulfur (% daf)	4.8
Oxygen *by diff.* (% daf)	7.2
Pyritic Sulfur (% db)	2.0
Sulfate (% db)	0.02
Organic Sulfur (% db)	1.9

Digestion of coal with anthracene oil was performed batch-wise in a heated Parr Instruments 2L stirred autoclave reactor. Coal was crushed to < 60 mesh and then slurried with anthracene oil in a coal to solvent ratio of 1:2 w/w and placed into the reactor, typical charge for the digestion was

about 900 g. Digestion of the coal was performed at 425 ^{o}C for 60 min and at a pressure of 200 psi. The reactor was maintained at 200 psi by slowly venting the reactor during digestion as required, the vent line was attached to a cold catch pot (-15 ^{o}C) to trap any light distillates generated during digestion. After the 60 min digestion time, the reactor was allowed to cool to approximately 260 ^{o}C, the reactor de-pressurized and the contents drained into a pre-weighed beaker. After allowing the reactor to cool to room temperature, the reactor, catch pot and vent lines were weighed and this data used to calculate a mass balance for the digestion. QI and THFI were determined on the digests.

Un-dissolved coal was separated from the digest by hot filtration. Filtration was preformed through a GFA filter at 250 ^{o}C with 10 psi of nitrogen over pressure. Filtering rate and cake resistivity was calculated using Darcy's Law [Purchas 1967]. The weight of filter cake and filtrate were also measured. Filtrates were vacuum distilled to recover anthracene oil and extracted pitch (pot residue). Vacuum distillation was used to control the softening point of the pitch, typically pitches with softening points in the range of 220 to 260 ^{o}C are desired for carbon fiber fabrication. A brief summary of extraction data from one of the batch extractions is shown below in Tables 2, 3 and 4.

Table 2 - Coal digestion data summary, digestion performed at 425 ^{o}C for 60 minutes.

	W.Ky	*units*
Coal IN (daf) =	224.5	g
Solvent IN =	584.9	g
Slurry IN (daf coal) =	809.4	g
Extraction Distillates OUT =	53.3	g
Digest OUT (daf coal) =	727.3	g
QI =	21.3	%
THFI =	24.8	%
% Conversion [based on QI] (daf coal) =	68.7	%
% Conversion [based on THFI] (daf coal) =	63.5	%
Mass Balance Extraction (daf coal) =	96.4	%

Table 3 – Summary of filtration parameters for coal/anthrancene oil digests.

	W.Ky	*units*
Filter Charge (daf coal) IN =	727.3	g
Cake (daf coal) OUT =	56.2	g
Filtrate (daf coal) OUT =	624.3	g
Distillates OUT =	4.7	g
Specific Cake Resistance =	2.1	10^{10}m/kg
Filter Rate =	214.5	kg/m^2/h
QI Filtrate =	0.8	%
Mass Balance Filtration (daf coal) =	97.6	%

Table 4 – Distillation Summary.

	W.Ky	***units***
Distillation Charge IN =	624.3	g
Distillate OUT =	391.2	g
Pitch (Pot Residue) (daf coal) OUT =	230.4	g
Pitch Softening Point =	255	^{o}C
Mass Balance Distillation (daf coal) =	99.6	%

Task 2.0 Production of Carbon Nanotubes – UK CAER.

The University of Kentucky Center for Applied Energy Research has developed a synthesis method for producing high purity multiwalled carbon nanotubes. The method is a chemical vapor deposition process and highly selective. A pilot process for producing high purity (>90 %) was installed and commissioned in January 2003, current production capacity is approximately 1 kg per day.

The synthesis process involves decomposition of an appropriate hydrocarbon over a dispersed iron catalyst that is deposited *in situ* on quartz substrates. The process has been described in detail elsewhere [Andrews et al 1999], but can be summarized as follows. The process configuration involves entraining a mixture of xylene and ferrocene into an inert gas stream. Decomposition of the ferrocene at temperatures in the range 625 – 775 °C, and at atmospheric pressure, produces a coating of iron nanoparticles on the quartz surfaces, and these metal sites function as catalysts for the formation and growth of multiwall carbon nanotubes. An example of the carbon nanotube mats produced is shown in Figure1.

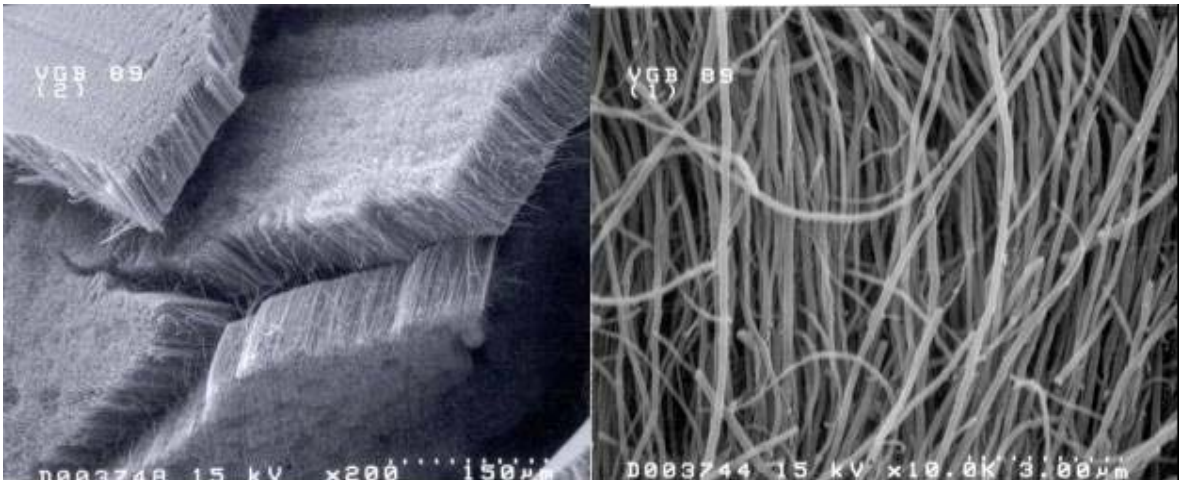

Figure 1 – Multiwall carbon nanotube mats.

In preparation of for fabrication of nanotube/pitch composite fiber and foams, approximately 500 g of multiwall carbon nanotubes was produced.

Task 3.0 Dispersion of nanotubes – UK CAER.

WVU provided UKCAER with a Koppers coal tar pitch, softening point 110 ^{o}C and a pitch/nanotube mix containing 2 wt % of nanotubes prepared. Dispersion of the MWNTs in the pitch matrix was achieved by heating the pitch to a temperature above its softening point in a Haake Polylab Rheomix, where high shear mixing could be applied. Tests were performed to determine the optimum conditions (temperature, mixing time and rotor speed) required to adequately disperse the MWNTs and yield a homogenous product, but without unduly degrading the pitch. At the completion of each test, the composite was allowed to cool, recovered from the mixer, and crushed to yield a granular product. Pitch/nanotube blends were prepared in 50 g batches (the optimum capacity of the mixing bowl), approximately 600 g of pitch/nanotube blend was prepared. The pitch blend was returned to WVU for carbon foam synthesis. Pitch/nanotube blends containing 2 and 4 wt% nanotubes were also prepared with W.Ky coal extract pitch and Ashland A500 pitch (for comparison) using the same techniques described above.

Task 4.0 Fiber forming, processing and testing – UK CAER

Pitches nanotube mixes were formed into continuous filaments using a Wayne bench scale extruder fitted with a 6.2mm diameter screw and 0.3mm dia x 1mm capillary die. Tests were conducted to determine the conditions under which the samples could be successfully extruded to produce a continuous thread. Feed size distribution and the temperature profile along the barrel and nozzle were crucial to this task. The extruded thread was attached to a wind-up drum rotating at speeds up to 1700rpm (12m/s) to draw filament in the range 15 to 30μm.

Tows of fiber cut from the wind-up drum were stabilized by heating slowly in air up to 310^{o}C. The stabilized fibers are then rapidly carbonized by heating to 1000^{o}C in nitrogen. Processing of control fiber samples is shown in Table 5.

Table 5 – Summary of fiber processing data for control fiber samples.

Pitch	**Stabilization**				**Carbonization**			**Carbon Yield (%)**
	Rate (^{o}C/min)	**Linear Shrink (%)**	**Weight Change (%)**	**Status**	**Linear Shrink (%)**	**Weight Change (%)**	**Status**	
WVU#BO44-NDK (QI Free Coal Tar)	0.2	13	-1.9	3	11	-21.3	3	76.8
WVU#BO81-NDK (Coal Extract)	0.2	12.5	-2.2	3	10	-24.3	3	73.5
W.Ky	0.2	11	-2.6	3	13	-31	3	71.2
Status: 0 = melted, 1 = stuck, 2 = slightly stuck, 3 = OK. *n/a = not applicable.*								

Table 6 – Summary of fiber processing data for pitch/nanotube composite fiber samples.

Pitch	Stabilization				Carbonization			Carbon Yield (%)
	Rate (^{o}C/min)	Linear Shrink (%)	Weight Change (%)	Status	Linear Shrink (%)	Weight Change (%)	Status	
W.Ky + 2 wt % MWNT	0.2	0	3.8	3	8	26.9	3	75.9
W.Ky + 4 wt % MWNT	0.2	4	3.4	3	11	22.4	3	80.2
A500 + 2 wt% MWNT	0.2	0	10	3	10	24	3	76
Status: 0 = melted, 1 = stuck, 2 = slightly stuck, 3 = OK. *n/a = not applicable.*								

SEM images of W.Ky pitch/nanotube composite fibers are shown below in Figure 2 and 3. Both images show dispersion of nanotubes as individual nanotubes, aligned axially in the fiber. Exhaustive attempts to measure mechanical properties of these fibers as single filaments produced ambiguous results. Overall mechanical properties measured appeared the same or lower than values determined for blank fibers (ie containing no nanotubes). Inspection of the above SEM images shows that the external surface of the fibers is rough, these “defect” sites in the surface may cause premature failure of the matrix before any stress can be transferred to the nanotubes (reinforcement), during testing of single fiber filaments. To avoid undue influence on the mechanical properties of the fiber by the fiber’s surface characteristics epoxy lay-ups of fiber tows were prepared.

Figure 2 – W.Ky pitch fiber containing 2 wt% nanotubes.

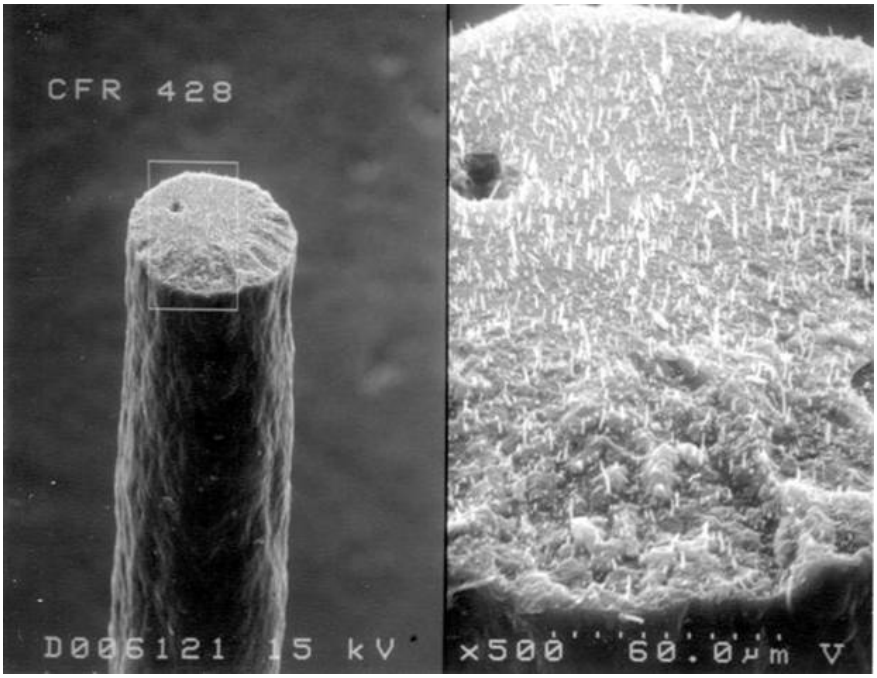

Figure 3 – W.Ky pitch fiber containing 4 wt% nanotubes.

Composite fibers were dip coated in epoxy to reduce the effect that surface defects had on the mechanical properties. Individual fibers were dip coated in epoxy, wiped and then cured at 120 ^{o}C for 1 hour. The resulting epoxy coated fibers were examined under SEM and some examples are shown in Figures 4 and 5. Inspection of these images shows that the epoxy significantly reduced the surface "roughness" of the composite fibers. The reduction in surface roughness also reduces surface defect sites that may have caused the ambiguous mechanical test results previously. Pitch fibers from both W.Ky and A500 feedstocks were also dip coated and used for comparisons with the epoxy coated composite fibers. Epoxy coated fibers were tested on an MTS tensile tester, 100 of each fiber type were tested. A summary of tensile strength and elastic modulus are shown in Table 7.

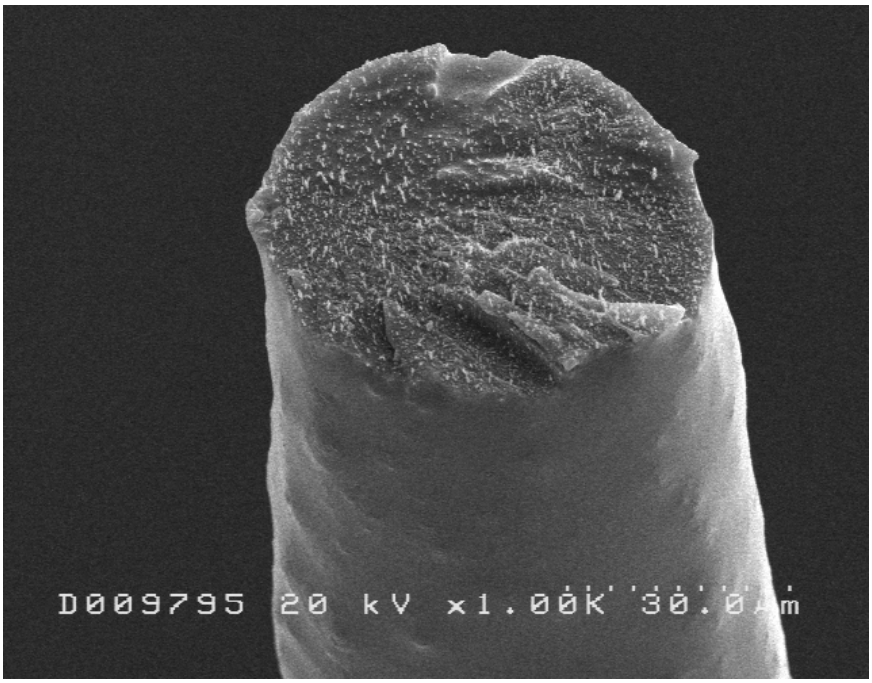

Figure 4 – Epoxy coated W.Ky pitch nanotube fiber.

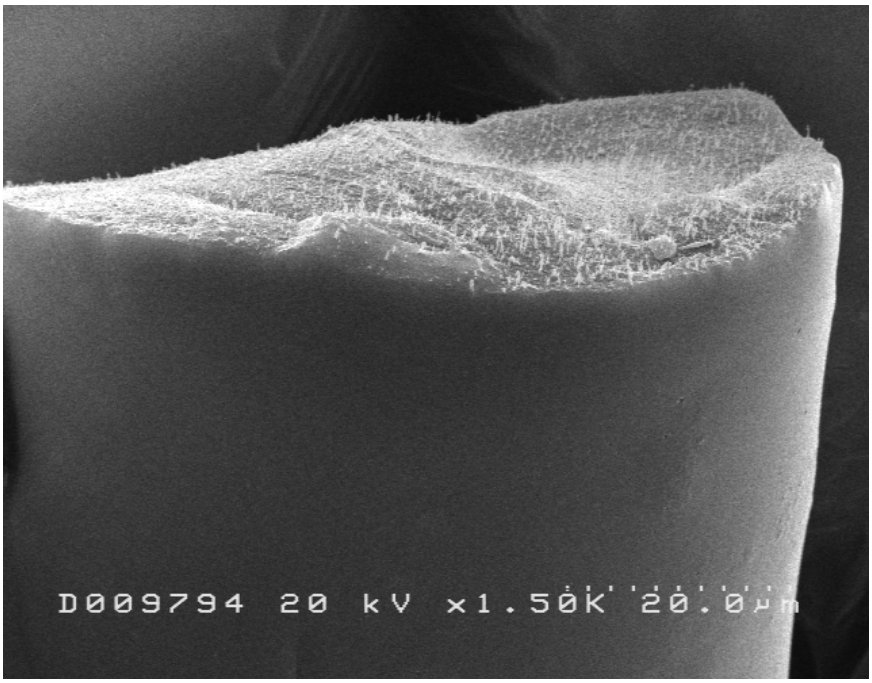

Figure 5 – Epoxy coated W.Ky pitch nanotube fiber.

Table 7 – Mechanical properties of epoxy coated pitch and pitch nanotube composite fibers.

Fiber	Mean Tensile Strength (MPa)	Std. Dev (MPa)	Mean Elastic Modulus (GPa)	Std. Dev (GPa)
A500	282.9	69.2	38.9	6.4
A500 + 2vol% nanotubes	372.2	61.0	36.4	2.8
W.Ky	526.3	60.5	36.0	3.6
W.Ky + 4vol% nanotubes	365.3	64.4	38.8	3.7

The results for the mechanical testing were not definitive. Although the A500 composite fibers did show increases in elastic modulus and tensile strength, the increases were moderate. The W.Ky composite fibers showed a decrease in tensile strength and modulus. These results can be explained by examining some of the fiber fracture surfaces, a sample of 10 fiber fracture surfaces retained after tensile testing were examined under SEM. A typical example of a W.Ky fiber

composite fracture surface is shown in Figure 6. This figure shows the presence of a large void within the fiber, such voids within the fiber were observed in several fiber fracture surfaces. The voids are detrimental to the fibers mechanical properties. The W.Ky composite fibers, which were spun with the highest nanotube loading, 4wt%, also had larger diameters compared to the fibers with lower loadings of nanotubes. Spinning larger diameter fibers also increases the likelihood of introducing larger defects during spinning. Further refinement of spinning techniques to reduce the fiber diameters of composite fibers is required.

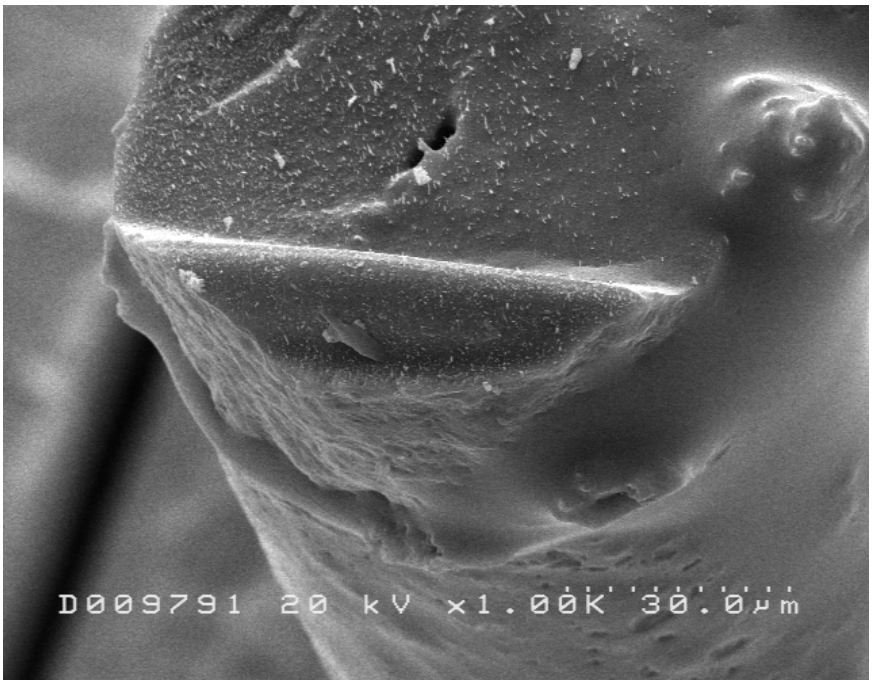

Figure 6 – W.Ky composite fiber fracture surface.

The thermal properties of composite foams were also assessed. The thermal diffusivity of the pitch derived foams and composite foams were measured using a laser flash method. Thermal diffusivities were measured on an Netzsch LFA 427 Laser Flash instrument. The laser flash

technique involves pulsing a laser onto the sample and measuring the heat diffused through the sample. Thermal diffusivity is directly proportional to thermal conductivity. Thermal conductivity can be calculated from the thermal diffusivity if the heat capacity and thermal expansion of the sample is known (or can be measured). Thermal diffusivity measurements require careful sample preparation to ensure that no penetration of the laser through the sample occurs during the measurement and that all of the lasers energy is absorbed by the sample.

Sample preparation of the carbon foams can be summarized as follows. Pitch foams and foam composites were cored to produce samples measuring 10mm diameter and approximately 2mm thick. Samples were coated, top, bottom and side with silicon carbide. The silicon carbide was used to fill the surface pores of the foam to prevent scatter or penetration of the laser pulse during measurement. The silicon carbide coated foam was cured at 400^{o}C for 1 hour, cooled and the polished to produce a smooth surface. The sample was then coated with graphite. Laser flash experiments were performed using a laser voltage of 450V and a pulse width of 0.8ms. Thermal diffusivity was measured in 100^{o}C increments from ambient to 700^{o}C, 3 shots per point were used with a delay time of 10 min between each shot. Results of thermal diffusivity test are summarized in Table 8.

Table 8 – Thermal diffusivity data for carbon foams.

	Thermal Diffusivity (mm^2/s)	
Temperature (^oC)	A240	A240 + 2wt% nanotubes
25	1.335	1.483
100	1.217	1.366
200	1.173	1.295
300	1.155	1.237
400	1.152	1.215
500	1.162	1.210
600	1.153	1.229
700	1.172	1.236

Comparison of thermal diffusivity between the foam and composite foam shows an approximate 30% increase in thermal diffusivity for the composite foam. It should be noted that this increase in thermal diffusivity was the result of only a 2wt% loading of nanotubes. It should also be noted that the thermal diffusivity of these foams did not change over the 700^{o}C temperature range. This is in comparison with graphite, where its thermal diffusivity drops dramatically above 400^{o}C.

2. SECTION TWO

WEST VIRGINIA UNIVERSITY

Task 5.0 Foam processing and testing - WVU

In last quarterly report, we reported on the pretreatment of pitches as a way of tailoring their foaming performance. In this report on we will report the subsequent foaming process and the characterization of the resultant foams.

Experimental:

Raw A240 petroleum-derived pitch and coal-based SynPitch were used as the starting pitches. A portion of each was sent to the CAER in Kentucky where 2% MWNT were incorporated into each pitch. Treated pitch samples, both with and without the addition of nanotubes, were ground to certain mesh size(50~100 mesh) and charged into a high pressure foaming reactor. The foaming was carried out in a N_2 atmosphere with pressure up to 500psi and temperature up to 500°C. The obtained green foam was then calcined at 1000°C in inert atmosphere to increase its strength and carbon content.

The carbon foams were characterized by SEM to investigate the distribution of nanotubes in carbon foam matrix. The general properties of carbon foam, such as bulk density and porosity and % of open cell structure were also measured. The porosity and % open cell were measured by means of a He pycnometer.

$$\text{Porosity}\% = (1 - D_b / D_p) \times 100$$

$$\%\ \text{open cell} = D_f / D_p \times 100$$

where D_b bulk density; D_f true density of the foam; D_p true density of pulverized foam

Results:

2 wt% MWNT was added into the raw pitch by the CAER workers, but after the heat treatment of pitch, foaming and calcinations, the amount of nanotubes in the carbon foam has been changed to 4.3%, 3.7% and 3.4%, respectively, as shown in Table 1. This is due to the loss of volatile matter during the various steps of foam preparation.

Table 1. Correction of the amount of nanotube in the carbon foam

Samples	Original MWNT added, wt%	Weight loss in different steps, wt%			Finial concentration of MWNT in the carbon foam, wt%
		pitch heat treatment	foaming	calcination	
A240	2	49.5	4.3	4.3	4.3
Coal-based SynPitch	2	36.4	10.7	5.7	3.7
Coal Tar Pitch	2	35.7	5.3	4.8	3.4

Table 2. General properties of carbon foam derived from pitches

Sample	Bulk density, g/cc	Porosity, %	% open cell
A240	0.34	82.9	97.2
A240/MWNT	0.41	78.6	95.7
Coal-based SynPitch	0.42	79.7	95.6
Coal-based SynPitch/MWNT	0.34	82.6	96.1
Coal Tar Pitch	0.67	64.8	83.5
Coal Tar Pitch/MWNT	0.68	65.4	82.9

The foam microstructure and the distribution of nanotubes in the foam matrix were investigated by SEM. Figure 1 shows the overall cross section of these pitch-derived carbon foams. A240 generates more uniform cell size, while SynPitch-dervived carbon foam shows a wider cell size distribution.

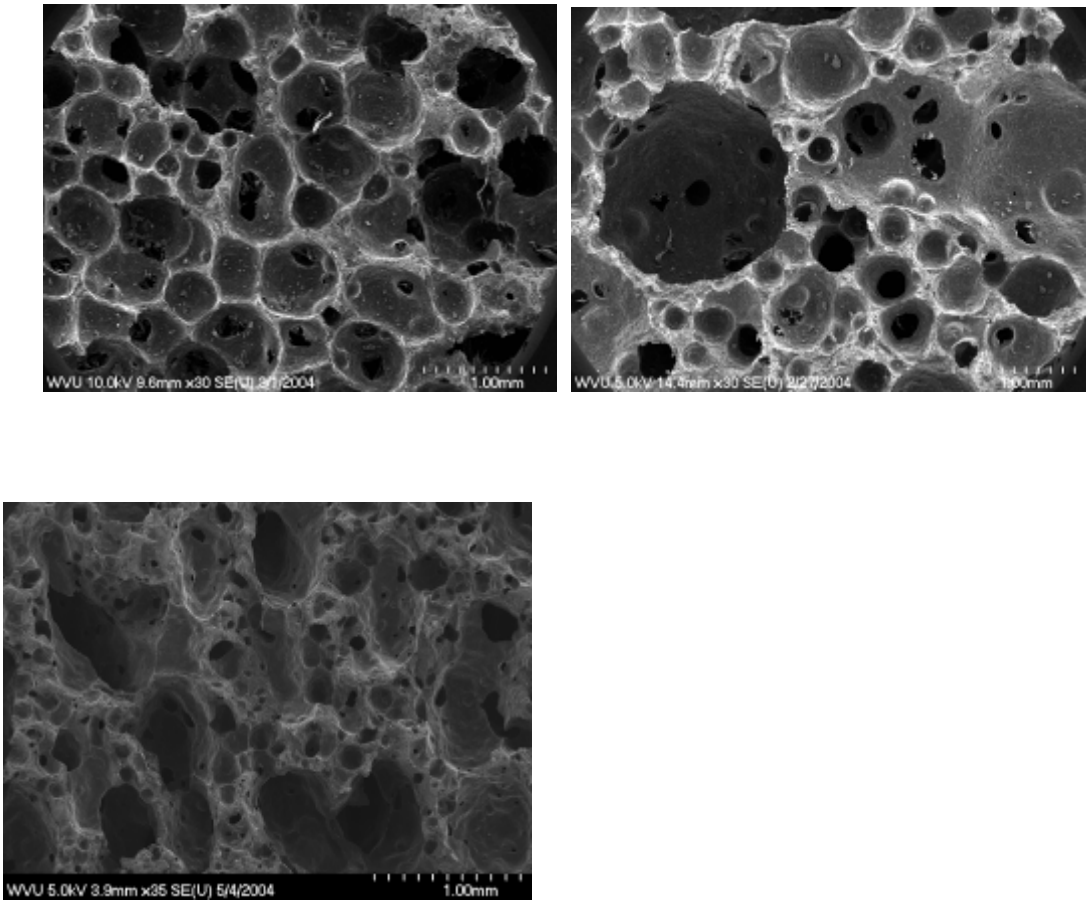

Figure 1. SEM images of MWNT reinforced carbon foam. A240-based, left, SynPitch-based, right and coal tar pitch-based, bottom center

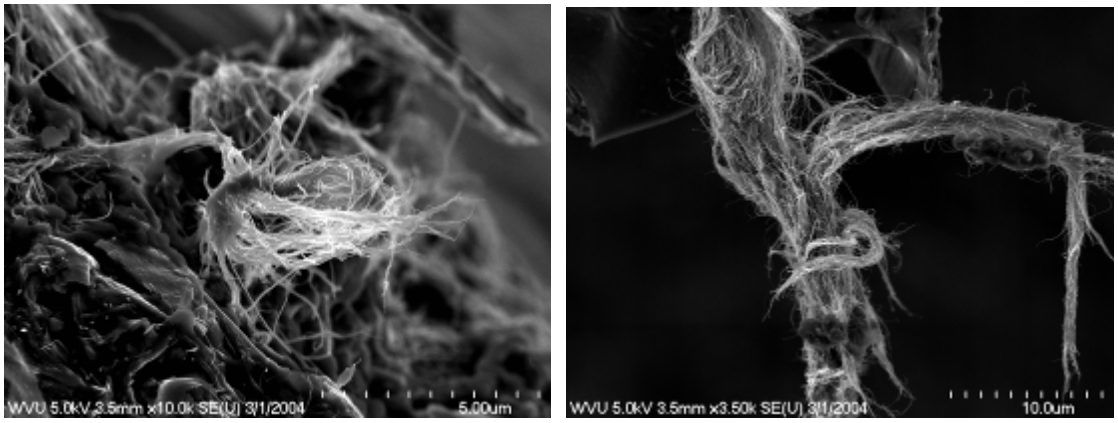

Figure 2. Agglomerated MWNT found in the carbon foam matrix

The interaction between the nanotube and composite matrix is in part responsible for the enhancement of mechanical strength. For the carbon foam/MWNT system, due to the lack of the knowledge of surface chemistry of nanotubes and carbon at this moment, we are unable to specify the precise interactions between nanotubes and carbon matrix, but *van Der Walls* and π-π interactions might be involved. The enhanced mechanical properties are believed to be due to the "bridging" effect of the nanotubes and the ability to transfer the load to the nanotubes. If the nanotubes are strongly bonding or interacting with the foam matrix, the nanotubes will bridge the microscopic cracks and the matrix residues should be observed adhering to the tube surface in the fracture sites. Figure 3 shows the nanotubes found on the fracture surface of foam matrix. Most of these tubes appear to have a clean surface without matrix residues adhering to it. The results indicate that the MWNT may have weak interactions with carbon foam matrix and hence not strongly bound to the matrix.

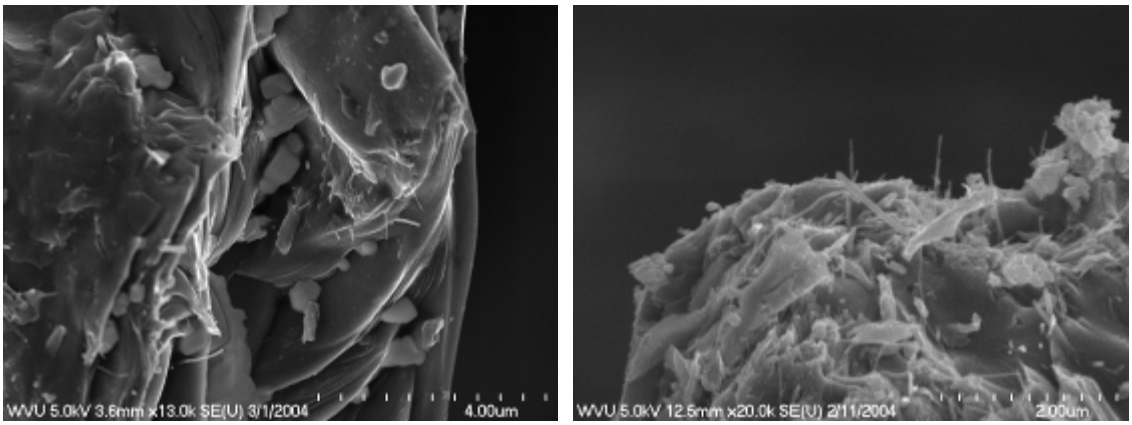

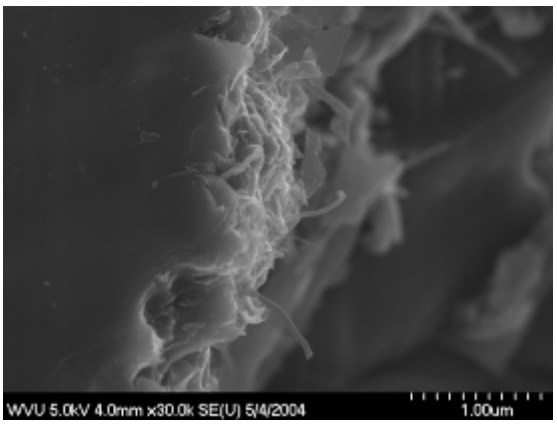

Figure 3. MWNT appeared on the cross section of carbon foam, A240-based, left and SynPitch-based, right, coal tar pitch-based, bottom.

The alignment(orientation) of nanotubes in the matrix also affects the property enhancement of the carbon foam. The nanotubes found on the fracture surface, as shown in Figure 3, were supposed to “bridge” the matrix together. This kind of alignment would be effective in enhancing the overall strength of the foam. However, the nanotubes found on the cell membrane are, for the most part, oriented perpendicular to the foam wall and are not effectively bridging the matrix together, as shown in Figure 4. In addition, the nanotubes bridging between the graphitic layers or microcracks should enhance the strength of the foam, but such structures were difficult

to find at least for the samples investigated here(see Figure 4). The nanotubes may need a high shearing force to align them in a certain direction. Unlike the spinning of the carbon fiber, which subjects the pitch a high shearing forces during extrusion from a nozzle, the shearing force applied to the carbon foam matrix during foaming is from the gas bubble evolution, which might not be strong enough to align the nanotubes parallel to the cell wall.

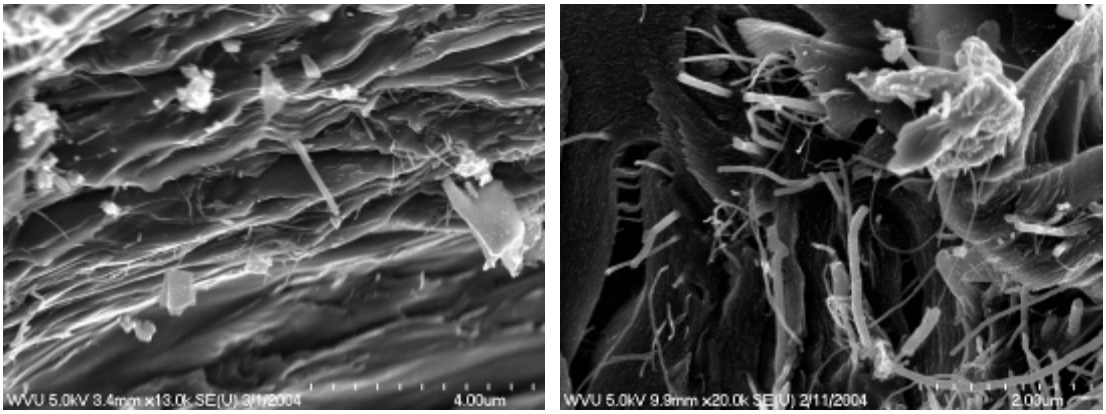

Figure 4. MWNT found on the foam cell membrane, A240-based, left; SynPitch-based, right.

Compressive strength was measured by means of Instron 5869 using a cylindrical shaped sample(25mm diameter by 20~30mm height) with a matched stainless steel sample holder cylinder and piston. The compressive strength is obtained from the yield strength of the stress-stain curve for the foam.

Figure 5 shows the compressive stress-strain curves. The stress increases as the load is applied to the sample and then the sample fractures but still resists the load as the cells are compressed. To compare the effect of nanotubes, the compressive strength along with the relative density of samples was measured and is listed in Table 3. An accurate comparison should be carried out among the samples with same relative density, but due to the technical difficulty, it is hard to get

the samples with and without nanotubes to have exactly the same relative density. However, the relative densities of the actual sample are close for the foams tested here. The results listed in Table 3 indicate that the nanotubes do not significantly affect the strength of carbon foam at least under compression. It is not clear at this moment what causes this result. Further testing of the tensile strength may be necessary to clarify the effect of nanotubes on the carbon foam strength and such tests are currently under way.

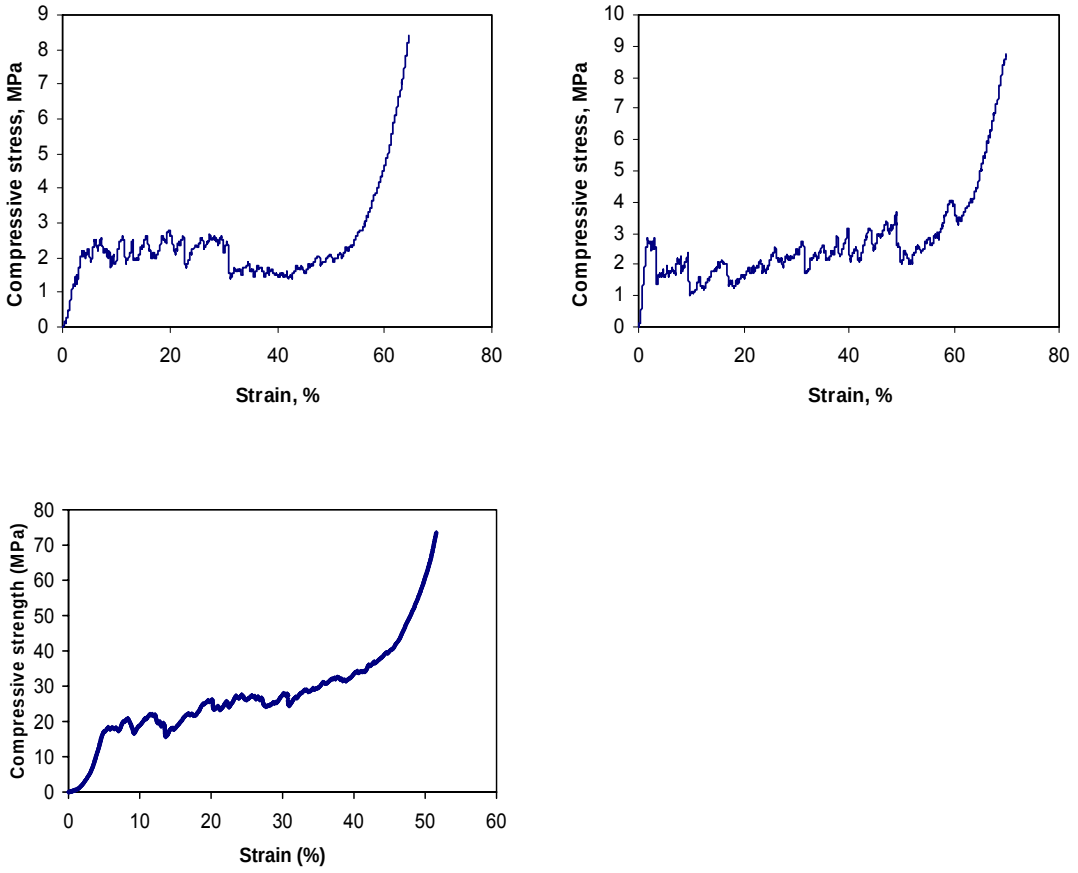

Figure 5. Compressive stress-strain curve. A240/MWNT, left; SynPitch/MWNT, right; and coal tar pitch/MWNT, bottom.

Table 3. Comparison of the compressive strength of carbon foam with and without MWNT addition

Sample	Compressive yield strength, MPa	Relative density
A240	3.9	0.17
A240/MWNT	2.3	0.21
SynPitch	2.5	0.20
SynPitch/MWNT	2.7	0.17
Coal Tar Pitch	18.2	0.35
Coal Tar Pitch/MWNT	18.2	0.35

References

Andrews, R., D. Jacques, A.M. Rao, F. Derbyshire, D. Qian, X. Fan, E.C. Dickey, and J. Chen, *Continuous production of aligned carbon nanotubes: A step closer to commercial realization.* Chemical Physics Letters, 1999. **303**(16): p. 467-474.

Purchas, D.B, 1967, “Industrial Filtration of Liquids”, Leonard Hill, London, England.

"Anthracite Coal for Cathode/Electrode Applications in Aluminum/Silicon Smelters"

Final Report

July 1, 2003 to June 30, 2004

John C. F. Chang
Irwin C. Lewis
Rick T. Lewis
Doug J. Miller

GrafTech International Ltd.
UCAR Carbon Company Inc.
Parma R&D Center
12900 Snow Road
Parma, OH 44130

Report Issued: August 15, 2004

Contract Number: 2562-UCAR-DOE-0350
Prime Award Number: DE-FC26-98FT40350

I. ABSTRACT

A pilot-plant study was carried out to investigate the use of high-temperature processed anthracite coals as a filler material for producing cathodes used in aluminum smelters and carbon electrodes used in silicon production. Electrically calcined Pennsylvania anthracite (ECA) was heat treated to temperatures of 2300 °C, 2700 °C, and 3000 °C and the products were used to fabricate 150 mm diameter artifacts. The artifacts were characterized by x-ray diffraction and microscopy techniques and by physical properties measurement after baking to 1100 °C for cathodes and 900 °C for electrodes. The results show that high-temperature processing of the coal filler leads to cathode and electrode artifacts with lower with-grain CTE, higher electrical and thermal conductivities and thus higher resistance to thermal shock. The sodium reactivity of cathodes was evaluated using the Rapoport test and the results showed increased resistance to sodium attack under simulated aluminum cell electrolysis conditions. The roles of catalytic graphitization from ash constituents and structural changes from thermal processing are discussed.

TABLE OF CONTENTS

LIST OF TABLES

LIST OF FIGURES

II. INTRODUCTION

II.1. Use of Anthracite Coal in Production of Carbon Electrodes and Cathodes

Anthracite coal is currently used as a filler material for two main bulk carbon products, carbon electrodes and cathode blocks. Carbon electrodes are employed for the refining of metals such as silicon, ferroalloys, and phosphorus in the submerged electric arc furnace. GrafTech produces carbon electrodes at its Columbia, Tennessee plant employing anthracite coal, electrically calcined to about 1800 °C as filler and coal tar pitch as binder. The formed electrodes are then baked to a final temperature of about 850 °C. A number of other manufacturers utilize petroleum coke rather than coal as the base filler material or use some graphite particles to achieve desired final properties. Since cost is a major issue for these applications, carbon electrodes are not processed beyond the bake stage required to carbonize the binder. Key properties for carbon electrodes and their typical values are listed in Table I.[1]

Table I
Ranges of Physical Properties of Typical Carbon Electrode Grades

Property	Range
Apparent Density, g/cc	1.50-1.68
Specific Resistance, μΩm	21-50
Flexural Strength, Mpa	3.1-6.9
Young's Modulus, Gpa	4.1-8.8
Ash Content, wt %	0.6-8.0

Cathode blocks are used throughout the world in the electrolytic production of aluminum by the Hall/Heroult process. Cathode blocks are produced in several different grades depending on the selection of raw materials and processing. The different block grades can be classified as graphitized, semi-graphitic and amorphous.[2]

Carbone Savoie, a subsidiary of GrafTech International Ltd. is a major world producer of cathode blocks. They produce a variety of grades with the following constitutions.

- Graphitized blocks (K grade) – using calcined petroleum coke filler and graphitized to above 2500 °C.

- Graphite blocks (HC-10) – using graphite filler and baked to a final temperature of 1000-1,100 °C.

- Semi-graphite blocks containing various amounts of calcined anthracite coal in combination with graphite filler and baked to 1000-1100 °C.

- Amorphous blocks (HC-3) – containing 100% of calcined anthracite coal as filler and baked to 1000- 1100 °C.

II.2. Challenges

The aluminum and silicon industries like all other metal refining industries are facing the same challenges of increasing productivity and efficiency.

In order to increase productivity, both aluminum and silicon smelters are significantly raising the power input into the smelting furnaces. For example, the normal technology in the aluminum smelting pot is AP18 and AP30 (developed by Aluminum Pechiney). AP18 was at one time the standard technology with 180,000-amp current going through the furnace. Most recently AP30 has become more prevalent with the use of 300,000 amps in most of the newly constructed aluminum smelters. A pilot unit of AP50 that uses 500,000 amps has been successfully developed by Aluminum Pechiney. It is anticipated that the AP50 technology will be commercialized in the near future.

Similarly, for the anode electrodes in silicon smelters, the current density going through the electrodes has been increased by at least by 50% in recent years. These increases in the current density will shorten the tap-to-tap times and increase productivity significantly.

For these reasons, the property requirements for the carbon electrodes and cathode blocks are becoming more stringent. Higher electrical conductivity and improved thermal shock resistance are required. Lower ash levels would lead to higher purity in the refined metals. Without improvements, the use of anthracite coal in both products is at risk.

Carbon electrodes made with petroleum coke are now being manufactured in China. For the cathode blocks, graphitized product made using calcined coke and graphite as filler are replacing the semi-graphite and amorphous grades produced with anthracite coal. There is, therefore, a need to improve the properties of coal-based electrodes and cathodes to maintain and hopefully expand the usage of anthracite coal for carbon products.

II.3. Processing of Anthracite Coal for Carbon Products

Currently anthracite coal is electrically calcined to a temperature in the range of 1600-1800 °C for both the carbon electrodes and cathode blocks. Processing to higher temperatures should increase crystallinity and lead to a filler material with higher electrical and thermal conductivities and less ash components.

There have been a number of previous studies on the effects of heat-treatment temperature on the properties of anthracite coal. Atria et al.[3] used X-ray diffraction (XRD) to measure the crystallinity of Pennsylvania anthracite coals heated at 2600°, 2700°, and 2900 °C. They found that significant increases in graphite order began to develop only at 2900 °C. Schobert and Papano,[4] in a program supported by the CPCPC, carried out a detailed XRD analysis of anthracite coal heat treated at temperatures of 2000-2600 °C. They concluded that ash components in the coal lead to carbide formation that act to increase graphite crystallinity at 2600 °C. As part of the same program, anthracite coal from Punxsutawney, Pennsylvania, was used as a filler material to produce specialty graphite[5].

Oberlin and Terriere[6] used High Resolution Electron Microscopy to study the structural changes that occur during the heat treatment of a variety of low ash (<2%) anthracite coals at 1700°-2500 °C. They concluded that the true transformation to graphitic carbon commences above 2500 °C for low ash anthracites. High ash anthracites exhibited catalytic graphitization by a carbide decomposition mechanism at 2500 °C.

Gonzales, et al.,[7] characterized Spanish anthracite coals heated at 2000°-2700 °C using XRD and Raman Spectroscopy. They reported that the graphite development occurs in stages with a rapid increase in crystalline order above 2000 °C to about 2400° or 2600 °C depending on the coal. They also concluded that ash constituents in the coal aid in catalytic graphitization. The effect of temperature on the ash content was also investigated[8]. A detailed analysis on the ash constitution of Pennsylvania anthracite coal heated at 2000°-2600°C was presented by Laumb, et al.[9]

II.4. Program Goal

The primary goal of the program was to determine how high-temperature heat treatment of domestic anthracite coal could be used to provide a filler that would give improved properties in carbon electrodes and cathode blocks. Electrically calcined anthracite coal was to be heat treated at several temperatures from 2300-3000 °C. The heat-treated coals would then be used to fabricate pilot-scale artifacts by simulating commercial manufacturing processing. Artifact properties would be compared to those for commercial materials to assess the benefits of the high-temperature treated anthracites. Optical microscopy and XRD analyses were also to be used to provide a fundamental understanding of the physical and chemical changes that accompany the high-temperature processing of anthracite coal.

III. EXECUTIVE SUMMARY

Anthracite coal is an important industrial raw material for various metal smelting applications. For example, electrically calcined anthracite (ECA) coal has been used extensively by producers of cathode blocks for aluminum cells. The percentage of anthracite coal used can vary from 0 to 100%. In another example, ECA coal is used to make carbon electrodes for silicon smelters to convert quartz to silicon metal (98 to 99+% pure).

As smelters increase their power inputs for increasing their productivity, there is a trend to use graphite particles to replace the ECA for those applications mentioned above. In order to reverse this trend and to utilize more anthracite coals, a pilot-plant study was carried out to investigate the use of high-temperature processed anthracite coals as a filler material for producing cathodes used in aluminum smelters and carbon electrodes for producing silicon.

Electrically calcined Pennsylvania anthracite was heat-treated to temperatures of 2300 °C, 2700 °C, and 3000 °C and the products were used to fabricate 150 mm diameter artifacts. The artifacts were characterized by x-ray diffraction and microscopy techniques and by physical properties measurement after baking to 1100 °C for cathodes and 900 °C for carbon electrodes. The sodium reactivity was monitored using the Rapoport test for the cathode artifacts. The results show that high-temperature processing of the coal filler leads to cathode artifacts with increased resistance to sodium attack. The physical properties of both cathodes and electrodes show higher electrical and thermal conductivities and lower with-grain coefficient of thermal expansion (CTE). As a result of these property enhancements, the calculated thermal shock resistance increases as the heat treatment temperature for ECA increases. This key performance indicator is especially important as the smelters increase the severity of their operations. The role of catalytic graphitization from ash constituents and structural changes from thermal processing and their contributions to the resultant physical properties are also discussed in detail. The optimal heat treatment temperature from this study seems to be in the range of 2300° to 2700 °C.

An economic assessment of the cost for heat treatment of anthracite coal is essential for the scale up in this work. Commercialization of the project depends on the economic assessment and the benefits from the field performance.

IV. EXPERIMENTAL

IV.1 Coal Preparation & Heat Treatment

IV.1.a. Starting Materials

Raw materials for this program were procured from GrafTech's Columbia, Tennessee plant. Three tons of #1 sized anthracite (60% < 3 mesh, 40% < 4 mesh), 2 tons of #3 sized anthracite (90% <6 mesh on 10 mesh), 1 ton of recycle graphite, and ½ ton of recycle baked carbon were received. The coal came from Jeddo Coal Company, Pennsylvania. The "as received" coal had been electrically calcined to a nominal temperature of 1800 °C. A one-gallon sample of raw uncalcined coal was also obtained for bench scale testing.

IV.1.b. Heat Treatment

The three heat treatment campaigns were carried out in pilot-plant induction furnaces. Each furnace run contained a total of 650 pounds of coal, about 400 pounds of #1 coal and about 250 pounds of #3 coal in separate graphite capsules. The furnaces were heated at 100 °C/hr to the final temperature and held for 1 hour. Heat treatment temperatures were monitored by optical pyrometery and verified by x-ray diffraction measurements on reference samples of carbon with a calibrated response to heat treatment. The weight loss for each heat treatment was determined by the difference between the starting and ending weights. Samples of particles from each heat treatment run, the as-received 1800 °C calcined ECA, and the raw anthracite were submitted for the following tests: ash, elemental analysis, sulfur, helium density, and XRD lattice parameters. All but the raw anthracite were also tested for sodium vapor uptake.

IV.1.c. Flour Sizing

The cathode mix design used a mixture of coarse particles up to about 1" in size and milled flour with a substantial fraction less than 200 mesh. Flours were prepared using a Micron Powder Systems Model 10 Air Classifying Mill. Particle size was measured using a Honeywell Microtrac Model X100. The silicon smelter mix design used some of the same coarse coal particles, a somewhat smaller particle size fraction, and a mixture of recycled electrode and coal flours sized the same as for the cathode mix. The cathode mix filler was 100% coal-derived. The electrode mix filler was 75% coal-derived with the remainder being recycled material.

IV.2. Billet Production

IV.2.a. Mixing and Forming

Four batches of each mix formulation were prepared, one with as received 1800 °C ECA and one with anthracite at each of the three heat treatment levels. Each experiment consisted of one 250-pound mix batch extruded and cut to make five 6" diameter by 13" long green billets. Coal tar pitch binder level was always adjusted to hold extrusion pressure in an acceptable range with the extrusion rate held constant. There was a strong trend of increasing binder level with increasing filler heat treatment temperature for both mix formulations. Microscopic examination of the particles revealed increased internal porosity, many in the form of cracks with increasing heat treatment temperature. The following graph (Figure 1) shows the increase of binder level with increasing HTT. Note that the change was more pronounced above 2300 °C.

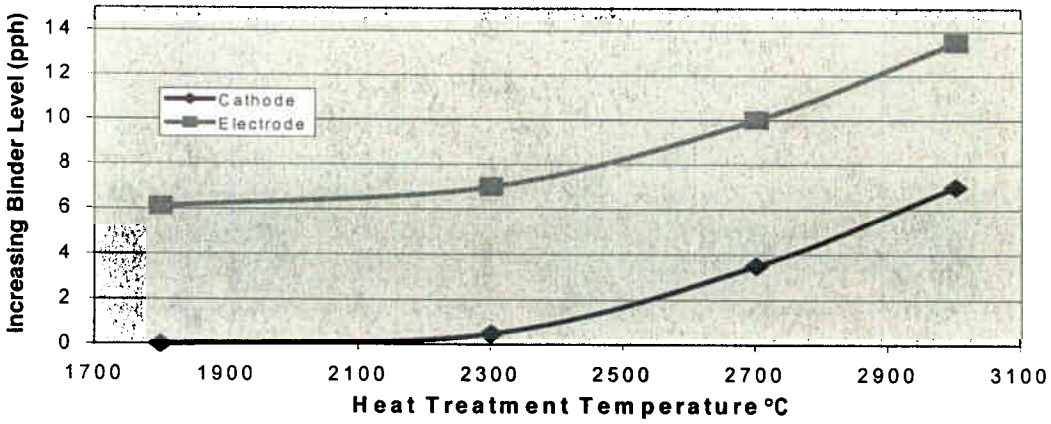

Figure 1. Binder Level Versus Coal Filler Heat Treatment Temperature.

IV.2.b. **Baking**

A total of 50 green billets were produced. Two billets from each extrusion were retained as green to insure against possible furnacing problems, and the other 3 billets were baked. The electrode mix formulation billets were packed in sand and baked to 900 °C. The aluminum cell cathode billets were baked with the electrode samples and then further heated to 1100 °C in an induction furnace.

IV.2.c. **Sample Testing Configuration**

After baking there were 3 billets of each variety available for testing. For both the electrode and cathode formulations, one of the billets was cut for physical property determinations. For electrodes the other two billets were tested for fracture toughness. For cathodes the other two billets were evaluated in the Rapoport test. The physical property cutting-diagram is shown below in Figure 2.

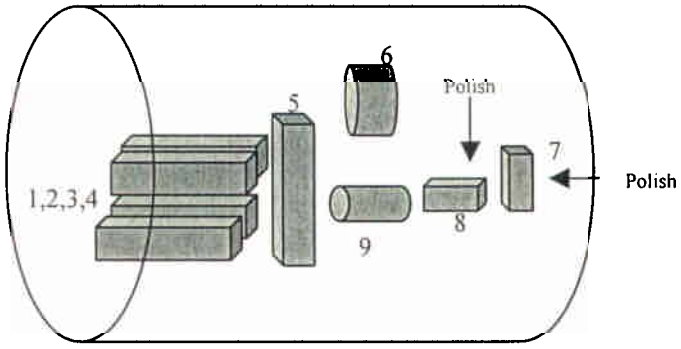

Figure 2. Baked Billet Cutting Diagram.

1, 2, 3,4	(1"x 1" x 5") *with grain,* flex strength, density, specific resistance, Young's Modulus, sample #1 for CTE.
5	(1" x 1" x 5") *against grain,* flex strength, density, specific resistance, Young's Modulus, CTE.
	6 (2"diameter x 2" long) *with grain,* for Anter Thermal Conductivity
7	(7/8" wide x 1 5/8" long) *against grain,* for Microscopy
8	(7/8" wide x 1 5/8" long) *with grain*, for Microscopy
9	(1" diameter x 2" long) sample for ash

IV.3. Fracture Toughness

The fracture toughness was measured on slotted bars machined from the test billets. This particular method is proprietary to GrafTech International but is consistent with other analogous methods. Two bars were obtained from each billet giving an average of four values for each heat treatment temperature.

IV.4. Rapoport Test for Measuring Sodium Expansion

The Rapoport test was published by Rapoport and Samoilenko in 1957[10]. It is a laboratory method for measuring expansion of carbon materials due to sodium incorporation. Several modifications of the Rapoport-Samoilenko test apparatus have been proposed[11-13]. Oye and Sorlie have published a good review on the sodium expansion of different carbon materials as a function of graphite content, current density, temperature, external pressure, cryolite ratio, etc., by analyzing the data collected from this test method.[2]

The Rapoport test apparatus set-up is shown in Figure 3. The apparatus is located at the Technical Center in France of Carbone Savoie, a subsidiary of GrafTech International. The operating conditions used for our tests, such as temperature, cryolite ratio, pressure, etc, were kept constant. The only difference is the cathode materials, which consist of cathodes made with ECA (1800 °C) and with ECA heat treated at 2300°, 2700°, and 3000 °C. A graphite crucible acts as the anode. The apparatus detects the length change during a two-hour test period.

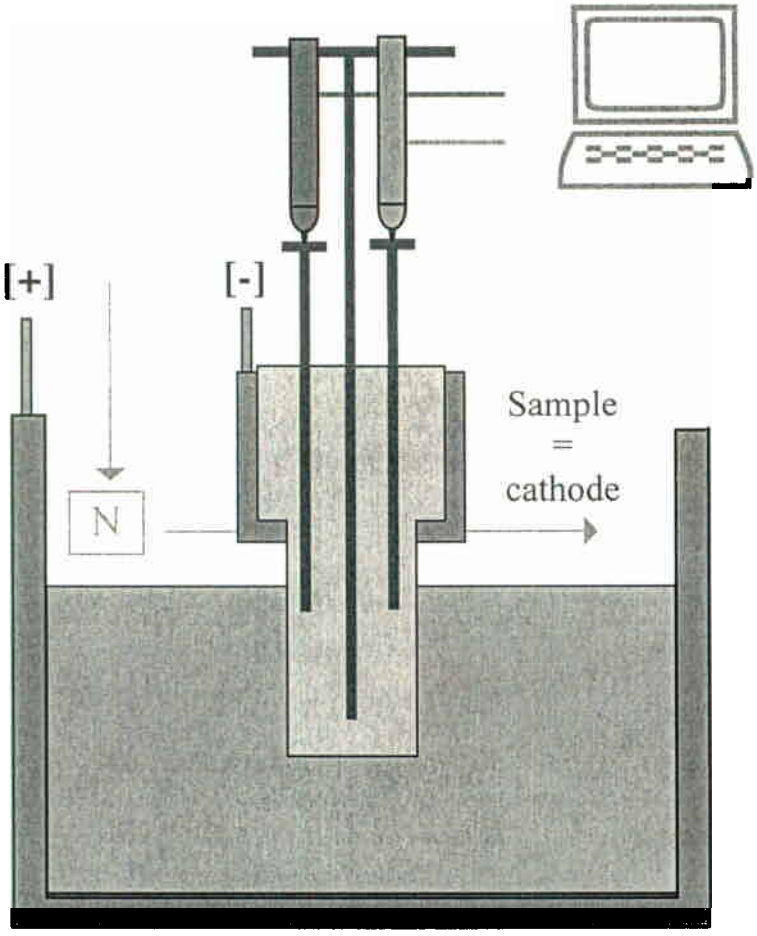

Graphite Crucible = Anode

Figure 3. Rapoport Test Apparatus.

IV.5. Characterization Tests

IV.5.a. Ash

The % ash was measured using procedure ASTM-C561.

IV.5.b. ICP-AES

Inductively Coupled Plasma – Atomic Emission Spectroscopy was used to measure the elemental composition of the ash samples. Eighteen elements are routinely analyzed on a Spectro Spectraflame Inductively Coupled Plasma Atomic Emission Spectrograph.

IV.5.c. Lattice Parameters-X-Ray Diffraction

These measurements were made on a Scintag Diffractometer X2 with a theta-theta goniometer, graphite monochrometer, and a scintillation detector. Samples were powdered to a sizing of -200 + 400 mesh, mixed with 3% NIST 640c Silicon as an internal peak position standard. The samples were loaded using a front packing method. A spinning sample holder was used. Measurement conditions were as follows:

Accelerating Voltage	45kV
Beam Current	40mA
Slit size	.015 mm
Step size	.020 Deg
Count time	0.02 Sec
Range	24 to 110 Deg 2 Theta

The software used included Scintag DMSNT v 1.37 for data Acquisition and K-Alpha 2 Stripping, Peak-Fit V-4.11, and Table-Curve v- 5.01 for peak finding, background subtraction, goodness of fit and line fitting.

Purified natural graphite standard SP-1 was used to determine instrumental and inherent line broadening. A shape factor of .95 was used in the Scherrer equation.

IV.5.d. Helium Density

The helium densities were measured with a Micrometrics Instrument Corporation Model AccuPyc 1330 Helium Pycnometer using procedure ASTM D2638.

IV.5.e. Optical Microscopy and SEM/EDS

Specimens for metallographic observations by optical microscopy and SEM/EDS were prepared using standard epoxy impregnation, encapsulation, and polishing procedures. Optical microscopy observations and photomicrographs were obtained with a Reichert MEF4 microscope. SEM micrographs were obtained using a JEOL JSM 5900LV unit equipped with an Oxford Model 7274 EDS unit for qualitative elemental analysis.

IV.5.f. Sodium Vapor Uptake

The sodium vapor test can be applied both to the filler materials in powder form or to the final carbon/graphite artifacts, for determining the sodium uptake at 700 °C. The test apparatus is depicted in Figure 4. The powder size is between 74 to 203 microns, and the operation is carried out under argon at atmospheric pressure. The sodium content is determined by titration.

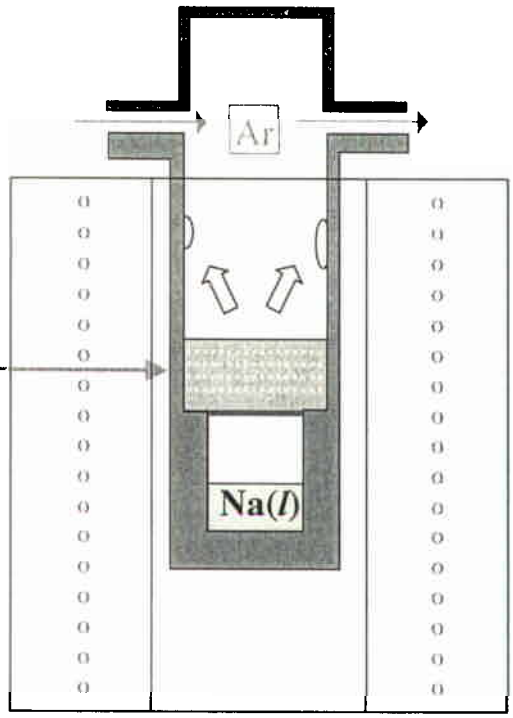

Operating conditions :

⇨Powder sample : 74μ-203μ

⇨Temperature : 700 °C

⇨Argon atmospheric pressure

Sample analysis :

⇨Sodium content by titration

At 700 °C, the sodium is vaporized, by diffusion it goes up towards the upper part of the cell to settle on the cooler surfaces.

Figure 4: Sodium Vapor Testing Apparatus.

V. RESULTS AND DISCUSSION

V.1. Coal Particle Test Results Before and After Heat Treatments

Table II summarizes the characterization test results for the raw and heat treated anthracite coals. The data for the heat-treated anthracite samples show a trend of reduced ash from 7.75% in the 1800 °C standard material to 0.43% after 3000 °C. The anthracite contained 6.31% ash. The ash content increase after calcination is due to the loss of volatiles during the 1800° C heat treatment. The helium density increased while the sodium vapor uptake decreased with higher heat treatment temperature.

Table II
Summary of Testing Results on Raw Coal, ECA and Heat Treated ECA Particles

Measurement	Raw Coal	As Received 1800 °C ECA	2300 °C	2700 °C	3000 °C
% Weight Loss in HT			4.9	8.3	9.2
Ash (%)	6.31	7.75	6.1	5.22	0.43
Sulfur (%)	0.629	0.46	0.162	0.02	0.02
Si (ppm)	13000	17000	12000	12000	290
Fe (ppm)	4200	1900	4200	2600	730
Al (ppm)	11000	15000	13000	9900	17
Ti (ppm)	640	1000	870	1700	36
Mg (ppm)	500	380	96	<.52	<.34
Na (ppm)	250	600	140	59	<.68
K (ppm)	760	1900	1300	32	<1.1
Ca (ppm)	1300	720	1500	580	170
He Density (g/cc)	1.582	1.845	1.958	2.107	2.183
Sodium Uptake (x of NaC_x)		30	37.5	43.5	85.5

V.2. X-ray Diffraction (XRD) Results

Table III shows the lattice parameter measurements by XRD for the raw and heat treated coal. As expected, the crystalline structure measured by all three parameters improves with higher heat treat temperature.

Table III
Summary of XRD Lattice Parameters Results

Heat Treatment Temp.	'd' spacing (002 ,nm)	Lc (002, nm)	La (110, nm)
Raw Anthracite	.3477	2.1	2.5
As Received ECA (1800°C)	.3373	17.2	21.4
2300°C	.3361	37.6	19.1
2700°C	.3362	48.6	35.1
3000°C	.3363	42.6	80.9
1800°C ECA +5% SP1	.3357	67.4	21.0

Examination of the XRD spectra (Figure 5) show silicon carbide peaks in the lower temperature samples that are missing from the 3000 °C sample. The microscopic examination of the samples described indicates catalytic graphitization at the outside surface and in pores of the particles. This indicates that a great deal of caution needs to be applied to the interpretation of the XRD data. The apparent crystallinity of the high temperature material may not be due solely to the bulk graphitization of the particles, but may be indicative of a mixture of some very good catalytic graphite with some very poorly graphitizing material. To check this possibility a blend of 1800°C anthracite and 5% SP1 graphite was measured. This experiment showed that even low levels of very crystalline material could dramatically skew the lattice parameters as shown by results in the last row of Table III. An overlay of the XRD spectra for raw coal and a blend of raw coal and 5% SP1 is shown in Figure 6. The changes in the resolution of the various reflection peaks and the sharpness and intensity of the 002 diffraction peak lead to the conclusion that both catalytic graphitization and improved general structure ordering are occurring with the higher heat treatment.

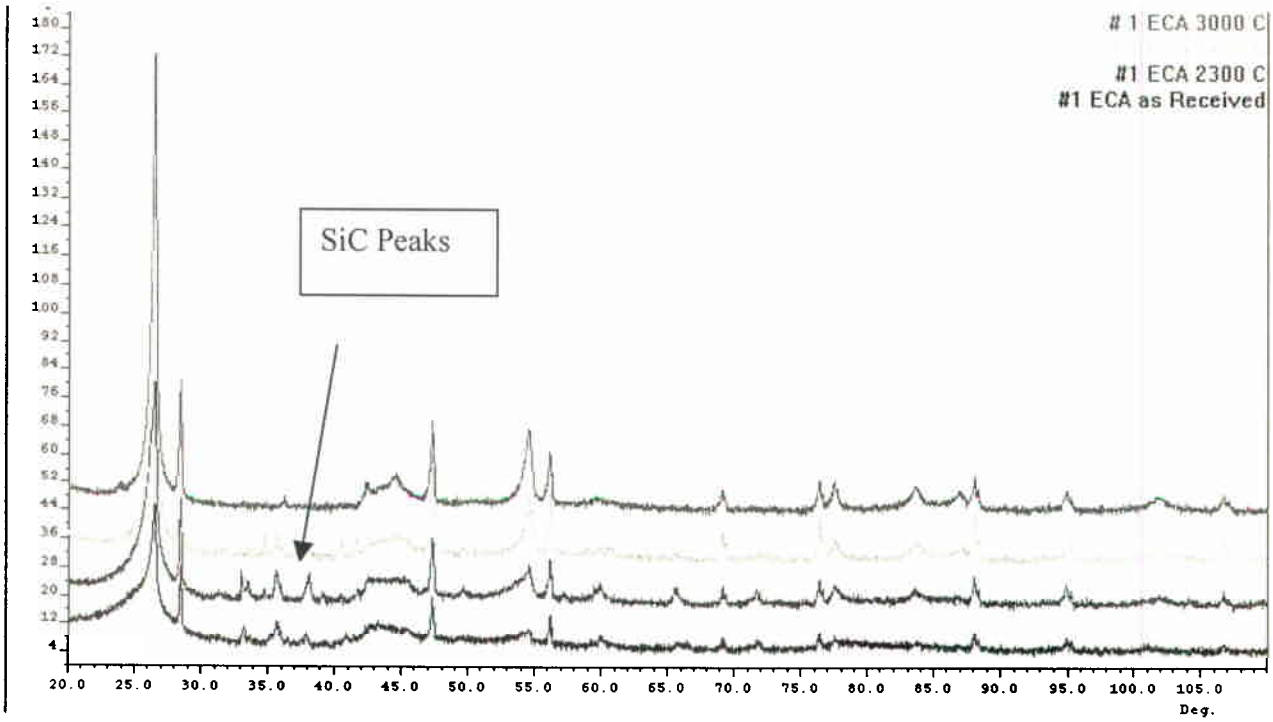

Figure 5. XRD Spectra of Coal Samples.

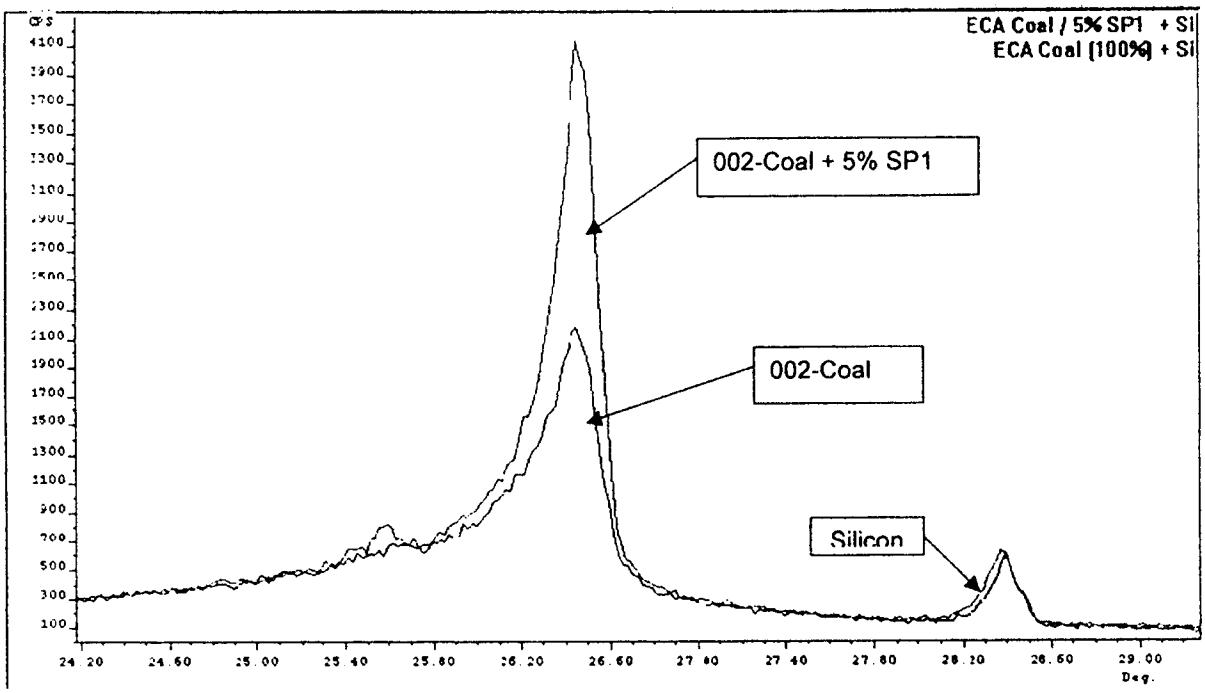

Figure 6. Overlay of XRD Spectra for Raw Coal and Raw Coal +5% SP1 Graphite.

V.3. Characterization of Raw Anthracite Coal, Electrically Calcined Coal (ECA) and Heat Treated ECA Products

Optical microscopy examinations were carried out initially to assess the structural characteristics of the electrically calcined Pennsylvania anthracite coal and each of the products from the heat treatments at nominal temperatures of 2300 °C, 2700 °C, and 3000 °C. SEM/EDS analyses were also carried out to characterize the ash phases in each of these materials. Subsequently, limited optical microscopy and SEM/EDS analyses were made on the raw anthracite precursor coal to obtain a better understanding of the structural evolution of the coal during the entire heat treatment range. Four or five large particles (>12 mm) of each material were examined to obtain reasonable statistics on these rather heterogeneous materials. The structural characterization results for each material are summarized below starting with the raw coal precursor.

V.3.a. **Raw Anthracite Coal**

Three broad structural categories were identified: (1) a relatively dense striated phase with elongated pores in a parallel array; this phase showed weak birefringence in polarized light indicating a modest degree of layer plane alignment (see Figure 7), (2) a dense, nearly glassy carbon-like phase with very weak birefringence in polarized light (see Figure 8), and (3) a very porous, almost "punky" phase with only local areas showing any orientation. Many of the pores in the punky regions were filled or partially filled with various types of inorganic materials.

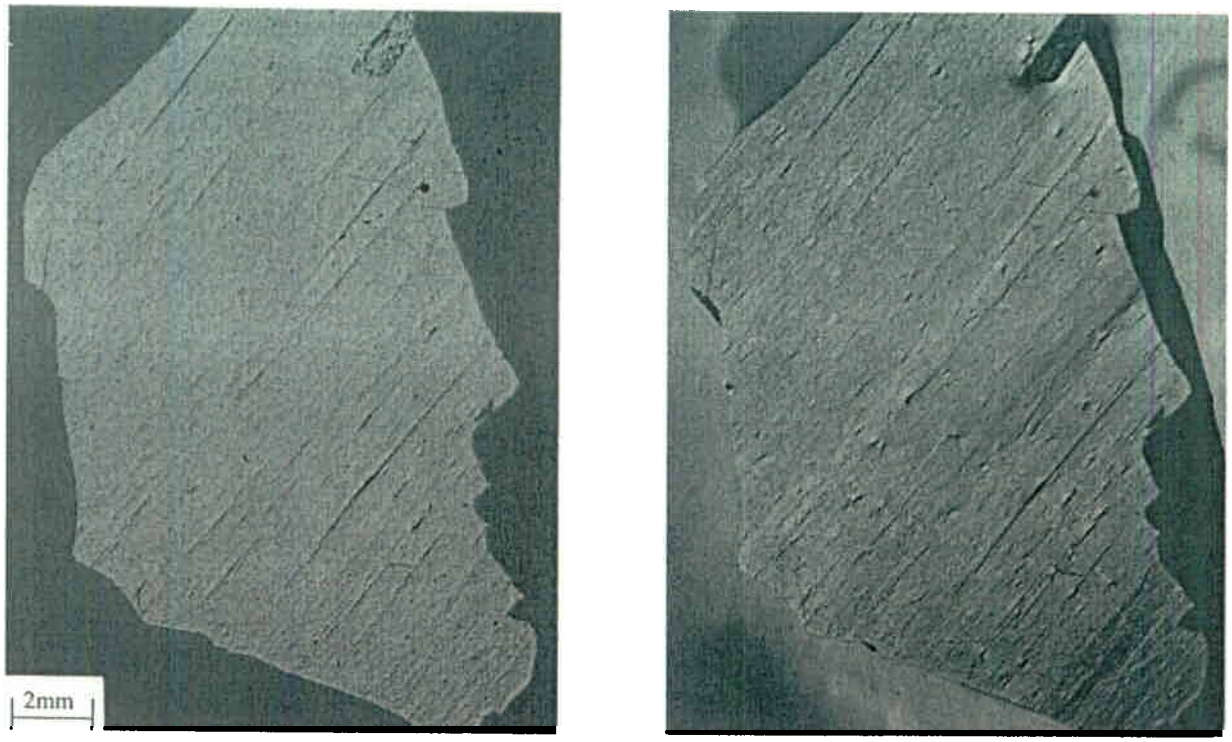

(a) Bright Field (b) Polarized Light

Figured 7. Raw Coal Particle with Striated Structure.
(Weak Birefringence is Visible in Polarized Light Photomicrograph.)

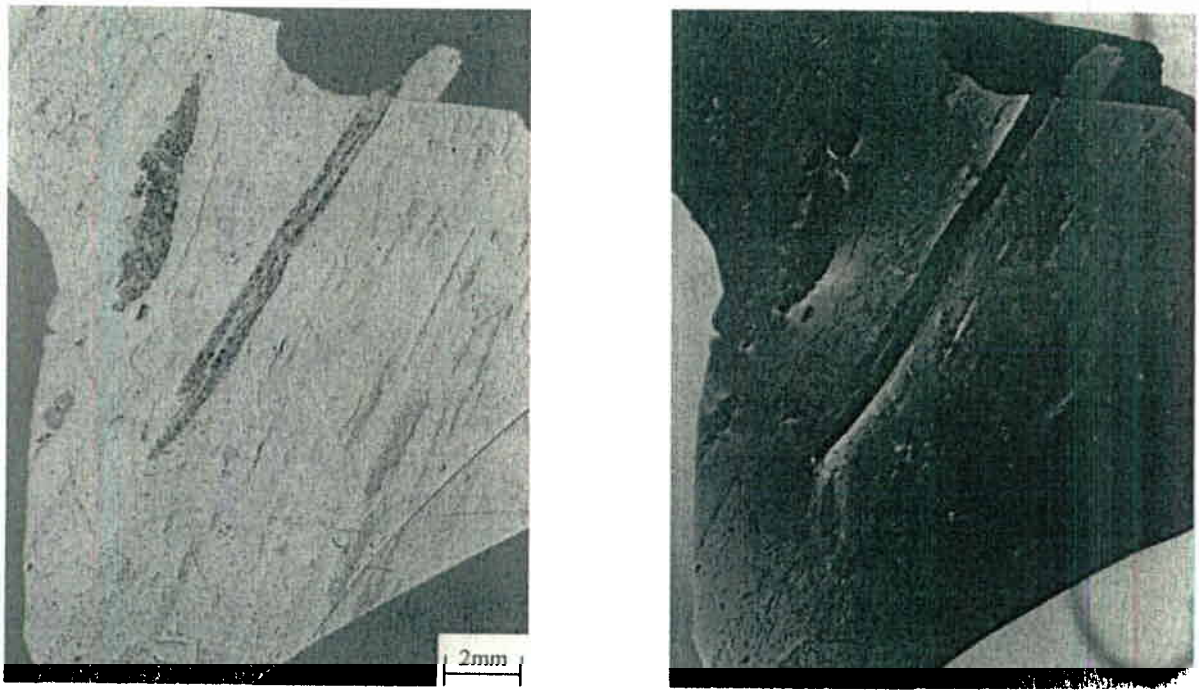

(a) Bright Field (b) Polarized Light

Figure 8. Raw Coal Particle with Predominantly Dense, Glassy Carbon Structure.
(Two Elongated Regions with Porous or Punky Structure are Visible in Bright Field Photomicrograph. Black Appearance of the Majority of the Particle in Polarized Light Shows the Glassy Carbon Character, i.e. Almost No Birefringence).

Most of the ash constituents were present as discrete phases in these porous areas as a shiny or bright phase in bright field illumination or as an apparent two-phase, inorganic glassy material. SEM/EDS analyses showed that most of the shiny phase particles were high in S and Fe with a peak height ratio closely matching that for a FeS_2 standard, confirming that pyrite areas or layers are present in this raw anthracite coal (see Figure 9). Of course, this is not surprising and is consistent with the ash constituent analyses reported by Laumb, et al[9].

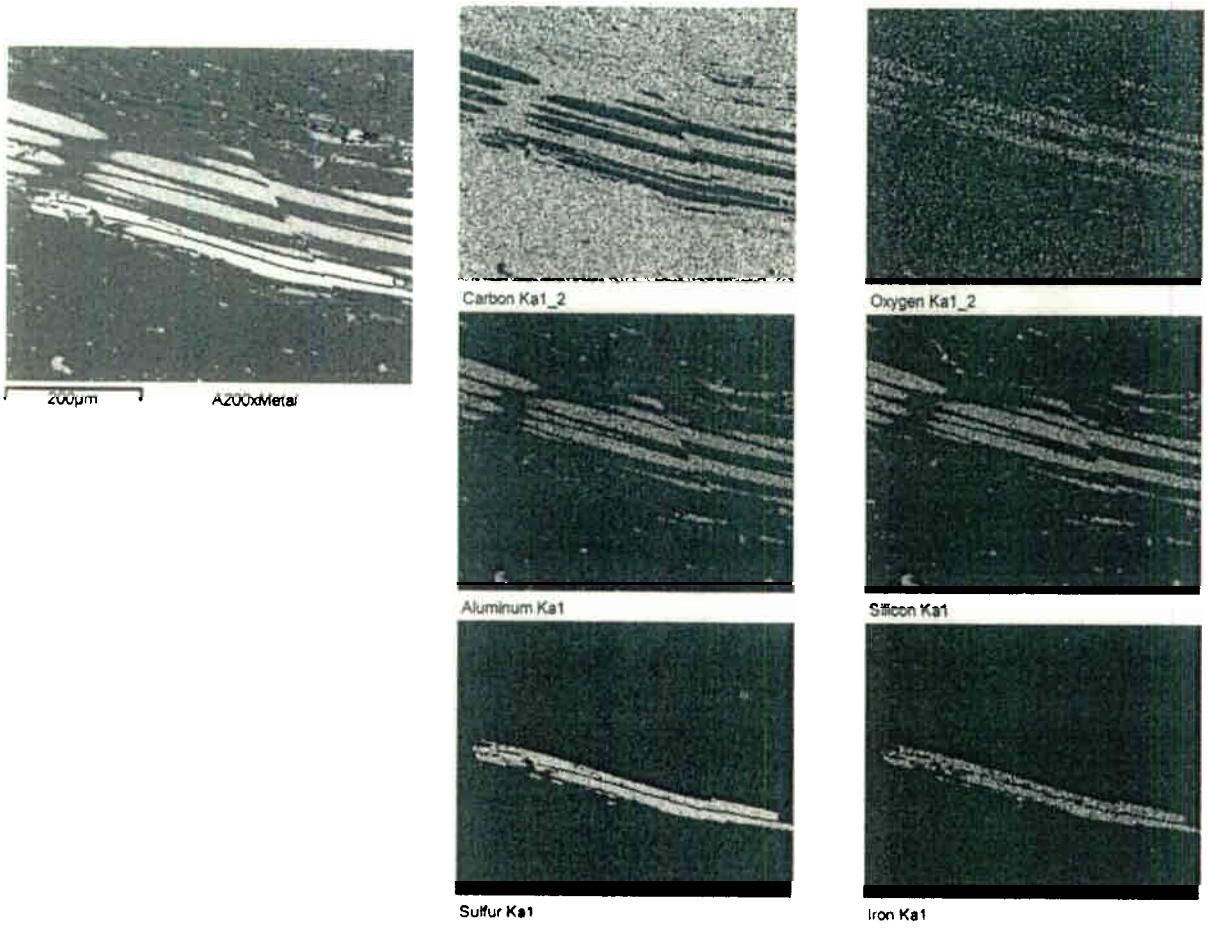

Figure 9. SEM and EDS Dot Map Images of Porous Area in Raw Anthracite Particle.
(Upper stripes appeared glassy and were rich in silicon, aluminum, and oxygen. Lower stripes were shiny "metallic" regions rich in iron and sulfur.)

Most of the apparent two-phase glassy areas actually had very uniform concentrations of Si, Al and O, so it appears that the two-phase character is probably due to devitrification of the aluminosilicates during cool down from the relatively high temperatures present during coalification. In contrast, a few apparent two-phase glassy areas actually did contain a distinct phase high in Si and O (SiO_2?) immersed in the high Al, Si, and O bulk glassy phase. Some of the glassy phase areas also contained high Ba, Ca, K or Na, as well as high Al, Si and O levels.

Small particles containing high Fe and O, high Ca and O and high Mg and O were also detected; these metal oxide phases were much smaller than the pyrite and glassy phases described above.

The bulk carbonaceous anthracite phase contained only C with a low S level by EDS. Almost all of the inorganic material was present in the ash particles described above.

V.3.b. Electrically Calcined Anthracite Coal

The three basic structural types identified in the raw precursor coal (striated, dense and nearly glassy, and punky or porous) were also found in the ECA particles. The amount of each phase in a given particle varied widely from particle to particle, as it did in the raw coal. The only noteworthy difference was that the birefringence of the striated phase was greater in the ECA than it was in the raw coal (see Figure 10 versus Figure 7). This is probably a reflection of the improved crystallinity and orientation produced by the calcination.

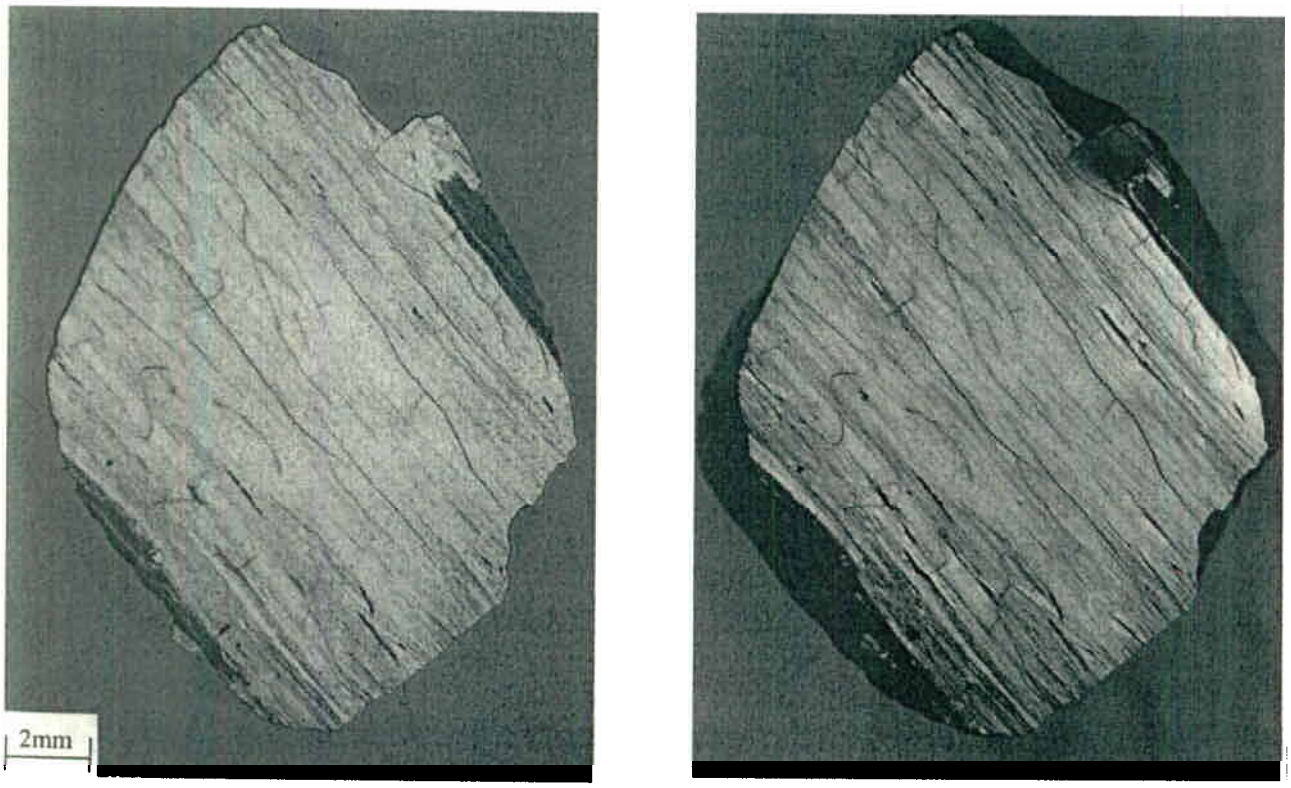

(a) Bright Field (b) Polarized Light

Figure 10. ECA Coal Particle with Striated Structure.
(Polarized Light Photograph Shows that ECA Striated Particle has more Birefringence than Raw Coal Striated Particle Shown in Figure 7(b).)

Many of the pores in the punky phase were still partially filled with an inorganic glassy material (see Figure 11). Some very small inorganic phase areas were also detected in the small pores in the other two dense phases as well (see Figure 12). Some small metallic particles, usually in clusters, were scattered throughout all

three phases. There was some indication that the walls of some medium-sized pores had developed some orientation parallel to the wall surface during the calcination process.

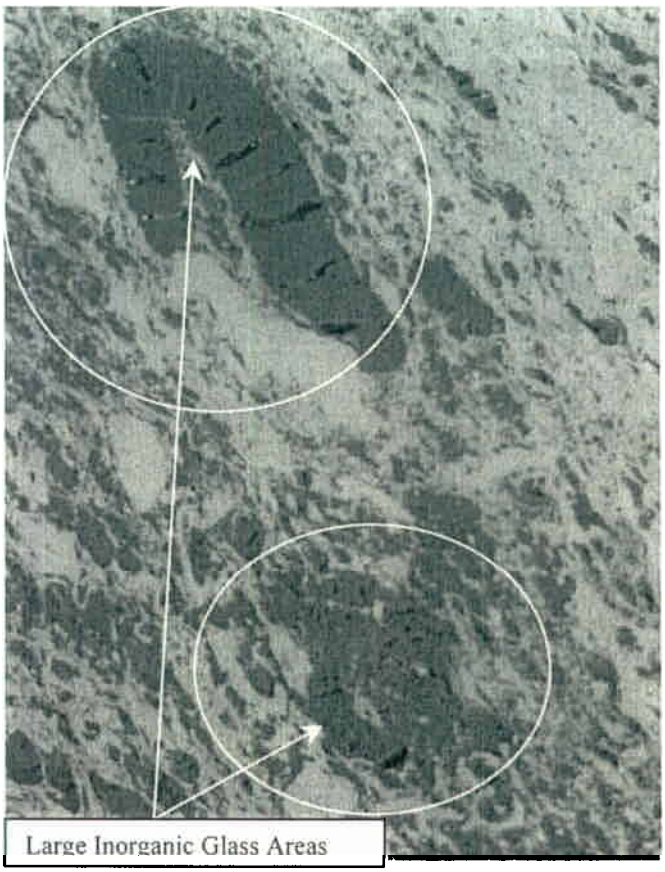

400X, Bright Field

Figure 11. ECA Particle with Large Inorganic Glass Areas

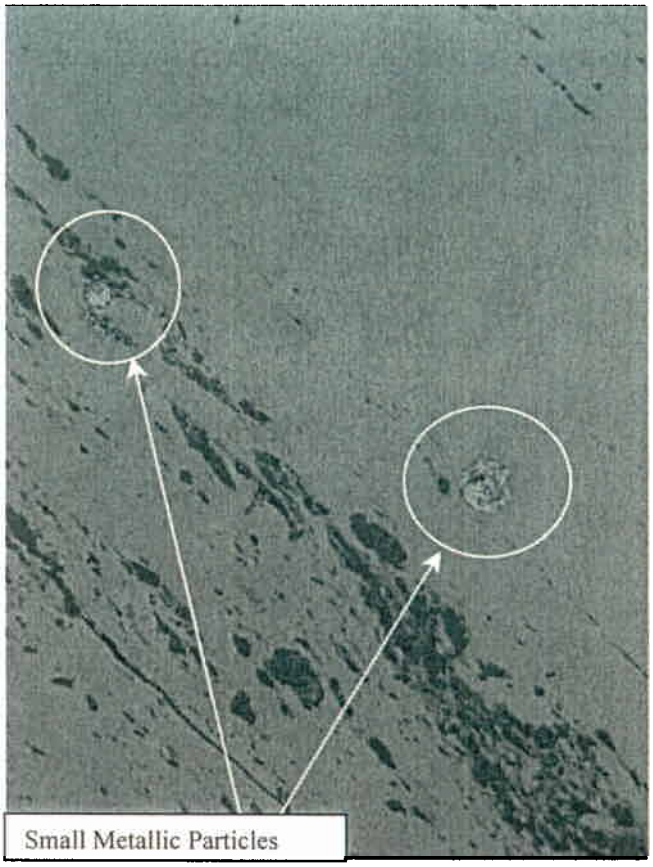

400X, Bright Field

Figure 12. ECA Particle with Small Metallic Particles.

The "metallic"-like particles, which appeared as a bright and highly reflective phase under bright field illumination in optical microscopy, were found to be rich in Fe and P or rich in Fe and S (see Figures 13 and 14). They also appear to contain some C, but do not contain much O. Apparently, the electric calcining process at a nominal 1800 °C converts (or carbon reduces) the iron pyrite, FeS_2, present in the raw anthracite into the more stable iron phosphide and iron sulfide, FeS_{1-x}, which are probably non-stoichiometric. As expected, the inorganic "glassy" phase present in some areas of the ECA particles was found to be rich in Si, Al, and O, but did not contain much C. The glassy phase composition is also visible in EDS dot maps in Figures 13 and 14. Presumably, the various silicon- and aluminum-containing ash components in the raw anthracite are fused into this glass-like phase during the 1800 °C calcination process.

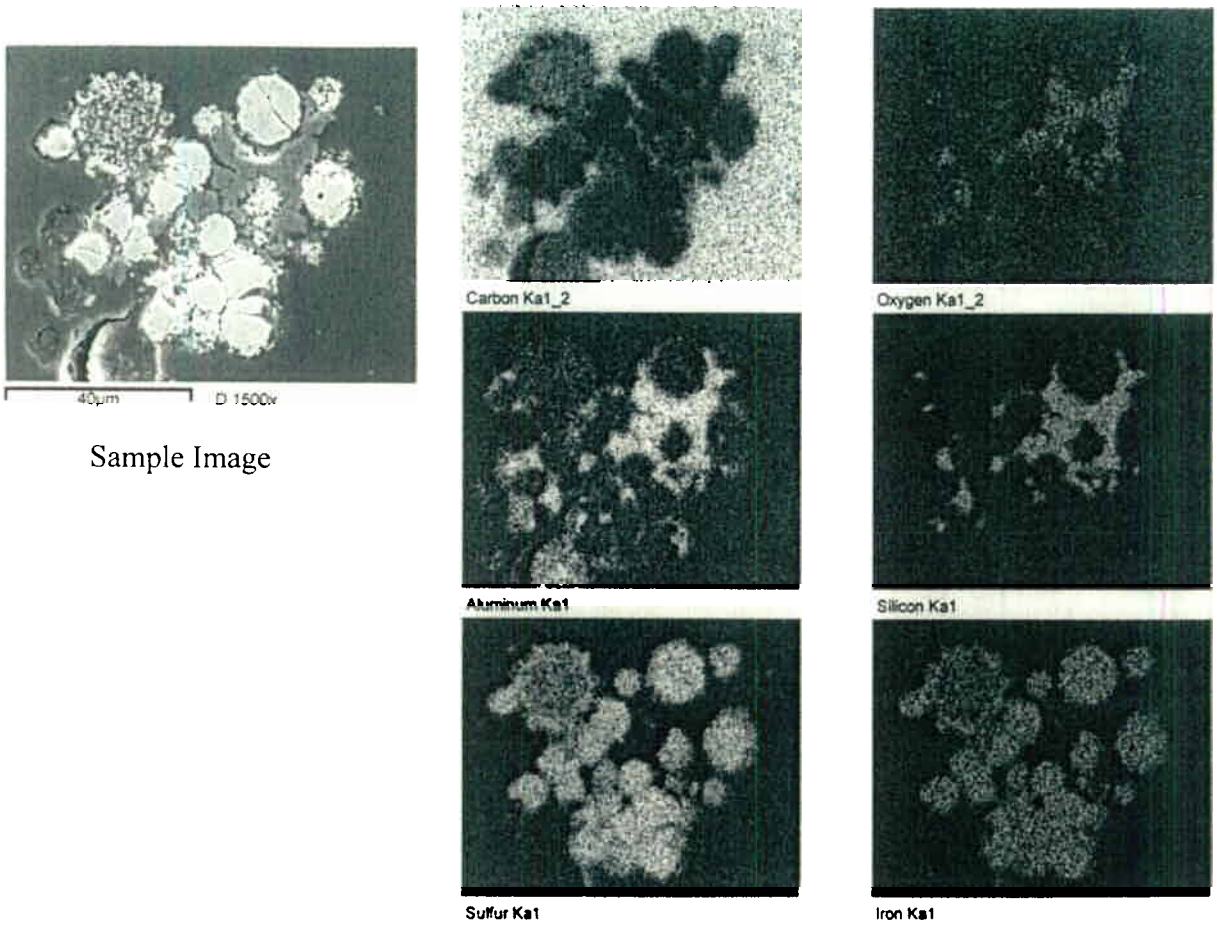

Sample Image

GRAFTech

Figure 13. "Metallic" particles with High Fe and S and Glassy Phase area with High Si, Al and O in ECA Particle.

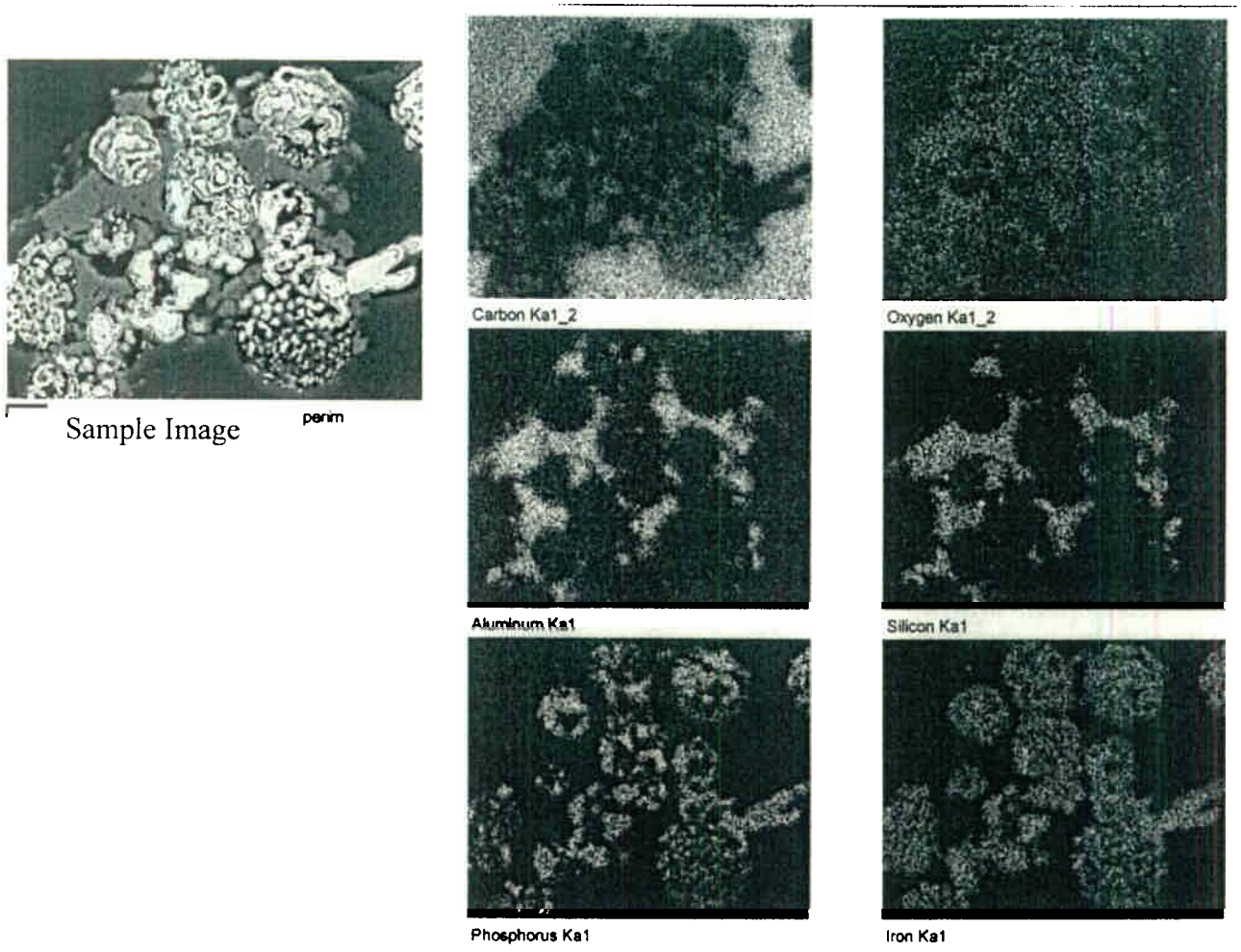

Figure 14. "Metallic" Particles with High Fe and P, and Glassy Phase with High Si, Al and O in ECA Particle.

V.3.c. Nominal 2300 °C Heat Treated ECA

The bulk continuous phase found in particles of this material was similar to that found in the dense phases in the ECA starting material. Small, local regions within these dense areas appeared to have developed a very small domain size texture that was not present in the original ECA. It is suspected that the inorganic glass phase in the very small pores in two dense ECA phases initiated a process akin to catalytic graphitization during the 2300 °C heat treatment. There was some evidence for an increase in the amount of alignment around pore walls, but this was not significant compared to the amount of the new fine texture areas. There was also some indication that the total amount of inorganic material (glassy and metallic) was lower in the 2300 °C particles and some of the largest pores were not as completely filled with this phase.

Some of the large coal particles appeared to have a deposit of very small acicular particles with a crystalline appearance on their external surfaces. SEM/EDS analyses showed that the crystals, deposited on the exterior surface and also present in some of the large cracks, actually were actually two different phases, one rich in Si and C and one rich in Al and C. Some of the particles did contain both Al and Si, but most were rich in one or the other (see Figure 15). The oxygen content appeared low in all cases. The presence of both Al rich and Si rich "carbide" phases at this high temperature is a surprise which has no obvious explanation, except for formation of the Al rich phase by some process during cool-down.

A thin layer with a "corroded" appearance was found on the surface of some of the heat treated coal particles in this sample, probably due to some catalytic graphitization produced by the ash vapors depositing on the surface during the heat treatment. "Metallic"-like particles within the catalytic graphite polyhedral balls in the corroded layer on the particle surface had variable composition, usually containing Fe, Si, Al, Ti and some C. Some evidence for two different phases within these metallic particles was also noted.

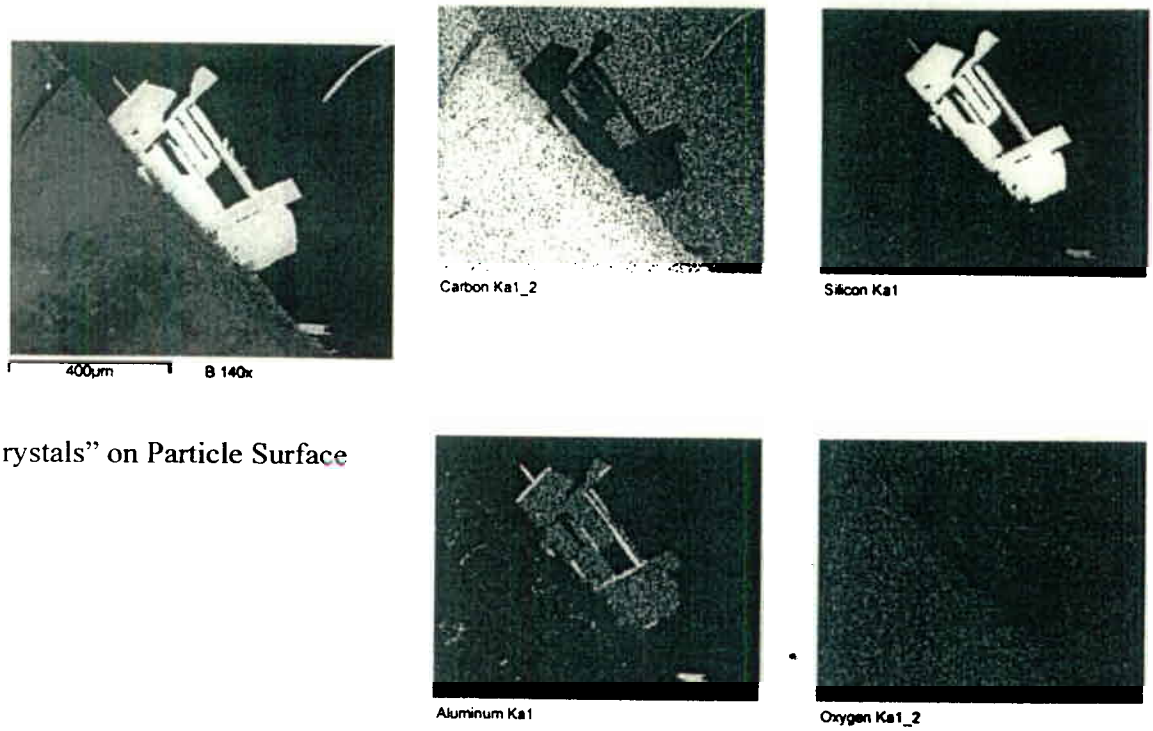

"Crystals" on Particle Surface

GRAFTech

Figure 15. Large Crystals with High Si and Low Al on Surface of 2300 °C HT Particle.
(Some surfaces of the bulk crystal have high Al and low Si.)

V.3.d. Nominal 2700 °C Heat Treated ECA

The initial examination of the nominal 2700 °C sample was carried out on two particles. Both had a distinct layer on their external surfaces which appeared to be a catalytic graphite material containing numerous hollow polyhedral "balls"(see Figure 16). Apparently, vapor phase species derived from the ash had deposited on these external surfaces and produced a more extensive catalytic graphitization than that on the surface of the 2300 °C particles. The internal areas, which were small and very fine textured in the 2300 °C sample, appeared considerably larger in the 2700 °C sample and had a larger domain size. There was some bulk continuous phase which had not been changed dramatically from that in the ECA starting material in one particle which had a relatively high density. The other particle was much more porous and had been converted almost completely into catalytic graphite; in fact it was so graphitic and soft that it could not be polished very well. The overall content of inorganic glass material and metallic particles was clearly reduced in the internal areas of these two particles compared to that in the ECA and the 2300 °C samples, but there was more of the SiC-like crystals deposited on the external surfaces of both particles.

200X Bright Field

Figure 16. 2700 °C Heat Treated Particle with Large Cluster of Catalytic Graphite Polyhedral Balls on Exterior Surface.

Optical microscopy analyses on several additional particles of this sample confirmed the preliminary results described above. The thicker "corroded" layer on the perimeter of each particle was clearly a catalytic

graphite material (see Figure 17). Interior fine-textured regions within the bulk of the particles also appeared to be the other type of catalytic graphite phase. SEM/EDS analyses on the "metallic" or reflective particles in the bulk regions of the particles in this sample were usually rich in Fe and Ti and contained some C. Small metallic particles in the catalytic graphite balls in the corroded surface layer were rich in Fe and Si or were rich in Si and Al; both types of particles also contained some C.

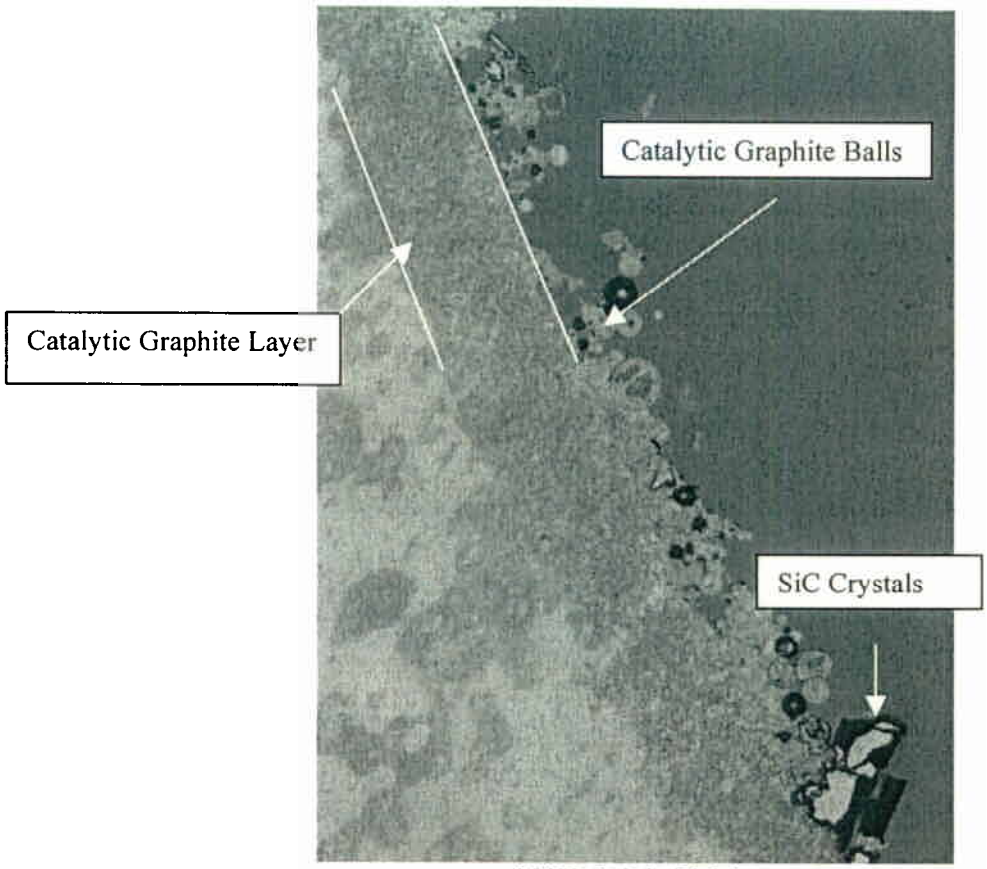

200X, Bright Field

Figure 17. 2700 °C Heat Treated Particle with Thin Surface Layer Converted to Catalytic Graphite

V.3.e Nominal 3000 °C Heat Treated ECA

Most of the particles in this sample showed a relatively thick, corroded surface layer of catalytic graphite material, but there were very few inorganic crystalline particles remaining on the exterior surface. Most of the catalytic graphite balls on the surface did not have any metallic particles remaining in their cores. Overall, the amount of metallic or inorganic phase particles detected within this sample was significantly lower than that in the other samples which is consistent with the lower measured ash level. The fine-textured, catalytic graphite areas within the bulk regions, noted in both the 2300° and 2700 °C samples, were also evident in the 3000 °C sample. However, the bulk regions, which did not appear to be affected by any of the catalytic graphitization processes, were still easily discernible and did not look much different in either bright field or polarized light from those present in the original ECA material. It appears that the this sample is

a composite of at least two types of catalytic graphite and a bulk phase which has only been altered by the inherent rearrangement and/or true crystallization processes during the graphitization heat treatment at 3000 °C.

SEM/EDS analyses of the clusters of very small metallic particles detected in the bulk of these particles showed that they had either high Ti, Fe and C contents or had high Fe, Si and C contents. Very few particles with only high Fe and C contents were noted.

V.4. Sodium Vapor Testing Of Heat Treated ECA Particles

One of the evaluation criteria used for cathode blocks in the aluminum Hall cell smelter is the susceptibility to sodium vapor attack on the cathodes. There are two testing methods used to determine sodium vapor attack: a sodium vapor pickup test and the Rapoport test. Both tests are set up in the Venissieux Technical Center of Carbone Savoie, a subsidiary of GrafTech International, based in France. Sodium vapor testing results presented in this section are for the as-received anthracite coal particles (1800 °C), and for those particles with 2300°, 2700° and 3000 °C heat treatment.

The test results are shown in Table IV and in Figure 18. The sodium pickups are expressed as x in the compound NaC_x. Thus the higher the value of x, the lower the sodium uptake.

Table IV
Summary of Sodium Vapor Testing Results

	HTT (°C)	x of NaC_x		
		Meas 1	Meas 2	Average
As-Received ECA	1800	30		30
	2300	39	36	37.5
	2700	54	33	43.5
	3000	86	85	85.5

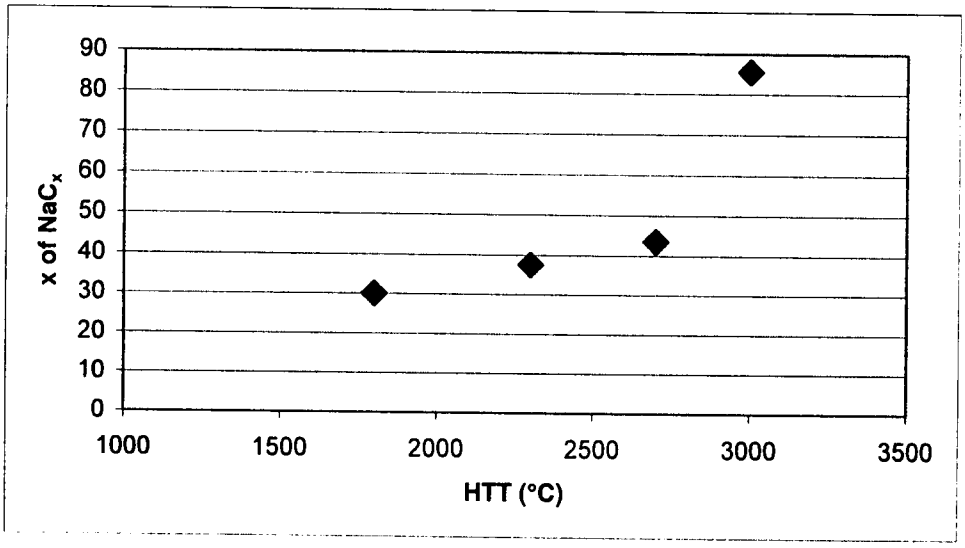

Figure 18: x of NaC_x as Function of Heat Treatment Temperature.

As the data indicate, the higher the heat treatment temperature, the lower the sodium vapor uptake by the anthracite coal particles. One could explain the results through two factors: (1) as the heat treatment temperature increases, the ash content in the coal particles decreases resulting in less interactions between ash components and sodium vapor, and (2) at higher temperatures the coal structure becomes more graphitic resulting in less incorporation of sodium.

V.5. Carbon Electrode Properties

The properties measured for the final carbon electrode artifacts are presented in Table V. Results include the following: specific resistance, modulus, and CTE measured in both extruded with grain (wg) and against grain (ag) directions, in addition to values of density, fracture toughness, thermal conductivity, and ash. Even though all the electrodes have been baked to the same final temperature of 900 °C, it is evident that the anthracite filler heat-treatment temperature has a large effect on properties. The specific electrical resistance and with-grain CTE decrease and the thermal conductivity increases with increasing filler heat treatment temperature. These effects would be expected to lead to improved performance in commercial applications. There appears to be no effect of filler heat treatment temperature on the flexural strength or fracture toughness, within the experimental limits of measurement. Although it is not considered valid to directly compare these pilot-scale artifact properties with those for commercial electrodes, the values do fall in the range of those for commercial product previously presented in Table I.

Table V
Properties of Pilot-Scale Carbon Electrode from Heat-Treated Anthracite Coal Fillers

		Carbon Electrode 1800°C Filler		Carbon Electrode 2300°C Filler		Carbon Electrode 2700°C Filler		Carbon Electrode 3000°C Filler	
Property	units	wg	ag	wg	ag	wg	ag	wg	ag
Bulk Density	g/cc	1.57		1.55		1.59		1.61	
Specific Resistance	μΩm	38.1	64.1	31.5	50.7	22.9	41	21.9	38.1
Young's Modulus	GPa	8.6	3.1	8.6	3.6	7.7	3.3	8.2	3.8
Flex Strength (4pt)	MPa	5.8	2.3	5.8	3.5	5.6	2.2	6.4	3.3
Fracture Toughness	J/m^2		448		383		446		452
CTE (30-100°C)	x10-6/°C	1.74	2.85	1.45	2.74	1.06	2.88	1.07	2.73
CTE anisotropy ratio (ag/wg)		1.64		1.89		2.72		2.55	
Volumetric CTE (30-100°C)	x10-6/°C	7.44		6.93		6.82		6.53	
Thermal Conductivity (R.T.)	W/mK	11		16		24		26	
Ash	%	4.74		4.19		2.82		1.36	

There appears to be no effect of filler heat-treatment temperature on the flexural strengths or fracture toughness, within the experimental limits of the measurements.

V.6. Cathode Properties

The properties of the pilot-scale cathode artifacts that were produced using anthracite coal fillers heat treated from 1800° to 3000 °C and then baked to a final temperature of 1,100 °C are listed in Table VI. The data include: bulk density, ash content, thermal conductivity, fracture toughness, and values of specific electrical resistance, Young's modulus and CTE measured in both wg and ag directions. From the results, it is evident that the with grain (wg) values of the CTE and specific resistance decrease and the thermal conductivity increases with higher filler heat-treatment temperatures. The cathodes also increase in anisotropy with increasing filler heat-treatment temperature, a point that will be discussed in the following section.

Table VI
Properties of Pilot-Scale Cathode Artifacts Prepared with Heat-Treated Anthracite Coal Filers

		Aluminum Cell Cathode 1800°C Filler		Aluminum Cell Cathode 2300°C Filler		Aluminum Cell Cathode 2700°C Filler		Aluminum Cell Cathode 3000°C Filler	
Property	units	wg	ag	wg	ag	wg	ag	wg	ag
Bulk Density	g/cc	1.57		1.52		1.52		1.55	
Specific Resistance	μΩm	51.8	78.6	50.7	84.7	49.8	93.9	30.1	51.5
Young's Modulus	GPa	7.49	3.81	4.51	1.75	1.86	0.54	3.35	1.61
Flex Strength (4pt)	MPa	5	3	2.8	1.6	1.3	0.7	2.1	1.8
Rapoport	vol%	0.58		0.18		0.17		0.19	
CTE (30-100°C)	x10-6/°C	1.69	2.7	1.41	2.63	1.17	2.86	0.932	2.98
CTE anisotropy ratio (ag/wg)		1.60		1.87		2.44		3.20	
Volumetric CTE (30-100°C)	x10-6/°C	7.09		6.67		6.89		6.89	
Thermal Conductivity (R.T.)	W/mK	8		13		16		27	
Ash	%	6.38		4.92		2.7		0.54	

Compiled in Table VII are properties for different commercial grades of cathodes.[2] The wg CTE values for the pilot-scale cathodes heat treated above 2300°C fall within the ranges of the semi-graphitic and semi-graphitized commercial products. The thermal conductivity and electrical resistivities for the pilot-scale cathodes with the 2700°C and 3000°C heat-treated fillers fall in the range of values for the commercial cathodes containing 50% graphite filler. It is, therefore, evident that higher heat-treated anthracite coal improves thermal and electrical properties and has the potential for increasing the usage of anthracite coal in cathodes by extending its use into other grades. The effect on performance of increasing anisotropy with temperature needs to be explored.

Table VII
Properties of Different Commercial Grades of Cathodes Used in Aluminum Production[2]

TYPE OF BLOCK		AMORPHOUS			SEMI-GRAPHITIC	SEMI-GRAPHITIZED
Filler material: Anthracite		100%	70%-80%	50%	-	-
Graphite		-	30%-20%	50%	100%	-
Petroleum Coke		-	-	-	-	100%
Bending strength,	Mpa	6-8	6-10	7-10	8-10	6-12
Specific electrical resistance,	μΩm	36-55	29-44	25-34	15-24	10-15
Linear thermal expansion coefficient,	μm/K·m	2.2-2.6	2.2-2.6	2.2-2.6	1.9-2.6	1.8-3.6
Thermal conductivity,	W/K·m	6-14	8-15	12-27	20-45	100-140
Ash content,	%	4-6	3-6	2-4	0.5-1.3	0.1-0.6
Sodium expansion,	%	0.5-1.3	0.3-1.0	0.2-0.7	0.1-0.4	<0.1-0.8

V.7. Rapoport Test Results for Sodium Expansion

The test results are presented in Table VIII and Figure 19. Table VIII shows that the cathode material made from ECA (1800 °C) has the greatest linear expansion during the electrolysis with a 0.58% length change. On the other hand, the cathode materials made from anthracite coals with higher heat treatment temperatures have significantly less expansion. One also notices that the cathode material made from coal with 2300 °C heat treatment temperature has as good a Rapoport response as that for cathodes made of coals with higher temperature heat treatment. The same conclusion is apparent from Figure 19. which compares the duplicate test results for the ECA 1800 °C cathodes with those for the cathodes from higher temperature heat-treated ECA.

Table VIII
Rapoport Test Results for Cathodes

Heat Treatment Temperature	1st Test	2nd Test	Average % Length Change
1800 °C	0.632	0.532	0.58
2300 °C	0.185	0.179	0.18
2700 °C	0.1798	0.166	0.17
3000 °C	0.1929	0.181	0.19

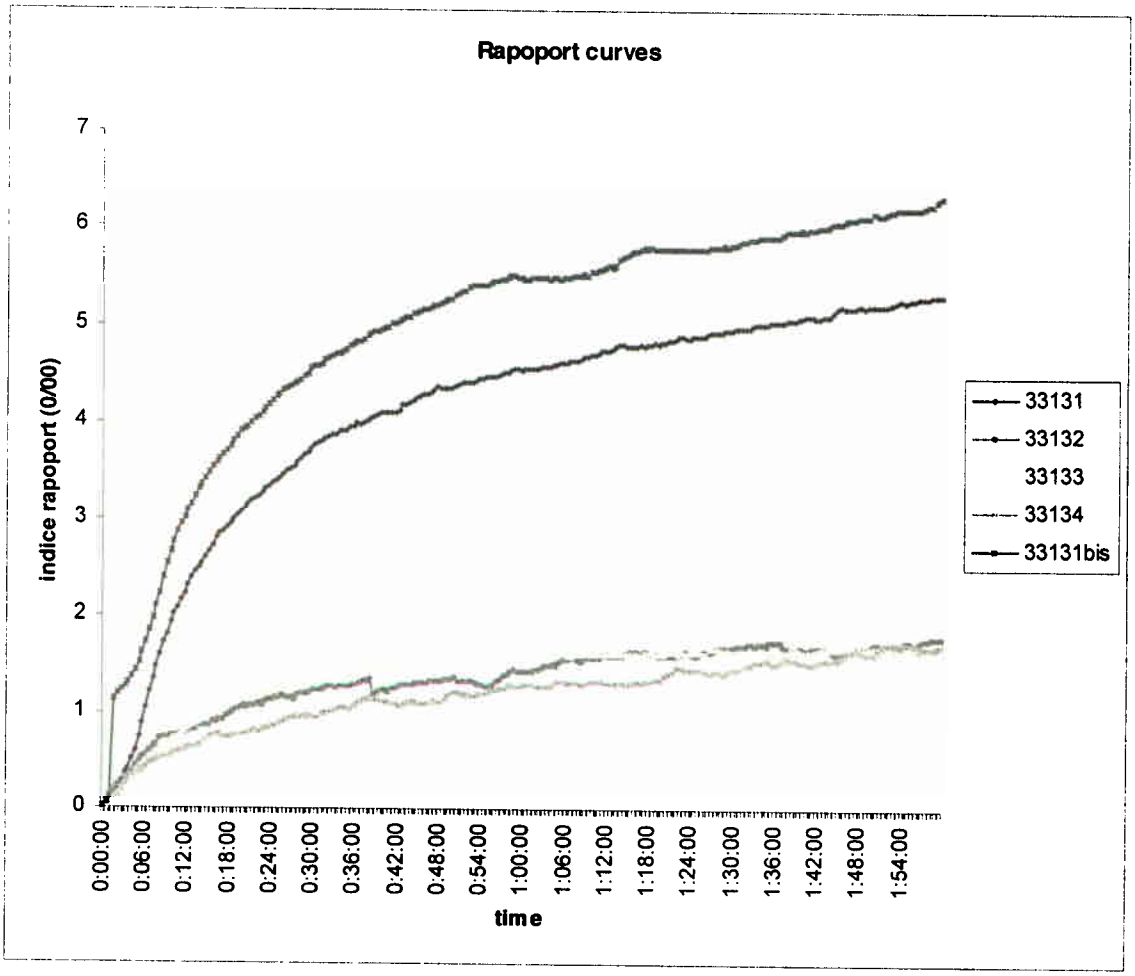

Figure 19. Rapoport Curves for Cathode Materials.

Note: Curve 33131 corresponds to cathode material made from ECA (1800 °C); 33132 for 2300 °C; 33133 for 2700 °C; and 33134 for 3000 °C respectively.

V.8. Thermal Shock Resistance Index for Cathodes and Electrodes

The thermal shock resistance index has been used to indicate how the carbon and graphite artifacts respond to sudden temperature changes. The index is very well known in the carbon industry and is expressed as:

$$\text{Index} = KS/CE$$

Where K= Thermal conductivity
S= Flexural strength of the artifact
C=Coefficient of thermal expansion
E=Young's modulus of the artifact

The property values for the carbon electrode and cathode artifacts given in Tables V and VI were used to calculate thermal shock resistance indices for these materials in Table IX.

Table IX
Calculated Thermal Shock Indices for Cathode and Electrode Artifacts

	Cathodes Index	Electrodes Index
1800 °C	3.16	4.26
2300 °C	5.72	7.44
2700 °C	9.56	16.47
3000 °C	18.16	18.97

Notice that the calculated thermal shock resistance for both electrodes and cathodes increases with increasing heat treatment temperature and is substantially better than those made with standard ECA.

V.9. Anisotropy Development With Filler Heat Treatment

V.9.a. Optical Microscopy Results on CTE Rods

Raw materials characterization for the starting ECA material and each of the heat-treated materials included measurements of the CTE of graphite rods prepared from each material. The CTE results showed a very significant decrease for the higher heat-treated fillers, 1.53 ppm/K for the starting ECA versus 0.69 ppm/K for the 3000 °C calcined sample. Briefly, these so-called CTE rods are made by milling the particles from each sample to a flour, mixing the flour and binder pitch, extruding a 19 mm diameter rod, baking and then graphitizing each rod to about 3000 °C. The with-grain or axial CTE of these rods in the 30°-100 °C range is the reported CTE value. Since all of the rods are graphitized to the same final temperature, one would not expect the calcining temperature to have such a dramatic effect on the rod CTE because the final 3000 °C graphitization should bring them all to similar levels of crystallinity. Optical microscopy examinations were carried out on each of the CTE rods to see if the reason for the large decrease in CTE could be determined.

The rod made with flour from the ECA starting material (CTE=1.53) contained a wide distribution of particle sizes and most of the particles had a fairly round shape. The largest particles were either glassy carbon-like (little birefringence in polarized light) or striated with considerable orientation (relatively strong birefringence in polarized light). There were essentially no large punky or porous particles in the rod, presumably because these relatively weak areas, found in all of the large particles before milling, did not survive the milling process. Figure 20 shows the structure of this rod.

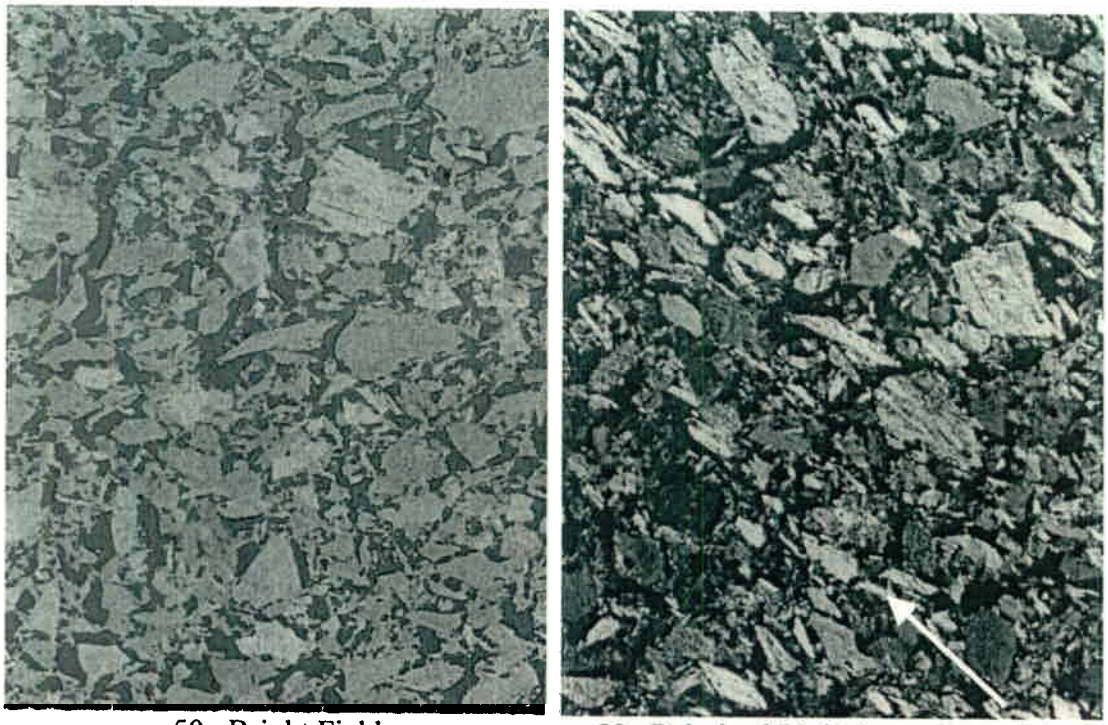

50x Bright Field

50x Polarized Light (extrusion axis)

Figure 20. CTE Rod from As-Received ECA.

The microstructure of the rod made with the flour from 2300 °C calcined material (CTE=1.26) was similar to the rod made with the ECA in most respects, except that there were considerably more very fine particles and most of these were platelet or needle- shaped. Most importantly, these platelet-shaped particles were better oriented in the extrusion direction and most of them were fairly crystalline because they showed optical activity in polarized light. The optical activity suggests that they originated in the striated phase or the catalytic graphite phase in the original large particles.

The microstructures of the rods made with the flours from the 2700 °C (CTE=0.77) and 3000 °C (CTE=0.69) calcined materials were similar to each other, but they both contained considerably more of the fine particles with platelet

shapes which were oriented extensively by the extrusion process. Again, most of these platelet-shaped particles contained fairly graphitic oriented material, rather than glassy carbon, because they showed optical activity in polarized light. Figure 21 shows the microstructure of the rod make with the 2700 °C calcined material.

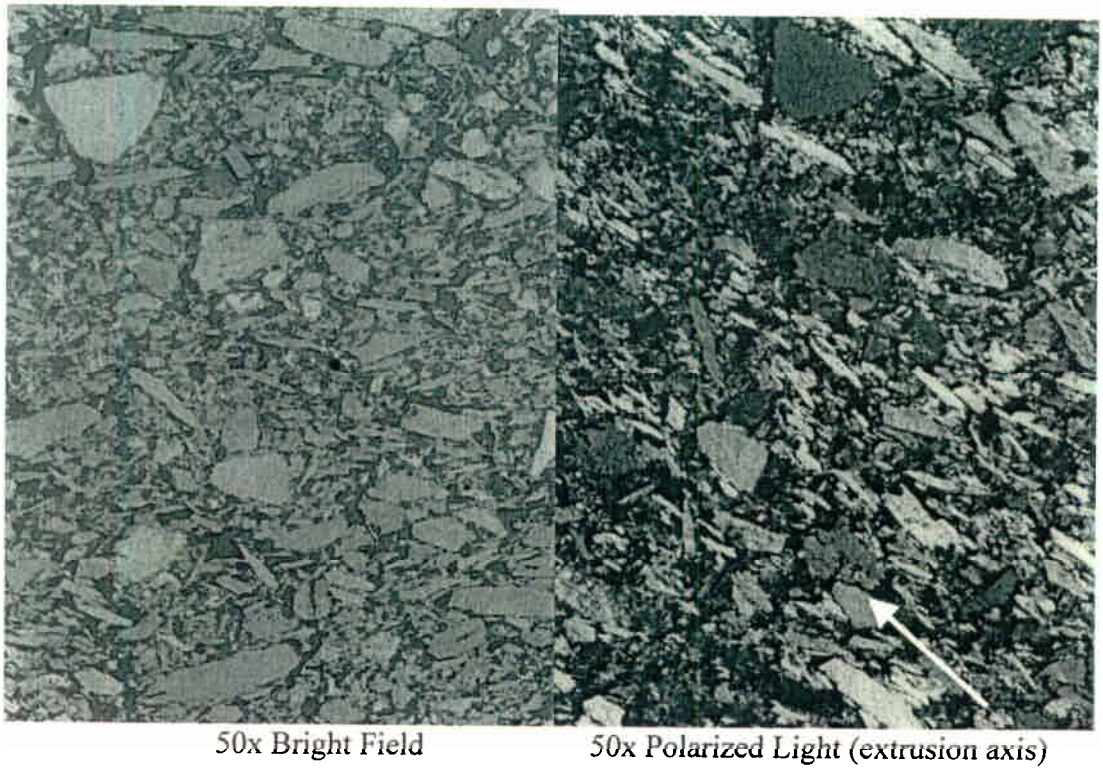

Figure 21. CTE Rod from 2700 °C Heat-Treated ECA.

In summary, it appears that the predominant factor in the CTE reduction in these graphitized rods was the effect of the calcining temperature on the milling process used to make the flour fillers. Both the size distribution and shape of the particles from milling were influenced by the calcining process. The most important effect is that the striated regions, and probably the catalytic graphite regions as well, present in the calcined coal particles are more easily cleaved into platelet-shaped particles as the calcining temperature increases.

V.9.b. Anisotropy in Physical Properties of Baked Carbon Electrodes and Cathodes

Examination of the physical property data shown in Tables V and VI for both types of baked electrodes showed a somewhat unexpected dependence of the anisotropy in the CTE on coal filler heat treatment temperature. The CTE Anisotropy Ratio and calculated Volumetric CTE results for the baked aluminum cell cathodes and silicon smelter electrodes are reproduced below in Tables X and XI, respectively.

Table X
CTE Anisotropy and Volumetric CTE of Aluminum Cell Cathodes

Property	Units	Aluminum Cell Cathode (1800 °C Filler)	Aluminum Cell Cathode (2300 °C Filler)	Aluminum Cell Cathode (2700 °C Filler)	Aluminum Cell Cathode (3000 °C Filler)
CTE Anisotropy Ratio (ag/wg)		1.60	1.87	2.44	3.20
Volumetric CTE (30-100°C)	10^{-6}/C	7.09	6.67	6.89	6.89

Table XI
CTE Anisotropy Ratio and Volumetric CTE of Silicon Smelter Electrodes

Property	Units	Silicon Smelter Electrode (1800 °C Filler)	Silicon Smelter Electrode (2300 °C Filler)	Silicon Smelter Electrode (2700 °C Filler)	Silicon Smelter Electrode (3000 °C Filler)
CTE Anisotropy Ratio (ag/wg)		1.64	1.89	2.72	2.55
Volumetric CTE (30-100°C)	10^{-6}/C	7.44	6.93	6.82	6.53

Inspection of Tables X and XI shows that the CTE Anisotropy Ratio increased significantly as the filler heat treatment temperature increased for both types of baked material, indicating a significant increase in the orientation of the coal-based filler particles. On the other hand, the Volumetric CTE data for both materials showed only a slight decrease with increasing filler heat treatment temperature. This is the anticipated behavior because the overall crystallinity of the coal-based filler particles increases with heat treatment temperature, and this would be expected to produce at least a slight reduction in the volumetric CTE of a baked product.

Since the heat treatment temperature of the ECA had already been found to have a significant effect on the milling behavior and the shape of the of small particles in the CTE rods described in the previous section, it appeared worthwhile to see if analogous particle shape and orientation effects could be detected in the baked artifacts by optical microscopy. The results are summarized below.

V.9.c. Optical Microscopy Results on Baked Cathodes and Silicon Electrodes

Optical microscopy examinations were carried out to evaluate the overall structural characteristics of the pilot-scale baked silicon electrodes and the baked cathodes to help explain some of the physical property results, especially the behavior described in the section above where the CTE anisotropy increased as the filler heat-treatment temperature was increased. Most of the effort was devoted to examining longitudinal

sections of the baked silicon electrodes to assess particle and flour orientation effects. Limited exams were made on the transverse sections of the baked silicon electrodes and both transverse and longitudinal sections of the baked cathodes.

In general, the large calcined anthracite particles in both baked artifacts were only weakly oriented in the extrusion direction, unless they were platelet-shaped with a significant aspect ratio. These platelet-shaped particles usually had a striated structure and were optically active (showed birefringence in polarized light). The medium sized calcined anthracite particles in the silicon electrodes tended to be more oriented in the extrusion direction than the larger anthracite particles because they tended to have a higher aspect ratio (see Figure 22).

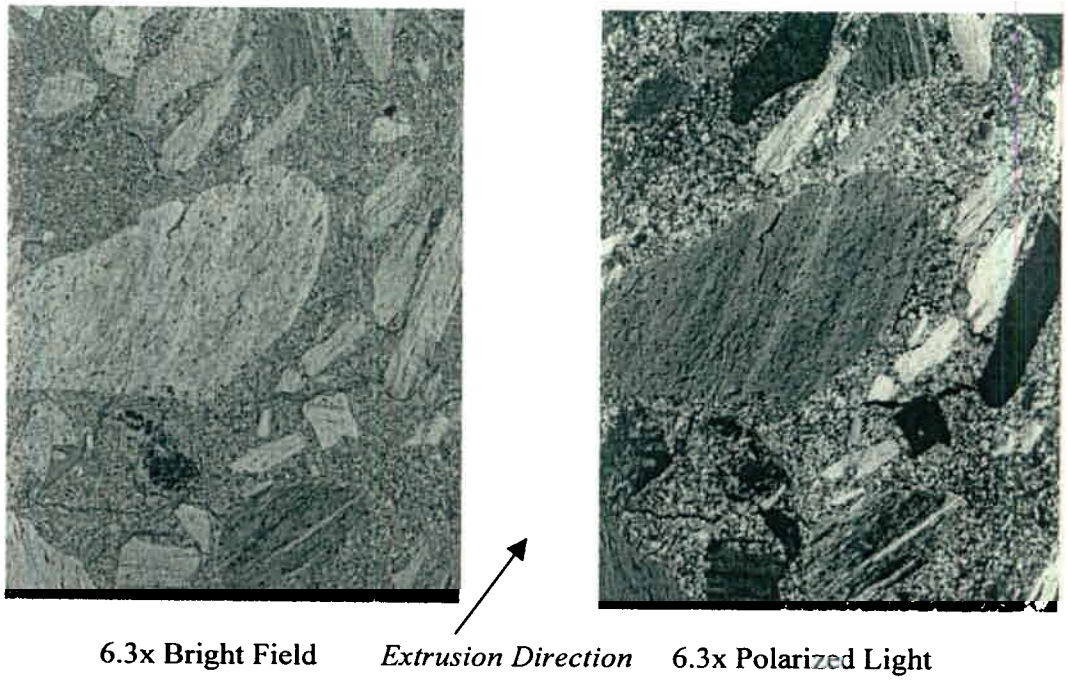

Figure 22. Low Magnification View Showing Macrostructure of Baked Silicon Electrode Made with 2300 °C Heat Treated ECA. (Note orientation of the medium size filler particles with a platelet shape in the extrusion direction.)

Portions of the perimeter of the large and medium sized anthracite particles were frequently debonded from the surrounding coked binder + flour matrix. The "mottled" structure, found to various extents in the calcined anthracite particles, was still evident in the large filler particles in the baked carbon electrodes and cathodes (see Figure 23).

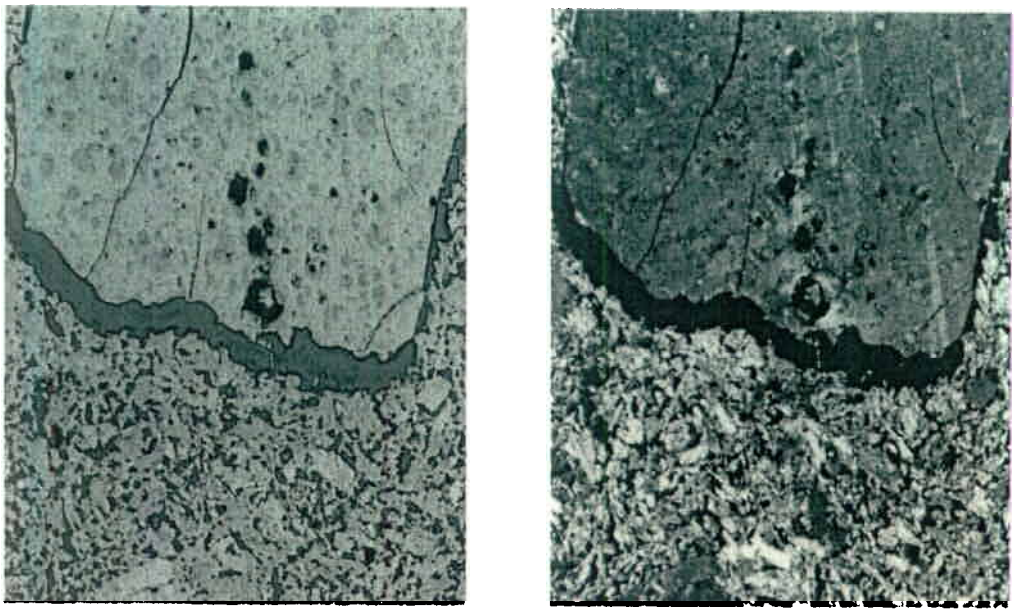

50x Bright Field

50x Polarized Light

Figure 23. Intermediate Magnification View Showing Debonding at the Interface Between Large Filler Particle and the Coked Binder/Flour Matrix in the Baked Silicon Electrode Made with 2300 °C Heat Treated ECA. (Note the "mottled" texture in the bulk of the large filler particle in bright field photograph.)

It proved to be difficult to assess the overall extent of orientation in the extrusion direction for both particles and flour in the baked silicon electrodes by optical microscopy alone. If one carefully examines fairly large longitudinal cross-sections of these electrodes at both high and low magnifications under both bright field and polarized light, there does appear to be a relation between calcining temperature and orientation. The overall orientation appears to be highest for the electrodes made with the 2700° and 3000 °C calcined ECA material. The electrodes made with the 2300 °C ECA appeared to have an intermediate level of orientation and the electrode made with the starting ECA had the least overall orientation. Unfortunately, it is virtually impossible to select a small set of micrographs to illustrate this result because there is so much variation in the microstructure from area to area in each sample. This is particularly true for the orientation of the flour particles in the small area that is encompassed in the high magnification micrographs which are required to show the structural detail in these regions. The net orientation behavior of the flour particles in a given small area is due to the combined effects of the flow in the extrusion direction and the local flow behavior around the neighboring large and medium size filler particles, and it is very difficult to assess the relative contributions of these two effects in any given matrix area. Hence, an observer must use a mental averaging process while scanning many such areas to evaluate qualitatively the extent of flour particle orientation. Analogous averaging observational procedures are required to assess the orientation of the larger filler particles.

VI. CONCLUSIONS AND RECOMMENDATIONS

VI.1. Conclusions

1. The heat treatment program for anthracite coal in the application of aluminum and silicon smelters was successfully carried out. The higher heat treatment leads to improved laboratory key performance-related test results for both cathodes and carbon electrodes. The anthracite coal quality is upgraded due to the heat treatment.

2. For aluminum smelter application, the cathodes made from higher heat treatment coal are lower in ash content and with-grain CTE, and higher in thermal conductivity. The sodium vapor test results show the lower sodium uptakes for the higher heat treatment coals. Similarly, the Rapoport tests show that the cathodes made from high heat treatment coals exhibit more resistance to electrolytic attack in the simulated electrochemical cell.

3. For silicon smelter application, the thermal shock resistance indices of the electrodes made from higher heat treatment coals are better than those from the lower heat treatment coals. For the fracture toughness tests, the results are inconclusive, primarily because the standard deviation for the test is too high to differentiate the toughness measurements. One would need to have a larger number of samples to get a definitive result.

4. The optimal heat treatment temperature from this laboratory study seems to be in the range of 2300° to 2700 °C. It is most evident in the Rapoport results, which shows significant effect from 1800° to 2300 °C, and very little additional effect at 2700° or 3000 °C heat treatment on the resistance to attack by sodium.

5. Binder demand in the manufacture of both the cathodes and carbon electrodes depends on the filler heat treatment severity. This is consistent with the structural observations which showed that particle shape is affected by heat treatment temperature.

6. Heat treatment of the ECA had two primary effects: (1) true "graphitization" which improved the crystallinity of the bulk regions that were essentially free of ash constituents in the precursor coal, and (2) "catalytic graphitization" of the regions of the coal particles that were adjacent to the ash particles in the interior of the original coal particles or at the perimeter of the coal particles where they were exposed to vaporized ash-derived species. Optical microscopy examinations showed conclusively that both types of material are present in the samples heated to 2300°-3000 °C with the amount of the catalytic graphite phase increasing with heat treatment temperature. SEM/EDS results showed the presence of various types of small ash-derived particles within the catalytic graphite regions with the composition varying with heat treatment temperature. The X-ray diffraction results are also consistent with the two-phase character of the heat treated ECA and clearly show the overall improvement in crystallinity with increasing heat treatment temperature. Real and helium density results, as well as the data on the amount of ash and its composition, are also consistent with this scenario.

7. The milling behavior of large coal particles showed a surprisingly large dependence upon heat treatment temperature. Optical microscopy examinations of graphitized rods made with milled flours showed that both the size distribution and the shape of the particles produced by milling were influenced by the heat treatment temperature with increasing temperature tending to increase the number of platelet-shaped particles which were more easily oriented during extrusion. The anisotropy in the physical properties of the baked carbon electrode and cathode products also appeared to be influenced by this milling effect from the filler heat treatment temperature.

VI.2. Recommendations

1. An economic assessment of the cost for heat treatment of anthracite coal is essential for the scale up in this work. Commercialization of the project depends on the economic assessment and the benefits from the field performance.

2. For the current ECA (electrically calcined anthracite coal) producers, the current project results could be implemented by modifying the existing ECA furnaces to operate a few hundred degrees higher in temperature and with a more uniform in temperature distribution inside the furnace.

3. It would be of interest to compare the physical and electrochemical properties in terms of erosion resistance, for the cathode materials produced in this study with those of graphitized cathodes made of petroleum coke.

4. It is recommended that a heat treatment series with a lower ash domestic anthracite coal should be carried out to delineate the mechanism for catalytic graphitization and bulk ordering due to thermal processing.

VII. REFERENCES

1. Kirk-Othmer Encyclopedia of Chemical Technology, 4th Ed., Volume 4, p. 994 (1992). Edited by J. Wiley & Sons.

2. "Cathodes in Aluminum Electrolysis," M. Sorlie and H. A. Oye. 2nd Edition, Aluminum-Verlag GmBH, Dusseldorf, (1994).

3. J. V. Atria, R. Rusinko, and H. H. Schobert, Energy and Fuel, 16, 1343 (2002).

4. H. Schobert and P. Papano, "Anthracite Fillers for Specialty Graphite-Feedstock Selection and Product Improvement," DOE Final Report, May 2002.

5. P. Stansberry, H. H. Schobert, D. P. Struble, and L. Lanzel, "Anthracite Filler and Coal-Extract Binder for the Development of Isostatically Molded Graphite, Final Report, DE-FC26-98FT40350 (March 2003).

6. A. Oberlin and G. Terriere, Carbon 13, 367 (1975).

7. D. Gonzales, M. A. Montes-Movan, I. Suarez-Ruiz and A. B. Garcia, Abstracts of Oviedo Carbon Conference (2002).

8. D. Gonzales, M. A. Montes-Moran, M. R. Martinez-Tarazona, and A. B. Garcia, Abstracts of Oviedo Carbon Conference (2002).

9. M. Laumb, S. A. Benson, P. Pappano, and H. H. Schobert, Prepr. Pap. Amercian Chemical Society, Div. Fuel Chem. 49, 165 (2004).

10. Rapoport, M.B., and Samoilenki, V.N., Tsvet. Met. 1957; 30(2); 44-51.

11. Newman, D.S., Dahl, O.T., Justnes, H, Kopperstand, S. and Oye, H.A., Lights Metals, 1986, 685-8.

12. Peyneau, J.M., Gaspard, J.R., Dumas, D., Samanos, B., Light Metals, 1992, 801-8.

13. Zolochevsky, Al, Hop, J.G., Servant, G., Foosnas, T., and H.A. Oye, Carbon, 2003, 41, 497-505.

"Remediation of Coal Impoundments: Efficacy of Coal for Activated Carbon"

Final Report

Reporting period start: June 2003
Reporting period end: June 2004
Principal Authors: David Mazyck, Ph.D., Matthew Tennant, Ph.D.
Date report issued: June 30th, 2004
DOE Award Number:DE-FC26-98FT40350

Submitting organizations:

University of Florida
PO Box 116450
Gainesville, FL 32611

and

Engineering Performance Solutions
5510 SW 41st Blvd., Suite 205
Gainesville, FL 32608

DISCLAIMER

ABSTRACT

The research project undertaken by the University of Florida and Engineering Performance Solutions addresses (a) treatment of coal slurry water to National Pollutant Discharge Elimination System (NPDES) standards, (b) the development of activation techniques for the recovered coal to produce a high surface area activated carbon, and (c) conduct a market analysis for potential use of the activated carbon product. Remediation of coal slurry water with a photocatalyst (TiO_2) proved to be more effective than adsorption with activated carbon. Since the solution pH was such a major factor on the removal of the metals, the current procedure calls for sodium hydroxide addition to raise the pH from 2 to around 7. The increase in pH removes the iron and aluminum from the coal slurry water. The photocatalyst along with UV is then used to remove the manganese. Research will continue in this direction in order to better determine the effectiveness of the technology. Activations of the raw coal recovered from coal impoundments were more effective employing a chemical activation strategy. Phosphoric acid and sodium hydroxide showed improvements in pore development over direct physical activation, however the most effective technique in producing an activated carbon was using raw coal that was first refined with a chemical washing procedure proceeded by physical activation. Steam activations using this refined coal produced activated carbon with well developed micro- and mesoporosity as seen by the BET surface area and tannin values.

TABLE OF CONTENTS

LIST OF TABLES

EXECUTIVE SUMMARY

The University of Florida and Engineering Performance Solutions collaborated to research the remediation of coal slurry impoundments. Coal slurry impoundments hold the effluents from washing processes that coal producers perform on raw coal once it is brought to the surface. The result is often large basins of highly acidic water with solid particulate matter, which are contained using dams made up of larger solid materials. Many of these dams are not adequately designed or built to hold the large volumes of water, particularly in heavy rains. Accidents involving coal slurry impoundments are tragic and costly, and therefore this is an extremely important issue to the coal industry and those living in coal mining regions. In order to effectively remediate coal slurry impoundments, new techniques must be developed in order to treat the coal slurry water and find uses for the solid coal refuse. In this research we attempted to remediate the coal slurry water using activated carbon adsorption and advanced oxidation with a photocatalyst. In addition we investigated the potential of the coal refuse from the impoundments as a precursor for activated carbon.

Coal slurry and acid mine drainage (AMD) water samples were received from five West Virginia sites. Characterization of these samples indicated extremely low pH values (approximately 2), and high levels of metals; particularly aluminum, iron, and manganese. A majority of the received water samples had concentrations of these metals well above the regulations set by the state of West Virginia. Moreover, the combination of the metals and the low pH levels makes the coal slurry and AMD water more difficult to treat as the metals are quite soluble in acidic environments.

The first treatment option selected was activated carbon. It was hopeful that adsorption onto activated carbon could effectively remove the metals from the coal slurry water, since another aim of this project was to produce carbons from the solid coal refuse. Unfortunately at 5 and 50 ppm dosages, activated carbon was unsuccessful in treating the coal slurry water, as less than 10% of any metal was removed. The next treatment technology attempted utilized pretreatment to the activated carbon by exposing the water to UV oxidation prior to adsorption. The hypothesis was that the UV would oxidize the metals, thus making them more adsorbable. The UV pretreatment did not increase removal however, as the removal values were very similar to activated carbon alone. The final treatment technology utilized was the photocatalyst TiO_2, with and without UV exposure, at various pH values. Three waters were used for these tests and TiO_2 showed excellent potential for metals removal in several of the test conditions. For example, iron removal values were near 90%, and approximately 70% of the aluminum was removed in two of three waters. The encouraging results have enabled us to continue investigating this technology in hopes of finding a cost effective treatment for coal slurry water.

The other principle objective of this work was to determine the efficacy of the raw coal refuse found in coal slurry impoundments for use as a precursor for activated carbon. The first activation protocols involved direct steam activation of the raw coal at temperatures between 840 and 950 °C and times between 2 and 3 hours. These techniques were unable to produce the desired porosity in the finished products, as none of the surface areas were

above 150 m^2/g. Chemical activation techniques utilizing concentrated phosphoric acid or 3 N sodium hydroxide followed by heat treatment were also unable to produce activated carbons with surface areas as large as those found in commercially available products (e.g., > 500 m^2/g). The chemical activations, however, did show an improvement over the physical activations with steam (BET surface areas: 260 m^2/g and 324 m^2/g, respectively), indicating that chemical activation can aid in the activation of the raw coal refuse. Even better yet, a third party chemical washing technique (hydrofluoric acid washing) that was used on the raw coal produced a precursor very high in carbon content (i.e., 99%). Steam activations on this refined coal had much more pore development with several surface area and tannin values similar to those of commercially available carbons (i.e., > 500 m^2/g and < 250). Therefore, the solid coal refuse from coal impoundments can be feedstock quality activated carbon if chemical pretreatment is used.

INTRODUCTION

Coal mining in the United States is extensive and essential to both regional and national economies as is evident by the fact that domestic coal powers more than 50% of the country's electricity. Production has increased to over 1 billion tons in 2001. However, this quantity of mechanized coal processing may potentially adversely affect environmental and human health through the byproducts that it produces. Innovative methods to store, treat, and utilize coal byproducts are necessary to discourage potential environmental disasters, which are also costly, that are possible with the current system. Clearly, coal is vital to our future, and therefore, a solution for the by-products is essential so that coal can remain a top resource for the nation.

The sophisticated, large-scale process used to clean raw coal produces a byproduct that is a fluid suspension of small particles of rock, clay, and fine coal that may also contain flocculants, lime, and heavy metals. This fine coal refuse, or slurry, is then pumped into an impoundment area with coarse coal refuse acting as a dam. Suspended materials are then left to settle in this storage pond that often holds millions of gallons of coal slurry. Many coal waste impoundments are not engineered to perfection and are unstable and even unsafe. Those built near old underground mines are more likely to overflow or collapse, in both cases releasing the slurry from the ponds into the environment. According to the Mine Safety Health Administration, in three West Virginia counties (Kanawha, Logan, and Boone) there are 37 coal slurry impoundments. Of these 37, 16 are ranked as having a moderate to high probability of breaking.

The proposed research herein seeks to address the problems associated with coal waste slurries by providing a suitable treatment methodology for coal slurry and acid mine drainage water and to identify the efficacy of activating the recovered coal from the slurry/refuse for producing activated carbon. The notion is that the coal refuse water could be cleaned for safe discharge to nearby receiving waters and the coal refuse could be manufactured in to activated carbon. The University of Florida and Engineering Performance Solutions (EPS) have teamed to focus on this problem.

EXPERIMENTAL

Activation of the coal slurry refuse and refined refuse took place in an apparatus built at Engineering Performance Solutions. A fluidized bed furnace similar to that used by Mazyck and Cannon (2000) was employed to activate the coal refuse/refined refuse. The samples were poured down the top of a 1-inch diameter quartz tube where they came to rest upon a quartz porous frit. Gases were distributed through this frit, and the coal refuse was fluidized. This reaction chamber was heated using an electrical clamshell furnace; the temperature inside the reaction chamber was monitored using a type K thermocouple. The inputs of N_2 and deionized water were controlled with flow meters, and the gases were distributed through 1/2-inch stainless steel tubing that was heated using heating tape with an external temperature of 550 ^{o}C.

The activation times (120 to 300 minutes) and temperatures (800 °C to 950 °C) were adjusted to investigate yield, BET surface area, and tannin values of the resulting product. For all steam activations, the oxidant to carbon ratio was held constant at 0.2 lb oxidant/lb GAC.

The resultant material (i.e., activated carbon) was then ground using an IKA A11 basic grinder and sieved using a 325 mesh sieve. The activated carbon that was passed through the 325 mesh sieve was then evaluated to determine its tannin value in accordance with ANSI/AWWA B600-90 Standard for Powdered Activated Carbon.

The BET model was applied to determine the surface area of the developed carbons by using a NOVA 1200 (Version 3.60) (Quantachrome Corporation, Boynton Beach, FL) located at the University of Florida's Engineering Research Center (ERC). The BET surface area (units of m^2/g), for example, expresses the surface that can be covered by nitrogen in a monomolecular layer. All samples were outgassed at 105 °C for a minimum of 4 hours prior to testing.

Batch tests were performed in Erlenmeyer flasks with coal slurry or AMD water on magnetic mixers. Activated carbon was weighed out and added to solution as a dry powder. Experiments with activated carbon and UV oxidation used carbons with 3% TiO_2 loading by weight.

Metals analyses for aluminum, manganese, and iron present in the AMD water before and after treatment were analyzed via inductively coupled plasma.

The same metals were analyzed for in the coal slurry water by a third party facility for QA/QC under the guidance of EPA-600/4-79-020, *Methods for Chemical Analysis of Water and Wastes*, Revised March 1983; and *EPA Test Methods for Evaluating Solid Waste, Physical/Chemical Methods*, SW_8420, December 1992, 3rd Edition incl. Updates I-III; and *Standard Methods for the Examination of Water and Wastewater*, 18th Edition, 1992.

RESULTS AND DISCUSSION

Characterization of the Water

Remediation of coal slurry impoundments is a two step process: treatment of the coal slurry and AMD water and also removal and reuse of the solid coal. Most of the coal refuse that is available for manufacturing has settled in the coal slurry pond. Therefore, to retrieve this coal, the water must be removed. Although an option is to pump the water from the pond to another location, ideally it would be treated for safe discharge to a nearby receiving body of water. Therefore, the first step in this project was to characterize the contaminants present in the coal refuse (i.e., coal slurry) water and acid mine drainage (AMD) water. The AMD water was not water that actually percolated through the earth and exited a mine, but rather that water which percolated through a coal refuse pile. Both water that exits mines and coal refuse piles is classified as AMD by the WV DEP.

Table 1. NPDES standards for special reclamation sites in West Virginia
1 below details the National Pollution Discharge Elimination System (NPDES) standards for the AMD and coal slurry water sites. More generally, these fall under the West Virginia category of special reclamation sites. In order to discharge treated water into a water body, these limitations must first be met.

Table 1. NPDES standards for special reclamation sites in West Virginia

Metal	NPDES Standards (mg/L)
Al	0.8
Fe	3.0
Mn	2.0

pH must between 6 and 9

Prior to treatment, the AMD and coal slurry waters were characterized, the results of which are presented in Table 2. Coal slurry water and AMD samples were collected at three sites throughout West Virginia, each of these are presently under evaluation by the West Virginia DEP to develop treatment strategies in the near future.

Table 2. Metal concentrations of AMD and coal slurry water

Metal	AMD Water			Coal Slurry Water	
	Site #23	Beckley Site #6	Sommersville	Sample #1	Sample #2
Al (mg/L)	4.5	49	0.12	86	182
Fe (mg/L)	27	34	6.9	159	345
Mn (mg/L)	32	11	4.4	1.6	3.1

In comparison to the NPDES permitted heavy metal concentrations required prior to release, Sommersville is the only location that would require minimal treatment in order to achieve the desired levels. Site #23 and Beckley Site #6 would require more extensive treatment prior to release. The coal slurry water as well requires substantial removal of aluminum and iron.

AMD and Coal Slurry Water Treatment Options

Adsorption via activated carbon

The next objective of the project was to investigate treatment strategies that would be cost effective and easily incorporated as a simple yet highly effective scheme. Typically, coal mines are located in remote areas where heavy equipment and expensive technologies are not at an easy grasp. Activated carbon has been one of the most easily retrofitted treatment chemicals in the water treatment industry. For the preliminary research, Beckley Site #6 was chosen because this location contains the most elevated concentrations of heavy metals and would most likely be the first target for required treatment.

Commercially available activated carbons were used in the bench-scale tests with the hopes that once suitable activation strategies of the coal refuse are complete, these would be used instead. Carbon doses of 5 and 50 mg/L were magnetically mixed with water from Beckley Site #6 for four hours. The percent removal using these carbon dosages are shown below (Table 3 and 4). However, the results are not too surprising in that increasing the carbon dose by an order of magnitude only increased metals removal marginally. This is true because the pH of the water is 2, where the metals are extremely soluble in water.

Table 3. Percent removal of heavy metals using 5 mg/L activated carbon dose

Carbon Type	Aluminum % Removal	Iron % Removal	Manganese % Removal
Bituminous (F400)	3.7	0	1.0
Lignite (HD4000)	5.4	0.3	2.9
Wood (Bark Char)	5.0	0	1.0
Chemically Activated Wood-Based (Bionuchar)	2.5	0	0

Table 4. Percent removal of heavy metals using 50 mg/L activated carbon dose

Carbon Type	Aluminum % Removal	Iron % Removal	Manganese % Removal
Bituminous (F400)	5.2	0	0.0
Lignite (HD4000)	7.4	0.3	1.9
Wood (Bark Char)	4.7	0	0.0
Chemically Activated Wood-Based (Bionuchar)	6.2	2.1	1.0

UV Oxidation and activated carbon adsorption

Adsorption onto activated carbon alone was not able to remove appreciable amounts of the contaminants from the Beckley Site # 6 due to the high solubility of metals at the low pH. The next step taken was activated carbon adsorption in concert with UV oxidation. It was believed that pretreatment of the water with UV oxidation would oxidize the metals and thereby make them more easily adsorbed onto the carbon. Table 5 shows the results of the trials using UV oxidation followed by four hours of contact with 50 ppm of two commercially available carbons. The results here show this technique to be unsuccessful and that other treatments are needed to adequately treat the AMD and coal slurry water. With this said, UV treatment did improve the overall removal for F400, and this lead to further pursuit of advanced oxidation techniques.

Table 5. Percent removal of heavy metals using UV oxidation followed by 50 mg/L activated carbon dose

Carbon Type	Aluminum % Removal	Iron % Removal	Manganese % Removal
Bituminous (F400)	8.6	2.1	0.5
Lignite (HD4000)	7.2	0.6	0.0

Photocatalysis

The next objective was to investigate if photocatalysis could effectively remove the metals below NPDES standards. The pH is a dominant variable for metal chemistry, so it was investigated to quantify its role in removal. Tables 6-8 show the results from three waters using the photocatalyst TiO_2 with and without UV.

Table 6. Beckley photocatalyst results

Fe Adsorption		**Fe Adsorption + Oxidation**	
pH	Percent Removal	pH	Percent Removal
2.4	3	2.4	6
4.4	7	4.4	0
6	12	6	0
Mn Adsorption		**Mn Adsorption + Oxidation**	
pH	Percent Removal	pH	Percent Removal
2.4	0	2.4	3
4.4	2	4.4	0
6	0	6	0
Al Adsorption		**Al Adsorption + Oxidation**	
pH	Percent Removal	pH	Percent Removal
2.4	1	2.4	3
4.4	3	4.4	5
6	MDL	6	MDL

MDL: below minimum detection level

Table 7. Site #23 Photocatalyst results

Fe Adsorption		**Fe Adsorption + Oxidation**	
pH	Percent Removal	pH	Percent Removal
3	31	3	23
4	14	4	64
5	46	5	91
6	62	6	62
Mn Adsorption		**Mn Adsorption + Oxidation**	
pH	Percent Removal	pH	Percent Removal
3	0	3	0
4	0	4	0
5	0	5	0
6	MDL	6	1
Al Adsorption		**Al Adsorption + Oxidation**	
pH	Percent Removal	pH	Percent Removal
3	12	3	10
4	0	4	0
5	29	5	69
6	MDL	6	NA

MDL: below minimum detection level

Table 8. Sommersville photocatalyst results

Fe Adsorption		Fe Adsorption + Oxidation	
pH	Percent Removal	pH	Percent Removal
3	20	3	20
4	0	4	0
5	13	5	2
6	15	6	24
7	87	7	78
Mn Adsorption		**Mn Adsorption + Oxidation**	
pH	Percent Removal	pH	Percent Removal
3	0	3	0
4	0	4	0
5	0	5	0
6	0	6	0
7	0	7	9
Al Adsorption		**Al Adsorption + Oxidation**	
pH	Percent Removal	pH	Percent Removal
3	0	3	0
4	0	4	0
5	0	5	0
6	39	6	0
7	0	7	71

The results summarized above are very intriguing. In some cases, adsorption by the TiO_2 photocatalyst alone was promising. When UV was added, which would have either reduced or oxidized the metal, the results improved for certain pH values, but was deleterious for others. In summary, increasing the pH from approximately 2 to 6 or 7 precipitated out the majority of iron and aluminum. Manganese however, is soluble up to a pH of 10, so it remained in solution. Therefore a plausible treatment strategy might consist of chemical precipitation to remove the iron and aluminum preceded by a technology to remove the manganese. Preliminary data not shown suggests that photooxidation of manganese can effectively remove initial concentrations of greater than 20 mg/L to below 2 mg/L. Research in this area in continuing.

Activation of Coal from Impoundments

Steam activation of raw coal

Producing activated carbons from coal often involves the use of a binder prior to activation. This technique takes additional resources and additional time to crush the raw material and then agglomerate it with the binder. The goal in this work was to determine the efficacy of creating an activated carbon from solids from coal impoundments by direct activation, i.e., without use of a binder. The first activations performed used the raw coal (BET surface area on the order of 1 m^2/g) received from the coal impoundment

without any pretreatment or additional materials. Steam was chosen as the oxidant and times and temperatures common to coal activation were utilized (Wigmans 1989). The results of six steam activations are shown in Table 9. Characterization of the activated samples showed little in the way of porosity development as the surface areas were all well below 150 m^2/g. Considering that commercially available coal-based carbons often have surface areas greater than 600 m^2/g, that other techniques are necessary in order to produce a viable activated carbon from the raw coal refuse.

Table 9. Raw coal activations using steam.

Sample	Temperature (°C)	Time (min)	Mass Loss (%)	Tannin Value	BET Surface Area (m^2/g)
Raw Steam 2	850	150	31	436	69
Raw Steam 4	840	120	28	477	72
Raw Steam 8	900	180	22	352	29
Raw Steam 9	950	180	35	205	46
Raw Steam 12	850	120	39	-	134
Raw Steam13	850	150	36	-	137

Chemical activation of raw coal

The next step was to activate the raw coal using chemical activation techniques. Phosphoric acid and sodium hydroxide are chemical agents that have shown excellent results for activating carbonaceous precursors into quality adsorbents. Tables 10 and 11 show the results of one phosphoric acid and one sodium hydroxide activation, respectively. These chemical activations did result in carbons with surface areas much higher than any produced via direct activation with steam. However, these surface areas were still far below those found in the market today.

Table 10. Raw coal activation using phosphoric acid

Sample	Temperature (°C)	Time (min)	BET Surface Area (m^2/g)
Raw Phosphoric 2	850	120	260

Table 11. Raw coal activation using sodium hydroxide

Sample	Temperature (°C)	Time (min)	BET Surface Area (m^2/g)
Raw NaOH 1	750	60	324

Physical activation of refined coal

The results of the physical and chemical activations did indicate that chemically pre-treating the raw coal did produce a better finished product. Thus, we decided to use a chemical refining process developed by a third-party private company. This proprietary technique utilizes hydrofluoric acid washing that creates a material high in carbon content, which is very encouraging for activated carbon production. Coal refuse was received in the laboratory after the refinement process. Table 12 lists 8 activation protocols used on the refined coal with steam as the oxidant. Many of these activations produced carbons with surface areas above 500 m^2/g, with one (Ref Steam 21) above 850 m^2/g. The carbons produced from physically activating the refined coal with steam indicated that quality activated carbons could be produced from the coal refuse found in coal impoundments.

Table 12. Activations using refined coal and steam

Sample	Temperature (°C)	Time (min)	Mass Loss (%)	Tannin Value	BET Surface Area (m^2/g)
Ref Steam 16	850	300	67	548	449
Ref Steam 18	900	240	95	70	683
Ref Steam 20	850	240	86	138	534
Ref Steam 21	850	300	81	221	850
Ref Steam 22	850	120	55	455	400
Ref Steam 28	950	120	79	-	523
Ref Steam 29	950	180	78	-	514
Ref Steam 30	850	180	47	-	382

In addition to the activations with steam, five physical activations were attempted using carbon dioxide as the oxidant. Despite similar activation protocols (i.e., time and temperature), carbon dioxide failed to develop any significant porosity. Longer times or higher temperatures would have likely increased pore development with carbon dioxide. However, since steam activations created quality carbons, the additional time or temperature needed for carbon dioxide did not appear justified.

Market Analysis of Coal Refuse for Use as an Activated Carbon Precursor

Direct activation of the coal refuse was unable to produce activated carbons with physical properties that would compete with those currently available commercially. The research indicated that chemical pretreatment was necessary in order to activate the raw coal. A chemical washing process (performed by a third party) produced a refined coal precursor very high in carbon content. Steam activations on this refined coal produced finished carbons with surface areas (> 500 m^2/g) similar to those on the market today. Therefore,

the costs of the refining process used here should be considered when analyzing the potential for commercialization of the solid refuse found in coal slurry impoundments.

The reported costs of the chemical pretreatment used in this research were approximately $0.01/ lb of raw material. Activated carbon manufacturers often buy raw material for approximately $0.04/ lb. Therefore, this refined coal could potentially serve as a viable feedstock for activated carbon. When considering the size and number of coal slurry impoundments in the Appalachian region alone, the amount of raw material available could allow for a sizable profit. In addition, the chemical pretreatment process produces particles roughly 1 mm in diameter. This is convenient for activated carbon production as GAC is often sold at this size, and the refined coal could be pulverized and sold as PAC.

SUMMARY

Remediation of coal slurry impoundments is a difficult yet important job for engineers in coal mining regions as well as across the United States. For efficiently treating these impoundments allows the United States to continue to rely on coal as a major resource for energy and quality products. The principle goal in the research was to determine the efficacy of coal refuse found in coal slurry impoundments as a precursor for activated carbon. In addition, we attempted to remediate the coal slurry water by removing the metals present at concentrations well above the regulated levels. Strategies for efficient removal and treatment of this potentially toxic water and commercial use of the solids found in coal impoundments would greatly aid the coal industries and the regions that rely on them.

The initial attempts to remove metals from the coal slurry and AMD water via activated carbon adsorption proved to be ineffective. Likewise, pretreatment with UV followed by adsorption was only slightly better. The only treatment option that showed any potential was the use of the photocatalyst TiO_2 with and without UV. This technique was able to effectively remove metals in some experimental conditions. The pH of the solution proved to be a major factor linked to metals removal. The potential of the photocatalyst for metal removal has lead EPS to team with Purifics, Inc.to continue research for this problem.

In order to determine the efficacy of the coal refuse for activated carbon, several activation strategies were employed. It was determined that direct physical activation of the raw coal could not produce a viable product. Chemical activations of the raw coal however, improved the surface areas found in the finished activated carbons. Although these techniques were unable to produce carbons as porous as those available today, the improvement did indicate that chemical pretreatment could be effective in converting the raw coal refuse into a quality carbonaceous precursor. Therefore, a third party was utilized to treat the coal refuse via a chemical washing technique. The result of this washing process is a material very high in carbon content. A sample of this was sent to us to determine its ability as a precursor to activation. Steam activations using this refined coal produced activated carbons with surface areas comparable to those from commercial producers. Therefore, it was determined that the coal refuse could be used to produce a quality activated carbon if chemical pretreatment was applied.

REFERENCES

Mazyck DW, Cannon FS. Overcoming calcium catalysis during the thermal reactivation of granular activated carbon. Part I. Steam-curing plus ramped-temperature N_2 treatment. Carbon 2000; 38(13):1785-1799.

Wigmans T. Industrial aspects of production and use of activated carbon. Carbon 1989; 27(1): 13-22.

"Expanding Supply for Fly Ash Derived Carbons"

Final Report

July 1, 2004 to April 30, 2004

Michael Sawayda
Dr. Thomas Weyand

Contract #: 2564-PMET-DOE-0350

Pittsburgh Mineral and Environmental Technology
700 Fifth Ave.
New Brighton, PA 15066

May 21, 2004

Table of Contents

List of Figures

List of Tables

Abstract

Pitt Carbon, a joint venture between Pittsburgh Mineral & Environmental Technology (PMET) and U.S. Natural Resources Inc. (USNR), is collecting carbon from fly ash with greater than 80% LOI at Reliant Energy's Niles cyclone burner (CB) power plant and marketing it as metallurgical carbon. New sources are required to meet the demand of metallurgical carbon from fly ash. It is the objective of this study to obtain and test samples from other CB power plants in the U.S. to determine whether the high carbon fly ash from these plants could be used to meet the demand.

An initial list of the 30 CB plants larger than 100 MW in the U.S. was compiled. The list later grew to 36 plants, with the addition of four pulverized coal (PC) fired plants and two spreader stoker plants. All the plants were contacted to gather information and request samples to evaluate the potential to market fly ash as carbon from these plants.

The carbon from a CB plant was evaluated for surface area by BET and iodine number and the surface morphology was analyzed. The results revealed that the carbon from fly ash from CB's cannot be utilized as activated carbon, but should be marketed as metallurgical carbon.

Of the 36 plants, four plants were considered "promising", producing a product with an LOI between 75 and 80%. One of these plants was not a CB, but a spreader stoker that produced a coarse carbon fly ash. The spreader stoker produced the most carbon per MW of plant capacity of any of the plants. Another CB plant produces an 80% LOI carbon product that could be drawn directly from the economizer hoppers, while the other plants require size classification to produce a 75+% LOI product. Three additional plants produce a "marginal" 65%+ LOI product. The remaining plants either produced fly ash with too low of an LOI, marketed their own fly ash, or no longer operated as a CB unit. Collecting the carbon available in fly ash from the top four plants could increase carbon usage by 37,000 tons per year.

Introduction

Coal-fired power plant fly ash represents a potentially significant source for certain types of commercial carbon products from coal. In analyzing the fly ash from Reliant Energy's Niles power plant, PMET (Pittsburgh Mineral & Environmental Technology) engineers noted that the unique high carbon fly ash produced from combustion in a cyclone burner (CB) seems to be suitable for utilization in certain carbon markets with some process upgrading. Fly ash obtained by Pitt Carbon, a joint venture between PMET and U.S. Natural Resources (USNR), from this plant's air heater hoppers and certain electrostatic precipitator field hoppers averages 80% LOI with beneficiation to remove the -100 mesh material. While the Niles fly ash carbon has no sorptive capability, this material is being utilized in several steel making operations to produce foamy slags and as sacrificial carbon in electric arc furnaces. Other CB fly ash sources may be appropriate for the same coke substitute applications or even in some granulated activated carbon markets, such as wastewater treatment and flue gas injection, where customers are highly price sensitive and the purity requirements are less demanding.

If the fly ash from other CB's is similar, a significant new source of carbon for certain applications would be available. The power plant owners of these CB's would have a new beneficial use for a portion of their fly ash as well as the potential through upgrading for access to additional markets. The objective of this project is to obtain and test samples from a representative group of CB power plants to establish whether or not the ash characteristics noted at the Niles power plant are common to other CB coal-fired plants.

Currently, Pitt Carbon is marketing high carbon material (82% LOI) from the Niles power plant. This plant consists of two CB units with a capacity of 220 MW. It is hoped that this project will help to expand this type of operation to other power plants and expose a normally overlooked supply of carbon that exists in fly ash. Currently, it is estimated that 78 CB power plants exist in the United States, producing 20,000 MW of power. If the Niles plant could be considered a "typical" CB power plant, there may be as much as 640,000 tons of high carbon material per year, based on extrapolation of this data. While the best candidates will be tested for sorptive potential, all materials will be tested for carbon content. Due to devolatilization of the coal in the CB, this material will be suitable at a minimum for metallurgical applications as coke.

Executive Summary

Pitt Carbon, a joint venture between Pittsburgh Mineral & Environmental Technology (PMET) and U.S. Natural Resources (USNR), is currently collecting and marketing carbon from fly ash at Reliant Energy's Niles cyclone burner (CB) power plant. This fly ash was recognized as having value as a carbon product since it exhibits an LOI greater than 80%. It is currently marketed as metallurgical carbon for use in electric arc furnaces (EAF's). The carbon is added to the EAF to make it more energy efficient, increase refractory life, and minimize nitrogen and hydrogen in the steel. Attempts to utilize this material as activated carbon were not successful.

Currently, all the high carbon fly ash collected at Niles is being sold, requiring new sources of high carbon material from fly ash to be found to meet increasing demand. It is thought that, like the Niles plant, other CB power plants may produce a similar, high carbon fly ash. It is the objective of this study to obtain and test samples from a representative sample of CB power plants to determine whether the high carbon fly ash at Niles is common to other CB power plants.

CB power plants are unique in that they burn coarser coal (crushed to -4 mesh) than pulverized coal burners (pulverized so that 65 to 80% is -200 mesh). Because of this, the unburned carbon leaving a CB is coarser. An initial list of 30 CB plants larger than 100 MW was compiled and all were contacted. Information regarding the plants fly ash collection system and fly ash characteristics were compiled. Based on this information, samples were requested from plants whose fly ash might serve as a source of carbon. Six additional plants were identified through these contacts, including two plants utilizing spreader stoker burners that reportedly produced high carbon fly ash.

The carbon from one of the plants found in this study was evaluated for surface area by BET and iodine number. Compared to powdered activated carbon (PAC), it showed no promise of being used as an activated carbon, with almost ten times less surface area than PAC and one-fifth of the iodine number of PAC. Morphology also showed that the carbon from CB's is covered by slag. Therefore, it was determined that the carbon from fly ash from CB's should not be marketed as activated carbon, but rather as metallurgical carbon based on carbon content measured via LOI.

In all, 36 plants were contacted. Of these, four plants were labeled as "promising." Three of these plants made fly ash in a CB from which a 75+% LOI carbon product could be obtained by collecting fly ash either directly from specific hoppers or through size classification from specific hoppers. The plants ranged from a total capacity of 135 to 720 MW. Three CB units at the Kammer plant are believed to produce 60 tons per day of an 80% LOI carbon that can be obtained by collecting material directly from the economizer hoppers. Two units at the Sheldon plant produce 18 tons per day of material with an LOI of 75+% LOI, obtained by size classification at +50 mesh. The larger unit at the Asbury plant is believed to produce around 6 tons per day of an 80+% LOI product, obtained by size classification at +20 mesh. A spreader stoker plant, W.N. Clark, was

also found to produce high carbon fly ash. Although much smaller (40 MW total) than the other "promising" plants, it is believed to produce a stream of fly ash from which 17 tons per day of a 75+% LOI product is obtainable.

Three other plants, including Crane, Conesville, and New Madrid, produce "marginal" material, from which a 65+% LOI product can be obtained. However, to produce a premium product (80% LOI), some beneficiation is required to increase the LOI of the fly ash streams.

Of the 30 total CB power plants evaluated in this study, 27 plants were still being utilized as CB's, while two had been re-powered (one as a circulating fluid bed and another using natural gas), and one was no longer operating. Results were finalized for 21 of the 27 plants (78%). The remaining six plants showed some initial interest in marketing their fly ash, but did not share enough information or supply samples for a complete evaluation. Of the evaluated plants, 14% produced what is believed to be a marketable carbon, 14% produced a marginal carbon containing fly ash, 29% produced fly ash that did not contain enough carbon to be marketable, 19% were considered geographically undesirable to supply carbon to metallurgical markets, 14% currently market their own fly ash, and 10% were uncooperative and it is believed that they may market their own fly ash as well.

Regarding the other six plants investigated, four were pulverized coal (PC) burners and two were spreader stoker burners. None of the pulverized coal burners produced a high carbon fly ash. Even if one had produced a high carbon product, the fly ash from PC burners is too fine since metallurgical applications require carbon greater than 100 mesh in size. However, one of the spreader stoker plants, W.N. Clark, produces 18 tons per day of 75+% LOI coarse carbon. While this plant is the smallest of any of the plants in terms of MW production (40 MW total), it produces almost five times more carbon per MW than the Kammer plant. Utilization of carbon from the fly produced in these four plants could increase the usage of carbon from fly ash by as much as 37,000 tons per year.

Experimental

CB's were initially selected for this study due to the success of collecting and marketing carbon from fly ash at the Niles plant. Unlike a pulverized coal (PC) burner, the coal in a CB is crushed to only four mesh. Fly ash from PC burners was not initially sought due to the fineness of coal that they combust. The coal combusted in the PC burners is typically pulverized so that 65 to 80% is smaller than 200 mesh (74 μm). PC burners operate by injecting the coal with primary air into a chamber utilizing a variety of configurations. Additional secondary and tertiary air is often injected to further combustion. The carbon that is found in the fly ash of PC burners is too fine to use in metallurgical markets, as these markets require carbon larger than 100 mesh.

In CB's, the coal is tangentially injected into the cylindrical "cyclone furnace" with primary air. The fine coal particles are burnt in suspension, while the coarser particles are thrown to the outer wall of the furnace that is covered by a sticky molten slag. The coarse coal particles, now stuck to the outer wall, remain there until combusted. Tangential secondary air is also added at the top of the furnace to combust the coarse particles. Slag is tapped continuously from the bottom of the furnace. It is estimated that 20% of the ash from a CB is fly ash, while the remaining 80% of the ash exits as slag. In a PC burner, 80% of the total ash is fly ash. Figure 1 illustrates how a CB or cyclone furnace operates.

Figure 1 – Cyclone Furnace (*From Baumeister*, Marks' Standard Handbook for Mechanical Engineers, *7th ed., McGraw Hill, New York, 1967*)

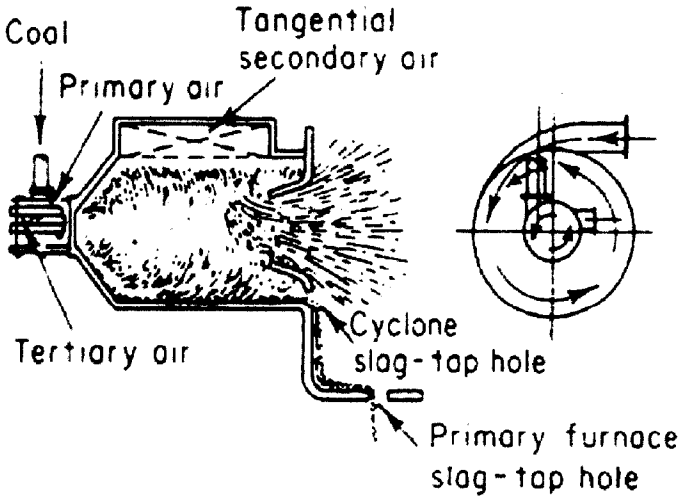

The large particle size of coal combusted in CB's helps to produce the large carbon particles that are recovered in the early fly ash recovery hoppers. The large size of the carbon particles also makes it easier to segregate the carbon from the ash using size classification.

Various power plant databases were accessed to identify the population of U.S. power plants utilizing CB's. After eliminating those plants smaller than 100 MW, the list of plants shown in Table 1 was developed. Originally, it was proposed to target 10-12 plants for visits and fly ash sampling and analyses. The results from these visits would have been extrapolated to the other CB plants. However, after several futile plant visits, it was determined that more progress could be made in the project by contacting the plants via phone to request information and samples. By doing so, information could be collected from all thirty CB plants found and listed in Table 1, instead of the 10-12 that were originally proposed. More detail regarding each plant is given in Appendix 1.

Table 1 – Cyclone Furnace Plants to be Screened for High Carbon Fly Ash

#	Plant Name	Location	# of Units	MW/Unit
1	England	Marmora, NJ	2	129 & 155
2	Conesville	Conesville, OH	2	125 each
3	Kammer	Moundsville, WV	3	210 each
4	Sioux	West Alton, MO	2	470 each
5	New Madrid	New Madrid, MO	2	580 each
6	Thomas Hill	Clifton Hill, MO	2	175 & 275
7	Crane	Baltimore, MD	2	190 each
8	Kincaid	Kincaid, IL	2	554 each
9	Stateline	Hammond, IN	2	187 & 303
10	Asbury	Asbury, MO	2	190 & 20
11	Muskingum River	Beverly, OH	2	240
12	Baldwin	Baldwin, IL	2	568 each
13	LaCygne	LaCygne, KS	1	682
14	Bailly	Chesterton, IN	2	160 & 320
15	Michigan City	Michigan City, IN	1	469
16	Schahfer	Wheatfield, IN	1	431
17	Sheldon	Hallam, NE	2	105 & 120
18	King	Bayport, MN	1	581
19	Riverside	Minneapolis, MN	1	222
20	Merrimack	Bow, NH	2	114 & 320
21	Big Stone	Big Stone City, SD	1	464
22	Powerton	Pekin, IL	2	782 each
23	Will County	Romeoville, IL	2	156 & 154
24	Marion	Marion, IL	4	34, 34, 34 & 170
25	Gannon	Tampa, FL	4	119, 199, 155, 189
26	Paradise	Drakesboro, KY	3	615, 615, 1036
27	Sibley	Sibley, MO	3	53, 52, 391
28	Allen	Memphis, TN	3	330 each
29	Dewey	Cassville, WI	2	109 & 105
30	Edgewater	Sheboygan, WI	2	71 & 327
		TOTAL	**62**	**18,678**

Information regarding coal sources, coal crushing size, burner types, fly ash collection system, and current fly ash marketing status were collected from each plant. Information regarding fly ash quantities and quality were also requested, although plant personnel often either did not have this knowledge or were unwilling to share it. More detailed individual plant reports are available in Appendix 2. After an understanding of the fly ash collection system was acquired, samples were requested from hoppers near the front end of the ash collection system, based on carbon collection experience at the Niles power plant. This experience has shown that carbon in fly ash from CB's exists as coarser particles than the ash portion. The coarse carbon typically drops out of the flue gas earlier than the fine ash particles. As each sample was received, it was screened for carbon content based on loss on ignition (LOI) tests according to ASTM standard C311. If the head LOI of the sample exceeded 50%, then the material was wet-screened by size fraction, and the LOI of each fraction was measured by the same ASTM standard. This was used to determine whether high carbon material could be collected by sizing only.

One fly ash found with greater than 80% carbon in large quantities (Kammer) was also tested to determine if it could be used as activated carbon. Other high carbon fly ashes were not tested since it was determined that carbon from CB's could not be used as activated carbon.

Through contacts made with the initial 30 plants listed in Table 1, leads to six additional plants were pursued. These additional plants are shown in Table 2. One lead led to the discovery of an additional CB. Three other potential leads turned out to be PC burners. The final two leads led to spreader stoker burners. This gave a total of 31 CB plants that were to be investigated and five other units.

Table 2 – Additional Plants Investigated

#	Plant	Location	# Units	MW	Notes
31	Coffeen	Montgomery County, IL	2	450 each	Cyclone Burners
32	Big Bend	Tampa, FL	4	450 each	PC Burners
33	Lake Road Plant	St. Joseph, MO	2	250 each	PC Burners
34	Seminole	Palatka, FL	2	650 each	PC Burners
35	Anheuser Busch	St. Louis, MO	2	13 each	Industrial Spreader Stoker
36	W.N. Clark	Canon City, CO	2	20 each	Spreader Stoker
		Total	**14**	**4,566**	

Although the spreader stoker units were smaller than the 100 MW cutoff used in this study, they were appealing due to the high LOI fly ash reportedly produced by them. Spreader stokers are more economical for applications requiring smaller power

requirements (typically less than 100,000 lbs/hr of steam). Similar to CB's, spreader stokers burn coarser coal than PC burners. They approximate the action of an overfeed stoker, propelling the coal into a furnace over a grating covering the bottom of the furnace. Air that passes through the grating combusts the coal. Approximately 30 to 50% of the coal fines are burnt in suspension before reaching the grating. The coarse particles and remaining fine particles reach the grate and are combusted. If excessive fines are present, more coal particles will be carried out of the furnace. Figure 2 is an illustration of an overfeed stoker in operation. Spreader stokers are more commonly found in industrial rather than utility applications. While the spreader stoker plants found in this study were much smaller than utility CB's (less than 100 MW), they are believed to be widely used in industrial applications. The quantity of spreader stokers is unknown at this time, as this information extends beyond the scope of this study. However, information was collected regarding two spreader stoker plants. They are listed in Table 2 and shown later in Figure 3 (represented by green circles).

Figure 2 – Overfeed Stoker (from Perry's Chemical Engineering Handbook, Sixth Edition, McGraw-Hill, 1984.)

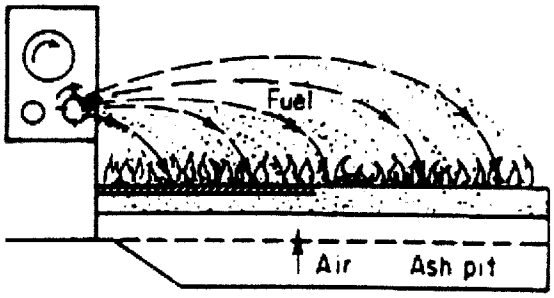

Figure 3 below shows the locations of all 36 plants investigated in the study, plotted on a map of the eastern half of the United States. The plant locations are primarily centered in the Midwest and are marked by solid colored shapes. Red squares indicate plants that have been sampled and are believed to be potential candidates for carbon marketing due to their elevated carbon content in some portion of the fly ash. Yellow diamonds indicate plants that have been eliminated as possibilities for a variety of reasons (described later in greater detail). Blue triangles indicate plants were unresponsive to requests for visits or samples. Green pentagons indicate spreader stoker plants that were found through contacts made during the study.

Figure 3 – Location and General Status of Power Plants to be Investigated

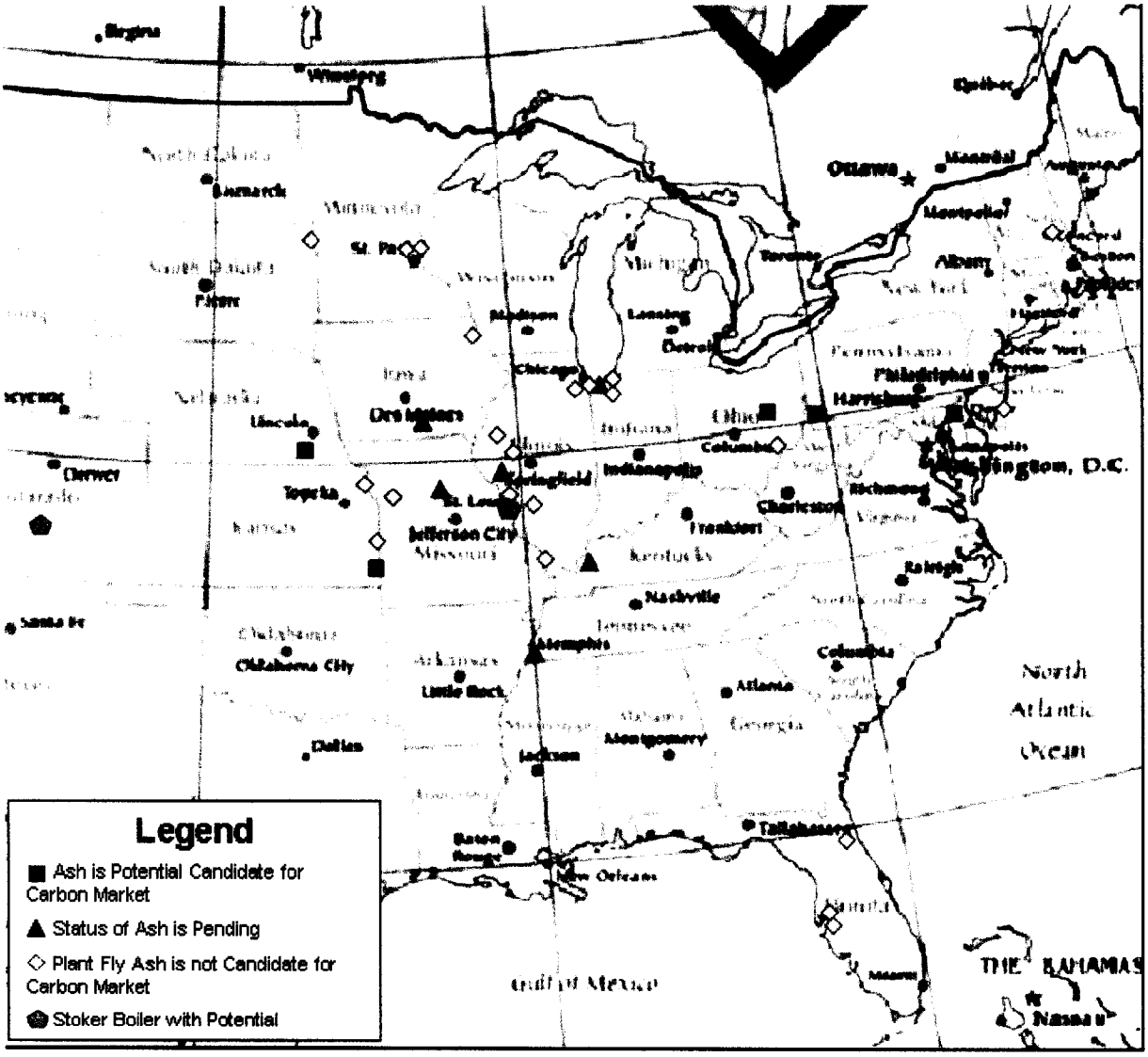

Paramount to the interpretation of the data is the understanding of where the fly ash samples come from in the flue gas handling train. The configuration of the flue gas handling system can be unique to each plant. A general configuration is described as follows:

1. Flue gas exits the burner and enters the "economizer" where it typically makes a sharp bend. The "economizer" can be used to pre-heat boiler water. The economizer hopper's function is to catch large pieces material that are airborne in the flue gas stream. Sometimes, large chunks of material, often carbon, can be found in these economizer hoppers.

2. The flue gas then enters the air pre-heaters. The purpose of this section is to pre-heat air used for combustion in the burner. The flue gas also makes a sharp turn through this section, causing additional fly ash to fall into the "air-heater" or "mechanical" hoppers. Coarse carbon material can also be collected here.
3. The flue gas exits the "mechanical air pre-heaters" and now contains mostly fine particles. It enters the electrostatic precipitators (ESP's) which function by imparting a negative charge on the fly ash particles by passing through negatively charged pipes. The flue gas next passes by positively charged plates which collect the negatively charged particles. The flue gas at this point is now entirely free of particles.

Figure 4 is a diagram of the New Madrid plant from AECI's website (Associated Electric Cooperative Inc.). The ash collection points are labeled in red as the Economizer Hopper, Air Heater Hoppers, and ESP hoppers. Additionally, the New Madrid power plant operates with selective catalytic reduction (SCR) between the economizer and air heater hoppers for NO_x control. This particular plant also collects fly ash in its SCR hoppers. Most plants use variations of this set-up. Fly ash may or may not be collected in hoppers in the economizer or air heaters. SCR's are not used at all plants. Another variation includes wet scrubbing the fly ash with water rather than ESP's to knock out the fine particles. Once the ash is sluiced, it would have to be dried before being used as metallurgical coke, making recovery less economically appealing. Another option is to replace or augment the ESP's with a baghouse. However, the ESP's are more economical in larger plants than a baghouse.

Figure 4 – Ash Collection at New Madrid Power Plant

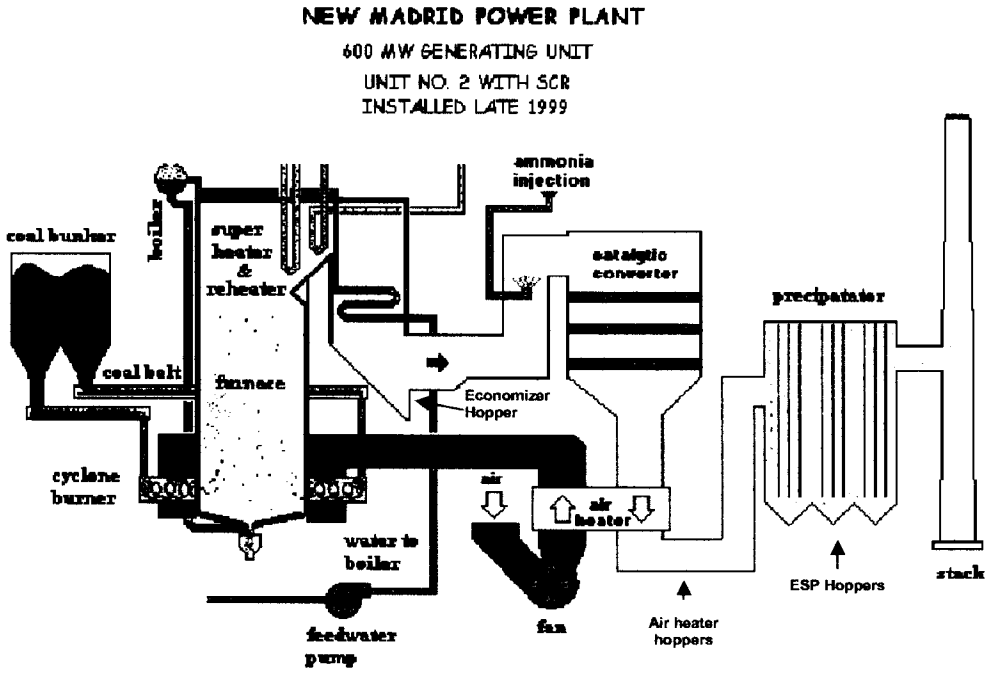

Results and Discussion

Carbon Markets

The carbon currently marketed by Pitt Carbon from the Niles plant is used in metallurgical applications. EAF's (electric arc furnaces) are the "...largest users of electric energy in industry[1]." The use of a foamy slag is considered the best method to make EAF's more energy efficient by performing a number of functions. Carbon injected to the alloy/stag interface can be oxidized, supplying between 30 and 40% of the heat input to the furnace[2]. The added carbon can also help to reduce iron oxide to iron, producing CO and some CO_2. The resulting CO and CO_2 gas produces bubbles which are caught in the slag layer, producing a foaming effect and providing a number of benefits. The foaming action of the slag helps to bury the arc, giving greater thermal efficiency by providing an "insulating" layer. This allows the furnace to operate at high arc voltages and increase the arc length without losing energy. The foamy slag reduces the amount of heat lost via radiation from the bath which extends refractory life and reduces energy loss. The foaming slag can also help to protect cooling panels by forming a frozen slag layer over them. Overall, foamy slag practices are estimated to save 3-10% in energy and decrease refractory consumption by 25-63%[3]. Foamy slags are also credited with reducing noise levels around EAF's. The foamy slag layer also provides a gas barrier, preventing atmospheric nitrogen from entering the steel. Carbon monoxide formed in the bath also aids in stripping nitrogen and hydrogen from the steel, both of which are detrimental to the strength of steel. Practical carbon injection rates are cited as "29 Nm^3 per tonne."[4]

Markets for metallurgical carbon can be found anywhere near steel production locations. Plants not within a reasonable location as determined by Pitt Carbon were eliminated. Pitt Carbon has estimated that the market demand exists to utilize carbon with a 75% LOI or greater.

Another potential use of carbon from fly ash is as activated carbon. In a study prepared for PMET by Dr. Mick Greenbank[5], it was concluded that in activated carbon markets, the most likely applications for carbon from fly ash were wastewater purification and flue gas injection. These carbons would require an iodine number of at least 550. Dr. Greenbank's report described the tests required to characterize carbons from fly ash to determine the highest value application for which they are suited. These tests were performed on a few samples of carbon from fly ash collected during the project.

Powdered activated carbon (PAC), along with carbon from Niles and Kammer (a plant found to produce 80% LOI carbon), were tested for surface area via BET and iodine number to determine their potential as an activated carbon. Table 3 summarizes these results.

Table 3 – Potential of Fly Ash Carbon for Activation

Material	Surface Area by BET (m^2/g)	Iodine No.
Powdered Activated Carbon	628	461
Kammer Carbon	24	63
Niles Carbon	18	70

The PAC was tested as a control to give relevance to the results generated by the Niles and Kammer carbons. Niles had already been determined not to be suitable for the activated carbon market. The same conclusion was drawn with regards to the Kammer carbon, as it exhibits a surface area that is a magnitude less than the PAC. Likewise, its iodine number is five times less than the PAC.

Morphology helps to explain why the carbon from CB's exhibits such a low surface area and iodine number. Figure 5 is an SEM at 25x of carbon from a CB. The carbon appears to be covered by a layer of slag. This is not surprising since the coal particles are stuck to the slag layer on the outer wall, thrown there by the centrifugal force of the CB.

Figure 5 – Carbon in Fly Ash from a CB (25x Magnification)

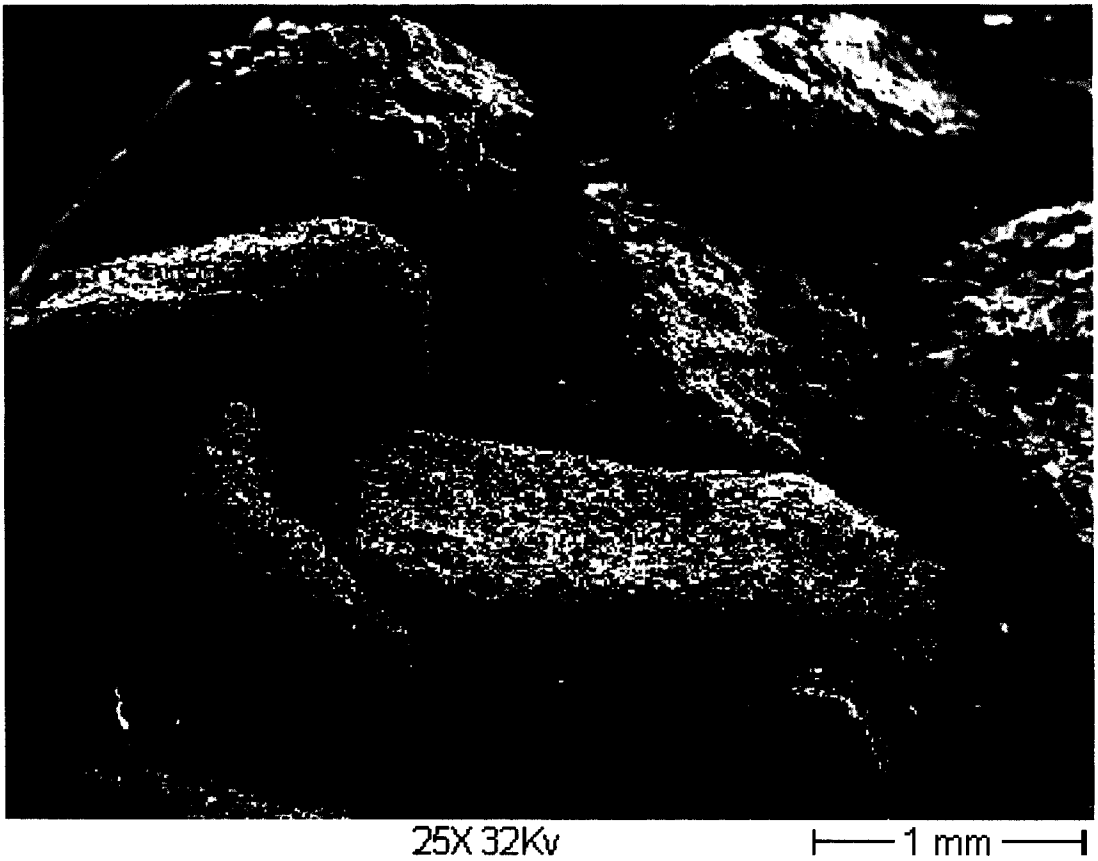

By comparison, Figure 6 is an SEM of carbon particles in fly ash produced by a PC burner. The pores can be seen in this carbon and the slag coating is not visible.

Figure 6 – Carbon from a PC Burner (500x Magnification)

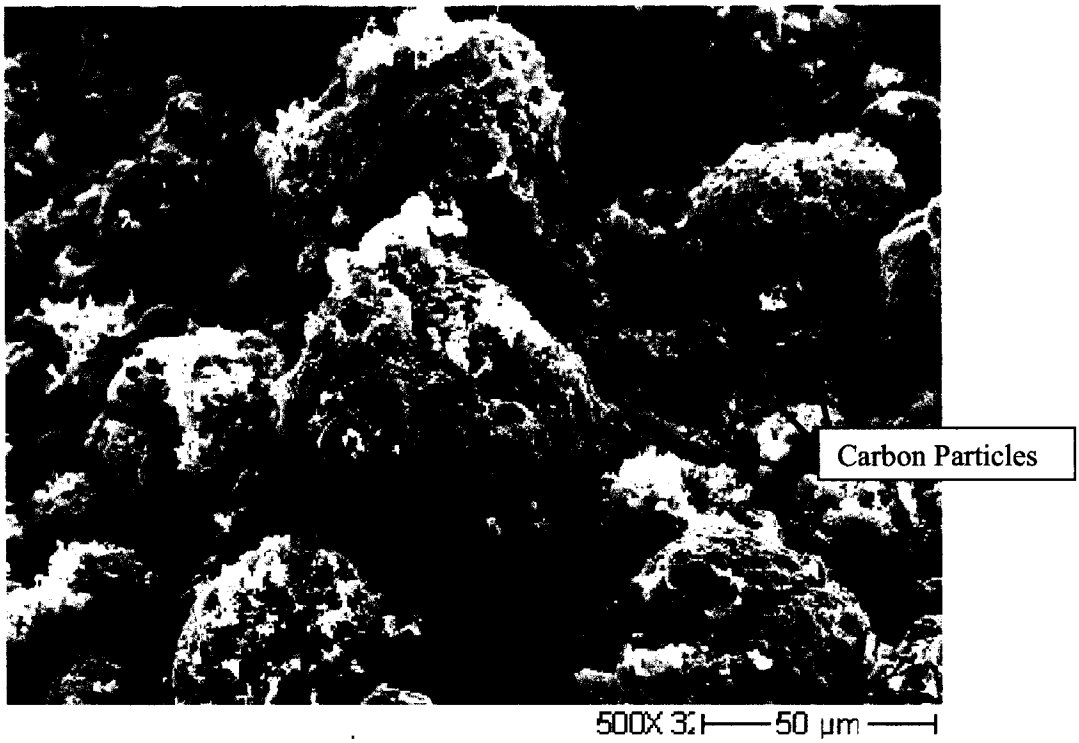

By combining the surface area, iodine number, and morphology study results, it was determined that carbon from fly ash generated in CB's was not suited for activated carbon applications. The best use for carbon in fly ash from CB's was determined to be metallurgical applications.

Summary of Carbon from CB Plants

Table 4 shows the status of the project with regard to all 31 CB power plants, 3 PC fired plants (marked with *), and two spreader stoker plants (marked with **). Conclusions regarding the marketability of carbon from each plant were made based on either tested samples or information gathered from the plant. Appendix 2 contains more detailed reports regarding each plant.

Table 4 – Project Status of Power Plant Fly Ash Evaluation for Carbon

Status	Plants Included	Detail
	Kammer (WV)	80+% LOI in +100 mesh material
	W.N. Clark Stn. (CO)**	75+% LOI in +50 mesh material
	Sheldon (NE)	75+% LOI in +50 mesh material
	Asbury (MO)	80+% LOI in +20 mesh material
	Crane (MD)	65+% LOI in +50 mesh material
	Conesville (OH)	60-65% LOI in +10 and +25 mesh material
	New Madrid (MO)	55+% LOI, in +50 mesh material
Out	Sioux (MO) Kincaid (IL) Stateline (IL) Muskingum River (OH) Michigan City (IN) Sibley (MO) Seminole (FL)*	LOI too low to be Useful in Carbon Market
	England (NJ) Baldwin (IL) LaCygne (KN) Lake Road Plant (MO)* Big Bend (FL)*	Already recycle fly ash, no interest to market carbon
	Schahfer (IN)	Not Cyclone Burner
	King (MN) Riverside (MN) Merrimack (NH) Big Stone (SD)	Geographically Undesirable for Metallurgical Carbon Market
	Powerton (IL) Dewey (WI)	No interest/cooperation from plant
	Will County (IL)	No longer operating
	Marion (IL) Gannon (FL)	Re-powered with Alternative Generation
Pending	Thomas Hill (MO) Bailly (IN) Paradise (KY) Edgewater (WI) Allen (TN) Coffeen (IL) Anheuser Busch (MO)**	Waiting for Sample

Promising Plants

Four plants whose samples were obtained are considered "promising".

Kammer Plant

The first promising plant to be found, Kammer, is located near Moundsville, WV. A plant visit was conducted in June of 2003 and samples from the plant were obtained. The plant produces a total of 720 MW utilizing 3 CB's. Each power generating burner at this plant collects fly ash utilizing five economizer hoppers and 5 rows of ESP's with 8 hoppers per row. While there are air pre-heaters in this plant, air heater hoppers are not utilized. Therefore, the best opportunity to collect carbon is from the economizer hoppers. Table 5 summarizes the LOI of fly ash in the economizers from units 1, 2, and 3.

Table 5 – Summary of Fly Ash LOI Collected from Kammer Economizer Hoppers

Cyclone Unit #	Hopper #	LOI
1	50	80.3%
	51	80.4%
	52	80.8%
	53	77.8%
	54	78.7%
	Average:	80%
2	50	81.9%
	51	80.3%
	52	79.7%
	53	81.4%
	54	82.8%
	Average:	81%
3	50	78.4%
	51	78.9%
	52	79.3%
	53	79.4%
	54	79.4%
	Average:	79%
	Overall Average:	**80%**

Each set of economizers collects approximately 20 tons per day of fly ash. This will produce almost 60 tons per day of 80%+ LOI material that can be marketed for metallurgical purposes. The -100 mesh fines, which are estimated to make up 3 to 6% of the overall material, must still be removed to make the carbon usable in metallurgical applications. The large quantity of carbon available makes installing an operation at this plant attractive. It is much larger than Niles (720 total MW vs. 218 total MW) and the estimated 60 tons per day of high carbon fly ash to be collected from the economizers is

three times the quantity available at Niles. The plant is located along the Ohio River and coal is barged to the plant. Moving the carbon via barge may be advantageous if far away markets are found. Collecting fly ash from the ESP hoppers is also a future option, but it will require size classification. However, this material has shown inconsistencies in LOI and quantities collected.

Based upon the LOI analysis of the Kammer Fly Ash, it is an ideal candidate to be used as metallurgical coke. Other material in the fly ash, such as ash and sulfur, would have to be considered when marketing the carbon to particular plants.

Sheldon

The Sheldon plant is located in Hallam, NE, approximately 80 miles southwest of Omaha, NE. The plant consists of two CB units producing 120 MW and 105 MW each. This plant is unique in that the fly ash is not collected in economizer or air-heater hoppers, but collected in the ESP hoppers only. After the flue gas passes through the ESP fields, additional material is collected in a baghouse. Samples were obtained from the hoppers under the first set of ESP fields since large pieces of carbon would most likely drop out of the flue gas stream in these hoppers

A sample of material from the first ESP hopper row was analyzed at PMET. Table 6 summarizes the LOI by size fraction results:

Table 6 – LOI by Size Fraction of Sheldon Fly Ash

Size Fraction	Weight %	LOI %	LOI Distribution	Cumulative Weight %	Cumulative LOI%
+20 mesh	24.7%	68.6%	22.6%	24.7%	68.6%
+35 mesh	29.9%	83.5%	33.3%	54.6%	76.8%
+50 mesh	16.9%	76.9%	17.1%	71.5%	**76.8%**
-50 mesh	28.5%	55.6%	27.1%	100%	70.7%
Total (Head)	100%	70.2%	100%		

Table 6 shows that pulling material from the first ESP hopper row results in a carbon product with a 70.2% LOI. However, this material could be upgraded to 76+% by removing the -50 mesh material (smaller than 300 microns). The coarser material is predominantly carbon, while the finer material contains more ash. Whether this upgrade in quality is worthwhile would be an economic decision based on the carbon quality requirement of customers.

The Sheldon plant is considered to be within range of the Nucor Steel plant in northeastern Nebraska. While the exact figure could not be pinpointed by plant personnel, it is estimated that this plant would generate between 17 and 34 tons per day

of 70+% LOI fly ash. Upgrading the product to 75+% LOI by size classification would decrease this figure to 12 to 24 tons per day of carbon.

W.N. Clark Station

If it were a CB, the small size of W.N. Clark Station (located in Canon City, CO, approximately 120 miles south of Denver, CO) would have excluded it from this study. Even though it is a small plant (40 MW total), the spreader stoker burner at W.N. Clark appears to be an excellent source of carbon. More commonly used in industrial burners rather than utility burners because of their lesser MW capacities, stoker burners burn coarser coal than PC burners, much like CB's. While a small individual spreader stoker may not generate as much energy or fly ash as the larger CB and PC burners, carbon from spreader stokers around the country may provide a significant source of carbon.

The W.N. Clark station collects fly ash using an economizer and baghouse. Air heater hoppers and ESP hoppers are not used to collect fly ash at this plant. Currently, fly ash collected in the economizers is used for reburn, common in spreader stokers. In this spreader stoker, 70% of the ash is estimated to be fly ash, while the 30% balance is bottom ash (CB's typically run at a 4:1 ratio of bottom ash:fly ash.) The fly ash is collected in economizer hoppers followed by a baghouse. Currently, the bottom ash is combined with the fly ash from the baghouse and land-filled. A carbon collecting operation would collect only the baghouse material. Table 7 provides a summary of the LOI by size fraction of the baghouse material.

Table 7 – LOI by Size Fraction of Baghouse Fly Ash from W.N. Clark Station

Size Fraction	Weight %	LOI %	LOI Distribution	Cumulative Weight %	Cumulative LOI%
+20 mesh	5.7%	87.3%	9.5%	5.7%	87.3%
+35 mesh	17.0%	82.8	27.0%	22.7%	83.9%
+50 mesh	16.6%	65.2%	20.8%	39.3%	**76.0%**
-50 mesh	60.7%	36.8%	42.8%	100%	52.2%
Total (Head)	100%	50.2%	100%		

Table 7 clearly shows that the baghouse material cannot be marketed without some classification. However, by recovering the +50 mesh material, a carbon product with a 75+% LOI could be obtained. This would produce a sellable product from 39% of the baghouse material that is currently land-filled. Estimates from that plant indicate that this would result in 17 tons per day of material that could be marketed as metallurgical coke based on the estimate that 70% of the ash is fly ash. Further analysis of Table 7 reveals that an 80+% LOI could be collected by sizing the fly ash at 35 mesh. However, this would decrease the baghouse recovery from 39% to 23%.

An analysis using X-Ray Fluorescence Spectroscopy (XRF) performed on the fly ash revealed that that 51% of the ash was SiO_2 and 38% of the ash was Al_2O_3. The remainder

of the ash consisted of CaO and Fe_2O_3 and other minor elements. The sulfur content of the material was less than 0.4%.

Historical data indicates that the LOI of the material is stable. Data obtained from 1997 shows a head LOI of 56.1% for fly ash from W.N. Clark Station. It also shows an LOI of 75% for material larger than 60 mesh, where the +60 mesh material made up 50% of the total fly ash. These results are very similar to those exhibited by the sample collected this year and summarized in Table 7.

Asbury

The Asbury plant is located in Asbury, MO, about 140 miles south of Kansas City, MO. This plant consists of two CB's, one rated at 205 MW and a second, much smaller unit, rated at 20 MW. Fly ash at the plant is collected in air heater hoppers and ESP hoppers. After exiting the air heater hoppers, a high LOI material is collected under the first ESP in the first row of ESP hoppers. Afterwards, on the inlet to the 2nd row of ESP hoppers, a second group of material is collected. Finally, in the 2nd row of ESP hoppers, a 3rd set of hoppers collect additional fly ash. Currently, all the fly ash at the plant is being placed in a pond.

Samples requested and received from all three sets of ESP hoppers showed a decrease in LOI of the fly ash as one proceeds through the system. The most promising material was collected from the 1st set of ESP hoppers. Table 8 below shows that the +20 mesh material appears to be very marketable with an 80+% LOI. Plant personnel could not give an estimate as to the quantity of fly ash collected in individual hoppers, although the total plant output is estimated at 15,000 to 25,000 tons per year. Assuming the fly ash is collected evenly among the three sets of hoppers, the first set of ESP hoppers might collect between 15 and 25 tons per day. Of this material, based on the LOI by size fraction in Table 8, this would give approximately 3.5 to 6 tons per day of material 80+% LOI fly ash. However, this estimate is probably conservative, as more material would drops out earlier in the ESP hoppers. Samples from the air heater hoppers have been requested, but not received. If additional, high LOI material can be found in these hoppers, this may make the plant worthy of pursuit.

Table 8 – LOI by Size Fraction of 1st ESP Row of Asbury Plant

Size Fraction	Weight %	LOI %	LOI Distribution	Cumulative Weight %	Cumulative LOI%
+20 mesh	24.3%	82.2%	39.9%	24.3%	**82.2%**
+50 mesh	33.9%	56.0%	38.0%	58.2%	66.8%
+80 mesh	4.2%	40.7%	3.4%	52.4%	65.1%
-80 mesh	37.5%	24.8%	24.8%	100%	50.0%
Total (Head)	100%	49.6%	100%		

Samples from the 2nd ESP row inlet and 2nd ESP hoppers exhibited LOI's of 28.3% and 6.9% respectively, making them unlikely to be sources of marketable carbon.

Marginal Plants

Three plants were contacted whose fly ash was considered marginal.

Crane

The Crane plant is located near Baltimore, MD. It consists of two CB's, each producing approximately 200 MW. Fly ash is collected using air heater hoppers and a baghouse to collect the fine material. All of the fly ash is combined in a silo and sent to a landfill. It is estimated that the plant produces 50,000 tons per year of fly ash (estimated at 137 tons per day). Table 9 summarizes the LOI by size fraction of the sample from the fly ash silo.

Table 9 – LOI by Size Fraction of Crane Fly Ash (Baghouse and Air Heater Hoppers Combined)

Size Fraction	Weight %	LOI %	LOI Distribution	Cumulative Weight %	Cumulative LOI%
+20 mesh	24.6%	64.1%	26.3%	24.6%	64.1%
+35 mesh	42.5%	71.0%	50.2%	67.1%	68.5%
+50 mesh	20.3%	60.4%	20.4%	87.4%	**66.6%**
-50 mesh	12.6%	14.9%	3.1%	100%	60.1%
Total (Head)	100%	54.2%	100%		

A carbon stream exhibiting greater than 65% LOI will be difficult to obtain from this fly ash unless it is beneficiated in some other manner to purify the carbon stream beyond size classification. However, the 65% LOI product that could be obtained from the +50 mesh fraction classifies it as marginal.

Conesville

The Conesville plant, located in Conesville, OH, was visited in June of 2003. It is powered by two CB units, rated at 125 MW each. Fly ash is collected at Conesville utilizing 2 economizer hoppers and 8 ESP hoppers for each unit. Each economizer hopper was sampled and the results are summarized in Table 10.

Table 10 – Potential Carbon Products from Conesville Economizer Hoppers

Recovery Point	Cut	Potential Carbon Product LOI	Recovery of Hopper
Unit 1, Hopper 1	+25 mesh	64%	83%
Unit 1, Hopper 2	+10 mesh	65%	16%
Unit 2, Hopper 1	+25 mesh	68%	87%
Unit 2, Hopper 2	+10 mesh	59%	4%

Table 10 shows that a 65% product can be obtained by collecting the favorable size fractions from each product. It is estimated that each hopper collects approximately 5 tons per day of fly ash. This results in approximately 9.3 tons per day of the 65% LOI product to be obtained. Due to the low output and low LOI of product, this plant was not placed in the promising category.

New Madrid

The final plant to be considered a marginal plant was the New Madrid plant, located in New Madrid, MO. This plant was one of the larger plants to be sampled, consisting of two 600 MW burners. It is estimated that this plant produces 92,500 tons of fly ash per year. The fly ash collected in the economizer, air heater, and SCR hoppers makes up approximately 20% of the fly ash collected, while the other 80% is collected in the ESP hoppers. The fly ash collected in the Economizer and ESP hoppers does not appear to be suitable as a carbon source, its LOI ranging from 10 to 24%. Samples from the air heater hopper and SCR hopper appeared to be more encouraging, as shown in Table 11.

Table 11 – Potential Carbon Products from New Madrid Air Heater and SCR Hoppers

Recovery Point	Cut	Potential Carbon Product LOI	Hopper Recovery
Air Heater Hopper	+35 mesh	49%	54%
SCR Hopper	+35 mesh	60%	50%

The fly ash recovered in the SCR Hopper appears to be the only material that could potentially be marketed. This quantity of fly ash from this hopper is estimated to be only 20 tons per day, small especially when considering the size of this plant. Most likely, the carbon content of this stream would be too low to successfully market.

Plants eliminated from consideration

A number of plants were eliminated from future consideration through this study. They are listed below, along with a few facts regarding the fly ash from each plant. A * indicates a PC burner plant.

Sioux (MO) – Economizer and air heater hopper fly ash samples were obtained. Neither exhibited high enough LOI to merit further study (13.5% and 6.1% respectively).

Kincaid (IL) – Fly ash from one air heater hopper exhibited a 50% LOI. However, quantity from one air heater hopper is too small to merit pursuit.

Stateline (IL) – LOI of fly ash from air heater hoppers measured only 15%.

Muskingum River (OH) – Best fly ash from one air heater hopper measured 45% LOI.

Michigan City (IN) – Fly ash sample from economizer exhibited 3.2% LOI.

Sibley (MO) – Fly ash from economizers measured 4.8% LOI.

Seminole (FL)* - This plant collects all of their fly ash using ESP hoppers since the economizer and air-heater hoppers were eliminated. Best LOI of fly ash from ESP's is estimated by plant personnel to be 17%.

Five other plants were eliminated as they already recycle their fly ash. These include England, Baldwin, LaCygne, Lake Road*, and Big Bend*. Normally, the fly ash was reportedly utilized for cement additive, indicating that the LOI was fairly low at any rate. Otherwise, it could not have been used in such an application.

The Schahfer plant in Indiana was found to be a "T-fired" PC burner, not a CB. Due to the poor success of finding high LOI fly ash from PC burners and given that they produce too fine of a carbon for metallurgical applications, this plant was not further pursued. Four plants (King, Riverside, Merrimack, and Big Stone), listed as "geographically undesirable", were eliminated since they did not fall within proximity of any end users of metallurgical coke. Two plants (Powerton and Dewey) refused to communicate any information. It is unknown whether these plants were already marketing their ash or were content to continue land-filling their ash. One plant (Will County) was no longer operating. Two plants, Marion and Gannon, were re-powered using alternative methods (natural gas and as a circulating fluidized bed reactor).

Seven plants that were contacted still have not supplied samples of fly ash. Of the seven, none appear to be overwhelmingly promising except one. Anheuser Busch currently operates their power generating facilities, including utilization of two spreader stokers, each producing approximately 13 MW. They are eager to utilize their fly ash from the spreader stokers, which are believed to produce fly ash with elevated LOI's. However, at the close of this report, further information is not available.

Conclusions

In all, evaluation of 36 plants was attempted. Of these plants, conclusions were drawn for 29 of the plants. Of the 30 CB plants initially scoped for this study, 26 are still operating as CB units. One of the plants has shut down, two plants were re-powered, and one plant was a PC burner. Of the six additional units added to the study, one was a CB, three were PC burners, and two were spreader stokers.

Of the 27 total operating CB's in the study, conclusions were drawn on 78% of them (21 plants). Table 12 summarizes the results found in these 21 plants.

Table 12 – Overall Summary of Carbon Collection Potential for 21 Operating CB Plants

Conclusion Drawn	% of Plants
Makes Marketable Carbon Material	14%
Make Marginal Carbon Material	14%
Fly Ash Unsuitable for Carbon Marketing	29%
Currently Markets Fly Ash	14%
Geographically Undesirable	19%
Unknown/Uncooperative	10%

Of the CB's, six plants remain without a final conclusion. Since it is known that these plants are in geographically desirable locations, they do not currently market their ash, and have offered some cooperation, these plants should fall along the same distribution of the first three categories in Table 12. By extrapolating the information from Table 12, of the remaining 6 plants, 1-2 plants should produce marketable material, 1-2 plants should produce marginal material, and 3 plants should produce material that will not be marketable. The only non-CB plant without a final conclusion was a spreader stoker plant owned by Anheuser Busch.

The only spreader stoker burner to be fully analyzed in this study, W.N. Clark Station, produced material that appears to be marketable with some size classification. The spreader stoker units were found to be similar to CB's in that they both burn fairly coarse coal, which is an important factor with regards to producing high LOI fly ash. It is very encouraging information considering that there may be many small spreader stokers whose fly ash is currently unmarketable due to its high carbon content

Of the four PC fired burners in this study, none showed any indication of producing material that could be marketed for carbon. It is believed that pulverizing the carbon has two effects:

1. Combustion is more efficient, leading to lower LOI's in the fly ash
2. Pulverized coal will lead to less of a difference in size between carbon and ash particles in the fly ash. This is most likely the reason high LOI material was not found in upstream hoppers (such as economizers or air heater hoppers.)

3. PC fired burners make fly ash that is too fine for the metallurgical carbon market

The spreader stoker found in this study is estimated to produce at least 3 times more marketable material per MW than any of the three CB's that also produced marketable material. The W.N. Clark plant produces almost five times more carbon product per MW than the Kammer plant. The spreader stoker at W.N. Clark Station is estimated to produce 17 tons per day of material from 40 MW of capacity. The Kammer plant is estimated to produce 60 tons per day from 720 MW. The Sheldon plant is expected to produce 18 tons per day from 135 MW. The Asbury plant is thought to produce as much as 6 tons per day from 205 MW of capacity. Table 13 summarizes the tons of carbon per day produced per MW at the three most promising plants and the current Niles operation.

Table 13 – Estimated Tons of Marketable Carbon per MW Capacity

Plant	Type	Capacity	Estimated Tons per Day of Carbon / MW
Niles	Cyclone Burner	220 MW	0.09
Kammer	Cyclone Burner	720 MW	0.08
Sheldon	Cyclone Burner	135 MW	0.13
Asbury	Cyclone Burner	205 MW	0.03
W.N. Clark	Spreader Stoker	40 MW	0.43

Of the two fly ash carbon samples analyzed for surface area and iodine number in this study (Niles and Kammer), both had a magnitude less surface area and approximately one fifth of the iodine number as activated carbon. Morphology determined by SEM of the carbon shows a layer of slag surrounding the carbon. Even if high purity carbon streams can be obtained from power plants, it appears that there is little hope to utilize carbon from fly ash for activated carbon applications. Metallurgical applications have been determined to be the best outlet for carbon from CB's.

This study has also further demonstrated a trend seen at Niles. At the Niles operation, the highest LOI fly ash is normally found upstream in the flue gas train. The highest LOI material from the ESP's is always found in the first few ESP hoppers. This is a trend that has shown to be consistent with the highest LOI fly ash collected in the first hoppers where fly ash is collected. Examples of this are the high LOI fly ash collected in the economizer hoppers at Kammer, the fly ash collected in the first row of ESP's at Sheldon, and the high LOI material collected in the first row of ESP's at Asbury. Other plants show the same general trends, indicating that the unburned carbon is often coarse, dropping out of the flue gas stream as soon as possible. Even though the ash portion of the fly ash is denser, it is a finer material and normally drops out later in the ESP's.

Overall, this study has found four additional "promising" plants in which operations to collect carbon from fly can be installed. Table 14 summarizes the quantity and quality of these carbon products.

Table 14 – Summary of Promising Plants Carbon Product's Quantity and Quality

Plant	Plant Capacity	Estimated Quantity	Estimated Quality
Kammer	720 MW	60 tons per day	80%+ LOI
Sheldon	135 MW	18 tons per day	75+% LOI
W.N. Clark	40 MW	17 tons per day	75+% LOI
Asbury	205 MW	6 tons per day	80+% LOI

This study has shown that there are carbon streams available from CB's. While the percentage of plants producing fly ash streams containing high levels of carbon is not as high as previously hoped, three new CB power plants and one spreader stoker plant were found where operations may be put in place to obtain and market this carbon from coal as metallurgical carbon or coke. Collecting carbon from all four plants would increase carbon usage from coal by as much as 37,000 tons per year. Of the 640,000 tons thought to exist from CB's, this covers 31,000 tons per year after sampling 17,250 MW of the 20,000 MW believed to exist in CB's. Other plants, labeled as marginal plants, also produce elevated levels of carbon in their fly ash. While the carbon from these plants is not as easily obtained as the top four plants in this study, the carbon from these plants may be later obtained using fly ash beneficiation methods to separate the carbon from the fly ash.

Appendix 1 – Plant Summaries

Plant Name	Unit	MW	Unit Number	State	Address	Phone Number	Fly Ash Production
England	1 2	129 155	2378	NJ	900 N Shore Rd. Marmora, NJ 08223	609-390-5104	All recycled
Conesville	1 2	125 125	2840	OH	47201 Cr 273 Conesville, OH 43811	614-829-2378	Combined Cyclone Units produce ~20 tpd
Kammer	1 2 3	210 210 210	3947	WV	PO Box K Moundsville, WV 26041	304-845-6220	22,000 tpy from the economizers
Sioux	1 2	470 470	2107	MO	8501 N. State, Rt. 94 West Alton, MO 63386	314-992-6201	55,000 tons
New Madrid	1 2	580 580	2167	MO	PO Box 159 New Madrid, MO 63869	314-643-2211	92,500 tons
Thomas Hill	1 2	175 275	2168	MO	Rt. 1, Box 87 Clifton Hill, MO 65244	816-261-4211	No data available for ash from cyclone units only

Plant Name	Unit	MW	Unit Number	State	Address	Phone Number	Fly Ash Production
Crane	1 2	190 190	1552	MD	Carroll Island Rd. Baltimore, MD 21027	410-787-5372	49,600 tons
Kincaid	1 2	554 554	876	IL	PO Box 80 Kincaid, IL 62540	217-237-4311	71,700 tons
Stateline	3 4	187 303	981	IN	103rd & Lake Michigan Hammond, IN 46320	219-659-0036	37,100 tons
Asbury	1 2	190 20	2076	MO	PO Box 53 Asbury, MO 64832	417-623-4700	29,000 tons
Muskingum River	1 2	240 240	2872	OH	PO Box 140 Beverly, OH 45715	614-984-2321	No data available for ash from cyclone units only
Baldwin	1 2	568 568	889	IL	PO Box 146 Baldwin, IL 62217	618-785-2294	147,400 tons
LaCygne	1	682	1241	KS	RR No 1 LaCygne, KS 66040	913-757-4451	129,000 tons
Bailly	7 8	160 320	995	IN	246 Bailly Station Rd. Chesterton, IN 46304	219-787-7301	46,000 tons

Plant Name	Unit	MW	Unit Number	State	Address	Phone Number	Fly Ash Production
Michigan City	12	469	997	IN	100 N. Wabash Michigan City, IN 46360	219-873-7204	39,000 tons
Schahfer	14	431	6085	IN	2723 E. 1500 N. Wheatfield, IN 46392	219-956-5101	Plant does not use cyclone burners
Sheldon	1 2	105 120	2277	NE	PO Box 88 4500 West Pella Rd. Hallam, NE 68368	402-787-2555	22,000 tons
King	1	581	1915	MN	1103 King Plant Road Bayport, MN 55003	612-330-7646	42,700 tons
Riverside	8	222	1927	MN	3100 Marshall St. N.E. Minneapolis, MN 55418	612-330-7646	38600 tons
Merrimack	1 2	114 320	2364	NH	97 River Road Bow, NH	603-224-4081	No fly ash data reported
Big Stone	1	464	6098	SD	PO Box 218 Big Stone City, SD 57216	605-862-8125	41,000 tons

Plant Name	Unit	MW	Unit Number	State	Address	Phone Number	Fly Ash Production
Powerton	5	782	879	IL	13082 E. Manito Rd	309-346-2165	95,000 tons
	6	782			Pekin, IL 61554		
Will County	1	156	884	IL	529 E. Romeo Rd.	815-886-1010	83,300 tons
	2	154			Romeoville, IL 60441		
Marion	1	34	976	IL	PO Box 607, Rt. 4	618-964-1448	23,000 tons
	2	34			Lake of Egypt Rd.		
	3	34			Marion, IL 62959		
	4	170					
Gannon	1	119	646	FL	PO Box 111	813-228-4111	107,000 tons
	2	119			Tampa, FL 33619		
	3	155					
	4	189					
Paradise	1	615	1378	KY	PO Box 800	502-476-3300	102000 tons
	2	615			Drakesboro, KY 42337		
	3	1036					
Sibley	1	53	2094	MO	33200 E. Johnson Rd.	816-249-6196	52,800 tons
	2	52			Sibley, MO 64088		
	3	391					

Plant Name	Unit	MW	Unit Number	State	Address	Phone Number	Fly Ash Production
Allen	1	330	3393	TN	2574 Plant Rd.	901-789-8400	48,500 tons
	2	330			Memphis, TN 38109		
	3	330					
Dewey	1	109	4054	WI	11999 CTH	608-725-5511	19,000 tons
	2	105			Cassville, WI 53806		
Edgewater	3	71	4050	WI	PO Box 356	920-459-6127	82,000 tons
	4	327			Sheboygan, WI 53082		
Coffeen	1	450		IL	Montgomery County, IL	217-534-7646	73,000 tons
	2	450					
Big Bend	1	450		FL	Big Bend Road		Currently
	2	450			Tampa, FL		Marketing
	3	450					*PC Burner
	4	450					
Lake Road Plant	1	250		MO	St. Joseph, MO	816-737-7558	Currently
	2	250					Marketing
Seminole	1	650		FL	890 North Hwy. 17	813-963-0994	Unknown
Generating Station	2	650			Palatka, FL 32177		*PC Burner
Anhueser Busch	1	13		MO	St. Louis, MO		Unknown
	2	13					*Stoker Burner
W.N. Clark	1	20		CO	Canon City, CO	719-546-6548	22,000
	2	20					*Stoker Burner

Appendix 2 – Detailed Plant Summaries

1. **England**

   Location: Marmora, NJ
   Capacity: Two cyclone burners, rated at 129 MW and 155 MW.
   Fly-Ash Notes: The plant currently recycles all of their fly ash. It is unknown how much fly ash the plant produces.

2. **Conesville**

   Location: Conesville, OH
   Capacity: Two cyclone burners, rated at 125 MW each
   Fly Ash Collection: Each cyclone unit utilizes two economizer hoppers followed by two fields of ESP's with eight ESP hoppers.
   Fly Ash Characteristics and Quantity Notes: The plant was visited in June of 2003. It is estimated that between the two units, approximately 20 tons per day of elevated LOI material would be available. A sample was drawn from each economizer and LOI by size fraction results are shown below.
   Other Notes: There are 3 other non-cyclone units at this facility. Coal is transported to the plant via rail
   Experimental Results:
   LOI by Size Fraction

PMET RFA # 4387
AEP Conesville
Fly ash from cyclone boiler

DATA SUMMARY

Unit 1 Economizer Hopper 9

Size Fraction	Weight %	LOI	LOI Dist.
+10	4.7%	64.6%	5.5%
+25	78.1%	63.4%	90.1%
+50	15.7%	13.4%	3.8%
+100	0.5%	20.2%	0.2%
-100	1.1%	15.5%	0.3%
Total	100.0%		100.0%
Calculated Head		54.9%	
Measured Head		61.1%	

Unit 2 Economizer Hopper 9

Size Fraction	Weight %	LOI	LOI Dist.
+10	4.7%	60.7%	4.3%
+25	82.4%	68.6%	86.2%
+50	12.3%	49.6%	9.3%
+100	0.2%	33.4%	0.1%
-100	0.4%	20.5%	0.1%
Total	100.0%		100.0%
Calculated Head		65.6%	
Measured Head		74.5%	

Unit 1 Economizer Hopper 10

Size Fraction	Weight %	LOI	LOI Dist.
+10	15.7%	64.7%	20.4%
+25	74.5%	50.0%	74.7%
+50	8.7%	24.5%	4.3%
+100	0.3%	23.4%	0.1%
-100	0.8%	29.3%	0.5%
Total	100.0%		100.0%
Calculated Head		49.8%	
Measured Head		63.6%	

Unit 2 Economizer Hopper 10

Size Fraction	Weight %	LOI	LOI Dist.
+10	4.0%	59.3%	5.1%
+25	75.7%	53.4%	87.8%
+50	18.9%	16.1%	6.6%
+100	0.8%	13.2%	0.2%
-100	0.7%	18.4%	0.3%
Total	100.0%		100.0%
Calculated Head		46.0%	
Measured Head		56.0%	

3. **Kammer**

Location: Moundsville, WV

Capacity: Three cyclone burners, rated at 240 MW each

Fly Ash Collection: Each cyclone unit utilizes five economizer hoppers followed by five fields of ESP's with eight ESP hoppers

Fly Ash Characteristics and Quantity Notes: The plant was visited in June of 2003. It is estimated that between the three units, approximately 60 tons per day of 80+% LOI material would be available (22,000 tons per year). A sample was drawn from each economizer and LOI by size fraction results are shown below. This material was also measured for its potential to be used as activated carbon by measuring the surface area via BET and iodine number. Results are also shown below. Without any size classification, the material appears to be marketable directly out of the hopper.

Other Notes: Ductwork for gas flow is parallel to the ESP fields. This causes the first row of 8 ESP hoppers to receive varying quantity and quality of material. Coal is transported via barge.

Experimental Results:

LOI by Size Fraction

PMET RFA # 4405
AEP
Kammer Fly Ash

DATA SUMMARY

Economizer Unit	Hopper	LOI
1	50	80.3%
	51	80.4%
	52	80.8%
	53	77.8%
	54	78.7%
2	50	81.9%
	51	80.3%
	52	79.7%
	53	81.4%
	54	82.8%
3	50	78.4%
	51	78.9%
	52	79.3%
	53	79.4%
	54	79.4%

Surface area of PAC (labeled as "Carbon Powder") and Kammer Carbon

SAMPLE DESCRIPTION: Carbon Powder SAMPLE LOG 0603-5B

TEST	PROCEDURE	RESULT	EQUIPMENT LOG NO.
Surface Area BET Method	NUCON 92 Rev 0	628 m^2/g	Control No. 37317
Iodine No.	NUCON 31 Rev 2	461	N/A

SAMPLE DESCRIPTION: Kammer SAMPLE LOG 0603-5C

TEST	PROCEDURE	RESULT	EQUIPMENT LOG NO.
Surface Area BET Method	NUCON 92 Rev 0	24.0 m^2/g	Control No. 37317
Iodine No.	NUCON 31 Rev 2	63	N/A

4. Sioux

Location: West Alton, MO

Capacity: Two cyclone burners, rated at 470 MW each

Fly Ash Collection: Each cyclone unit collects ash utilizing economizers, air heater hoppers, and ESP's. The economizers and air heater hoppers collect a total of 38 tons per day for both units combined.

Fly Ash Characteristics and Quantity Notes: Plant produces a total of 55,000 tons per year of fly ash. Two samples were requested and received from this plant, one from an economizer hopper and one from an air heater hopper. Analyses via LOI were completed on each. The LOI of the fly ash samples were to low to merit further pursuit (6.1% for air heater hopper and 13.5% for economizer hopper)

Other Notes: The coal burnt at this plant is typically 85% PRB and 15% Illinois Coal.

5. **New Madrid**

Location: New Madrid, MO

Capacity: Two cyclone burners, rated at 600 MW each

Coal Type: Plants burns 100% PRB

Fly Ash Collection: Each cyclone unit collects ash utilizing economizers, air heater hoppers, SCR hoppers, and ESP's.

Fly Ash Characteristics and Quantity Notes: The plant produces a total of 90,000 tons per year of fly ash. Approximately 20% of the total fly ash is collected by the economizers, air heater hoppers, and SCR hoppers. The remaining 80% is collected in the ESP hoppers. LOI for the ESP collected fly ash is estimated to run between 10 and 20 %. The fly ash collected in the economizers and air heater hoppers is sent to a pond with the bottom ash. The fly ash collected in the ESP hoppers is sent to a landfill. Fly ash samples were requested and received from the economizer, air heater hopper, SCR hopper, and two ESP hoppers. Analyses are shown below. The +35 mesh material from the Air Heater Hoppers is marginal.

Experimental Results:

LOI by Size Fraction

New Madrid Fly Ash

4534-3

Unit 1 Air Heater Hopper

DATA SUMMARY			
Size Fractions	Weight %	LOI	LOI Dist.
+20m	27.44%	38.05%	25.55%
+35m	26.82%	59.45%	39.01%
+50m	15.37%	44.65%	16.79%
-50m	30.36%	25.10%	18.64%
Total	100.00%		100.00%
Calculated Head		40.87%	
Measured Head		43.90%	

4534-1

Unit 1 Economizer

Head LOI: 23.6%

4534-4

ESP Hopper - 1D Precipitator - Hopper 1D

Head LOI: 10.4%

4534-5

Unit 2 ESP - 2C Precipitator - Hopper 1B

Head LOI: 13.9%

4534-6

SCR Hopper Unit 1

DATA SUMMARY			
Size Fractions	Weight %	LOI	LOI Dist.
+20m	26.14%	52.30%	29.19%
+35m	23.71%	67.70%	34.28%
+50m	16.66%	55.60%	19.77%
-50m	33.49%	23.45%	16.76%
Total	100.00%		100.00%
Calculated Head		46.84%	
Measured Head		46.90%	

6. **Thomas Hill**

Location: Clifton Hill, MO

Capacity: Two cyclone burners, rated at 175 and 275 MW

Coal Type: 100% PRB

Fly Ash Collection: Each cyclone unit collects ash utilizing economizers, air heater hoppers, and ESP's.

Fly Ash Characteristics and Quantity Notes: Quantities of fly were unknown by plant personnel. Average LOI of material is reported as 6-10%. Currently, much of the fly ash is being disposed of in a landfill. Doesn't appear to be much potential for marketing of fly ash for carbon.

Experimental Results: Samples were requested three times, but no cooperation from plant personnel.

7. Crane

Location: Baltimore, MD

Capacity: Two cyclone burners, rated at 200 MW each

Coal Type: Lower Pittsburgh Seam

Fly Ash Collection: Each cyclone unit collects ash utilizing air heater hoppers and a baghouse.

Fly Ash Characteristics and Quantity Notes: Total production of fly ash is estimated 49,600 tons per year. All fly ash is currently being land filled. During NO_x season, LOI of material from air heater hoppers is estimated to be greater than 20%. Otherwise, LOI of this material runs 5-10%. Samples requested and received from air heater hoppers. Material in +50 mesh exhibits LOI between 60-70% LOI. See analysis below. Considered marginal product for marketing, may require some beneficiation.

Experimental Results:

LOI by Size Fraction

Crane
Cyclone Boiler
DATA SUMMARY

4545-2

Size Fractions	Weight %	LOI	LOI Dist.	
+20m	24.6%	64.1%	26.3%	
+35m	42.5%	71.0%	50.2%	68.5% <---LOI of +35m material
+50m	20.3%	60.4%	20.4%	66.6% <---LOI of +50m material
-50m	12.6%	14.9%	3.1%	
Total	100.0%		100.0%	
Calculated Head		60.1%		
Measured Head		54.20%		

4545-3

Size Fractions	Weight %	LOI	LOI Dist.	
+20m	26.65%	67.81%	27.32%	
+35m	46.85%	75.23%	53.27%	72.5% <--LOI of +35 material
+50m	16.69%	60.89%	15.36%	70.4% <---LOI of +50m material
-50m	9.80%	27.29%	4.04%	
Total	100.00%			
Calculated Head		66.16%		
Measured Head		46.83%		

8. Kincaid

Location: Kincaid, IL

Capacity: Two cyclone burners, rated at 600 MW each

Coal Type: 100% PRB

Fly Ash Collection: Each cyclone unit collects ash utilizing economizer hoppers, air heater hoppers and ESP hoppers.

Fly Ash Characteristics and Quantity Notes: Plant was visited July 2003. Total production of fly ash is estimated at 71,700 tons per year. ESP hopper fly ash runs 3-4%. Qualifies as cement additive, but transportation costs prohibits use. Economizer and air heater hopper fly ash is currently ponded. Samples of six air heater hoppers were requested and received. The +20 mesh material (about 50% of fly ash in hopper) of air heater hopper 11 appeared promising (69% LOI), while the other five hoppers showed no potential. See results below. Not enough high LOI material to pursue.

Experimental Results:

LOI by Size Fraction

Kincaid
4507-1
Air Heater Hopper 11
DATA SUMMARY

Size Fractions	Weight %	LOI	LOI Dist.
+20m	44.3%	69.4%	68.3%
+35m	37.9%	28.5%	24.0%
+50m	12.4%	11.2%	3.1%
-50m	5.4%	38.2%	4.6%
Total	100.0%		100.0%
Calculated Head		45.0%	
Measured Head		50.0%	

4507-4
Air Heater Hopper 21
Head LOI: 2.5%

Kincaid
4507-2
Air Heater Hopper 12
DATA SUMMARY

Size Fractions	Weight %	LOI	LOI Dist.
+20m	29.20%	37.63%	53.78%
+35m	34.08%	19.33%	32.25%
+50m	21.24%	5.60%	5.82%
-50m	15.48%	10.75%	8.14%
Total	100.00%		100.00%
Calculated Head		20.43%	
Measured Head		15.95%	

Kincaid
4507-5
Air Heater Hopper 22
DATA SUMMARY

Size Fractions	Weight %	LOI	LOI Dist.
+20m	15.9%	22.8%	32.5%
+35m	37.5%	9.6%	32.5%
+50m	32.9%	3.5%	10.2%
-50m	13.7%	20.1%	24.8%
Total	100.0%		100.0%
Calculated Head		11.1%	
Measured Head		13.0%	

Kincaid
4507-3
Air Heater Hopper 13
DATA SUMMARY

Size Fractions	Weight %	LOI	LOI Dist.
+20m	9.51%	4.60%	23.15%
+35m	35.49%	2.50%	46.98%
+50m	38.31%	0.95%	19.27%
-50m	16.68%	1.20%	10.60%
Total	100.00%		100.00%
Calculated Head		1.89%	
Measured Head		1.40%	

Kincaid
4507-6
Air Heater Hopper 23
DATA SUMMARY

Size Fractions	Weight %	LOI	LOI Dist.
+20m	15.77%	23.15%	30.35%
+35m	30.09%	11.90%	29.77%
+50m	31.24%	5.75%	14.93%
-50m	22.90%	13.10%	24.95%
Total	100.00%		100.00%
Calculated Head		12.03%	
Measured Head		14.55%	

9. **Stateline Power Plant**

Location: Hammond, IN

Capacity: Two cyclone burners, rated at 187 MW and 303 MW.

Fly Ash Collection: Each cyclone unit collects ash utilizing air heater hoppers and ESP hoppers.

Fly Ash Characteristics and Quantity Notes: Plant was visited August 2003. Total production of fly ash is estimated at 37,100 tons per year. ESP hopper fly ash runs at 1-2% LOI and is currently marketed as a concrete additive. Currently, fly ash from air heater hoppers is re-injected. Sample requested and received from air heater hoppers. LOI of air heater hopper fly ash is not high enough to market for carbon product. See analysis below.

Experimental Results:

LOI by Size Fraction

State Line Plant
4508-1
Common AHH
DATA SUMMARY

Size Fractions	Weight %	LOI	LOI Dist.
+20m	6.8%	68.2%	39.5%
+35m	22.1%	14.2%	26.6%
+50m	25.5%	2.8%	6.1%
-50m	45.5%	7.2%	27.8%
Total	100.0%		100.0%
Calculated Head		11.8%	
Measured Head		16.9%	

10. Asbury

Location: Asbury, MO

Capacity: Two cyclone burners, rated at 20 MW and 205 MW.

Coal Type: Mostly PRB, with a blend of bituminous coal from KS or MO.

Fly Ash Collection: Each cyclone unit collects ash utilizing one row of air heater hoppers, followed by two sets of ESP's. Fly ash is sluiced and sent to a pond.

Fly Ash Characteristics and Quantity Notes: The plant produces between 15,000 to 25,000 tons per year of fly ash. Samples were requested from the ESP hoppers and received. For fly ash in the first ESP row, the +50 mesh material appears very promising. The quantity of material going to the first ESP rows is unknown by plant personnel.

Experimental Results:

LOI by Size Fraction

Asbury
4554-1 (First ESP Row)
Cyclone Boiler
DATA SUMMARY

Size Fractions	Weight %	LOI	LOI Dist.	
+20m	24.3%	82.2%	39.9%	
+50m	33.9%	56.0%	38.0%	67.0% <---LOI of +50m material
+80m	4.2%	40.7%	3.4%	65.2% <---LOI of +80m material
-80m	37.5%	24.8%	18.6%	
Total	100.0%		100.0%	
Calculated Head		50.0%		
Measured Head		49.6%		

	LOI
4554-2 (Inlet Row of 2nd ESP)	28.3%
4554-3 (2nd ESP Row)	6.9%

11. Muskingum River

Location: Beverly, OH
Capacity: Two cyclone burners, each rated at 240 MW
Fly Ash Collection: ESP fields are only means of collecting fly ash.
Fly Ash Characteristics and Quantity Notes: The plant was visited in June of 2003. Samples were obtained from the row of ESP's from both units. While the material ran an elevated LOI, it does not appear that the LOI is high enough to market this fly ash as carbon.
Other Notes: Coal is shipped by rail.
Experimental Results:
LOI of ESP Hoppers and ESP Inlet of Unit 3 and ESP Inlet of Unit 4

AEP
Muskingum River Plant
PMET RFA 4388

DATA SUMMARY

Unit	Hopper	LOI
3	ESP 1	38.5%
	ESP 2	43.2%
	ESP 3	38.9%
	ESP 4	44.1%
	ESP Inlet	34.0%
4	ESP Inlet	37.9%

12. Baldwin

Location: Baldwin, IL
Capacity: Two cyclone burners, each rated at 600 MW
Coal Source: PRB
Fly Ash Collection: Air heater hoppers and ESP's are used to collect fly ash.
Fly Ash Characteristics and Quantity Notes: Approximately 500 tons per day of fly ash are produced at this plant. Approximately 80% of the fly ash is collected in the ESP's and marketed as a Class C fly ash. Remaining 20% is captured in air heater hoppers and LOI runs 10-15%. Air heater hopper material exhibits too low of an LOI to be marketed for carbon.

13. LaCygne

Location: LaCygne, KS
Capacity: One cyclone burner rated at 750 MW
Coal Source: PRB
Fly Ash Collection: ESP's are used to collect fly ash.
Fly Ash Characteristics and Quantity Notes: Produces approximately 129,000 tons per year of fly ash. Material is sent through a wet scrubber, rendering material useless for marketing for carbon. All other fly ash at the plant is currently marketed.

14. Bailly

Location: Chesterton, IN

Capacity: Two cyclone burners, one rated at 160 MW and 320 MW.

Coal Source: Midwest Illinois Basin

Fly Ash Collection: For the smaller, 160 MW unit, the fly ash is wet scrubbed and sluiced with the bottom ash. The larger unit (320 MW) uses 1 economizer hopper, 3 air heater hoppers, and 2 SCR hoppers to collect fly ash.

Fly Ash Characteristics and Quantity Notes: A plant visit was conducted in August, 2003. At that time, the plant was shut down for installation of SCR units. Since that time, numerous requests have been ignored for samples from air heater hoppers, economizers, and SCR hoppers.

15. Michigan City

Location: Michigan City, IN

Capacity: One cyclone burner rated at 469 MW

Fly Ash Characteristics and Quantity Notes: A plant visit was attempted in July, 2003, without access being granted upon arrival. ISG currently markets ash. Fly ash from economizers sent to PMET for evaluation. This material exhibited a 3.2% LOI. With ISG currently marketing material, most likely for cement additive, the material is probably not suitable for carbon marketing.

16. Schahfer

Location: Wheatfield, IN

Capacity: Plant was found to be incorrectly identified in database as cyclone unit. It is a PC burner.

17. Sheldon

Location: Hallam, NE

Capacity: Two cyclone burners, rated at 120 MW and 105 MW

Coal Type: PRB

Fly Ash Collection: Air heater hoppers were removed. First row of ESP's are deactivated to remove large particles. A baghouse also collected fine particles.

Fly Ash Characteristics and Quantity Notes: Total fly ash production is estimated at 22,000 tons per year. Samples were requested and received from the deactivated ESP hoppers. The material in these hoppers appears very promising, with an LOI ranging from 70-75% for the +50 mesh fraction. See LOI by size fraction below. Estimates are that these hoppers collect 500 – 1000 tons per month, giving an estimated production of 360 to 720 tons per month.

Experimental Results:

LOI by Size Fraction

Sheldon
4545-1
Cyclone Boiler
DATA SUMMARY

Size Fractions	Weight %	LOI	LOI Dist.	
+20m	24.7%	68.6%	22.6%	
+35m	29.9%	83.5%	33.3%	
+50m	16.9%	76.0%	17.1%	76.6% <---LOI of +50m material
-50m	28.5%	71.4%	27.1%	
Total	100.0%		100.0%	
Calculated Head		75.1%		
Measured Head		70.16%		

18. King

Location: Bayport, MN

Capacity: One cyclone unit rated at 581 MW.

Fly Ash Characteristics and Quantity Notes: This plant was eliminated from this study due to its lack of proximity to metallurgical carbon markets.

19. Riverside

Location: Minneapolis, MN

Capacity: One cyclone unit rated at 222 MW.

Fly Ash Characteristics and Quantity Notes: This plant was eliminated from this study due to its lack of proximity to metallurgical carbon markets.

20. Merrimack

Location: Bow, NH

Capacity: Two cyclone units, rated at 114 MW and 320 MW.

Fly Ash Characteristics and Quantity Notes: This plant was eliminated from this study due to its lack of proximity to metallurgical carbon markets.

21. Big Stone

Location: Big Stone City, SD

Capacity: One cyclone unit rated at 464 MW.

Fly Ash Characteristics and Quantity Notes: This plant was eliminated from this study due to its lack of proximity to metallurgical carbon markets.

22. Powerton

Location: Pekin, IL

Capacity: Two cyclone burners, each rated at 782 MW

Fly Ash Characteristics and Quantity Notes: Powerton currently has a group looking at their fly ash and had no interest in sharing any information with us.

23. Will County

Location: Romeoville, IL

Capacity: Plant has been shut down.

24. Marion

Location: Marion, IL

Capacity: No longer operating as cyclone burner. This plant has been re-powered as a circulating fluidized bed.

25. Gannon

Location: Tampa, FL

Capacity: By the end of 2004, coal firing will have ceased at Gannon. The plant is currently being converted to natural gas.

26. Paradise

Location: Drakesboro, KY

Capacity: Three cyclone burners, rated at 700 MW, 700 MW, and 1150 MW

Coal Type: ~80% PRB, 20% Utah bituminous

Fly Ash Collection: All three units use economizer and air heater hoppers to collect some fly ash. None of the units use ESP's. Fly ash from the two smaller units (700 MW) is currently sludged and the largest unit (1150 MW) has been retrofitted with a scrubber. All fly ash collected in the air heater hopper is sluiced to a pond.

Fly Ash Characteristics and Quantity Notes: Total fly ash production is estimated at 102,000 tons per year. Samples have been requested for fly ash from the economizer hoppers and air heater hoppers, but have not been received. Even though this plant produces a great deal of fly ash, most of it is collected wet, making it difficult to market.

27. Sibley

Location: Sibley, MO

Capacity: Three cyclone units, rated at 52 MW, 53 MW, and 391 MW

Fly Ash Collection: Fly ash is collected using economizer and ESP hoppers (no air heater hoppers).

Fly Ash Characteristics and Quantity Notes: Total fly ash production is estimated at 52,800 tons per year. Samples were requested and received from the economizer hoppers. ESP hopper ash was believed to run at ~5% LOI. Analysis of samples at PMET showed that economizer hopper fly ash exhibited a 4 – 5% LOI, too low for carbon marketing.

28. Allen

Location: Memphis, TN

Capacity: Three cyclone burners, each rated at 330 MW.

Coal Type: 70% PRB, 30% Western Bituminous

Fly Ash Collection: Unlike other TVA plant (Paradise), fly ash is not scrubbed. The material is collected dry using ESP's and air heater hoppers and sluiced to a pond.

Fly Ash Characteristics and Quantity Notes: Total fly ash production is estimated at 48,500 tons per year. Samples were requested from the air heater hoppers, but have not yet been received.

29. Dewey

Location: Cassville, WI

Capacity: Two cyclone burners, rated at 109 MW and 105 MW

Fly Ash Collection: The Dewey plant had no interest in marketing their fly ash as carbon or sharing any information with us. It is believed that Dewey produces about 19,000 tons per year of fly ash.

30. Edgewater

Location: Sheboygan, WI

Capacity: Two cyclone burners, rated at 71 MW and 327 MW

Coal Type: PRB

Fly Ash Collection: Economizer hoppers collect fly ash that is sluiced out with the slag in the bottom of the cyclone burner. The remainder of the fly ash is collected in air heater hoppers, ESP hoppers, and a baghouse.

Fly Ash Characteristics and Quantity Notes: Currently, fly ash is being land filled. Fly ash is occasionally sold into stabilization markets. Total fly ash production is estimated at 32,000 tons per year. Samples from economizers and first set of ESP hoppers were requested numerous times, but never received.

31. **Coffeen**
Location: Montgomery County, IL
Capacity: Two cyclone burners, rated at 450 MW each
Coal Type: PRB and Illinois Coal
Fly Ash Collection: Fly ash collected in the economizer hoppers is currently sluiced with the slag out of the bottom of the cyclone burner. Fly ash is also collected in air heater hoppers, ESP hoppers, and a baghouse.
Fly Ash Characteristics and Quantity Notes: Total fly ash production is estimated at 200 tons per day. The LOI is estimated to average between 12 and 20% for the fly ash. Samples from the air heater hoppers and first set of ESP hoppers were requested but not received.

32. **Big Bend**
Location: Tampa, FL
Capacity: Four PC fired burners, rated at a total of 1800 MW.
Fly Ash Characteristics and Quantity Notes: All fly ash is currently being marketed. Low LOI material, not suitable for carbon market.

33. **Lake Road Plant**
Location: St. Joseph, MO
Capacity: Two PC burners, each rated at 250 MW each
Fly Ash Collection: Use only ESP's to collect Fly Ash. All ESP hopper fly ash is currently being marketed.

34. **Seminole**
Location: Palatka, FL
Capacity: Two PC burners, rated at 650 MW each
Coal Type: 66% Southern Illinois Coal, 33% Pet Coke
Fly Ash Collection: Economizer hoppers collect some fly ash, which is then simply blown in the ESP's. Air heater hoppers removed from service. All fly ash is collected by ESP's.
Fly Ash Characteristics and Quantity Notes: The LOI of the fly ash collected in the ESP hoppers averages 18%, which is too low for carbon market consideration.

35. **Anheuser Busch**
Location: St. Louis, MO
Capacity: Two cyclone burners, rated at 13 MW each
Coal Type: PRB
Fly Ash Collection: This is a spreader stoker burner that uses an economizer and ESP hoppers to collect fly ash.
Fly Ash Characteristics and Quantity Notes: Since this is an industrial burner, there was not much known about the fly ash. The LOI is elevated, but plant personnel did not know how high. Currently awaiting sample.

36. W.N. Clark

Location: Canon City, CO

Capacity: Two spreader stokers each rated at 20 MW

Coal Type: Mixture of sub-bituminous and bituminous coals

Fly Ash Collection: Fly ash collected in the economizer is used for re-burn. All other fly ash is collected in a baghouse.

Fly Ash Characteristics and Quantity Notes: It is estimated that the plant produces a total of 60 tons per day of ash. Of that total, it is estimated that 70% is fly ash (balance is bottom ash). Based on samples sent from the baghouse to PMET, it appears that a carbon product with a 75% LOI can be obtained from the +50 mesh material (which is 40% of the baghouse material). This is estimated to give 17 tons per day of a +75% LOI product. See LOI by size fraction analysis below. Currently, the plant is land-filling their ash and are looking for a market for the material.

Experimental Results:

LOI by Size Fraction

Canon City
4541-2
Stokker Boiler
DATA SUMMARY

Size Fractions	Weight %	LOI	LOI Dist.	
+20m	5.7%	87.3%	9.5%	
+35m	17.0%	82.8%	27.0%	
+50m	16.6%	65.2%	20.8%	76.0% <--LOI of +50m
-50m	60.7%	36.8%	42.8%	
Total	100.0%		100.0%	
Calculated Head		52.2%		
Measured Head		50.15%		

References

1. Aminorroaya, S., Edris, H., "The Effect of Foamy Slag in the Electric Arc Furnaces on Electric Energy Consumption"

2. AISI Learning Center: Coal Utilization in the Steel Industry

3. Kwong, K.-S., Bennett, J.P., "Recycling Practices of Spent MgO-C Refractories", Journal of Minerals & Materials Characterization & Engineering, Vol 1, No 2, 69-78, 2002.

4. Rummley, T., Anderson, E., Hamy, M., Bunemann, G., Apfel, J., "Efficient Steelmaking has Environmental Benefits", AISE Steel Technology, March 2003.

5. Greenbank, M., "Carbon from Fly Ash as a Sellable Carbon", prepared for PMET, January 2, 2003.

Turbostratic Carbon Powder

FINAL REPORT

Reporting Period
September 10, 2003 to July 30, 2004

Report Prepared by
John W. Zondlo
Department of Chemical Engineering
College of Engineering and Mineral Resources
P.O. Box 6102

Report Issued
July 31, 2004

Subcontract No.: 2566-WVU-DOE-0350

Other Contributors

Abha Saddawi, Peter Stansberry and Elliot Kennel
Department of Chemical Engineering
College of Engineering and Mineral Resources
P.O. Box 6102
West Virginia University
Morgantown, WV 26506-6102

DISCLAIMER

Abstract

Fine particulate carbon was created by grinding Solvent Extracted Carbon Ore (SECO), lightly oxidizing it, and heat treating it to various temperatures to produce a dense micropowder. Eight SECO samples were prepared and analyzed via proximate (dry) and elemental analyses, as well as with XRD and SEM. The electrical resistivity of some of the samples was also assessed. Dr. Cooper's group at Lawrence Livermore National Laboratory (LLNL), as well as Dr. Steven Chuang's group at the Department of Chemical Engineering, University of Akron, Akron, OH, were supplied with these SECO samples for testing in their Direct Carbon Fuel Cells (DCFC). It was found that heat-treated samples demonstrated a continuous increase in carbon, and a decrease in volatile matter, nitrogen, hydrogen and sulfur as the heat-treated temperature was raised. The oxygen content jumped significantly following oxidation, and then decreased dramatically upon heat treatment. XRD results indicated some degree of order in the structure of these heat-treated SECO samples, where a higher degree of order was observed for the samples heated at higher temperatures. Carbon foams consisting of coal tar pitch (CTP) combined with one of the oxidized SECO samples were made and assessed for their properties. The SECO/CTP foam sample showed properties consistent with other similar foam samples. The SECO heat-treated to 800 °C and above proved to be a more conductive carbon for use in the fuel cell, and showed favorable performance in LLNL's fuel cell. The University of Akron also reported favorable results for the oxidized SECO. The low ash, low sulfur, and highly conductive character of these samples makes them very attractive for application in the direct carbon fuel cell.

TABLE OF CONTENTS

LIST OF TABLES

LIST OF FIGURES

Executive Summary

This program is focused on the production of a low cost coal-derived turbostratic carbon powder for structural and other applications, and investigates the suitability of such a material for use in a carbon fuel cell, such as that which has been demonstrated by Lawrence Livermore National Laboratory (LLNL). The Direct Carbon Conversion (DCC) process, pioneered by a LLNL team led by Dr. John Cooper, employs a unique fuel cell to produce electric power. The overall cell reaction is combustion of carbon with oxygen (from ambient air) forming carbon dioxide and electricity. Cooper's results at LLNL suggest that the ideal carbon feed for a carbon fuel cell should be a turbostratic carbon with microscopic domain size of 30 nm or smaller, with an ash value less than 0.5%, low VM, a sulfur level between 0.25% to 1.0%, low graphitization, and high electrical conductivity.

Solvent-extracted carbon ore (SECO) was initially suggested due to its low ash and sulfur content, as well as its presumed high friability enabling the production via grinding of extremely small particles. Fine particulate carbon was created by grinding Pilot Plant and lab-scale SECO, where the lab-scale SECO was lightly oxidized and coked to 400 °C, 600 °C 800 °C, 1000 °C, to produce a dense micropowder. The SECO samples were analyzed via proximate (dry) and elemental analyses, as well as with XRD and SEM. The electrical resistivity of some of the samples was also assessed. For testing purposes, Dr. Cooper's group was supplied with these SECO samples as well as cokes prepared from condensed byproducts from other CPCPC projects. Dr. Steven Chuang's group at the Department of Chemical Engineering, University of Akron, Akron, OH, is

also working on the development of a carbon fuel cell and collaborated in evaluating the SECO samples produced by WVU.

Additionally, carbon foams consisting of coal tar pitch (CTP) combined with one of the oxidized SECO samples were made and assessed for their properties. The SECO/CTP foam sample was successfully created and showed properties consistent with other similar foam samples with a crush test value of 12.3 MPa.

WVU Coal Extraction Pilot Plant SECO samples SECO-4 and SECO-6/7 were found to be low in ash and sulfur. However, both samples had a large VM content (~40%) and difficulties were encountered during testing in the fuel cell. Thus, the lab-scale SECO batch was made, where heat treatment resulted in a dramatic decrease of volatile matter. Heat-treated samples also demonstrate a continuous increase in carbon, and a decrease in nitrogen, hydrogen and sulfur. The XRD results show some degree of order in the structure, and data indicate higher order for the samples heated at higher temperatures. All the samples thus produced have domain sizes less than 30 nm, indicating turbostratic carbon. No unusual surface effects due to heat-treatment are evident in the SEM images of the SECO. Resistivity measurements indicated that the higher the heat-treatment temperature, the lower the resistivity of the SECO becomes. Thus, the 800°C or above heat-treated SECO proved to be a more conductive carbon for use in the fuel cell, and showed favorable performance in LLNL's fuel cell. The University of Akron also reported favorable results for the oxidized SECO.

Introduction

This program is focused on the production of a low cost coal-derived turbostratic carbon powder for structural and other applications. This material will differ from carbon black in that it will be a turbostratic carbon with low surface area, as opposed to carbon black, which is usually a high surface area amorphous material. The turbostratic carbon powder, when combined with an appropriate binder pitch, can be used as part of a carbon composite manufacturing process. In addition, such a material can be suitable for use in a carbon fuel cell, such as that which has been demonstrated by Lawrence Livermore National Laboratory (LLNL). The Direct Carbon Conversion (DCC) process, pioneered by a LLNL team led by Dr. John Cooper, employs a unique fuel cell to produce electric power. The overall cell reaction is combustion of carbon with oxygen (from ambient air) forming carbon dioxide and electricity. A schematic diagram of the direct carbon fuel cell concept is shown in Figure 1.

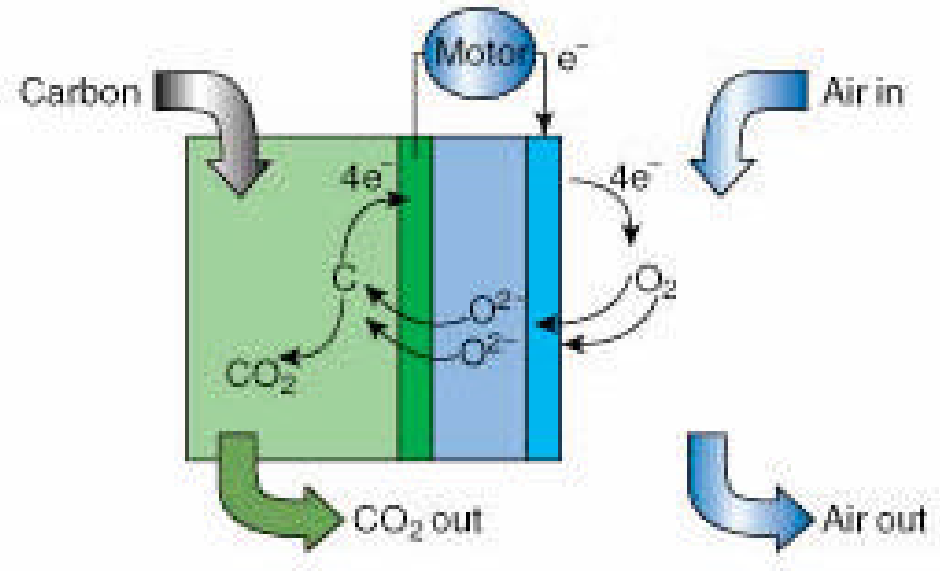

Figure 1. Direct Carbon Conversion Concept (by LLNL)

The reactions involved in this process are as follows[1]:

$C + 2CO_3^{2-} = 3CO_2 + 4e^-$	Anode
$O_2 + 2CO_2 + 4 e^- = 2CO_3^{2-}$	Cathode
$C + O_2 = CO_2$	Overall Reaction
	?G ~32.8 MJ/kg;
	E = 1.02 V at T=800 °C

LLNL results to date have shown that the fuel cell reaction yields 80 percent of the carbon-oxygen combustion energy as electricity[1]. It provides up to 1 kilowatt of power per square meter of cell surface area, which is comparable to other electrochemical systems. Laboratory cells tested at LLNL consist of a nickel anode current collector, a ceramic matrix for containing the molten electrolyte, a nickel screen for reacting the oxygen from the air, and a thermocouple (see Figure 2). The solid carbon fuel is fed as a fine powder to the cell. Currently the cell is operated in the batch mode but continuous operation is possible.

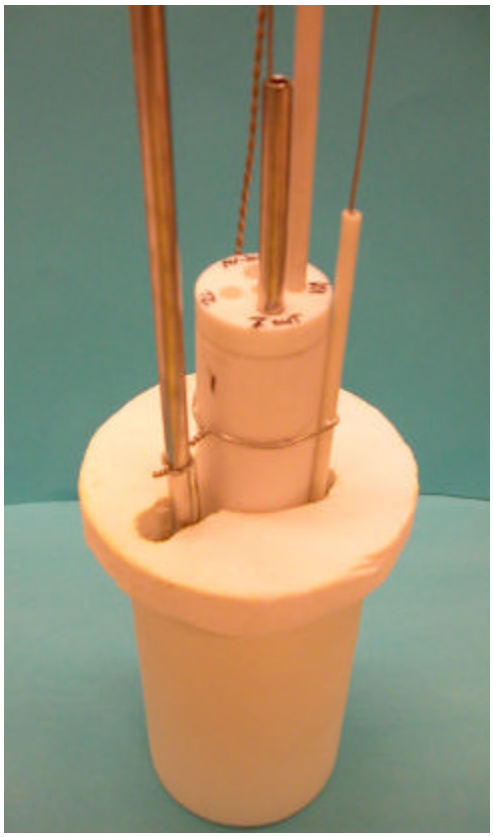

Figure 2. LLNL Fuel Cell (1.8cm^2)

Cooper's results at LLNL suggest that the ideal carbon feed for a carbon fuel cell should be a turbostratic carbon with microscopic domain size of 30 nm or smaller.[1] It also must have an ash value less than 0.5% to prevent excessive contamination of the molten salt electrolyte. Ranging degrees of volatile matter (VM) are of interest, but low VM is preferred. The sulfur level should be between 0.25% to 1.0% so that the metal electrodes are not chemically attacked and degraded excessively. Cooper's results also indicate that the electrochemical performance of the carbon improves with less graphitization as that increases reactivity of the carbon to oxidation. Performance is also enhanced with carbon of increased electrical conductivity which improves performance due to enhanced charge transport.[1]

In this project, the use of solvent-extracted carbon ore (SECO) was evaluated as a feedstock for the direct carbon fuel cell. The SECO was initially suggested due to its low ash and sulfur content, as well as its presumed high friability enabling the production via grinding of extremely small particles. Fine particulate carbon was created by grinding SECO, lightly oxidizing it, and heat-treating it to produce a dense micropowder. Eight SECO samples were prepared and analyzed via proximate (dry) and elemental analyses, as well as with XRD and SEM. The electrical resistivity of some of the samples was also assessed. For testing purposes, Dr. Cooper's group was supplied with these SECO samples as well as cokes prepared from condensed byproducts from other CPCPC projects. Dr. Steven Chuang's group at the Department of Chemical Engineering, University of Akron, Akron, OH, is also working on the development of a carbon fuel cell and collaborated in evaluating the SECO samples produced by WVU.

Additionally, carbon foams consisting of coal tar pitch (CTP) combined with one of the oxidized, heat-treated SECO samples were made and assessed for their properties.

Experimental

A reconfiguration of the Coal Extraction Pilot Plant at West Virginia University was completed in the Fall of 2003. Figure 3 shows an overall view of the pilot plant as it currently is configured. In a typical extraction run, approximately 30 pounds of SECO can be produced.

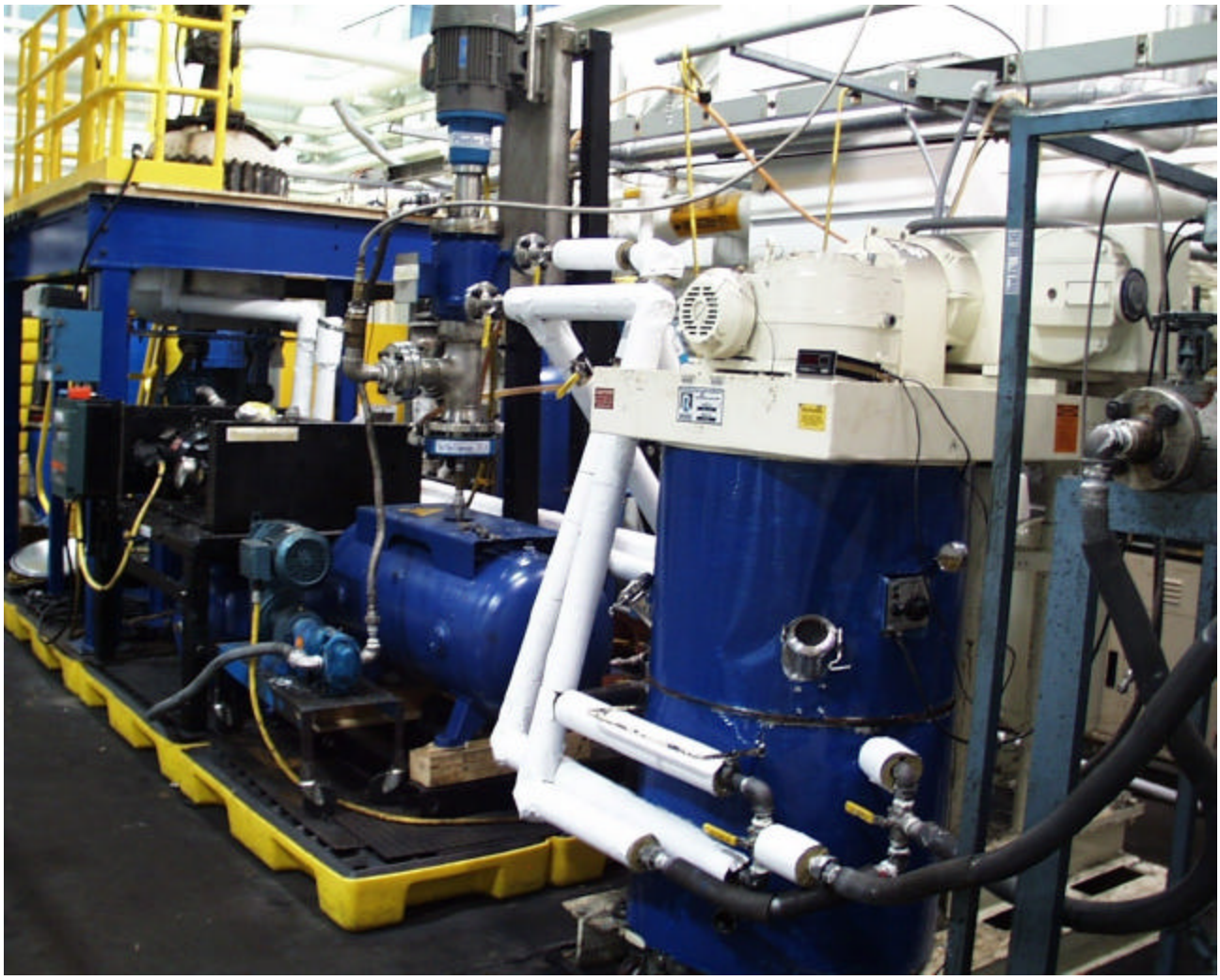

Figure 3. Solvent Extraction Pilot Plant Facility at WVU

Samples from two runs at the pilot plant, SECO-4 and SECO-6/7, were obtained for use in this project. These SECO samples were produced from a raw Kingwood coal

mined in Preston Co., WV. The proximate and elemental analyses for the raw coal are shown in Table 1. The SECO samples were ground to ~200 mesh and were also characterized via proximate and elemental analysis. Results of these tests are shown in Table 1 as well.

Table 1. Proximate and Elemental Analysis Results of raw Kingwood Coal and SECO samples 4, 6/7 made in the WVU Pilot Plant

a) Proximate:	Moisture (wt %)	Volatile Matter (wt %)	Fixed Carbon (wt %)	Ash (wt %)
Raw Kingwood Coal	6.86	30.07	55.03	8.04
SECO-4	0.66	36.73	62.11	0.50
SECO-6/7	2.10	40.60	56.79	0.51
b) Elemental Composition:	C	N	H	S
Raw Kingwood Coal	77.44	1.18	4.95	1.58
SECO-4	83.36	2.78	5.73	0.62
SECO-6/7	80.01	3.86	6.04	0.54

As can be seen from the analysis, these two SECO samples are similar in composition. It should also be noted that the samples are very low in ash and contain only 0.5% sulfur, a considerable reduction from the ash and sulfur in the raw coal. Roughly 30 grams of SECO-4, 6/7 were sent to LLNL for testing and evaluation.

For more efficient operation of the direct carbon fuel cell, it is advantageous to grind the SECO to the micron range. To this end, an ultra sonic grinder (Ultrasonic Processor for Industrial Application, Model UIP2000) was obtained and tested for this purpose. The device was found to reduce the size of smaller particles to about 3 microns. However it was ineffective at reducing large particles of SECO. Thus, conventional grinding, via the ball mill, was still necessary. Figure 4 shows an electronmicrograph of

SECO ground using conventional ball milling equipment. It can be seen that particle sizes on the order of 1µm can easily be obtained.

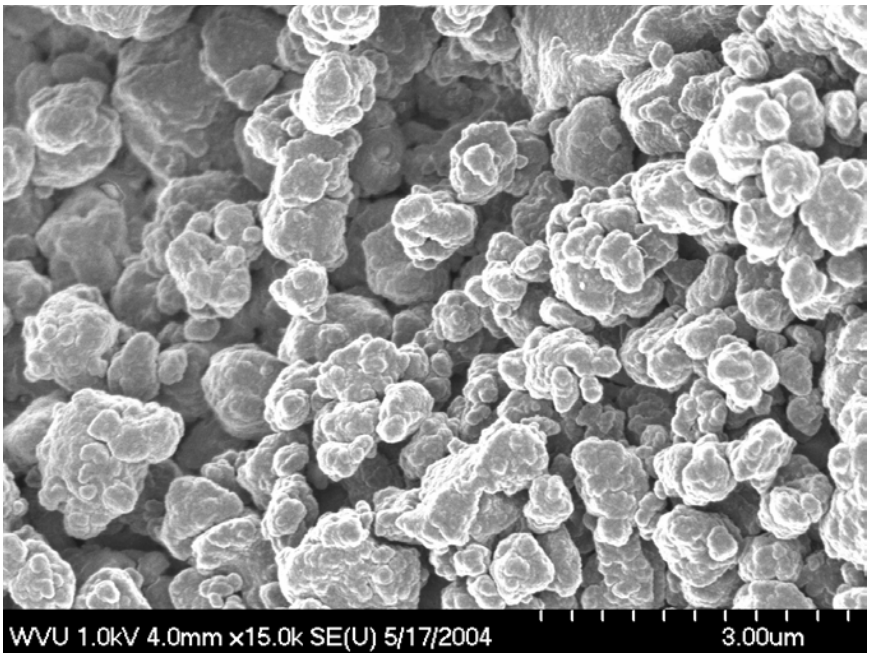

Figure 4. SEM image of ground SECO using a conventional ball mill

Feedback from Dr. Cooper indicated that the high volatile matter content (~40%) created difficulties in testing and determining accurate cell efficiency since some of the fuel left the cell as unburned volatiles. To rectify this problem, another batch of SECO from the same coal was prepared on the lab scale.[2] A block flow-sheet of the process is shown as Figure 5.

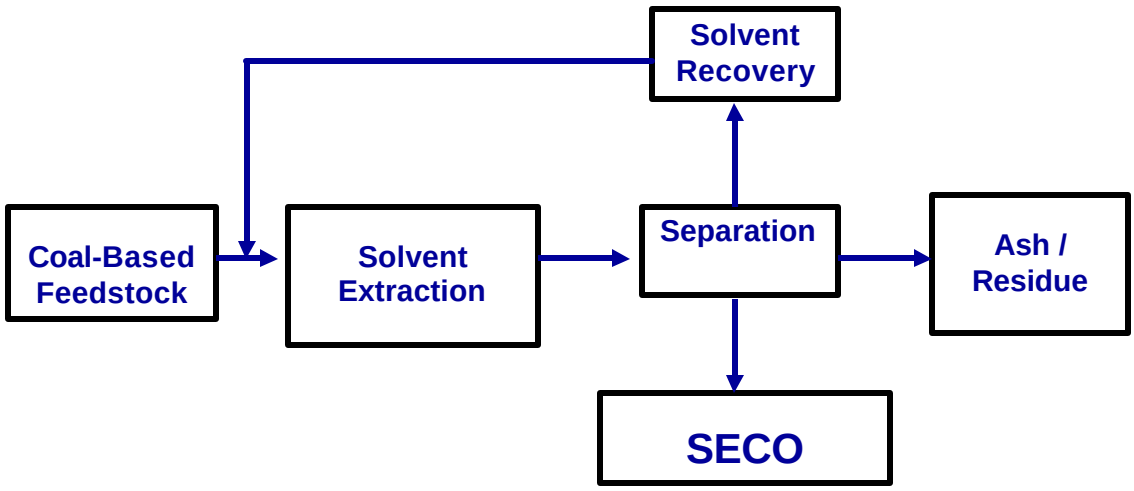

Figure 5. Flowchart of the solvent extraction process for SECO

Kingwood Coal, first air-dried for two days, was ground and vacuum-dried overnight at about 120°C. N-methyl pyrrolidone (NMP) was heated to about 200 °C after which coal was mixed in a ten-to-one solvent-to-coal ratio (10mL of NMP = 1g of coal) while being continuously stirred under nitrogen. This solution was left to reflux for 30 minutes. Following extraction, the solution was cooled and vacuum-filtered. Final evaporation of the NMP in a rotary evaporator precipitated the desired SECO as a solid product.

The resultant SECO was then heat-treated to varying temperatures to drive off some of the volatile matter. However, upon heat-treatment, the raw SECO was found to foam violently and boil out of the vessel. To prevent this, the sample was first partially oxidized at 250 °C for 4 hours in air so that cross-linking could be effected. Following oxidation, the sample was again heat treated, this time with no foaming noted. Four different levels of heat treatment were performed: 4 hours each at 400 °C, 600 °C, 800 °C, 1000°C in an inert atmosphere. These samples were then subjected to elemental and proximate analysis along with evaluation by x-ray diffraction (XRD) and SEM.

The electrical resistivity of the compacted heat treated SECO powders was also assessed by placing the powder in a nonconductive piston/cylinder assembly with electrodes on each end. Figure 6 shows photographs of the resistivity cell.

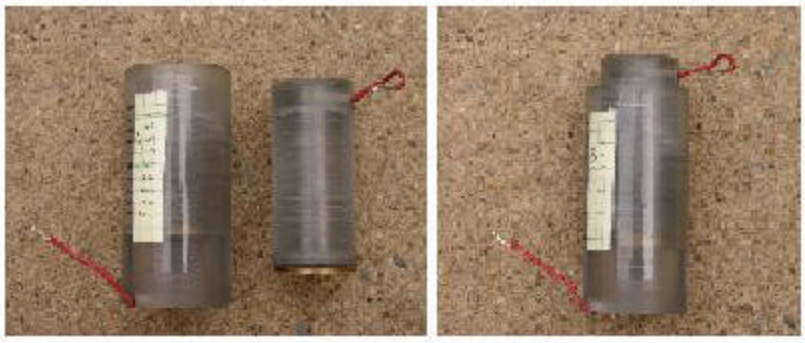

Figure 6. Electrical resistivity cell (WVU)

The resistance measurements were made by placing a known amount of sample in the cell. Electrical contact was made with the sample by means of two polished brass discs placed on either side of the sample bed. The diameter and the height (i.e. distance between the electrodes) of the sample bed was measured. A Keithley Model 2700 DVM was connected to the electrodes and resistance measurements were made as various amounts of weight were placed on the piston so that the powders could be compacted. The weight was increased until no further change in resistance was noted. Unfortunately, for highly conductive powders (like graphite and heat-treated SECO), the lower limit of the ohm meter was reached and further measurements were not possible. Hence reliable data were obtained only for the SECO samples heated to 600 °C and 800 °C. The 1000 °C sample had a resistivity too low for accurate measurement.

Three additional coke samples were prepared by Dr. Stansberry from a related CPCPC project. These samples were cokes made from the by-product coal liquids driven off during preparation of hydrogenated coal extracts. During processing, one of the steps

is a partial distillation to raise the softening point of the desired product. This step produces a volatile stream of by-product hydrocarbons which when coked produces a low-sulfur, low-ash carbon. These recovered liquids were then coked at a rate of 3 °C per minute pausing at 300 °C for 2 hours and then raised the temperature at the same rate to 700 °C. This temperature was held for 2 hours before cooling to room temperature. The entire operation was performed in a covered crucible which was itself immersed in coke breeze to prevent burning. These samples were sent to LLNL. Samples were also sent to Dr. Chuang's group at the University of Akron.

A calcined carbon foam was produced from one of the previously mentioned SECO samples and tested for density, porosity and crush strength. The SECO powder that was oxidized and heat treated to 800 °C was ground to less than 200 mesh and mixed with CTP, which was also ground to under 200 mesh, in a ratio of seven parts coke to 3 parts CTP. The mixed powder was then put into a mold and heated under nitrogen to 500 °C at a rate of 5 °C per minute for 5 hours. Then the sample was calcined at 1000 °C for 5 hours. For comparison, a similar sample was made of only CTP without the addition of the coke. It was heat treated by the identical protocol.

Results and Discussion

Elemental and proximate analyses of the raw coal used in this project, Kingwood coal mined in Preston Co., WV, and WVU Coal Extraction Pilot Plant SECO samples SECO-4 and SECO-6/7 are listed in Table 1. Both SECO samples were low in ash and sulfur. However, due to the samples' large VM content (~40%), difficulties during the testing of the DCFC were experienced and an accurate determination of the cell efficiency was not possible since some of the fuel left the cell as unburned volatiles.

With the goal of decreasing VM and ash content, another lab-scale SECO batch was made (also from Kingwood Coal).[2] To prevent foaming during heat treatment, the samples were first partially oxidized at 250°C for 4 hours in air so that cross-linking could be effected. Following oxidation, the samples were again heat treated, this time with no foaming noted. Four different levels of heat treatment were performed: 4 hours each at 400 °C, 600 °C, 800 °C, and 1000 ºC in an inert atmosphere. The extract and oxidized heat-treated samples were subjected to elemental and proximate analysis. These results are shown in Table 2.

Table 2. Proximate (Dry) and Elemental Analysis of Raw and Heat-Treated SECO (Kingwood) made in the laboratory

Proximate Analysis			VM wt%	FC wt%	Ash wt%
Kingwood Coal			33	58	8.92
SECO Extract			32	67.82	0.18
Oxidized SECO Extract			32.17	67.54	0.29
Oxidized SECO, HT 400°C			28.87	70.90	0.24
Oxidized SECO, HT 600°C			9.05	90.66	0.29
Oxidized SECO, HT 800°C			3.84	95.90	0.27
Oxidized SECO, HT 1000°C			1.78	97.82	0.40
Elemental Analysis	**C**	**N**	**H**	**S**	**O**
Kingwood Coal	77.44	1.18	4.95	1.58	ND
SECO Extract	85.80	1.78	5.83	0.64	3.91
Oxidized SECO Extract	75.50	1.90	3.77	0.65	11.70
Oxidized SECO, HT 400°C	80.37	1.88	3.50	0.64	8.60
Oxidized SECO, HT 600°C	84.24	1.69	2.19	0.61	2.52
Oxidized SECO, HT 800°C	88.75	1.35	0.80	0.56	1.51
Oxidized SECO, HT 1000°C	91.00	1.48	0.34	0.44	ND

Table 3. XRD Analysis of Bench Samples

Sample	2? (002)	2 ? (110)	d(002) (nm)	d(110) (nm)	La (nm)	Lc (nm)
Raw SECO	22.9	81.43	0.3884	0.11819	2.4151	1.126
Ox/SECO	23.21	81.4	0.3832	0.11822	2.7072	1.0678
Ox/SECO 400°C	23.79	81.24	0.374	0.11842	2.3795	1.4925
Ox/SECO 600°C	23.94	81.45	0.3717	0.11816	2.7219	1.832
Ox/SECO 800°C	24.08	79.34	0.3696	0.12077	3.3361	2.2706
Ox/SECO 1000°C	ND	ND	ND	ND	ND	ND
Graphite Sample	26.33	73.83	0.3385	0.12835	27.851	45.118

XRD results can be seen in Table 3 and Figure 7, and a typical SEM image is show in Figure 8.

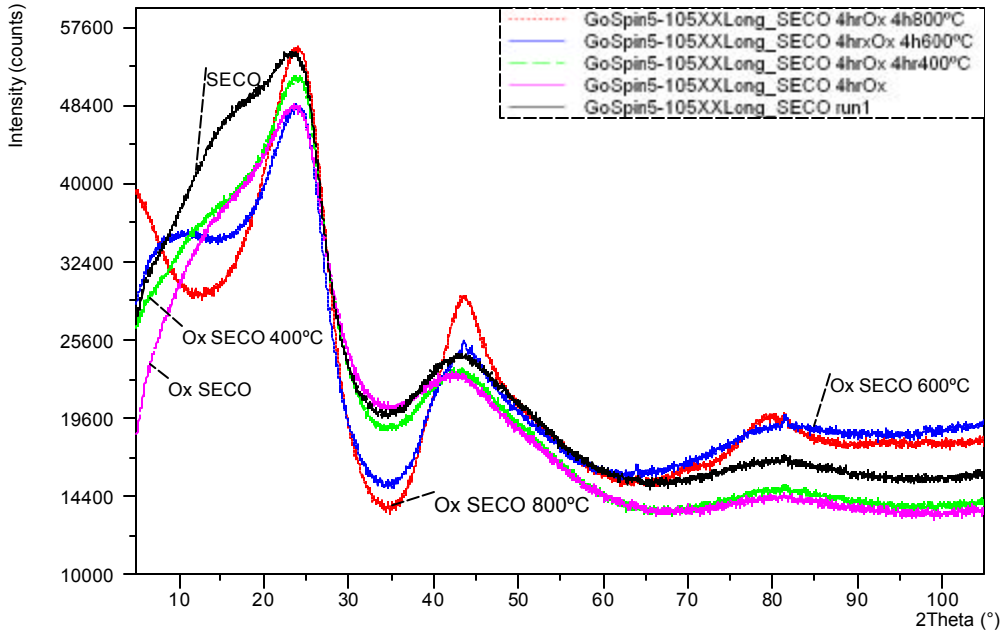

Figure 7. XRD analysis of bench samples

One may note, from the proximate analysis, the heat treatment results in a dramatic decrease in volatile matter. Heat-treated samples also demonstrate a continuous increase in carbon, and a decrease in nitrogen, hydrogen and sulfur. The oxygen content jumps significantly following oxidation, as is expected, and then decreases dramatically upon heat treatment. The XRD results show that the d (002) spacing consistently decreases upon heating to higher temperatures indicating some degree of order in the structure. In addition, the crystallographic domain sizes Lc and La increase steadily as a result of heat treatment. For reference, a sample of graphite was also tested in the XRD for comparison. These data indicate higher order for the samples heated at higher temperature. As can be seen, all the carbons thus produced have domain sizes less than 30 nm, indicating turbostratic, carbons.[4,5]

From the SEM image for the SECO treated at 800 °C, shown as Figure 8, one may see that any unusual effect of heat-treatment is not evident on the surface. The

image resembles that of a friable glassy carbon, and is representative of the other images taken of the Oxidized SECO samples treated at different temperatures.

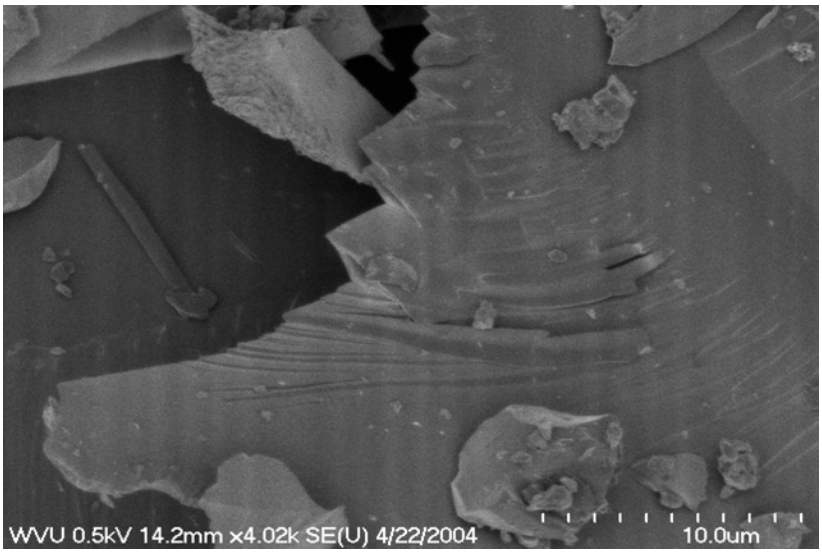

Figure 8. SEM image of oxidized SECO coked to 800 ºC

The electrical resistivity of the compacted heat treated SECO powders was assessed by placing the powder in a nonconductive piston with electrodes on each end. The resistivity was measured with respect to packing weight loaded on top of the piston. The results are listed in Table 4, as well as in Figures 9 and 10. From the results listed in Table 4, one can clearly see that the higher the heat-treatment temperature, the lower the resistivity of the SECO becomes. Thus the 800 °C sample represents one with low VM and resistivity and should perform well in the carbon fuel cell.

Table 4. Electrical Resistivity Measurements of some heat treated SECO samples

Sample Name	Resistivity (Ocm)
Oxidized, Heat-Treated to 400 °C SECO	Too high for accurate measurement
Oxidized, Heat-Treated to 600 °C SECO	$6.1 X10^{6}$
Oxidized, Heat-Treated to 800 °C SECO	29
Oxidized, Heat-Treated to 1000 °C SECO	Too low for accurate measurement

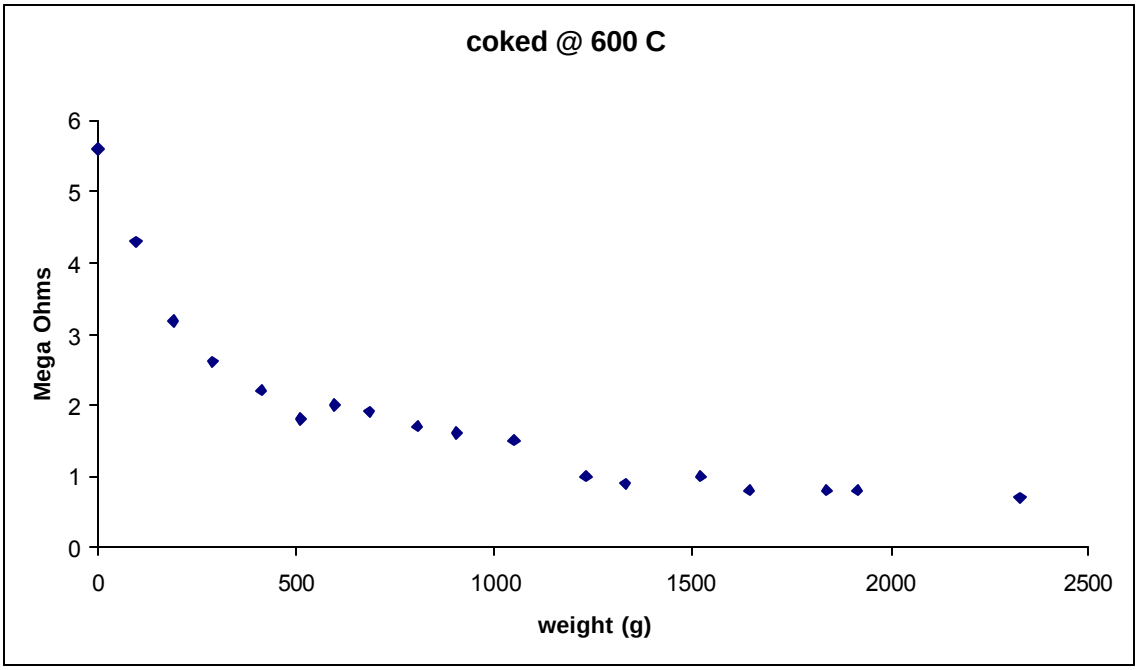

Figure 9. Electrical resistance measurements versus weight loading for Oxidized SECO heat treated to 600 °C

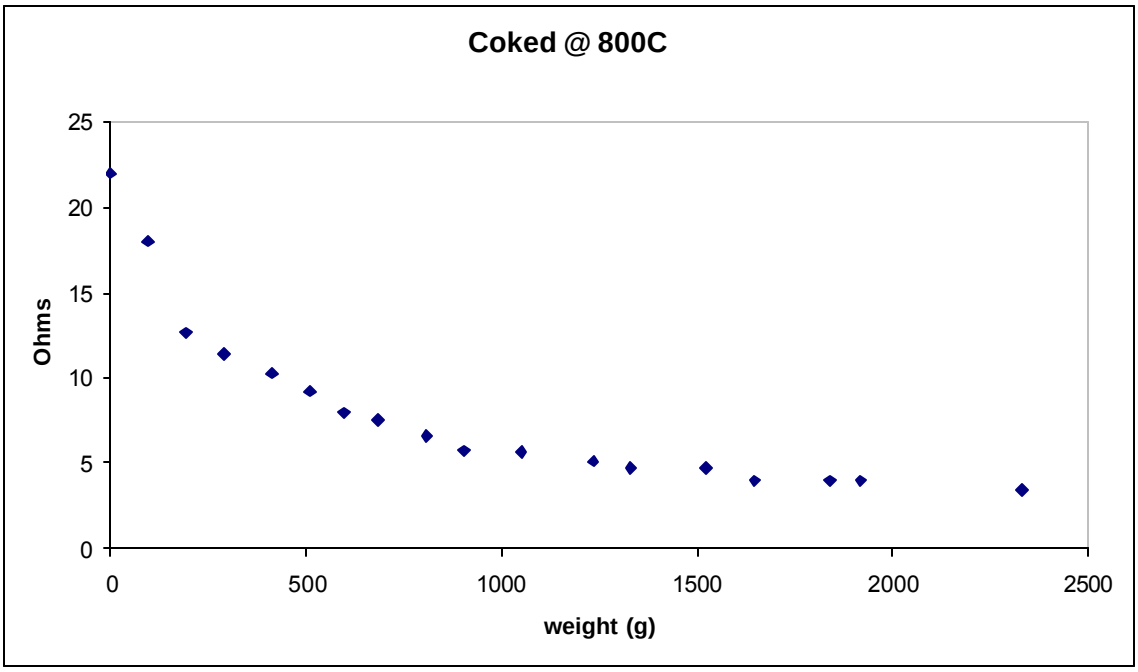

Figure 10. Electrical resistance measurements versus weight loading for Oxidized SECO heat treated to 800 °C

Dr. Cooper's group at LLNL was only able to test two of the samples sent to them by WVU. These two samples were the Oxidized, 400 °C heat-treated SECO and the oxidized, 800°C heat-treated SECO. In the case of the 400°C fuel, the cell voltage was reported to be poor due to sulfur interference with the cathode activation. However, the 800°C sample showed very favorable performance. These results are shown in Figures 11 and 12.

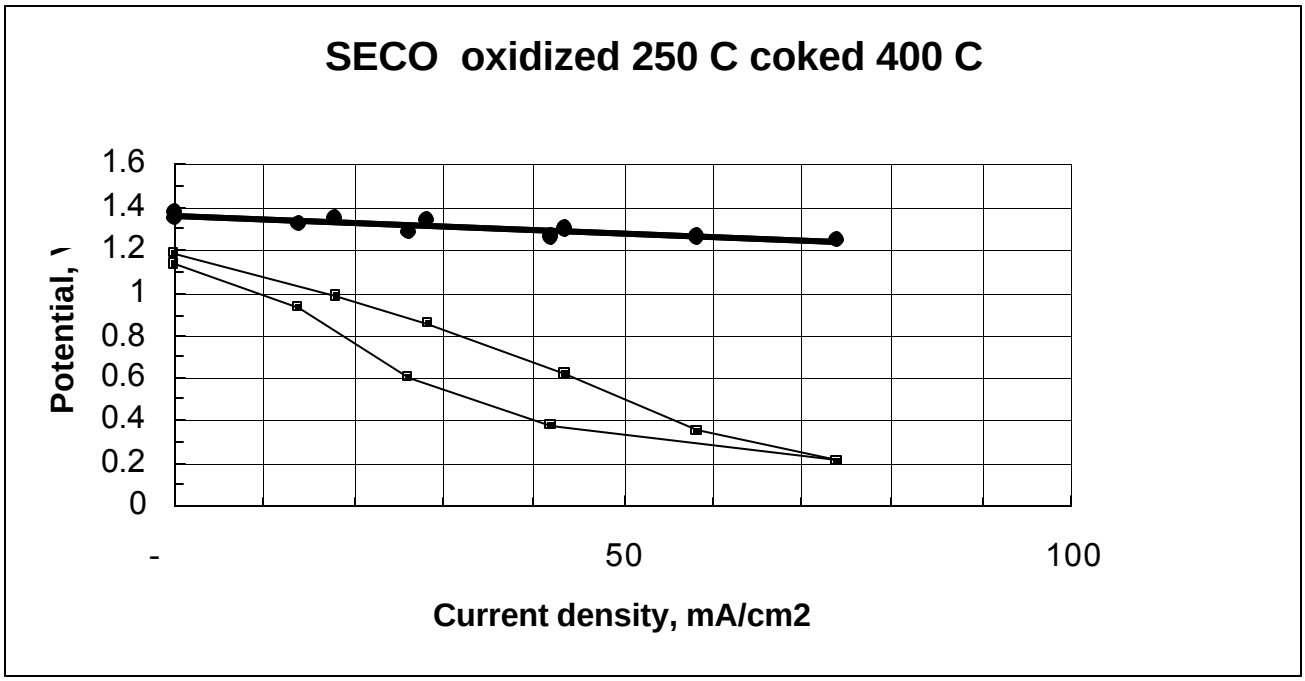

Figure 11. Polarization of Coked Solvent-Derived Sample
In this cell, we attempted to activate cathode in presence of C. The polarization of the carbon (upper trace) was favorable

Vcarbon ° Ecarbon - Eref (Au/ 5/7 air, 2/7 CO2)

Cell voltage was poor because S interfered with cathode activation

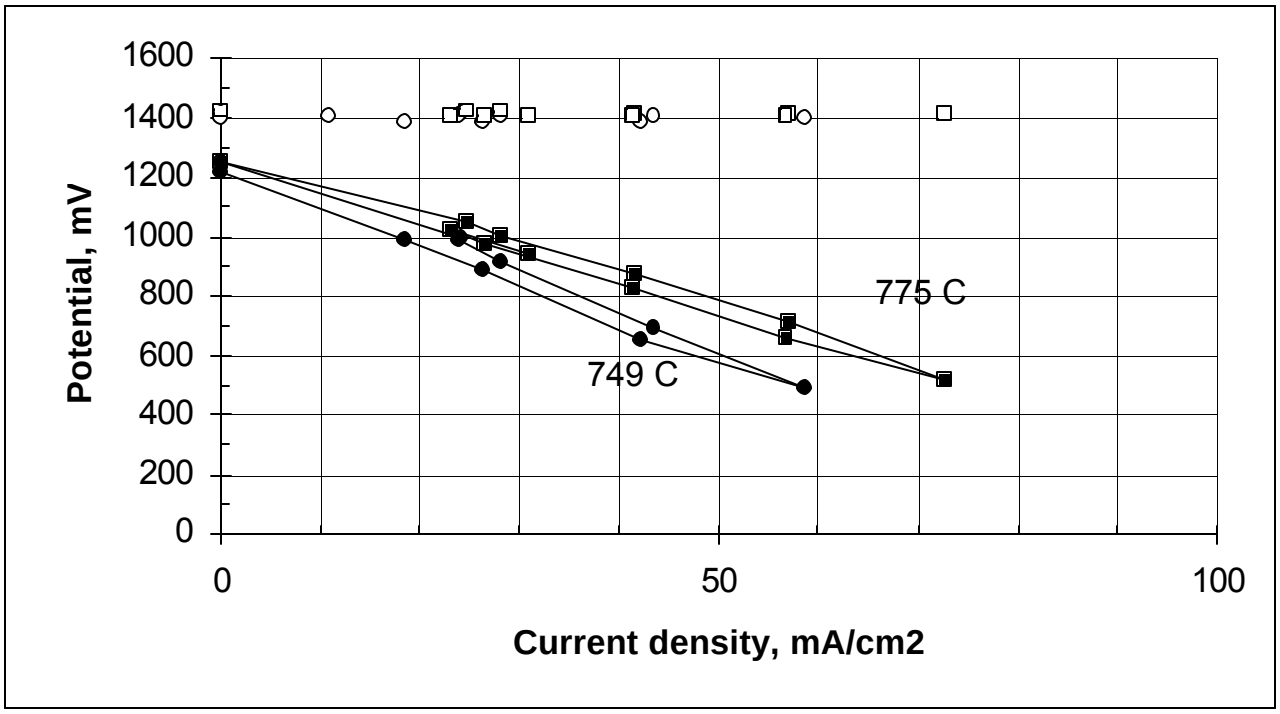

Figure 12. Pre-activation of Nickel Cathode Maximizes Performance of Carbon/Air Cell

- **Sample: WVU low-ash SECO; oxidized 250 °C, coked at 800 °C**
- **Cathode: activated prior to adding carbon to cell**
- **Favorable performance: 0.8 V at ~ 50 mA/cm2**

Dr. Chuang's assessment of the lab-scale SECO was as follows:

> "Your clean coal performed at the same level as Ohio no. 5 coal without producing much ash. The problem is the current density of our fuel cell remains to be very low. The low current density is not due to your clean coal. It is due to the problem inherent to our fuel cell. We are working to improve our fuel cell. Once I get good results, I will let you know immediately."[3]

Finally, Figure 13 shows a photograph of two foam samples produced during this work. The one on the left is a foam made from only CTP and the one on the right is the foam made from the blend of 30% CTP and 70% oxidized SECO which was heat-treated to 800°C. As can be seen, the CTP-only foam was very porous, of low density and of

low strength. In contrast, the SECO/CTP was very dense with much smaller pores and with much greater strength.

Figure 13. Carbon foam produced from SECO powder and CTP (right), and from CTP alone treated under the same conditions (left)

A crush test was conducted on the SECO/CTP foam sample and resulted in a value of 12.3 MPa. The density of the foam was found to be 0.87 g/cm^3 and the porosity was found to be 47%. These results are comparable to other carbon foams produced from a variety of feedstocks at WVU.

Conclusions

Elemental and proximate analyses of WVU Coal Extraction Pilot Plant SECO samples, SECO-4 and SECO-6/7, showed that the samples were low in ash and sulfur. However, a significant reduction in the VM content was needed in order to minimize difficulties during the testing of the DCFC. With the goal of decreasing the VM, and minimizing ash, a lab-scale SECO batch was successfully made from Kingwood Coal. This SECO was partially oxidized to prevent foaming during the heat-treatment process which was conducted at four different temperature levels (400, 600, 800, 1000 °C). Heat treatment resulted in a dramatic decrease in volatile matter. Heat-treated samples also demonstrated a continuous increase in carbon, and a decrease in nitrogen, hydrogen and sulfur. The oxygen content jumped significantly following oxidation, as was expected, and then decreased dramatically upon heat treatment.

XRD results indicated some degree of order in the structure of these heat-treated SECO samples. A higher degree of order as indicated by both the d-spacing and L values was observed for the samples heated at higher temperatures. All the carbons thus produced had domain sizes less than 30 nm, indicating turbostratic carbons.

Electrical resistivity measurements showed that the higher the heat-treatment temperature, the lower the resistivity of the SECO becomes. Thus, with the oxidized SECO heat-treated to 800°C or above, a more conductive carbon is obtained. Unfortunately, an accurate value for the resistivity of the 1000 °C heat-treated sample was not possible with the equipment available in the laboratory.

A SECO/CTP foam sample was successfully created and showed properties consistent with other similar foam samples.

The oxidized, 800 °C heat-treated SECO showed favorable performance in LLNL's fuel cell. The lab-scale SECO was also shown to perform well according to Dr. Chuang's findings. The low ash character of these samples makes them very attractive for application in the direct carbon fuel cell. Further work is this direction will be pursued in the future.

REFERENCES

1. N.J. Cherepy, R. Krueger, K.J. Fiet, A.f. Jankowski, J.F. Cooper, "Direct Conversion of Carbon Fuels in a Molten Carbonate Fuel Cell," (Journal of the Electrochemical Society February 25, 2004)
2. K. Renganathan, J.W. Zondlo, E.A. Mintz, P. Kneisl, A.H. Stiller, "Preparation of an Ultra-Low Ash Coal Extract under Mild Conditions," (Fuel Processing Technology, 18 (1988) 273-278)
3. Personal communication between Dr. Steven S.C. Chuang at the University of Akron and Dr. John W. Zondlo at West Virginia University.
4. Norio Iwashita, Chong Rae Park, Hiroyuki Fujimoto, Minoru Shiraishi, Michio Inagaki, "Specification for a standard procedure of X-ray diffraction measurements on carbon materials," (Carbon 42 (2004) 701-714)
5. "Standard Test Method for Determination of Crystallite Size (Lc) of Calcined Petrolium Coke by X-ray Diffraction," (ASTM Designation: D 5187 – 91 (Reapproved 1997))
6. Ron Walker, "Direct Carbon Fuel Cells: Assessment of the ir Potential as Solid Carbon Fuel Based Power Generation Systems," (Ron Wolk, Wolk Integrated Technical Services, San Jose, CA, (Report to Directors' Review Committee April 9, 2004; Report No. UCRL-SR-203880))

LIST OF ACRONYMS AND ABBREVIATIONS

LLNL:	Lawrence Livermore National Laboratory
DCC:	Direct Carbon Conversion
VM:	Volatile Matter
SECO:	Solvent-Extracted Carbon Ore
XRD:	X-ray diffraction
SEM:	Scanning Electron Microscopy
VM:	Volatile Matter
CTP:	Coal Tar Pitch
NMP:	N-methyl pyrrolidone
DCFC:	Direct Carbon Fuel Cell
WVU:	West Virginia University

CONSORTIUM FOR PREMIUM CARBON PRODUCTS FROM COAL

Pitch Derived Fiber Reinforced Fly Ash Concrete

Subcontract No. 2565-UK-DOE-0350

FINAL REPORT
for Period 1 July 2003 through 30 June 2004

by

University of Kentucky
Center for Applied Energy Research

August 2004

Disclaimer

ABSTRACT

The results of Laboratory and supporting technical assessments conducted under DOE Subcontract No. 2565-UK-DOE-0350 are reported for the period July 1, 2003 to June 30, 2004. This contract is with the University of Kentucky Research Foundation, which supports work with the University of Kentucky Center for Applied Energy Research, Koppers Industries. The work involves the production of bulk carbon fiber fabricated from a range of pitch precursors using a centrifugal melt spinning (CMS) process, production of concrete mixtures that utilize coal combustion fly ash as a pozzolan and utilization/assessment of bulk carbon fiber reinforcement in concretes.

TABLE OF CONTENTS

EXECUTIVE SUMMARY

This report describes the methods and results for the evaluation of CMS carbon fibers as a reinforcement in fly ash concrete and mortar composites. Preliminary work on modifying and then commissioning a CMS fiber production unit was carried out. This involved re-design of the pitch feed system and the addition of a cyclone fiber collection system.

The main focus of the experimental study was to assess common performance improvements associated with the addition of fiber reinforcement in concrete. Test specimen sizes were maintained at a relatively small scale to facilitate ease of storage, handling, and testing. Quantitative tests performed on concrete and fiber composite concrete specimens included: indirect tensile strength; unconfined compressive strength; modulus of elasticity; and a brief study on nuclear shielding. Tests performed on mortar composites included: drying shrinkage; flexural strength properties; and thermal conductivity. Additional investigations and studies to determine air content, admixture demand, and workability effects on wet and hardened concrete, mortar, and cement paste were also performed.

1. SECTION ONE

UNIVERSITY OF KENTUCKY
CENTER FOR APPLIED ENERGY RESEARCH

INTRODUCTION

This project is the integration of two developing areas in value-added products derived from coal. The first area is the production of low cost discontinuous carbon fiber from coal derived pitch, the second, utilization of recovered coal combustion fly ash in concrete. In this project, pitch was fabricated into discontinuous carbon fiber and used as reinforcement in fly ash concretes and mortars. The addition of pitch derived fiber to fly ash concrete should maintain stress transfer capability across a matrix crack to improve toughness, impact resistance and fatigue endurance in fly ash concrete.

Since the 1930s, the benefits of using pulverized coal combustion fly ash as a concrete admixture have been recognized in the U.S. [Davis et al., 1937]. With the advent of more stringent environmental regulations such as the Clean Air Act, large amounts of high-quality fly ash became available in the late 1960's and early 1970's [ACI, 2000]. Using fly ash as a partial replacement for Portland cement not only improves the “workability” of fresh concrete, but also improves long-term strength and durability. In a Portland cement-water system fly ash behaves as a pozzolan, which is defined as a glassy silicate or aluminosilicate that does not possess cementitious properties when mixed with water, but will react with aqueous calcium hydroxide at ordinary temperatures to form a cement [ACI, 2000]. Replacing a portion of Portland cement with a high quality fly ash reduces the amount of calcium hydroxide that is responsible for secondary destructive reactions in concrete such as sulfation, while simultaneously increasing the formation of calcium aluminosilicate hydrate gels, which serve as “binders” in concrete. Consuming the calcium hydroxide in the interstitial pore waters to form additional cement thus imparts many structural benefits to the concrete including greater compressive strength, lower permeability and increased durability. A reduction in permeability is particularly important for prevention of corrosion in reinforcing steel.

In addition to the structural benefits imparted to concrete by the addition of fly ash and carbon fiber, the replacement of Portland cement with coal combustion fly ash can indirectly lower the amount of CO_2 emitted to the atmosphere. The production of Portland cement is the third largest man-made source of CO_2 emissions. As a rule of thumb, the production of one ton of Portland

cement releases one ton of CO_2 to the atmosphere. In the conterminous United States alone there were approximately 89 million metric tons of cement manufactured in 2002 [USGS, 2003]. Thus, an important environmental benefit can be realized by replacing more Portland cement in concrete with fly ash. This benefit occurs because the CO_2 emission that occurs when fly ash is produced is caused by electricity, not fly ash, production, there is also far more fly ash produced than is utilized. In other words, increasing the use of fly ash in concrete will not cause additional fly ash to be produced to meet demand. In fact, when the improvements in concrete strength and durability are factored in, there may not be a more effective and unobtrusive technology for CO_2 reduction. Therefore, in addition to determining the performance of the coal derived pitch fibers in concrete, a goal of this project will be to design the pitch fiber reinforced concrete mixes to maximize the proportion of fly ash that can be added to the concrete while also achieving a high synergistic performance with the fibers (i.e. increasing the paste volume to better accommodate the fibers).

Corrosion of steel in concrete has lead to a significant amount of effort aimed at finding alternative ways of reinforcing concrete. One possibility is to reinforce concrete with randomly distributed fibers such that fibers maintain the stress transfer capability across a matrix crack, and in turn, improve the toughness, impact resistance, and fatigue endurance of concrete [Bentur and Mindess, 1990]. Various applications such as slabs on grade, bridge decks, and tunnel linings, where steel is provided mainly to combat secondary stresses, the use of fiber is proven to be practical and cost-effective [Bantha et. al., 1995].

Concrete contains a significant volume fraction of coarse aggregate larger than 5 mm, and consequently a much smaller paste (cement and water) volume fraction available to accommodate the fibers. Therefore, the maximum fiber content without excessive mixture stiffening and loss of workability is rather small, often less than 1%, and usually not more than 2% by volume of mixture. Rigorous mechanical mixing is usually needed to blend the fibers with coarse and fine aggregates, cement, and filler materials present. Fly ash, slag, or silica fume are used to increase the paste volume fraction and facilitate accommodation of fibers. Steel fibers are most commonly used, but fibrillated polypropylene, and monofilament forms of polypropylene, polyethylene, polyvinyl alcohol and polyacrylonitrile can also be incorporated

into concrete by mechanical mixing, or in some cases by dry-process shotcreting [Johnston, 2001].

Coal derived pitch carbon fiber may be a viable performance and cost alternative to traditional concrete fiber reinforcements. The carbon fibers produced for this project will be fabricated from isotropic pitch, supplied by Koppers Industries. Fibers will be formed using a novel technique, Centrifugal Melt Spinning (CMS), previously developed at the University of Kentucky Center for Applied Energy Research. The CMS process is capable of producing fibers from feedstocks containing significant quantities of solids, offering the potential for utilizing low cost feedstocks and reduced processing economics. Furthermore, regardless of the purity of the pitch feedstock, the high throughput of the CMS process makes it eminently suitable for producing large quantities of material in bulk fiber applications like concrete reinforcements.

CMS generates discontinuous fiber in the form of large fiber mats. CMS fibers have characteristic variations in diameter over the length of fiber, they also tend to be curved. These features do not necessarily detract from their performance in bulk filler applications and in fact may actually enhance adhesion of the fiber in the matrix. Variations in fiber geometry cause the matrix to "lock" around the fiber more effectively, allowing more effective stress transfer from the matrix to the fiber without allowing the fiber to slip within the matrix.

Literature Review

Zhang et al. (2002) uses a fiber-reinforced strip of mortar in concrete slabs in hopes of replacing typical jointing in concrete slabs. The idea is to localize cracking in the strip. They use 1.5 % by volume of polyethylene fibers E = 120 Gpa, tensile strength = 2700 Mpa, diameter = 0.038 mm, and length = 19.05 mm. Strain hardening was observed after first crack. The composite strains at 5% as opposed to 0.02% for regular concrete. Fiber composite mix proportions were cement = 1, sand = 0.5, water = 0.32, superplasticizer = 0.02, methyl cellulose = 0.0007, and antifoamer = 0.0005. Slabs were broken in uniaxial tension in a MTS 810 material testing system at 3, 7, 14, 21, and 28 days. Stress / strain and tensile strengths were reported.

Zollo states that ASTM C1018 is the typically accepted test for strength and toughness, but mentions that post cracking testing may be better. It reduces the sudden energy release associated with typical failure tests. For a flexure test, the specimen is placed between two steel plates and loaded in flexure to a specified deflection where the specimen is beginning to fail by cracking. The steel plates are then removed and the specimen is tested by itself to a chosen deformation, and load deformation relationships are obtained. An example of a 4"x4"x14" specimen in a four-point loading was given. Value added applications mentioned include low fiber volume, 0.5 vol%. Slab on grade and composite deck applications were given because of improved serviceability such as durability and toughness. Cast in place and precast applications include dam, bridge deck, mine, tunnel, canal, and reservoir lining, security and utility vaults, caisson, pile and pile cap foundation elements, slope stabilization, highway and airport slabs and many others. Typical applications are for crack control and utilize the energy-absorbing capabilities of fibers.

Tatro used steel fiber reinforcement in concrete composites with large size (1.5") aggregate. 3 types of steel fibers were used. Properties are as follows: yield strength = 170, 140, and 55 ksi, length = 60, 76, 19 mm, diameter = 0.8, 0.8, 0.4 mm, fibers had hooked ends, corrugated shape or were smooth. Beams were tested for fatigue and in flexure (ASTM C1018) and load deflection were curves plotted. Cylinders were tested for compressive strength and impact resistance. Impact testing was performed on 2 5/8" thick specimens sawed from 6" cylinder cross-sections by dropping a 10.5 lb weight from a height of 18in. The number of blows to first crack and ultimate failure (deformation to 6 3/8") were recorded for impact testing. Cylinder mix fiber content varied and beam fiber contents were 80 lbs/cyd for hooked and corrugated and 200 lbs/cyd for smooth. Flexural toughness, impact resistance, and fatigue properties were improved. Cylinder mix proportions were: Cement = 637 and 575 lb/cyd, water = 255 and 230 lb/cyd, 1.5" coarse aggr. = 778 and 709 lb/cyd, ¾" coarse aggr. = 1246 and 1162 lb/cyd, fine aggr. = 1091 and 1354 lb/cyd. Fatigue specimen mix proportions were: Cement = 597 lb/cyd, water = 229 lb/cyd, 1.5" coarse aggr. = 707 lb/cyd, ¾" coarse aggr. = 1157 lb/cyd, fine aggr. = 1348 lb/cyd. Entrained air was kept at 5%.

ACI suggests that section thickness may be reduced by use of fibers. ASTM C1116 is standard spec. for fiber reinforced concrete and ASTM A820 covers steel fibers. They recommend mix proportions as follows: cement = 500-900 lb/cyd, w/c =0.35-0.50, percent fine to coarse aggr. = 45-55, air content 4-6, smooth fiber = 0.3-0.8 vol%, deformed fiber = 0.6-1.6 vol%. Slab joints should be sawed 1/3 to ½ way through slabs to prevent random cracking elsewhere in the slab due to increased performance of the FRC at the joint.

Uomoto et al. mentions applications for FRC such as prestressed concrete, anchors for slope stabilization, and in special structures such as high speed motor railway tracks, MRI units of hospitals, and repair and rehabilitation works.

Zhang and Li (2001) state that Mangat and Azari (1988) performed shrinkage tests on steel fiber reinforced concrete and mortar beams with dimensions of 100x100x500mm. The specimens were cured at 20C at a relative humidity of 55%. The shrinkage was measured with an extensometer with regular measurements up to 120 or 520 days of age. The concrete mix proportions by weight were 1:2.5:1.25:0.58 (cement:sand:stone:water) and the mortar proportions by weight were 1:2.75:0:0.58 (cement:sand:stone:water). Three fiber types were used: hooked, crimped, and smooth extract. The fiber contents varied from 0 to 3%, fiber radius = 0.2-0.57mm, E = 210 Gpa, L = 22.5-48.7, depending upon the fiber type. Shrinkage vs. age was reported. FRC showed less shrinkage after about 50 days.

Zhang (2003) also states that Mangat et al. (1985) measured creep of FRC beams with smooth and hooked steel fibers. The mix was the same as mentioned above. The specimen was placed in a creep rig and loaded to a stress/ strength ratio of 0.3 and 0.55 respectively. The load was kept constant for 90 days and the creep measured with an extensometer. Creep strain versus time was reported. The FRC demonstrated less creep strain.

Bischoff performed axial tension tests on 100x100x1100mm concrete beams reinforced with a central 15 or 20 M steel bar and steel fiber. The FRC mix consisted of Cement = 450 kg/m^3, coarse aggr. = 764 kg/m^3, fine aggr. = 928 kg/m^3, water = 188 kg/m^3, 60kg/m^3. It appears that some of the coarse aggregate was taken out to accommodate the steel fiber and keep the

yield at 1 m^3. Specimens were moist cured for 7 days the air-dried for 64 or 65 days until testing. Stress strain and crack spacing and widths were reported.

In a run through of some of the remaining abstracts, the same tests keep surfacing as mentioned in the summaries above, ASTM C1018, compression, tension and impact resistance as well as shear tests and shrinking and cracking. The tests seem to result in improved characteristics, especially toughness, when performed on FRC. Resistance to wear heat and corrosion was noted with carbon fibers. Fiber volumes are consistent from 0 to 2 or 3%. The main applications that are continuously mentioned are slabs. Repair and rehabilitation are also mentioned as well as use of fibers in shotcrete.

It is suggested that fiber length should exceed the maximum aggregate size in the matrix (Blood, 1970; Tatro, 1985). Fibers currently marketed for use in concrete are rarely shorter than 15 mm or longer than 65 mm. Guidelines for water-cement ratio, cement content and fine/total aggregate contents for mechanically mixed steel fiber-reinforced concrete have been developed (ACI Committee 544, 1993). The process has been utilized primarily with steel fibers at fiber contents up to 20% by volume (Lankard, 1986; Bayasi and Zheng, 1997).

Task 1.0 Fabrication of CMS Carbon Fiber

Further to the work completed under a previous CPCPC Project and described in, “Production of Bulk Carbon Fibers and Activated Carbon Fibers via Centrifugal Melt Spinning” Final Report, March 2002 through June 2003 Subcontract No. 2191-UK-DOE-0350, the CMS processor was modified. Modifications included the addition of cyclone fiber collection system that dramatically reduced the amount of damage and breakage of the green fibers during production. The extruder feed system was also rebuilt using a slightly smaller i/d extruder bore, to improve the precision and consistency of the feed rate delivery to the spin head. The entire CMS unit was also skid mounted. CMS process modifications are shown below in Figure 1.

Figure 1 – Skid mounted CMS with cyclone collection system.

Koppers Industries Inc supplied two coal tar pitches, one low QI low softening point pitch (Stickney pitch) and one high QI high softening point pitch (Clairton pitch). As reported previously, "Production of Bulk Carbon Fibers and Activated Carbon Fibers via Centrifugal Melt Spinning" Final Report, March 2002 through June 2003 Subcontract No. 2191-UK-DOE-0350, the high QI Clairton pitch was successfully converted into CMS fiber mats. However, carbon fibers produced from this feedstock showed lower tensile strength and elastic modulus compared to other fibers produced from lower QI feedstocks. To produce fiber concrete composites that fully exploit the properties of the fiber reinforcement, CMS fibers were produced from the low QI Stickney pitch. However, before the Stickney pitch could be converted into CMS fibers its softening point was increased so that CMS fibers could be thermally processed to CMS carbon fibers.

Air blowing was used to increase the softening point of the Clairton pitch from 110 ^{o}C to 250 ^{o}C. The air blowing process can be described as follows. The pitch was heated to 300 ^{o}C while air flowing at approximately 1 L/min was bubbled through the pitch. Air blowing was performed in batches of approximately 2.5 kg of pitch for 12-17 h. Samples of pitch were removed and their softening points measured during the treatment.

After a desired softening point of 250 ^{o}C was reached, the pitch was allowed to cool and then crushed to a particle size of < 2 mm. The crushed pitch was transferred to the CMS extruder feed system and the molten pitch fabricated into discontinuous fiber mats and collected by the cyclone collection system. Approximately 2 kg of CMS fibers was produced during each spinning run. The green fibers were then processed to carbon fibers in two steps. The first step was oxidative stabilization. Green fiber mats were heated in air at 5 ^{o}C/min to 180 ^{o}C, then at 0.1 ^{o}C/min to 320 ^{o}C and held for 3 h. The cross-linking reactions that occur during stabilization are exothermic, hence the very slow heating rate was necessary to prevent the fiber mats from overheating and igniting during stabilization. The stabilized fiber mats were then carbonized by heating at 20 ^{o}C/min to 1000 ^{o}C in nitrogen. During the course of this project approximately 10 kg of CMS pitch derived carbon fiber was produced. Table 1 shows fiber processing for CMS fibers derived from Stickney pitch.

Table 1 – Data summary for processing of Stickney pitch fibers.

Pitch	Stabilization				Carbonization			Carbon Yield (%)
	Rate (^{o}C/min)	Linear Shrink (%)	Weight Change (%)	Status	Linear Shrink (%)	Weight Change (%)	Status	
Stickney	0.1	n/a	4.2	3	n/a	28.1	3	76.1
Status: 0 = melted, 1 = stuck, 2 = slightly stuck, 3 = OK. *n/a = not applicable.*								

The discontinuous fiber mat nature of CMS fibers makes assessment of their physical properties difficult. To determine approximations of tensile strength and elastic modulus of fibers derived from Stickney pitch, continuous filaments where melt spun using a ¼" Wayne Yellow Jacket bench top extruder. Continuous filaments were spun from a 330 μ die and the filaments wound onto a rotating drum. By controlling the extruders screw speed and the speed of the wind up drum the diameter of the resultant filaments can be controlled. Continuous filaments were cut of the wind up drum as fiber tows and processed to carbon fibers using the same methods described above. The mechanical properties of the continuous filaments were measured according to ASTM D3379 using an MTS Qtest tensile tester, Table 2.

Table 2 – Mechanical properties of Stickney pitch derived continuous filament carbon fibers.

Diameter (μm)	25.3
Tensile Strength (MPa)	408
Modulus (Gpa)	32

Figure 3 shows an example of CMS fibers produced from Koppers Stickney pitch. Inspection of Figure 3 shows the typical characteristics of CMS fibers. The fibers have variable diameter, are curved and may be tapered along the axis. A small batch (~500g) of CMS fibers were treated with boiling nitric acid for 2 hours. The nitric acid treatment was used to modify the surface

functionality of the fibers. These acid treated fibers were used for different investigations described below.

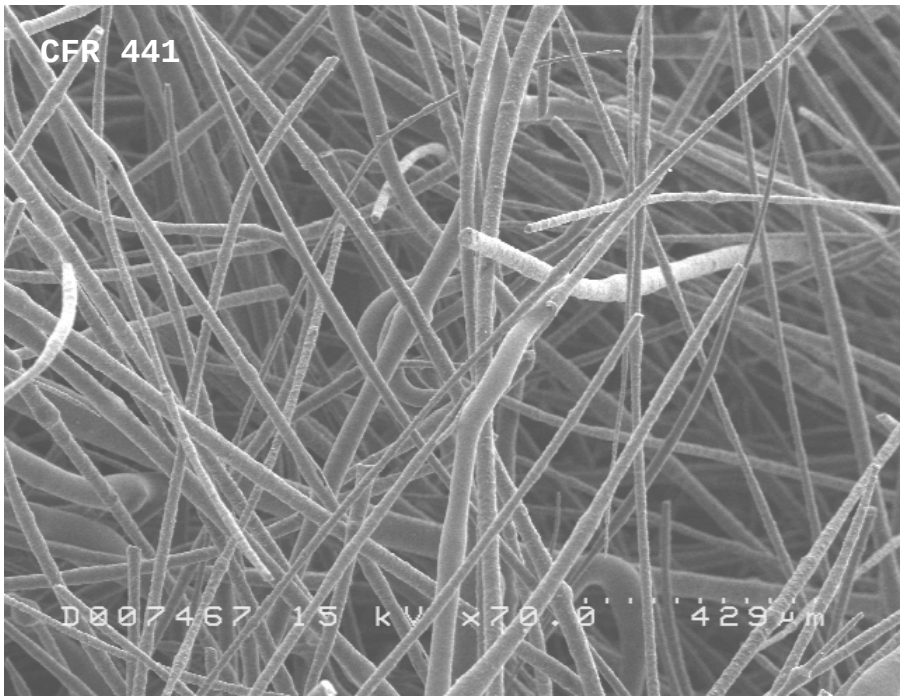

Figure 3 – CMS fiber produced from Stickney pitch.

Task 2.0/3.0 Fly Ash Concrete Test Specimens/Fabrication of fiber reinforced concrete

CMS carbon fibers were evaluated as reinforcements in both concrete and mortar mixes. The concrete mix design chosen for this project was the Class AAA mix, outlined in the Kentucky Transportation Cabinet (KYTC) Standard Specifications for Road and Bridge Construction 2000 Edition. The AAA mix was an ideal candidate for the addition of CMS carbon fibers. The mix produces a high performance concrete primarily utilized for bridge deck construction. However, because of its high cement content use of the AAA mix has for the most part been discontinued by the KYTC due to problems with shrinkage and cracking during curing. The addition of CMS carbon fiber should not only further improve the concrete strength but may also help control shrinkage during curing. Mortar mixes matched those outlined in ASTM standards C596 (for shrinkage specimens) and C109 (for flexure specimens).

A 20% by weight replacement of flyash for cement was used in all concrete and mortar mixes. Fiber contents of 0.1, 1.0, and 2.0% by volume were chosen to span typical ranges found in literature. A volume of sand, equal to the volume of fiber used, was removed in all mixes to maintain a constant yield. The concrete mix designs are presented in Table 3.

Table 3 - Class AAA Concrete Mix Proportions

		AAA Mix							
		Control		**0.1% Fiber**		**1% Fiber**		**2% Fiber**	
	SG (cc/g)	**wt (kg)**	**vol (m^3)**	**wt (kg)**	**vol (m^3)**	**wt (kg)**	**vol (m^3)**	**Wt (kg)**	**vol (m^3)**
Cement	3.2	325.6	0.1	325.6	0.1	325.6	0.1	325.6	0.1
Fly Ash	2.4	81.4	0.0	81.4	0.0	81.4	0.0	81.4	0.0
Water	1.0	162.8	0.2	162.8	0.2	162.8	0.2	162.8	0.2
Sand	2.6	673.2	0.3	670.6	0.3	646.9	0.2	620.6	0.2
Gravel	2.7	1029.0	0.4	1029.0	0.4	1029.0	0.4	1029.0	0.4
Fiber	1.8	0.0	0.0	1.8	0.0	18.0	0.0	36.0	0.0
Air	-	0.0	0.1	0.0	0.1	0.0	0.1	0.0	0.1
Total		**2272.0**	**1.0**	**2271.2**	**1.0**	**2263.7**	**1.0**	**2255.4**	**1.0**

The coarse concrete aggregate consisted of crushed limestone (No. 57 and No.8 size), and the fine aggregate comprised washed river sand. Admixtures used included an air-entraining admixture (AEA) as well as mid- and high-range water reducing admixtures. It should be noted that the high range plasticizer was only used in the 2 % fiber mixes. The fly ash was obtained from a central Kentucky power plant, and meets C 618 requirements for use as a pozzolanic admixture in concrete. The sand used for mortar strength and shrinkage testing comprised ASTM standard (graded) Ottawa sand, whereas that used for mortar air entrainment tests comprised ASTM 20-30 sand.

Concrete was prepared in a portable concrete mixer with a capacity of 2.3 m^3. Fibers were added to the wet concrete using two methods: 1) dispersion of the fibers into a slurry using a 4 L blender and adding the slurry to the mix, or 2) separation and distribution of the fibers into the mix by hand. All aggregates, water, and plasticizers were charged into the mixer and tumbled slowly for approximately 10 min to free the fine particles that had adhered to the surface of the coarse aggregate. The cement, ash, and AEA was then charged into the mixer and mixed at full speed for approximately 2 min, allowed to set for approximately 4 min, while the sides of the mixer were scraped down, and then mixed for an additional 2 min at full speed. Mortars were mixed with a 4.7 L (5 qt) stand mixer in accordance with ASTM C 305.

Workability, Air Entrainment and Admixture Demand

Investigations were performed to determine the effect that CMS fibers had on entrained air content and workability of concrete and mortar. All water contents and admixtures dosages were held constant, unless otherwise noted. Concrete workability and air content was determined using the methods outlined in ASTM C 143 and ASTM C 231, respectively. Mortar workability and air content was determined by using the methods outlined in ASTM C109 and ASTM C185, respectively. Table 4 and 5 present the workability and air data for concrete and mortar mixes.

Table 4 – AAA concrete mixes air content and workability

	Slump (in)	Air (%)
Control	7	6
0.1% Fiber	6.5	6.5
1% Fiber	5	9
1% Fiber **	nd	9

****** Note: No air entraining admixture used in this mix

Inspection of Tables 4 and 5 reveals that the addition of CMS fibers reduced the workability and flow of the mortar and concrete mixes. This is to be expected given that any alteration or addition to a standard concrete or mortar mix will affect the workability. Table 5 also shows a slight increase in air content for the 1% fiber mortar mix. Additional tests were performed to determine the origin or source of the additional air observed for the fiber mortar mixes.

Table 5 – Mortar workability and air content

	Flow (%)	Mortar Air (%)
Control	86	18
0.1% Fiber	44	19
1% Fiber	32	20

A modified version of Dodson's foam index test (modified by Boral Material Technologies) and Ultraviolet-Visible (UV-Vis) spectroscopy were used to quantify adsorption of the air entraining admixtures (AEAs) by the carbon fibers. The foam index is essentially a titration where the endpoint is indicated by the formation of a stable foam on the surface of an aqueous cement-air entrainment admixture mixture. The test is performed by blending the materials together and adding aliquots of the air entrainment admixture (AEA) are added and the mixture re-blended. The solution surface is inspected after each aliquot addition until a stable foam is observed (defined as an unbroken foam covering the entire surface). The larger the volume of AEA added indicates higher adsorption of AEA by the CMS fiber. Tests were performed using two different

AEA's, abietic acid and sodium laural sulfate on cement-fly ash mixtures with and without CMS fibers. The results from the foam index tests are presented in Table 6.

Table 6 – Modified foam index test results

	Abietic Acid, sodium salt	**Sodium Laural Sulfate**
Cement	2.2	3.2
Cement + Fibers	2.2	2.8
Cement + Acid Treated Fibers	2.5	3.3

In the UV-Vis spectroscopy experiments, different mixtures of Portland cement, fly ash, carbon fibers, water, and AEAs were prepared. After mixing for 5 min the aqueous mixture was filtered through a 0.45 micron filter and the solutions AEA concentration measured. Abietic acid (5.9%) and sodium dodecylbenzosulfonate (NaDDBS) were used as model compounds representing two classes of commercial concrete AEAs. The results of UV-Vis tests results for CMS fibers and nitric acid treated fibers are presented in Tables 7 and 8.

Table 7 – Adsorption of AEA by CMS fibers

	ppm remaining in solution	
	Abietic Acid	**NaDDBS**
Standard Solution	1945	1100
Cement Only	1434	NA
Cement and Flyash	1759	367
Cement, Flyash and Fibers	1609	344

Table 8 – Adsorption of AEA by CMS fibers treated with nitric acid

	ppm remaining in solution	
	Abietic Acid	**NaDDBS**
Standard Solution	1200	1299
Cement Only	NA	454
Cement and Flyash	1184	413
Cement, Flyash and Fibers	931	440

The results for the modified foam index and UV-vis tests show that the CMS fibers do not have any affinity for the AEAs. This also indicates that any additional air observed in fiber concrete and mortar mixes is likely due to air trapped within agglomerates of CMS fibers.

For concretes to resist the effects of freezing and thawing there must be sufficient air voids in the cured concrete. It is generally considered that the maximum distance from any point in the cement paste to the periphery of an air void should be 0.20 mm or less. This distance is referred to as the spacing factor (L). The spacing factor (L) was measured using optical microscopy analysis of polished cross sections of concrete fiber composites, Table 9. Inspection of Table 9 shows that the spacing factor (L) to be below the desired value of 0.20 mm, hence the concrete fiber composites should not be adversely affected by freeze/thaw conditions.

Table 9 – Optical microscopy results for air and fiber content

Sample	**Air Content (%)**	**Fiber Content (%)**	**L (spacing factor)**
No fiber	7.64	0	0.16
0.1% Fiber	5.84	0.24	0.18
1% Fiber	8.23	0.97	0.15

Task 4.0 Evaluation of fiber reinforced concrete

Mechanical Properties

All specimens were cast according to American Society for Testing Materials (ASTM) accepted practices and cured submerged in water at a controlled temperature of 23^{o}C, Figure 4. Cylindrical concrete specimens, with dimensions of 76x152 millimeters (3 in X 6 in), were cast and cured in accordance with ASTM C 192. Strength parameters are to be tested after 29, 57 and 113 days of curing. Compressive strength and elastic modulus data will be obtained following the procedures outlined in ASTM C 39 / C 39M-99 and C 469-94, respectively, and tensile strength will be determined through the indirect split cylinder method outlined in ASTM C 496-96. The results of the concrete cylinder testing can be seen in Tables 10, 11, 12 and 13.

Figure 4 – Curing of concrete test specimens.

Addition of CMS fibers to concrete and mortar composites appears to have little if no effect on the tensile, compressive, and flexural strength of the specimens over the relatively short time span of this project. However, closer inspection of the data does show a small trend toward improved strength of the fiber composites, above the control specimens, in the long term. This is particularly evident for the 1 vol% fiber content specimens, Table 13, where this sample showed slightly higher tensile and compressive strength after 29 days of curing compared to the standard concrete, Table 10. It should also be noted that the fibers for these composite concretes were dispersed into the concrete by hand before being mechanically mixed. This procedure involved "teasing" the fibers apart into smaller agglomerates rather than adding the fibers as one large mat. Addition of the fibers as smaller agglomerates should have reduced excessive shortening of the fiber during mechanically mixing and indeed these composites did show moderately improved strength. Unfortunately, due to the time constraint of the project, longer term curing and strength measurements could not be completed.

Table 10 – AAA concrete standard cylinder test results

Curing Time (days)	Tensile Strength (MPa)	Compressive Strength (MPa)	Elastic Modulus (MPa)
29	4.7	35.5	15169
57	4.5	36.5	16893
113	5.2	46.4	18237

Table 11 – AAA concrete containing 0.1 vol% fiber cylinder test results (mechanically dispersed)

Curing Time (days)	Tensile Strength (MPa)	Compressive Strength (MPa)	Elastic Modulus (MPa)
29	4.5	36.5	15169
57	4.8	37.6	16962

Table 12 – AAA concrete containing 1.0 vol% fiber cylinder results (mechanically dispersed)

Curing Time (days)	Tensile Strength (MPa)	Compressive Strength (MPa)	Elastic Modulus (MPa)
29	4.4	31.0	12917
57	4.8	33.5	14893

Table 13 – AAA concrete containing 1.0 vol% fiber cylinder results (hand dispersed)

Curing Time (days)	Tensile Strength (MPa)	Compressive Strength (MPa)	Avg. Elastic Modulus (MPa)
29	5.1	38.5	15031

The flexural strength of fiber composite mortars was also assessed. Mortar bars with dimensions of 25 x 25 x 305 mm were cast with CMS fibers added in loadings of 0.1, 1 and 2 vol%, nitric acid treated fibers were also cast into fiber mortar composites. The specimens were cured at 23 ^{o}C and 100 % humidity for periods up to 61 days. Specimens were sawn into 152 mm lengths and tested via three-point bending on an MTS Q-test instrument. Mortar bars were tested across a span of 89 mm with a point load applied to the center of the sample and a constant cross head speed of 0.1 mm/min. The results of the flexural testing are presented in Tables 14, 15, 16, 17, and 18.

Table 14 – Standard mortar bar flexural test results

Curing Time (days)	Peak Flexural Strength (MPa)	Strain at Break (%)	Flexural Modulus (MPa)
28	6.8	0.18	3820
56	6.9	0.18	3873

Table 15 – 0.1 vol% CMS fiber mortar bar flexural test results

Curing Time (days)	Peak Flexural Strength (MPa)	Strain at Break (%)	Flexural Modulus (MPa)
28	6.1	0.16	3813
61	6.5	0.17	3980

Table 16 – 1 vol% CMS fiber mortar bar flexural test results

Curing Time (days)	Peak Flexural Strength (MPa)	Strain at Break (%)	Flexural Modulus (MPa)
28	5.8	0.17	3375
57	7.1	0.19	3753

Table 17 – 2 vol% CMS fiber mortar bar flexural test results

Curing Time (days)	Peak Flexural Strength (MPa)	Strain at Break (%)	Flexural Modulus (MPa)
28	4.8	0.16	3308
56	5.8	0.15	3871

Table 18 – 1 vol% nitric acid treated CMS fiber mortar bar flexural test results

Curing Time (days)	Peak Flexural Strength (MPa)	Strain at Break (%)	Flexural Modulus (MPa)
28	5.7	0.15	3897

Inspection of the above data shows that the addition of CMS fibers at varying loadings did not significantly increase or decrease the flexural strength of the mortars. Closer examination of the composite concretes and mortars was performed to determine why addition of CMS fibers had no impact on mechanical properties.

The fracture surfaces of composite concrete and mortars were examined under optical microscopy, Figure 5 and 6. Inspection of the fracture showed that the majority of CMS fibers were well dispersed within the matrix, however, there was evidence of small fiber agglomerates in both concretes and mortars. Evidence of fracture bridging by the fibers was also noted, Figure 7. However, the length of fibers within the composites was well below the desired lengths identified in the literature (see Introduction). Although fiber length was not quantified, generally fibers less than 10 mm were observed.

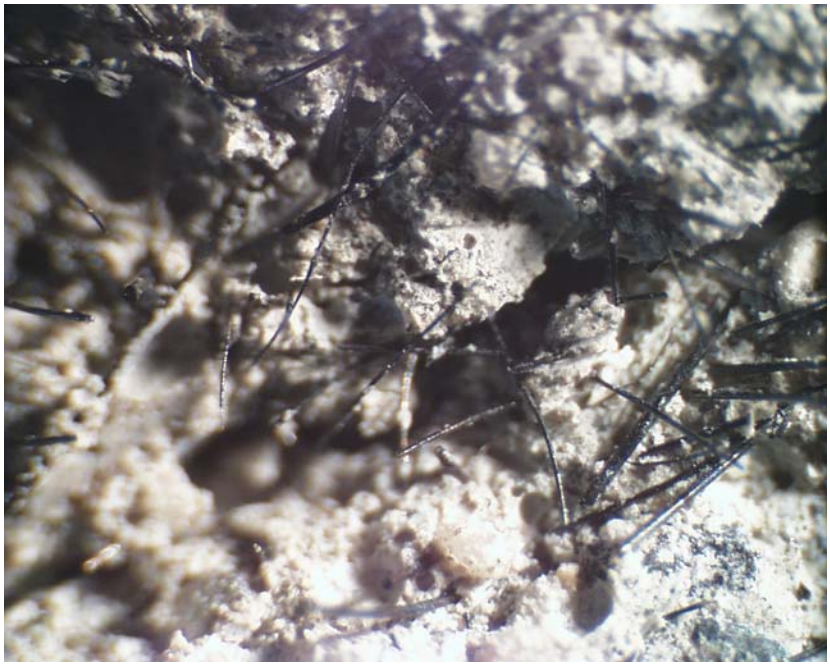

Figure 5 – Composite concrete fracture surface

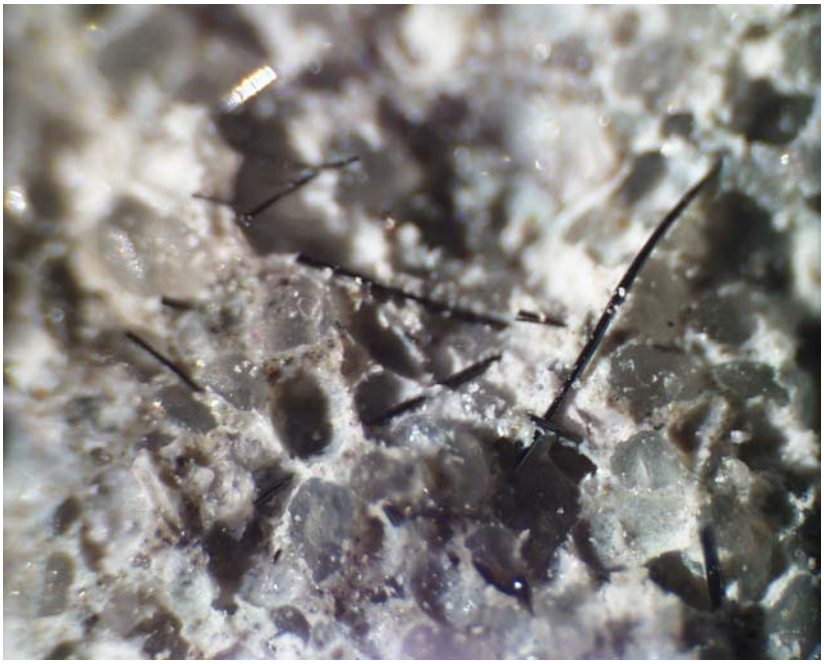

Figure 6 – Composite mortar fracture surface

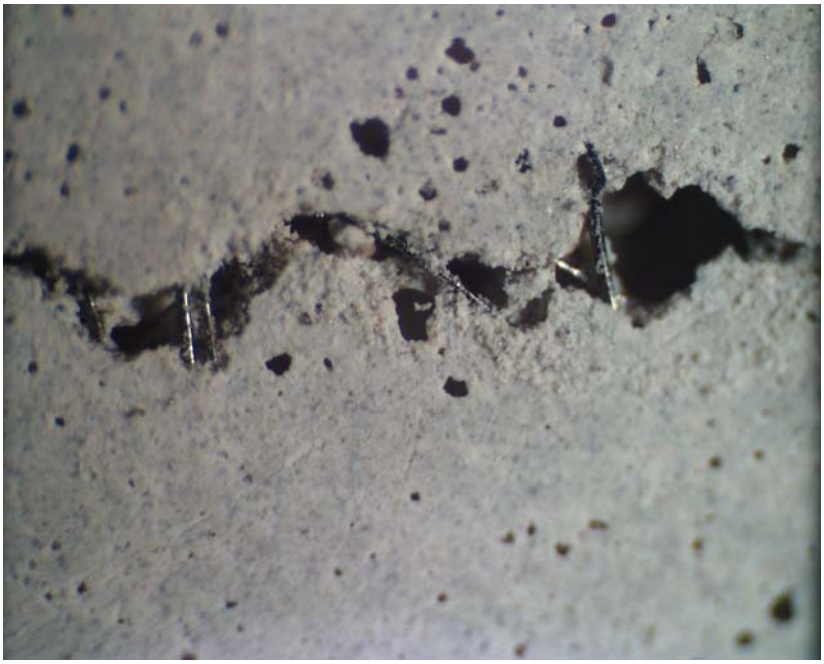

Figure 7 – Bridging of concrete composite fracture by CMS fibers

The lack of mechanical property enhancement by the CMS fibers can be attributed to two factors. The first was the short length of the fibers. Indeed, this was partly confirmed by the results obtained for tensile strength of composite concretes prepared by hand dispersing the fibers prior to mechanical mixing, Table 13. The strength results for these composites showed slight improvements over the mechanically dispersed fiber composites. The second was the small agglomerates of fibers in the composites. The presence of such agglomerated fibers was not primarily responsible for the absence of improved mechanical properties, as the results did not show large decreases in the mechanical properties. However, these small agglomerates of fibers were a source of trapped macroscopic air pockets within the mix, causing these agglomerated fibers to act as weak aggregates. This would have lead to an overall weakening of the composite and effectively canceling out any synergistic reinforcing effects the fiber may have had. This problem had been identified previously [Chung, 1992] where increases in the air content of fiber reinforced concretes was observed. Results shown in Table 4, support this hypothesis, where 1 vol% fiber concrete mix showed 9% air content without the addition of an AEA. Furthermore, data presented in Table 6, 7 and 8 show that the fibers themselves have no significant demand for AEAs.

Mortar Shrinkage Tests

Specimens for drying shrinkage experiments were cast, cured, stored, and tested in accordance with ASTM C 596, with the exception of curing conditions, Figure 8. The ambient humidity was approximately 55-60%, but was not rigorously controlled at that level. However, the humidity was monitored using a data logger and both the control and fiber mortar bars were prepared at the same time and exposed to identical curing conditions. Plots of shrinkage versus dry storage time for standard and fiber mortar composites with varying fiber contents are presented in Figures 9, 10 and 11.

Figure 8 – Curing of CMS fiber composite mortar bars for shrinkage tests

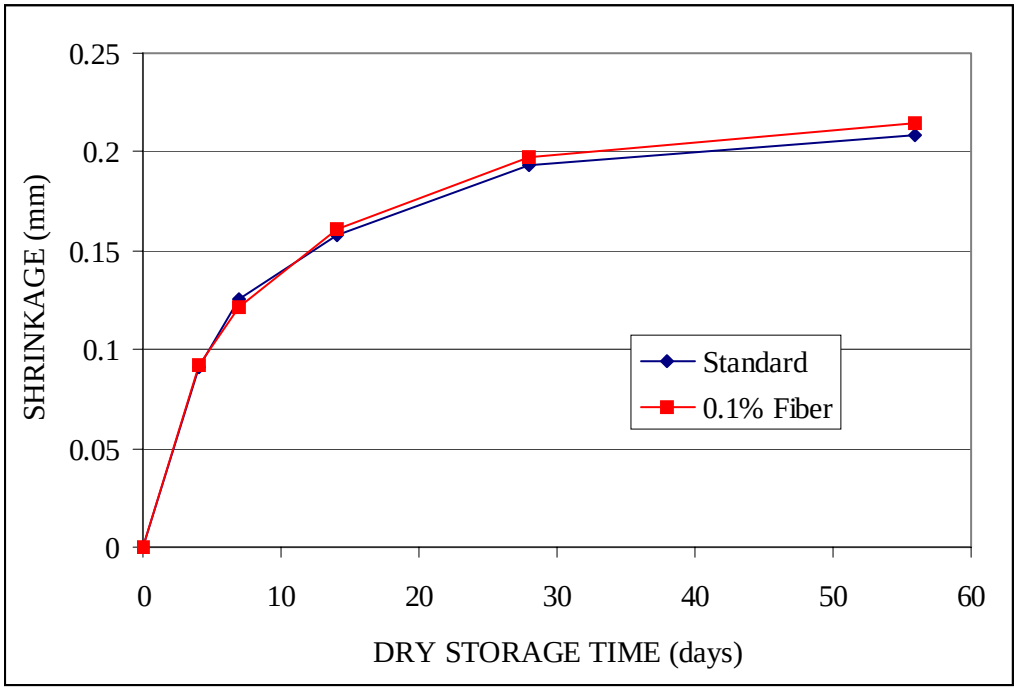

Figure 9 – Drying shrinkage vs. storage time for standard and 0.1% fiber mortar bars

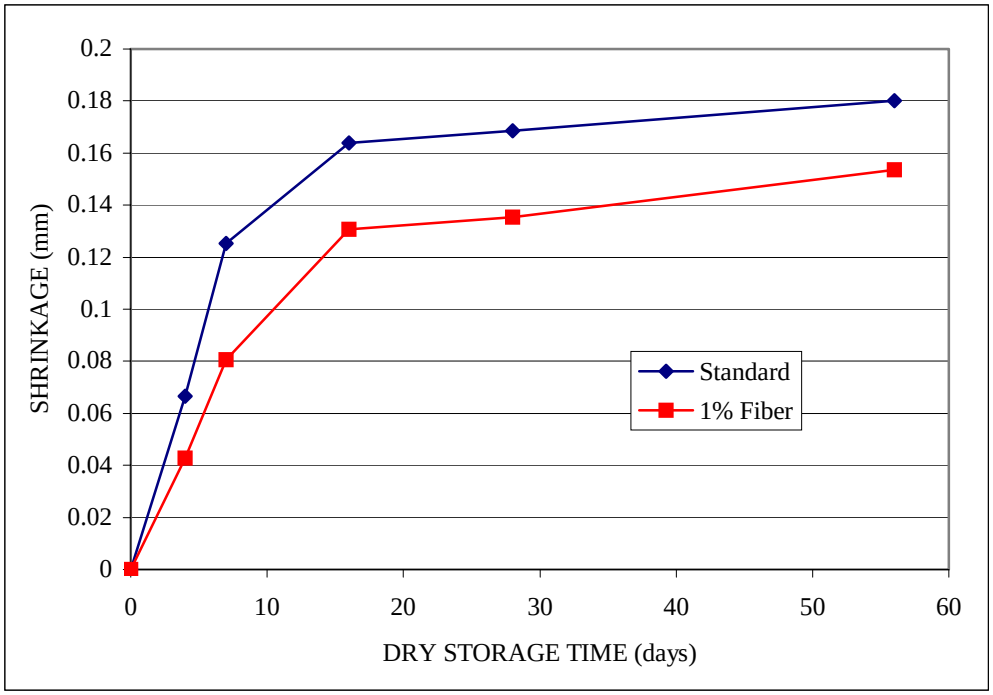

Figure 10 - Drying shrinkage vs. storage time for standard and 1% fiber mortar bars

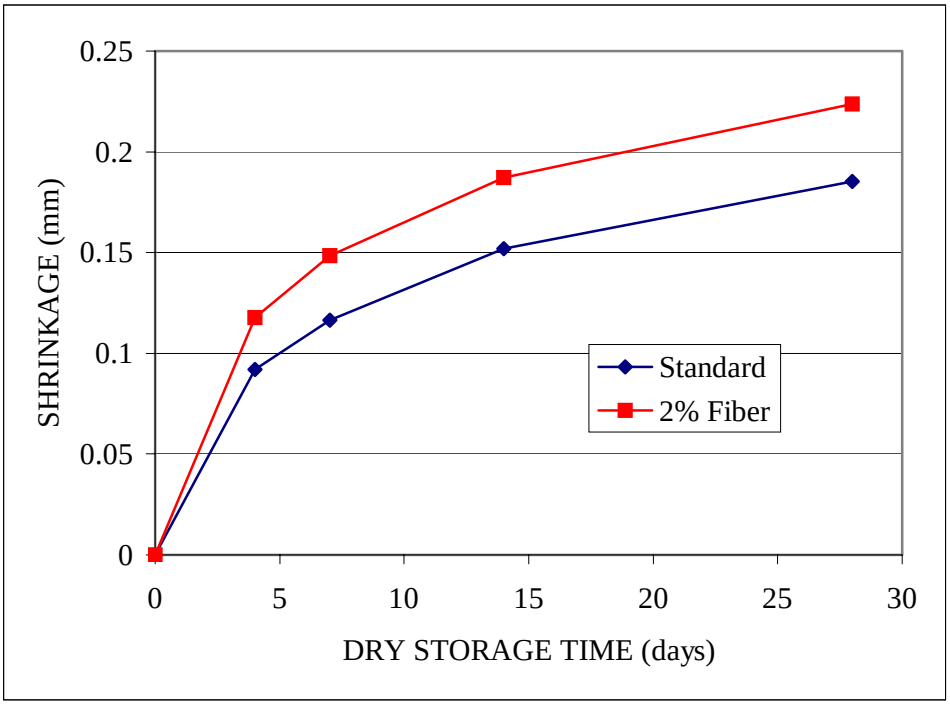

Figure 11 - Drying shrinkage vs. storage time for standard and 2% fiber mortar bars

The addition of CMS had a significant effect on the drying shrinkage of composite mortars, showing approximately 36 % less mortar shrinkage for the addition of 1 vol% CMS fiber. The marked reduction in mortar shrinkage is quite significant. As discussed above, many high performance concrete mixes have been discontinued because of excessive shrinkage and cracking problems. The results attained during this work show that mortar shrinkage can be significantly reduced by the addition of CMS fibers.

Task 5.0 Full Scale Field Test / Test Specimen

The research proposal for this project described the production of a $2m^3$ concrete pour for field testing evaluation. Unfortunately due to the time constraints of this project a full scale test was not completed. The time required to fabricate and process the necessary quantity of CMS fibers, as well, as, the time required to study the properties and characteristics of a large scale test specimen during curing was beyond the time available for this project. In place of the large scale field test, two additional studies on CMS fiber concrete composites were performed.

Nuclear Shielding

A brief investigation into the nuclear radiation abatement capability of carbon fiber reinforced concrete composites was performed. Concrete composites produced with carbon fiber reinforcement might offer some degree of shielding to nuclear radiation. A control concrete slab and a slab containing 2 vol% CMS fibers were cast. Each slab measured 406 mm in diameter and 152 mm thick, Figure 12 and 13 and both cured under identical conditions. Water content of each slab was held constant; this included accounting for an approximate 114 wt% absorption of water by the carbon fibers. A 16 mm diameter hole was cast through the depth of each slab to be used for density and moisture measurements.

The nuclear shielding tests were performed with a Surface Moisture-Density Gauge, manufactured by Troxler Electronic Laboratories Inc., as a radiation source. The gauge contains a ^{137}Cs point source to emit gamma radiation through a sample, a detector quantifies the intensity of the gamma radiation emitted through the sample. The intensity reading is correlated to the density of the specimen. A lower number of gamma photons reaching the detector indicates higher scattering/absorption of photons within the test specimen, resulting in a higher density measurement. Moisture within the slab was also measured with the Troxler gauge. Moisture content is measured using 40mCi Am and ^{241}Be sources to emit neutrons. Neutrons are "thermalized" or slowed by water molecules in the sample. A ^{3}He detector measures the flow of neutrons through the sample, this measurement is directly proportional to the moisture content of the slab. The density and moisture content of the slabs were measured at 17 days curing age.

The results of these measurements along with calculated theoretical densities are presented in Table 19.

Figure 12 – Concrete slab for nuclear shielding tests

Figure 13 – CMS fiber concrete composite slab for nuclear shielding tests

Table 19 – Density and moisture data for concrete and CMS concrete composites

	Control Slab	2 vol% Fiber Slab
Measured Density (kg/m3)	2148.1	2002.3
Calculated Density (kg/m3)	2184.9	2066.4
Measured Moisture (%)	6.0	7.9

Thermal Conductivity

Generally concretes and mortars are insulating materials, however, the addition of CMS fibers to mortar mixes may affect the thermal conductivity of the material. A brief investigation to determine the difference in thermal conductivity of mortar and fiber mortar composites was performed. The thermal conductivity of fiber mortar composites was determined by measurement of the thermal diffusivity at ambient temperature. Thermal conductivity cannot be measured directly. However, thermal diffusivity can be measured directly and is directly proportional to thermal conductivity. Samples of fiber mortar composites measuring 10 mm x 8 mm were cut and then coated with graphite. Thermal diffusivity measurements were performed with Netzsch Instruments Laser Flash Apparatus LFA 427. Thermal diffusivity measurement involves pulsing the sample with a laser and measuring the radiated heat emitted through the sample. Thermal diffusivity measurements were performed at ambient temperature, under an atmosphere of flowing Ar, laser voltage was 450 V and pulse width 0.8 ms. The results shown in Table 20 are mean values for 5 shots per sample. Inspection of the data reveals that the addition of CMS fibers did not significantly alter the thermal diffusivity of the mortar.

Table 20 – Thermal diffusivity data for mortar and CMS fiber composite mortar

Sample	Mean Thermal Diffusivity (mm2/s)	Standard Deviation (mm2/s)
Control Mortar	1.570	0.044
2 vol% CMS Fiber Mortar	1.606	0.047

Conclusions

The results obtained during the course of this project support the following conclusions:

- The addition of CMS carbon fibers decreased the workability of concrete and mortar mixes.
- CMS carbon fibers did show any affinity for adsorption of air entraining admixtures (AEAs) in the concrete and mortar mixes. Optical microscopy studies showed that CMS fiber composite concretes had sufficient air contents to resist the detrimental effects of freeze/thaw conditions.
- Addition of CMS fibers to concrete and mortars did not significantly decrease or increase the mechanical properties of concretes or mortars compared to control concrete and mortar mixes. This was attributed to the following:
    - Although the majority of the CMS fibers were dispersed, majority of these fibers were too short, <10mm, to be effective in bridging fractures and failures in the matrix.
    - The presence of small fiber agglomerates increased the air content of the fiber, effectively negating any potential improvements in strength.
- Addition of CMS fibers where shown to be effective in controlling concrete shrinkage during curing. This result is significant, as many high performance concrete mixtures (such as the AAA mix studied here) suffer from excessive shrinkage and premature cracking during cure and significant effort is required to control the rate of shrinkage for these concretes.

References

ACI Committee 544, (1993), Guide for Specifying, Proportioning, Mixing, Placing and Finishing SFRC, MCP-5, Report ACI 544.3r, 10pp.

American Concrete Institute (ACI), *Manual of Concrete Practice: Part 1*, 116R-90, pp. 116R-1 to 116R-68, 2000.

Banthia, N, M. Al-Asaly, and S. Ma. (1995). "Behavior of Concrete Slabs Reinforced with Fiber-reinforced Plastic Grids", Journal of Materials in Civil Engineering, Nov., 1995, 252-257.

Bentur, A. and Midness, S. (1990). Fiber Reinforced Cementitious Composites, Elsevier Applied Science, New York, N.Y.

Bischoff, P. H. (2003). "Tension Stiffening and Cracking of Steel Fiber-Reinforced Concrete" Journal *of Materials in Civil Engineering*., March/April 2003, 174-182.

Blood, G.W. (1970), Material Science Thesis, University of Calgary.

Bayasi, Ziad, Jack Zeng, (1997), "Flexural Behavior of Slurry Infiltrated Mat Concrete (SIMCON)", Journal of Materials in Civil Engineering, Nov, 1997, 194-199.

Chung, D D L (1992), Carbon Fiber Reinforced Concrete, Strategic Highway Research Program, National Research Council, Washington DC, 1992.

Davis, R.E., Carlson, R.W., Kelly, J.W. and Davis, H.E., Properties of Cements and Concretes Containing Fly Ash, *Journal of the American Concrete Institute*, Vol. 33, pp. 577-612.

Johnston, Colin D. (2001). Fiber-Reinforced Cements and Concretes, Gordon and Breach Science Publisher, Canmet, Ottawa, Ontario Canada.

Kentucky Transportation Cabinet. *Standard Specifications for Road and Bridge Construction* (2000).

Lancard, D.R., (1986), Steel Fiber Concrete, (Ed. Shah and Skarendahl), Elsevier, pp. 200-217
Tatro, S.B.,(1985), Master's Thesis, Purdue University, Lafayette, Indiana, U.S.A.

Tatro, S. B., (1986). "The Effect of Steel Fibers on the Toughness Properties of Large Aggregate Concrete." Purdue University, Joint Highway Research Project, 1986.

United States Geological Survey (USGS), *Mineral Commodities Summaries: Cement*, http://usgs.gov, January 2003Annual Book of ASTM Standards (2000).
Uomoto, T., Mutsuyoshi, H., Katsuki, F., Misra, S. (2002). " Use of fiber reinforced polymer as reinforcing material for concrete." *Journal of Materials in Civil Engineering*., May/June 2002, 191-210.

Zhang, J., Li, V. C. (2001). "Influences of fibers on drying shrinkage of fiber reinforced cementitious composite" *Journal of Engineering Mechanics*., January 2001, 37-44.

Zhang, J.,(2003). "Modeling of the influence of fibers on creep of fiber reinforced cementitious composite" *Composites Science and Technology*., Vol. 63, 2003, 1877-1884.

Zhang, J., Li, V. C., Nowak, A. S., and Wang, S. (2002). "Introducing Ductile Strip for Durability Enhancement of Concrete Slabs." *Journal of Materials in Civil Engineering*., May/June 2002, 253-260.

Zollo, R. F., (1995). "Fiber Reinforced Concrete: and Overview after 30 Years of Development." *Cement and Concrete Composites*., Elsevier 1997, 107-122.

DEVELOPMENT OF ANTHRACITE-BASED CARBON CATALYSTS

Final Report

Report Period: March 1, 2003-February 28, 2004

Principal Investigator: Dr. John W. Larsen and
Dr. Harold H. Schobert
Author: Francelys Medina
Report Issue: October 2004

Internal Agreement No.,
For Award No.: DE-FC26-98FT40350

The Energy Institute
Penn State University
C 211 CUL
University Park, PA 16802

ABSTRACT

An exploratory study has been made of the kinetics of the carbon-catalyzed reduction of nitrobenzene to aniline by hydrazine and the carbon-catalyzed decomposition of hydrazine in refluxing *iso*-propyl alcohol. The reactions are thermodynamically highly feasible, but do not proceed at measurable rates in homogeneous solutions. The catalytic mechanism for the nitrobenzene reduction by hydrazine was previously proposed to be adsorption of the reactants on the surface of the carbon followed by electron transfer.[1] The principal goal of this project was to provide additional information on the catalytic mechanisms of these reactions. The ultimate goal of this program at The Energy Institute is to develop carbon catalysts for existing commercial reactions and for new reactions. This requires a better understanding of how different carbons catalyze reactions so that carbon catalysts can be developed in the most efficient and expeditious manner.

Various commercial carbons, with widely differing physicochemical properties, were characterized and their catalytic activity for both reactions was investigated. The carbon samples studied included activated carbons, carbon blacks, non-activated charcoals and graphite. The reactions were followed by measuring the production of gases as a function of time using a gas burette. All of the carbon samples brought about easily detectable rates of hydrazine decomposition and nitrobenzene reduction by hydrazine. The reaction rates were proportional to the catalyst concentration, increased with surface area, and were independent of the stirring conditions, providing evidence that both reactions may be surface-controlled. However, the nitrobenzene reduction may

be, in part, controlled by pore diffusion as determined by the almost linear relationship between the initial reaction rates and the external surface area and pore volume of the carbon catalysts.

For both reactions, the catalytic activity of carbon catalysts was found to vary linearly with the surface area (of carbon blacks in the case of the nitrobenzene reduction) and bulk oxygen content at low oxygen content. The surface area dependence can be separated into two different straight lines corresponding to acidic and basic carbons, which was proposed as due to the presence of two different types of oxygen surface groups affecting the adsorption of hydrazine and nitrobenzene.

The kinetics of the hydrazine decomposition reaction exhibited a change of reaction order from first order at low concentrations of hydrazine to zero order at high concentrations. The observed kinetics have been explained by postulating a Langmuir adsorption process is involved in the slow step of the reaction, in which the hydrazine molecules are nondissociatively adsorbed on the carbon surface. A subsequent reaction between liquid-phase hydrazine molecules and hydrazine molecules adsorbed on the carbon surface, followed by a reaction between two adsorbed diimide molecules, leads to the final products.

The kinetics of the nitrobenzene reduction by hydrazine were complicated by the simultaneous decomposition of hydrazine. The observed kinetics for the nitrobenzene reduction exhibited a pronounced order change from a fractional positive value at low nitrobenzene concentrations to a fractional negative order at high nitrobenzene concentrations. This behavior has been explained by deriving the overall rate equation on the assumption that the rate-determining step is the reaction between an adsorbed

nitrobenzene molecule and an adsorbed hydrazine molecule, according to a Langmuir-Hinshelwood model.

Table of Contents

List of Figures

List of Tables

Chapter 1.

Introduction

Carbons are known to catalyze a wide range of reactions.[2-11] For several reactions, catalytic mechanisms have been investigated. We are continuing the investigation of the mechanism of the carbon-catalyzed reduction of nitrobenzene by hydrazine and the carbon-catalyzed decomposition of hydrazine in *iso*propanol. Earlier studies[1,12] indicated that these reactions may proceed by adsorption of the reacting species at the carbon surface followed by electron transfer—a mechanism originally proposed by Spiro for other reactions catalyzed by carbons and noble metals.[13] If this reaction pathway is common, it raises the possibility of replacing expensive and environmentally troublesome metal catalysts with carbon in some processes.

Carbons are attractive as catalysts because of their low cost, environmental acceptability, reasonably high electrical conductivity, relatively low chemical and electrochemical reactivity, and easily reproducible and controllable surface chemistry. Current market price for a carbon black is about 30 ¢/lb.[14] Carbon poses little risk of environmental contamination and is generally considered non-toxic with only minor effects to the respiratory and cardiovascular systems. In fact, carbon does not appear on any of the lists of hazardous or toxic substances.[15] Carbon may display the electronic properties of metal, semiconductor, or insulators, and often has electrical conductivity comparable to common metals.[16] At ordinary temperatures, carbon is one of the most chemically inactive of the elements due to its high tendency to form covalent bonds.[16] Carbon possesses only a rather limited area of thermodynamic stability, but both oxidation and reduction of carbons are extremely slow reactions (electrochemically

irreversible) and cannot actually be brought about under normal conditions of temperature and pressure.[17]

In addition, carbon is suitable as a catalyst because of its availability in a wide variety of physical structures, ranging from highly oriented pyrolytic graphite to amorphous carbon black and activated carbon. In between the two extremes of highly graphitic and amorphous carbons, there is a host of carbons with a wide range of differing and reasonably well-defined morphologies (e.g. small particles, fibers, large solid blocks, etc.) and physicochemical, chemical, electrical and thermal properties. These materials are obtained by the use of different precursors, manufacturing processes, and subsequent treatment steps.[16] For instance, heat treatment at progressively higher temperatures produces carbons with physicochemical properties that start with amorphous carbon and end with graphitized carbon.

A perusal of the literature shows the diversity of reactions catalyzed by carbons. Carbon is used commercially to catalyze the formation of phosgene and sulfuryl chloride.[18] Carbon as a catalyst for other industrially useful reactions represents a potential new market for premium carbon products. These catalysts could be cheaper and more environmentally acceptable than traditional, heavy-metal, supported catalysts. To intelligently select reactions that might be catalyzed by carbons, the mechanisms by which carbon catalyzes reactions must be understood. However, there is no published summary of the mechanisms of carbon catalysis.

The objective of this thesis is to further explore the catalytic mechanisms of two carbon-catalyzed reactions for which there exists some mechanistic information in the literature: the reduction of nitrobenzene to aniline by hydrazine[1] and the decomposition

of hydrazine.[12] In doing so, we attempt to understand the fundamentals of carbon as catalyst in order to develop the knowledge to design carbon catalysts for existing commercial reactions.

1.1. Hypotheses of this project

The hypothesis of this research is that carbon may catalyze the nitrobenzene reduction by hydrazine and the hydrazine decomposition reactions by the same mechanisms that occur with some metals.

Chapter 2. Literature Review

2.1. Heterogeneous catalysis

A catalyst is a substance that increases the rate at which a chemical system attains equilibrium without itself undergoing an irreversible chemical change.[19] In other words, the primary result of catalysis is to enhance the reaction rate and sometimes to yield the desired products with high selectivity. To do so, the catalyst has to reduce the activation barrier of the rate-determining step. The type of catalysis where the catalyst exists in a different phase from the reactant molecules (usually as a solid in contact with either gaseous reactants or with reactants in a liquid solution) is known as **heterogeneous catalysis**.

The sequence of elementary steps by which a reaction proceeds is known as its reaction mechanism. If a reaction proceeds by a multistep mechanism (stepwise reaction) one of the steps may be much slower than the others and so be the rate-determining step. The rate-determining step governs the rate law for the overall process.

Heterogeneous catalysis must involve interaction between the surface and at least one of the reactants. In general, if the reaction

$$A + B \rightarrow C + D$$

occurs at the surface of a catalyst, several pieces of information are required before it is possible to understand or unravel the mechanism.[19] These may include the following:

1. Are both A and/or B molecules adsorbed at the catalyst surface? Will A displace B or vice versa?

2. If both A and B are adsorbed, what are their relative surface concentrations?
3. Are there changes taking place in A and B if they are adsorbed? What is the nature of the bond between the catalyst and the adsorbed species?
4. What is the nature of the surface intermediates?
5. What features of the catalyst are the important ones that make it catalytically active?
6. Do the products influence the reaction in any way?
7. What is the rate-determining step in the catalytic process?

Obtaining these key pieces of information requires studying the kinetics of the reaction. In general, studies of reaction mechanism begin with a study of the reaction kinetics. In this study, we want to explore questions (5) and (7).

A heterogeneous catalytic process involves five distinct steps:[20]

- mass transport of reactant(s) to the catalytic surface from the bulk solution;
- adsorption of the reactant(s) on the surface;
- chemical reaction at the surface, which involves the chemical rearrangement (bond breaking, bond, formation, molecular rearrangement) of the adsorbed reaction intermediates;
- desorption of product(s) from the surface; and
- mass transport of product(s) away from the surface into the bulk solution.

Any of these steps could be the rate-determining step in a catalytic process. However, the processes of adsorption or desorption are *usually* too fast to be rate-

determining steps in solution catalysis.[20] In addition, the majority of reactions in liquid solutions are not diffusion-controlled; instead only a small fraction of encounters lead to reaction. We will show that the reduction of nitrobenzene to aniline by hydrazine and the decomposition of hydrazine are surface-controlled reactions, i.e., the rate-determining step involves the reaction on the surface of an adsorbed reactant or of a derived species. The terms "surface-controlled reaction" and "surface reaction" will be used interchangeably throughout this thesis.

2.1.1. Rates of surface reactions

In a kinetic experiment, the change in the amount of a reactant or product with time is measured to learn the rate law. The discussion that follows is mainly based on that of Spiro's review on heterogeneous catalysis of solution reactions.[20] Consider the elementary reaction of the form

$$a\mathrm{A} + b\mathrm{B} \rightarrow c\mathrm{C} + d\mathrm{D} \tag{2.1}$$

where a, b,…are the coefficients in the balanced chemical equation and A, B,…are the chemical species. If the reaction takes places in a closed, isothermal system, the **reaction rate** may be defined as the time derivative of the extent of reaction,

$$R = -\frac{1}{a}\frac{dn_a}{dt} = -\frac{1}{b}\frac{dn_b}{dt} = \frac{1}{c}\frac{dn_c}{dt} = \frac{1}{d}\frac{dn_d}{dt} \tag{2.2}$$

where n_i is the amount (in moles) of species i. The reaction rate defined in this way is independent of the particular reactant or product chosen, so no ambiguity arises if any of the terms in this expression is taken to be the rate of the reaction. Equation (2.2) may be used even when there are volume changes during the reaction or two or more phases are

present. It should be noted that the reaction rate as defined by Eq. (2.2) is an extensive quantity, but in fundamental reaction kinetics, an intensive reaction rate is needed. In this case, Eq. (2.2) is divided by a reference variable that may affect concentration through means other than destruction of reactant or creation of product. In closed homogeneous systems, volume is the most important variable of this kind.[*] In dealing with heterogeneous systems, the mass of the solid, as well as the surface area of the solid, may be taken as the reference variable but with certain caution because the dependence of the reaction rate on the mass or surface area of the catalysts may not be straightforward. Besides, the active surface area of the catalyst is seldom known precisely. Since we are dealing with initial rates in this thesis, we will use Eq. (2.2) as the reaction rate divided by the total volume of solution, which is either constant or changes by a negligible amount at the beginning of the reaction even for concentrated solutions.

The rate of a reaction may be expressed in the form of an empirically determined equation called the **rate law** of the reaction

$$R = k[\mathrm{A}]^{\alpha}[\mathrm{B}]^{\beta}... \tag{2.3}$$

where the brackets [ ] represent concentration (customarily molar) and α, β…are constants, known as the **orders** of the reaction with respect to A, B…The overall reaction order, *n*, is equal to the sum of the individual orders. The proportionality constant *k* in the rate law is referred as the **rate constant**. *It is important to note that the reaction orders are not necessarily determined by the stoichiometric coefficients of the balanced*

---

[*] If the volume is constant during the reaction, the reaction rate may be expressed in terms of the change of the concentration (for diluted solutions) of one of the reactants or products.

chemical equation, except in the special case of an elementary reaction[†]*, so the reaction orders must be determined in kinetic experiments.* In addition, although there are some heterogeneous reactions which exhibit simple orders of reaction, for example the copper-catalyzed hydrogenation of ethylene at high temperatures, the majority of surface reactions cannot be assigned a simple order.[19]

One can determine the rate law for a reaction by using the solution of the differential rate equations (integration method), and comparing the time evolution of the concentrations of the reacting species (or an equivalent quantity that expresses the extent of the reaction) predicted by the possible rate laws with the experimental data. Laidler[21] refers to the order determined from the integration method as the order with respect to time. The integration method is useful for providing accurate rate constants if the order of a reaction has been well established. However, the method creates prejudice in favor of integral or half-integral orders.[21] The rate law can also be determined by observing the effect of changing initial reactant concentrations on the initial rate of the reaction (differential method). The order determined in this way is referred to as the order with respect to concentration. This procedure, dealing with initial rates, avoids or minimizes the effects of complicating factors (e.g., interference by products, sintering or poisoning of the catalyst, etc.) contributing to the change in the reaction rate. A full discussion of the kinetic methods and their advantages and disadvantages can be found in Laidler.[21]

In addition to its variation with reactant concentration at the surface, the rate of a surface reaction varies with the surface area of the catalyst. The surface area determines

---

[†] An elementary reaction is a reaction that occurs in a single step, with no experimentally detectable reaction intermediates.

the number of active sites for adsorption and catalysis. In a constant volume system, the number of molecules reacting in unit time is proportional to the number of collisions with the surface. Thus the reaction rate will vary directly with the area of the catalyst surface.[19]

A problem in the kinetics of heterogeneous reactions is the difference in dimensionality of a molecule in solution and on a surface, and the inclusion of adsorption onto a surface in the kinetic treatment. This problem is handled by the use of adsorption isotherms. Before considering each type of surface reactions, it is important to introduce the concept of adsorption since the extent of adsorption has a profound effect on the rate of a heterogeneous reaction.

2.1.2. Adsorption isotherms

Adsorption refers to the binding of molecules to a surface. In practice, not all the molecules bound to a catalyst surface are reactive. Besides, various impurities may be adsorbed at the surface, and these may occupy potential reaction sites and block the reaction. The places where adsorbed molecules may become reactive are called **active sites**. The number of active sites per unit amount of catalyst depends on the nature of the catalyst, on its method of preparation, and on its treatment before use.

The most common isotherm equations used to describe adsorption are those by Langmuir and Freundlich, which represent reasonably well the adsorption from dilute solutions. Both Langmuir and Freundlich isotherms are applicable to chemisorption and physisorption processes.[22] Adsorption isotherms of nitrobenzene from its aqueous

solutions on activated carbons and carbon blacks appear to be of the Type I or Langmuir variety.[23,24]

Three important assumptions are made in the derivation of the Langmuir adsorption isotherm. These are as follows:[19]

(1) the species are adsorbed in definite, localized sites in a monolayer;

(2) adsorption involves one and only one adsorbed molecule per site;

(3) the energy of an adsorbed molecule is the same at any site and is unaffected by adsorption on neighboring sites, i.e. the heat of adsorption is independent of surface coverage.

Deviations from the Langmuir equations are often observed. This may be because the surface is not uniform, and also there may be interactions between adsorbed molecules. Another reason for deviations from the Langmuir isotherm is that there may be adsorption in more than one layer, that is, multilayer adsorption. When such deviations occur, the adsorption results can sometimes be fitted to an empirical adsorption isotherm due to Freundlich.

The Freundlich isotherm is an empirical relationship between concentration and surface coverage. However, it can be derived theoretically if the following assumptions are made:[19]

(1) the heat of adsorption falls exponentially as the coverage is increased;

(2) the decrease in heat is due to surface heterogeneity, rather than to repulsive forces between adjacently adsorbed species.

(a) Langmuir isotherm without dissociation

A brief derivation of the Langmuir adsorption isotherm is as follows. If θ is the

fraction of surface which is covered by a molecule, then (1 – θ) is the fraction which is bare. Let us assume that [a] is the concentration of the adsorbing species in solution and k_a and k_{-a} are the kinetics rate constants for adsorption and desorption respectively. Then for adsorption without dissociation to cover a single surface site, the rate of adsorption is

$$v_a = k_a[a](1-\theta) \tag{2.4}$$

Desorption involves one adsorbed species and the rate is

$$v_{-a} = k_{-a}\theta \tag{2.5}$$

At equilibrium the rates are equal, so that

$$k_a[a](1-\theta) = k_{-a}\theta,$$

$$\frac{\theta}{1-\theta} = \frac{k_a}{k_{-a}}[a] = K_a[a],$$

and

$$\theta = \frac{K_a[a]}{1+K_a[a]} \tag{2.6}$$

where $K_a = k_a/k_{-a}$, is an equilibrium constant for the adsorption-desorption process.

The variation of θ with [a] is the following:

(a) at low concentrations [a] is small and $K_a[a] << 1$, so

$$\theta = K_a[a], \tag{2.7}$$

the fraction of surface covered being proportional to the concentration of the reactant;

(b) at high concentrations [a] is large and $K_a[a] >> 1$, so

$$\theta \approx 1, \tag{2.8}$$

and the fraction of surface covered is independent of the concentration of the reactant. At intermediate concentrations the fraction of surface covered is proportional to the

concentration of the reactant to some power between one and zero.

(b) Langmuir isotherm with dissociation

Langmuir's derivation of the isotherm for adsorption with dissociation to cover two surface sites is as follows. The rate of adsorption is

$$v_1 = k_1[a](1-\theta)^2 \tag{2.9}$$

Desorption involves two adsorbed species and the rate is

$$v_{-1} = k_{-1}\theta^2 \tag{2.10}$$

At equilibrium the rates are equal, so that

$$k_1[a](1-\theta)^2 = k_{-1}\theta^2,$$

$$\frac{\theta}{1-\theta} = \left(\frac{k_1}{k_{-1}}[a]\right)^{\frac{1}{2}} = K_a^{\frac{1}{2}}[a]^{\frac{1}{2}},$$

and

$$\theta = \frac{K_a^{\frac{1}{2}}[a]^{\frac{1}{2}}}{1+K_a^{\frac{1}{2}}[a]^{\frac{1}{2}}} \tag{2.11}$$

The variation of θ with $[a]$ is the following:

(a) at low concentrations $[a]$ is small and $K_a^{\frac{1}{2}}[a]^{\frac{1}{2}} << 1$, so

$$\theta = K_a^{\frac{1}{2}}[a]^{\frac{1}{2}}, \tag{2.12}$$

the fraction being proportional to the square root of the concentration of the reactant;

(b) at high concentrations $[a]$ is large and $K_a^{\frac{1}{2}}[a]^{\frac{1}{2}} >> 1$, so

$$\theta \approx 1, \tag{2.13}$$

and the fraction of surface covered is independent of the concentration of the reactant. At

intermediate concentrations the fraction of surface covered is proportional to the concentration of the reactant to some power between ½ and zero.

(c) Freundlich isotherm (nonlinear adsorption)

According to this adsorption equation due to Freundlich,[21] the amount of a substance adsorbed is related to the concentration by the equation,

$$\theta = K_a [a]^m \tag{2.14}$$

where K_a and m are empirical constants. This equation does not give saturation of the surface; the amount adsorbed keeps increasing as $[a]$ increases. If Eq.(2.14) applies, a plot of $\log_{10} x$ versus $\log_{10} [a]$ gives a straight line of slope m.

2.1.3. Kinetics of heterogeneous reactions

(a) Unimolecular reactions

In a unimolecular surface reaction, one molecule of a single reactant species is adsorbed and reacts on the surface. This type of surface reaction is usually treated in terms of the Langmuir adsorption isotherm as follows. The rate R of a heterogeneous reaction is proportional to the fraction of surface which is covered, i.e.

$$R = k\theta = \frac{kK_a[a]}{1 + K_a[a]} \tag{2.15}$$

for adsorption without dissociation and,

$$R = k\theta = \frac{kK_a^{\frac{1}{2}}[a]^{\frac{1}{2}}}{1 + K_a^{\frac{1}{2}}[a]^{\frac{1}{2}}} \tag{2.16}$$

for adsorption with dissociation. Here, k is the rate constant defined earlier in this chapter.

The dependence of rate on [a], shown in Figure 2.1, is exactly the same as that given by the Langmuir isotherm.

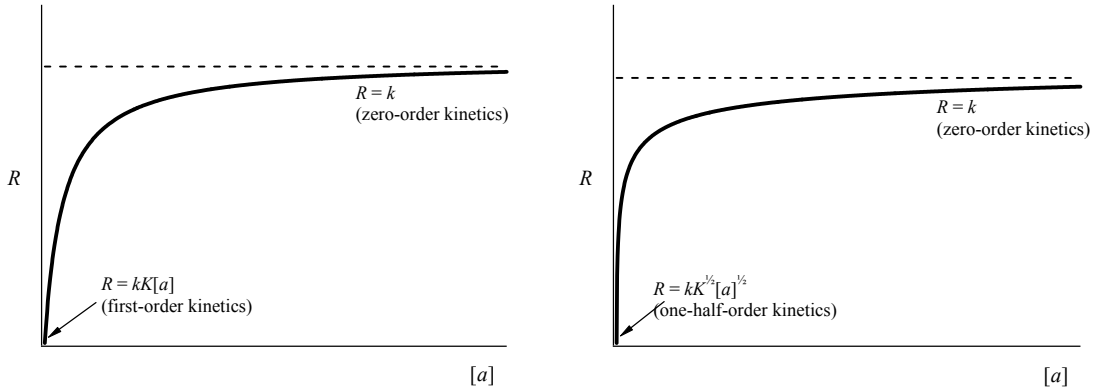

Figure 2.1. Variation of rate with concentration for unimolecular reactions with nondissociative adsorption (*left*) and dissociative adsorption (*right*).

Suppose now that the adsorption of a reactant A is the rate-determining step, the *net* rate of adsorption will be the difference between the rate of adsorption of A and its rate of desorption. Applying the notion of Langmuir we can write[25] the rate of adsorption of A,

$$R = \frac{k_a[a]}{1 + K_a[a]} \tag{2.17}$$

(b) Bimolecular reactions

(i) Langmuir-Hinshelwood mechanism

In a Langmuir-Hinshelwood mechanism, the reaction occurs between two adsorbed molecules, as shown in Figure 2.2. Suppose that the fraction of surface covered by molecules of type A is θ_a and that the fraction covered by B is θ_b. The bare fraction is

$1-\theta_a-\theta_b$. If both substances are adsorbed without dissociation, the rates of adsorption of *a* and *b* are

$$v_a = k_a[a](1-\theta_a-\theta_b) \tag{2.18}$$

and

$$v_b = k_b[b](1-\theta_a-\theta_b) \tag{2.19}$$

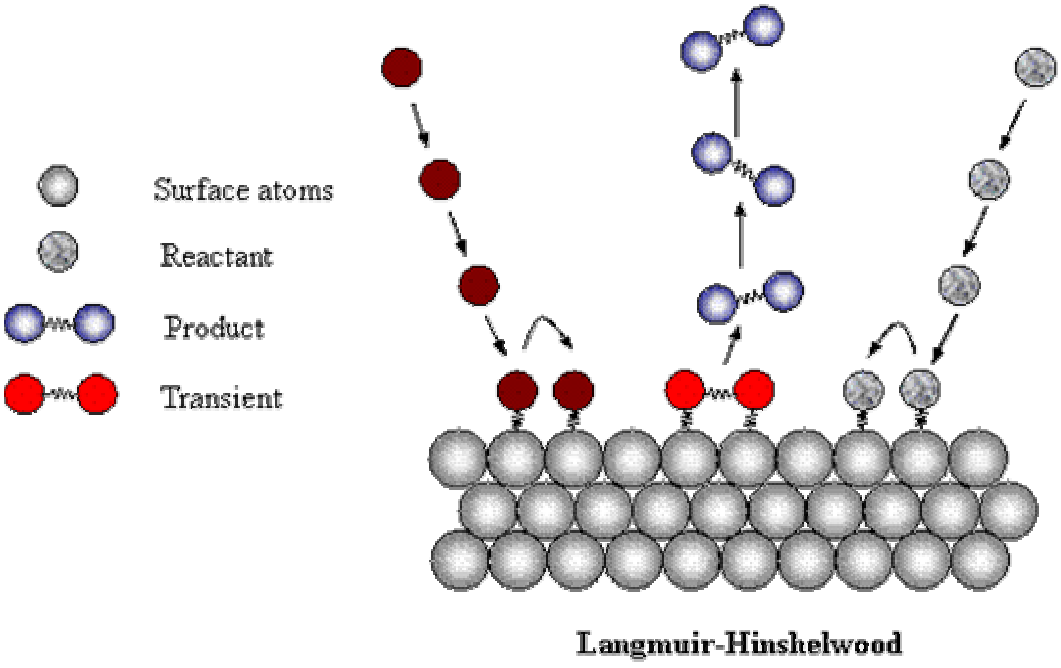

Figure 2.2. Graphic illustration of the Langmuir-Hinshelwood mechanism, where the reactants are equilibrated on the surface prior to reaction.

The rates of desorption are

$$v_{-a} = k_{-a}\theta_a \tag{2.20}$$

$$v_{-b} = k_{-b}\theta_b \tag{2.21}$$

Equating Eqs. (2.18) and (2.20) leads to

$$\frac{\theta_a}{1-\theta_a-\theta_b} = K_a[a] \tag{2.22}$$

where $K_a = k_a/k_{-a}$. From Eqs. (2.19) and (2.21) it follows that

$$\frac{\theta_b}{1-\theta_a-\theta_b} = K_b[b] \tag{2.23}$$

where $K_b = k_b/k_{-b}$. Equations (2.22) and (2.23) are two simultaneous equations that can be solved to give, for the fractions covered by *a* and *b*, respectively,

$$\theta_a = \frac{K_a[a]}{1+K_a[a]+K_b[b]} \tag{2.24}$$

$$\theta_b = \frac{K_b[b]}{1+K_a[a]+K_b[b]} \tag{2.25}$$

This simple derivation requires that a number of assumptions are met: (a) each adsorption site accommodates only one molecule; (b) molecules are adsorbed without dissociation; (c) all sites are energetically equal (i.e., the adsorption enthalpy is independent of coverage).

A clear consequence of the first assumption follows from Eqs. (2.24) and (2.25), that is, that the fraction of the surface covered by one substance is reduced if the amount of the other substance is increased. This is because the molecules of A and B are competing with one another for limited number of surface sites, and we speak of competitive adsorption.

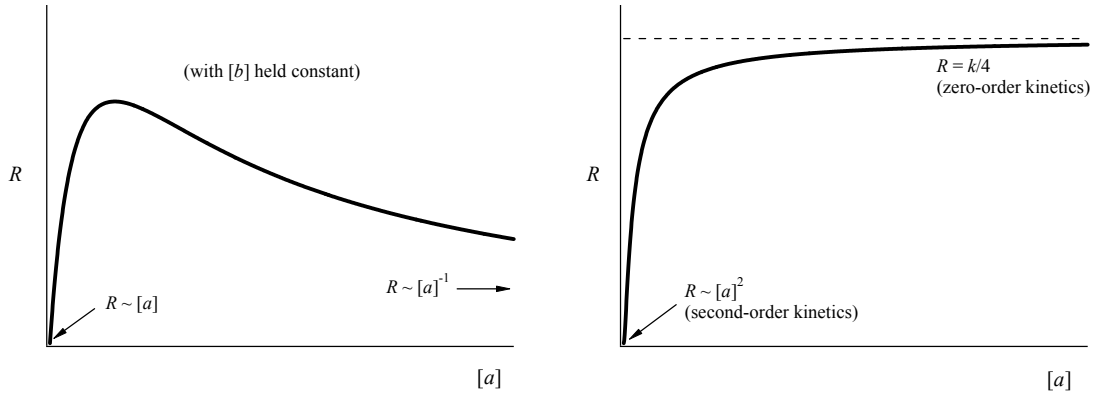

Figure 2.3. Variation of rate with concentration for a bimolecular reaction occurring by a Langmuir-Hinshelwood mechanism between two different molecules (*left*) and two molecules of the same type (*right*).

In the Langmuir-Hinshelwood mechanism, the rate is proportional to the fractions of the reacting molecules A and B that are adsorbed. The reaction rate is therefore

$$R = k\theta_a\theta_b = \frac{kK_aK_b[a][b]}{(1+K_a[a]+K_b[b])^2} \tag{2.26}$$

where k is the rate constant of the reduction reaction. If [b] is held constant and [a] is varied, the rate varies in accordance with Figure 2.3(a):

(a) at sufficiently low concentrations [a] and [b] are small, $K_a[a] << 1$ and $K_b[b] << 1$, so

$$R = kK_aK_b[a][b] \tag{2.27}$$

The reaction is therefore second order, being first order in both A and B.

(b) at high concentrations [b] is large and $K_b[b] >> 1$, so

$$R = \frac{kK_a[a]}{K_b[b]} \tag{2.28}$$

The rate is now inversely proportional to [b], and the order with respect to B is -1.

(c) the rate is maximum when $\theta_a = \theta_b$, i.e., when $[a] = \frac{K_b}{K_a}[b]$.

If both A and B are the same reactants, the rate equation for the Langmuir-Hinshelwood mechanism is therefore

$$R = \frac{kK_a^2[a]^2}{(1+2K_a[a])^2} \tag{2.29}$$

The kinetics become second-order and zero-order at low and high concentrations, respectively, as shown in Figure 2.3(b).

(ii) Eley-Rideal mechanism

In an Eley-Rideal mechanism, the reaction occurs between an adsorbed B molecule and a molecule of A in the liquid phase, as shown in Figure 2.4. The rate is proportional to the fraction of surface covered by B and to the concentration of A in solution:

$$R = k\theta_b[a] = \frac{kK_b[a][b]}{1+K_a[a]+K_b[b]} \tag{2.30}$$

Note that adsorbed A molecules do not enter directly into reaction, but they reduce the rate by occupying surface that might otherwise be occupied by B molecules.

If both A and B are the same reactants, the rate equation for the Eley-Rideal mechanism is therefore

$$R = \frac{kK_a[a]^2}{1+2K_a[a]} \tag{2.31}$$

The kinetics become second-order and first-order at low and high concentrations, respectively, as shown in Figure 2.5(a). For like molecules, the rate varies with concentration in the manner shown in Figure 2.5(b).

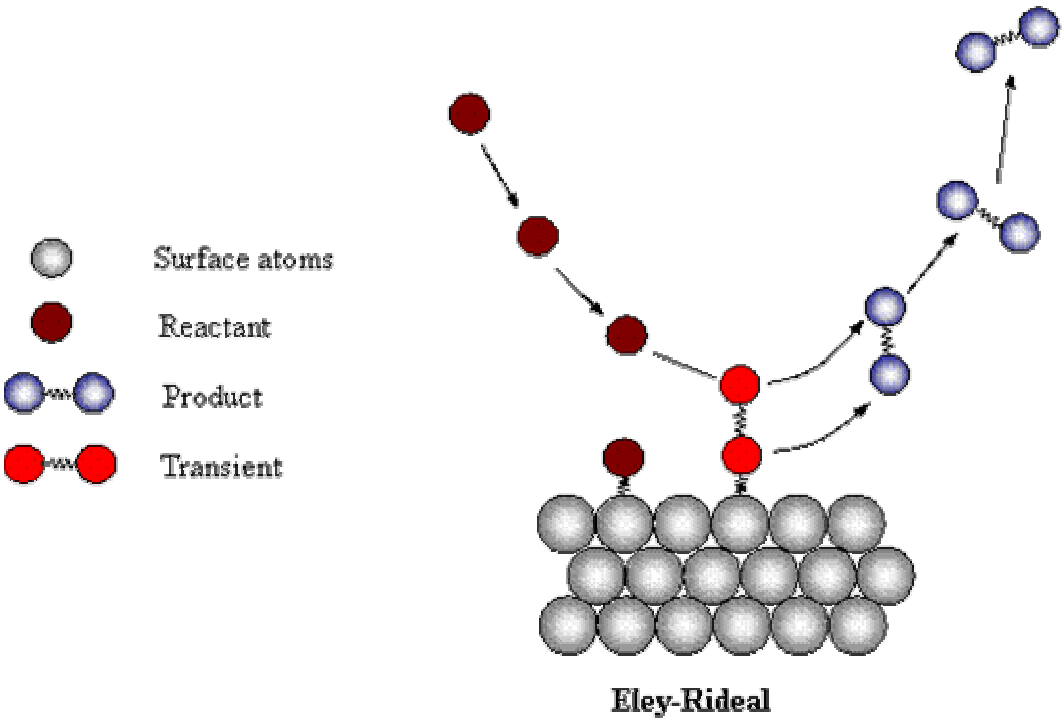

Figure 2.4. Graphic illustration of the Eley-Rideal mechanism, where an adsorbed species reacts by a direct collision with a liquid-phase species.

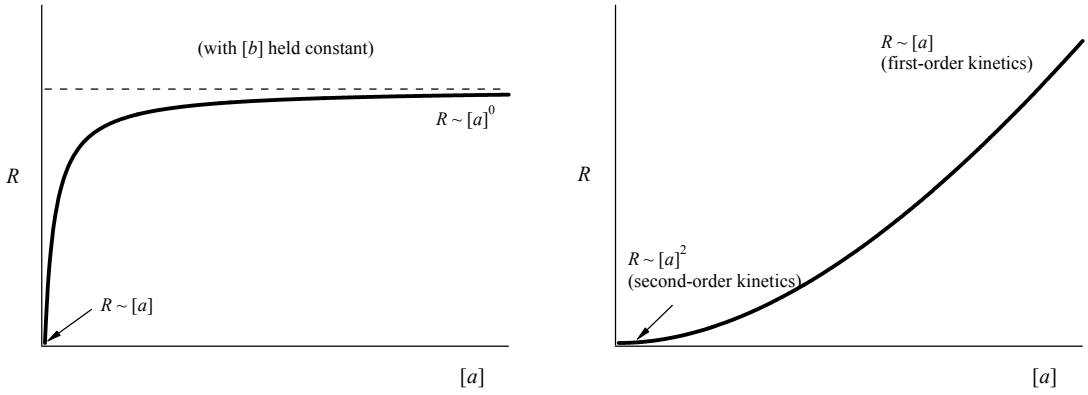

Figure 2.5. Variation of rate with concentration for a bimolecular process occurring by an Eley-Rideal mechanism between two different molecules (*left*) and two molecules of the same type (*right*).

The third category of bimolecular surface reactions is peculiar to redox reactions catalyzed by metals and semiconductors. The discussion of this mechanism, known as the

electrochemical mechanism, is postponed for later in this chapter.

2.2. Carbon as a catalyst

Carbon catalyses a variety of liquid-phase reactions including decomposition, polymerization, halogenation, substitution, isomerization, hydrocracking, and redox reactions.[2-11] There is neither a comprehensive list of reactions known to be carbon-catalyzed, nor a codified list of the mechanisms for carbon-catalyzed reactions. The literature on carbon-catalyzed reactions is fragmented, with many single reports scattered in the literature.

The earliest review on carbon catalysis seems to be the monograph by Hassler,[3] in which an incomplete list of reactions catalyzed by activated charcoal is presented. No space is devoted to catalytic mechanisms in that review. The reviews by Coughlin[4,5] and Weiss[2] deal with an arbitrarily selected group of reactions and attempt to describe most catalytic properties of carbon in terms of electronic effects of metals, semiconductors or insulators. No serious attempt was made to sample the patent literature. In the article by Tripathi and Ramachandran,[7] reactions catalyzed by carbon were reviewed for the effect of surface area, pore size and nature of surface complexes. Trimm[6] also briefly discussed carbon-catalyzed reactions in terms of the surface groups present on the carbon materials. Jüntgen and Kühl[8] summarized briefly the role of activated carbon catalysts in environmentally relevant reactions and correlated catalytic activity to the physical properties of the carbon catalyst. Kalra *et al*.[9] presented the status of investigations on an arbitrary group of carbon-catalyzed reactions. A more recent review deals with a group of

carbon-catalyzed reactions in solution.[10] The monograph by Radovic and Rodriguez-Reinoso[11] devoted little space to carbon catalysts. None of these reviews is exhaustive and none attempts a general understanding of the mechanisms by which carbons catalyze reactions.

Several examples of reactions known to be catalyzed by carbons are presented next. The reactions have been selected to provide a breadth of examples:

1) Isomerization reactions: α-methyl mono-olefin and straight-chain olefins (e.g., 2-methyl-1-butene, 2-methyl-1-pentene, and 1-pentene),[26-28] oximes,[29,30] optically active 1,1'-binaphthyl and disubstituted derivatives,[31-33] optical isomers of *tris*(ethylenediamine)-cobalt(III) ion $[Co(en)_3]^{3+}$,[34-39] optically active unsymmetrical facial bis[di(2-aminoethyl)sulfide]-cobalt(III) ion $(-)_D$-$[Co(daes)_2]^{3+}$,[40,41] *tris*(propylenediamide)-cobalt(III) ion $[Co(pn)_3]^{3+}$,[42] (ethylenediamide)tetraacetato-cobalt(III) Co(EDTA),[43] and $[Pt(en)_3]^{4+}$.[44]

2) Substitution (solvolysis) reactions: 2,2'-binaphthyl methyl phosphate ester of 1,1'-bi-2-naphthol,[45] methyl acetate to acetic acid,[46] ethyl acetate,[47] benzyl acetate,[20] alkyl halides (e.g. ethyl iodide) by metallic nitrates (e.g., $AgNO_3$),[48,49] and compounds of cobalt or chromium ions coordinated to nitrogen atoms (e.g. cobaltammine).[50-54]

3) Oxidative hydrogenation and dehydrogenation reactions: conversion of ethylbenzene to styrene,[55-62] conversion of primary alcohols (e.g., 2-propanol and butan-2-ol) to acetals,[63-66] conversion of cyclohexanol to cyclohexene, cyclohexanone, and phenol,[67] and conversion of aliphatic and aromatic carboxylic acids and carboxylic acid anhydrides with CCl_4 to the corresponding acid chlorides.[68-70]

4) Oxidation-reduction reactions: oxidation of hydrogen sulfide by oxygen,[71-77]

oxidation of sulfur dioxide,[78-82] reduction of nitric oxide,[83-87] oxidation of fluorene to fluorenone,[88] oxidation of *o*-xylene to phthalic anhydride,[89-92] oxidation of olefinic compounds (e.g., cyclohexene),[93] oxidation of hydrochloric acid,[94] oxidation of aqueous oxalic acid,[95-98] oxidation of *n*-hexane,[99] and reduction of nitroaromatic compounds.[1]

5) Decomposition reactions: hydrogen peroxide,[100-110] peracids, peracid salts and alkyl hydroperoxides,[111] 1,2-dicholoethane,[112-114] benzoyl peroxide,[105,115,116] nitrogen dioxide,[117] and hydrazine compounds.[12]

6) Polymerization reactions: methyl olefins (e.g. 2-methyl-propene and isobutene),[26] methyl methacrylate,[118] N-vinylcarbazole,[119,120] isobutyl vinyl ether,[121] α-methylstyrene,[122] and N-vinyl-2-pyrrolidone.[123]

7) Halogenation and dehalogenation reactions: production of phosphene[124-126] and sulfuryl chloride,[127] chlorination of toluene and benzene,[128,129] conversion of chloride into hydrochloric acid,[130,131] hydrodehalogenation of halogenated aromatic compounds (e.g. 9-bromophenanthrene, 1-chloronaphthalene, 1-bromonaphthalene, 4-chlorobiphenyl),[132] dehydrochlorination of 1,1,2,2,-tetrachloroethane to trichloroethylene,[133] and synthesis of hydrobromic acid[134-141] and hydrogen iodide.[142]

8) Hydrocracking reactions: degradation of polyethylene to aromatic hydrocarbons, [143]cracking of Decalin, *n*-hexadecane, paraffin wax, and *iso*propylbenzene,[144] and bond cleavage of 4-(1-naphthylmethyl)bibenzyl.[145-147]

9) Exchange reactions: hydrogen-deuterium exchange,[148,149] and ortho-para hydrogen exchange.[150,151]

10) Other reactions: Friedel-Crafts acylation of aromatic compounds (e.g. anisole, toluene and *o*-xylene) with acyl halides,[152] Kemp elimination,[153] Menschutkin reaction,[154]

alkylation of imidazole[155] and dealkylation of polymethylbenzene (e.g. toluene to benzene).[156]

It is obvious from the forgoing list that carbons are versatile catalysts capable of effectively increasing the rate of a broad range of reaction types. It seems likely that in doing so, a variety of reaction mechanisms are involved. Our concern here is with a pair of reactions in which the carbon-catalyzed reactions seems to be similar to metal-catalyzed reactions. There are important industrial uses to carbon catalysts. For example, the synthesis of phosgene and sulfuryl chloride is performed over activated carbons.[3] With increasing awareness of the problem of air and water pollution by industrial wastes, carbonaceous materials are finding new applications in the removal of a wide spectrum of unwanted chemical species. In these applications, carbons initiate conversions of pollutants to less toxic or nontoxic chemical species. For example, the oxidation of SO_2, NO, H_2S are industrial processes for the simultaneous removal of these species, especially from flue gases downstream of an SO_2 scrubbing process.[8]

Few fundamental studies have been published on the mechanisms of most of these catalytic reactions and the nature of the active sites is usually unknown. In general, many of the catalytic properties of carbon can be understood in terms of textural properties (e.g. surface area, pore shape and pore size), structure, electronic behavior, and surface chemistry, which in turn, depend on treatment and preparation. In many instances, these considerations suggest how selecting and pretreating a carbon might enhance its activity, capacity, and selectivity as a catalyst or adsorbent. To mention a few examples, the decompositions of hydrogen peroxide[110] and nitrous oxide[117] were suggested to be controlled by the presence of surface complexes. On the other hand, the microporosity of

carbons has been suggested to be very important in the catalyzed oxidation of hydrogen sulfide.[72,73]

One problem which will emerge in the consideration of carbons as catalysts is that of impurities in the carbon. Traces of impurities may have a large effect on the catalytic behavior of a given carbon. For instance, Cariaso and Walker[74] found that impurities in the carbon could also have a strong influence on the carbon-catalyzed oxidation of hydrogen sulfide.

Catalytic reactions involve adsorption of one or more reactants on the carbon surface. The course and extent of such reactions, therefore, are often found to be related to surface complexes already present on the carbon surface. The most common groups on the surface of carbons involve oxygen. The importance of surface complexes in the behavior of carbons has been reflected in several surveys of the field.[105,157-160] A real problem here involves the difficulty in quantifying accurately these functional groups on the carbon surface, so the exact catalytic role of carbon surface is often open to considerable question.

Although the state-of-the-art for carbon as a catalyst is not as well developed as for carbon-supported catalysts, it is clear that the future will be promising once it is understood that carbon offers unparalleled flexibility in tailoring catalyst properties to specific needs. However, the future growth of the use of carbon materials in catalysis will depend on the better understanding of the role of carbon surface chemistry and the clear identification of the catalytically active sites for given reactions, which can then be exploited in the design of truly unique catalysts.

2.2.1. Catalysis by carbons of redox reactions

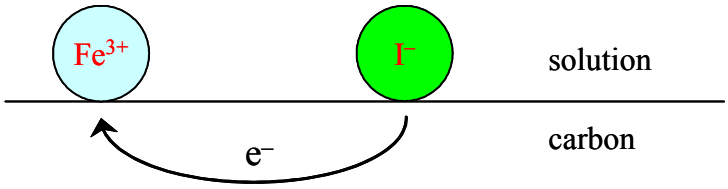

Figure 2.6. Catalytic mechanism of electron transfer through the carbon for the reaction between Fe(III) and iodine ions (Adapted from Spiro[10]).

An electrochemical mechanism was proposed to account for the widespread catalysis by carbons of redox reactions in solution.[13] In this mechanism both reactants sit on the surface, not necessarily on adjacent sites, and the electrons are transferred from the reducing to the oxidizing species through the solid catalyst, as depicted in Figure 2.6. The catalyst acts simply as an adsorbent and a conductor of electrons. This mechanism is important because it is a common catalytic mechanism of noble metal catalysts and perhaps they can be replaced for some uses by carbons.[20]

In the electrochemical model the reaction is split into its component half-reactions. In the presence of both couples the catalyst adopts an appropriate "mixture" or "mixed" potential (a potential of zero net current) at which the rate (i.e., the current) of both half-reactions is the same. The rate is identical to that at which electrons are transferred through the carbon and it is therefore also the rate at which the carbon catalyzes the overall heterogeneous reaction. From the electrochemical point of view, the cathodic current due to one couple must equal the anodic current of the other couple at the carbon surface at the mixture potential. The catalytic rate equation can thus be derived from the electrochemical theory. It is worth noting that the rate constant is no longer independent of concentration, unlike the case of other bimolecular surface reactions.[20]

One typical example of a carbon-catalyzed redox reaction is the reaction of Fe(III) and iodine ions.[13] The initial heterogeneous rates at 25 ºC can be represented by the equation

$$R = k \cdot m\left[\mathrm{Fe}^{3+}\right]^{0.87}\left[\mathrm{I}^{-}\right]^{0.51} \tag{2.32}$$

where m is the mass of the carbon. One could easily misunderstand this outcome as indicative of a Langmuir-Hinshelwood mechanism with two reactants adsorbed next to each other by Freundlich isotherms, a warning against too facile an interpretation of the observed rate law.

2.3. Reduction of nitrobenzene by hydrazine

The transformation of a nitroaromatic compound to the corresponding aromatic amine is an important synthetic and industrial process. For instance, the reduction of nitrobenzene is used on a large scale today for the production of aniline—an important feedstock for manufacturing polyurethane foams, dyes, rubber, pesticides, drugs, photographic chemicals, varnishes and explosives. The reduction of nitroaromatic compounds is also significant for hazardous waste treatment.[161] This transformation can be accomplished by using a variety of reducing agents which have been reviewed and discussed extensively.[162] Hydrazine as a reducing agent for the conversion of nitroaromatic compounds to aromatic amines has been investigated.[163] The hydrazine reduction of nitrobenzene follows the overall reaction:

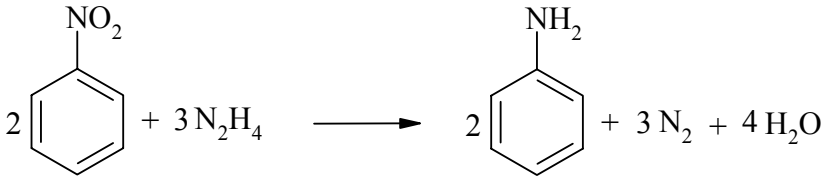

$$\Delta H_f^\circ = -151\,\text{kcal/mol}\,C_6H_5NO_2 \qquad (2.33)$$

Hydrazine is an attractive reducing reagent for the reaction because the reduction is clean and complete. The by-products from the catalyzed hydrazine reduction, nitrogen and water, are easily separated from the aromatic amine and are not environmentally hazardous.

Table 2–1. Selected studies of catalyzed nitrobenzene reduction by hydrazine

Catalyst	Nitrobenzene moles	Hydrazine equivalents	Time (hrs)	*T* (ºC)	Yield (%)
Zn-Cu (2 g):[164]					
prepared	0.01	4	2	25	86
commercial	0.01	4	2	25	7
Fe-Cu-$(NH_2)_2H_2O$[164]	0.01	4	2	25	71
Cu-$(NH_2)_2H_2O$[164]	0.01	4	2	25	42
Montmorillonite (3 g)[165]	0.01	6.25	3	78	85
Graphite (3 g)[166]	0.01	2	2	78	95
$NaNO_3$-C[167]	0.01	6	2	78	87
Oxidized C (3 g)[168]	0.24	5.25	4		80

This reaction is a thermodynamically favored process. The enthalpy change for the reaction is calculated to be –151 kcal/mol $C_6H_5NO_2$ at 25 ºC. In spite of the strongly

favorable thermodynamics, this reaction does not occur in uncatalyzed homogeneous solution. In fact, the first reported reduction of nitrobenzene with hydrazine hydrate, carried out in 1893 by Rothenburg[169] in the absence of a catalyst, achieved very low yields.

Nitrobenzene, as well as other nitro compounds, is reduced with great specificity and efficiency using hydrazine and a catalyst.[163] Table 2–1 compares the reduction of nitrobenzene by hydrazine over some selected catalysts. Metal catalysts used for the hydrazine reduction of nitroaromatic compounds include platinum, palladium, ruthenium, and Raney nickel, among others.[163] Endrey and Reilly[170] observed the catalytic action of carbon black on the reduction of nitroaromatic compounds. In 1985 it was reported that graphite, in large amounts, is an effective catalyst for the reduction of aromatic nitro groups by hydrazine in refluxing ethanol.[166] One advantage over conventional methods is the elimination of use of expensive metals and improvements on reaction conditions as well as yield. The reduction has also been reported on carbon activated with $FeCl_3$ or by the presence of nitrate ion.[167,171] Oxidized carbons have also been used as catalysts and the reported yields are lower than those obtained with graphite.[168] More recent reports showed that the reduction of nitroaromatic compounds by hydrazine is catalyzed by carbon blacks (e.g. Black Pearls L) and graphite.[1] The reaction was optimized to provide complete conversion to the amine without the formation of side products.

2.3.1. Stepwise reaction pathway

The reduction of nitrobenzene may proceed in a stepwise fashion through a

nitrosobenzene and β-phenylhydroxylamine intermediates.[163]

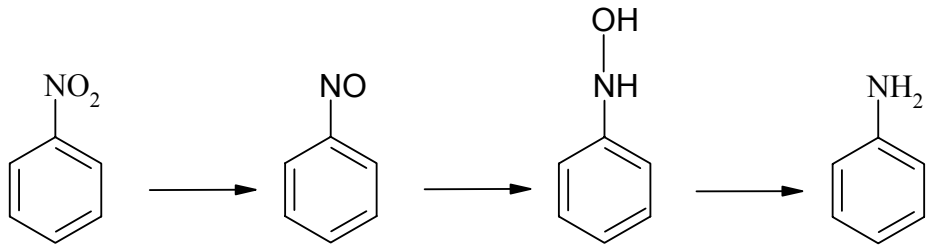

For example, during the reduction of nitrobenzene by hydrazine catalyzed by palladium on charcoal, nitrosobenzene was postulated but not observed.[172] It is possible that once formed the nitrosobenzene is rapidly transformed to the β-phenylhydroxylamine. This pathway has been supported by isolation of a phenylhydroxylamine and formation of coupled products (azobenzene and azoxybenzene), which are attributed to the reaction of nitrosobenzene and/or phenylhydroxylamine intermediates.[172] The reaction may stop with the formation of coupled products or the coupled products may be further reduced, depending on the pH of the solution.[173] Formation of phenyltriazine as an intermediate has been suggested for the Raney nickel catalyzed nitrobenzene reduction by hydrazine hydrate, but there is no evidence to support triazine formation.[174]

2.3.2. Electrochemical mechanism

The nitrobenzene reduction by hydrazine may proceed by redox reactions, comparable to an electrochemical reaction.[20] The electrochemical reduction of nitrobenzene to phenylhydroxylamine proceeds in a single four-electron overall process at all pH values.[173]

$$C_6H_5NO_2 + 3H_2O + 4e^- \rightarrow C_6H_5NHOH + 4OH^- \qquad (2.34)$$

In basic solutions, aniline has been observed to form at various electrodes along with azoxybenzene, azobenzene, and hydrazobenzene.[175-177]

The electrochemical oxidation of hydrazine in alkaline aqueous solutions is represented by the overall equation[178]

$$N_2H_4 + 4OH^- \rightarrow N_2 + 4H_2O + 4e^- \quad E° = +1.16\,\text{V vs. NHE} \quad (2.35)$$

Mostly, one oxidation peak is found, corresponding to the four-electron process to yield nitrogen as the final product. This reaction was proposed to proceed via sequential oxidation steps involving the formation of either the ion $N_2H_3^+$ or the radicals N_2H_3 and N_2H_2, among other intermediates.[178]

Larsen *et al.*[1] provided evidence that the carbon-catalyzed reduction of nitrobenzene by hydrazine occurs by Spiro's electron transfer mechanism. If correct, this mechanism is important for two reasons. First, noble metals catalyze many reactions by this mechanism; these metals can in principle be replaced by an appropriate carbon that acts by the same mechanism. Second, there is a possibility that this behavior can be generalized to other reactions.

The most compelling evidence for this mechanism in carbon-catalyzed reduction of nitroaromatic compounds can be summarized briefly. The identification of phenylhydroxylamine by NMR during the reduction reaction indicated that the initial nitro group reduction is a four-electron process. Hydrazine can act as a two-electron reducing agent and the intermediate formed in the two-electron process (diimide HN=NH) has been observed in this reaction. If hydrazine (two-electron reducer) is to react with a nitroaromatic compound requiring four electrons in the first step, a ternary complex of two hydrazine molecules and one nitroaromatic molecule is required. This is

highly improbable. Carbons catalyze the reaction by adsorbing both hydrazine and nitroaromatic molecules and by allowing the necessary electron flow to occur. This raises the possibility that carbons will be effective catalysts for many reactions in which the number of electrons required for the oxidation and reduction steps is not matched. There is a conflict between the trapping of diimide (a two-electron intermediate) and the normal four-electron kinetics of the hydrazine in carbons in base solutions. Careful kinetics can resolve this issue.

As we move towards a more complete understanding of this reaction mechanism, we are moving towards exciting possibilities, not only the possibility of replacing metal catalysts by carbons, but also the possibility of developing new reactions catalyzed by carbons.

2.4. Decomposition of hydrazine

The decomposition of hydrazine may occur during the hydrazine reduction of a nitroaromatic compound because many catalysts that are used for the reduction are also effective for hydrazine decomposition.[179] The decomposition of hydrazine is an important industrial reaction because of hydrazine's use as a monopropellant rocket fuel. Indeed, the consumption of hydrazine as high-energy fuel dominated the market through the 1960's. The transient decomposition of liquid hydrazine in a space vehicle forms a high-temperature gas mixture ejecting from the nozzle of the thruster to change the flight orbit or to regulate the flight attitude of the space vehicle.[180] The use of hydrazine in satellite attitude control is due to the low activation energy of its decomposition and the high

exothermicity of this reaction.[179]

Hydrazine, both in alkaline and in acid solutions, is capable of undergoing thermal decomposition.[181] In the absence of hydrogen, the decomposition proceeds mainly through

$$3N_2H_4 \rightarrow 4NH_3 + N_2 \qquad (2.36)$$

Under ordinary circumstances this reaction does not take place readily, even though it is thermodynamically favored. The free energy change of this reaction was calculated to be –64.3 kJ/mol at 25 ºC.

Table 2–2. Relevant studies on heterogeneous decomposition of hydrazine in the liquid phase.

Author(s)	Catalyst	*T* (K)	Condition(s)	Stoichiometry‡
Audrieth and Jolly[182]	Raney Ni	274-327	Liquid	(2.36)&(2.39)
Sayer[183-186]	Ir on Al_2O_3	273-327	15-100% H_2O	(2.36)
	Rh on Al_2O_3			(2.38)
Davis and Sayer[187]	20 % Rh on Al_2O_3	273-323	0-100% H_2O	(2.38)
Sayer[188]	20% Ru on Al_2O_3	273-323	0-100% H_2O	(2.36)&(2.38)
Sayer[189]	20% Pd on Al_2O_3	273-327	1.2-3.1 *M* H_2O	(2.38)
	20% Pt on Al_2O_3			
Larsen *et al*.[12]	Carbon	355	*Iso*propanol solution	(2.36)

With a variety of catalysts such as noble metals, hydrazine decomposition does

‡ The stoichiometry of the reaction is determined by Eqs. (2.36)-(2.39).

take place readily in accordance with the above equation.[179] In addition to molecular nitrogen and ammonia, hydrogen was also observed as product of the catalytic decomposition of hydrazine, and at least three other equations can be used to describe the heterogeneous decomposition of hydrazine:[179]

$$3N_2H_4 \rightarrow 2NH_3 + 2N_2 + 3H_2 \quad (2.37)$$

$$2N_2H_4 \rightarrow 2NH_3 + N_2 + H_2 \quad (2.38)$$

$$N_2H_4 \rightarrow N_2 + 2H_2 \quad (2.39)$$

These reactions may take place simultaneously or preferentially. In general, the composition of the gases liberated will depend upon the nature of the catalysts employed and the reaction conditions.[179] For example, a product gas composition corresponding to Eq. (2.38) was found by using platinum black as a catalyst. Upon addition of alkali, the gas composition approached that expected for Eq. (2.37).[190,191] Other investigations did not yield any detectable amount of hydrogen, which supports Eq. (2.36).[192] Apparently, Eq. (2.36) describes the overall reaction when hydrazine decomposition proceeds at lower temperatures, while the reaction described by Eq. (2.38) becomes evident only at higher temperatures.[179] Table 2–2 gives a group of relevant publications devoted to the study of heterogeneous hydrazine decomposition in the liquid phase.

Vitvitskaya and Grabovskaya[193] first observed the catalytic decomposition of hydrazine on AG-3 activated carbon. Larsen *et al.*[12] reported the carbon-catalyzed decomposition of hydrazine during the study of the carbon-catalyzed reduction of nitroaromatic compounds by hydrazine.

2.4.1. Nondissociative bimolecular mechanism

Sayer[185] proposed the following mechanism for hydrazine decomposition in aqueous solution on Shell 405 catalyst:

$$N_2H_{4(aq)} \rightarrow N_2H_{4(ads)} \quad (2.40)$$

$$N_2H_{4(ads)} + N_2H_{4(aq)} \rightarrow N_2H_{2(ads)} + 2NH_3 \quad (2.41)$$

$$2N_2H_{2(ads)} \rightarrow N_2H_{4(ads)} + N_{2(g)} \quad (2.42)$$

$$N_2H_{2(ads)} \rightarrow H_{2(g)} + N_{2(g)} \quad (2.43)$$

The hydrazine molecule may be adsorbed on the surface through the two lone pairs of electrons. An adsorbed hydrazine molecule transfers two hydrogen atoms to another hydrazine molecule in solution to cleave the N-N bond and form two molecules of ammonia and an adsorbed *cis*-diimide (N_2H_2) on the surface. The diimide then reacts by either one of two possible mechanisms. The first mechanism involves the disproportionation reaction with neighboring diimide forming nitrogen that then desorbs and one molecule of hydrazine, which remains adsorbed on the surface. The second mechanism for the decomposition of diimide occurs if diimide adsorbed on the surface cannot find an adjacent diimide to react with, so the diimide molecule decomposes directly to nitrogen and hydrogen. The diimide disproportionation to hydrazine is well established and is a significant complication in the use of diimide to reduce double bonds.[194]

Sayer's suggestions are consistent with isotope studies of hydrazine decomposition using ^{15}N-labeled hydrazine.[185] In these studies, the nitrogen produced consisted only of ^{15}N-^{15}N or ^{14}N-^{14}N, indicating that the N-N bond of the hydrazine

remained intact during the decomposition reaction.

2.4.2. Dissociative bimolecular mechanism

Fouché *el al*.[195] proposed the mechanism illustrated below based on their kinetic studies on iridium-alumina catalysts:

$$N_2H_{4(aq)} \rightarrow N_2H_{4(ads)} \quad (2.44)$$

$$2N_2H_{4(ads)} \rightarrow 2NH_3 + 2NH_{(ads)} \quad (2.45)$$

$$2NH_{(ads)} \rightarrow N_2H_{2(ads)} \quad (2.46)$$

$$N_2H_{4(ads)} + N_2H_{2(ads)} \rightarrow N_{2(g)} + 2NH_3 \quad (2.47)$$

Diimide is assumed as an intermediate in the decomposition of hydrazine. However, the mechanism through N-N bond splitting proposed by Fouché *el al*. is not supported by isotope studies.

2.4.3. Electrochemical mechanism

Spiro and Ravnö[196] first proposed that hydrazine decomposition may proceed by redox reactions in acid or neutral solutions, where the metal catalyst acts simply as an electron-conductor. Hydrazine decomposition could take place by a redox reaction in basic solutions as well. The standard redox potentials for half reactions involving hydrazine have been calculated[181]

$$N_2H_4 + 4OH^- \rightarrow N_2 + 4H_2O + 4e^- \quad E° = +1.16\,\text{V vs. NHE} \quad (2.48)$$

$$N_2H_4 + 2H_2O + 2e^- \rightarrow 2NH_3 + 2OH^- \quad E° = +0.15\,\text{V vs. NHE} \quad (2.49)$$

The overall reaction is spontaneous (E^o = + 1.31 V vs. NHE).

Chapter 3.

Experimental Techniques

3.1. Carbonaceous Samples

A variety of carbonaceous materials were examined as catalysts. They included:

a) Carbon blacks: Monarch 1000, Monarch 1300, Regal 400R, Vulcan XC-72 R, Black Pearls 2000, and Mogul L (Cabot Corporation).

b) Activated carbons: Nuchar SN-20, Nuchar SA-20, Nuchar SA, and Nuchar WV-A 900 (MeadWestvaco Corporation). Darco G60 and Norit SX2 (Norit Americas, Inc.)

c) Charcoals: Coconut (Fisher Scientific, Inc.) and Bone (Ebonex Corporation)

d) Natural graphite (Fisher Scientific, Inc.)

Carbon black[197] is a very fine particulate form of elemental carbon, consisting of well-developed planes of carbon atoms (graphene sheets) stacked roughly parallel to one another, but randomly in orientation with respect to adjacent layers to form spherical particles, which in turn form structures or aggregates. All carbon blacks are produced either by incomplete combustion or thermal decomposition (vapor-phase pyrolysis) of a hydrocarbon feedstock, such as heavy petroleum distillates and residual oils, coal-tar products, natural gas and acetylene. The carbon blacks used here (all from Cabot Corporation) are oil-furnace blacks that exhibit a rather wide range of particle aggregation in which carbon particles are fused into grape-like clusters and/or reticulate

chains or branches. Of all carbon blacks used in this study, Black Pearls 2000 has the highest structure or particle aggregation (average structure level) as determined by the dibutyl phthalate absorption number (330 cc/100 g), as shown in Table 3–1. Carbon blacks from Cabot Corporation are produced by subjecting heavy residual oil feedstock to extremely high temperatures (> 1500 °C) in a carefully controlled combustion process.

Table 3–1. Selected properties of carbon blacks[198]

Carbon black	pH	DBP Oil Absorption (cc/100 g)	Particle size (nm)
Monarch 1300	2.5	100	13
Monarch 1000	3.0	110	16
Mogul L	3.0	62	24
Regal 400R	4.0	71	25
Black Pearls 2000	8.6	330	12
Vulcan XC-72R	8.5	192	30

Activated carbons,[3,199] another form of amorphous carbon, consist of a twisted network of defective layers or stacks of graphene sheets that are less regularly organized than in carbon blacks, and cross-linked by aliphatic bridging groups. They are produced by a process called “activation” where a number of naturally occurring and synthetic carbon-containing substances (coal, peat, wood, nutshells, coconut husks, animal bones, etc.) are first carbonized. The carbon so produced (charcoal) is then washed with acid to remove impurities and "activated" by heating in steam at 600–900 °C or in air. Due to the activation process, the carbon layer planes are separated by micropores, most of which

are slit-shaped. Depending on the precursor, there may also exist a large fraction of the pore volume in meso- and macropores. Activated carbons from MeadWestvasco Corporation are manufactured from hardwood, so they are inherently low in extractable minerals and lower in moisture than other carbons.

Charcoal[16] is the raw material used to produce activated carbon. It contains other organic residues, is much less porous, and has a lower surface area than activated carbons. The relevant properties of these carbons are summarized in Table 3–2 and Table 3–3.

Table 3–2. Selected compositional properties of carbon samples used

				% Elemental analysis (dry basis)				
Carbon	**Type**	**Source**	**% Ash**	**C**	**H**	**N**	**S**	**O**
Graphite		Fisher	1.43	98.85	~ 0	0.07	0.05	~ 0
Coconut charcoal	Charcoal	EM Science	5.38	92.01	0.04	0.55	0.14	1.89
Bone charcoal	Charcoal	Ebonex	83.83	13.66	0.32	0.69	0.06	1.44
Nuchar SA	Activated	Westvaco	4.26	89.60	1.67	0.48	0.02	3.97
Nuchar SA-20	Activated	Westvaco	3.81	89.78	1.86	0.46	0.01	4.08
Nuchar SN-20	Activated	Westvaco	5.62	88.25	1.44	0.40	0.01	4.28
Nuchar WV-A 900	Activated	Westvaco	3.59	89.99	1.75	0.48	0.01	4.18
Norit SX2	Activated	Norit	3.95	93.66	0.04	0.84	0.18	1.34
Darco G60	Activated	Norit	4.76	92.38	0.08	0.72	0.18	1.87
Mogul L	Black	Cabot	0.34	96.13	0.09	0.25	0.95	2.25
Regal 400R	Black	Cabot	0.17	97.76	~ 0	0.35	0.91	0.81
Black Pearls 2000	Black	Cabot	0.47	96.68	0.10	0.46	1.58	1.18
Monarch 1300	Black	Cabot	0.50	94.27	0.11	0.28	0.64	4.20
Monarch 1000	Black	Cabot	~ 0	94.54	0.06	0.39	0.93	4.08
Vulcan XC-72R	Black	Cabot	0.31	99.06	~ 0	0.39	0.62	~ 0

3.1.1. Characterization and Techniques

The BET surface areas, *S*, were determined by N_2 physisorption at 77 K using a Quantachrome Autosorb 1 analyzer (Table 3–3). Prior to the adsorption experiments, samples were outgassed at 150 ºC for 10 hrs. The BET equation was used to calculate the apparent surface area from nitrogen adsorption data in the range $0.1 < P/P_0 < 0.3$.[200] The experimental error associated with these measurements was in the order of ± 10 m^2/g, as determined from the standard deviation of three independent trials.

The external surface area or non-microporous surface, S_{ext}, was determined with the deBoer *t*-method using nitrogen adsorption isotherms in the range $0.2 < P/P_0 < 0.5$. This surface corresponds essentially to the walls of the meso- and macropores in activated carbons. The determination of the external surface using deBoer *t*-method is a standard technique for carbon blacks.[200] For activated carbons other methods, also involving the adsorption isotherm, are more realistic.[201] However, the various techniques used for the determination of the external surface of activated carbons are fairly consistent and produce an overall scatter of 10–15%, which has been interpreted as due to possible errors inherent to the individual techniques.[202] Other textural parameters were evaluated from nitrogen adsorption isotherms: the total pore volume, V_p (amount of N_2 adsorbed at a relative pressure of $P/P_0 = 0.99$), and the mean pore radius, *r* (estimated from the equation $r = 2V_p/S$).[200]

Elemental analysis of the carbon samples was carried out with a LECO CHN-600 elemental analyzer, a LECO SC-132 sulfur determinator and a LECO MAC-400 proximate analyzer. The method consists in the determination of the moisture, volatile

matter, and ash yield using the LECO MAC-400 proximate analyzer. Moisture content is determined by establishing the loss in weight of a sample when heated between 104–110ºC. This quantity is used for calculating other analytical results to a dry basis. Ash yield is determined by weighting the residue remaining after burning the sample between 700–750ºC in the presence of air. Volatile matter is determined by establishing the loss in weight resulting from heating a sample at ~ 950ºC. The total sulfur content, and the total carbon, hydrogen and nitrogen contents are determined using the LECO SC-132 sulfur determinator and the LECO CHN-600 elemental analyzer, respectively. C, H, and S are measured by infrared absorption while N is determined by thermal conductivity. The experimental error associated with the elemental analysis is ~ ± 2%.

Table 3–3. Selected textural properties of carbon samples used

Carbon	Type	S (m^2/g)	S_{ext} (m^2/g)	V_p (cm^3/g)	r (nm)
Graphite		11	8.8	0.043	7.77
Coconut charcoal	Charcoal	934	41	0.527	1.13
Bone charcoal	Charcoal	112	109	0.231	4.13
Nuchar SA	Activated	1350	382	1.060	1.57
Nuchar SA-20	Activated	1342	355	1.211	1.81
Nuchar SN-20	Activated	1193	340	1.008	1.67
Nuchar WV-A 900	Activated	1403	374	1.134	1.62
Norit SX2	Activated	750	171	0.639	1.70
Darco G60	Activated	655	173	0.577	1.76
Mogul L	Black	148	148	0.796	10.75
Regal 400R	Black	96	96	0.745	15.52
Black Pearls 2000	Black	1448	447	3.268	4.52
Monarch 1000	Black	350	289	1.088	6.21
Monarch 1300	Black	494	301	0.867	3.51
Vulcan XC-72R	Black	229	102	0.685	5.98

The bulk oxygen content is determined by weight difference. Therefore, it is

expected that this quantity carries a propagated error from the determination of the content of the other quantities involved in its calculation. The pH values at 24 ºC of the "as received" carbon samples were determined according to the ASTM method D1512, and using a pH meter (Beckman Φ240) with a precision of ± 0.01.

3.2. Kinetic Measurements

The reduction of nitrobenzene (99.5 vol%, Fischer Scientific, Inc.) by hydrazine (98.5 vol%, Alfa Aesar, Co.) using carbon catalysts was studied. All compounds were used as received. The reactions were conducted in refluxing[§] *iso*propyl alcohol (Fisher Scientific, Inc.), which was also used as received. The reaction is then conducted at the normal boiling point of *iso*propanol (~ 82 ºC). *Iso*propanol was chosen as the solvent because it is inexpensive and environmentally sound. In addition, the aromatic amines are readily isolated from *iso*propanol due to its low boiling point.

The experimental setup for kinetic measurements is shown in Figure 3.1. A three neck 100 mL round bottom flask with 24/40 joints was used with a reflux condenser connected to a gas burette, a 30 mL pressure-balanced addition funnel, and a thermometer. The gas burette was composed of two 1L volume calibrated addition funnels connected together at their bottoms with Tygon® tubing. The amount of gas produced as a function of time was measured using the gas burette at a constant pressure

---

[§] Refluxing is the simplest and most convenient way to control the temperature of the reaction mixture by using a reaction solvent that has a boiling point within the desired temperature range for the reaction.

of 1 atm. This is achieved by adjusting the level of the manometric liquid (water), changing the height of the burette. The gas volume is measured with an experimental error ± 5 mL, and each experiment was performed at least three times from which deviations of the experimental data (i.e., gas volume at a particular time) were determined to be less than 5%.

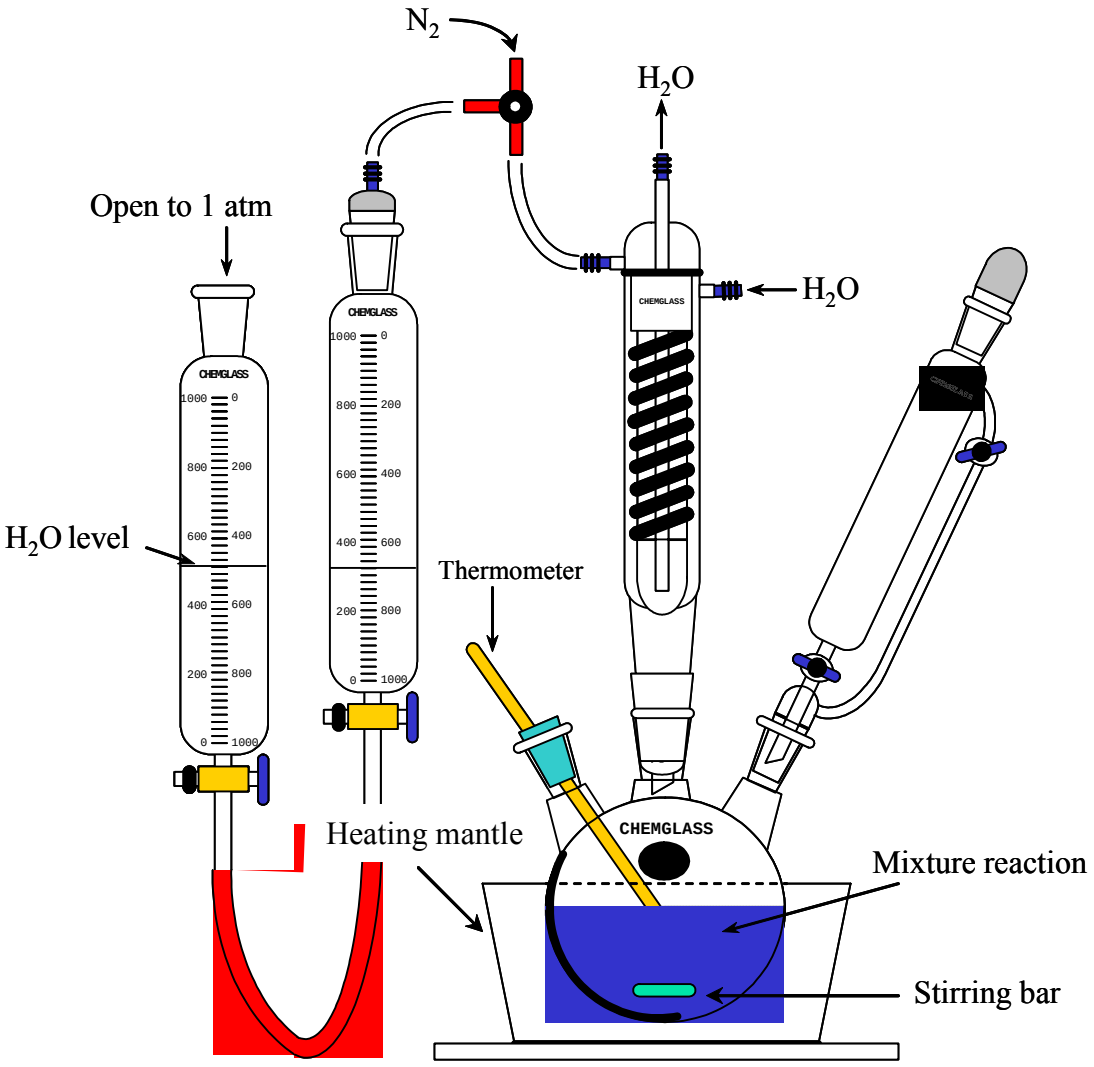

Figure 3.1. Schematic diagram of the experimental setup used to follow the reaction kinetics of the nitrobenzene reduction and hydrazine decomposition.

The standard procedure used for the nitrobenzene reduction follows. All reactions were carried out in a hood and care was taken to ensure safety when working with

hydrazine. The carbon catalyst was added to a solution of nitrobenzene and *iso*propanol in the round bottom flask. A magnetic stir bar and a magnetic stir plate were used to mix the reactants. Hydrazine was placed in the addition funnel. Nitrogen was passed through the system from the top of the reflux condenser for 20 minutes before the ground glass stopper was placed on the addition funnel. All of the ground glass joints were thoroughly greased to insure a tight seal. After the system has been purged with nitrogen, the flask was heated using an electric heating mantle controlled with a variable power controller. The system was brought to reflux and connected to the gas measuring apparatus. When the system was stable, determined by no change in gas volume for at least 30 minutes, the reaction was initiated by the addition of hydrazine to the refluxing mixture of the compound and carbon in *iso*propanol. The reaction was followed by measuring the volume of water displaced from the gas burette at atmospheric pressure.

In a typical experiment, 0.017 moles of nitrobenzene, 0.025 moles of hydrazine, 0.70 g of carbon material and 25 mL of *iso*propanol was charged into the measuring apparatus. The mixture was refluxed until the produced gas volume remained constant. When the reaction was complete, the product mixture was filtered by suction filtration to remove the carbon catalyst.

The decomposition of hydrazine on several carbonaceous catalysts was also examined. The procedure and apparatus were the same as for the reduction of nitrobenzene, except that the nitrobenzene was not included. In addition, 20 mL of *iso*propanol was used to increase the initial concentration of hydrazine with a subsequent increase of the reaction kinetics.

Measurement of the amount of gas produced from the reaction as a function of

time was used to determine a rate of reaction. The rate of gas production is approximately equal to the rate of nitrobenzene reduction if the rate of hydrazine decomposition is slow compared to the reduction rate and the adsorption equilibrium is established instantaneously.

Chapter 4.

Carbon-catalyzed decomposition of hydrazine

4.1. Kinetics of the reaction

Figure 4.1 shows plots of gas volume versus time for refluxing solutions of hydrazine in *iso*propanol to which the indicated carbon had been added. The gas evolution plots show simple time dependence. In the absence of added carbon, hydrazine solutions are stable under the reaction conditions. The production of gas upon addition of carbons to otherwise stable hydrazine solutions demonstrates carbon-catalyzed decomposition. All of the carbons catalyze the reaction to different extents. Based on the amount of gas produced at a given time, we found that graphite is the least effective catalyst and Nuchar WV-A 900 is the most effective catalyst (see Table 4–1).

Nitrogen and ammonia are the only decomposition products according to previous studies by Larsen *et al.*[12] on Black Pearls L (carbon black). The decomposition of hydrazine on a supported iridium catalyst (the Shell 405 catalyst) was also shown to yield nitrogen and ammonia, and the overall reaction is represented by Eq. (2.36).[183] If the overall reaction over carbon catalysts follows Eq. (2.36), the total gas volume expected (V_C) from 0.025 moles of hydrazine used is about 1050 mL if ammonia is in the gas phase or V_C = 210 mL if ammonia remains totally dissolved in *iso*propanol and the water in the gas burette. For some carbons, the observed gas volumes are somewhat larger than the amount of N_2 expected. For example, as shown in Figure 4.2, the amount of gas

produced in the presence of Nuchar WV-A 900 was on the order of 430 mL; twice the amount of N_2 gas expected.

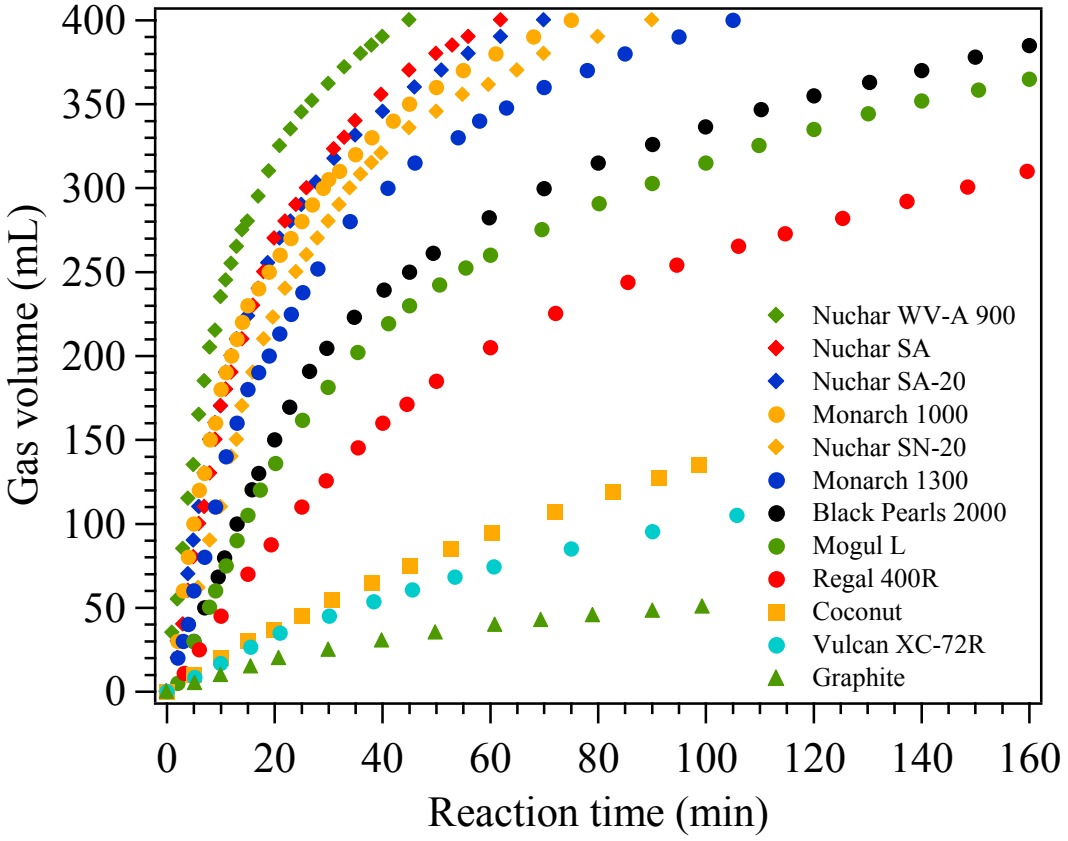

Figure 4.1. Gas evolution from hydrazine decomposition in refluxing *iso*propanol catalyzed by carbons.

There are three possibilities for gases in addition to nitrogen. One is ammonia. Ammonia produced in the decomposition reaction is first dissolved in *iso*propanol, so initially only nitrogen is expected to be produced. At 80 ºC, ~400 mL of ammonia dissolve in 1L of *iso*prpanol.[203] After *iso*propanol saturation with ammonia, the reaction proceeds with the production of both nitrogen and ammonia in the gas phase. However, the solubility of ammonia in water is quite high. At 24 ºC, 692 mL of ammonia gas dissolves in 1 mL of water.[204] Therefore, ammonia produced in the gas phase, after

*iso*propanol saturation, is expected to dissolve quickly in the water of the gas burette.

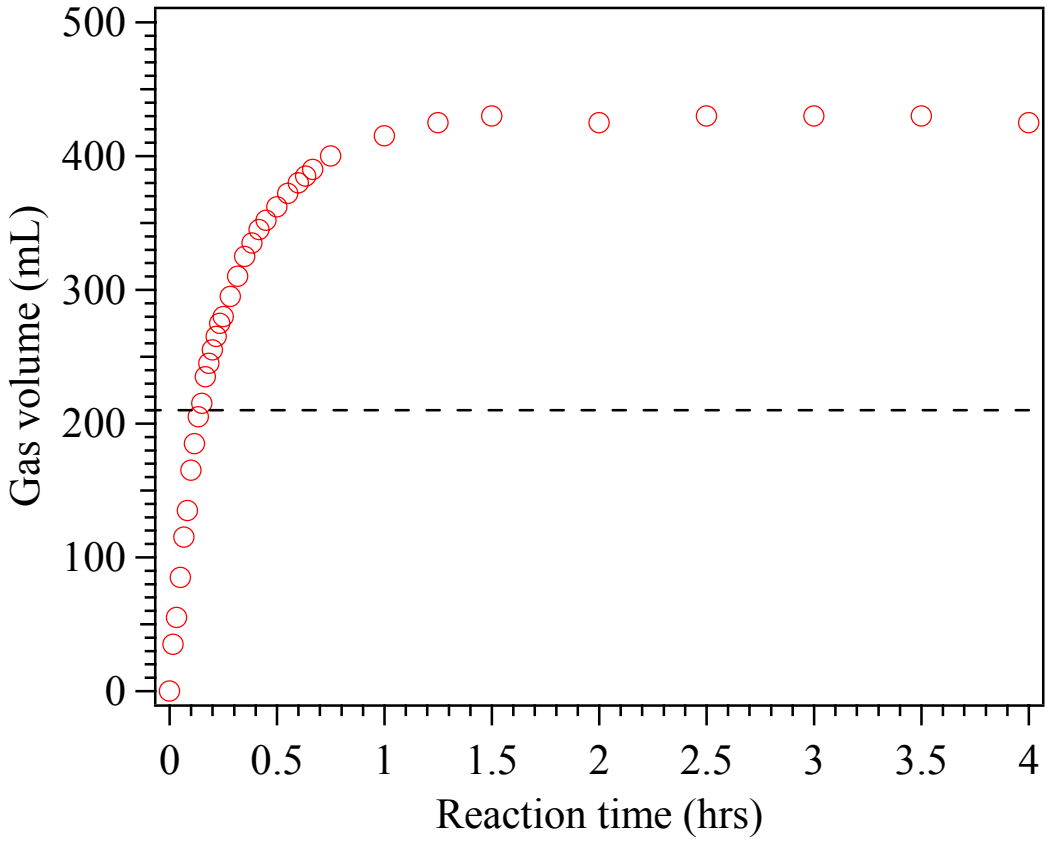

Figure 4.2. Gas evolution from hydrazine decomposition in refluxing *iso*propanol catalyzed by Nuchar WV-A 900 (activated carbon).

The second possibility for the additional gas produced is hydrogen, if the reaction is proceeding by pathways in addition to Eq. (2.36). However, the absence of hydrogen was demonstrated for Black Pearls L using GC techniques.[12]

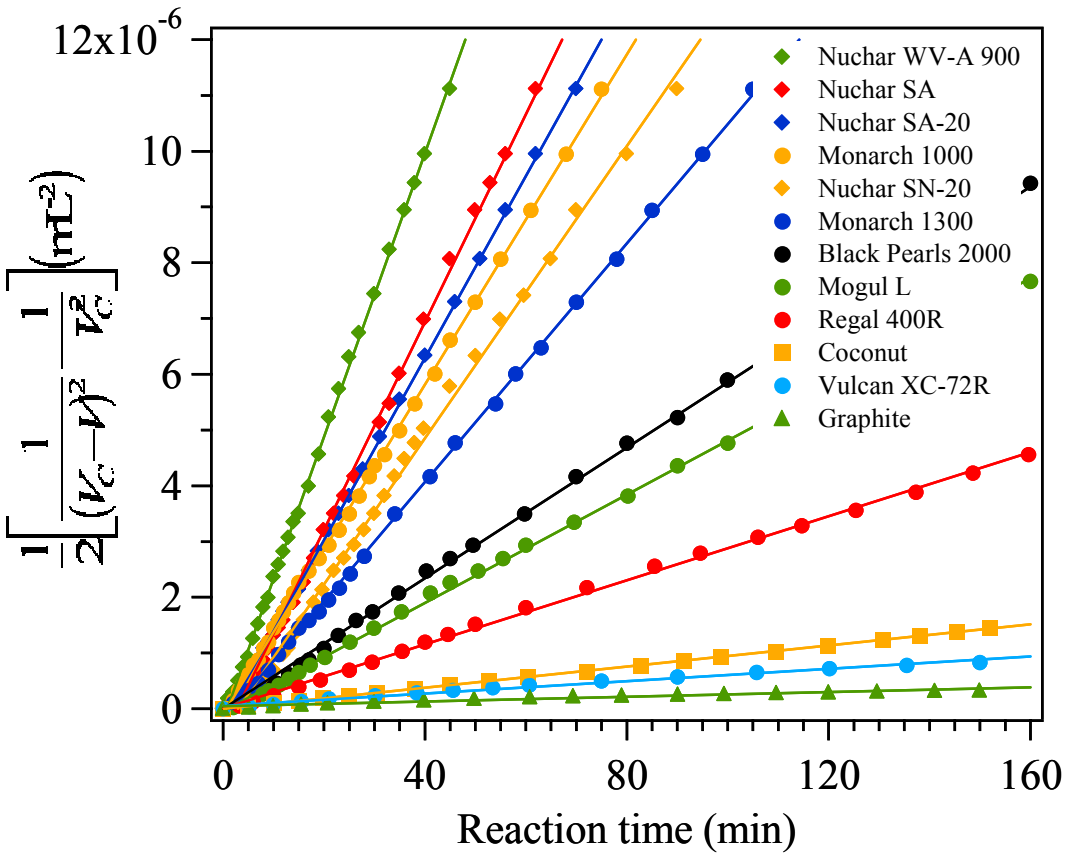

Figure 4.3. Third-order plots for the decomposition of hydrazine in the presence of several carbon catalysts (V is the gas volume at time t, and V_C is the calculated final gas volume using the stoichiometry of Eq (2.36). Solid lines are linear fits to the data.

The third possible explanation for the extra amount of gas produced is that a simultaneous reaction is taken place which is also contributing to the production of gases. Szymanski and Rychlicki[64,65] reported that oxidized carbon and its metal cation-substituted forms catalyze the decomposition of *iso*propanol vapors. Dehydration of *iso*propyl alcohol vapor to propene and *iso*propyl ether, and dehydrogenation to acetone were observed in the temperature range 100º–190 ºC. The authors also found that the presence of adsorbed metal cations enhances the dehydrogenation activity at the expense of the total dehydration activity.[64] It was suggested that dehydrogenation activity requires the simultaneous presence on the carbon surface of acidic and basic Lewis sites, while

dehydration activity results from the presence of carboxylic acid groups of varying strength. This is consistent with the very low or no catalytic activity exhibited by ordinary (non-oxidized) activated carbons, which are basic carbons. Systematic studies are needed on the decomposition of *iso*propanol in the liquid phase over commercial carbons. So far, we have found no clear indication that this reaction is occurring during the decomposition of hydrazine.

To avoid the complications introduced by possible side reactions and ammonia in the gas phase, initial rates were used to analyze the reaction kinetics. At the beginning of the reaction, neither side reactions nor ammonia will contribute to the reaction rate. Surprisingly, the data were found to fit very well a third-order reaction in hydrazine, as shown in Figure 4.3. This is an interesting finding since termolecular reactions are very rare in heterogeneous catalysis. For instance, only one example third-order carbon-catalyzed reaction could be found in the literature: the racemization of *tris*(ethylenediamine)-cobalt(III) ion $[Co(en)_3]^{3+}$ by iodide in the presence of a carbon black.[38] On the other hand, the electrochemical oxidation of hydrazine on glassy carbon electrodes in acetonitrile[205,206] shows a third-order behavior where one-third of the hydrazine molecules are oxidized to N_2H_2 and the other two-thirds act as proton acceptors, but this not a reasonable mechanism for the hydrazine decomposition where there is no oxidative driving force.

Table 4–1. Kinetic parameters for the decomposition of hydrazine on different carbons

Carbon sample	$R \times 10^8$ (mol cm $^{-3}$ s^{-1})	V_{30} (mL)	% dec (30 min)
Graphite	0.069	25	2.5
Coconut	0.312	54	5.4
Nuchar SA	6.138	320	32.0
Nuchar SA-20	5.373	316	31.6
Nuchar SN-20	4.314	280	28.0
Nuchar WV-A 900	8.107	362	36.2
Mogul L	1.599	181	18.1
Regal 400R	0.947	126	12.6
Black Pearls 2000	1.949	205	20.5
Monarch 1000	4.872	305	30.5
Monarch 1300	5.223	260	26.0
Vulcan XC-72R	0.183	45	4.5

Several kinetic parameters were measured for each carbon catalyst; these are (1) the initial rate of reaction, R, (2) volume of gas evolved up to t = 30 min, V_{30}, and (3) percent decomposition at t = 30 min, (%dec = $V_{30}/V_C \times 100$). The results are colleted in Table 4–1. The varying initial rates (0.069–8.107)$\times 10^{-8}$ mol cm^{-3} s^{-1}, as shown in Table 4–1, also confirm the diversity of activity of the carbon catalysts. These differences could be associated with individual differences in the physicochemical properties of the carbon. This issue will be explored later in this chapter. Unfortunately, due to the differences in the reaction conditions employed (i.e., temperature, initial concentrations, etc.), we cannot compare the reaction rates obtained in this study with those in previous studies on metal catalysts.

4.2. Effect of impurities

Many of the carbon catalysts used in this study contain mineral matter, so it was necessary to determine whether any of the catalytic activity is due to the presence of minerals. Evidence that mineral matter plays no role in this reaction is provided by the scattered data in Figure 4.4, where the initial rate of the reaction is plotted as a function of the ash yield. As shown in this figure, carbon blacks with little or no ash yield (~0-0.5%) exhibit wide changes in the initial rates. For instance, the initial rate of the reaction on Monarch 1000 (~0% ash yield) is a factor of ~20 higher than that on Vulcan XC-72R (0.31% ash yield). Also, note the scattering of the data and the wide range of initial rate changes for carbons with ash yield over 3% with high surface area. This is the scattering observed for carbons with medium and low surface area. In addition, the highest initial rates are observed for carbons with high oxygen content. The relationship between the initial rates of the reaction and the oxygen content of the carbons will be discussed later in section 4.6.

Further evidence that the observed reaction is not due to minerals comes for the absence of catalysis by ash. On combustion, most of the carbons used yield some ash (see Table 3–2). Ash is the product of a variety of thermally driven reactions of mineral matter that occur while the carbonaceous portion of the carbon sample is undergoing combustion. Therefore, the composition of ash should resemble that of the oxidized portion of the mineral matter. Ash residue consists of silicates and aluminosilicates of alkali, alkaline earth and other metals such as iron. Some minerals will be oxidized, so the absence of catalytic activity by ash is not definitive. One experiment was carried out to detect the

possible role of mineral matter, by igniting an activated carbon (Nuchar SA, 4.26% ash yield) at 900 °C followed by the determination of the catalytic activity of the ash formed. We observed no detectable catalytic action when 0.3 g of ash was used, i.e., gas was not produced. This amount of ash is 10 times higher than that collected from the combustion of 0.7 g of carbon—the amount of carbon employed to produce the plots in Figure 4.1.

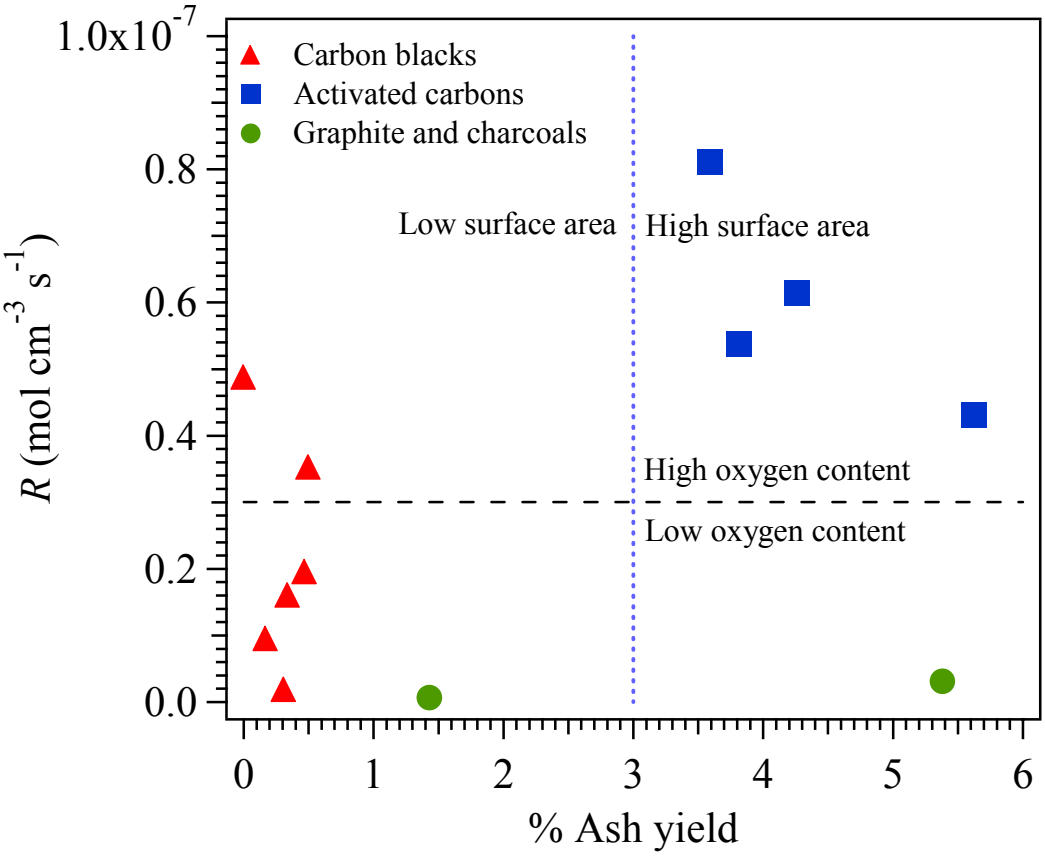

Figure 4.4. Effect of ash yield of carbon catalyst on the initial rate of hydrazine decomposition.

4.3. Variation of rate with mass of catalyst and stirring

The chemical reaction at the surface is likely to be rate-determining in heterogeneous catalysis of solution reactions.[20] It is clearly an essential part of a kinetic

investigation to ascertain whether any other factors (e.g., adsorption, desorption, diffusion) influence the rate of the overall catalytic process. Two main diagnostic criteria have been employed for this purpose:[20]

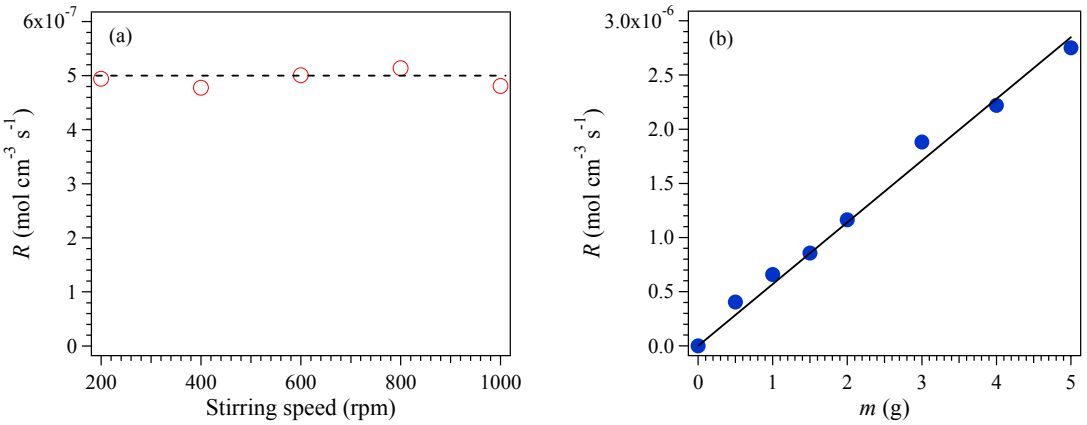

Figure 4.5. Effect of stirring (*left*) and carbon mass (*right*) on the initial rate of hydrazine decomposition over Nuchar SA activated carbon. Solid line is a linear fit of the the data and dashed line is a guide to the eye.

(1) Variation of stirring

More effective agitation of the solution around the solid catalyst does not affect surface-controlled processes but markedly increases external diffusion rates. Figure 4.5(a) illustrates how the overall reaction rate responds to increased agitation of the solution. The constant reaction rate over the experimental range of stirring speed indicates that the carbon-catalyzed hydrazine decomposition is NOT a diffusion-limited reaction but a surface-controlled reaction.

(2) Variation of catalyst area

The catalytic rate is usually directly proportional to the total surface area for reactions controlled by surface kinetics. This is clearly understood if one considers that the reaction rate is directly proportional to the frequency of effective collisions between

reactants. If the molecules can collide only at a surface then more molecules can collide per unit of time when there is a higher number of available catalytic active sites, which in turn, is determined by the surface area of the catalyst. For a given catalyst preparation, when not only surface heterogeneity but also particle size distribution is expected to be uniform from sample to sample, the most appropriate way to change the surface area is by changing the amount of catalyst used. Thus, for surface reactions, the reaction rates are usually directly proportional to the mass of catalyst. Figure 4.5(b) shows that the initial rate of hydrazine decomposition is indeed directly proportional to the amount of carbon used.

4.4. Effect of hydrazine concentration

The variations of the initial rate of carbon-catalyzed hydrazine decomposition with hydrazine concentration [N_2H_4] are shown in Figure 4.6 and Figure 4.7. As the hydrazine concentration is increased the reaction rate increased to saturation, i.e., the reaction rate did not change as the concentration varied. The reaction rate R and the concentration of hydrazine [N_2H_4] may be related by an expression of the form $R = k[N_2H_4]^n$, where k is a rate constant and n is the order of reaction. Writing this equation in the form $\log_{10} R = \log_{10} k + n \log_{10}[N_2H_4]$, we may plot the data in Figure 4.6 and Figure 4.7 in the form of $\log_{10} R$ with respect to $\log_{10}$ [N_2H_4] as in the insert to these figures. Linear fittings of these plots show that at hydrazine concentrations up to ~ 2 M the rate of decomposition is almost proportional to the concentration, the value of n being in the range 0.90-0.95 (i.e., $n \sim 1$). Above ~ 2 M the value of n falls, becoming zero for

high concentrations.

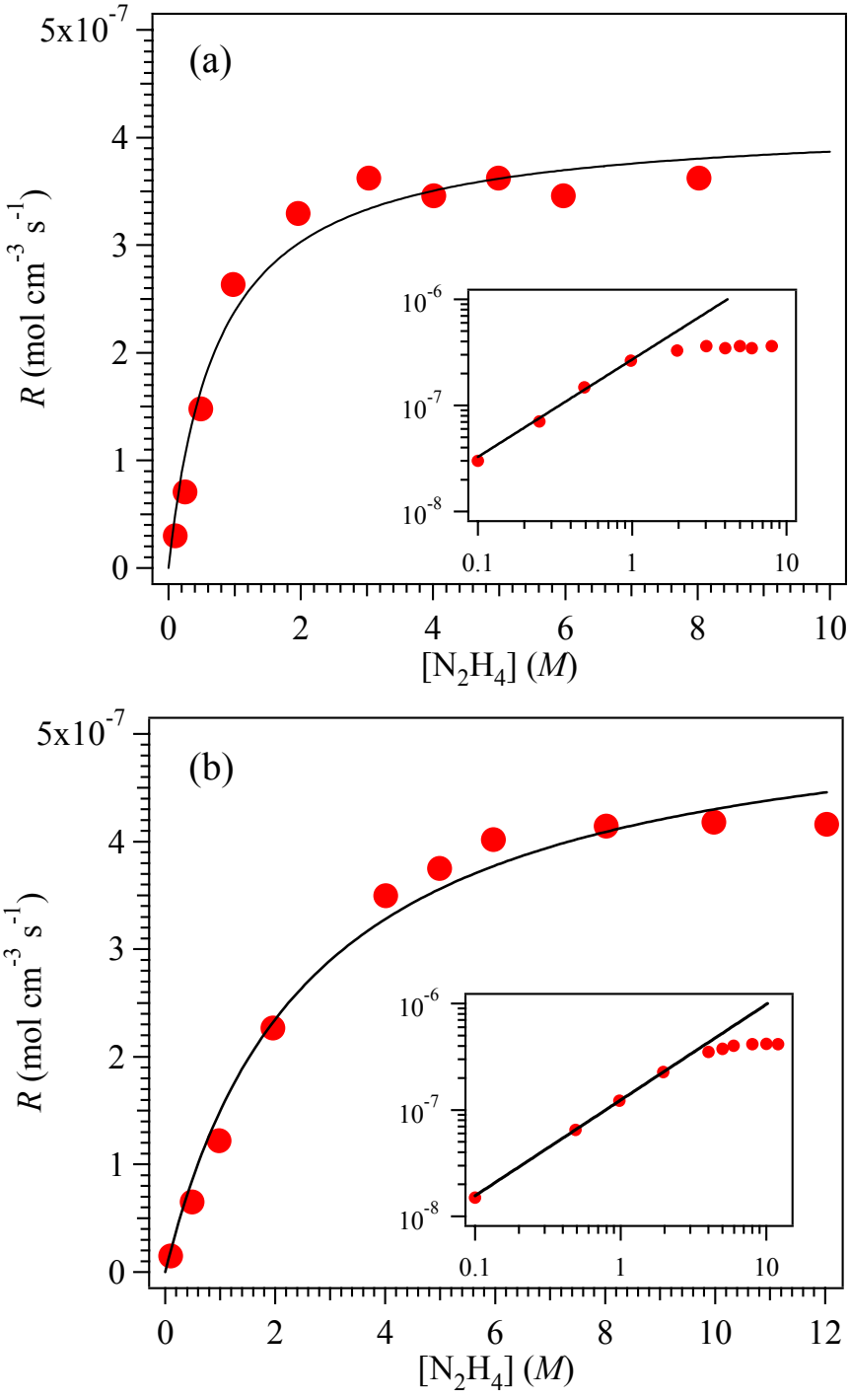

Figure 4.6. Effect of hydrazine concentration on the initial reaction rate of decomposition over carbon blacks: (a) Black Pearls 2000 and (b) Mogul L. Solid line is a fit of the data to Eq. (2.17). The insert shows the log-log plots of the same data with a linear fit at low hydrazine concentrations.

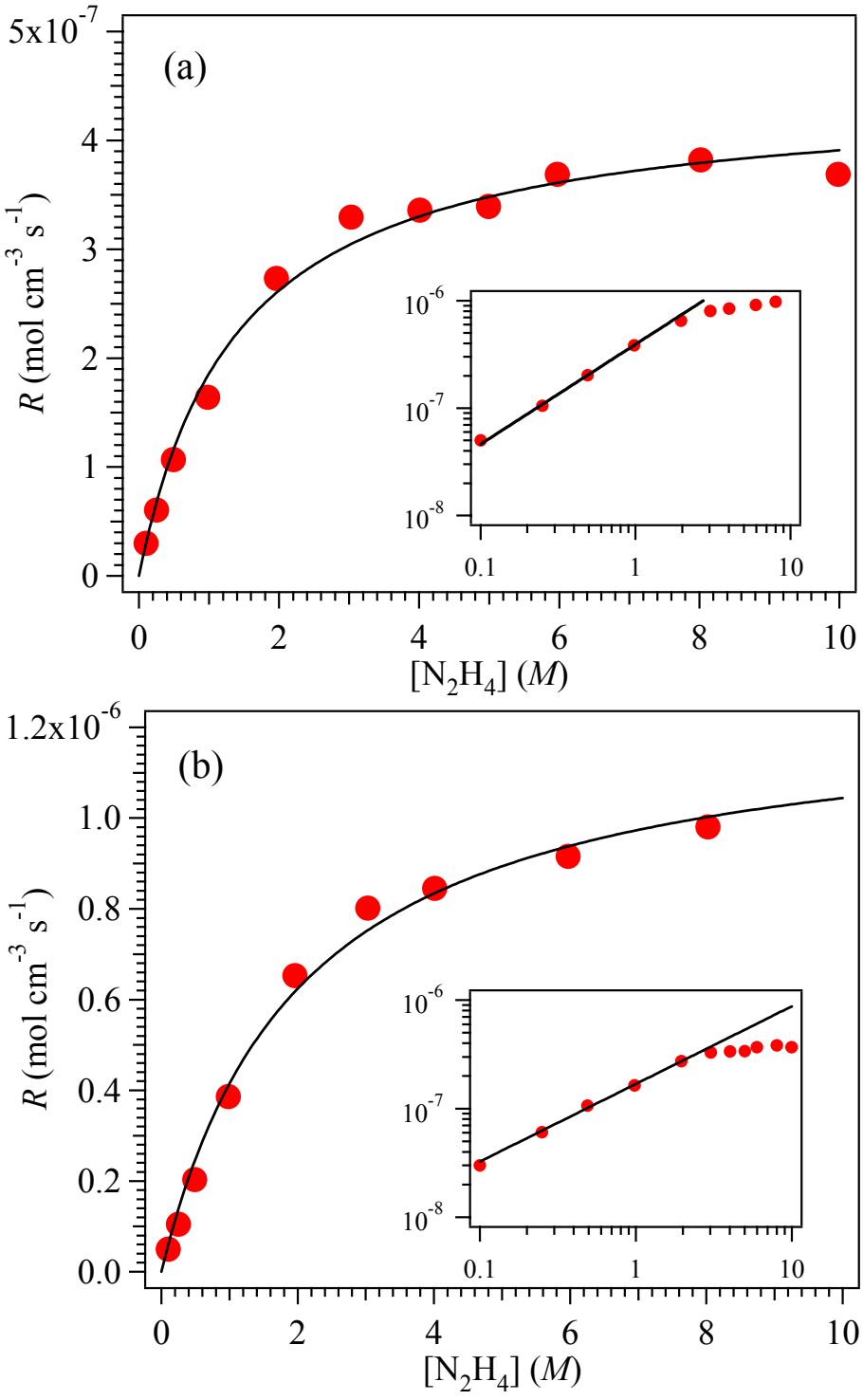

Figure 4.7. Effect of hydrazine concentration on the initial reaction rate of decomposition over activated carbons: (a) Darco G60 and (b) Nuchar SA. Solid line is a fit of the data to Eq. (2.17). The insert shows the log-log plots of the same data with a linear fit at low hydrazine concentrations.

Similar results were obtained in kinetic studies of the decomposition of hydrazine over a supported rhodium catalyst by Davis and Sayer,[186,187] and over platinum catalyst by Sayer.[189] In those cases, however, the authors found that the rate of decomposition is almost proportional to the square root of the hydrazine concentration, i.e, $n \sim 0.5$. According to the authors "the way in which the kinetics change with respect to hydrazine concentration indicates that the [dissociative] adsorption of hydrazine [in the form of amine radicals] on the catalyst surface is involved in the slow step of the reaction." It is worth noting that, unlike the case of carbons, hydrogen is a product of the hydrazine decomposition on rhodium and platinum catalysts.

Here, the relationships of reaction rates to concentrations as shown in Figure 4.6 and Figure 4.7 are commonly found in heterogeneous catalysis when the rate-controlling step of the surface reaction is either the (non-dissociative or molecular) adsorption of the reactant on the catalyst surface or the reaction of the adsorbed species on the surface (unimolecular surface reaction, cf. Figure 2.1).[21] It is difficult to envision a mechanism in which a single hydrazine molecule decomposes to form the products, so we discarded a unimolecular surface reaction as a possibility to explain the kinetic results.

The data are best fit by Eq. (2.17) which is based on the non-dissociative adsorption of hydrazine. The curve fittings were performed using Igor Pro (WaveMetrics, Inc.) Igor Pro is an integrated program for visualizing, analyzing, transforming and presenting data. The reader is referred to Appendix C for details on the curve fitting procedure. The best values for the fitting parameter are shown in Table 4–2. Unfortunately, hydrazine adsorption isotherm could not be measured due to its decomposition. However, it is not surprising that our data can be fitted with a Langmuir

isotherm since hydrazine adsorption on metals (see section 4.6) has been proposed to be a chemisorption process.

Table 4–2. Best fit parameter values achieved with Eq. (2.17)

Carbon	$k_a \times 10^7$ (s^{-1})	K_a (mol^{-1} cm^3)
Black Pearls 2000	5.59	1.344
Mogul L	3.19	0.381
Darco G60	2.07	0.715
Nuchar SA	6.20	0.494

Cosser and Tompkins[207] postulated a dual-plane mechanism to explain the decomposition of hydrazine on different surfaces. They suggested that (i) on more active surfaces where N_2H_4 is dissociatively adsorbed as amide radicals, only H_2 and N_2 will be produced, and (ii) on weakly adsorbing surfaces, dissociative chemisorption of N_2H_4 should be absent and decomposition will occur yielding only NH_3 and N_2. Our kinetic results are in agreement with this postulate, i.e., hydrazine is shown to non-dissociatively chemisorb on carbons and its decomposition produces only N_2 and NH_3.

4.5. Reaction mechanism

The observed kinetics of the decomposition of hydrazine in liquid solutions over carbon catalysts may then be explained by assuming that nondissociative adsorption of hydrazine is the initial step and applying this to the Langmuir adsorption isotherm to derive the overall rate equation. Based on the evidence, we suggest that a scheme

analogous to Sayer's mechanism,[185] with all of the diimide disproportionating to N_2 and hydrazine, is a strong possibility to explain the kinetics of the hydrazine decomposition over carbon catalysts. In this mechanism, the surface reaction occurs between one adsorbed hydrazine molecule and one hydrazine molecule in the liquid phase. In this reaction, the adsorbed hydrazine transfers two hydrogen atoms to the solution hydrazine molecule, to cleave the N-N bond and form two molecules of ammonia and an adsorbed diimide molecule. From stereochemical considerations, the adsorbed diimide exists in the *cis* form due to the abstraction of two *cis* hydrogen atoms by the solution hydrazine molecule. The *cis*-diimide may then disproportionate by reacting with a neighboring diimide, which re-arranges with bonds breaking and reforming to produce nitrogen, which is desorbed, and one molecule of hydrazine, which remains adsorbed on the surface. The desorption of nitrogen leaves a vacancy to be filled by another hydrazine molecule on adsorption. Sayer's mechanism is outlined below:

$$N_2H_{4(aq)} \rightarrow N_2H_{4(ads)}$$

$$N_2H_{4(ads)} + N_2H_{4(aq)} \rightarrow N_2H_{2(ads)} + 2NH_3$$

$$2N_2H_{2(ads)} \rightarrow N_2H_{4(ads)} + N_{2(g)}$$

This mechanism was proposed by Sayer[185] to explain the kinetics of the decomposition of liquid hydrazine on a supported iridium catalyst (Shell 405 catalyst), which also follows the stoichiometry of Eq. (2.36), as in the case of carbon catalysts. According to the authors "The observed first order kinetics over the range 15-100% hydrazine may be explained by the rate controlling step being either the attack by a solution hydrazine molecule on the adsorbed hydrazine molecule…or the adsorption of a hydrazine molecule to fill the vacancy left by the desorption of the nitrogen molecule."

We proposed that, in the case of hydrazine decomposition on carbon catalysts, the rate controlling step is the chemisorption of hydrazine molecules. Thus, in this reaction, the behavior of carbons and metal catalysts seems to be similar.

4.6. Dependence of the catalytic decomposition on carbon properties

Since the catalytic decomposition is a heterogeneous reaction, the available carbon surface is expected to play an important role in the catalysis. We found a correlation between the total surface area of carbon blacks and the initial rates for the reaction, as shown in Figure 4.8. No clear correlation could be established with the use of non-activated and activated carbons. The data in Figure 4.8 show that the initial rate of hydrazine decomposition is directly proportional to the surface area of the carbon blacks. This observation is consistent with the hypothesis that higher surface area carbons contain a relatively higher concentration of active sites for the reaction. Two distinct linear curves with different slopes fitted the data in Figure 4.8. The high-slope curve fitted the data for acidic carbons and the low-slope curve fitted the data for basic carbons. Since the pH characteristic of the carbons is a measure of the total acidic and basic character of the myriad of various functional groups present on carbon surfaces, the trend of the data shown in Figure 4.8 indicates that not only the surface area is relevant for the reaction but also the nature of the surface groups present on the carbon surface. We will discuss the effect of surface functional groups later in this section. Let us first concentrate our attention on the observed change in initial rate with pH and surface area.

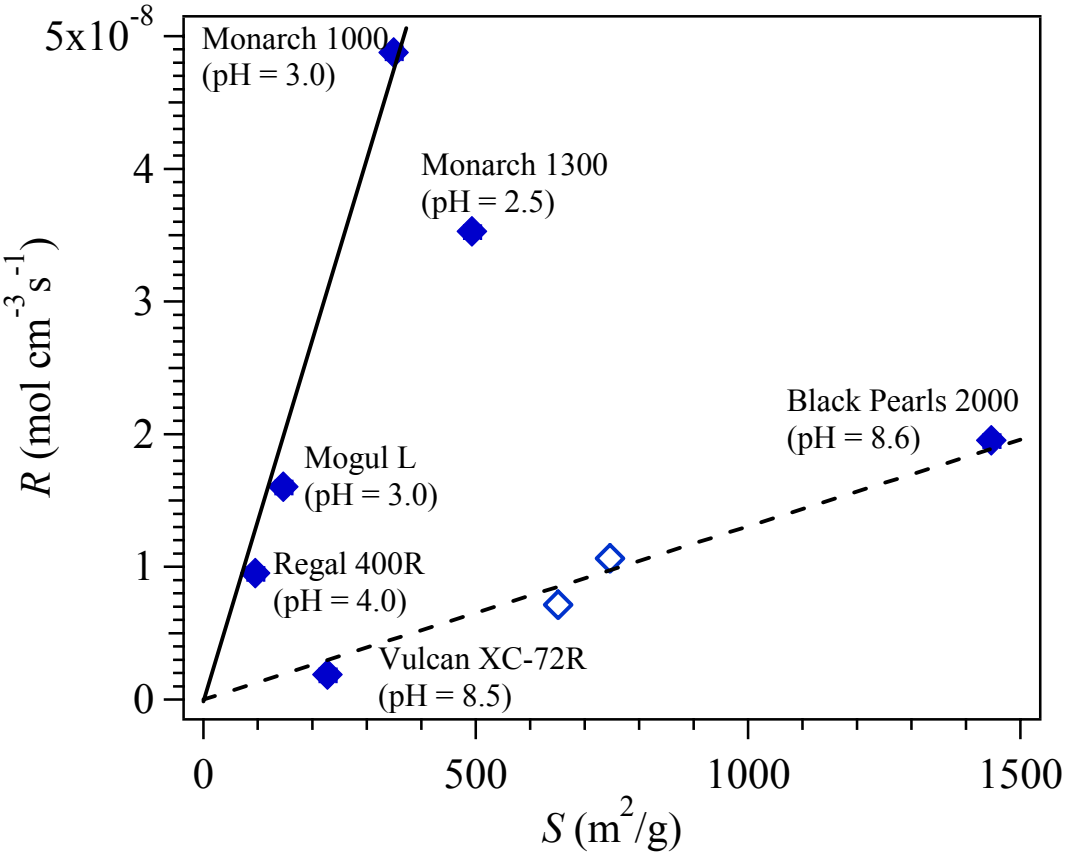

Figure 4.8. Influence of surface area of various carbon blacks on the rate of hydrazine decomposition. Number in parenthesis is the pH of the corresponding carbon. Lines indicate the trend of the data. Data for two activated carbons (open symbols) are included for comparison purposes only.

The pH change for basic carbon blacks is ~ 0 (from Vulcan XC-72R to Black Pearls 2000), and the change in reaction rate is ΔR ~ 0.8% per unit area. A similar change in reaction rate is observed for a pH change of ~ 1.5 (from Regal 400R to Monarch 1300) and for no pH change at all (from Mogul L to Monarch 1000) on acidic carbon blacks. These results suggest that the change in initial rate for these carbons is entirely due to a change in total surface area, but not to a pH change.

The high-slope curve in Figure 4.8 indicates that the reaction rate is enhanced by the presence of surface groups with a much stronger acid character. The acidity of carbon

blacks is generally attributed to the presence of chemisorbed oxygen.[105] The oxygen content of the furnace blacks is probably picked up by the carbon during the various treatments such as pulverizing, pelleting, drying or storage.[208] In particular, the acidic furnace blacks from Cabot Corporation have been further treated *via* an oxidative post production process to increase the amount of chemisorbed oxygen groups present.[198]

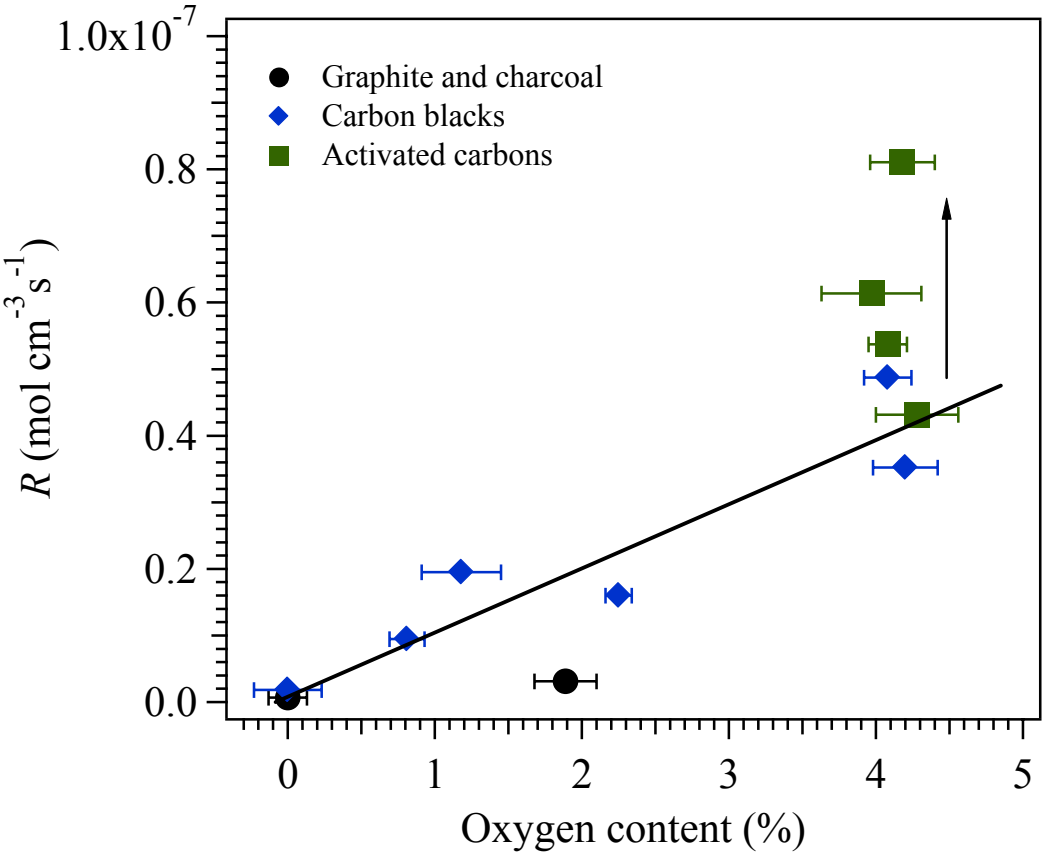

Figure 4.9. Influence of oxygen concentration on the rate of the carbon-catalyzed hydrazine decomposition. Solid line indicates the trend of the data.

To further understand the effect of oxygen functionality on the rate of hydrazine decomposition, we plotted the initial rate of decomposition as a function of the total oxygen content of carbons. The results in Figure 4.9 indicate that the initial rate increases with an increase in the total oxygen content of the carbon catalyst. Most of the data for

carbon blacks, non-activated carbons and graphite in Figure 4.9 could be accommodated on a straight line, but the initial rate varies by a factor of 2 for activated carbons with similar oxygen content. It is possible that the activation procedure of these carbons introduces a variable concentration of different acidic groups or that the change in rate is due to a change in the total surface area. Because the total bulk oxygen content is plotted, no information is available as to the importance of different functional groups on the rate of hydrazine decomposition.

Since the slow step of the reaction was proposed to be the adsorption process of hydrazine on the carbon surface, it is expected that acidic surface groups affect the reaction rate by enhancing the adsorption of hydrazine. The hydrazine molecule exits predominantly in the *gauche* form.[179] It was theorized that the two lone electron pairs (electron pairs which are not involved with bonding to other atoms) in hydrazine interact with unfilled orbitals in the early stages of adsorption and chemisorption of hydrazine on metals.[179] Here, the lone electron pairs of hydrazine may establish a bond to the carbon surface by interacting with partially unfilled π bands. These bands are formed by the overlapping of the p_z-orbital with those from neighboring carbon atoms, in a sideways manner, to form the distributed π-bonds that reside above and below each graphite sheet. It is documented in the literature[23] that heterogeneous oxygen groups chemically bound on the edges can attract and localize the electrons of the basal planes, hence, removing them from the π electron system and forming partially positive "islands" in the basal planes. This effect may improve the adsorption of hydrazine on acidic carbons and enhance the catalytic action of these carbons. Molecular simulations of adsorption of hydrazine on graphene sheets either positive or negatively charged could help to

understand this better.

Chapter 5.

Nitrobenzene reduction to aniline by hydrazine

5.1. Kinetics of the reaction

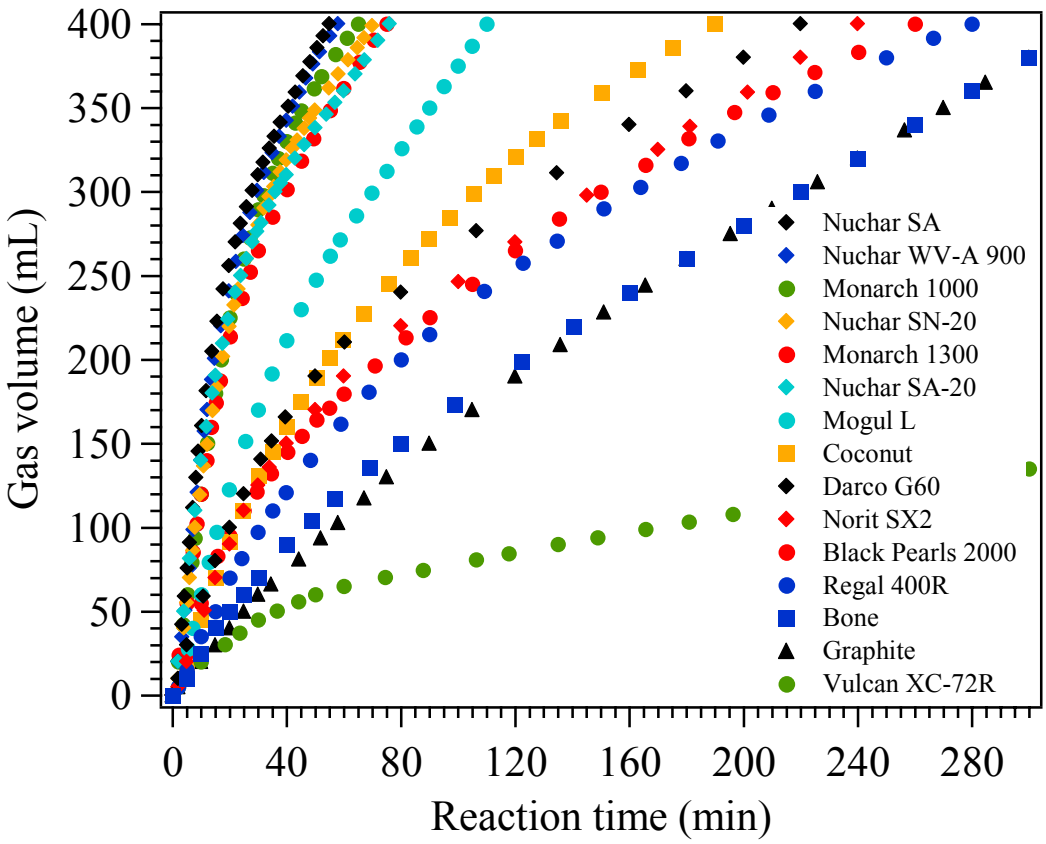

Figure 5.1. Gas evolution from the reduction of nitrobenzene by hydrazine in refluxing *iso*propanol, in the presence of several carbon materials.

The results for nitrobenzene reduction by hydrazine in the presence of different carbons are shown in Figure 5.1, plotted as gas volume evolution vs. time. The gas evolution plots show simple time dependence. In the absence of carbon, no reaction was

observed. The production of gases upon addition of carbons to the reactants demonstrates that the carbons tested catalyze the nitrobenzene reduction by hydrazine with different activities.

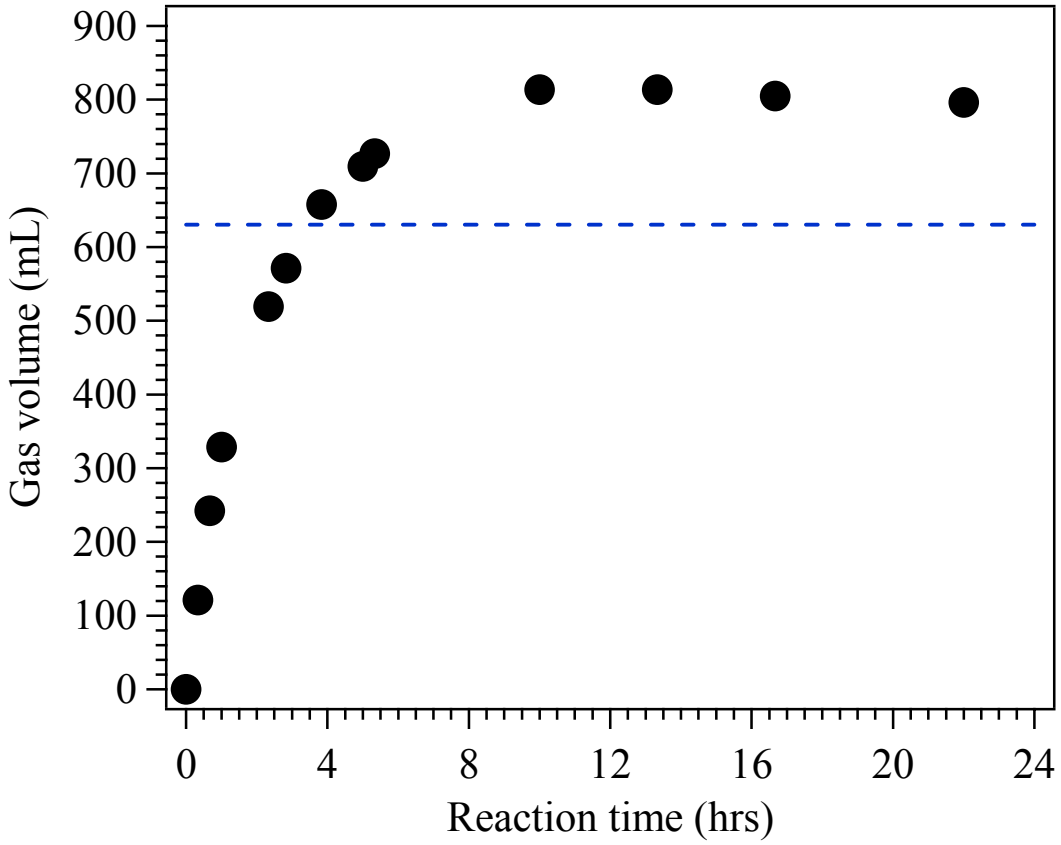

Figure 5.2. Gas evolution from the reduction of nitrobenzene by hydrazine in refluxing *iso*propanol, catalyzed by graphite.

If the overall reaction for the nitrobenzene reduction follows Eq. (2.33), the total nitrogen gas volume expected is about V_C = 630 mL using 0.017 mol of nitrobenzene (see Appendix B). Therefore, based on the amount of gas produced at a given time, we found that Vulcan XC-72R (carbon black) is the least effective catalyst and Nuchar SA (activated carbon) is the most effective catalyst.

Unfortunately, two reactions are occurring simultaneously and this complicates the data analysis of the carbon-catalyzed gas formation. The reactions are given by Eqs. (2.33) and (2.36). For a stoichiometric reaction mixture, we found that certain amount of nitrobenzene is still left in solution, even in the cases where almost the total expected amount of gas is produced. In addition, for some carbons, the observed gas volumes are somewhat larger than the amount of N_2 expected. For example, as shown in Figure 5.2, the amount of gas produced in the presence of graphite was in the order of 800 mL; about 26% higher than the amount of N_2 gas expected.

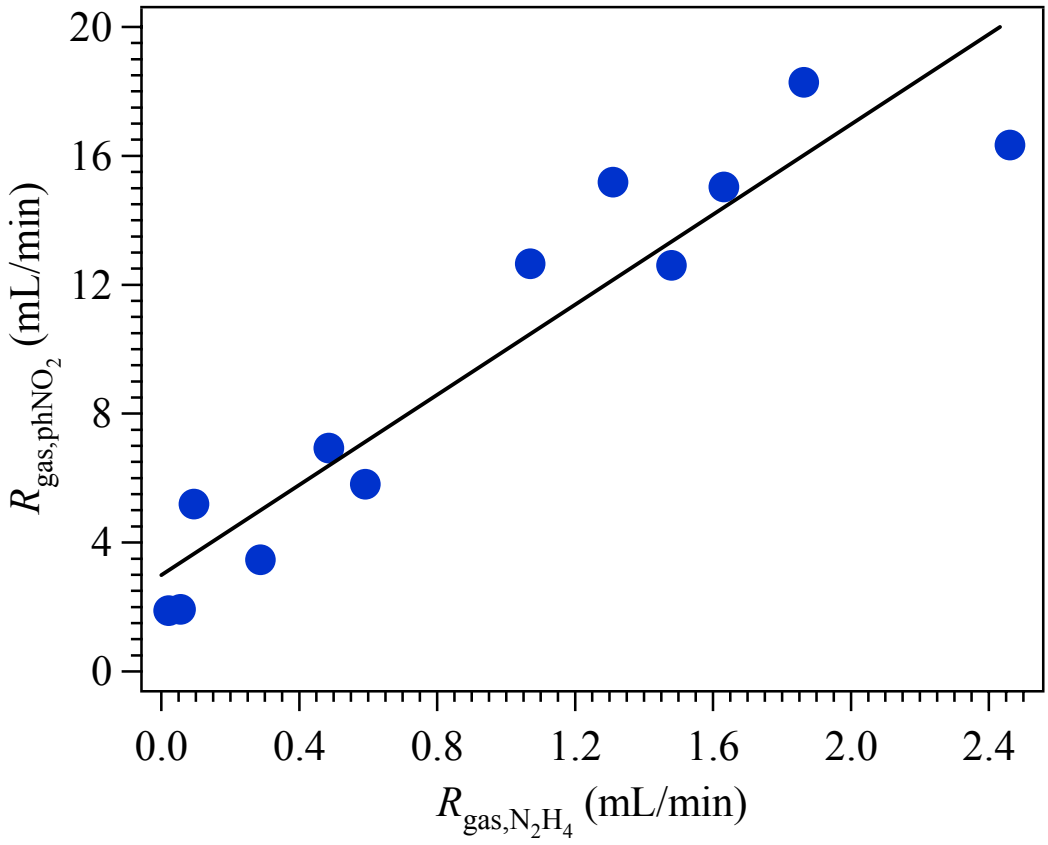

Figure 5.3. Comparison between the initial rates of gas production in the nitrobenzene reduction ($R_{gas,phNO_2}$) and in the hydrazine decomposition (R_{gas,N_2H_4}) reactions on several carbons.

We believe that these effects are due to complications introduced by the carbon-

catalyzed decomposition of hydrazine. However, Figure 5.3 shows that the initial rate of gas production due to hydrazine decomposition is at least 10 times lower than the initial rate of gas production in the nitrobenzene reduction. The data in Figure 5.3 were taken using the same initial amount (0.025 moles) and initial concentration of hydrazine (1 *M*) for both reactions, the hydrazine decomposition and the reduction of nitrobenzene. The hydrazine decomposition may become faster as the two reactions proceed. As explained in the previous chapter and later in this chapter, both the hydrazine decomposition and the reduction of nitrobenzene are surface reactions, where the reactants adsorb competitively on the carbon surface. Since nitrobenzene is first added to the solution of carbon and *iso*propanol, then nitrobenzene molecules are first adsorbed on the carbon surface and promote the reduction reaction at the beginning of the overall reaction. Later in the reaction, nitrobenzene molecules must compete with hydrazine molecules for a limited number of surface sites. If hydrazine molecules adsorb more easily than nitrobenzene molecules on a carbon surface, then the hydrazine decomposition reaction is favorable.

Figure 5.4 shows first-order and second-order plots for the reduction of nitrobenzene on different carbons. The kinetics of the reaction are complex as evidenced by deviations from either first-order or second-order behavior for most of the carbons. This is not surprising for a heterogeneous reaction. Control experiments where nitrobenzene and hydrazine are added together to the reactor showed that this behavior was not due to any progressive deactivation of catalyst by standing with nitrobenzene in *iso*propanol.

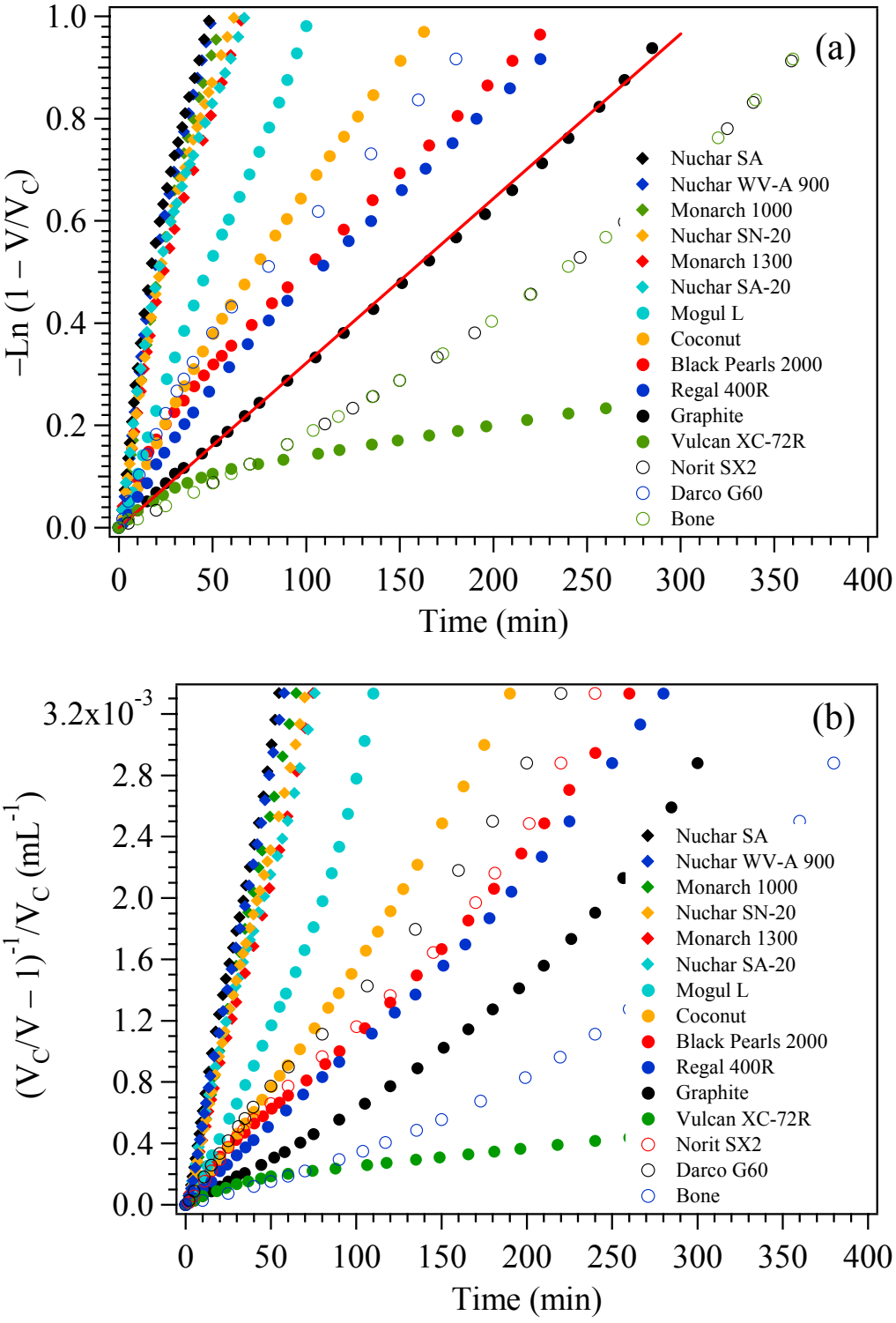

Figure 5.4. First-order (*top*) and second-order (*bottom*) plots for the reduction of nitrobenzene by hydrazine in the presence of various carbon samples.

In any case, we will analyze the kinetics of this reaction using initial rates as determined by initial slopes of the gas evolution plots (see Appendix B). This way we minimize the effect of factors (e.g., interference by products, sintering or poisoning of the catalyst) contributing to the change in the reaction rate other than the changes in concentrations of reactants as the reaction proceeds.

5.2. Effect of impurities

As in the case of the hydrazine decomposition reaction, we performed an experiment to determine the catalytic activity due to the presence of mineral matter in the carbon catalysts. We direct the reader's attention to that section for additional details. In this experiment, no detectable catalytic activity was found when ash was used as a catalyst instead of the carbon. Figure 5.5 shows a plot of the rate of reduction as a function of the ash yield of the carbon catalyst. The lack of a correlation also indicates that mineral matter may play a minor or no role in this reaction. Note that bone charcoal (not shown in Figure 5.5 for clarity) which yields ~83% ash has the same behavior and initial rate (see Figure 5.1) than graphite with ~1.5% ash yield.

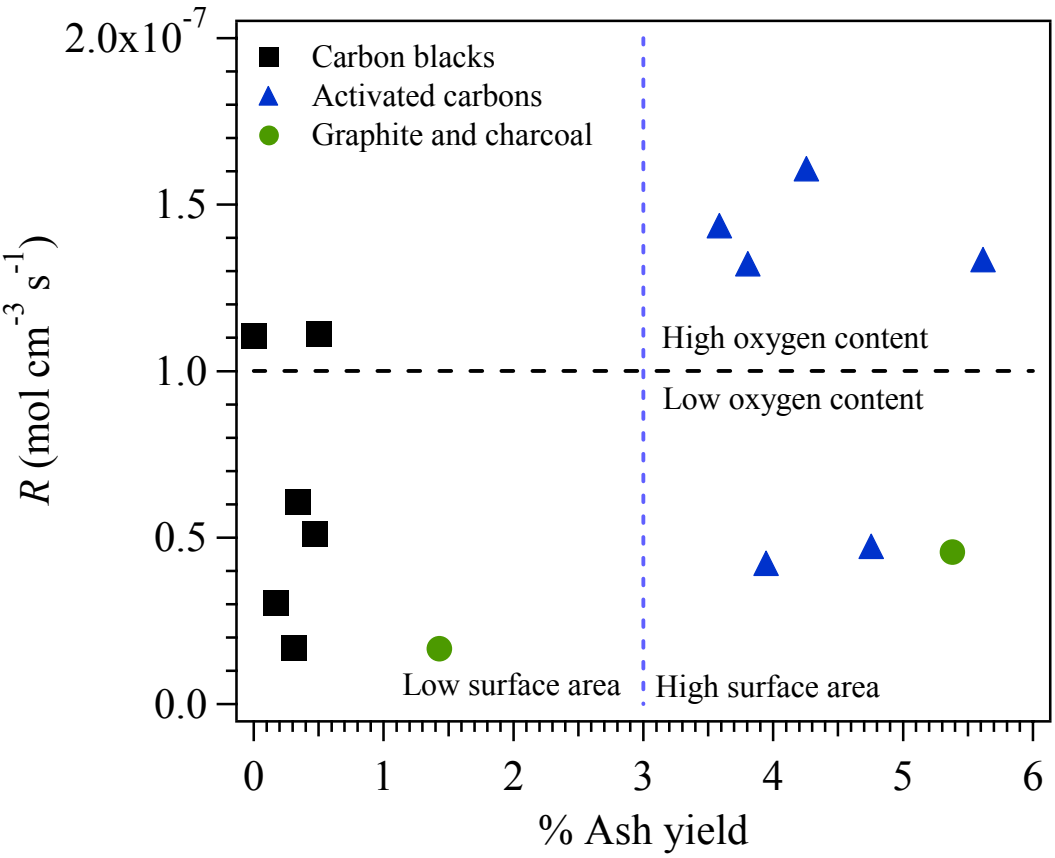

Figure 5.5. Effect of ash yield of carbon catalyst on the rate of nitrobenzene reduction.

5.3. Variation of rate with mass of catalyst and stirring

The initial rate of nitrobenzene reduction as a function of the amount of carbon was found to increase linearly with an increase in the mass of catalyst from 0 to 5 g. The functional dependence shown in Figure 5.6(b) is typical of heterogeneous reactions. The rate of gas production was also found to be independent on the stirring rates as shown in Figure 5.6(a), suggesting that the reaction is NOT mass transport limited.

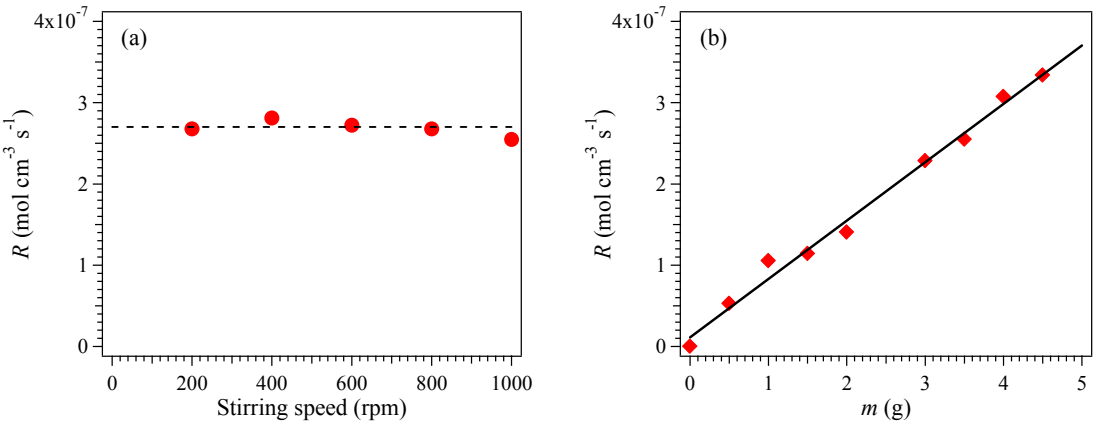

Figure 5.6. Effect of stirring (*left*) and carbon mass (*right*) on the rate of nitrobenzene reduction by hydrazine over coconut charcoal. Solid line is a linear fit of the data and dashed line is a guide to the eye.

5.4. Effect of nitrobenzene concentration

The activity of Black Pearls 2000 (carbon black) and Nuchar SA (activated carbon) was determined for a series of nitrobenzene-hydrazine mixtures ranging from 0.25 to 12 *M* with respect to nitrobenzene at a constant hydrazine concentration of 1 *M*. These data are shown graphically in Figure 5.7. As the nitrobenzene concentration is increased the rate first increases, then passes through a maximum, and finally decreases. The explanation of the fall off in the rate at high concentrations is that one reactant displaces the other from the surface as its concentration is increased. The maximum rate corresponds to the existence of the optimum number of hydrazine and nitrobenzene molecules on the carbon surface.

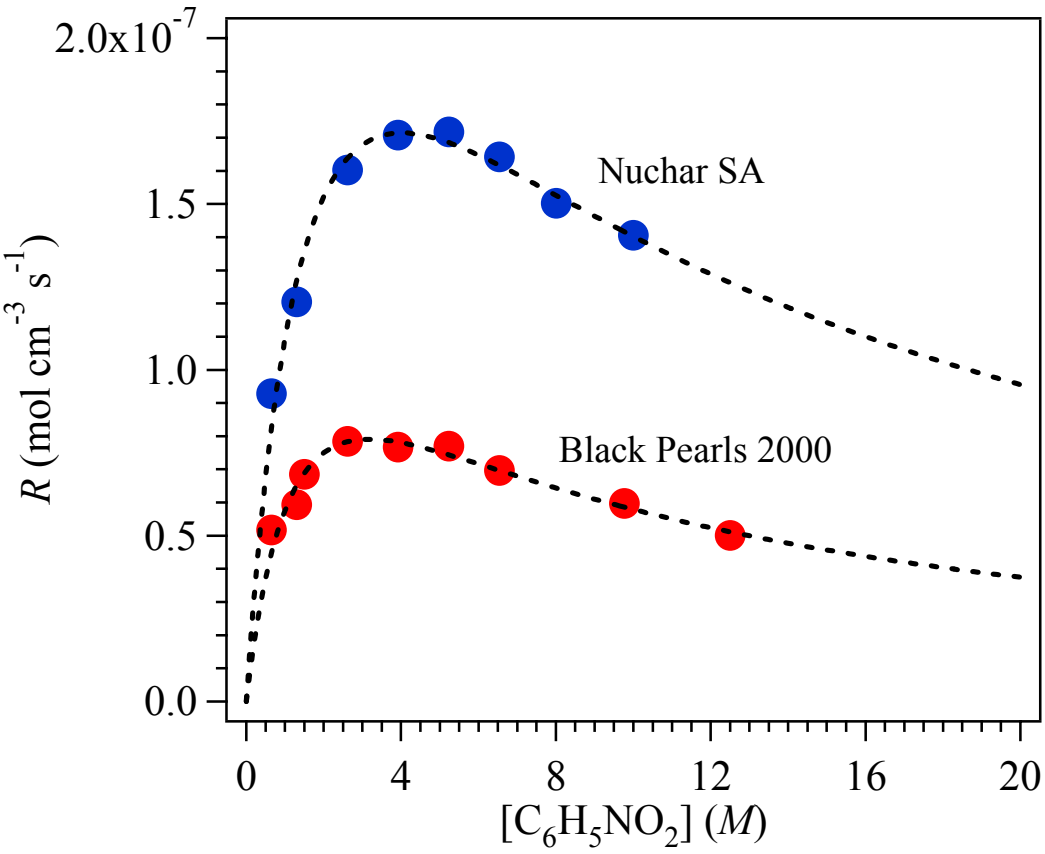

Figure 5.7. Effect of nitrobenzene concentration on the rate of reduction over Black Pearls 2000 (carbon black) and Nuchar SA (activated carbon). Dashed lines are fit of the data to Eq. (2.26).

The relationship of the rate of reaction to concentration as shown in Figure 5.7 is commonly found in heterogeneous reactions when the rate-controlling step is the reaction between two adsorbed molecules, according to a Langmuir-Hinshelwood mechanism (see Figure 2.3(a)).[21] Dashed lines in Figure 5.7 represent fits of the data to the corresponding rate law equation for a Langmuir-Hinshelwood mechanism, Eq. (2.26). As can be seen, excellent fits of the data can be obtained with the use of this equation. The best fit parameters are shown in Table 5–1. Note that the equilibrium adsorption-desorption constants for hydrazine (K_a) and nitrobenzene (K_b) are approximately equal for a particular carbon.

Table 5–1. Best fit parameter values achieved with Eq. (2.26)

Carbon	$k\times10^{6}$ (mol cm^{-3} s^{-1})	$K_a\times10^{-3}$ (mol cm^{-3})	$K_b\times10^{-3}$ (mol cm^{-3})
Nuchar SA	2.76	0.331	0.330
Black Pearls 2000	1.09	0.444	0.411

The observed kinetics of the nitrobenzene reduction by hydrazine in liquid solutions over carbon catalysts may therefore be explained by assuming that the slow step is the reaction between two adsorbed molecules on the carbon surface.

Our kinetic results for the reduction of nitrobenzene may also be explained by quite a different mechanism: the electrochemical mechanism. Catalysis occurs by the electrochemical mechanism if both couples are electrochemically reversible on the catalyst or, should one or even both couples be electrochemically irreversible, if the difference in their Nernst potentials is sufficiently large.[196] The electrochemical oxidation of hydrazine on carbon electrodes is an irreversible 4-electron process (to N_2) in aqueous solutions[209] and methanolic solutions[210] but a reversible 2-electron process (to N_2H_2) in acetronitrile solutions.[205,210] The difference seems to come from the presence or absence of polarized oxygen-containing groups in the electrolyte solution, which can affect the stability of diimide and other intermediates.[206] The electrochemical reduction of nitrobenzene on carbon electrodes is a reversible 4-electron process to phenylhydroxylamine in basic aqueous, alcoholic or mixed aqueous-organic media.[211,212] Phenylhydroxylamine was identified by NMR during the chemical reduction of nitrobenzene by hydrazine over carbon catalysts.[1] Unfortunately, not enough electrochemical data are available on carbon electrodes for a qualitative test of the

electrochemical mechanism.

Larsen *et al.*[1] concluded that a strong evidence for the applicability electrochemical mechanism to the carbon-catalyzed reduction of nitrobenzene by hydrazine was the observation of an electrical potential in an emf cell, where a carbon electrode was immersed in a solution of hydrazine and an identical carbon electrode was immersed in a solution of nitrobenzene. The presence of *this* voltage is irrelevant for a test of the electrochemical mechanism. First, the catalytic potential taken up by a carbon catalyst in the presence of *both couples* (hydrazine-nitrogen and nitrobenzene-phenylhydroxylamine) should be equal to the electrochemically-determined mixture potential at equal anodic and cathodic currents, in order for an electrochemical mechanism to be applicable to a redox reaction.[213] Second, a catalytic potential in the presence of *only* either hydrazine or nitrobenzene can be due to many factors, the most promising candidate being the adsorption of these compounds on the carbon surface.

Adsorption on a metal surface is always accompanied by a change in the distribution of the local electronic states on the substrate atoms.[214] Changes can also occur in the atomic arrangement and—from the thermodynamic viewpoint—in the surface energy. The nature and magnitude of the surface redistribution of electrons are largely dependent on the electronegativity of the adsorbed species and of the metal atoms, but also on the surface symmetry and the shape of the orbitals involved. It is also easy to imagine that when a foreign atom or molecule is adsorbed, the electron density around it will be modified and this will lead to the appearance of an electric dipole. Thus, an electric field is induced on the metal due to the distribution of electric charges near the metal surface as well as the creation of random electric dipoles upon adsorption. One

should expect that chemisorption of hydrazine molecules will have a stronger effect than the physisorption of nitrobenzene on the carbon surface. Indeed, the potential difference between both carbon electrodes was reported to drop steadily to a constant potential in a time period comparable to that required for the complete decomposition of hydrazine over the carbon electrode.[1]

Further evidence for our interpretation on the origin of the potential measured by Larsen *et al*.[1] is provided by the investigations of the noncurrent potentials (with respect to a reference electrode) in hydrazine solutions on several metal electrodes.[215-218] The potential of a metal electrode was usually found to be more positive than the standard potential of reaction in Eq. (2.35), and dependent upon the nature of the metal, the condition of the surface, and the electrode rotation.[218] The noncurrent potential was also found to be more positive than the standard potential of water electrolysis reaction

$$2H_2O + 2e^- \rightarrow H_2 + 2OH^- \quad E° = -0.828\,V \qquad (5.1)$$

so it is very unlikely that the potential of the electrode represents a mixture potential of reactions in Eqs. (2.35) and (5.1). It was concluded that the potential of an electrode in hydrazine solution without current is determined by adsorption processes, and the magnitude of this potential depends on the polarity of the bonds between the dissociative chemisorption products and the surface.[218]

The fact that an alternative explanation exits for previous results of Larsen *et al*. does not mean that the original conclusion from those authors was wrong, but that it was not the only possibility.

5.5. Dependence of catalytic reduction on carbon properties

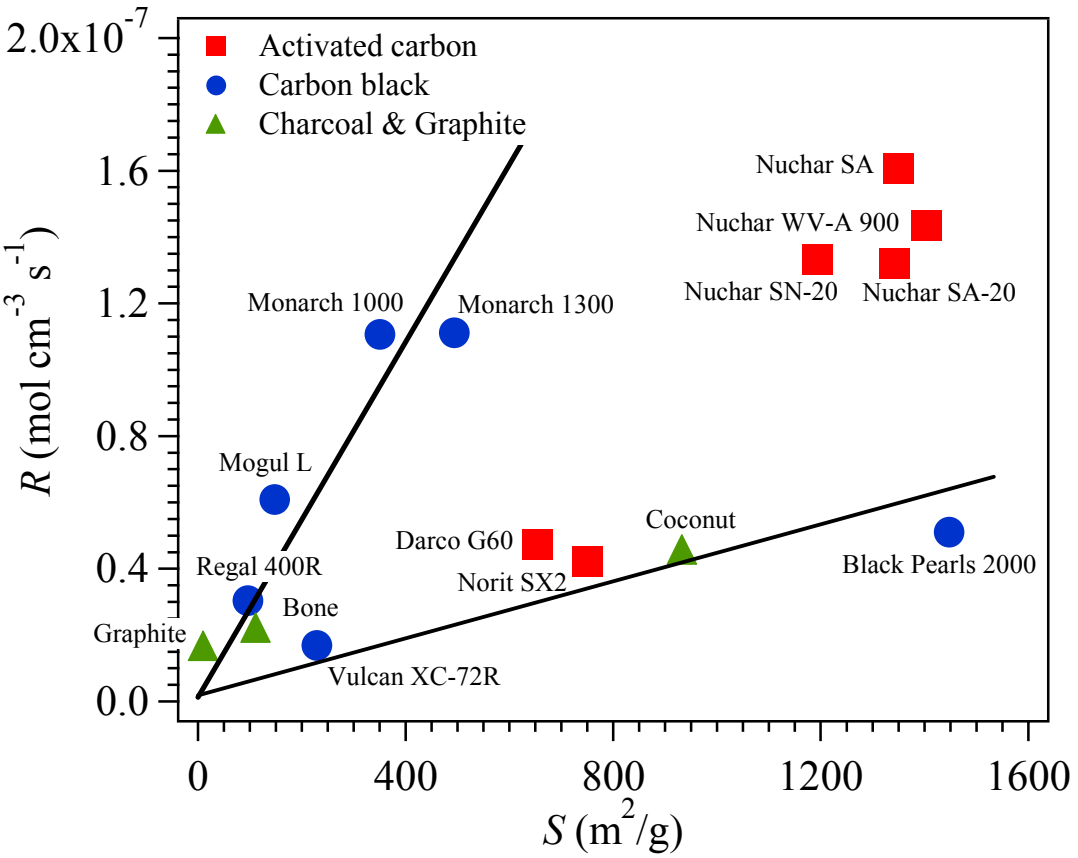

Figure 5.8. Influence of surface area of various carbons on the rate of nitrobenzene reduction. Solid lines indicate the trend of the data.

The observed catalytic activity for the reduction of nitrobenzene by hydrazine as a function of the surface area of the carbon catalyst is shown in Figure 5.8. Despite the scatter in the data, the trend in this figure suggests that the nitrobenzene reduction rate increases with the surface area. At first glance, this is in agreement with the generalized hypothesis that higher surface area carbons contain a relatively higher concentration of active sites for the carbon-catalyzed reaction. The typical active sites for carbon-catalyzed reactions are basal planes of the graphitic crystallites of carbons, edge sites,

surface functional groups, etc. [2-11]

We notice in Figure 5.8 a clear separation between the trends observed for neutral and basic carbons and acidic carbon blacks. A series of acidic activated carbons is grouped together in the higher surface area and higher initial rate region. The fact that the data for basic carbons fall on the same linear curve suggests that carbon structure plays no dominant role in the catalysis. These observations also indicate that surface area is not the only factor which determines the initial rate of the reaction. Aggarwal *et al*.[24] also found that nitrobenzene adsorption depends upon surface area but there is no direct relationship between the maximum amounts of nitrobenzene adsorbed and the surface area of carbon, and concluded that surface area is not the only factor which determines the adsorption of nitrobenzene.

The data in Figure 5.8 also indicate that the rate of the reaction is enhanced by the presence of surface groups with a much stronger acid character. For instance, the reaction rate is increased by ~ 370% for a pH change of ~1.5 in the acidic range. We already discussed the effect of surface acidity on the adsorption of hydrazine. The adsorption equilibrium for nitrobenzene on carbons is also dependent, to a large extent, on the chemistry of the carbon surface.[23,24] Heterogeneous oxygen groups have been reported in the literature to play an important role in the process. Aggarwal *et al*.[24] reported that nitrobenzene adsorption on activated carbons increased on degassing but decreased on oxidation. The maximum adsorption in case of a sample degassed at 600ºC and a subsequent decrease at higher degassing temperature was explained on the basis of the existence of two types of carbon-oxygen surface structures.[199] The carbon sample degassed at 600ºC is devoid of a larger portion of its CO_2-yielding complexes (carboxylic

acid or lactonic groups) but still retains a large proportion of its CO-yielding complexes (quinonic groups), while a carbon sample degassed at 1000ºC is almost free of any of these surface complexes. It thus appears that the presence of acidic CO_2-yielding complexes tends to suppress the adsorption, while emergence of CO-yielding complexes as the dominating oxygen complex enhances its adsorption capacity for nitrobenzene. Following the idea of Aggarwal *et al*., we propose that two different types of acidic groups, one in carbon blacks and another in activated carbons, are responsible for the behavior observed between these two groups of carbons in Figure 5.8.

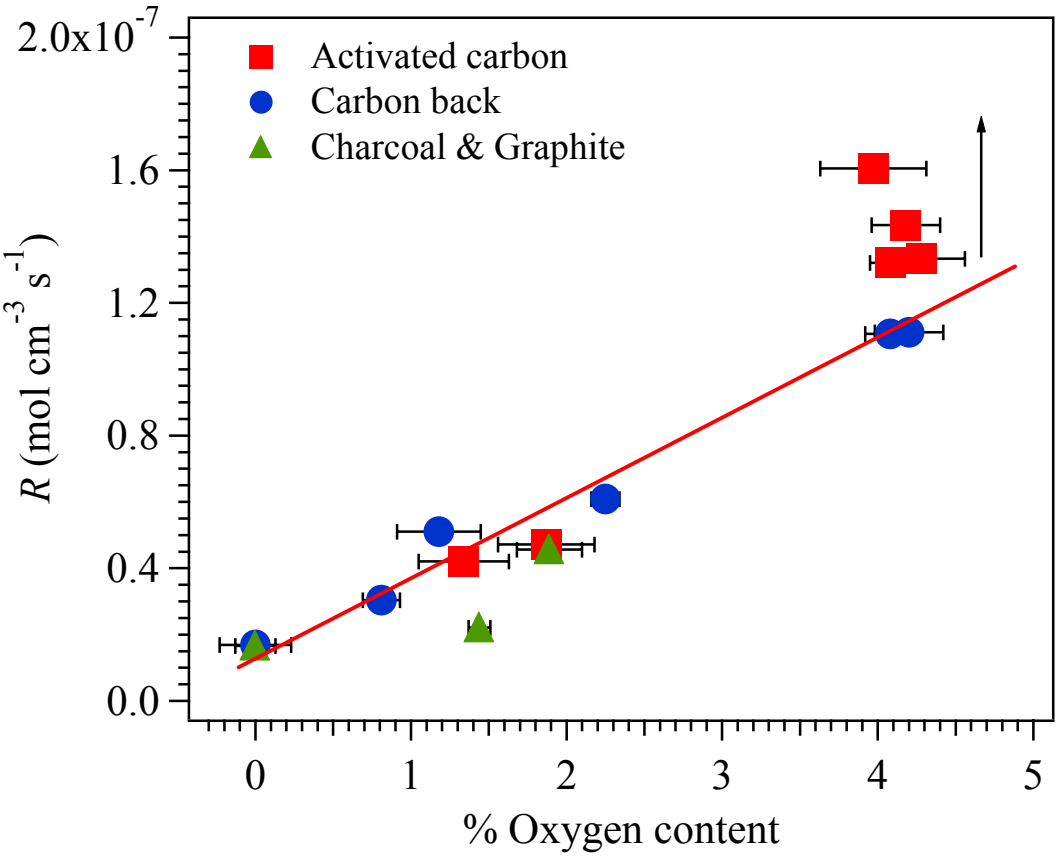

Figure 5.9. Influence of oxygen concentration of various carbon catalysts on the rate of nitrobenzene reduction. Solid line indicates the trend of the data.

Figure 5.9 shows the effect of oxygen concentration on the rate of nitrobenzene reduction. The results demonstrate that the rate of nitrobenzene reduction increases with increasing total oxygen content of the catalyzing carbon. Because the total oxygen content is plotted, no information is available about the relative importance of different oxygen functional groups. The fact that the reaction rate differs considerably for activated carbons with similar oxygen contents indicates that not all of the oxygen functional groups are equally important to this reaction. It is possible that the concentration of acidic CO-yielding complexes increases in these activated carbons without a significant change of the total oxygen content.

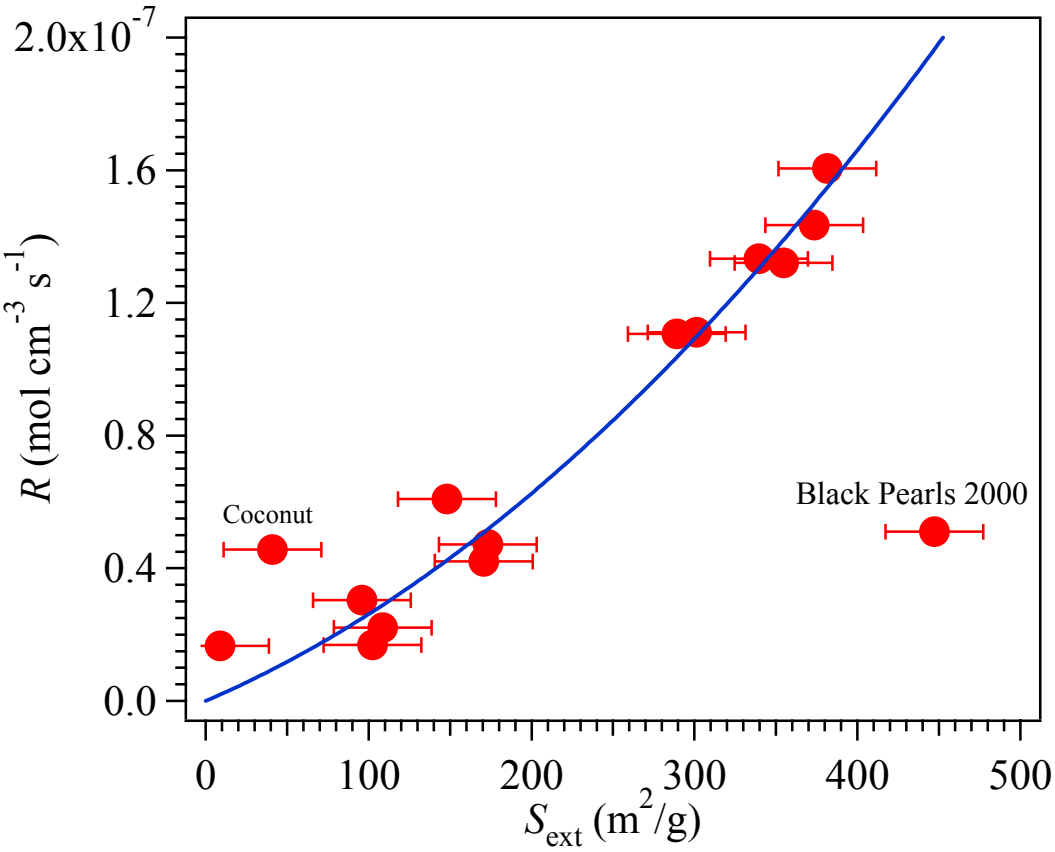

Figure 5.10. Influence of the external surface area of various carbons on the rate of nitrobenzene reduction. Solid line indicates the trend of the data.

It is tempting to suggest that due to the relatively high accessibility of the carbon blacks and ground graphite surfaces (little intraparticle microposity), the whole of their surfaces can be wetted and available for reaction. If this hypothesis is extended to include the activated carbon surfaces and carbon blacks (with high BET surface areas), then it implies that only part of their surface area is available for reaction involving a large molecule such as nitrobenzene and small pores. This hypothesis is reasonable, since most of this surface area is internal microposity. Figure 5.10 displays the initial rate as a function of the external surface area of the carbon catalyst with wide variation in surface area ranging from ~ 10 to 500 m^2/g. It is seen that the initial reaction rate and the external surface area are almost directly proportional, except for a few data points. A relationship of this type is usually observed when the reaction is controlled by external diffusion of the reactants. However, more effective agitation of the solution around the solid catalysts is expected to markedly increase external diffusion rates; an effect not seen in Figure 4.5(a). The catalytic rate is also proportional to the external surface area of the catalyst when a narrow pore structure limits the reaction rate and the reaction is in the pore (or internal) diffusion regime, which is little influenced by stirring.[20] In this case, if the reactant diffuses slowly but reacts rapidly, conversion to product will occur near the pore entrances and the interior of the pores will play no role in the catalysis. It is possible that the nitrobenzene reduction reaction is, in part, limited by pore diffusion. Further tests are needed to prove this hypothesis.

The pore volume per unit mass (V_p) (a measure of the particle porosity) is also a parameter which is important and is implicitly contained in relations of the rate of pore diffusion.[20] When the reaction rate is controlled by pore diffusion, it is either directly

proportional or proportional to the square root of the pore volume. However, Figure 5.11 shows the initial rate of the nitrobenzene reduction increases in a superlinear fashion with the pore volume of the catalyzing carbon, except for a few carbons.

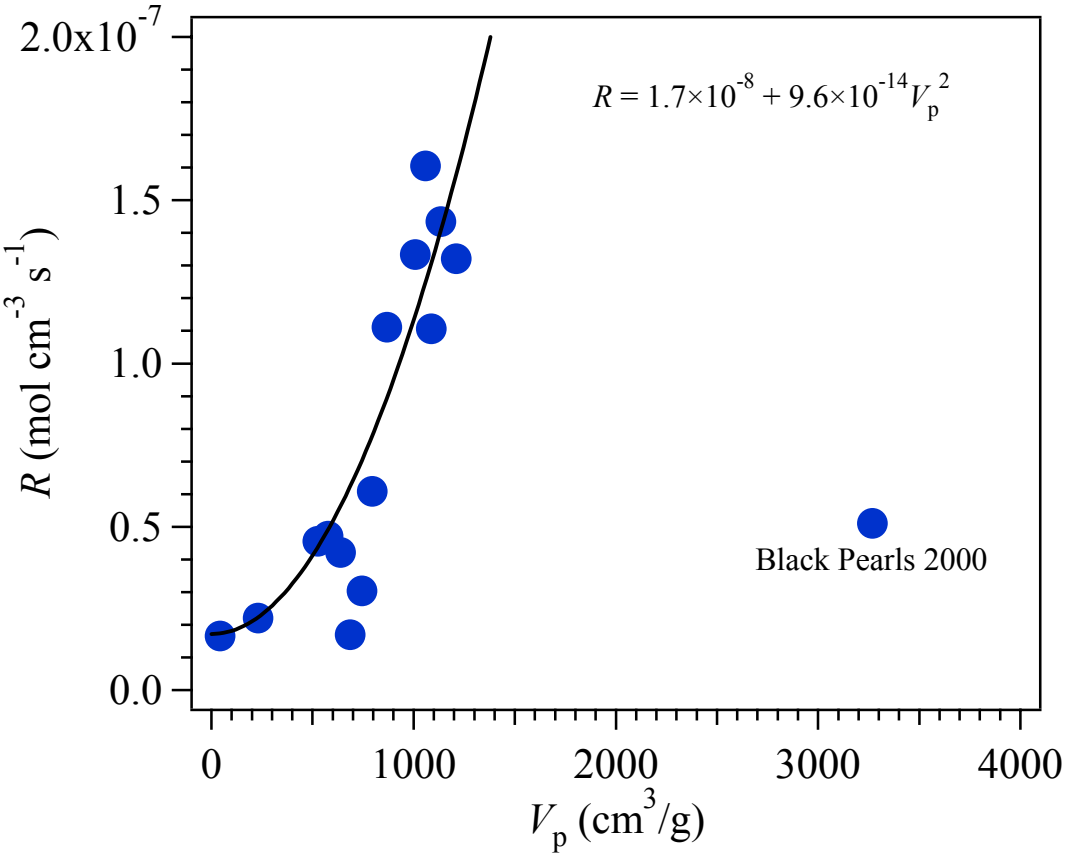

Figure 5.11. Effect of pore volume of various carbons on the initial rate of nitrobenzene reduction. Solid line is a fit of the data to a power law function.

Chapter 6.

Summary and Conclusions

The kinetics of the nitrobenzene reduction to aniline by hydrazine and the decomposition of hydrazine over carbons in refluxing *iso*propyl alcohol solutions were investigated. The results presented in this thesis confirm previous results[1,12] that carbons catalyze both reactions, although with different activities. Both reactions exhibited well-known behaviors for heterogeneous catalysis.

The kinetics of the hydrazine decomposition over carbons exhibited a change of reaction order from first order at low concentrations of hydrazine to zero order at high concentrations. The observed kinetics may be explained using the Langmuir adsorption isotherm to derive the overall rate equation on the assumption that the nondissociative chemisorption of hydrazine is the slow step in the reaction mechanism. A reaction is then postulated to occur where an adsorbed hydrazine molecule reacts with a hydrazine molecule in the liquid phase to form two molecules of ammonia and an adsorbed *cis*-diimide (N_2H_2) on the carbon surface. The overall reaction then proceeds with the reaction between neighboring diimide molecules on the carbon surface, forming nitrogen that then desorbs and one hydrazine molecule which remains adsorbed on the carbon surface. This is the same catalytic mechanism proposed for metals such as iridium and rhodium.

The kinetics of the nitrobenzene reduction to aniline by hydrazine exhibited a pronounced order change from a fractional positive value at low nitrobenzene concentrations to a fractional negative order at high nitrobenzene concentrations. The observed kinetics may be explained by assuming that the slow step is a Langmuir-

Hinshelwood type reaction where an adsorbed nitrobenzene molecule reacts with an adsorbed hydrazine molecule to yield phenylhydroxylamine. Our kinetic results do not allow us to differentiate between catalytic processes where molecules adsorbed either side by side or at distant sites. In the latter case, the electron transfer is expected to occur through the carbon solid.

Both the hydrazine decomposition reaction and the nitrobenzene reduction by hydrazine may be surface-controlled reactions. This conclusion is based on the aforementioned variation of the reaction order with reactant concentrations, the lack of dependence of the reaction rates with stirring and the proportionality between the reaction rates and the catalyst mass. All these behaviors are characteristics of surface-controlled reactions. The nitrobenzene reduction reaction may be, in part, controlled by pore diffusion as determined by the almost linear relationship between the reaction rates and the external surface area and pore volume of the carbon catalysts. Further studies are needed to determine the validity of this assumption.

Comparison of the physicochemical properties of the carbon catalysts and kinetic studies showed that the structure and the nature of the carbon surface play a role in the catalysis. For instance, the reaction rate increased linearly with the surface area of carbon blacks, non-activated charcoals, graphite and weakly basic activated carbons. Both reactions are enhanced by the presence of acidic surface groups on the carbon surface. The effect of acidic surface groups on the reactants' adsorption can be understood by assuming that hydrazine molecules are adsorbed by interactions between their lone electron pairs with partially unfilled π bands of the carbon surface. The π electrons of the basal planes are attracted and localized by the acidic surface groups in the carbon edges.

The effect of oxygen surface groups is further evidenced by the linear relationship between the oxygen content of carbons and the reaction rates at low oxygen content. Acidic activated carbons are an exception to this trend due to changes in the relative concentration of the relevant oxygen surface groups for constant total oxygen contents.

Our hypothesis that carbon catalyzes both nitrobenzene reduction by hydrazine and hydrazine decomposition reactions in the same way that metals do appears to have been supported by our kinetic studies. However, more work needs to be done to account for possible factors influencing the results, such as the production of extra gases during the reactions.

Chapter 7.

Future Work

We have postulated a mechanism for hydrazine decomposition where both nitrogen atoms in the nitrogen molecule produced come from the same N_2H_4 molecule. It is thus of interest to check a possible redistribution of nitrogen atoms by using ^{15}N label and, more precisely, by studying the hydrazine decomposition reaction of equimolar mixtures of nitrogen-15 labeled hydrazine ($H_2{}^{15}N\text{-}{}^{15}NH_2$) and normal hydrazine ($H_2{}^{14}N\text{-}{}^{14}NH_2$). Mass spectrometric analysis (for mass numbers 28, 29 and 30) of the nitrogen gas resulting from this reaction can be used to determine whether randomization of molecular nitrogen (i.e., $^{15}N\text{-}{}^{15}N$ and $^{14}N\text{-}{}^{14}N$ do not exchange) does occur in the nitrogen product. For example, if there is no randomization at all the decomposition of an equimolar mixture of $H_2{}^{15}N\text{-}{}^{15}NH_2$ and $H_2{}^{14}N\text{-}{}^{14}NH_2$ should give an equimolar mixture of $^{14}N_2$ and $^{15}N_2$, whereas a complete randomization should lead to the following distribution:

$[^{14}N_2] = 25\%$;

$[^{15}N_2] = 25\%$;

$[^{14}N^{15}N] = 50\%$.

Previous ^{15}N-labeled hydrazine decomposition investigations reveal a lack of scrambling in some cases, namely, on supported rhodium[187] and supported iridium[185] in the liquid phase, on supported iron in the gas phase,[219] and even in thermal decomposition in a quartz or glass vessel.[220] Conversely, scrambling was observed during hydrazine oxidation over several electrocatalysts.[187,221,222] The only experiments found in the literature on ^{15}N-labeled hydrazine decomposition in the liquid phase[185,187] were performed over catalyst in the form of pellets and without stirring of the hydrazine

solution. Besides, the authors used a small sample (1 mole) of ^{15}N enriched hydrazine in the presence of a large excess of normal hydrazine (65.3 or 122.3 moles). These observations suggest that these experiments may have not been done properly. Unfortunately, ^{15}N enriched hydrazine is very expensive.

As mentioned before, our results on the nitrobenzene reduction by hydrazine can also be explained by an electrochemical mechanism. It was suggested that here the carbon catalyst acts as an electron conductor. It accepts electrons from adsorbed hydrazine and donates them to adsorbed nitrobenzene and its reduced intermediates. One or more tests should be applied to check that the catalysis does indeed proceed by electrochemical mechanism. The experimental tests of the electrochemical model are provided by a combination of kinetic and electrochemical experiments:

(a) Comparison of the observed kinetics (with respect to reaction rate and reaction orders) of heterogeneous catalysis with that predicted from independent current-voltage curves of the two redox couples individually at the same carbon surface. Moreover, judicious changes in the experimental conditions should alter the rate equations in a predictable way.[213]

(b) Comparison of the observed potential taken up by the carbon catalyst during heterogeneous catalysis with the electrochemically determined mixture potential at equal anodic and cathodic currents.[213]

(c) Carrying out a specially designed experiment in which the two reactants are in contact with the carbon catalyst but are separated from each other.[223,224] If reaction still takes place under these circumstances, it must do so via electron transfer through the carbon catalyst.

(d) Imposing upon the catalyst a potential equal to the equilibrium potential of one of the redox couples. This will stop the overall reaction.

(e) Measurement of the steady-state potential of the catalyst and of its polarization characteristics in the reaction mixture.

Many of the factors involved in the mechanisms proposed here are general to all carbon-catalyzed reactions and so will be broadly useful. The effect of the carbon surface functionality on the reactions remains to be explored. Three approaches are proposed. We have already observed that the rate of the reactions studied here increases as the oxygen content of the carbon catalyst increases. Standard Fourier transform infrared spectroscopy (FTIR) can be used to identify the oxygen functional groups present in the carbon catalysts to correlate them with catalytic ability, but it provides relatively little quantitative information. The technique has already been applied to carbon blacks.[225,226] X-ray photoelectron spectroscopy (XPS) can be used to determine the concentration of surface oxygen functionality for several of the most effective carbon catalysts. XPS is ideal for this use because it is a surface-sensitive technique that yields functional group populations and has already been applied to coals and chars, so its application to commercial carbons does not involve any technique development.[227] Surface oxides of carbons can be identified by their reaction (or failure to react) with bases and acids of different strengths. The procedure has been described and discussed earlier.[157] From this work it would be possible to tailor the carbon surface to achieve maximum catalysis.

It would be interesting to evaluate the prospects for producing premium carbon catalysts from commercial carbon precursors. This requires the study of the catalytic activity of, for example, anthracitic coals. This represents new markets, which in turn,

provides additional sales opportunities for coals. Anthracites have the highest electrical conductivity of any rank of coal; as the structure approaches that of graphite via heat-treatment, conductivity should also approach that of graphite. The heat-treating of anthracitic coals to various degrees to produce a sequence of samples ranging from the native anthracite to a nearly graphitic carbon provides a suite of samples in which conductivity will vary over several orders of magnitude.

If anthracites are able to catalyze these reactions, it would raise the possibility of using anthracite coal waste (culm) to develop catalysts for the reduction of nitroaromatics. This development would simultaneously represent a potential new market for this carbonaceous material and a means of removing culm from the environment. The low-coal-content waste material that remains after mining for anthracite coal is an extremely low cost feedstock. In fact, it may be possible to obtain credit via the Department of Environmental Protection for "remining" this material and getting it out of the environment. This waste causes air and water pollution problems, danger from waste pile fires, and is an aesthetic blight on the landscape. Currently, there are at least 800 million, and possibly billions, of tons of culm within the anthracite region of Pennsylvania. Such a project could look at converting anthracite waste in Pennsylvania into high-quality, environmentally friendly catalysts for an environmentally relevant reaction: the reduction of nitroaromatics.

Diesel engines are major contributors to the emission of toxic substances into the atmosphere.[228] These toxic substances are a vital concern nationwide due to human health and environmental effects.[229] For example, nitroaromatic compounds such as nitronaphthalenes—major components of diesel exhaust emissions—are potent mutagens

and carcinogens for humans.[230,231] Reductive transformation of nitroaromatic compounds into their corresponding aromatic amines could play a major role in the detoxification process of diesel exhaust emissions. Thus, such a project would aim to address the following environmental concerns:

(a) Removal of culm banks that have accumulated as a result of coal mining.

(b) Detoxification process of diesel exhaust emissions.

(c) Development of environmentally friendly catalysts.

The first concern would be addressed by showing experimentally that anthracite waste can be used as a catalyst in the reaction of nitroaromatic compounds with hydrazine. The demonstrated reduction of large nitroaromatic compounds, typical of diesel exhaust, would address the second concern. This represents an extension of our present work, which so far has looked only at nitrobenzene reduction. The third concern is being addressed by the general theme of this work, which is to replace expensive catalysts containing heavy metals with the much less expensive and safer carbon.

Unfortunately, due to the differences in the reaction conditions employed (i.e., temperature, initial concentrations, etc.), we cannot compare the reaction rates obtained in this study with those in previous studies on metal catalysts. It would be interesting to perform a systematic study on the performance of carbons compared to typical metal catalysts.

Even though, we are confident that mineral matter has a minor or none effect on the catalytic properties of the carbon used in this study, a comprehensive and more systematic study is needed on this issue. For instance, mineral matter content of the carbon can be reduced or eliminated by washing the carbon with HCl and HF to remove

trace metal impurities.

References

[1] J. W. Larsen, M. Freund, K. Y. Kim, M. Sidovar, and J. L. Stuart, "Mechanism of the carbon catalyzed reduction of nitrobenzene by hydrazine." Carbon **38** (5), 655 (2000).

[2] D. E. Weiss, "The catalytic properties of amorphous carbons." Proceedings of the 5th Conference on Carbon **1**, 65 (1962).

[3] J. W. Hassler, *Activated carbon*. (Chemical Publishing Co., New York, 1963).

[4] R. W. Coughlin, "Carbon as adsorbent and catalyst." Industrial & Engineering Chemistry, Product Research and Development **8** (1), 12 (1969).

[5] R. W. Coughlin, "Predicting the activity of carbon catalysts." Proceedings on the 4th International Congress on Catalysis **2**, 322 (1971).

[6] D. L. Trimm, in *Catalysis* (Royal Chemical Society, London, 1981), Vol. 4, Chap. 8.

[7] V. S. Tripathi and P. K. Ramachandran, "Carbon as catalyst." Defence Science Journal **35** (1), 115 (1985).

[8] H. Juntgen and H. Kuhl, in *Chemistry and Physics of Carbon*, edited by P. A. Thrower (Marcel Dekker, New York, 1989), Vol. 22, Chap. 2.

[9] K. C. Kalra, P. Katyal, and K. C. Singh, "Catalytic reactions of carbons." Journal of Scientific and Industrial Research **48** (4), 186 (1989).

[10] M. Spiro, "Catalysis by carbons of reactions in solution." Catalysis Today **7** (2), 167 (1990).

[11] L. R. Radovic and F. Rodriguez-Reinoso, in *Chemistry and Physics of Carbon*, edited by P. A. Thrower (Marcel Dekker, New York, 1997), Vol. 25, 243.

[12] J. W. Larsen, J. Jandzinski, M. Sidovar, and J. L. Stuart, "Carbon-catalyzed decompositions of hydrazine and hydroxylamine." Carbon **39** (3), 473 (2001).

[13] J. M. Austin, T. Groenewald, and M. Spiro, "Heterogeneous catalysis in solution. Part 18. The catalysis by carbons of oxidation-reduction reactions." Journal of the Chemical Society: Dalton Transactions (6), 854 (1980).

[14] Anonymous, "Carbon black: chemical profile." Chemical Market Reporter **261** (25), 35 (June 24, 2002).

[15] N. P. Cheremisinoff, *Handbook of industrial toxicology and hazardous materials*. (Marcel Dekker, New York, 1999).

[16] C. L. Mantell, *Carbon and graphite handbook*. (Interscience Publishers, New York, 1968).

[17] M. Pourbaix, *Atlas of electrochemical equilibria in aqueous solutions*. (Pergamon Press, New York, 1966).

[18] J. I. Kroschwitz, *Kirk-Othmer concise encyclopedia of chemical technology*, 4th ed. (Wiley, New York, 1999).

[19] S. J. Thomson and G. C. Webb, *Heterogeneous catalysis*. (John Wiley & Sons, Inc., New York, 1968).

[20] M. Spiro, in *Comprehensive chemical kinetics*, edited by R. G. Compton (Elsevier, New York, 1989), Vol. 28, Chap. 2.

[21] K. J. Laidler, *Chemical kinetics*, 3rd ed. (Harper & Row, New York, 1987).

[22] J. M. Thomas and William John Thomas, *Introduction to the principles of heterogeneous catalysis*. (Academic Press, New York, 1967).

[23] R. W. Coughlin and F. S. Ezra, "Role of surface acidity in the adsorption of organic pollutants on the surface of carbon." Environmental Science and Technology **2** (4), 291 (1968).

[24] P. Aggarwal, J. C. Kapoor, S. K. Kapoor, A. K. Bhalla, and R. C. Bansal, "Adsorption of nitrobenzene on activated carbon from dilute aqueous solutions." Indian Journal of Chemical Technology **3** (4), 187 (1996).

[25] J. M. Thomas and W. J. Thomas, *Principles and practice of heterogeneous catalysis*. (VCH, New York, 1997).

[26] P. H. Given and L. W. Hill, "Catalysis of the isomerization and polymerization of olefins on carbon blacks." Carbon **6** (4), 525 (1968).

[27] L. W. Hill, V. K. Acharya, and W. E. Wallace, Jr., "Carbon black catalyzed olefin isomerizations." Carbon **9** (2), 219 (1971).

[28] J. A. Meier and L. W. Hill, "Carbon black catalyzed olefin isomerization. I. Heterogeneous site model based on rate dependence on catalyst concentration." Journal of Catalysis **32** (1), 80 (1974).

[29] T. W. J. Taylor and E. M. W. Lavington, "The heterogeneous catalysis of stereoisomeric change in oximes." Journal of the Chemical Society, 980 (1934).

[30] T. W. J. Taylor and Sally Marks, "The conversion of alpha-benzil monoxime into the beta-oxime by animal charcoal." Nature **125**, 636 (1930).

[31] R. E. Pincock, W. M. Johnson, and J. Haywood-Farmer, "Carbon catalyzed organic reactions: racemization of 1,1'-binaphthyl by carbon surfaces." Canadian Journal of Chemistry **54** (4), 548 (1976).

[32] R. E. Pincock, W. M. Johnson, K. R. Wilson, and J. Haywood-Farmer, "Carbon catalyzed racemization of 1,1'-binaphthyl." Journal of the American Chemical Society **95** (19), 6477 (1973).

[33] L. G. Hutchins and R. E. Pincock, "Heterogeneous catalytic racemization of 4,4'-disubstituted 1,1'-binaphthyls by active carbons and by modified carbon catalysts." Journal of Organic Chemistry **45** (12), 2414 (1980).

[34] B. E. Douglas, "Racemization of tris(ethylenediamine)cobalt(III) ion in the presence of decolorizing carbon." Journal of the American Chemical Society **76**, 1020 (1954).

[35] W. C. Erdman, H. E. Swift, and B. E. Douglas, "The racemization of complex ions on activated carbon. II. The racemization of D-tris(ethylenediamine)cobalt(III) chloride and other complexes." Journal of Inorganic and Nuclear Chemistry **24**, 1365 (1962).

[36] F. P. Dwyer and A. M. Sargeson, "Catalytic racemization of tris-(ethylenediamine)cobalt(III) ion." Nature **187**, 1022 (1960).

[37] R. J. Mureinik and M. Spiro, "Heterogeneous catalysis in solution. Part 10. Racemization and reduction by solids of (+)589-tris(ethylenediamine)cobalt(III)." Journal of the Chemical Society: Dalton Transactions (23), 2480 (1974).

[38] R. J. Mureinik and M. Spiro, "Heterogeneous catalysis in solution. Part 12.

Racemization of (+)589-tris(ethylenediamine)cobalt(III) by a carbon black and kinetics of reacting systems involving racemization." Journal of the Chemical Society: Dalton Transactions (23), 2493 (1974).

[39] P. D. Totterdell and M. Spiro, "Heterogeneous catalysis in solution. Part 13. Kinetics of racemization in two immiscible phases with rapid exchange across the interface, illustrated by the racemization of (+)589-tris(ethylenediamine)cobalt(III) catalyzed by a carbon black." Journal of the Chemical Society: Faraday Transactions I **72** (6), 1477 (1976).

[40] G. H. Searle and E. Larsen, "The bis[di(2-aminoethyl)sulfide]cobalt(III) ion. Existence of only the unsymmetrical-facial geometric isomer and its optical resolution." Acta Chemica Scandinavica A **A30** (2), 143 (1976).

[41] A. Hammershoi and E. Larsen, "The stability of u-fac-bis[di(2-aminoethyl)sulfide]cobalt(III) and the charcoal-catalyzed racemization of the (-)D enantiomer in acidic solution." Acta Chemica Scandinavica A **32** (6), 485 (1978).

[42] F. P. Dwyer, F. L. Garvan, and A. Shulman, "Stereospecific influences in metal complexes containing optically active ligands. I. Some of the optical isomers of tris(propylenediamine)cobalt(III) ion." Journal of the American Chemical Society **81**, 290 (1959).

[43] W. C. Erdman and B. E. Douglas, "The racemization of complex ions on activated carbon. I. The racemization of potassium D-ethylenediaminetetraacetatocobaltate(III)." Journal of Inorganic and Nuclear Chemistry **24**, 1355 (1962).

[44] D. Sen and W. C. Fernelius, "Catalytic racemization of optically active complexes: Tris(ethylenediamine)cobalt(III), -platinum(IV), and -rhodium(III) halides." Journal of Inorganic and Nuclear Chemistry **10**, 269 (1959).

[45] Y. Y. Hoyano and R. E. Pincock, "Carbon catalyzed organic reactions: carbon promoted solvolysis of a phosphate ester derived from 1,1'-bi-2-naphthol." Canadian Journal of Chemistry **58** (2), 134 (1980).

[46] F. J. Waller, J. B. Appleby, and S. C. Webb, in *Chemical Industries*, edited by M. E. Ford (Marcel Dekker, Inc., New York, 2001), Vol. 82 (Catalysis of Organic Reactions), 169.

[47] B. R. Puri, S. Kumari, and K. C. Kalra, "Acidoid behavior of charcoal as a function of its oxygen complexes. VIII. Strength of charcoal acidoid." Journal of the Indian Chemical Society **49** (2), 127 (1972).

[48] P. S. Walton and M. Spiro, "Heterogeneous catalysis in solution. Part 4. Effect of solids on some organic substitution reactions." Journal of the Chemical Society B (1), 42 (1969).

[49] J. M. Austin, O. D. E. S. Ibrahim, and M. Spiro, "Heterogeneous catalysis in solution. Part 5. Catalysis by charcoal and silver iodide of the ethyl iodide-silver nitrate reaction." Journal of the Chemical Society B (6), 669 (1969).

[50] J. Bjerrum and E. Christensen, *Metal ammine formation in aqueous solution: theory of the reversible step reactions*. (P. Haase & Son, Copenhagen, 1941).

[51] J. C. Bailar, Jr. and J. B. Work, "The role of catalysis in the preparation and reactions of some Co(III) and Cr(III) ammines." Journal of the American

Chemical Society **67**, 176 (1945).

[52] R. J. Mureinik, "Carbon-catalyzed formation of hexamminecobalt(III) in solution." Journal of Catalysis **50** (1), 56 (1977).

[53] A. Tomita and Y. Tamai, "Catalytic effect of surface groups on carbon in the hydrolysis of a hexanitrocobaltate(III)." Journal of Colloid and Interface Science **36** (1), 153 (1971).

[54] A. Tomita and Y. Tamai, "Effect of surface groups of carbon on the adsorption and catalytic base hydrolysis of a hexaamminecobalt(III) ion." Journal of Physical Chemistry **75** (5), 649 (1971).

[55] T. G. Alkhazov, A. E. Lisovskii, Yu A. Ismailov, and A. I. Kozharov, "Oxidative dehydrogenation of ethylbenzene on activated carbons. I. General characteristics of the process." Kinetika i Kataliz **19** (3), 611 (1978).

[56] A. E. Lisovskii, A. I. Kozharov, Yu A. Ismailov, and T. G. Alkhazov, "Oxidative dehydrogenation of ethylbenzene on activated carbons. II. Study of the nonsteady-state activity of carbons." Kinetika i Kataliz **19** (4), 950 (1978).

[57] T. G. Alkhazov, A. E. Lisovskii, and T. K. Gulakhmedova, "Oxidative dehydrogenation of ethylbenzene over a charcoal catalyst." Reaction Kinetics and Catalysis Letters **12** (2), 189 (1979).

[58] G. C. Grunewald and R. S. Drago, "Oxidative dehydrogenation of ethylbenzene to styrene over carbon-based catalysts." Journal of Molecular Catalysis **58** (2), 227 (1990).

[59] M. F. R. Pereira, J. J. M. Orfao, and J. L. Figueiredo, "Oxidative dehydrogenation

of ethylbenzene on activated carbon catalysts. I. Influence of surface chemical groups." Applied Catalysis A: General **184** (1), 153 (1999).

[60] M. F. R. Pereira, J. J. M. Orfao, and J. L. Figueiredo, "Oxidative dehydrogenation of ethylbenzene on activated carbon catalysts 2. Kinetic modelling." Applied Catalysis A: General **196** (1), 43 (2000).

[61] M. F. R. Pereira, J. J. M. Orfao, and J. L. Figueiredo, "Oxidative dehydrogenation of ethylbenzene on activated carbon catalysts 3. Catalyst deactivation." Applied Catalysis A: General **218** (1-2), 307 (2001).

[62] A. Schraut, G. Emig, and H. Hofmann, "Kinetic investigations of the oxydehydrogenation of ethylbenzene." Journal of Catalysis **112** (1), 221 (1988).

[63] G. S. Szymanski and G. Rychlicki, "Importance of oxygen surface groups in catalytic dehydration and dehydrogenation of butan-2-ol promoted by carbon catalysts." Carbon **29** (4-5), 489 (1991).

[64] G. S. Szymanski and G. Rychlicki, "Catalytic conversion of 2-propanol on cation-substituted forms of oxidized carbon." Reaction Kinetics and Catalysis Letters **43** (2), 475 (1991).

[65] G. S. Szymanski and G. Rychlicki, "Catalytic conversion of propan-2-ol on carbon catalysts." Carbon **31** (2), 247 (1993).

[66] G. S. Szymanski, G. Rychlicki, and A. P. Terzyk, "Catalytic conversion of ethanol on carbon catalysts." Carbon **32** (2), 265 (1994).

[67] I. F. Silva, J. Vital, A. M. Ramos, H. Valente, A. M. B. do Rego, and M. J. Reis, "Oxydehydrogenation of cyclohexanol over carbon catalysts." Carbon **36** (7-8),

1159 (1998).

[68] V. N. Dubchenko and V. I. Kovalenko, "Chlorination of carboxylic acid anhydrides by carbon tetrachloride on activated charcoal." Zhurnal Prikladnoi Khimii **41** (11), 2568 (1968).

[69] V. N. Dubchenko and V. I. Kovalenko, "Transformation of carboxylic acid anhydrides in the gas phase on activated carbon." Zhurnal Prikladnoi Khimii **41** (9), 2048 (1968).

[70] V. N. Dubchenko, "Thermocatalytic reaction of carboxylic acids with carbon tetrachloride in the gas phase." Zhurnal Prikladnoi Khimii **46** (8), 1822 (1973).

[71] B. R. Puri, B. Kumar, and K. C. Kalra, "Studies in catalytic reactions of carbon. IV. Oxidation of hydrogen sulfide." Indian Journal of Chemistry A **9** (9), 970 (1971).

[72] M. Steijns and P. Mars, "Role of sulfur trapped in micropores in the catalytic partial oxidation of hydrogen sulfide with oxygen." Journal of Catalysis **35** (1), 11 (1974).

[73] R. Sreeramamurthy and P. G. Menon, "Oxidation of hydrogen sulfide on active carbon catalyst." Journal of Catalysis **37** (2), 287 (1975).

[74] O. C. Cariaso and P. L. Walker, Jr., "Oxidation of hydrogen sulfide over microporous carbons." Carbon **13** (3), 233 (1975).

[75] M. Steijns, F. Derks, A. Verloop, and P. Mars, "The mechanism of the catalytic oxidation of hydrogen sulfide. II. Kinetics and mechanism of hydrogen sulfide oxidation catalyzed by sulfur." Journal of Catalysis **42** (1), 87 (1976).

[76] M. Steijns, P. Koopman, B. Nieuwenhuijse, and P. Mars, "The mechanism of the catalytic oxidation of hydrogen sulfide. III. An electron spin resonance study of the sulfur catalyzed oxidation of hydrogen sulfide." Journal of Catalysis **42** (1), 96 (1976).

[77] B. R. Puri, D. D. Singh, and S. K. Verma, "Studies on catalytic reaction of carbon. Part VIII. Oxidation of hydrogen sulfide by air in the presence of active carbons." Indian Journal of Chemistry A **18A** (5), 388 (1979).

[78] W. O. Stacy, F. J. Vastola, and P. L. Walker, Jr., "Interaction of sulfur dioxide with active carbon." Carbon **6** (6), 917 (1968).

[79] T. Otake, S. Tone, Y. Yokota, and K. Yoshimura, "Kinetics of sulfur dioxide oxidation over activated carbon." Journal of Chemical Engineering of Japan **4** (2), 155 (1971).

[80] H. Komiyama and J. M. Smith, "Sulfur dioxide oxidation in slurries of activated carbon." AIChE Journal **21** (4), 664 (1975).

[81] E. Richter, "Carbon catalysts for pollution control." Catalysis Today **7** (2), 93 (1990).

[82] X. S. Zhao, G. Y. Cai, Z. Z. Wang, Q. X. Wang, Y. H. Yang, and J. S. Luo, "Influences of surface functional groups on catalytic activity over activated carbon catalysts for sulfur dioxide removal from flue gases." Applied Catalysis B: Environmental **3** (4), 229 (1994).

[83] M. N. Rao and O. A. Hougen, "Catalytic oxidation of nitric oxide on activated carbon." Chemical Engineering Progress Symposium Series **48** (Reaction Kinetics

and Transfer Processes), 110 (1952).

[84] H. Jüntgen, E. Richter, and H. Kühl, "Catalytic activity of carbon catalysts for the reaction of nitrogen oxides (NOx) with ammonia." Fuel **67** (6), 775 (1988).

[85] H. Jüntgen and H. Kühl, in *Chemistry and Physics of Carbon*, edited by P. A. Thrower (Marcel Dekker, New York, 1989), Vol. 22, Chap. 2.

[86] H. Kuhl, H. Baumann, H. Juentgen, P. Ehrburger, J. Dentzer, and J. Lahaye, "The importance of active surface area on the nitric oxide reduction with ammonia on carbon catalysts." Fuel **68** (1), 129 (1989).

[87] E. Richter, H. J. Schmidt, and H. G. Schecker, "Adsorption and catalytic reactions of nitric oxide and ammonia on activated carbon." Chemical Engineering and Technology **13** (5), 332 (1990).

[88] K. Yang and M. A. Johnson, "Novel carbon catalysis: oxidation in basic solution." Journal of Organic Chemistry **42** (23), 3754 (1977).

[89] Y. I. Pyatnitskii, G. I. Golodets, and T. G. Skorbilina, "Vapor-phase oxidation of o-xylene to phthalic anhydride on carbon." Kinetika i Kataliz **17** (3), 814 (1976).

[90] Y. I. Pyatnitskii, T. G. Skorbilina, and I. A. Tarkovskaya, "Catalytic vapor-phase oxidation of o-xylene on activated carbon." Kataliz i Katalizatory **19**, 41 (1981).

[91] A. Y. Lukomskaya, "Mechanism of the catalytic oxidation of o-xylene on active coals." Reaction Kinetics and Catalysis Letters **23** (1-2), 85 (1983).

[92] A. Y. Lukomskaya, I. A. Tarkovskaya, and V. V. Strelko, "Influence of chemical-composition of carbon catalysts on their adsorptive properties in catalytic-oxidation of ortho-xylene." Reaction Kinetics and Catalysis Letters **31** (2), 435

(1986).

[93] A. Tomita, S. Mori, and Y. Tamai, "Catalytic behavior of carbon on the oxidation of cyclohexene." Carbon **9** (2), 224 (1971).

[94] M. Voll and H. P. Boehm, "Catalytic hydrogen chloride oxidation on carbon black." Carbon **8** (1), 99 (1970).

[95] E. K. Rideal and W. M. Wright, "Low-temperature oxidation at charcoal surfaces. I. The behavior of charcoal in the absence of promoters." Journal of the Chemical Society **127**, 1347 (1925).

[96] E. K. Rideal and W. M. Wright, "Low-temperature oxidation at charcoal surfaces. III. The behavior of blood charcoal and the influence of temperature on the reaction rate." Journal of the Chemical Society, 3182 (1926).

[97] E. K. Rideal and W. M. Wright, "Low-temperature oxidation at charcoal surfaces. II. The behavior of charcoal in the presence of promoters." Journal of the Chemical Society, 1813 (1926).

[98] W. M. Wright, "Low-temperature oxidation at charcoal surfaces. IV. The active areas for different acids and their relative rates of oxidation." Journal of the Chemical Society, 2323 (1927).

[99] J. Barkauskas and A. Kareiva, "Investigation of n-hexane oxidation on the surface of activated charcoal." Reaction Kinetics and Catalysis Letters **53** (1), 7 (1994).

[100] G. Lemoine, "On some reactions effected by means of charcoal as a catalytic agent." Comptes Rendus **144**, 357 (1907).

[101] A. King, "Chemisorption on charcoal. VIII. Influence of temperature of activation of charcoal on (a) catalytic oxidation of salts and (b) catalytic decomposition of hydrogen peroxide." Journal of the Chemical Society, 1688 (1936).

[102] E. C. Larsen and J. H. Walton, "Activated carbon as a catalyst in certain oxidation-reduction reactions." Journal of Physical Chemistry **44**, 70 (1940).

[103] G. Brinkmann, "Chemical character and catalytic behavior of activated carbon." Angewandte Chemie **61**, 378 (1949).

[104] G. Brinkmann, "Catalytic reactions of active carbon." Kolloid-Zeitschrift **123**, 116 (1951).

[105] M. L. Studebaker, "Chemistry of carbon black and reinforcement." Rubber Chemistry and Technology **30**, 1400 (1957).

[106] V. A. Garten and D. E. Weiss, "Ion- and electron-exchange properties of activated carbon in relation to its behavior as a catalyst and adsorbent." Reviews of Pure and Applied Chemistry **7**, 69 (1957).

[107] A. S. Fomenko, I. L. Gankina, and T. M. Abramova, "Study of the mechanism of decomposition of hydrogen peroxide on activated carbon by the isotope method." Kinetika i Kataliz **2**, 732 (1961).

[108] R. N. Smith, A. J. Miles, and S. F. Watkins, "Carbon-catalyzed decomposition of hydrogen peroxide." Transactions of the Faraday Society **62** (9), 2553 (1966).

[109] B. R. Puri and K. C. Kalra, "Catalytic reactions of carbon. II. Catalytic decomposition of hydrogen peroxide." Indian Journal of Chemistry A **7** (2), 149 (1969).

[110] B. R. Puri and K. C. Kalra, "Decomposition of hydrogen peroxide in the presence of carbon blacks." Carbon **9** (3), 313 (1971).

[111] R. Davis, T. C. Lovelace, N. J. Martinez, and A. Millar, "Decomposition of peracids and their salts with activated carbon." Catalysis Letters **31**, 307 (1995).

[112] C. R. Walter, "Kinetics of ethylene chloride pyrolysis using a pumice catalyst." Journal of Chemical and Engineering Data **5**, 468 (1960).

[113] K. Okamoto, N. Tanaka, K. Adachi, and H. Shingu, "Catalytic dehydrochlorination of 1,2-dichloroethane on active carbon in the presence of some hydrocarbons." Bulletin of the Chemical Society of Japan **39** (7), 1522 (1966).

[114] J. J. Prinsloo, P. C. Van Berge, and J. Zlotnick, "Catalytic decomposition of 1,2-dichloroethane with activated carbon catalysts." Journal of Catalysis **32** (3), 466 (1974).

[115] M. Braden, W. P. Fletcher, and G. P. McSweeney, "Vulcanization of rubber by organic peroxides." Rubber Chemistry and Technology **28**, 190 (1955).

[116] B. R. Puri, V. K. Sud, and K. C. Kalra, "Studies in catalytic reactions of carbon. III. Catalytic decomposition of benzoyl peroxide." Indian Journal of Chemistry A **9** (9), 966 (1971).

[117] V. V. Kislykh and A. E. Sidel'nikov, "Decomposition of nitrous oxide in the presence of carbon." Kinetika i Kataliz **16** (3), 776 (1975).

[118] W. J. Snyder and D. Kunzru, "Effect of active carbon on the kinetics of polymerization of methyl methacrylate." Journal of Macromolecular Science:

Chemistry A **5** (2), 297 (1971).

[119] K. Ohkita, N. Tsubokawa, M. Noda, and M. Uchiyama, "Polymerization of N-vinylcarbazole initiated by carbon black surface." Carbon **15** (3), 194 (1977).

[120] K. Ohkita, M. Uchiyama, and H. Nishioka, "The polymerization of N-vinylcarbazole in the presence of carbon black." Carbon **16** (3), 195 (1978).

[121] N. Tsubokawa, N. Takeda, and K. Kudoh, "Carbon black as an initiator of cationic polymerization of isobutyl vinyl ether." Carbon **18** (2), 163 (1980).

[122] N. Tsubokawa, "Cationic polymerization of alpha-methylstyrene initiated by channel black surface." Journal of Polymer Science: Polymer Letters **18** (6), 461 (1980).

[123] N. Tsubokawa, N. Takeda, and A. Kanamaru, "The cationic polymerization of N-vinyl-2-pyrrolidone initiated by carbon black surface." Journal of Polymer Science: Polymer Letters **18** (9), 625 (1980).

[124] E. N. Shapatina, V. L. Kuchaev, B. E. Pen'kovoi, and M. I. Temkin, "Kinetics of the catalytic synthesis of phosgene." Kinetika i Kataliz **17** (3), 644 (1976).

[125] E. N. Shapatina, V. L. Kuchaev, and M. I. Temkin, "Kinetics of the catalytic synthesis of phosgene." Kinetika i Kataliz **18** (4), 968 (1977).

[126] E. N. Shapatina, V. L. Kuchaev, and M. I. Temkin, "Kinetics of phosgene synthesis at low chlorine concentrations." Kinetika i Kataliz **20** (5), 1183 (1979).

[127] W. J. Pope, "The preparation of sulfuryl chloride." Recueil des Travaux Chimiques **42**, 939 (1923).

[128] B. R. Puri, D. D. Singh, and S. K. Verma, "Studies in catalytic reactions of carbons: Part VII. Catalytic chlorination of toluene in presence of active carbons." Indian Journal of Chemistry A **16A** (12), 1026 (1978).

[129] B. R. Puri, D. D. Singh, N. C. Kaura, and S. K. Verma, "Studies in catalytic reactions of carbons. Part X. Catalytic chlorination of benzene and toluene at ambient temperature in the presence of activated carbons." Indian Journal of Chemistry A **19A** (2), 109 (1980).

[130] B. R. Puri, D. D. Singh, J. Chander, and L. R. Sharma, "Interaction of charcoal with chlorine water." Journal of the Indian Chemical Society **35**, 181 (1958).

[131] B. R. Puri, O. P. Mahajan, and D. D. Singh, "Interaction of charcoal with chlorine water. II." Journal of the Indian Chemical Society **37**, 171 (1960).

[132] M. Farcasiu, S. C. Petrosius, and E. P. Ladner, "Hydrodehydroxylation and hydrodehalogenation of substituted polycyclic aromatics using carbon catalysts." Journal of Catalysis **146** (1), 313 (1994).

[133] T. Sankarshana and M. B. Rao, "Catalytic dehydrochlorination of 1,1,2,2-tetrachloroethane." Indian Chemical Engineer **31** (1), 38 (1989).

[134] B. Neumann, W. Steuer, and R. Domke, "The conversion of bromine and hydrogen into hydrobromic acid in the presence of charcoal." Zeitschrift fur Angewandte Chemie **39**, 374 (1926).

[135] N. C. Jones, "The activation of halogen and carbon monoxide." Journal of Physical Chemistry **33**, 1415 (1929).

[136] G.-M. Schwab and F. Lober, "The halogen-transporting action of carbon."

Zeitschrift für Physikalische Chemie **A186**, 321 (1940).

[137] U. Hofmann and G. Ohlerich, "The surface chemistry of carbon." Angewandte Chemie **62**, 16 (1950).

[138] A. Clauss, H. P. Boehm, and U. Hofmann, "The adsorbing and catalytically effective surfaces of carbon blacks." Zeitschrift für Anorganische und Allgemeine Chemie **290**, 35 (1957).

[139] R. N. Smith, "The chemistry of carbon-oxygen surface compounds." Quarterly Reviews **13**, 287 (1959).

[140] E. Stumpp and W. Ruedorff, "Catalytic investigations on metal chloride-graphite compounds." Zeitschrift für Elektrochemie **66**, 648 (1962).

[141] B. R. Puri and K. C. Kalra, "Catalytic reactions on carbon. I. Catalytic combination of hydrogen and bromine." Indian Journal of Chemistry A **5** (12), 638 (1967).

[142] B. R. Puri and K. C. Kalra, "Carbons as catalysts for combination of hydrogen and iodine." Chemistry & Industry (50), 1810 (1969).

[143] Y. Uemichi, Y. Kashiwaya, A. Ayame, and H. Kanoh, "Formation of aromatic hydrocarbons in degradation of polyethylene over an activated carbon catalyst." Chemistry Letters (1), 41 (1984).

[144] B. S. Greensfelder, H. H. Voge, and G. M. Good, "Catalytic and thermal cracking of pure hydrocarbons. Mechanisms of reaction." Industrial & Engineering Chemistry **41**, 2573 (1949).

[145] M. Farcasiu and C. Smith, "Modeling coal liquefaction: Decomposition of 4-(1-

naphthylmethyl)bibenzyl catalyzed by carbon black." Energy & Fuels **5** (1), 83 (1991).

[146] M. Farcasiu, C. M. Smith, E. P. Ladner, and A. P. Sylwester, "Carbon materials - activity and selectivity in hydrocracking reactions." Preprints of Symposia - American Chemical Society, Division of Fuel Chemistry **36** (4), 1869 (1991).

[147] M. Farcasiu and S. C. Petrosius, "Heterogenous catalysis: mechanisms of selective cleavage of strong carbon-carbon bonds." Preprints of Symposia - American Chemical Society, Division of Fuel Chemistry **39** (3), 723 (1994).

[148] R. Burshtein, "Exchange between light and heavy hydrogen on charcoal." Acta Physicochimica U. R. S. S. **8**, 857 (1938).

[149] M. J. Rossiter, R. N. Smith, and J. R. Ludden, "The carbon-catalyzed hydrogen-deuterium exchange reaction." Journal of Physical Chemistry **67** (12), 2541 (1963).

[150] K. F. Bonhoeffer, A. Farkas, and K. W. Rummel, "Heterogeneous catalysis of the para-hydrogen conversion." Zeitschrift fur Physikalische Chemie **B21**, 225 (1933).

[151] J. Turkevich and J. Laroche, "Catalytic activity of a graded set of charcoals for hydrogen-deuterium equilibration and ortho-parahydrogen conversion and electron spin resonance." Zeitschrift fur Physikalische Chemie **15**, 399 (1958).

[152] M. Kodomari, Y. Suzuki, and K. Yoshida, "Graphite as an effective catalyst for Friedel-Crafts acylation." Chemical Communications (16), 1567 (1997).

[153] H. Shulman and E. Keinan, "Catalysis of the Kemp elimination by natural coals." Organic Letters **2** (23), 3747 (2000).

[154] E. F. G. Barbosa and M. Spiro, "Joint homogeneous and heterogeneous catalysis: a new synergistic effect." Journal of the Chemical Society: Chemical Communications (13), 423 (1977).

[155] R. M. Martin-Aranda, M. L. Rojas Cervantes, A. J. Lopez-Peinado, and J. D. Lopez-Gonzalez, "Alkaline carbons as base catalysts: alkylation of imidazole with alkyl halides." Journal of Molecular Catalysis **85**, 253 (1993).

[156] F. J. Weigert, "Carbon catalyzed polymethylbenzene dealkylation." Journal of Molecular Catalysis **85** (2), 229 (1993).

[157] H. P. Boehm, E. Diehl, W. Heck, and R. Sappok, "Surface oxides of carbon." Angewandte Chemie **76** (17), 742 (1964).

[158] B. R. Puri, in *Chemistry and Physics of Carbon*, edited by P. A. Thrower (Marcel Dekker, New York, 1970), Vol. 6, 191.

[159] D. Rivin, "Surface properties of carbon." Rubber Chemistry and Technology **44** (2), 307 (1971).

[160] H. P. Boehm, "Some aspects of the surface chemistry of carbon blacks and other carbons." Carbon **32** (5), 759 (1994).

[161] J. Klausen, S. P. Troeber, S. B. Haderlein, and R. P. Schwarzenbach, "Reduction of substituted nitrobenzenes by Fe(II) in aqueous mineral suspensions." Environmental Science and Technology **29** (9), 2396 (1995).

[162] N. V. Sidgwick, *The organic chemistry of nitrogen*. (Clarendon Press, Oxford, 1967).

[163] A. Furst, R. C. Berlo, and S. Hooton, "Hydrazine as a reducing agent for organic

compounds (catalytic hydrazine reductions)." Chemistry Reviews **65** (1), 51 (1965).

[164] B. H. Han, D. H. Shin, H. R. Lee, and B. H. Ro, "Reduction of aromatic nitro compounds with hydrazine catalyzed by activated zinc-copper." Bulletin of the Korean Chemical Society **10** (3), 315 (1989).

[165] B. H. Han and D. G. Jang, "Montmorillonite-catalyzed reduction of nitroarenes with hydrazine." Tetrahedron Letters **31** (8), 1181 (1990).

[166] B. H. Han, D. H. Shin, and S. Y. Cho, "Graphite catalyzed reduction of aromatic and aliphatic nitro compounds with hydrazine hydrate." Tetrahedron Letters **26** (50), 6233 (1985).

[167] M. K. Park, D. G. Jang, and B. H. Han, "Reduction of aromatic nitro compounds with hydrazine in the presence of sodium nitrate-carbon." Bulletin of the Korean Chemical Society **12** (6), 709 (1991).

[168] T. F. Stepanova and O. F. Ginzburg, "Use of oxidized SKT and BAU carbons as catalysts during the reduction of aromatic nitro compounds by hydrazine hydrate." Zhurnal Prikladnoi Khimii **46** (5), 1159 (1973).

[169] R. V. Rothenburg, "Performance of hydrazine hydrates in the removal of nitro-, nitroso- and isonitroso-groups." Chemische Berichte **26**, 2060 (1893).

[170] A. L. Endrey and T. A. Reilly, "Reduction mechanism of aromatic nitro compounds." Proceedings of the Annual Power Sources Conference **22**, 91 (1968).

[171] T. Hirashima and O. Manabe, "Catalytic reduction of aromatic nitro compounds with hydrazine in the presence of iron(III) chloride and active carbon." Chemistry

Letters (3), 259 (1975).

[172] P. M. G. Bavin, "The preparation of amines and hydrazo compounds using hydrazine and palladized charcoal." Canadian Journal of Chemistry **36**, 238 (1958).

[173] L. Holleck and R. Schindler, "Polarographic behavior of aromatic nitroso compounds." Zeitschrift fur Elektrochemie **60**, 1138 (1956).

[174] A. Furst and R. E. Moore, "Reductions with hydrazine hydrate catalyzed by Raney Nickel. II. Aromatic nitro compounds to intermediate products." Journal of the American Chemical Society **79**, 5492 (1957).

[175] C. Nishihara and H. Shindo, "Reduction of nitrobenzene in aqueous alkaline solution at a silver electrode. Observation by SERS, RRDE and UV absorption." Journal of Electroanalytical Chemistry and Interfacial Electrochemistry **202** (1-2), 231 (1986).

[176] A. Cyr, P. Huot, J. F. Marcoux, G. Belot, E. Laviron, and J. Lessard, "The electrochemical reduction of nitrobenzene and azoxybenzene in neutral and basic aqueous methanolic solutions at polycrystalline copper and nickel electrodes." Electrochimica Acta **34** (3), 439 (1989).

[177] A. Cyr, P. Huot, G. Belot, and J. Lessard, "The efficient electrochemical reduction of nitrobenzene and azoxybenzene to aniline in neutral and basic aqueous methanolic solutions at Devarda copper and Raney nickel electrodes: electrocatalytic hydrogenolysis of nitrogen-oxygen and nitrogen-nitrogen bonds." Electrochimica Acta **35** (1), 147 (1990).

[178] W. J. Plieth, in *Encyclopedia of electrochemistry of the elements*, edited by A. J. Bard (Marcel Dekker, New York, 1979), Vol. 8, 321.

[179] E. W. Schmidt, *Hydrazine and its derivatives: preparation, properties, applications*, 2nd ed. (Wiley-Interscience, New York, 2001).

[180] H. W. Schiessl, "Hydrazine - rocket fuel to synthetic tool." Aldrichimica Acta **13** (2), 33 (1980).

[181] L. F. Audrieth and B. A. Ogg, *The chemistry of hydrazine*. (John Wiley & Sons, New York, 1951).

[182] L. F. Audrieth and W. L. Jolly, "Catalytic decomposition of highly concentrated hydrazine by Raney nickel." Journal of Physics & Colloid Chemistry **55**, 524 (1951).

[183] C. F. Sayer, "The heterogeneous decomposition of hydrazine. Part 1: Kinetics of the liquid phase decomposition on a supported iridium catalyst." Technical Report No. RPETR688 (Rocket Propulsion Establishment, Westcott, Oct. 1968).

[184] C. F. Sayer, "The heterogeneous decomposition of hydrazine. Part 2: Use of N15 as a tracer to study the decomposition of hydrazine on the Shell 405 catalyst." Technical Report No. RPETR6910 (Rocket Propulsion Establishment, Westcott, Dec. 1969).

[185] C. F. Sayer, "The decomposition of hydrazine on the shell 405 catalyst." Technical Papers of the AIAA 6th Propulsion Joint Specialist Conference, Paper 70606 (1970).

[186] C. F. Sayer, "The heterogeneous decomposition of hydrazine. Part 4: Kinetics of

the decomposition of liquid hydrazine on a supported rhodium catalyst." Technical Report No. RPETR7116 (Rocket Propulsion Establishment, Westcott, Nov. 1971).

[187] K. M. C. Davis and C. F. Sayer, "Heterogeneous decomposition of hydrazine. 1. On a supported rhodium catalyst." Journal of the Chemical Society: Faraday Transactions I **68** (10), 1884 (1972).

[188] C. F. Sayer, "The heterogeneous decomposition of hydrazine: Part 5: Kinetics of the decomposition of liquid hydrazine on a supported ruthenium catalyst." Technical Report No. RPETR721 (Rocket Propulsion Establishment, Westcott, Jan. 1972).

[189] C. F. Sayer, "The heterogeneous decomposition of hydrazine. Part 6: Kinetics of the decomposition on supported palladium and platinum catalysts." Technical Report No. RPETR31 (Rocket Propulsion Establishment, Westcott, Nov. 1974).

[190] S. Tanatar, "Catalysis of hydroxylamines and hydrazine." Zeitschrift fur Physikalische Chemie **40**, 475 (1902).

[191] S. Tanatar, "Catalysis of hydrazines." Zeitschrift fur Physikalische Chemie **41**, 37 (1902).

[192] A. Gutbier and K. Neundlinger, "Catalysis of hydrazine by platinum black." Zeitschrift fur Physikalische Chemie **84**, 203 (1913).

[193] G. V. Vitvitskaya and G. B. Grabovskaya, "Catalytic decomposition of hydrazine over platinized carbon in an alkaline solution." Journal of Applied Chemistry **42** (10), 2091 (1969).

[194] S. Huenig, H. R. Mueller, and W. Thier, "Decomposition of diimine." Angewandte Chemie **75**, 298 (1963).

[195] S. Fouche, J. C. Goudeau, and M. L. Bernard, "Kinetic study of the catalytic decomposition of liquid hydrazine in a constant volume static reactor." Journal de Chimie Physique et de Physico-Chimie Biologique **71** (10), 1275 (1974).

[196] M. Spiro and A. B. Ravno, "Heterogeneous catalysis in solution. Part 2. The effect of platinum on oxidation-reduction reactions." Journal of the Chemical Society, 78 (1965).

[197] J.-B. Donnet, R. C. Bansal, and M.-J. Wang, *Carbon black: science and technology*, 2nd. ed. (Marcel Dekker, Inc., New York, 1993).

[198] Special Blacks Division, "Carbon blacks for specialty applications." Technical Report No. S-136 (Cabot Corporation, Billerica, MA, Apr. 2003).

[199] R. C. Bansal, J.-B. Donnet, and F. Stoeckli, *Active carbon*. (Marcel Dekker, Inc., New York, 1988).

[200] S. Lowell and J. E. Shields, *Powder surface area and porosity*, 3rd ed. (Chapman & Hall, New York, 1991).

[201] S. J. Gregg and K. S. W. Sing, *Adsorption, surface area, and porosity*, 2nd ed. (Academic Press, New York, 1982).

[202] F. Stoeckli and F. Kraehenbuehl, "The external surface of microporous carbons, derived from adsorption and immersion studies." Carbon **22** (3), 297 (1984).

[203] A. Seidell and W. F. Linke, *Solubilities: a compilation of solubility data from the periodical literature*, 4th ed. (Van Nostrand, Princeton, 1958).

[204] J.A. Dean and N. A. Lange, *Lange's handbook of chemistry*, 11th ed. (McGraw-Hill, New York, 1973).

[205] B. Wang and X. Cao, "The anodic oxidation of hydrazine on glassy carbon electrode." Electroanalysis **4** (7), 719 (1992).

[206] X. Cao, B. Wang, and Q. Su, "Anodic oxidation of hydrazine on glassy carbon electrodes in acetonitrile." Journal of Electroanalytical Chemistry **361** (1-2), 211 (1993).

[207] R. C. Cosser and F. C. Tompkins, "Heterogeneous decomposition of hydrazine on tungsten films." Transactions of the Faraday Society **67** (2), 526 (1971).

[208] B. R. Puri and R. C. Bansal, "Surface chemistry of carbon blacks. I. High-temperature evacuations." Carbon **1** (4), 451 (1964).

[209] N. V. Korovin and A. G. Kicheev, "Anodic oxidation of hydrazine on graphite." Elektrokhimiya **6** (9), 1330 (1970).

[210] S. Antoniadou, A. D. Jannakoudakis, and E. Theodoridou, "Electrocatalytic reactions on carbon fiber electrodes modified by hemin. II. Electro-oxidation of hydrazine." Synthetic Metals **30** (3), 295 (1989).

[211] P. Pouillen, A.M. Martre, and P. Martinet, "Electrochemical reduction of nitrobenzene in aqueous micellar solutions of various pH. Influence of the type of surfactant." Electrochimica Acta **27** (7), 853 (1982).

[212] I. Rubinstein, "Voltammetric study of nitrobenzene and related compounds on solid electrodes in aqueous solutions." Journal of Electroanalytical Chemistry and Interfacial Electrochemistry **183** (1-2), 379 (1985).

[213] M. Spiro and P. W. Griffin, "Proof of an electron-transfer mechanism by which metals can catalyze oxidation-reduction reactions." Chemical Communications (6), 262 (1969).

[214] J. Bénard and Y. Berthier, *Adsorption on metal surfaces: an integrated approach*. (Elsevier Scientific Publishing Co., New York, 1983).

[215] T. O. Pavela, "Hydrazine-platinum, a low-pressure hydrogen electrode." Suomen Kemistilehti **30B**, 240 (1957).

[216] G. Susbielles and O. Bloch, "Electrochemical study of the reaction of catalytic decomposition of hydrazine on platinum electrodes, in basic medium." Comptes Rendus de l'Académie des Sciences **255**, 685 (1962).

[217] S. Szpak, P. Stonehart, and T. Katan, "Electrode reactions of hydrazine in aqueous solutions." Electrochimica Acta **10** (6), 563 (1965).

[218] B. P. Nesterov and N. V. Korovin, "Anodic oxidation of hydrazine on smooth nickel in alkaline solution." Elektrokhimiya **2** (11), 1296 (1966).

[219] J. Block and G. Schulz-Ekloff, "Catalytic decomposition of nitrogen-15-labeled hydrazine on magnesium oxide-supported iron." Journal of Catalysis **30** (2), 327 (1973).

[220] A. Kant and W. J. McMahon, "Thermal decomposition of nitrogen-15-labeled hydrazine." Journal of Inorganic and Nuclear Chemistry **15**, 305 (1960).

[221] W. C. E. Higginson and D. Sutton, "Oxidation of hydrazine in aqueous solution. II. Use of N15 as a tracer in the oxidation of hydrazine." Journal of the Chemical Society, 1402 (1953).

[222] K. Arnolds, J. Heitbaum, and W. Vielstich, "Rupture of the nitrogen-nitrogen bond in the anodic oxidation and catalytic decomposition of hydrazine." Zeitschrift fur Naturforschung A **29** (2), 359 (1974).

[223] W. Jaenicke and F. Sutter, "Mechanism of photographic development with hydroquinone, Metol, and p-phenylenediamine." Zeitschrift für Elektrochemie **63**, 722 (1959).

[224] I. R. Jonasson and D. R. Stranks, "Heterogeneous catalyzed electron-exchange reactions. I. The thallium(I)-thallium(III) system." Electrochimica Acta **13** (5), 1147 (1968).

[225] P. L. Antonucci, L. Pino, N. Giordano, and G. Pinna, "A comparative analysis of structural and surface effects in the electrochemical corrosion of carbons." Materials Chemistry and Physics **21** (5), 495 (1989).

[226] N. Giordano, P. L. Antonucci, E. Passalacqua, L. Pino, A. S. Arico, and K. Kinoshita, "Relationship between physicochemical properties and electrooxidation behavior of carbon materials." Electrochimica Acta **36** (13), 1931 (1991).

[227] S. R. Kelemen, M. Afeworki, M. L. Gorbaty, and A. D. Cohen, "Characterization of organically bound oxygen forms in lignites, peats, and pyrolyzed peats by X-ray Photoelectron Spectroscopy (XPS) and Solid-State ^{13}C NMR methods." Energy & Fuels **16** (6), 1450 (2002).

[228] U.S. Environmental Protection Agency: Office of Transportation and Air Quality, "Diesel Exhaust in the United States." Report No. EPA420-F-02-048 (September

2002).

[229] G. M. Solomon, T. R. Campbell, T. Carmichael, G. R. Feuer, and J. S. Hathaway, "Exhausted by diesel: how America's dependence on diesel engines threatens our health." Natural Resources Defense Council Report (1998).

[230] E. T. Wei and H. P. Shu, "Nitroaromatic carcinogens in diesel soot: a review of laboratory findings." American Journal of Public Health **73** (9), 1085 (1993).

[231] M. Stiborova, "Nitroaromatic compounds: Environmental pollutants with carcinogenic potential for humans." Chemicke Listy **96** (10), 784 (2002).

Appendix A:

Nitrogen Adsorption Isotherms

V_{gas} = volume of N_2 gas adsorbed

P = N_2 equilibrium pressure

P_0 = N_2 saturated equilibrium vapor pressure

P/P_0 = relative pressure

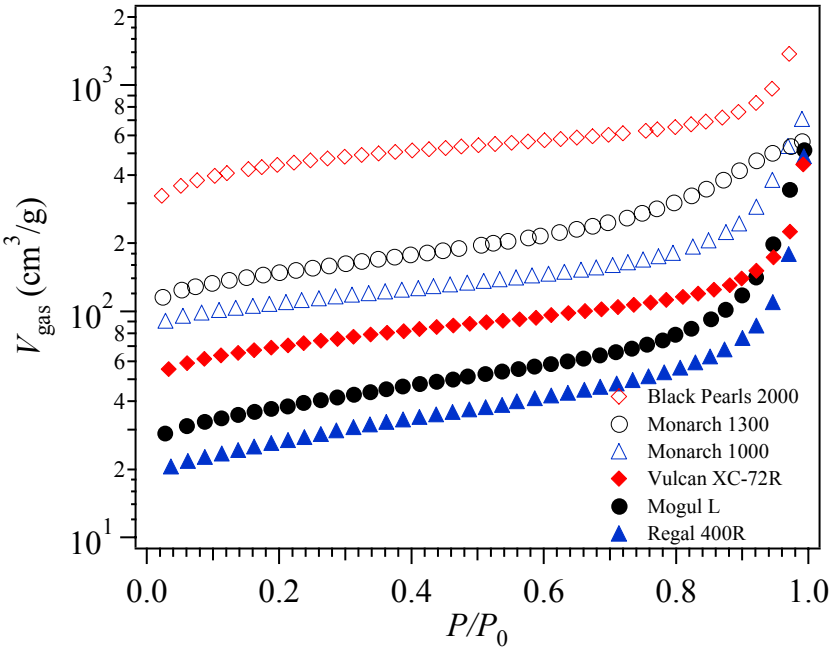

Adsorption isotherm of carbon blacks

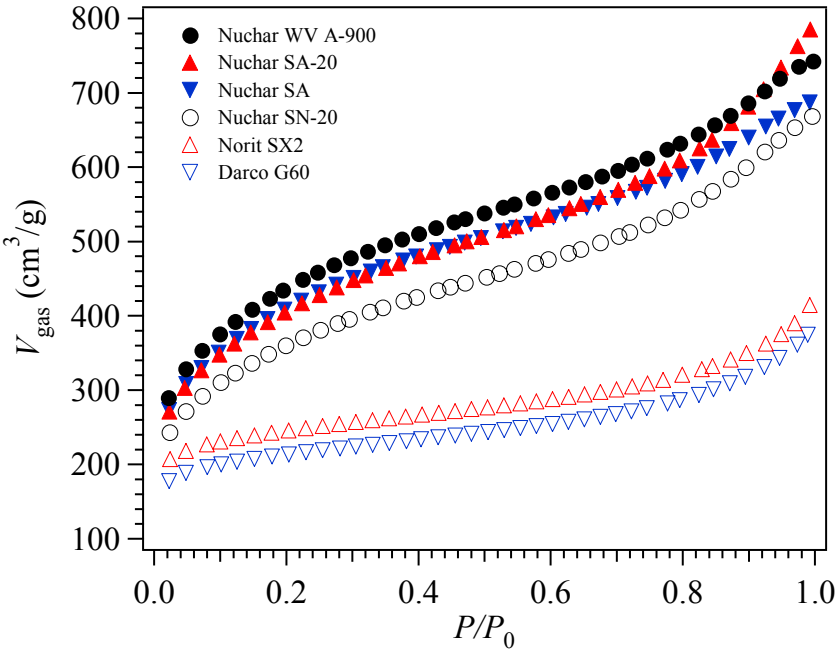

Adsorption isotherms of activated carbons

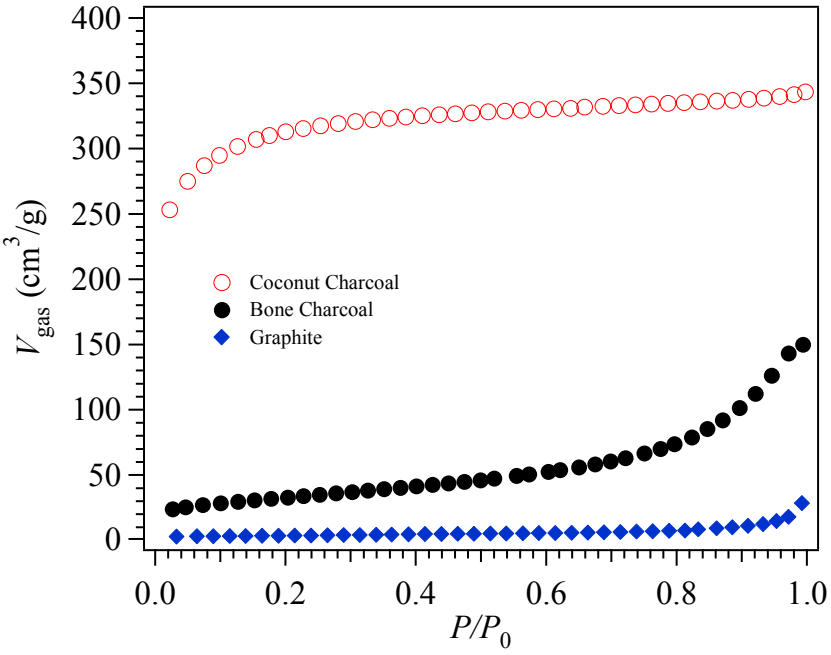

Adsorption isotherm of charcoals and graphite

Determination of the BET surface area

The weight of N_2 adsorbed is given by

$$W = \frac{V_{\text{liq}}}{\rho_{\text{liq}}},$$

where $\rho_{\text{liq}} = 0.807$ g/cm^3 is the liquid nitrogen density at 77 K, and V_{liq} is the volume of liquid N_2 adsorbed. The latter can be calculated from the moles of N_2 gas adsorbed, i.e.

$$\begin{aligned} V_{\text{liq}} &= n\overline{V} \\ &= \left(p\frac{V_{gas}}{RT} \right) \cdot \overline{V} \end{aligned}$$

Here, V_{gas} is the volume of N_2 gas adsorbed at standard conditions ($T = 273.15$ K, $p = 1$ atm), $R = 82.058$ cm^3·atm/mol·K is the universal gas constant, and $\overline{V} = 34.6$ cm^3/mol is the molar volume of liquid nitrogen.

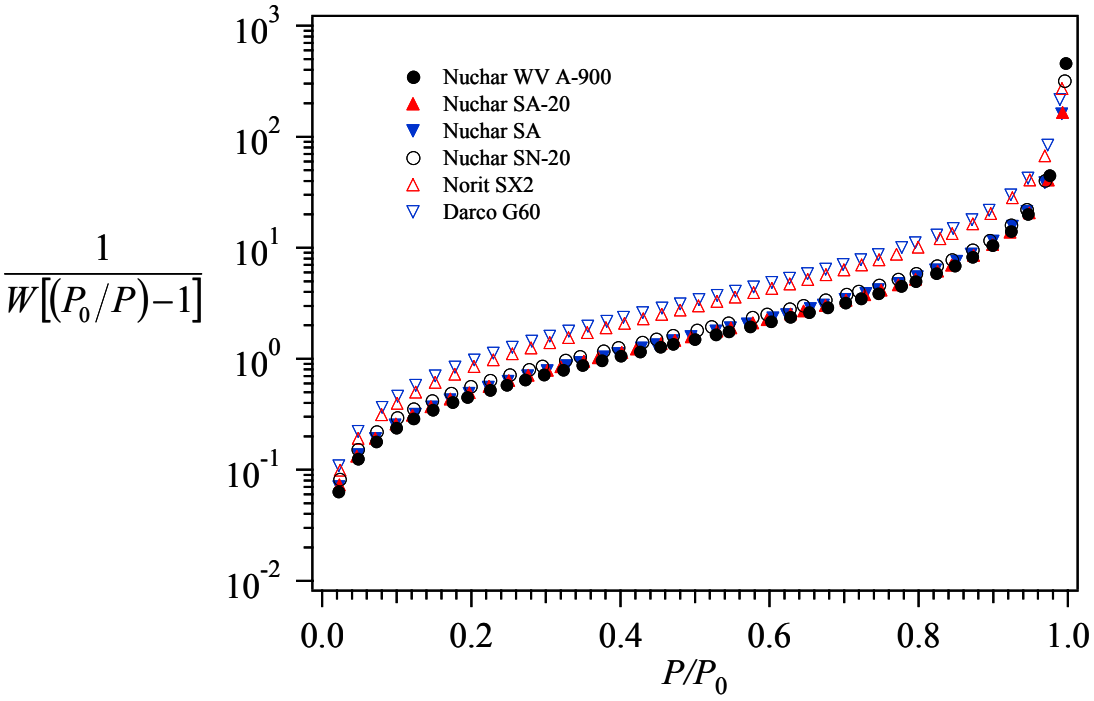

BET plots for activated carbons

BET surface area, S, is determined from a linear fitting of the BET plots in the range $0.05 < P/P_0 < 0.35$:

$$S = \frac{W_m \overline{N} A}{\overline{M}}$$

where $A = 16.2 \times 10^{-20}$ m^2 and $\overline{M} = 28.014$ g/mol are the cross-sectional area and the molecular weight of nitrogen, and $\overline{N} = 6.02214 \times 10^{23}$ mol^{-1} is the Avogadro number. The N_2 weight adsorbed in a monolayer is given by

$$W_m = \frac{1}{s + i}$$

where s and i are the slope and intercept of a BET plot.

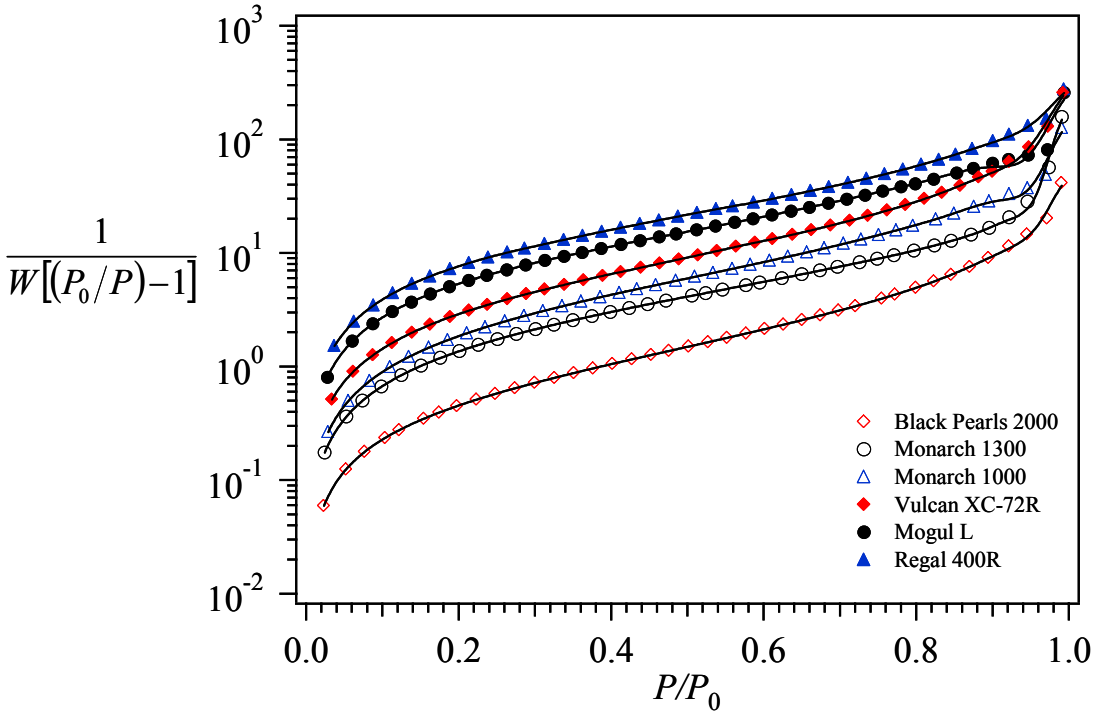

BET plots for carbon blacks

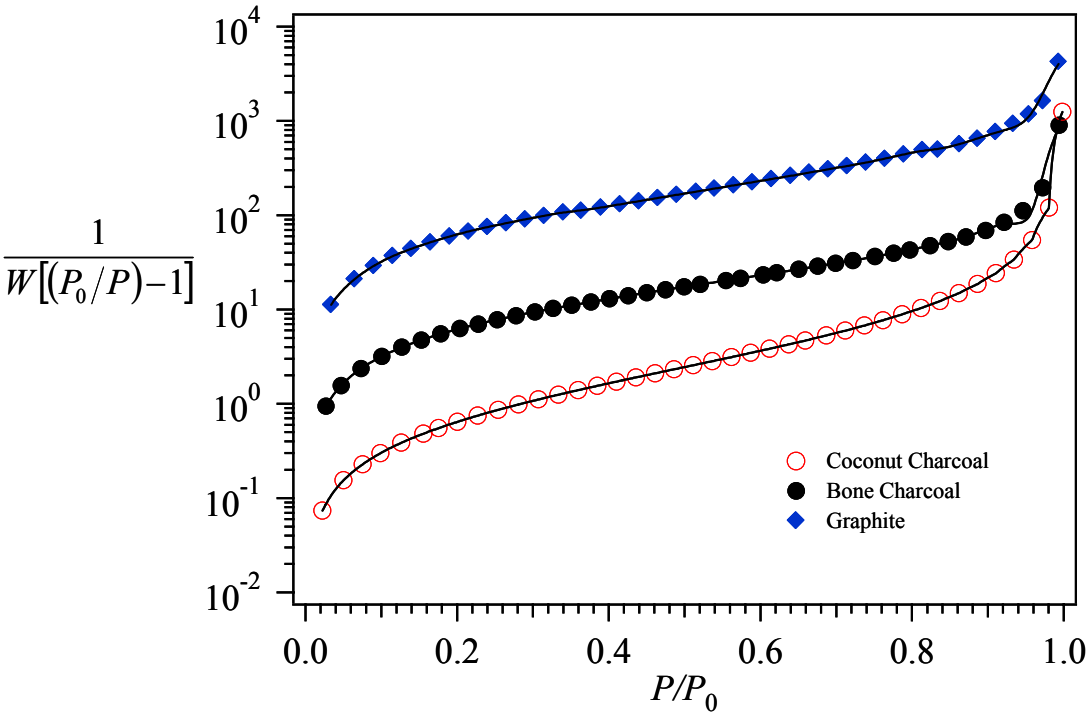

BET plots for charcoals and graphite

Determination of the external surface area: de Boer *t*-method

The determination of the external surface area is based on the *t*-curve, a plot of *t*, the statistical thickness, versus the relative pressure, P/P_0. The standard *t*-curve is expressed by the empirical de Boer equation:

$$t = \left(\frac{13.99}{\log P_0/P + 0.034} \right)^{\frac{1}{2}}$$

The calculated statistical thickness at various relative pressures is then used to replot the analysis isotherm as a *t*-curve, a plot of the volume of gas adsorbed versus *t*. Typical *t*-plots are shown below with the linear fitting to the upper linear portion. The external surface area is obtained from the slope of the upper linear portion of the *t*-plot, as follows

$$S_{\text{ext}} = \left(\frac{V_{\text{liq}}}{t} \right)_{\text{upper}} \times 10^4$$

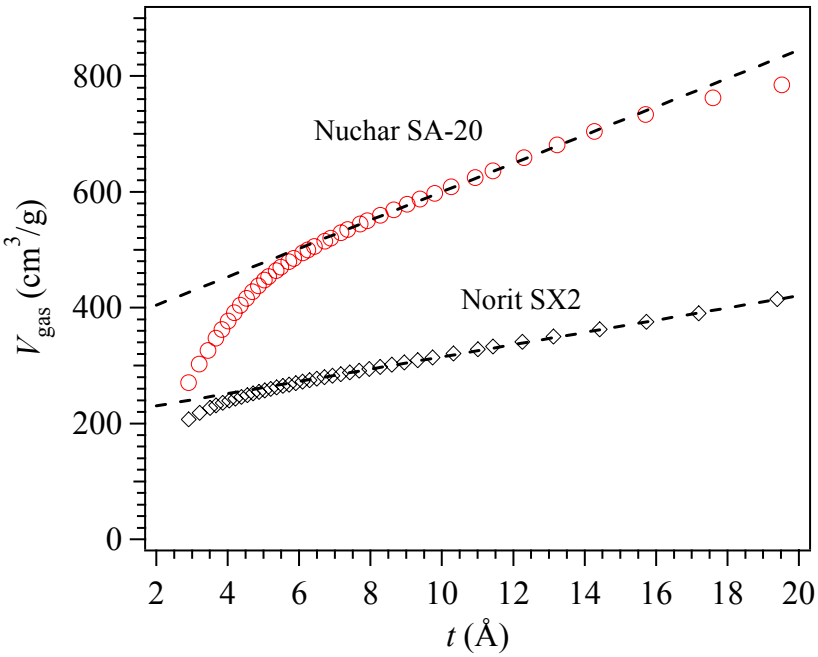

***t*-plot for selected activated carbons**

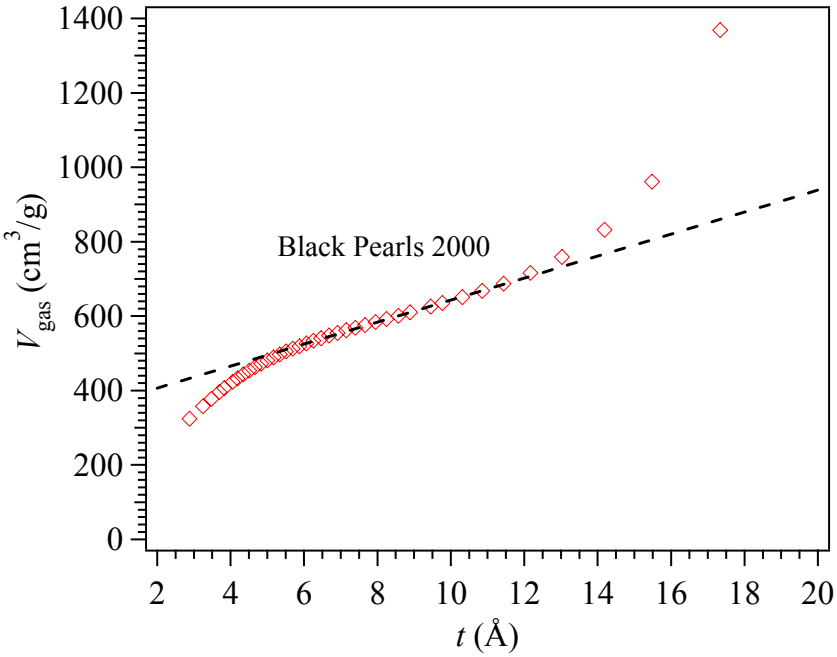

***t*-plot for a carbon black sample**

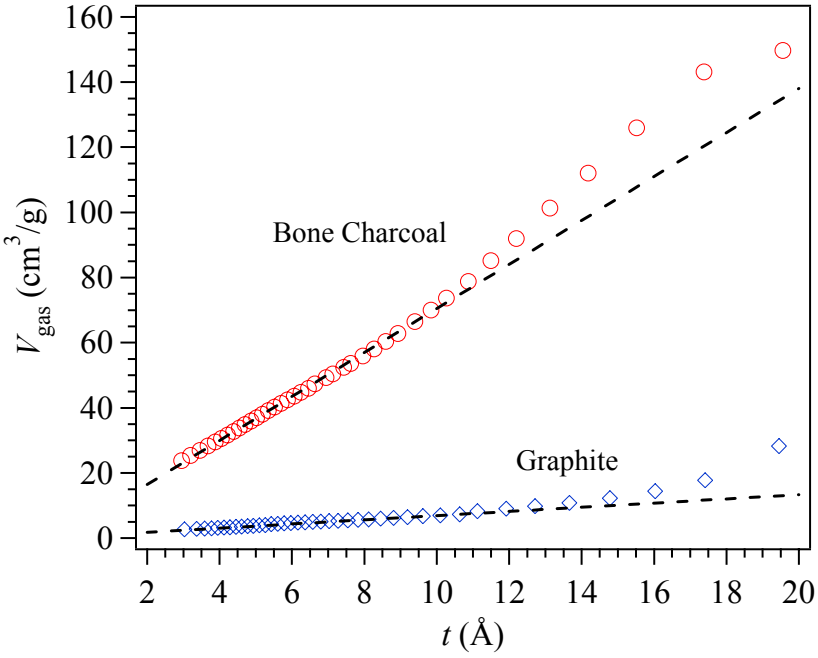

***t*-plot for a charcoal and graphite samples**

Appendix B:

Sample Calculations

1. Calculation of concentration of chemicals

The molarity (M) of a compound is calculated using the standard procedure,

$$M = \frac{n}{V_{\text{solution}}}$$

where n is the number of moles of solute and V_{solution} is the total volume of solution. The number of moles of solute is given by

$$n = \frac{\rho V_{\text{solute}}}{\overline{M}}$$

where ρ is the density, V_{solute} is the volume and $\overline{M}$ is the molecular weight of the solute.

A. For 0.8 mL of hydrazine (98.5 vol%) in 25 mL of solution

$$n = \frac{(1.028\ \text{g/mL})(0.8\ \text{mL})(0.985)}{32.04\ \text{g/mol}} = 0.025\ \text{moles}$$

$$M = \frac{0.025}{25\ \text{mL}} \times \frac{1000\ \text{mL}}{1\ \text{L}} = 1M$$

B. For 1.7 mL of nitrobenzene (99.5 vol%) in 25 mL of solution

$$n = \frac{(1.2037\ \text{g/mL})(1.7\ \text{mL})(0.995)}{123.11\ \text{g/mol}} = 0.017\ \text{moles}$$

$$M = \frac{0.017}{25\ \text{mL}} \times \frac{1000\ \text{mL}}{1\ \text{L}} = 0.68M$$

2. Calculation of the total volume of gas expected

To convert number of moles of gas to volume, we assume that either nitrogen or ammonia (at 0.967 atm, 25 ºC) behave as an ideal gas, so

$$V_C = n\overline{V}$$

where n is the number of moles expected and $\overline{V} = 25.30\ \text{L/mol}$ is the molar volume of the ideal gas.

A. From 0.025 moles of hydrazine in the reduction of nitrobenzene

$$V_C = (0.025\ \text{moles})(25.30\ \text{L/mol}) = 630\ \text{mL of } N_2$$

B. From 0.025 moles of hydrazine in the decomposition reaction

$$V_C = \frac{1}{3}(0.025\ \text{moles})(25.30\ \text{L/mol}) = 210\ \text{mL of } N_2$$

2. Calculation of the rate of reaction

The apparent rate of reaction (dV_g/dt) was calculated from the initial slope of the plot of volume of gas evolved with respect to time, as shown in the figure below. Additional approaches can be used with similar results: (a) volume of gas produced in certain unit of time at the beginning of the reaction (e.g., at 15 min of reaction time), and (b) graphical differentiation of the gas evolution plots. We assume that the traces of ammonia formed at the beginning of the reaction remained dissolved in the *iso*propanol solution. Thus, the gas evolved consisted of only nitrogen.

To convert apparent rate of reaction to reaction rate as expressed by Eq. (2.2), we assume that nitrogen (at 0.967 atm, 25 ºC) behave as an ideal gas, whose molar volume is $\overline{V} = 25.30\ \text{L/mol}$. The reaction rate (normalized by the total volume V of reaction mixture) is given by

$$R = \frac{1}{V\overline{V}\nu}\frac{dV_g}{dt}$$

where ν is the nitrogen coefficient in the balanced equation ($\nu = 1$ for the hydrazine

decomposition reaction, ν = 3 for the nitrobenzene reduction reaction)

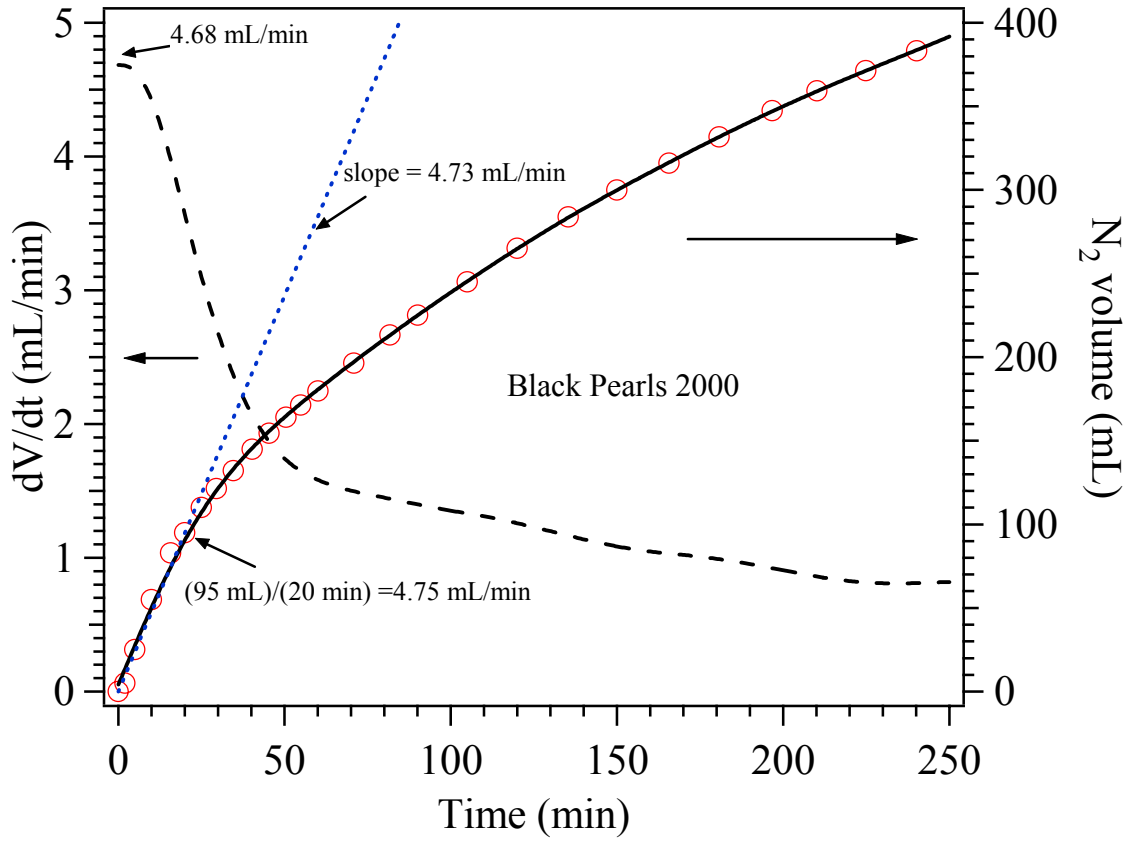

Typical determination of the reaction rate. Solid line represents the interpolation curve of the raw data. Dashed line represents the derivative of the interpolation curve. Short dashed line is the linear fitting of the first points of the gas evolution plot. Note that the slope of this line is very close to the derivative at $t = 0$ and the rate determined using the gas produced at 20 min.

Appendix C:

Igor Pro Curve Fitting

Igor's curve fitting capability is one of its strongest analysis features. The idea of curve fitting is to find a mathematical model that fits your data. The curve fit finds the specific coefficients which make that function match your data as closely as possible. Igor can fit to either built-in functions or user-defined functions. One creates a user-defined function by entering the function in the New Fit Function dialog. Very complicated functions may have to be entered in the Procedure window.

If we want to fit the data to a function of the form

$$R = \frac{k_a[a]}{1 + K_a[a]},$$

the user-defined fitting function used in our analyses has the following form:

Function Adsorption(w, x) : FitFunc

Wave w; Variable x

Variable r

r =w[0]*x/(1+w[1]*x)

return r

End

A typical example of the Curve Fitting Dialog is shown below

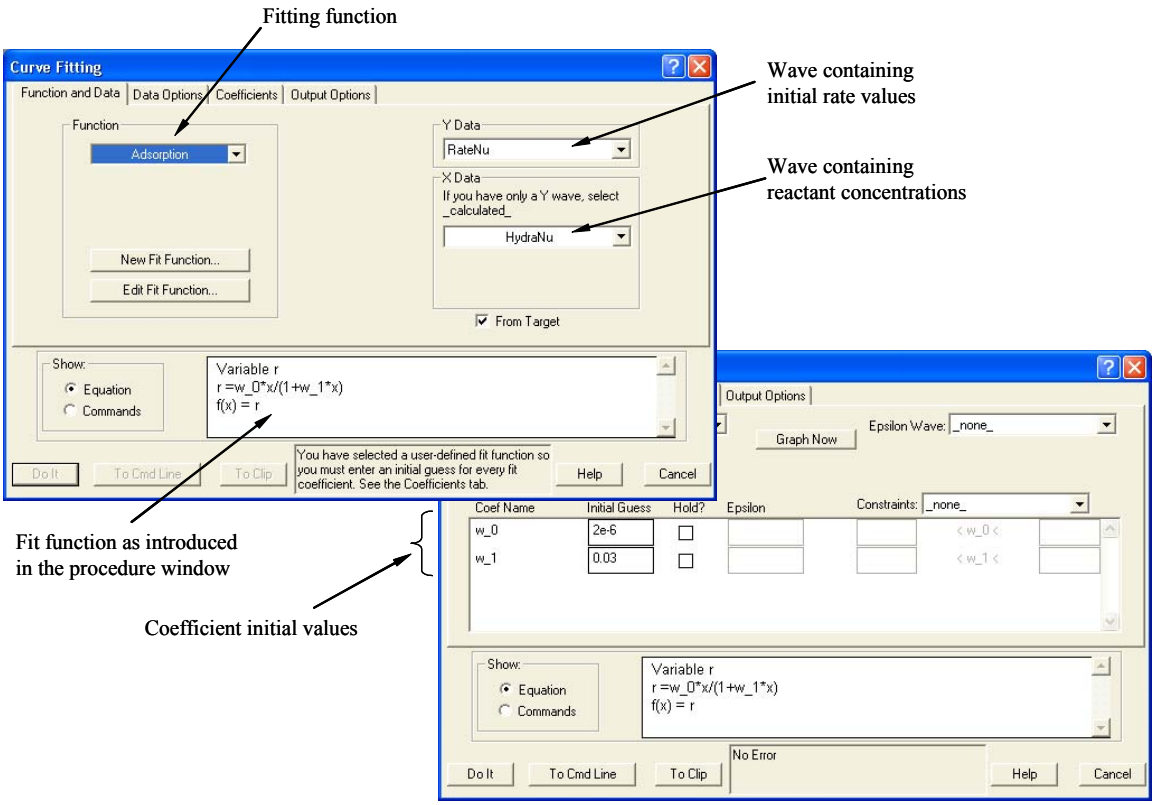
Fitting function
Wave containing initial rate values
Wave containing reactant concentrations
Curve Fitting
Function and Data
Data Options
Coefficients
Output Options
Function
Adsorption
New Fit Function...
Edit Fit Function...
Y Data
RateNu
X Data
If you have only a Y wave, select _calculated_
HydraNu
From Target
Show:
Equation
Commands
Variable r
r =w_0*x/(1+w_1*x)
f(x) = r
Do It
To Cmd Line
To Clip
You have selected a user-defined fit function so you must enter an initial guess for every fit coefficient. See the Coefficients tab.
Help
Cancel
Graph Now
Epsilon Wave: _none_
Coef Name
Initial Guess
Hold?
Epsilon
Constraints: _none_
w_0
2e-6
w_1
0.03
< w_0 <
< w_1 <
No Error
Fit function as introduced in the procedure window
Coefficient initial values

Synthetic Coal Tar Enamel Using Solvent Extraction

FINAL REPORT

Reporting Period
March 1, 2003 February 29, 2004

Report Prepared by

Peter G. Stansberry
Department of Chemical Engineering
College of Engineering and Mineral Resources
P. O. Box 6102
West Virginia University
Morgantown, WV 26506-6102

Report Issued
April 15, 2004

DOE Award Number DE-FC26-98FT40350

Other Contributors

Elliot B. Kennel and Lloyd Ford
Department of Chemical Engineering
College of Engineering and Mineral Resources
P. O. Box 6102
West Virginia University
Morgantown, WV 26506-6102

DISCLAIMER

ASTRACT

Producing a synthetic coal tar enamel proved to be both feasible and moderately successful. After characterizing a commercial grade coal tar enamel, a synthetic coal tar enamel was made using solvent extracted coal, heavy oil, bituminous coal and talc. The synthetic enamel was developed in a 1L autoclave reactor at temperatures up to 300°C with stirring at a rate of 1000rpm for digestion times up to 3 hours. The resulting synthetic enamel has properties that fall within most specifications of commercial grade coal tar enamel. The synthetic enamel had slightly higher volatile loss, very similar viscosity, and lower sulfur content than that of commercial enamel. Penetration values for the synthetic enamel generally were slightly lower, but were still within the specified range for commercial enamels. In cathodic disbonding, the synthetic enamel did not perform as well as the commercial product. It was demonstrated that synthetic enamel can be used as an adhesive for carbon foam-steel composites, and the bond strength to carbon foam can be adequate for some applications.

TABLE OF CONTENTS

LIST OF FIGURES

LIST OF FIGURES
(Continued)

Page

LIST OF TABLES

1 EXECUTIVE SUMMARY

Coal tar enamels suitable for wide-temperature or hot-applied applications are generally produced by digesting bituminous coal in pitch, heavy oil, and inorganic fillers. Sourcing of the pitch (and heavy oil) components is typically reliant on the byproducts recovered from metallurgical coke ovens. As such, because of the continuing decline of the byproduct coke oven industry in the United States, an alternative method for producing the pitch ingredient of coal tar enamel is timely.

Extraction of bituminous coal was used to produce a pitch-like material for testing in laboratory enamels. In all evaluations, the performance of the synthetic enamel was compared to a commercial product. Several synthetic enamel formulations with the coal extract were produced by digestion at 200°C, with resultant properties that varied in penetration behavior, viscosity, and volatility. However, optical microscopic examination of these enamels indicated that the digestion conditions were not severe enough to dissolve or digest the coal because the coal particles remained essentially unchanged. Therefore, other formulations were produced at 300°C and the samples again observed with the optical microscope. It appeared that preparation at 300°C produced partially dissolved coal particles very similar in appearance to commercial coal tar enamel.

One of the synthetic coal tar enamels was judged suitable for additional testing. In comparisons with the commercial product, the synthetic enamel had penetration values that, while lower than the commercial sample, were still within industrial specifications. Volatile content was similar to the commercial material as well, and the composition of the synthetic enamel did not contain any detectable organic compounds not already

evident in the commercial product. Additionally, the sulfur content of the synthetic enamel was only 0.18wt% and the commercial enamel was 0.46wt%.

Cathodic disbonding tests were conducted with enamel-coated steel coupons placed in an aqueous salt solution for four weeks under an applied potential of 1.5V. The synthetic enamel allowed significant corrosion to occur, possibly because of poor adhesion to the surface of the metal.

Resistance to moisture penetration of carbon foams coated with the synthetic and commercial enamels under ambient conditions was very good within the time constraints of the research project. Accelerated tests were devised in which the coated carbon foams were tested under pressurized water. These tests indicated that the synthetic enamel coating resisted water uptake more than the commercial coating initially, but after a longer period of time both behaved similarly.

Finally, the synthetic enamel was used as an adhesive in a steel-carbon foam composite with an encouraging degree of success. The enamel had a usable strength when subjected to a tensile test.

2 INTRODUCTION

Coal tar enamel is used as coatings for pipelines and other objects that need to be protected from environmental conditions. Since coal tar enamel is thermoplastic, it softens when heated for ease of application. After cooling, coal tar enamel hardens to form a flexible water and vapor-proof barrier. The desirable features of coal tar enamel include long lifetime during underground burial and resistance to salt water exposure and freeze-thaw cycles. Coal tar enamel has been, and continues to be, one of the most cost effective and forgiving corrosion mitigation coatings available.

Based on years of experience in real-world uses, coal tar enamel is preferred in certain applications to petroleum-based asphalt in barrier and cathodic protection applications. Unlike asphalt, which exhibits aliphatic characteristics, coal tar enamel is a stable complex of aromatic ring structures, which result in a denser and tighter molecular barrier. Thus, coal tar enamel is very stable, forming strong molecular associations that are difficult to disrupt.

Coal extraction is a well-known process for obtaining pitch-like materials. Coal extracts, being similar to the components in coal tar enamel, are also predominately comprised of aromatic hydrocarbons. Through control of extraction conditions, a wide range of low-ash, low-sulfur pitch-like products can be made from coal.

Currently, the pitch (and oil) component of coal tar enamel is obtained from the high-temperature carbonization of coal during the production of metallurgical coke. As such, the pitch used in enamel formulations is a byproduct similar to coal tar binder pitch. Because domestic coke production is expected to continue to decline, there are concerns about adequate sourcing. Thus being able to produce synthetic coal tar enamel via a new

approach is especially important considering the declining domestic production of coal tar pitch.

The specific objectives of this research were to 1) produce a coal extract as a surrogate for conventional coal pitch, 2) develop a synthetic coal tar enamel that closely matches a commercial product in penetration behavior, 3) compare the volatility of synthetic enamel to commercial product, 4) establish the upper sulfur content in the synthetic enamel at no more than 1wt%, 5) test the performance of the synthetic enamel with regards to cathodic protection, 6) determine the applicability of synthetic enamel as a vapor-barrier coating on carbon foam artifacts and, 7) fabricate a compliant seal between carbon foam and steel using a synthetic enamel and evaluate mechanical properties of the composite.

3 BACKGROUND

Coal tar enamels and coatings are a diverse family of materials. The diversity arises, in part, from the specifications and performance characteristics established by the customer. Figure 1 indicates some of the groups into which these materials are classified. Modern coal tar enamels are comprised of essentially four components: coal pitch, heavy coal tar distillate (heavy oil), coal, and inorganic fillers. Coal pitch in its own right is an effective water vapor barrier but suffers from brittleness and poor temperature susceptibility, while heavy oils sag and flow from surfaces at relatively low temperatures.

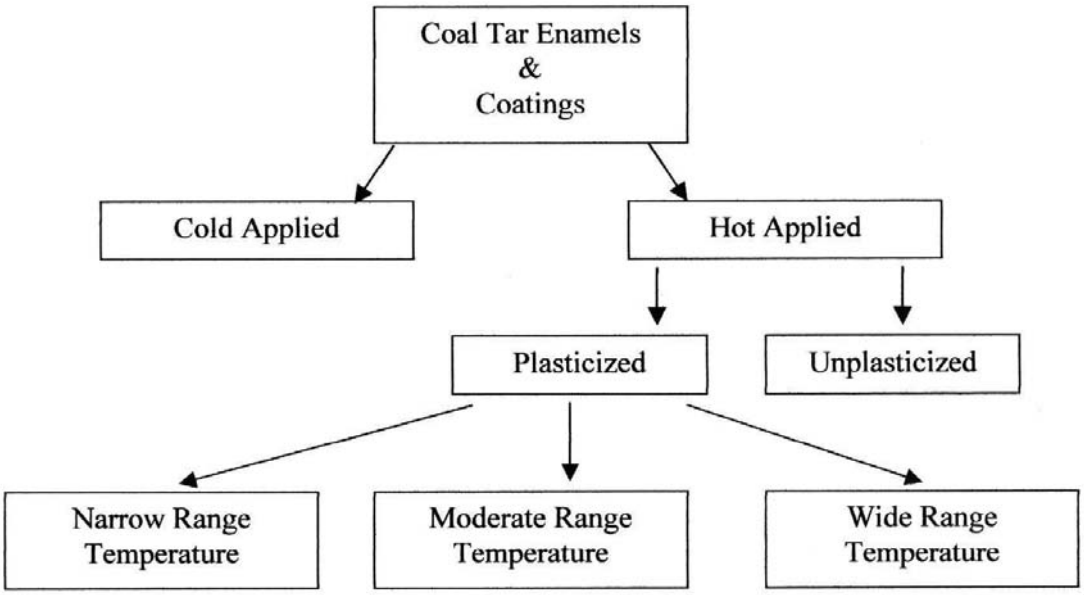

Figure 1. Categories of coal tar enamels and coatings.

The simplest method to reduce cold flow and to prevent sagging in enamels is to raise the softening point of the pitch by distillation. Chemical methods such as oxidation and dehydrogenation are optional treatments, but are rarely used. The addition of inorganic fillers to coal tars is quite effective in reducing brittleness and improving the mechanical properties of enamels. Further reduction in enamel brittleness, especially at low-temperature service, is achievable by digestion of bituminous coal in the pitch or oils. The digestion of coal results in enamels being "plasticized". Coal digests consist of mixing bituminous coal with coal pitch, heavy coal tar oil, or a combination thereof. Heating the mix below the thermal decomposition temperature of the coal, the pitch and oil partially dissolve the coal to form a "colloid" or "gel". The effectiveness of coal tar enamels can be attributed in large measure to the forces established between the solvent components, in this case pitch and oil, and the coal itself.

Development of coal tar enamel still remains a black art. The processes and ingredients used in enamel formulations that affect performance have evolved over many decades, if not centuries, through trail-and-error or cook-and-look methods. Ultimately, it is the result of extended field service that guides the manufacturer of coal tar enamel to produce a spectrum of specifications.

Laboratory studies of enamels made with charges of the same coal (18wt% VM), pitch (45°C softening point), and creosote oil have been previously reported.[1] Digestion took place in a stirred-batch mixer for 3 hours at 315°C. In Figure 2 are shown the effects of increasing coal content during digestion in *pitch* alone. There is about 3.8°C increase in softening point temperature for each percent increase in coal. Increasing the coal content makes the enamels more rigid, as evident by the penetration trends.

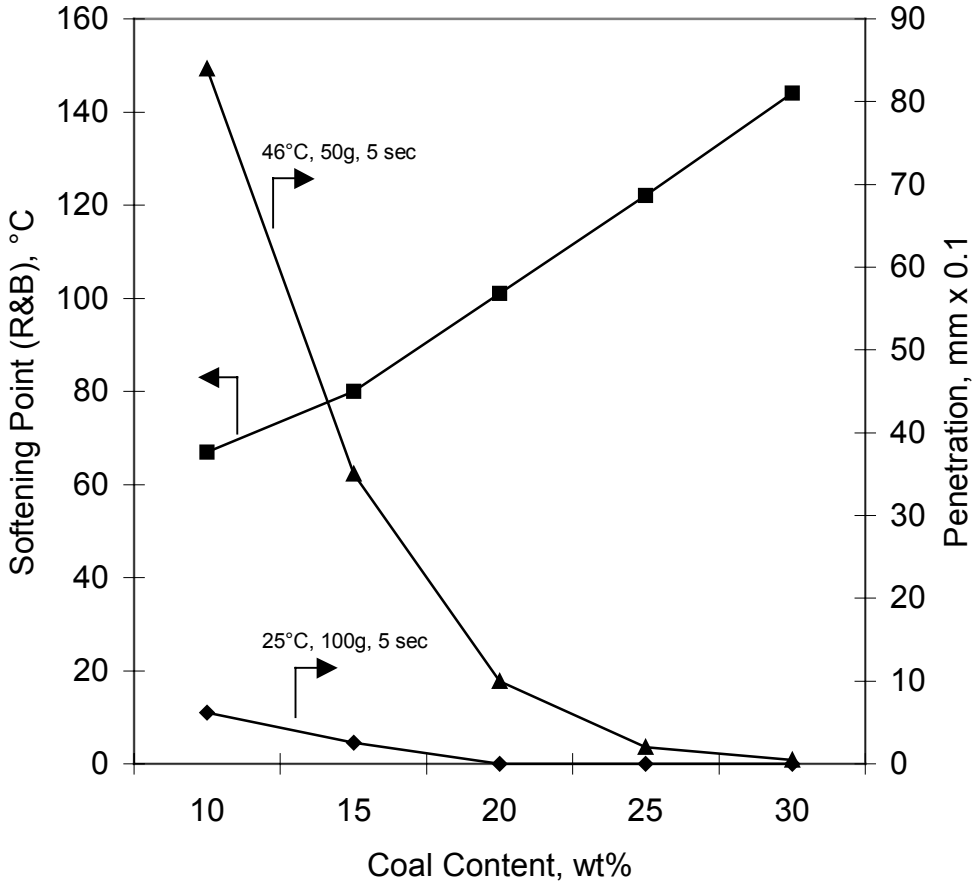

Figure 2. Effects of increasing coal content in pitch-alone digestion.[1]

The effects of digestion of coal in *oil* alone are indicated in Figure 3. Similar to the case involving only pitch, increasing the content of coal decreases softening point and penetration. Note that penetration behavior is much more pronounced because of the greater plasticizing power of the oil. Normally oil content is kept to a minimum, however, to reduce volatile emission during application and in service.

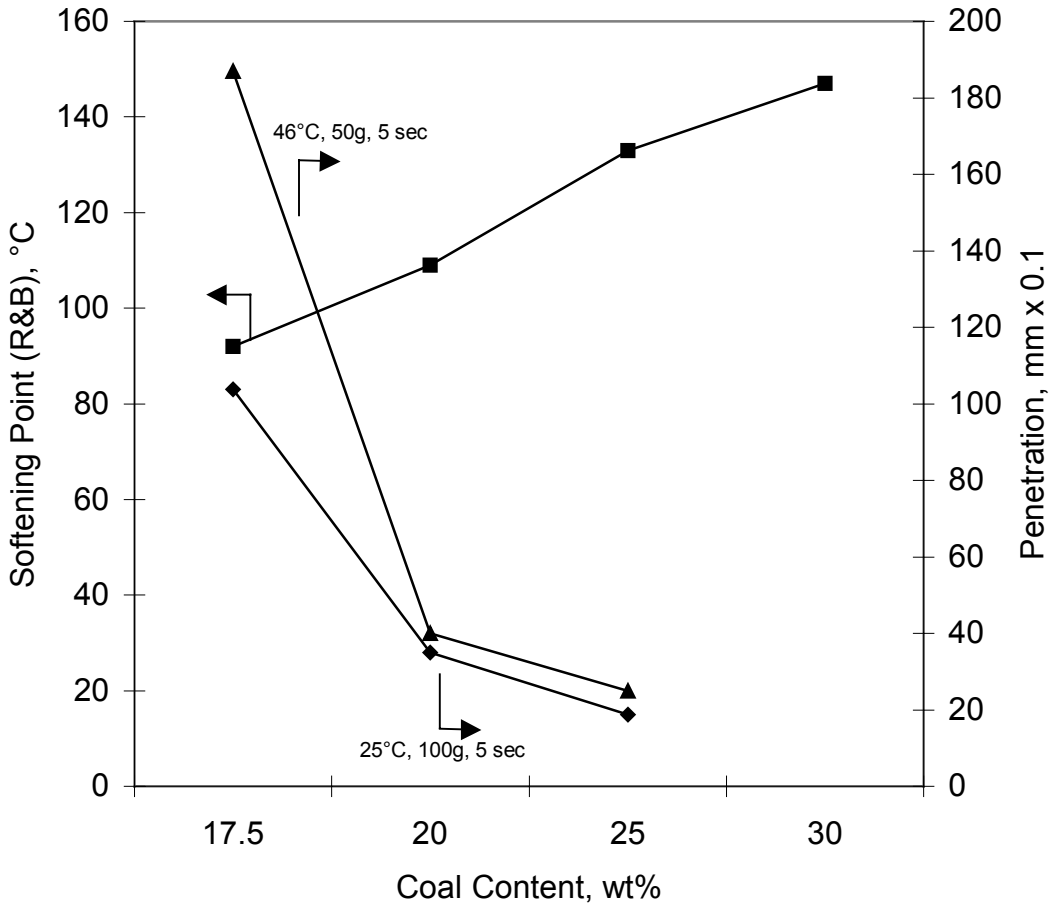

Figure 3. Effects of increasing coal content in oil-alone digestion.[2]

Several observations can be drawn from the results. The combination of coal and pitch alone produces enamels that are very hard and brittle. The enamels exhibit wide-temperature susceptibility as well, i.e., the 46 to 25°C penetration ratios are large. On the other hand, coal in oil alone produces high-softening point, but very soft enamels. An advantage in using oil over pitch is the narrow-temperature susceptibility, i.e., the 46 to 25°C penetration ratios do not change dramatically with softening point temperature. Interestingly, it was noted that the coal digested readily in the pitch but the oil required considerably longer processing time to complete its action on the coal. The effect agrees

with what is known about coal extraction processes in that condense aromatic molecules can extract or disperse large percentages of coal.[3-4]

Satisfactory enamels can be produced by combining separate pitch- and oil-digested coal together. For example, two enamels were prepared by digesting 25wt% bituminous coal in either pitch or oil. A composite was made by blending the separate enamels in a 50:50 ratio. As shown in Figure 4, penetration increases as the proportion of oil increases, as expected. Curiously, the softening point temperature for the blend is significantly lower than the softening point temperature of either individual enamel. This phenomenon is often encountered, demonstrating that many of the properties of enamels cannot be predicted based on simple mixing rules.

Normally, enamels are not made by combining separate pitch- and oil-digested coal because of the difficulty in controlling the characteristics of the blend. Once the amount of coal is determined and held relatively constant, the quantities of pitch and oil are manipulated until the desired softening point temperature and penetration are obtained. The results in Figure 5 are for enamels containing 33.3wt% coal digested in various proportions of pitch and oil. Similar to the results shown in Figure 4, the softening point temperature of coal digested in both pitch and oil is lower than in either coal liquid itself.

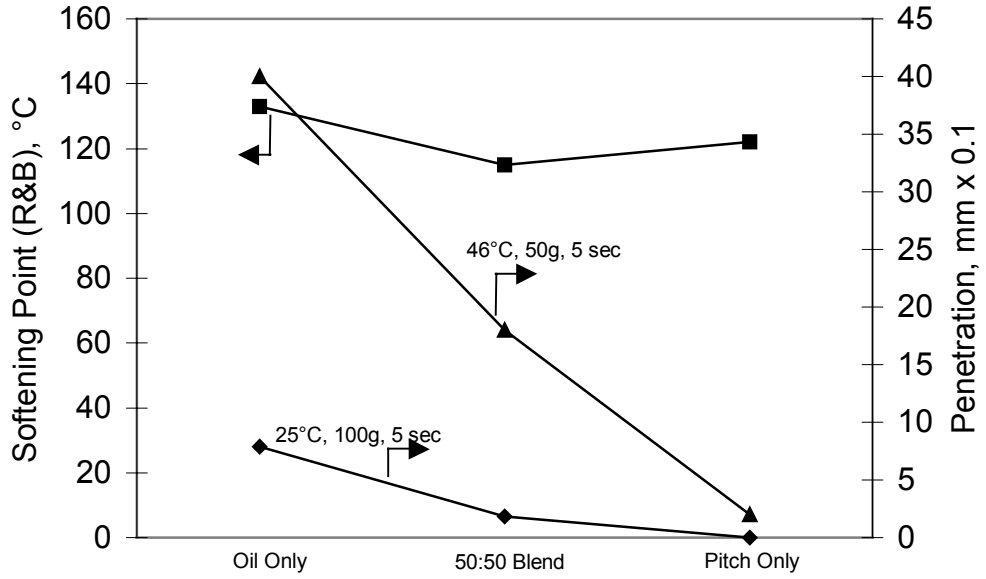

Figure 4. Effects of blending coal-digested enamels on softening point and penetration.[5]

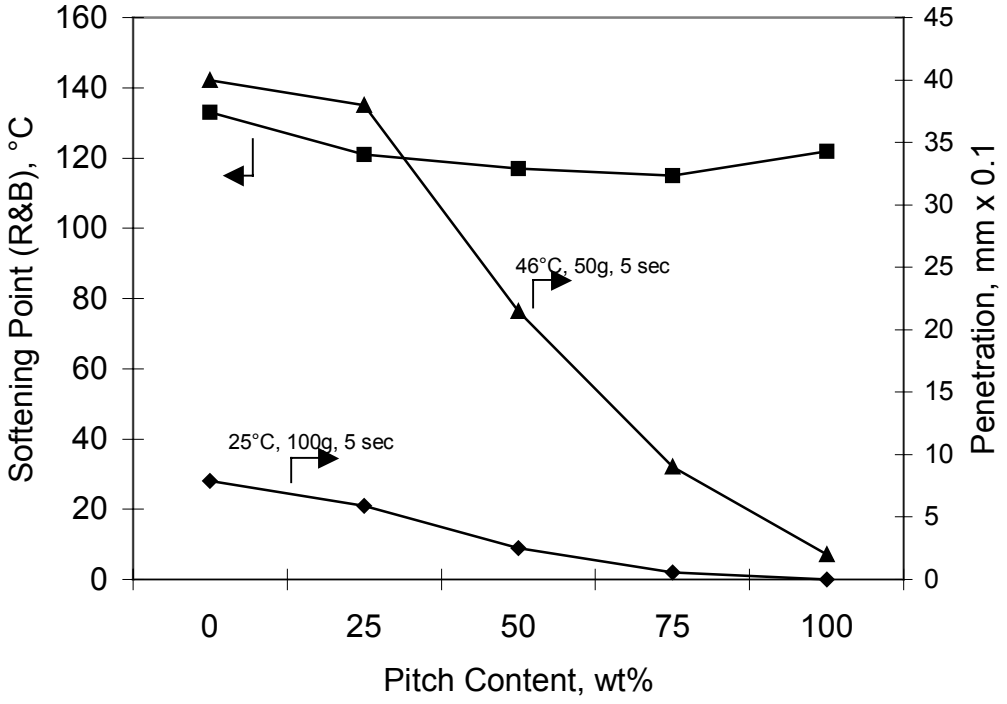

Figure 5. Effects of coal digestion in pitch and oil at constant coal content.[6]

Fillers are added to coal tar enamel to impart further reduction in brittleness and to increase mechanical strength. By far the most common fillers are pulverized talc and related minerals. These substances are nonabrasive and their foliated nature prevents settling in mixing and holding tanks. The characteristics of three fillers on enamel softening point temperature are shown in Figure 6. Note the relative insensitivity of softening point on the addition of talc.

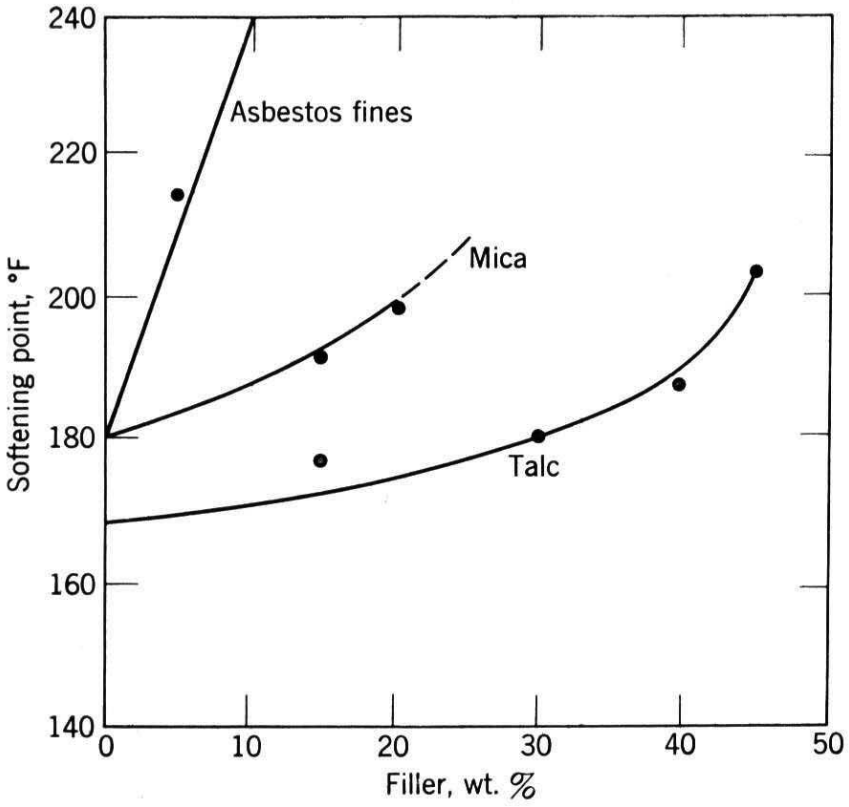

Figure 6. Effect of filler content on softening point temperature.[7]

4 EXPERIMENTAL

This research project focused on the development of synthetic coal tar enamel that would be categorized as a wide-range temperature product. Thus, the intent was to match the properties of synthetic coal tar enamel with those of commercial enamel as closely as possible.

4.1 Characterization of Commercial Coal Tar Enamel

A 5-gallon container of commercial coal tar enamel was obtained and subjected to testing to determine some if its gross properties. The test methods employed are shown in Table 1, and the average of duplicate measurements is shown in Table 2. The properties of the commercial coal tar enamel provided by the manufacturer are shown in Table 3.

Table 1. Test methods used to characterize coal tar enamel and pitches.

Determination	Test Method
Softening Point, °C	ASTM D3104
Toluene Insoluble (TI), wt%	Soxhlet Extraction
Pyridine Insoluble (PI), wt%	Soxhlet Extraction
Conradson Carbon Residue, wt%	ASTM D189
Ash Content, wt%	ASTM D2415
Viscosity, cP	Brookfield Viscometry

Table 2. Measured properties of commercial coal tar enamel.

Softening Point, °C	121.2
Toluene Insoluble, wt%	56.0
Pyridine Insoluble, wt%	53.4
Conradson Carbon Residue, wt%	60.5
Ash Content, wt%	30.0

Table 3. Manufacturer's specifications for coal tar enamel.

Measurement	Specification
Softening Point, °C	120 to 130
Ash Content, wt%	25 to 35
Application Temperature, °C	232 to 260
Penetration, 25°C, 100g, 5sec	2 to 9

The softening point temperature confirmed that this particular type of enamel is suited for hot-applied coatings. The high-temperature ash content of 30wt% indicates significant addition of inorganic fillers while the amount of pyridine and toluene insolubles suggests that the oil and/or pitch used in this formulation are highly soluble. The Conradson carbon residue is high, undoubtedly resulting from significant amounts of filler. The effect of temperature on viscosity of the coal tar enamel is shown in Figure 7, with a conventional coal tar binder pitch (110°C softening point) used for comparison.

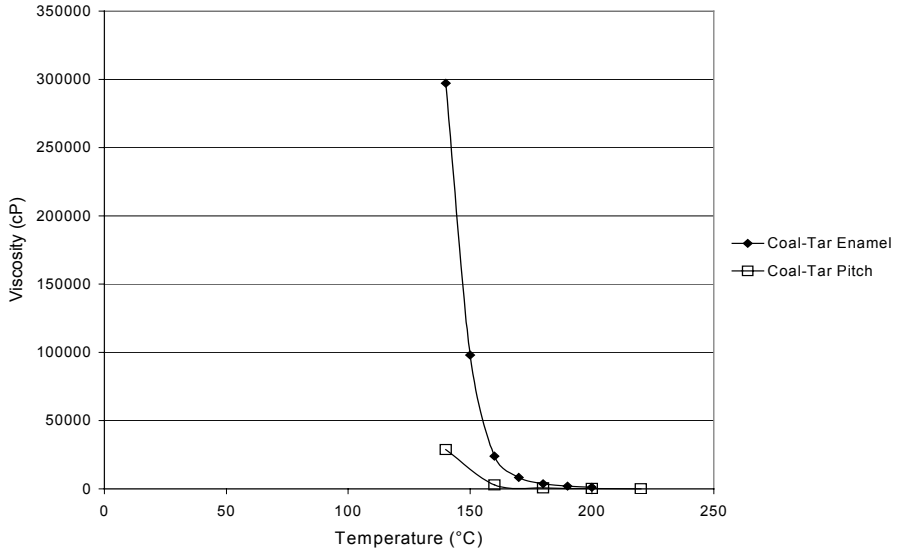

Figure 7. Effect of temperature on coal tar enamel viscosity.

4.2 Development of Coal-Extract Pitch

A West Virginia bituminous coal was extracted in tetralin and deashed by solvent extraction using N-methyl pyrrolidone as described elsewhere[8]. Characterization results of the feed coal are presented in Table 4 and properties of the coal-extract pitch are shown in Table 5.

Table 4. Basic characteristics of bituminous coal feed used in extraction.

Proximate (as received), wt%	
Moisture	0.82
Fixed Carbon	60.49
Volatile Matter	34.41
Ash	4.27
Petrographic Composition, vol%	
Vitrinite	71.4
Liptinite	5.5
Inertinite	21.7

Table 5. Characterization results of coal-extract pitch.

Softening Point, °C	130.5
Conradson Carbon, wt%	40.6
Ash Content, wt%	0.15
Density, g/cm^3	1.189
C/H Atomic Ratio	1.10

4.3 Development of Synthetic Coal Tar Enamels

As mentioned previously, coal tar enamels are made from bituminous coal, pitch, oil, and inorganic fillers. The bituminous coal used as the plasticizer is mined in West Virginia. Some of the basic characteristics of the coal are provided in Table 6. The oil, which is a coal tar distillate, was acquired from a commercial vender. The vender called the material “heavy oil,” which was a room temperature liquid containing about 1-2wt% insoluble solids. For some of the formulations the heavy oil was vacuum-distilled in

conventional laboratory glassware at 10mm Hg up to an end point of 250°C. The distillation was required to reduce volatility of the heavy oil. Talc (hydrous magnesium silicate, <350 mesh) was purchased from a chemical supply company and used as is.

Table 6. Characteristics of coal used as a plasticizer in synthetic enamels.

Proximate (dry basis), wt%	
Fixed Carbon	57.91
Volatile Matter	33.17
Ash	8.92
Petrographic Composition, vol%	
Vitrinite	74.6
Liptinite	5.0
Inertinite	16.1

Processing protocols were developed using a 1L-stirred autoclave by adding the appropriate proportion of feeds. The coal was dried and ground to a 150-mesh sieve top size. In all experiments, the total mass added to the vessel was held constant at 158g. Heat was applied until the mixture became sufficiently fluid after which the autoclave lid was bolted to the body. Stirring rate was 1000rpm and the reactor contents were brought to temperature and held there for 2 to 3 hours. After the coal digestion period, the reactor was opened and the contents poured into a metal pan to cool.

4.4 Determination of Pitch Volatility

The standard test of pitch volatility (ASTM D4893) stipulates that a sample of pitch must be placed into a preheated 350°C zone of a specific design. After 30 minutes the loss in mass is determined. For this research project, volatility was determined on a Leco thermoanlyzer by placing 1 to 2 grams of an enamel sample into a tared ceramic crucible. The sample was then placed into the instrument and brought to 350°C as rapidly as possible (about 20 to 25 minutes) and held at this temperature for thirty

minutes while monitoring weight changes. For an additional test, in order to ascertain weight loss at higher temperature, the sample was heated rapidly to 400°C and held at the higher temperature for 30 minutes while monitoring weight changes. The volatility tests were all conducted under a nitrogen blanket.

Select enamels were distilled in a Saybolt distillation flask. About 20g of sample were introduced into the flask and the bottom portion buried in sand for the even distribution of heat. Heat was applied by a gas burner to vaporize the volatile components, which were condensed and collected. The distillates were analyzed on a Saturn gas chromatograph/mass spectrometer (GC/MS) to determine composition.

4.5 Cathodic Disbonding Testing

A cathodic disbonding test was developed by modifying the ASTM G8-96 method. Steel coupons (3 ½ x 1 x ⅜ inches) were polished with fine abrasives to remove surface corrosion and dirt. The coupons were rinsed with de-ionized water and dried at 110°C, then wiped clean with acetone and dried again before coating with enamel. Coating was accomplished by first melting the enamel in a beaker to 250°C in an oven and quickly dipping the room-temperature steel coupon to a depth of about 2 inches. However, this procedure did not result in firm bonding of the enamel to the surface of the steel. Thus the test coupon was preheated to 250°C and then dipped twice into the 250°C molten enamel to form a smooth covering between 2 to 3mm in thickness. The adhesion using this approach appeared to be better than dipping the cold coupons into the molten enamel. Prior to the disbonding experiment, a circular holiday of about 6mm in diameter was made to expose some of metal surface to the salt solution.

A conductive, alkaline electrolytic solution was prepared by dissolving 1wt% each of the technical-grade salts, sodium chloride, sodium sulfate, and sodium carbonate, in de-ionized water. An imposed electrical potential of 1.5V was supplied by a potentiostat (BAS Power Module, model PWR-3) to the coupon at about 3mA for the duration of 4 weeks. At the end of the experiment the coupon was inspected visually for defects and the coating removed carefully to determine corrosion. Figure 8 is a schematic of the experimental set up.

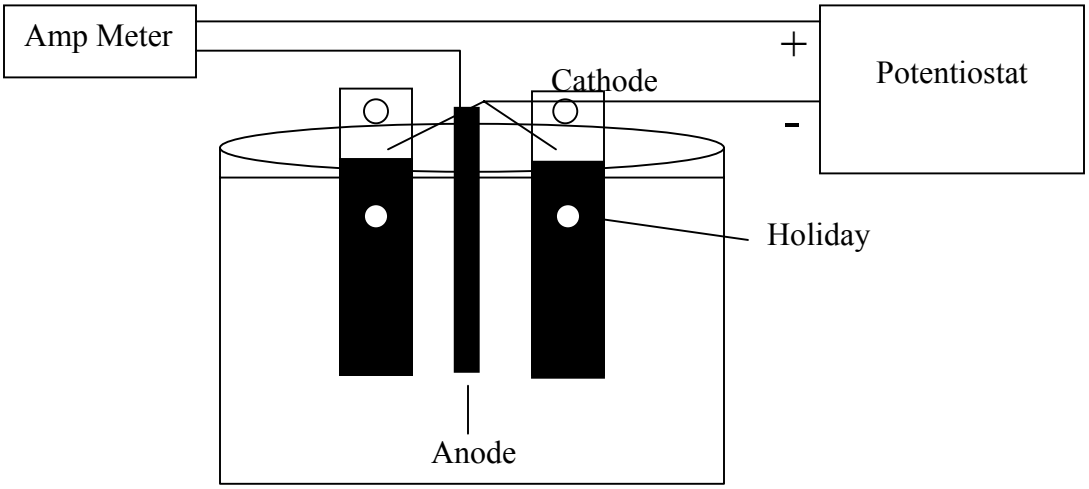

Figure 8. Schematic of cathodic disbonding experiment.

4.6 Carbon Foam Coatings and Metal Composites

4.6.1 Water Penetration of Enamel Coated Carbon Foam

Two pieces of carbon foam were cut into approximately 0.4 x 0.8x 0.5-inch rectangles. Coatings were made by first preheating both the enamel and foam to 250°C and then dipping the foam rapidly into the molten enamel two times and then allowing

them to cool to room temperature. The samples were submerged in a beaker of de-ionized water for a week and weighed to determine water weight gain.

The ASTM G9-87 procedure for determining water vapor requires several months to complete. Because of the time constraints of this research project, an accelerated water-penetration method was devised. The accelerated method was conducted under pressure. The coated carbon foam was inserted into a $50cm^3$ tubing bomb along with $25cm^3$ of de-ionized water. The reactor was pressurized with 500psig nitrogen. At various time intervals, the reactor was de-pressurized and the samples removed and allowed to air dry. After weighing to determine weight gain, the samples were reinserted the reactor and pressurized with nitrogen for another determination.

4.6.2 Carbon Foam/Steel Composite

Carbon foam/steel composites were produced using coal tar enamel as an adhesive. Two different types of composites were produced, one for tensile testing and the other for flexural testing via three-point bending. The steel for the tensile sample was 2.54cm 1018 carbon steel round stock machined into the shape shown in Figure 9. This particular shape was needed in order to secure the sample properly for testing. The grips are 0.4763cm thick and approximately 1.90cm to 2.50cm long. The foam was cut using a 3.18cm hole-saw that had the pilot bit removed.

Figure 9. Foam-steel composite for tensile test.

The enamel adhesive was heated to 250°C and allowed to become molten. The metal tabs were dipped into the enamel to coat and then were attached to the foam and allowed to cool. Tensile testing for the samples was done on an Instron tester.

The second type of composite, Figure 10, was made from automotive grade sheet metal cut into 2.54cm by 15.24cm sections and then attached to carbon foam 1cm thick by pouring some molten enamel onto the metal sheets and pressing the foam onto the enamel. The composite was then placed into the 250°C oven for approximately 1 minute to help set the enamel onto the foam.

This composite was tested using a three point bending method by modifying ASTM D790. Two pieces of the cut sheet metal, one set upon the other, and a tri-layer of sheet metal and packing foam cut to the same dimensions as the carbon foam, were used for comparison. The steel-packing foam-steel tri-layer was held together with rubber cement. This was done to allow for testing of objects of the same geometry. There were several differences between the method used and the ASTM standard, most notably the span to depth ratio was less than the 16:1 specified by ASTM D790. The composite had

a span to depth ratio of 6.89:1, while the sheet metal reference had a span to depth ratio of 60:1.

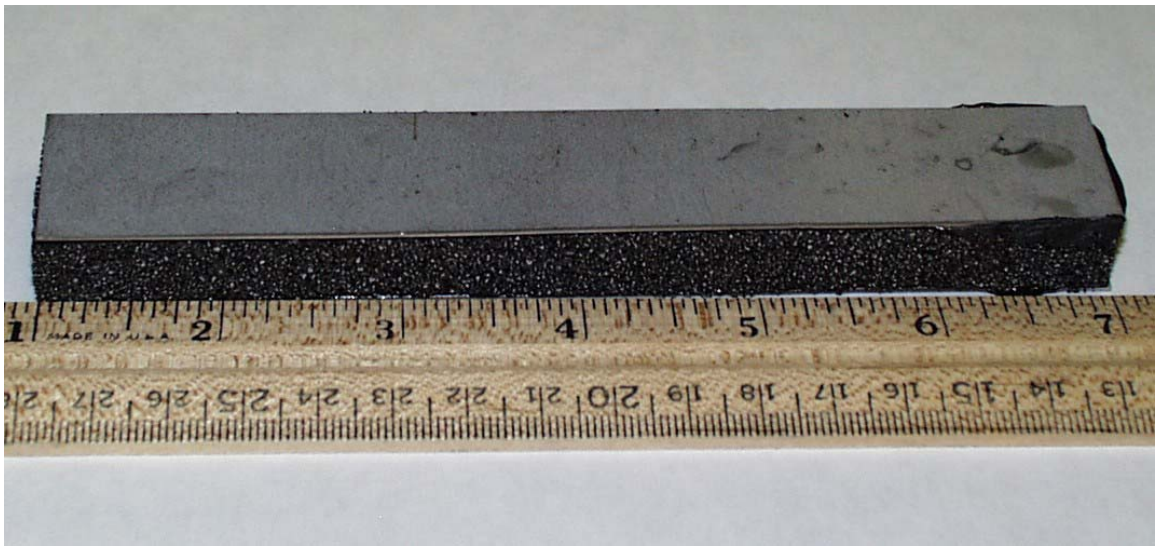

Figure 10. Foam-steel composite for flexural testing.

4.7 Other Characterization Testing Methods.

Penetration tests were conducted on a Humboldt H-1240 penetrometer following the ASTM method D5-97 at 22, 46, and 55°C under applied force of 50, 100, 150 and 200 grams for 5 seconds. Four penetration determinations were made at each temperature and the average penetration reported. Elemental analysis was accomplished on a ThermoQuest analyzer and the average of three determinations is reported. Select samples of enamels were embedded in plastic and polished following conventional procedures for examination by optical microscopy. Photomicrographs were taken on a Zeiss Axioskop reflected light microscope.

5 RESULTS AND DISCUSSION

5.1 Preparation and Characterization of Synthetic Enamels

A commercial coal tar enamel was used as the control material in all of the characterization and performance tests. Several synthetic enamels were produced by digestion of coal at 200°C. The formulations are summarized in Table 7 along with softening point temperatures.

Table 7. Synthetic coal-tar enamel formulations and softening point temperature.

	Component Concentration, wt%				
Sample ID	Coal	Coal Pitch	Oil	Talc	SP, °C
J025	20	31	33	15	87.0
J026	25	37	19	19	100.2
J028	18	27	41	14	83.6
J029	18	41	27	14	84.7
J030	25	19	37	19	107.2
J031	35	26	26	13	96.9
J032	18	27	28	27	58.7
J033	16	48	24	12	77.3
J034	0	40	40	20	Tacky
J036	44	22	22	11	113.7
J037	16	24	24	36	76.7
J038	31	46	0	23	135.1

The data in Table 7 indicate that the softening point temperature increased and the enamel became more brittle as the amount of coal was increased. When the amount of pitch was increased, a decrease of the softening point temperature resulted. As the amount of oil was increased, the softening point temperature decreased, and the enamel appeared to be less brittle.

A sample of the synthetic enamel was prepared for optical microscopy. Figure 11 compares the optical features of the commercial enamel with one of the synthetic enamels.

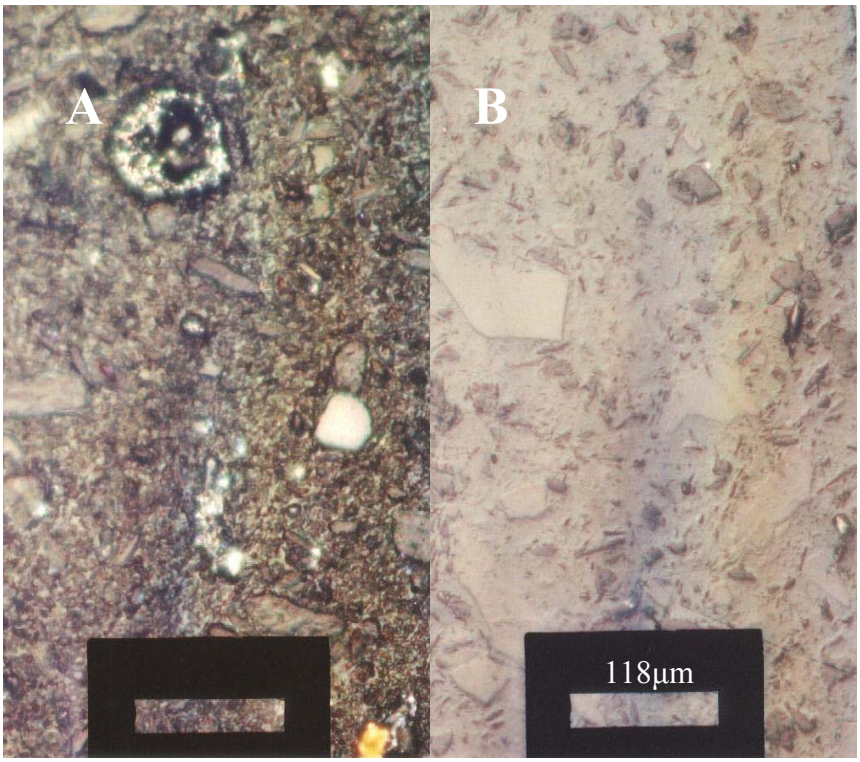

Figure 11. Optical photomicrographs of enamels: A, commercial coal tar enamel; B, synthetic enamel.

It was judged that the coal particles of the synthetic enamel were, for the most part, unchanged. The surface characteristics and particle shapes of the coal did not appear to be affected by digestion. This observation suggested the process temperature of 200°C was too low for the coal to be partially dissolved or digested. Thus the preparation temperature was raised to 300°C for two hours in order to digest the coal more fully, yet a low enough temperature to prevent complete thermal degradation of coal. All subsequent synthetic enamel formulations were prepared at the higher temperature.

Optical examination of these products confirmed that the morphology of the coal particles had been altered, becoming rounded and less distinct, as shown if Figure 12.

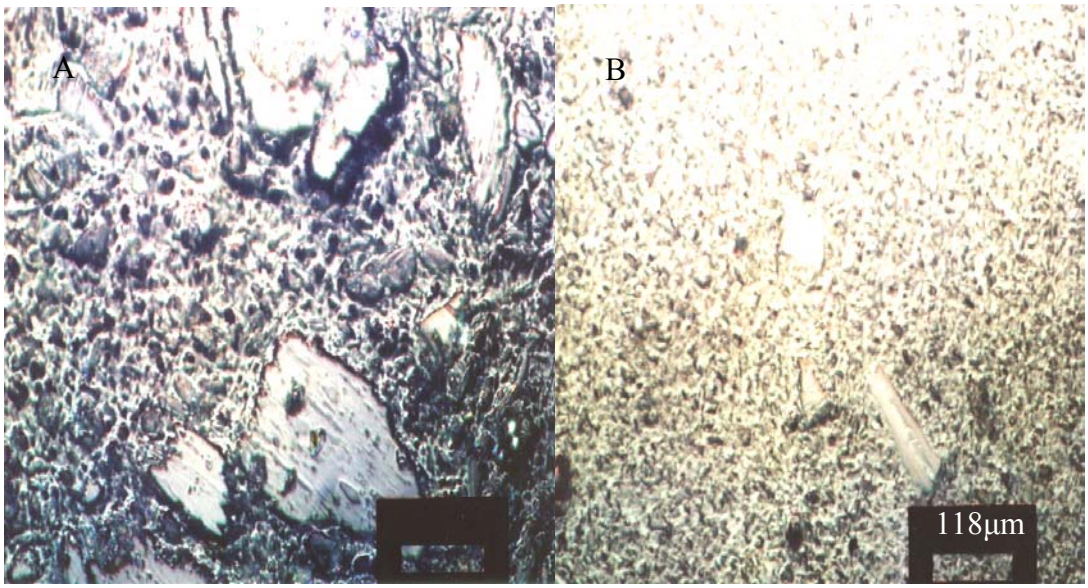

Figure 12. Photomicrographs of synthetic enamels: A at 200°C; B at 300°C

Table 8 shows the compositions of synthetic coal tar enamels that were prepared at 300°C. Figures 13 through 15 show the penetration behavior at 22, 46 and 55°C, respectively.

Table 8. Composition of synthetic enamels digested at 300°C.

	Component Concentration, wt%				
Sample ID	Coal	Coal Extract	Oil	Talc	SP, °C
J040	25	20	30	25	157.9
J041	25	15	35	25	138.1
J042	20	31	33	15	119.2
J044	20	10	42	28	126.0

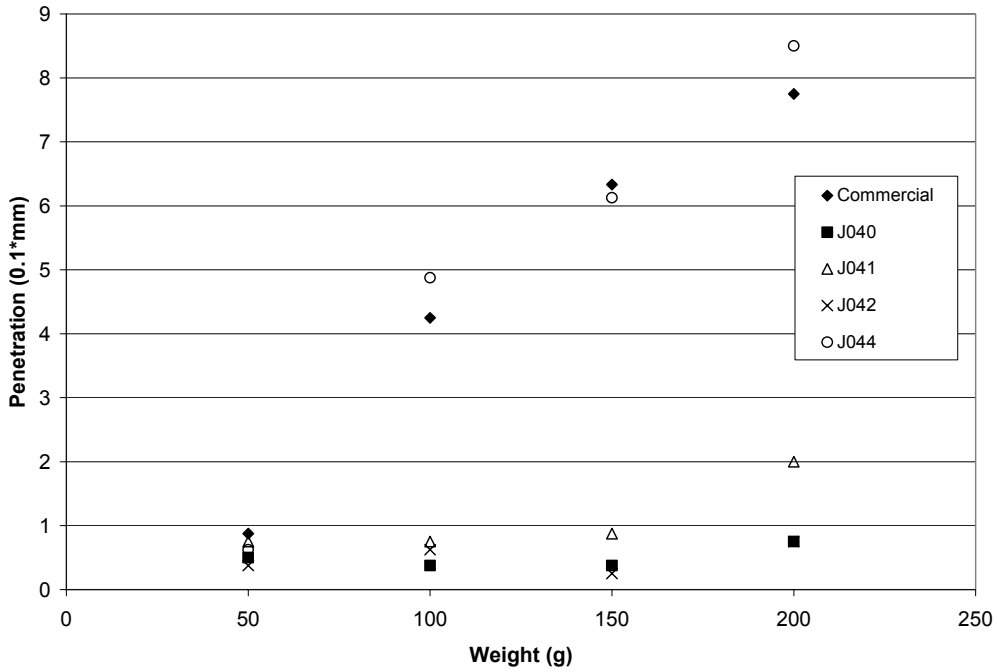

Figure 13. Penetration results at 22°C.

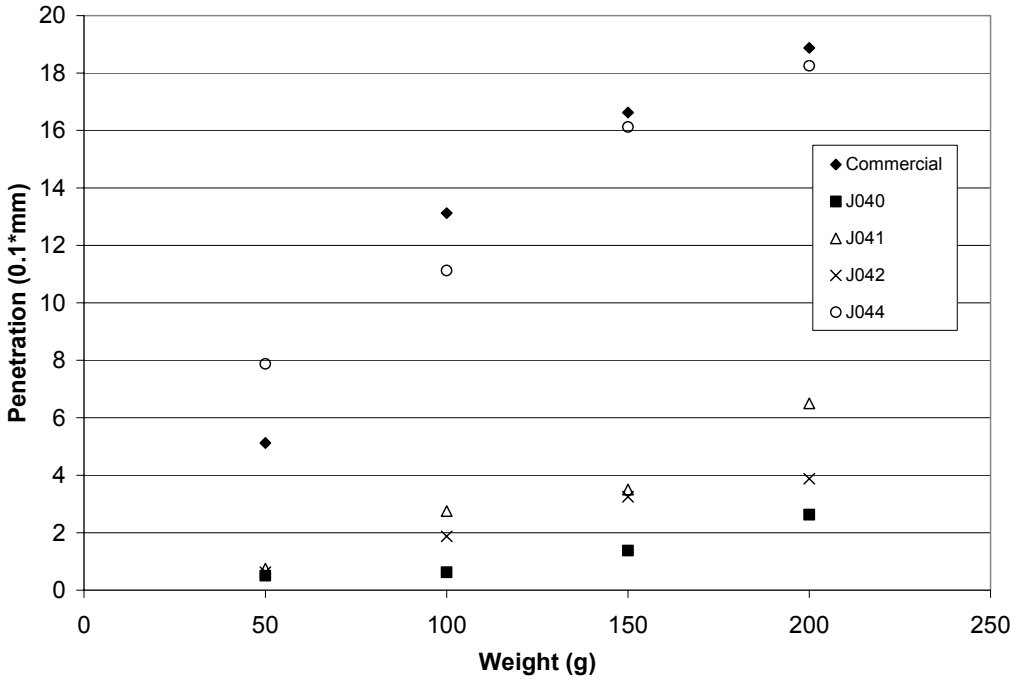

Figure 14. Penetration results at 46°C.

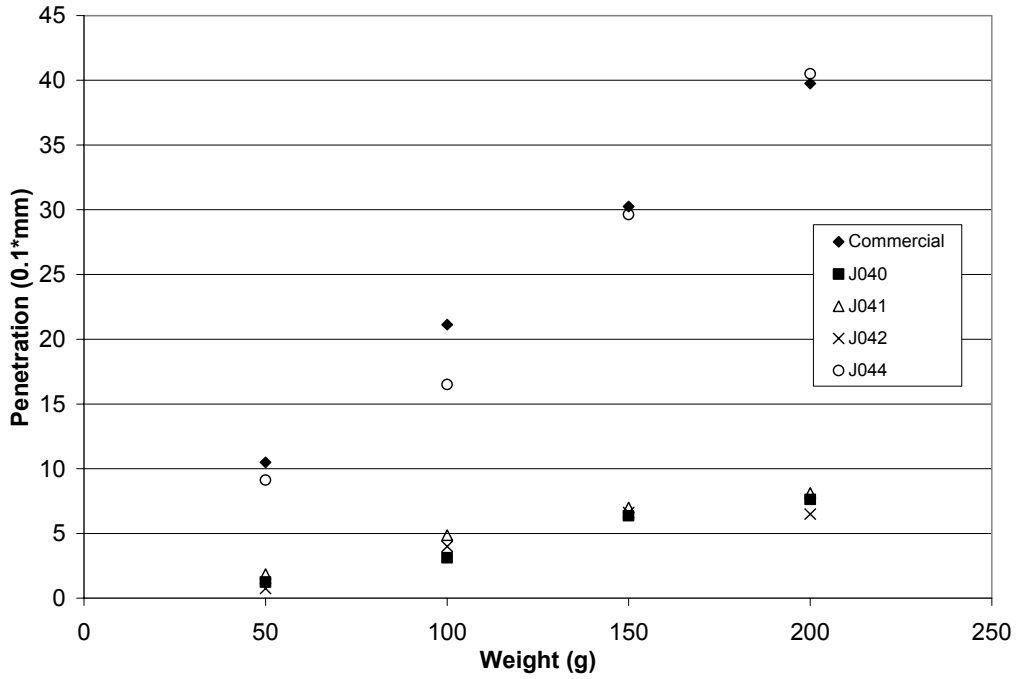

Figure 15. Penetration results at 55°C.

Formulations J040, J041, and J042 were relatively high in coal extract and low in heavy oil content. This combination produced synthetic enamels that were stiff and resistant to penetration when compared to the commercial material. Adjustments were made in the mix recipe (Table 8) to produce synthetic enamel J044. As can be seen, sample J044 behaved quite similarly to the commercial enamel in nearly all respects in terms of penetration.

Although the penetration performance of synthetic enamel J044 matches that of the commercial product very well, the volatile content of J044 was significantly higher, as shown in Figure 16. High volatility is undesirable because of safety concerns.

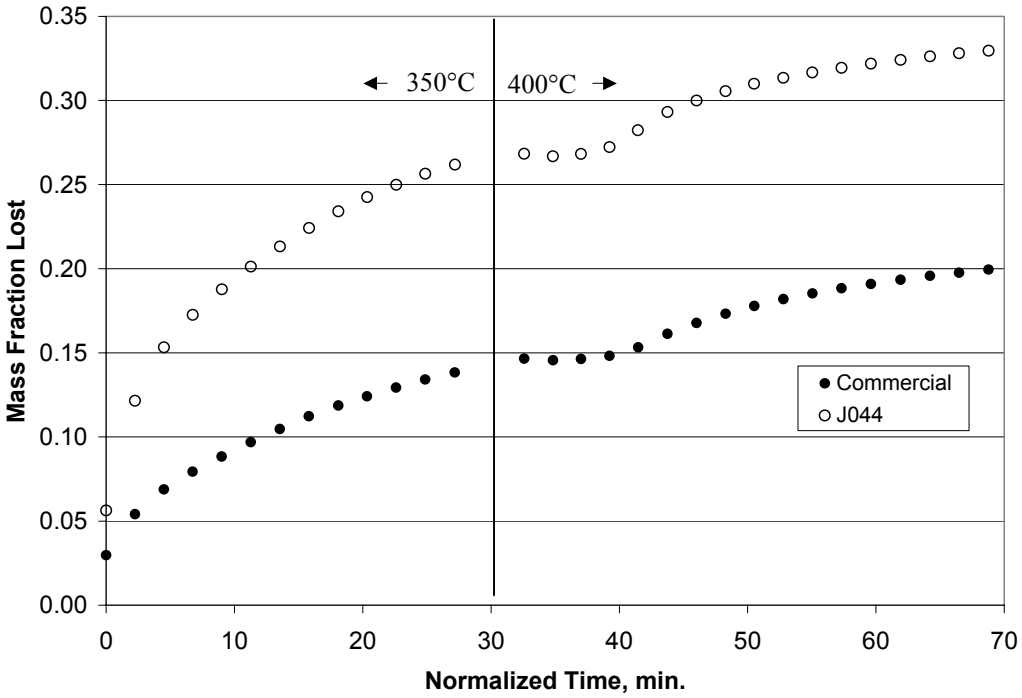

Figure 16. Volatility of sample J044 and commercial coal tar enamel.

It was concluded that the volatility of the synthetic enamel originated with the heavy oil. Thus, a couple of fomulations with similar composition were prepared with distilled heavy oil, as listed in Table 9, and digested at 300°C for 2 hours.

Table 9. Synthetic enamel formulations with distilled heavy oil.

	Component Concentration, wt%				
Sample ID	Coal	Coal Extract	Oil	Talc	SP, °C
*J044	20	10	42	28	126.0
J049	20	10	42	28	130.7
J056	20	10	42	28	126.7

* Prepared with undistilled heavy oil.

Although synthetic enamels J049 and J056 were prepared under similar conditions, the former exhibited penetration behavior more like the commercial enamel than the latter, as seen in Figures 17, 18, and 19. The reason is not known. Part of

reason might be attributed to the greater amount of volatile material in sample J046, as can be seen in Figure 20.

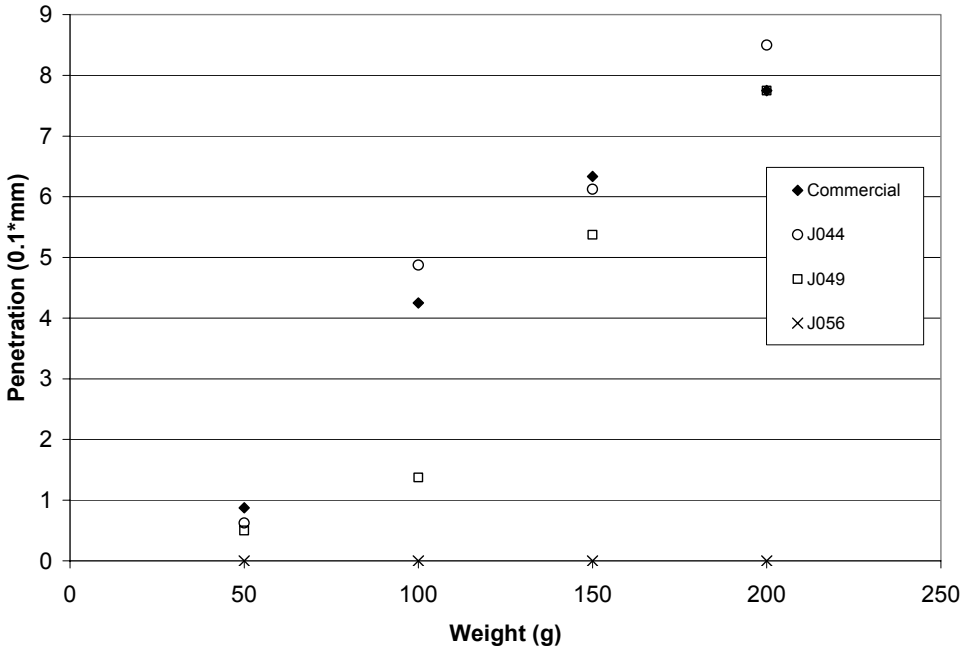

Figure 17. Penetration results at 22°C with formulations containing distilled heavy oil.

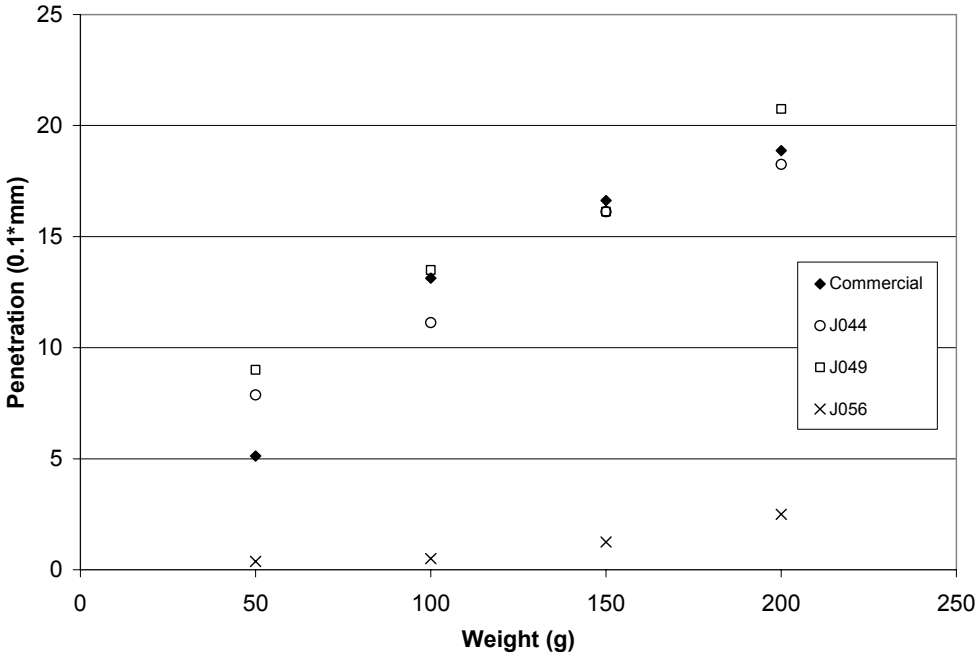

Figure 18. Penetration results at 46°C with formulations containing distilled heavy oil.

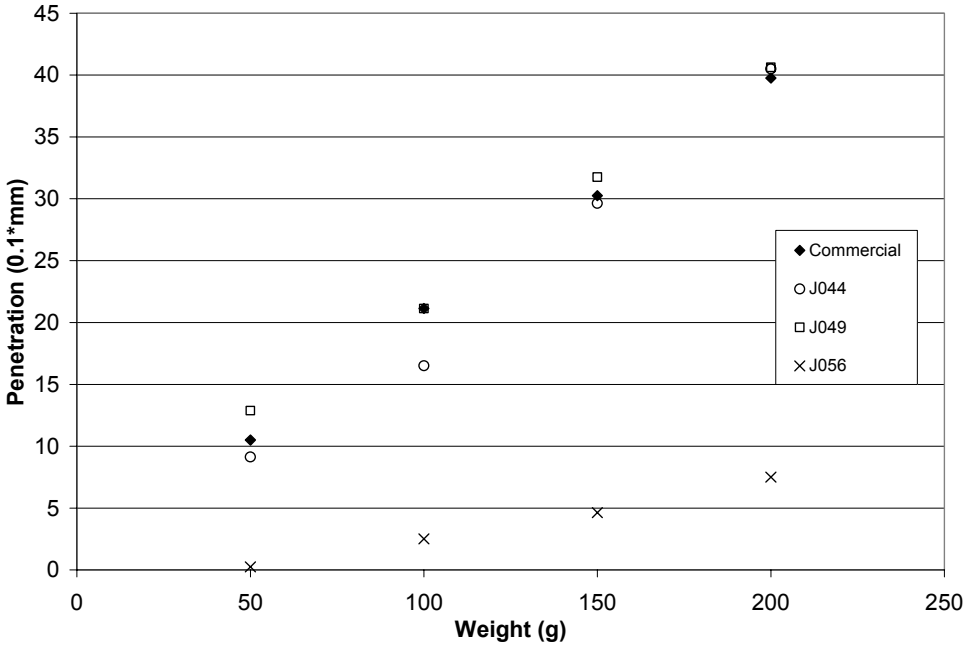

Figure 19. Penetration results at 55°C with formulations containing distilled heavy oil.

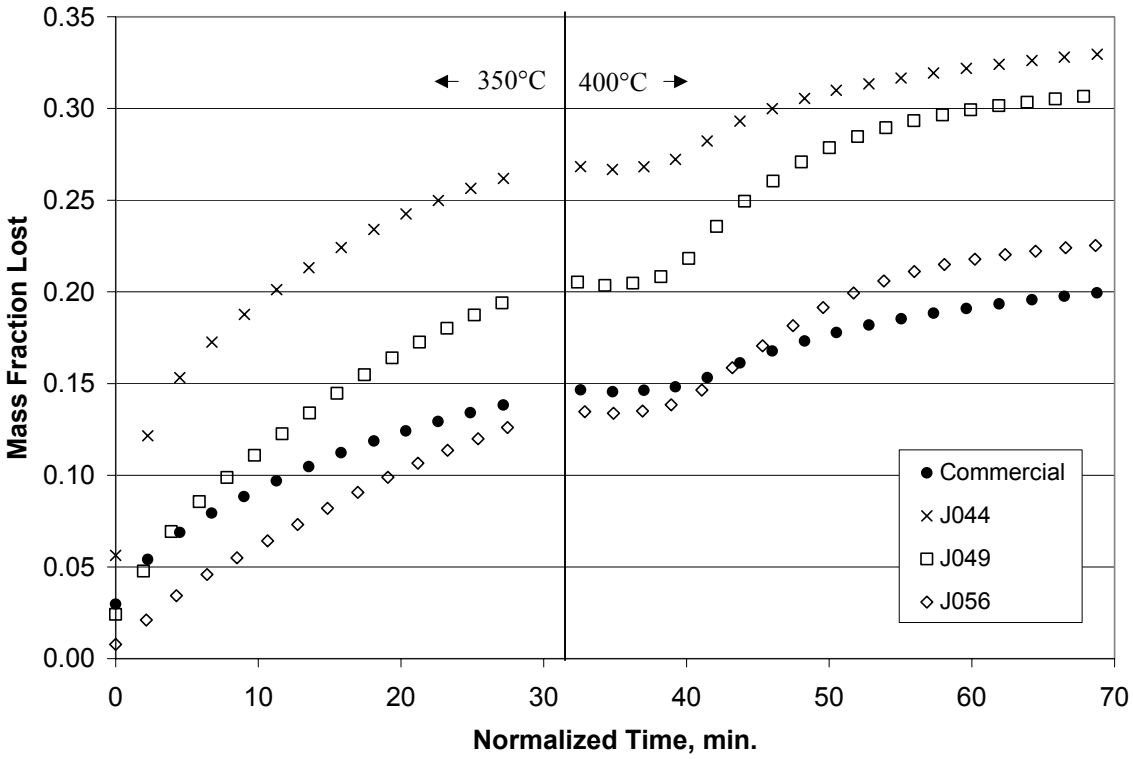

Figure 20. Volatility of samples prepared with distilled heavy oil.

Since the volatile content of J056 is less and J049 more than the volatile content of the commercial enamel, it was possible to make a blend of the two synthetic enamels in order to match the commercial product more closely. Thus, the synthetic enamels J049 and J056 were mixed in a 1:1 ratio at 200°C with the goal of making a blend that would match the commercial material in both penetration and volatility behavior. The blend is identified as sample J060. Penetration behavior of sample J060 (softening point 112.6°C) was less than the commercial enamel for all temperatures, as is evident in Figures 21, 22, and 23. Nonetheless, the volatile content of the blend was judged quite acceptable up to the test temperature of 350°C, as shown in Figure 24.

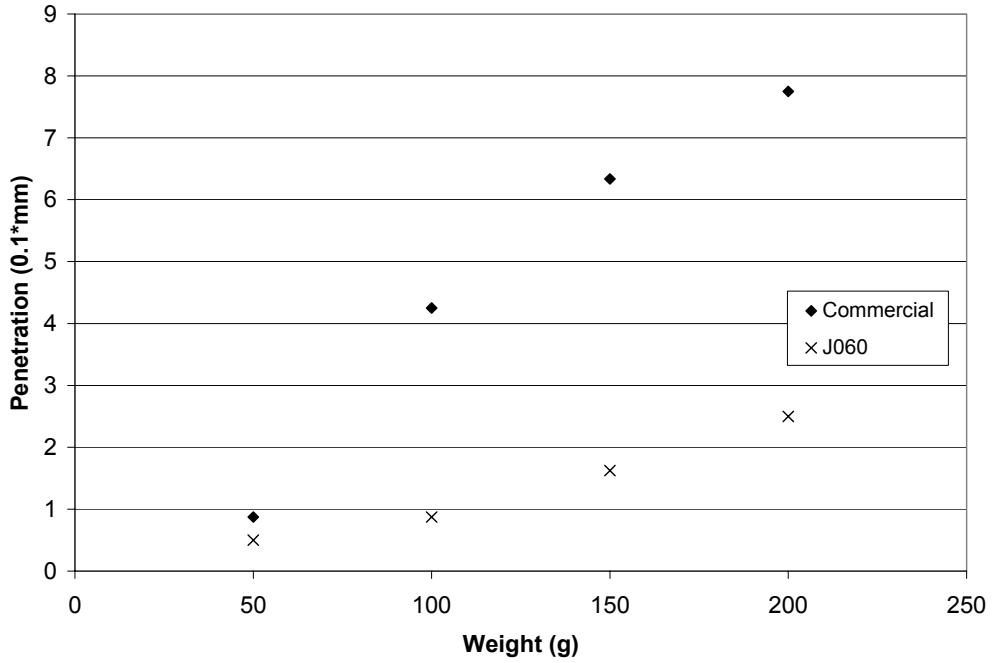

Figure 21. Penetration of synthetic enamel J060 at 22°C.

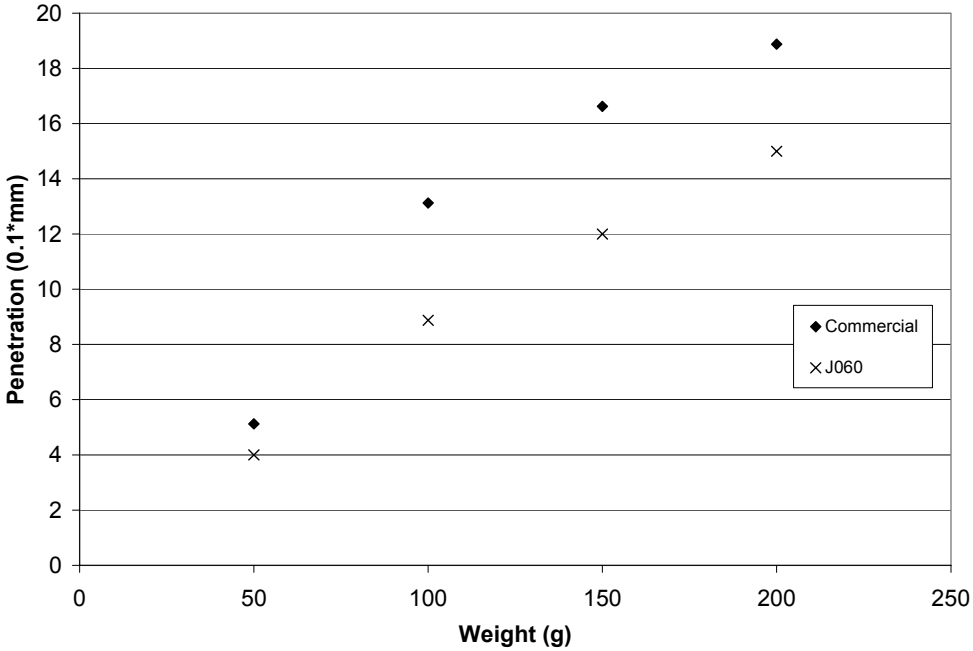

Figure 22. Penetration of synthetic enamel J060 at 46°C.

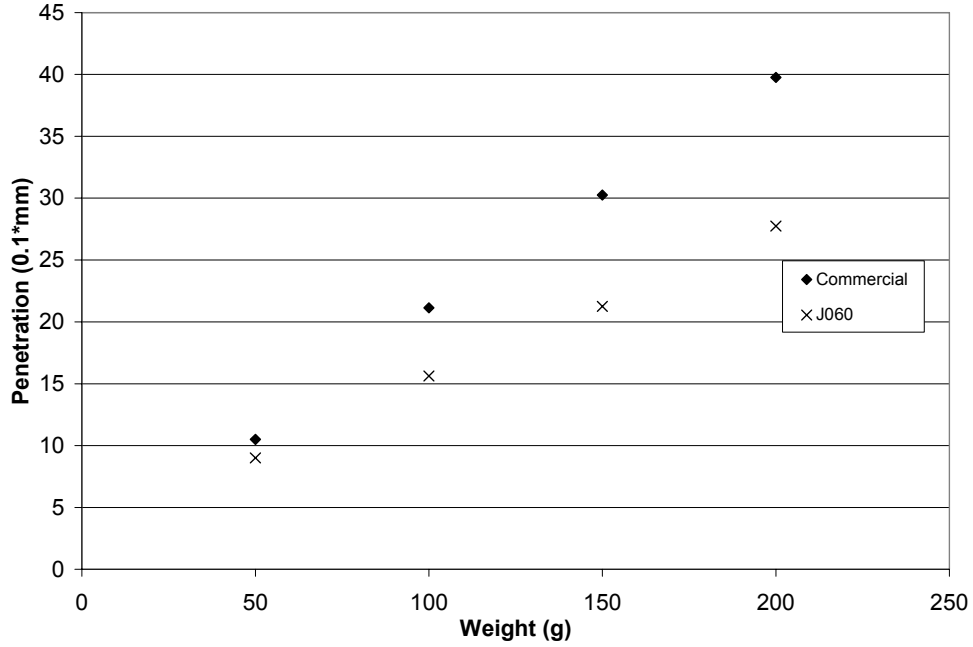

Figure 23. Penetration of synthetic enamel J060 at 55°C.

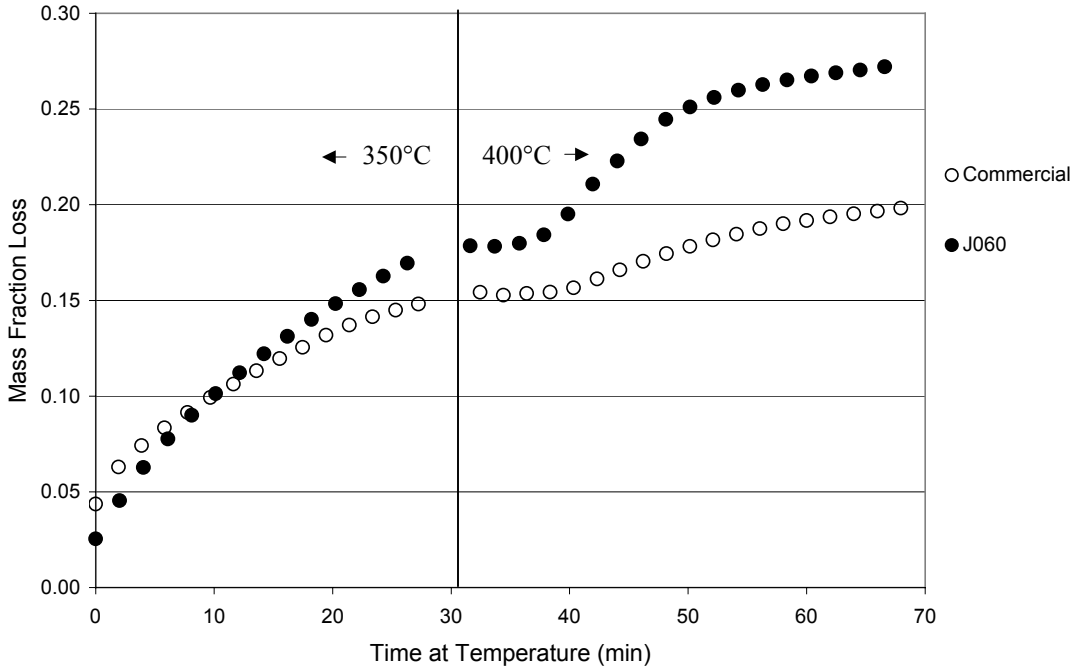

Figure 24. Volatility of sample J060 compared to commercial enamel.

In Figure 25 are shown the effects of temperature on the viscosity of sample J060 and the commercial enamel. The viscosity behavior of J066 is similar, except the synthetic pitch has a lower viscosity at the lower temperatures and somewhat higher viscosity at the higher temperatures compared with the commercial enamel control.

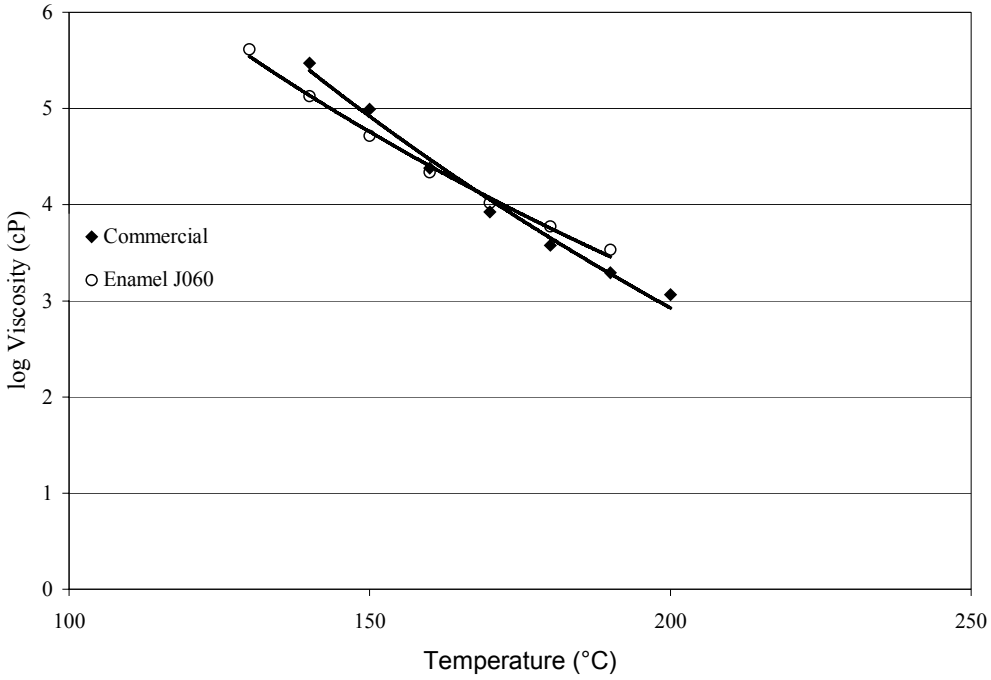

Figure 25. Effects of temperature on viscosity.

5.2 Testing of Synthetic Enamel J060 in Coating and Composite Applications

It was judged that synthetic enamel J060 was the best compromise attainable under the current research project. Consequently, synthetic enamel J060 was then used for the remaining tests related to coatings and composites.

5.2.1 Moisture Resistance

The enamel-coated carbon foam samples were prepared as described in section 4.6.1. After a week of immersion in water, neither the commercial nor the synthetic enamel-coated foam gained any weight. Thus both coated foams were able to resist water penetration under these conditions. The results of accelerated tests (conducted under pressure) are shown in Figure 26, where it can be seen that the synthetic enamel was more effective during the initial period of exposure to water under pressure.

However, both specimens behaved similarly after about an hour. The resistance of J060 during the initial period of the test might be related to its lower penetration numbers and volatile content.

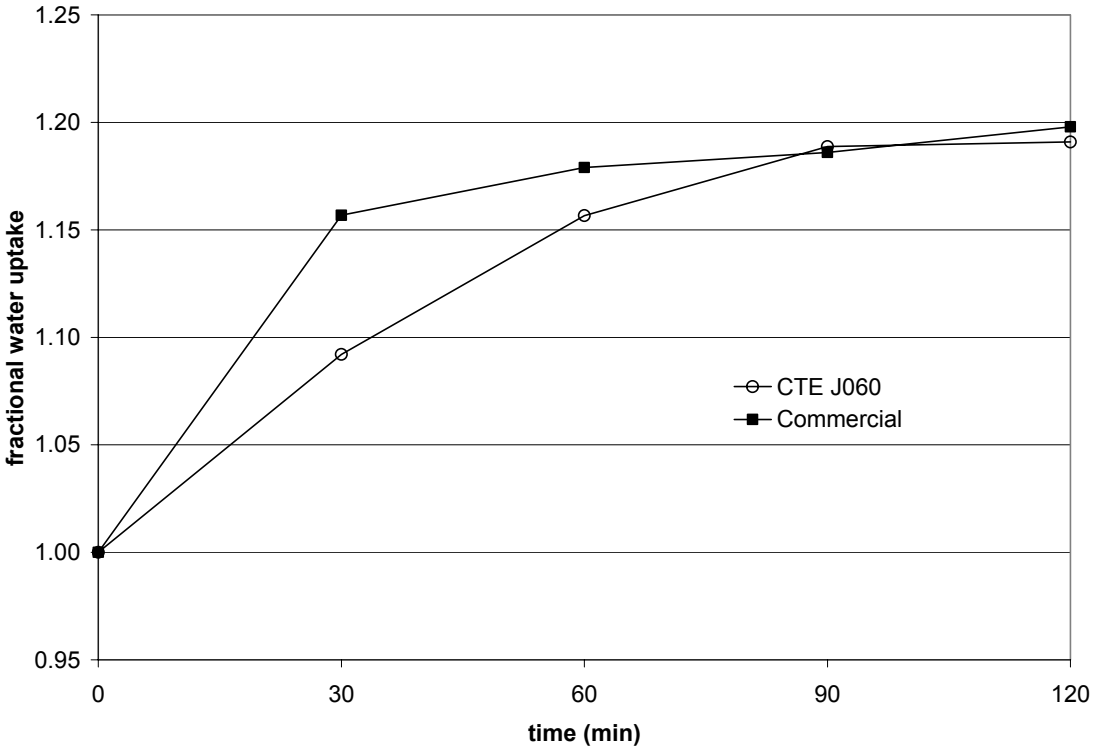

Figure 26. Water uptake of coated foam samples under pressure.

5.2.2 Identification of Organic Composition of Commercial and Synthetic Enamels.

The commercial enamel and synthetic enamel J060 were distilled as described in section 4.4. The condensed material was analyzed by gas chromatography/mass spectrometry, with the chromatographs shown in Figure 27. Both enamels were essentially comprised of the same volatile organic compounds, although the relative proportions were not the same. The synthetic enamel did not contain any measurable components that were not evident in the commercial enamel.

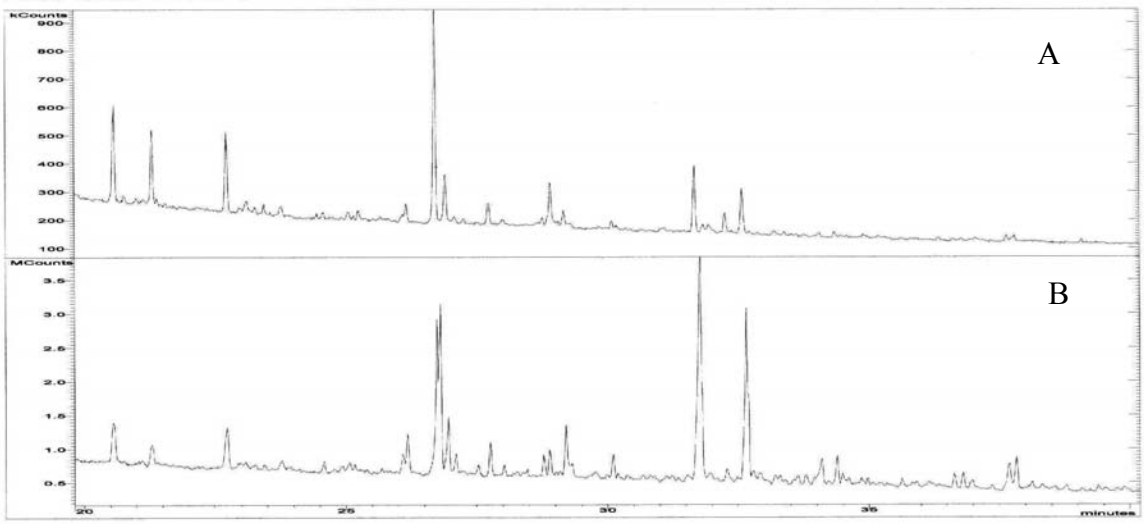

Figure 27. Gas chromatographs of enamel distillates: A, commercial enamel; B, synthetic enamel J060.

5.2.3 Results of Cathodic Protection

Visual inspection of the test coupons revealed no apparent disbonding of the coating from the surface of the metal. However, it was noticed that some "wicking" had occurred since there was a small amount of precipitated salts where the top portion where the enamel coating started. The coatings were removed carefully to reveal the nature of the metal surface underneath, as shown in Figure 28. The synthetic coating came off easily in single layers or pieces but the commercial enamel exhibited greater adhesion to the metal surface. The greater bonding of the commercial product was probably more effective in prohibiting corrosion than the synthetic material.

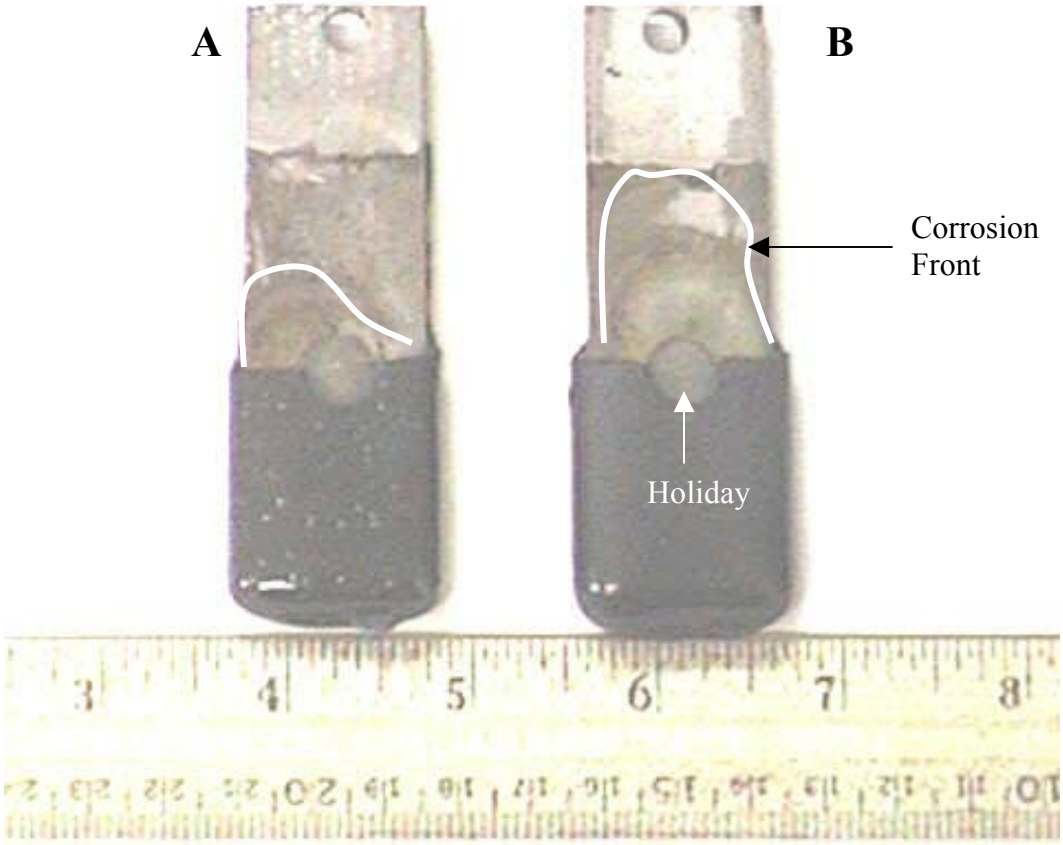

Figure 28. Comparison of cathodic disbonding between commercial enamel and J060: A, commercial enamel; B, synthetic enamel J060

5.2.4 Composite Testing and Evaluation

As discussed in Section 4.6.2, testing for all of the composite samples was performed on an Instron machine. The stress-strain curves shown in Figure 29 represent the result of the tensile test on the first composite type. The graph shows that the commercial enamel has a slightly higher tensile stress; however, the difference between the two is only about 100kPa. However, disbonding occurred at the enamel-metal surface and not at the enamel-foam surface. This is not surprising given the difference in surface area available to the enamel on the foam interface as opposed to the steel interface.

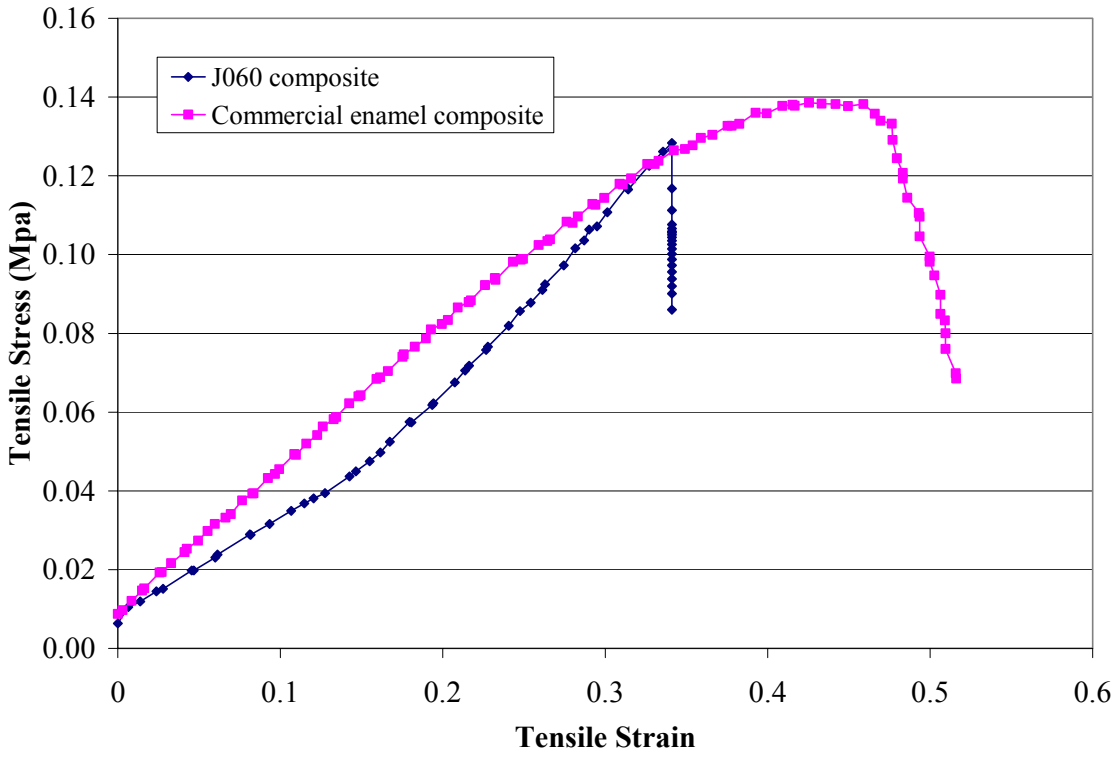

Figure 29. Stress-strain curve for tensile test

The results from the testing of the second composite type are shown in Figures 30 and 31. The most likely explanation for the low flexural stress of the composite in Figure 30 can be attributed to the relative weakness of the carbon foam when compared to steel. The carbon foam was simply crushed between the two pieces of sheet metal, whereas the steel physically bent. In essence, difference in the strength between the carbon foam composite and the steel plates turned the 3-point bend test into a distributed load test. However, Figure 31 shows that it did indeed take more force to get the same displacement out of the carbon foam composite than out of either the steel plates or the packing foam-steel tri-layer.

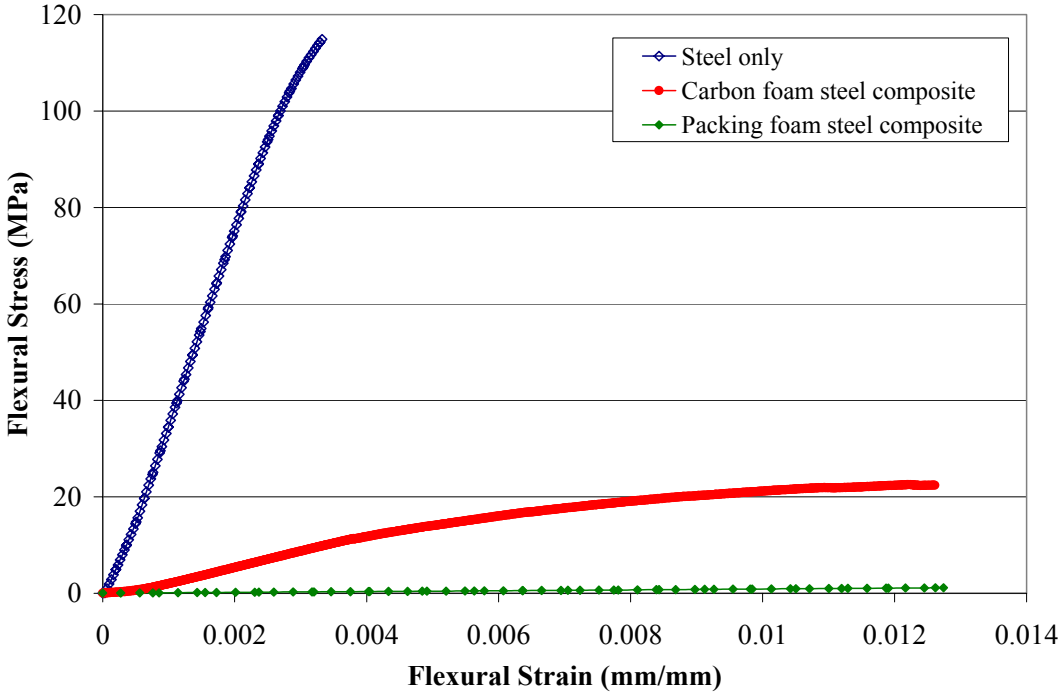

Figure 30. Flexural properties for foam-steel composite

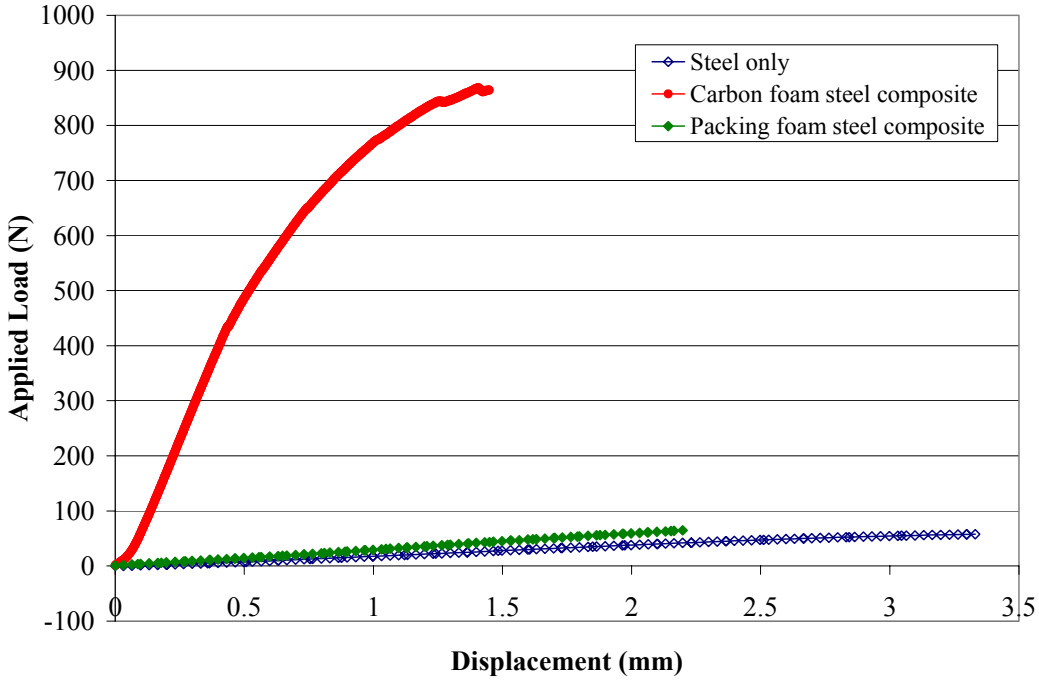

Figure 31. Loading diagram for three-point bending test

6 CONCLUSIONS

In the creation and production of synthetic coal tar enamel using solvent extraction, many interesting findings have been made. It is possible to produce coal tar enamel out of a solvent extracted pitch and commercial grade heavy oil. The results of that synthetic coal tar enamel produce properties that are within the specifications of commercial grade coal tar enamel, for the most part. The volatility of the synthetic is slightly higher than that of commercial enamel, but is not so much higher that it would not be usable. Penetration values, while lower than those of the commercial enamel available, were still within in range of standard, commercial grade enamel. Cathodic disbonding tests show that there are still improvements to be made to the synthetic coal tar enamel, but overall, given the difference in the timeframe used to develop commercial grade enamel and the timeframe used to develop synthetic enamel, the results are quite impressive. Also, it has been shown that enamel can be used as an adhesive for carbon foam-steel composites, and the bond strength to carbon foam is quite usable.

7 REFERENCES

[1] Whittier, F. "Pipeline Coatings" In: *Bituminous Materials: Asphalts, Tars, and Pitches*, Vol. III, Chap. 10, pg. 300, Hoiberg ed., John Wiley & Sons, Inc., New York (1966).
[2] Whittier, F. "Pipeline Coatings" In: *Bituminous Materials: Asphalts, Tars, and Pitches*, Vol. III, Chap. 10, pg. 301, Hoiberg ed., John Wiley & Sons, Inc., New York (1966).
[3]Donath, E. E. "Hydrogenation of Coal and Tar" In: *Chemistry of Utilization, Supplementary Volume*, H. H. Lowry ed., Chap. 22, National Academy of Sciences-National Research Council, John Wiley & Sons, Inc., New York (1963).
[4]Clarke, J. W., Kimber, G. M., Rantell, T. D., and Shipley, D. E. "Reactivity of British Coals in Solvent Extraction" In: *Coal Liquefaction Fundamentals*, ACS Symposium Series 139, Chap. 6, Whitehurst ed., American Chemical Society, Washington, D. C. (1980).
[5] Whittier, F. "Pipeline Coatings" In: *Bituminous Materials: Asphalts, Tars, and Pitches*, Vol. III, Chap. 10, pg. 302, Hoiberg ed., John Wiley & Sons, Inc., New York (1966).
[6] Whittier, F. "Pipeline Coatings" In: *Bituminous Materials: Asphalts, Tars, and Pitches*, Vol. III, Chap. 10, pg. 303, Hoiberg ed., John Wiley & Sons, Inc., New York (1966).
[7] Whittier, F. "Pipeline Coatings" In: *Bituminous Materials: Asphalts, Tars, and Pitches*, Vol. III, Chap. 10, pg. 296, Hoiberg ed., John Wiley & Sons, Inc., New York (1966).
[8] Stansberry et al., DOE/CPCPC final report *Development of an All-Coal Anode, 2003.*

Characterization of Coal Solvent Extraction Processes Using Petrographic, Chemical, and Physical Methods

FINAL REPORT

Reporting Period
March 1, 2003 to February 29, 2004

Report Prepared by

Peter G. Stansberry
Department of Chemical Engineering
College of Engineering and Mineral Resources
P. O. Box 6102
West Virginia University
Morgantown, WV 26506-6102

Report Issued
April 15, 2004

DOE Award Number DE-FC26-98FT40350

Other Contributors

Kevin DeVanney & Ralph J. Gray
Coal Tech Petrographic Associates
3100 Braun Avenue
Murrysville, PA 15668

DISCLAIMER

ASTRACT

Nine bituminous coals were selected based on petrographic composition for solvent extraction in N-methyl pyrrolidone (NMP). The lowest rank coal had a vitrinite reflectance of 0.53 and the highest rank coal 1.53. All of the coals underwent laboratory extraction to determine which petrographic features were most amenable to solvent processing. In addition to detailed petrographic analyses of the feed coals, the NMP-insoluble residues and NMP-soluble extracts were also examined by a wide range of chemical and physical characterization methods. It was found that the liptinite and inertinite macerals and mineral matter were not significantly affected nor solubilized by the solvent. Vitrinite had the largest influence on yield and quality of the extract. Solvent etching of polished coal surfaces with NMP proved informative on describing the nature by which NMP attacks the organic coal portion. A combination of conventional test methods can be used to identify candidate coals. Coals most suitable to NMP extraction should be comprised predominantly of vitrinite with a mean maximum reflectance of about 1.1, should exhibit extensive Gieseler plasticity and Audibert-Arnu dilatometry, and should produce high free-swelling index buttons. Not only did the analysis show that rank parameters were important in establishing yields but also were influential in determining the optical microtexture of the cokes following simulated carbonization in the free-swelling index test: low rank bituminous coal extracts produced more isotropic cokes than extracts from high rank bituminous coals. Based on selection criteria developed in this project, a bituminous coal was chosen and successfully processed through the WVU coal extraction pilot plant.

TABLE OF CONTENTS

TABLE OF CONTENTS
(Continued)

LIST OF FIGURES

LIST OF FIGURES
(Continued)

LIST OF TABLES

1 EXECUTIVE SUMMARY

The objective of the current proposal was to determine what petrographic, physical, and chemical characteristics of bituminous coals lead to the production of maximum extraction yield in N-methyl pyrrolidone (NMP). Detailed analyses of the feed coals and the examination of the coal maceral components that were solubilized by NMP were of great importance in establishing criteria for the selection of candidate coals. Normally petrographic data are determined on a volume percent basis by microscopic point techniques. Conversion of these data to a weight percent basis was made for comparison with the extract and residue weights. The characterization of extract quality and quantity as well as the coke textures and structures produced from carbonization of the extracts provided insight into the mechanism of NMP-solvent extraction.

Nine bituminous coals were chosen for extensive testing based on petrographic composition. The lowest rank coal had a vitrinite reflectance of 0.53 and the highest rank coal 1.53. All of the coals underwent laboratory extraction to determine which petrographic features were most amenable to solvent processing. It was found that coals with mean maximum vitrinite reflectance below about 1.0 were difficult to process by filtration. Some of these low rank bituminous coals appeared to generate solutions that were colloidal in nature, which resulted in blockage of the filter. Coals with vitrinite reflectance above about 1.20 processed well but produced moderate extraction efficiencies. Extraction of high rank coals produced low yields of soluble material. The coal most suitable for NMP extraction exhibited vitrinite reflectance of about 1.10 with yields approaching nearly 75wt% the mass of feed material.

In addition to detailed petrographic analyses of the feed coals, the NMP-insoluble residues and NMP-soluble extracts were also examined by a wide range of chemical and physical characterization methods. It was found that the liptinite and inertinite macerals and mineral matter were not significantly affected nor solubilized by NMP. Vitrinite had the largest influence on yield and quality of the NMP extract. Solvent etching polished coal surfaces with NMP showed that the lower rank coals were most affected by NMP in terms of physical alteration and staining of vitrinite.

Conventional test methods can be used to identify candidate coals. Coals most suitable to NMP extraction should be comprised predominantly of vitrinite with a mean maximum reflectance of about 1.1, should exhibit extensive Gieseler plasticity and Audibert-Arnu dilatation, and should produce high free-swelling indexes. Coals with these characteristics would generally fall within the hvA bituminous rank.

Analyses showed that rank parameters were important not only in establishing yields but also were influential in determining the optical microtexture of the cokes following simulated carbonization in the free-swelling index test: low rank bituminous coal extracts produced more isotropic cokes than extracts from high rank bituminous coals.

Based on selection criteria developed in this project, a bituminous coal was chosen to test whether laboratory-scale extraction processes could be verified on a larger level. This was successfully accomplished with the Kingwood bituminous coal through the WVU coal extraction pilot plant.

2 INTRODUCTION

The Consortium for Premium Carbon Products from Coal has as its mission the development of coal-based materials of high value. As prior CPCPC research efforts have shown, a wide range of carbon precursors is attainable by solvent extraction of coal. By manipulating solvent extraction conditions, materials suitable for binder pitches, anode cokes, carbon fibers, and isotropic graphites can be obtained. Potential applications of the solvent-extract technology that are attracting considerable attention are the use of coal extracts in the development of nuclear-grade graphite and low-cost cellular structures otherwise know as carbon foams.

Solvent processing under mild conditions in which the coal is not thermally degraded results in an essentially mineral-matter-free extract. These extracts often exhibit rheological and carbonization characteristics similar to that of the original coal. Little, if any, CPCPC-sponsored work has focused on the characterization of coals prior to, during, and after exhaustive solvent extraction or of the nature of the coal on extract quality and yield. Thus, this research effort sought to establish criteria necessary for the selection of optimal coals for solvent extraction and to develop an accurate model for predicting extract yields.

The coal extracts were produced in this project under mild conditions using solvent extraction technology developed at West Virginia University (WVU). Porosity development, pore size distribution, and chemical characterization of the coal and its insoluble residue were followed as a function of extraction efficiency. Coal Tech Petrographic Associates (CPA) examined the feed coals, extracts, and residues petrographically. In addition, the research groups co-operated on measuring pertinent

rheological and other chemical properties. Moreover, petrographic techniques were used in determining the development of optical microstructure of the coal extracts from cokes made in the Free Swelling Index (FSI) determination. The resultant optical microtexture relating to coal rank, type, and extract yield were determined. Finally, a bituminous coal was chosen, based on the results of the research, for processing through the WVU coal extraction pilot plant.

3 BACKGROUND

3.1 Coal Formation Primer

Coal is a complex organic mixture consisting primarily of the elements carbon, hydrogen, oxygen, nitrogen, and sulfur. How these elements are bonded, their relative proportion, spatial distribution and conformation, give rise to a very nearly infinite variability in terms of reactivity and utility. The presence of inorganic matter is an additional facet affecting coal in all of its uses. Whether as discrete minerals or chemically associated with the organic portion of coal, mineral matter can be troublesome, by forming ash during combustion, or beneficial, by catalyzing reactions during direct coal liquefaction or gasification. Furthermore, since coal is solid, inherent porosity can trap or release gas, water, or solvent-soluble material, and influence accessibility of reagents. The interplay among the organic, inorganic, and physical components ultimately determines many of the applications for which coal can be used.

It certainly is not possible to cover all aspects of coal formation, structure, or analyses within the confines of this project. Nonetheless, despite the lack of depth covered here, it is pertinent to address various aspects on the nature of coal, especially as they pertain to solvent extraction. For those so inclined, a wealth of detailed information

on a wide range of coal topics can be found in earlier texts of Lowry [1,2], Elliot [3], and Stach [4], more recently van Krevelen [5], and in the prevalent refereed journals. An updated review on solvent extraction of coal is also available by Dilo Paul [6].

Since the crust is not fixed, the Earth is a dynamic celestial body and its surface features continually change over eons of time. Imagine that the continental United States was at one time much closer to the equator but because of plate tectonics, now resides in northern latitudes. While the continents were gradually shifting and environments and climates slowly changing, the prevailing vegetation evolved, from primitive mosses and horsetails, to more modern spore producers, and eventually to seed producing plants. The basic organic compounds comprising all of these plants were probably similar chemically, but their proportions could be quite different: the building blocks of plants—cellulose, lignin, waxes, and resins—are variable in quantity from species to species and from era to era. This is important because the composition of plant material going into forming coal could have an effect on its properties [7].

Although the process of plant evolution proceeded uninterrupted, the conditions necessary for the deposition of coal were specialized and sporadic on a geological time scale. When a plant dies and lies on the forest floor, the usual outcome is decay, resulting in the complete conversion of tissues and specialized structures into carbon dioxide and water. To form coal, however, the dead plant material should be deposited in swampy or boggy conditions. Under water, attack of the dead plants by oxygen and microorganisms can still occur, but is greatly retarded. In this environment, the plant materials become peat, which is enriched in carbon compared to the original organic input, because of the loss of methane, carbon dioxide, and water. Additional plants could continue to grow,

die, and deposit in the swamp intermittently or continually for many years until thin seams or thick deposits are made. Eventually, the peat becomes covered with sediment and forced by geological processes to subside.

Coalification is a two-part process that plant materials undergo on their course toward coal. The first, the biochemical stage, ends by the time peat is formed. The second, the geochemical stage, depending on pressure, temperature, and time, transforms the peat material into either lignite, subbituminous coal, bituminous coal, or ultimately anthracite. Lignite can be considered an "immature" coal since it has undergone the least metamorphosis and, at the other extreme, anthracite the most "mature" coal.

Differences in plant material and the conditions during decomposition and burial result in petrographic entities known as macerals. Macerals are fossilized plant remains, distinguishable by observation under the optical microscope, and are categorized into three main groups: vitrinite (huminite in low rank coals), liptinite, and inertinite. Within each main group there are a number of other maceral components that can be identified by their size, morphology, and reflective properties: it is abundantly apparent that coal is not homogeneous. Neavel [8] said the assemblage of macerals in coal is analogous to a fruitcake, as is evident in Figure 1.

The predominant macerals fall within the vitrinite group and exert the greatest influence on the behavior of coal during its utilization. Vitrinite is derived primarily from woody antecedents. Liptinite is higher in hydrogen content than vitrinite and is comprised of more-specialized fossilized plant remains such as spores, pollen, cuticles, and resins. Inertinite is higher in carbon content than vitrinite and often displays a

charcoal-like structure. Although occurring in lesser amounts than vitrinite, the affects of liptinite and inertinite must not be ignored or underestimated.

Upon moving from the low-rank lignite to the high-rank anthracite, many chemical and physical characteristics change in a more or less systematic manner [9,10]. Correlations between coal behavior and extent of coalification are very useful in most

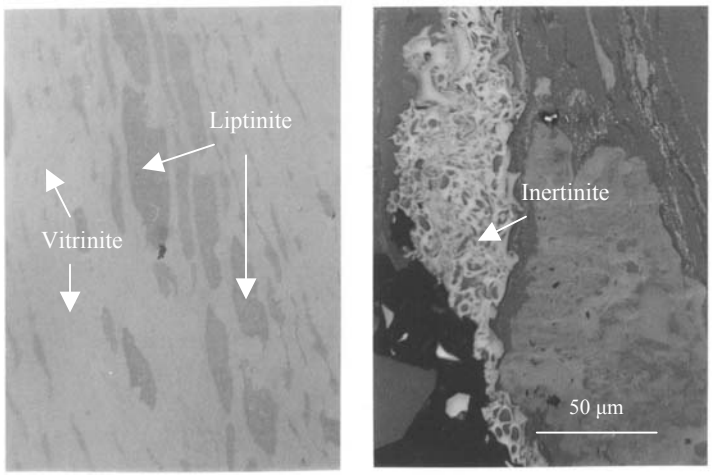

Figure 1. Photomicrographs of main maceral groups in a bituminous coal.

applications, especially in the establishment of a coal classification system. Classifying coals helps in determining whether carbonization or gasification, for example, would be appropriate. Attempts to place coals into certain groups or similar categories have evolved since the early 19th century in parallel with the growth of the industrial revolution, which became increasingly reliant on worldwide-coal trade for fuel. Some of the classification tests are based on 1) chemical analysis, 2) thermoplastic behavior, or 3) petrographic analysis. The Economic Commission for Europe Coal Committee developed a comprehensive system that involves a 14-digit code based on the results of all three tests [11].

In the United States, coals are classified according to rank as defined by the American Society for Testing Materials (ASTM D388). The U.S. classification is based on volatile matter content or calorific value, as indicated in Table 1.

Table 1. Coal classification according to ASTM.

Class		Group	Abbreviation	Fixed carbon limits, % dmmf		Volatile matter limits, % dmmf		Calorific value limits, MJ/kg mmmf[a]		limits Btu/lb mmmf		Agglomerating character
				Equal or greater than	Less than	Greater than	Equal or less than	Equal or greater than	Less than	Equal or greater than	Less than	
I	Anthracitic	1 meta-anthracite	ma	98			2					non-agglomerating[b]
		2 anthracite	an	92	98	2	8					
		3 semi-anthracite‡	sa	86	92	8	14					
II	Bituminous	1 low volatile bitiminous coal	lvb	78	86	14	22					
		2 medium volatile bituminous coal	mvb	69	78	22	31					
		3 high volatile A bituminous coal	hvAb		69	31		32.56[c]		14000		commonly agglomerating[d]
		4 high volatile B bituminous coal	hvBb					30.24[e]	32.56	13000	14000	
		5 high volatile C bituminous coal	hvCb					26.75	30.24	11500	13000	
								24.42	26.75	10500	11500	agglomerating
III	Subbituminous	1 subbituminous A coal	subA					24.42	26.75	10500	11500	
		2 subbituminous B coal	subB					22.10	24.42	9500	10500	
		3 subbituminous C coal	subC					19.31	22.10	8300	9500	non-agglomerating
IV	Lignitic	1 lignite A	ligA					14.65	19.31	6300	8300	
		2 lignite B	ligB						14.65		6300	

Several physicochemical tendencies are evident on going from low rank coal to high rank coal. Some of these trends include increases in carbon content; decreases in oxygen, moisture, and volatile matter content; and increases in maceral reflectance, molecular weight, and aromaticity. For coals with about 87-89wt% carbon, a minimum in true density, surface area, and porosity is measured, and a maximum in extractable material and fluidity is obtained.

3.2 Action of Solvents on Coal

Solvent extraction under mild conditions has been and continues to be actively pursued, primarily as a tool to probe the molecular properties and structure of coal and, in

some instances, for commercial applications. Research shows that the effectiveness of solvents for coal extraction is influenced by coal type, rank, and petrographic composition, and by the chemical nature of the solvent.

Whether the vitrinite in coal is a micellar complex [12] or three-dimensional network [13] remains to be proven, and whether solvent effectiveness can be explained entirely by solubility parameter [14], donor-accepter number [15], hydrogen-bonding [16], solvent-synergism [17], or other associative forces [18] continues to be investigated. These fundamental aspects on coal-solvent interactions are beyond the scope of this project.

Though still relevant today, Oele et al. more than fifty years ago classified solvents used to extract coal into four groups [19]. In general, the efficiency of solvents in this system is closely related to temperature. Solvents in the first category, *non-specific extraction*, extract only a few percent of the coal at temperatures below about 100°C. These solvents (for example benzene, hexane, carbon tetrachloride, and ethanol) extract only a few percent coal thought to be primarily resins and waxes. In *specific extraction* the coal material solubilized can typically amount to about 20-40wt% at temperatures up to about 200°C. Many of these solvents are nucleophilic, have electron donor-acceptor properties and high internal pressure. Pyridine, quinoline, and N-methyl pyrrolidone are examples of solvents used for specific extraction. It is noteworthy that remarkable ambient-temperature extraction efficiencies have been reported by Iino with mixed carbon disulfide—N-methyl pyrrolidone solutions [20]. During *extractive disintegration* temperatures approaching the thermal decomposition of coal, up to 350°C, can be encountered. Under these conditions it can be anticipated that solvent components

which can redistribute hydrogen from and to reactive coal components by a shuttling mechanism appear to be most effective [21-22]. For example, extraction of a bituminous coal with phenanthrene (boiling point 340°C) produced 95wt% extract yield, but extraction of the same coal in anthracene (boiling point 354°C) produced only 24wt% extract [23]. Since the two solvents are isomers of similar boiling point, it was suggested that phenanthrene was more active than anthracene in hydrogen exchange reactions [24]. The *extractive chemical disintegration* process can be called direct coal liquefaction. Here, solvents rich in hydroaromatic components are especially suited in extracting nearly all of the reactive coal macerals. These types of solvents actively participant chemically in bond breakage and stabilization, are consumed or structurally changed, and are normally used at temperatures considerably in excess of 300°C. One should be mindful, however, that there could be no clear operational or mechanistic distinction between extractive disintegration and extractive chemical disintegration processes.

3.3 Role of Extracts on Thermoplastic Properties

When certain bituminous coals are heated, they soften and become fluid commensurate with the evolution of gas and tar [25-26]. The plastic behavior is transient and the mass eventually thickens, swells, and fuses to form a porous solid or coke. This phenomenon is of the utmost importance to the production of metallurgical coke, and in other processes sensitive to coal caking and agglomeration. Because of the impact of plastic behavior on industrial processes, a great deal of early research effort was directed toward understanding coal composition and the relation of soluble extracts to the "coking" principle [27-29]. The plastic behavior in coals has been explained by the hypothesis that the development of plasticity is a transient, in situ, hydrogen donor

process [30]. The solvent-soluble material contains more hydrogen than the parent coal, and is thought to be responsible for solvation and hydrogen stabilization of the molecular units in coal as they become mobile with increasing temperature. It is believed that the stability of the metaplast produced by coking coals during their softening and resolidification, which is emulated in their plastic range, is responsible for the quality and quantity of extract produced. These extractable components are also influential in other processes such as direct coal liquefaction [31].

It is well established that there is a correspondence between the amount of material extractable from coal using specific solvents and rank, as shown in Figure 2. The quantity of extracts in pyridine increases as the carbon content increases, peaks around 86wt% carbon, and then drops precipitously.

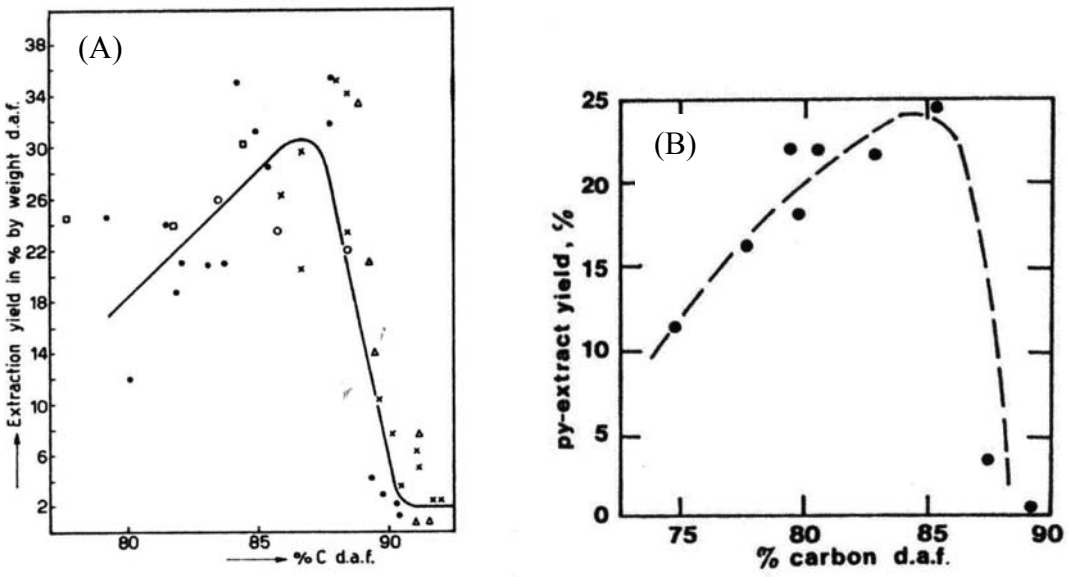

Figure 2. Yield of pyridine extracts vs. coal rank: A from ref. 35; B from ref. 36.

Furthermore, there also is a correspondence or relationship between the amount of material extractable from bituminous coal and thermoplascitity, see Figure 3. The significance of the extracts on plasticity is made clear when extracts from good coking coals are blended with non-coking coals to induce fluidity [32-33], and extracting prime coking coals leaves a residue devoid of plastic behavior [34].

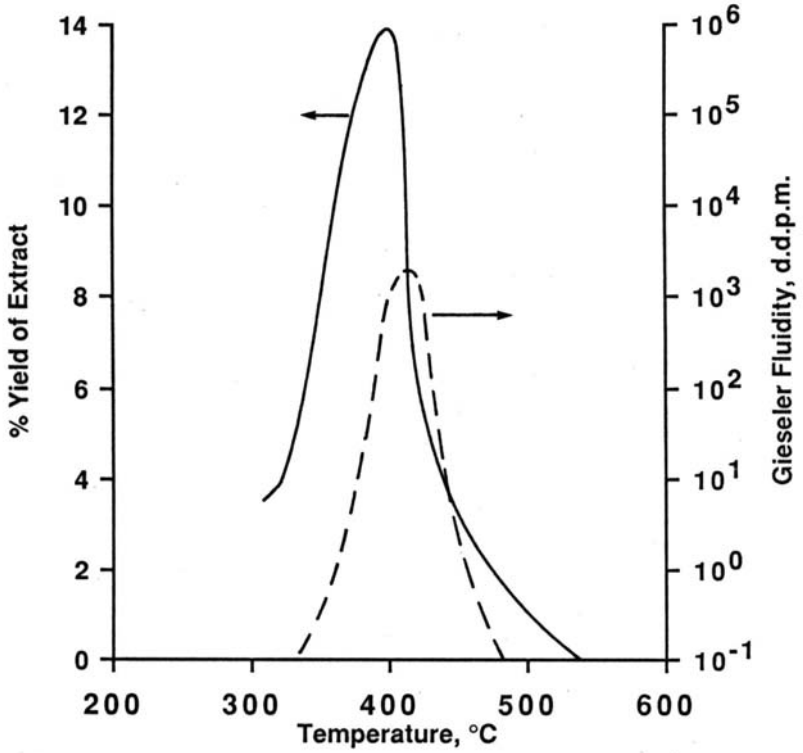

Figure 3. Variation of extract yield and Gieseler fluidity [37].

3.4 Optical Microscopy as Applied to Coal, Coal Products, and Coke/Carbon Forms

Coals are bioclastic sedimentary solid fossils of plant origin that consist of macerals, minerals, water, and gas. In addition to variations in rank, coals also vary in type, from sapropelic to banded, and in grade, from carbonaceous rock to relatively pure organic material. The one technique that uniquely fingerprints coal in terms of rank,

type, and grade is optical microscopy. Petrographic analysis of coal has become immensely important on a worldwide scale in selection of coals for development, utilization, and marketing. As such, the American Society for Testing Materials has developed standards for preparing coal samples for microscopical analysis by reflected light [38], for megascopic description of coal seams and microscopical determination of volume percent of coal components [39], and for the microscopical determination of the reflectance of organic components of coal [40].

Petrology is that branch of geological science that deals with the study of rocks in the earth's crust. Petrography of coal is the descriptive part of petrology, and deals with the characterization and designation of coal as a rock. The simplest method of characterization can be accomplished by casual observation. To the unaided eye coal can appear either banded or non-banded. Examples of the latter include cannel and boghead coals: sporinite is predominant in cannel coal and algonite in boghead coal. However, we usually are more familiar with the banded coal varieties, in which a systematic effort to describe the visible bands, or lithotypes (literally "rocktype"), began to emerge in the 1920's. Differences in the appearance, luster, and hardness identify lithotypes as 1) vitrain: a black, lustrous, relatively homogeneous bands in bituminous coals that break conchoidally; 2) clarain: a finely banded, lustrous black material, with a silky texture, that breaks horizontally; 3) durain: a dull, matt-like, granular appearing, black solid material; 4) fusain: a dull, generally lenticular, friable solid that resembles charcoal: 5) duroclarain and clarodurain: intermediate between clarain and durain. Presently coal petrography centers mostly around microscopic techniques to identify and

quantify the individual fossilized plant components which makeup the lithotypes and, since 1957, to use spectral reflectance in identifying coal according to rank.

When light strikes a flat surface of coal, a portion, not all, is reflected. The nature and intensity of the reflection can provide information on the chemical and physical state of coal [42]. Of the macerals in the vitrinite group, shown in Table 2, collinite is selected to determine coal rank because of its preponderance and homogeneity. The reflectance of all macerals differs and changes with rank, but the reflectance of collinite changes in a very regular fashion with changes in rank, see Figure 4. A collinite reflectance of R = 1.5, for example, means that 1.5 percent of the incident light is reflected: the magnitude of only 1.5 means coals absorb a large portion of visible light. Reflectance values are often reported as V-types. For instance, V-6 includes all of the vitrinite with a reflectance of 0.60 through 0.69 percent.

Table 2. Maceral groups and macerals in hard coals (from ref. 5, pg. 118).

Group	*Maceral*	*Characteristics*
Vitrinite	telinite	cell walls
	collinite { telo-	amorphous (gel or gelified { tissue)
	collinite { detro-	amorphous (gel or gelified { detritus)
	corpocollinite	cell fillings
	vitrodetrinite	detritus
Liptinite (formerly exinite)	sporinite	spores, pollen
	cutinite	cuticles
	suberinite	suberinised cell walls (cork)
	fluorinite	plant oils
	resinite	resins, waxes, latex
	alginite	algae
	bituminite	amorphous (bacterial, algal, faunal)
	chlorophyllinite	chlorophyll
	exsudatinite	secondary exudates
	liptodetrinite	detritus
Inertinite[1]	fusinite	cell walls (charred, oxydised)
	semi-fusinite	cell walls (partly charred, oxydised)
	sclerotinite	fungal cell walls
	macrinite	amorphous gel (oxydised, metabolic)
	micrinite	secondary relics of oil generation (mainly)
	inertodetrinite	detritus

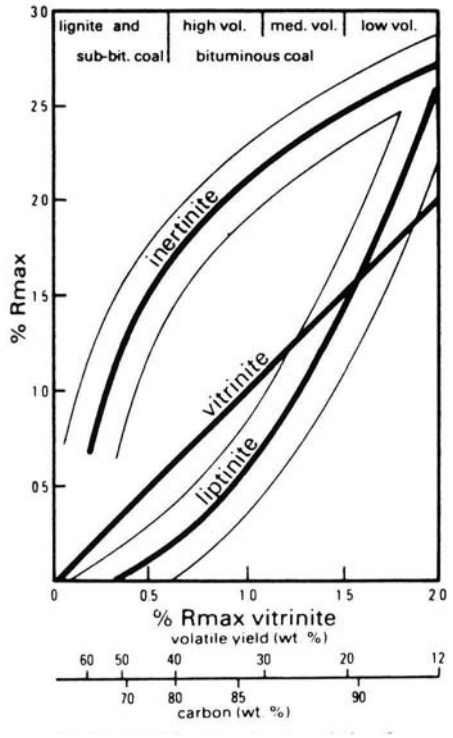

Figure 4. Reflectance of macerals vs. rank (from ref. 5, pg. 373).

In the maceral analysis of coal, the sample is prepared by mounting a representative sample of minus 20 mesh coal in a plastic binder and forming the mixture into a cylindrical pellet under pressure to exclude air. After the plastic has cured, the surface of the pellet containing the coal is ground and polished to a mirror-smooth finish for microscopic examination. Magnifications of about 300 to 700 with oil immersion objectives are commonly used. The specimen is observed through an ocular equipped with a measuring device, such as a whipple disc, and the stage moved in fixed incremental distances in the x and y directions to permit counting.

In conducting a quantitative analysis the sample is moved in fixed increments or fields of at least one-half the size of the largest particle in the sample. The fields are spaced along a traverse or line through the sample. Parallel traverses are run through the sample until sufficient materials are identified. A uniform sampling grid is used to sample randomly dispersed particles. Each field along a traverse is sampled identifying materials that occur at the intersections of the corner lines in a rectangular grid in the ocular. In general, two sets of 500 macerals are counted. If the separate sets are near duplicates then the 1000 points are averaged and reported as volume or area percentages. If the duplicate 500 points counted do not reproduce then additional points are counted up to 2000 points.

Petrographic techniques are also applicable in the characterization of carbon and coke forms obtained from coal [43]. The cokes from coals have a variety of microstructures that are optically distinct in polarized light. The graphitizability, electrical resistivity, reactivity to CO_2 at elevated temperatures, and strength of carbons are related to the optical properties of the coke carbon forms, which vary in amount, size, and degree of anisotropy. The system of coke microscopy used in this project is shown in Table 3 and some of the forms that cokes exhibit are shown in Figure 5.

Cokes from coals consist of binder and filler phases. Binder phase carbons are produced from the reactive macerals vitrinite, exinite, resinite, and reactive semifusinite. All reactive macerals soften during carbonization. Filler phase carbon forms are derived from inert semifusinite, fusinite, possibly micrinite, macrinite, and inertodetrinite macerals, which do not soften appreciably during carbonization. The binder and filler phase coke analyses are combined to complete the petrographic examination. The

relation of coal rank based on vitrinite reflectance to coke carbon forms (microstructures) in the binder phase is also shown in Table 3.

Table 3. A system of coke microscopy.

Coke Binder-Phase Carbon Form Classification

Binder Phase	Width (in microns)	Length to Width Relation	Parent Coal Vitrinite Type	Bituminous Coal (Volatility)
Isotropic	0.0	None	6, 7	High
Incipient (anisotropic)	0.5	L=W*	8	High
Circular (anisotropic)				
Fine circular	0.5 – 1.0	L=W	9	High
Medium circular	1.0 – 1.5	L=W	10	High
Coarse circular	1.5 – 2.0	L<2W	11	High to Med.
Lenticular (anisotropic)				
Fine lenticular	1.0 – 3.0	L≥2W L<4W	12	High to Med.
Medium lenticular	2.0 – 8.0	L>2W L<4W	13	Medium
Coarse lenticular	8.0 – 12.0	L>2W L≤4W	14	Medium to Low
Ribbon (anisotropic)				
Fine ribbon	3.0 – 12.0	L>4W	15	Medium to Low
Medium ribbon	12.0 – 25.0	L>4W	16	Low
Coarse ribbon	25.0+	L>4W	17, 18	Low

Coke Filler-Phase Carbon-Form Classification

Filler-Phase	Size (in microns)	Precursor material
Organic Inerts		
Fine	<50	Micrinite, macrinite, inertadetrinite
Coarse**	>50	Semifusinite, Fusinite, macrinite
Miscellaneous Inerts		
Oxidized coal (coke)		Oxidized coal – slight moderate and advanced.
Brecciated coal (coke)		Brecciated coal – fine, intermediate and coarse.
Noncoking Vitrinite (coke)		Vitrinite too high or low in rank.
Inorganic Inerts		Various types of mineral matter
Fine	<50	Coal mineral matter and bone coal
Coarse	>50	Coal mineral matter and bone coal

Miscellaneous Categories Quantified in Carbon Form Analysis***

Depositional Carbons	Sooty, spherulytic, and pyrolytic.
Additive Carbons	Coke breeze, anthracite, petroleum coke, etc.
Miscellaneous Observations	"Green" coke, burnt coke, etc.

Notes: * L = length of carbon form domain (long dimension).
W = width of carbon form domain (short dimension).

** Includes coarse inert-rich microlithotypes which retain distinct particle boundaries and appear to act as filler instead of binder phase. These are kept separate during microscopic analysis.

*** Miscellaneous observations can be quantified or presence can be indicated as rare or abundant.

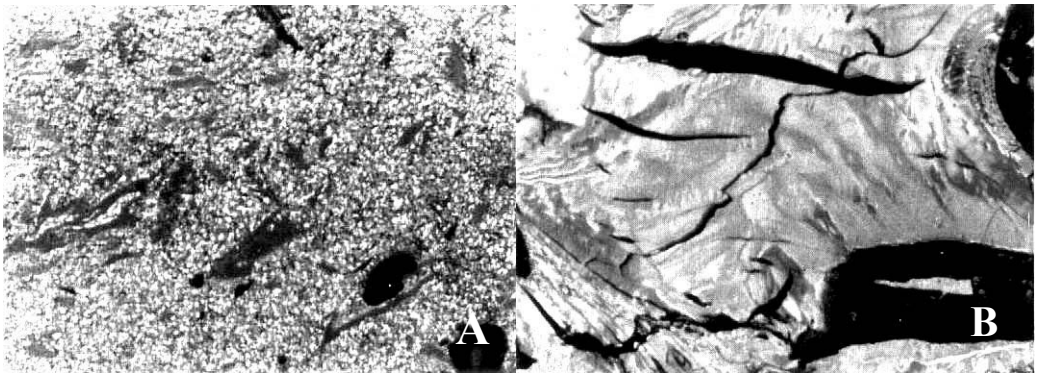

Figure 5. Two examples of coal coke microstructure: A, circular anisotropic (coarse); B, ribbon anisotropic (coarse).

4 EXPERIMENTAL

4.1 Feed Coal Characterization and Solvent Processing

4.1.1 Coal Selection, Preparation, and Characterization

Twelve different coals or fractions (9 for coal rank, 3 for coal type) were acquired for this project, ranging from about 0.5 to about 1.6% vitrinite reflectance. Figure 6 is an outline of the steps followed in the preparation of the coal for characterization and solvent extraction. Approximately 80 pounds or more of as-received coal were air dried and then crushed to ¼ x 0 inch. The coal was riffled and 15 pounds of this material crushed to 8 x 0 mesh. The remainder was sealed and retained for other testing, such as washability. Five pounds of the riffled material was ground to minus 20 mesh. A portion of the minus 20-mesh coal underwent reflectance measurements, and maceral type and content determination. The remaining minus 20-mesh coal was ground and sized as shown in order to undergo other tests. Table 4 identifies the coals and provides some of their basic characteristics. Additional data are located in Appendix 1.

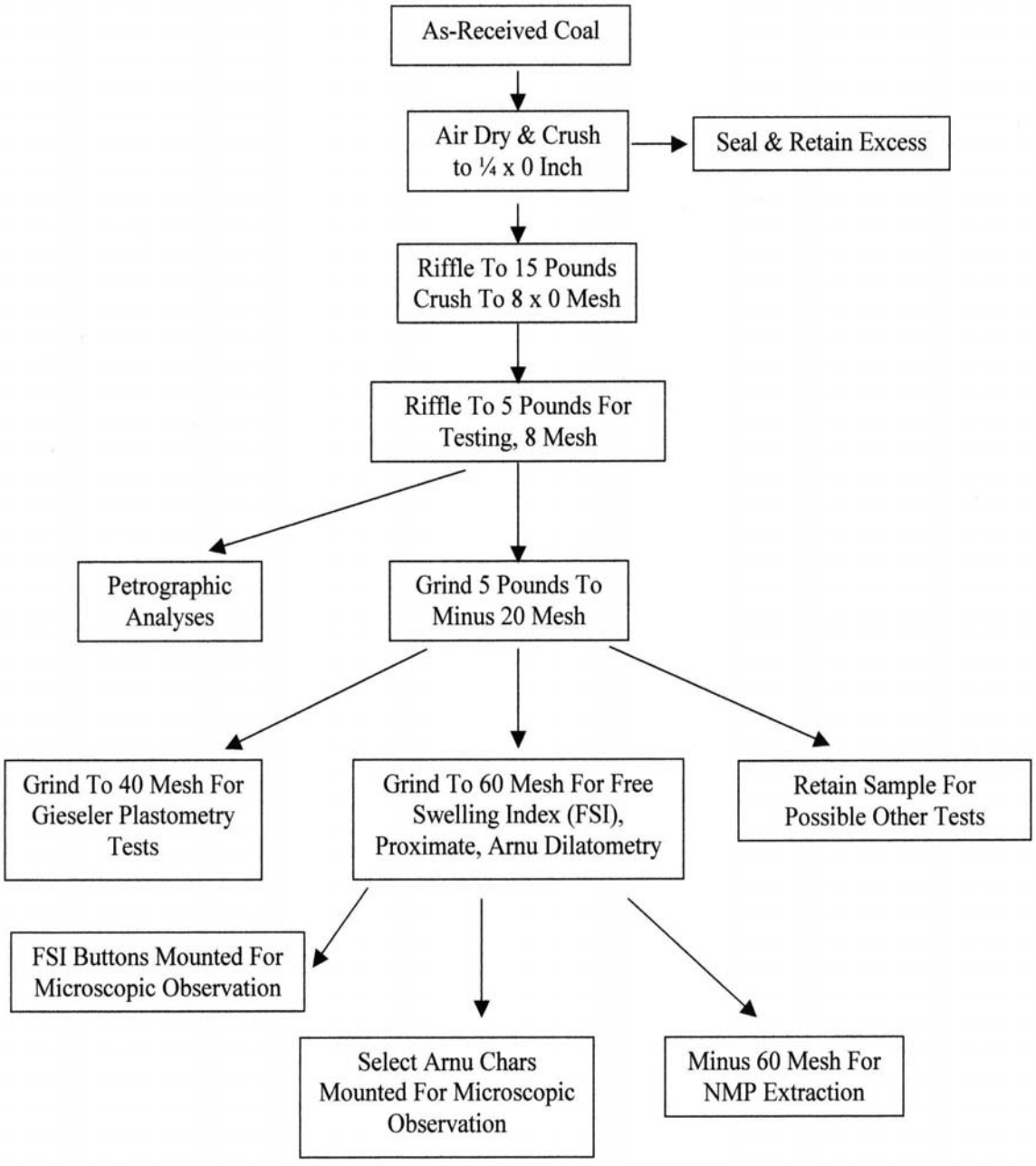

Figure 6. Coal preparation and testing outline steps.

Table 4. Characteristics of bituminous coals selected for testing in this project.

Coal Name	Ky #9	Shoemaker	Bailey	Mingo Logan	Marfork	Kingwood	Litwar	Jewell-Tiller	Poca #12
Seam	No. 9	Pittsburgh	Pittsburgh		70/30 Pow/CG	Kittanning	Litwar	Tiller	McDowell /WV
County/State	KY	Marshall/WV	PA	WV	WV	Preston/WV	WV	Buch./VA	WV
Mean Max Vitrinite Reflectance R_o, %	0.53	0.77	0.83	0.98	1.02	1.08	1.23	1.36	1.53
Sulfur, %dry	3.26	3.12	1.91	0.76	1.06	1.02	0.74	0.92	1.11
Proximate Analysis, %dry									
VM	36.65	38.06	36.22	35.00	33.45	33.17	27.42	22.77	19.54
FC	53.52	51.92	56.11	59.27	60.05	57.91	68.09	70.63	76.63
Ash	9.83	10.02	7.67	5.73	6.50	8.92	4.49	6.60	3.83

4.1.2 Coal Extraction in NMP (N-methyl pyrrolidone)

The coal samples (<60mesh, dry) were tested to determine extraction efficiency. Ten grams of coal were added to 100mL of NMP in a 250mL ground-glass-joint Erlenmeyer flask. A water-cooled condenser was attached to the flask and provision was made for purging the system with nitrogen gas. Mixing was accomplished with a magnetic stirrer and heating supplied by a temperature-variable hotplate. The solution was brought to reflux at about 202°C for one hour after which the solution was vacuum filtered hot through a 1.6μm glass-fiber filter using a conventional Buchner-type filtration apparatus. The filter cake was washed with about 100mL of hot NMP and then was dried overnight in a vacuum oven at about 150°C while maintaining a slow purge of nitrogen gas. The filtrate was isolated from the NMP by rotary evaporation before vacuum drying along with the insoluble residue. After cooling to room temperature, the coal residue was weighed to determine extraction yield according to the following equation:

Yield = [(wt dry coal – wt residue)/(wt dry coal)] X 100.

Each coal extraction was repeated four times to establish statistical reliability. In addition, each coal underwent solvent extraction sufficient to produce about 40-50g each of soluble extract and insoluble residue for additional characterization.

4.1.3 Determination of Plastic Properties and Proximate Analysis

Standard tests were used to characterize feed coal, extracts, and residues for thermoplastic behavior according to dilatation, fluidity, and free swelling. The changes

in coal length during heating under controlled conditions can be accomplished using an Audibert-Arnu dilatometer. A sample of powdered coal material is pressed into a pencil and inserted into a steel tube. A piston is inserted into the tube on top of the pencil. The assembly is then heated at a proscribed rate. As the sample changes dimensions to the response of heat, the piston is displaced and the distance traveled is recorded. The movement of the piston is expressed as a percentage relative to the original length of sample. The determinations are reported as percent maximum contraction, percent maximum expansion, initial softening temperature, initial dilatation temperature, and maximum dilatation temperature.

Plasticity was determined in a Gieseler plastometer. A powdered coal sample is compressed in a cylindrical container fitted with a rabble-arm stirrer. The cylinder is placed in a solder bath and heated at a controlled rate. A constant torque is applied to the stirrer, which moves in response to changes in coal fluidity. The units of plasticity are reported as dial divisions per minute (ddpm). The information collected includes maximum fluidity, temperature at maximum fluidity, softening temperature, solidification temperature, and plastic-range temperature.

The free-swelling index (FSI) is a measure of the increase in volume of coal material when heated under specified conditions. Since the determination is conducted such that the swelling and dimensional changes occur unimpeded, it is possible for the coal sample to flow and form a button. The free-swelling index is then determined by comparing the button with a series of standard profiles, which are numbered 1 to 9 in 0.5 units. A large FSI value indicates considerable expansion of the coal upon heating.

Proximate analysis is determined by heating coal material under controlled conditions and recording associated weight changes. The method provides percentage moisture, volatile matter, and ash. Fixed carbon is determine by subtracting the percentages of moisture, volatile matter, and ash from 100

4.2 Analyses of Feed Coals, Residues, and Extracts

4.2.1 Petrographic Method Applied to Feed Coals, Residues, Extracts, and Cokes

Conventional sample preparation and polishing techniques, and established quantitative microscopical methods were followed in the petrographic examination of coals, extracts, and residues. Chars and cokes produced from the extracts in the free-swelling index determination were also mounted in plastic and prepared for optical microscopy. In addition, coal samples were mounted to determine whether a solvent etching procedure with NMP could be developed and correlated with extraction yield and some microscopic feature. The solvent etching consisted of placing a drop of NMP onto the polished surface of coal in an identifiable area. The pellet with NMP was then placed in a microwave oven for various periods of time. It was determined that 30 seconds in the microwave was sufficient to etch the various ranks of coal being tested. The etched surface was then rinsed in water and/or alcohol and allowed to air dry before optical microscopy.

4.2.3 Physical and Chemical Characterization of Feed Coals, Residues, and Extracts

Several analyses were conducted to determine surface and bulk properties, and chemical nature of the feed coals, extracts, and residues. Surface and bulk characteristics were determined by helium pycnometry (ASTM D-4892), surface area by the BET

method using liquid nitrogen, and porosity by mercury intrusion (ASTM-4284). The chemical characterization tests consisted of elemental analysis, thermogravimetric analysis, and infrared spectroscopy. The determination of carbon, hydrogen, nitrogen, and sulfur was conducted on a ThermoQuest elemental analyzer. Following calibration of the instrument with compounds of known composition, coal samples were analyzed and the average of at least three determinations reported. Infrared spectra were collected on a Nicolet 510P Fourier-transform infrared (FTIR) spectrometer by co-adding 256 interferograms at a resolution of 2 cm^{-1}. Samples were prepared using a conventional KBr pellet process with a specimen concentration of about 3wt%. Sample weight loss with temperature was determined on a Leco TGA analyzer under nitrogen at a heating rate of 3°C/min up to 900°C.

5 RESULTS AND DISCUSSION

All of the experimental data are tabulated in Appendix 1 through 16. Several hundred photomicrographs were produced and, thus, it was not possible to include them all in this report. The more relevant findings are presented in the following sections.

5.1 Results of NMP Extraction

Early in the project there was discussion as to whether channel samples from newly mined areas, free from weathering, should be selected. However, it was acknowledged that this might not be always possible or cost effective. If channel samples or raw-run-of-mine samples were to be used, they would require laboratory washing using solvents of select specific densities. It was not known if specific gravity

chemicals would affect the solvent extraction process or extract quality. To address the concern, coal sample A was washed in Centigrav (1.45 specific gravity) and the float/sink fractions combined. In addition, the 1.35 specific gravity float fraction of coal B was extracted in NMP. The results presented in Table 5 indicate that laboratory washing of coal B had little, if any, affect on extraction efficiency. However, the float fraction of coal A appeared to extract slightly more than the feed coal perhaps because of the reduction in the mass of mineral matter or the more dense maceral components, or a concentration of fractions more amenable to extraction. In any case, the results for coal A sample are nearly within experimental error.

Table 5. NMP-extraction of laboratory washed coals.

	Coal A		Coal B	
	Feed Coal	1.35sg Float	Washed Centigrav F/S Combined	Not Washed
NMP Extraction Yield, wt%	66.7 $\sigma = 0.35$	71.7 $\sigma = 2.12$	37.5 $\sigma = 1.74$	36.8 $\sigma = 0.69$

σ = Standard deviation of four extractions.

A suite of about 10 different coals or fractions (7 for coal rank, 3 for coal type) was initially planned for sampling, detailed microscopic analysis, rheological properties, and limited chemical analyses to be undertaken prior to NMP extraction. Testing some of the initial candidate coals did not accomplish the objective in determining the lower and upper rank boundaries amenable to solvent extraction. Thus, two additional coals were selected and ordered to clarify the upper, lower, and optimum rank and fluidity ranges where extraction yield diminishes or reaches optimum. Therefore, coal "type" studies were very limited under the current constraints of this year's budget allocation. Consequently, coal sampling entailed all production samples. For each sample, location,

seam, mine name, depth, mine section, and other important information were obtained whenever possible.

Thus, it was decided that solvent extraction and detailed characterization would be focused on the nine coals based solely on rank rather than type. The results of NMP extraction of these coals are provided in Table 6 and shown graphically in Figure 7.

Table 6. Yield of NMP-soluble extracts from bituminous coals.

Coal Name	Ky #9	Shoemaker	Bailey	Mingo Logan	Marfork	Kingwood	Litwar	Jewell-Tiller	Poca #12
Mean Max Vitrinite Reflectance R_o, %	0.53	0.77	0.83	0.98	1.02	1.08	1.23	1.36	1.53
Yield, wt%	30.3	34.1	30.9	32.4	45.3	66.7	40.6	30	5
Standard Deviation	0.73	2.1	0.69	0.55	1.97	0.35	0.84	1.96	0.41
Yield, daf%	33.6	37.9	33.5	34.4	48.4	73.2	42.5	32.1	5.2

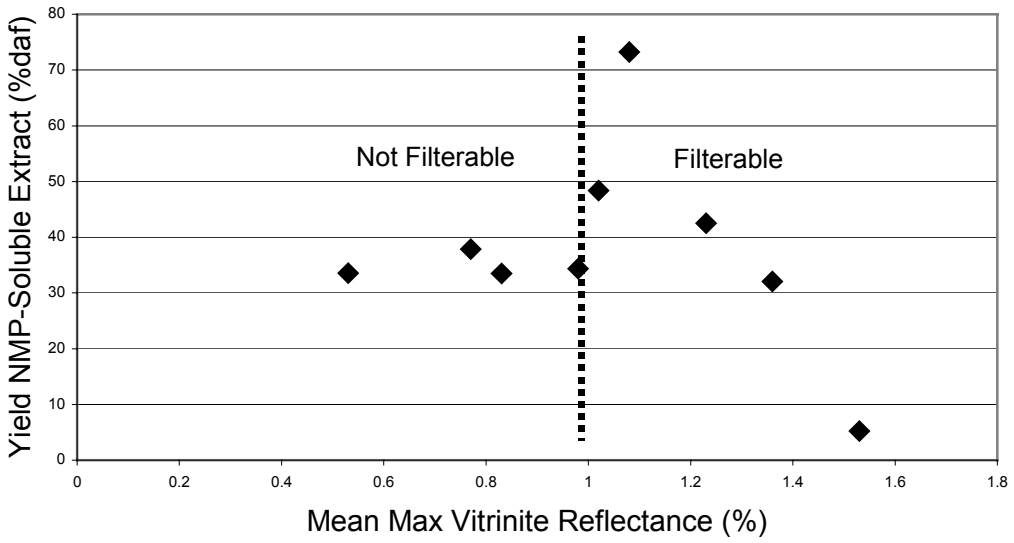

Figure 7. Effect of coal rank on NMP extraction efficiency.

There is a trend in increasing extraction yield up to a vitrinite reflectance of about 1.0 with decreasing yields evident at the higher ranks. Important in terms of processing

was the observation that coal solutions to the left of the vertical dotted line in Figure 7 were extremely difficult to filter. For these coals the solutions immediately blind the filter, which had to be replaced frequently to allow reasonable filtration rates. A drop of filtrate from the Shoemaker coal (reflectance 0.77) was placed on a glass slide and examined under a microscope where reticulated coal fragments suspended in the solution were observed. Presumably the extracts from the low rank bituminous coals are not true solutions but are colloidal-like mixtures, which would be difficult to remove by simple filtration. Coals with reflectances above 1.0 filtered without any difficulty. The highest extraction was obtained with the Kingwood coal at 73.2% on a daf basis. This coal filtered quite easily.

5.2 Correlation of Coal Characteristics with Solvent Extraction Performance

There was no clear relationship between extraction behavior and rank with true density, surface area, or porosity of the feed coals and insoluble residues, see the data compiled in Appendix 2. This lack of correspondence is probably because of the small population of coals and the fact that these physical attributes do not vary much within the range of rank investigated [44].

On the other hand, firm correlations were noted with extraction and thermoplastic behavior with a range of coal rank parameters. Some examples are provided in Figures 8 through 12. Although arguments with Audibert-Arnu dilatometry and FSI would lead to similar conclusions drawn with the Gieseler plastometry results, correspondence with the former two methods were more scattered.

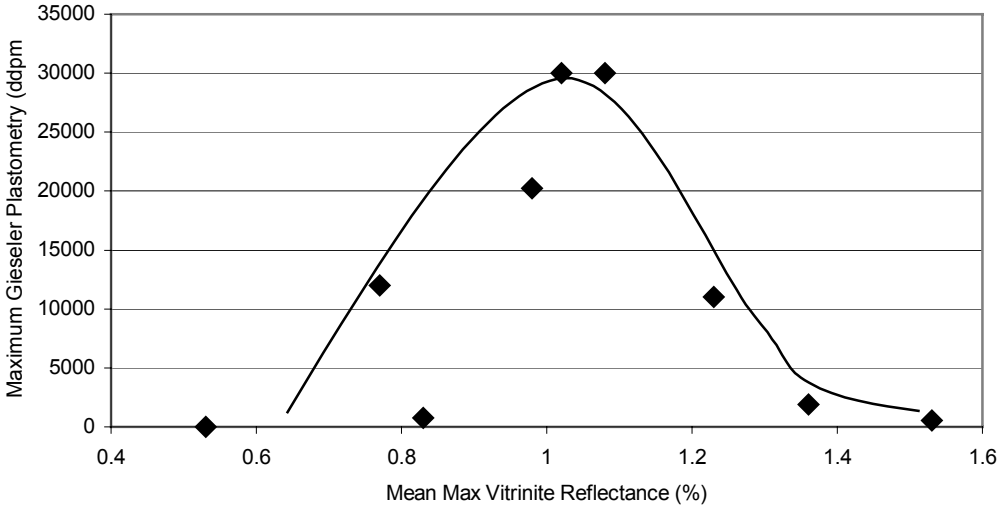

Figure 8. Reflectance (rank) vs. maximum Gieseler plasticity.

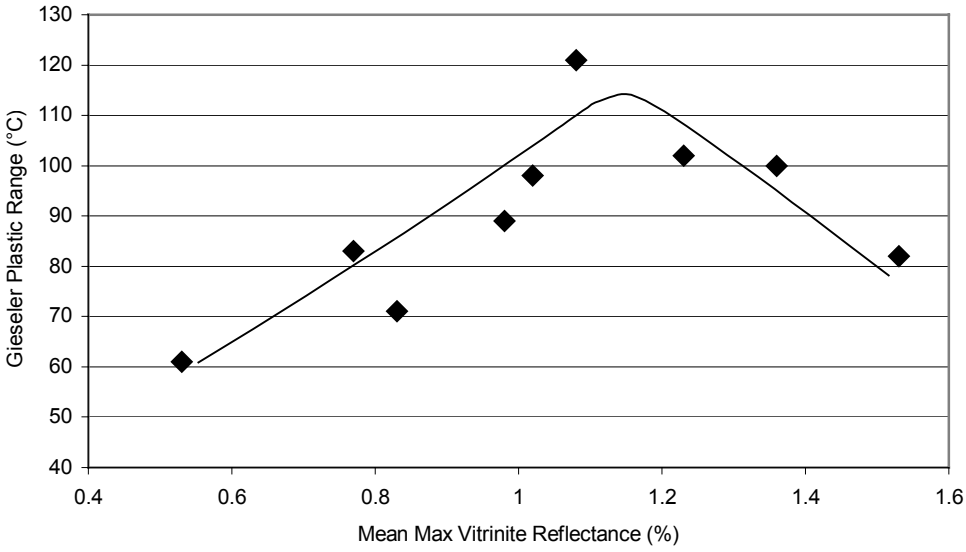

Figure 9. Reflectance (rank) vs. Gieseler plastic range.

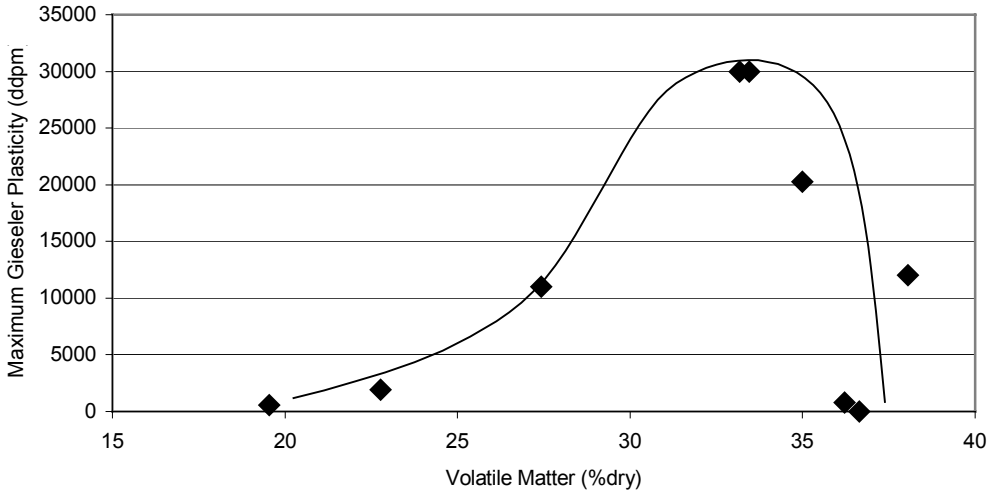

Figure 10. Volatile matter vs. maximum Gieseler plasticity.

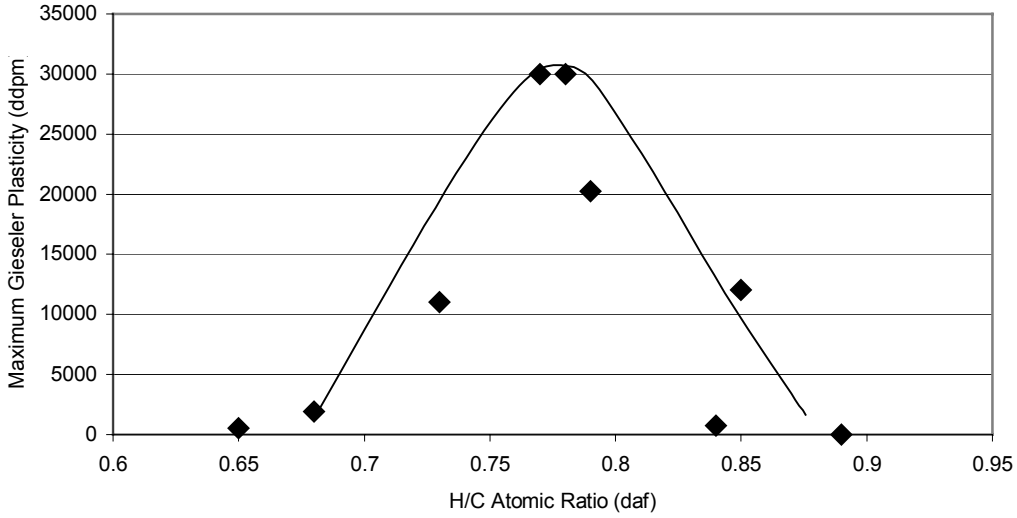

Figure 11. H/C atomic ratio of feed coals vs. maximum Gieseler plasticity.

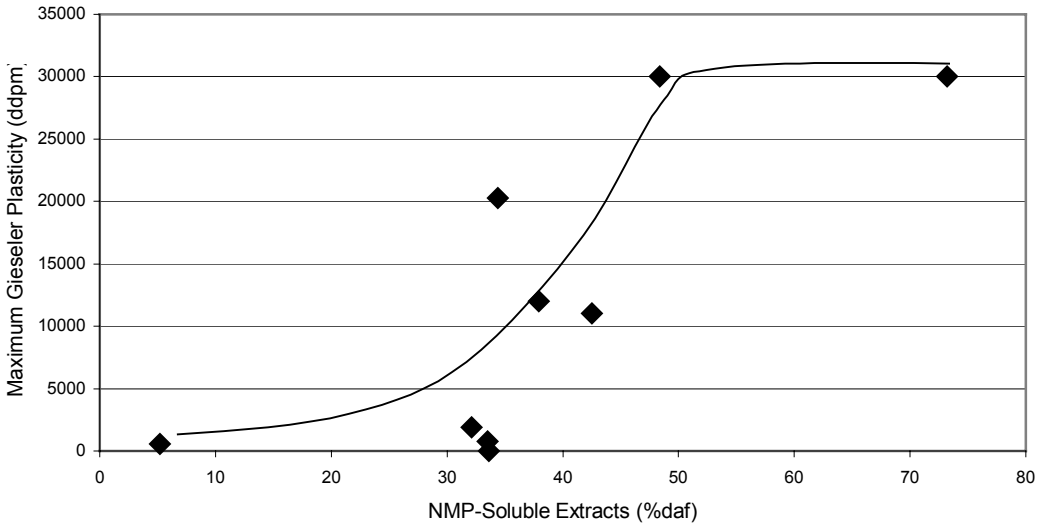

Figure 12. NMP extract yield vs. maximum Gieseler plasticity.

All feed coals and their residues and extracts were examined by FTIR for functional group comparisons. In particular, the peaks associated with the aromatic C-H (H_{ar} at about 3050 cm^{-1}) and aliphatic C-H (H_{al} at about 2900cm^{-1}) vibrational stretching modes were integrated after baseline correction. The ratio H_{ar}/H_{al} can be used as an indicator of aromaticity [45] and, thus, can be considered a rank parameter. Example spectra are provided in Figure 13, which compares the infrared spectra for the Kingwood feed coal, extract, and residue. Figure 14 compares the H_{ar}/H_{al} ratio with C/H atomic ratio calculated from knowing the elemental composition of the feed coals. Not unexpected, the two ratios appear to be correlated in that the feed coals become more aromatic as rank increases. Interestingly, the H_{ar}/H_{al} ratio of the feed coal and extracts increase as their respective reflectances increase, as seen in Figure 15. Using FTIR to determine H_{ar}/H_{al} ratio was not possible for all of the residues, however, because for some of these products the peak intensities were too weak to integrate. FTIR and elemental analysis are summarized in Appendix 5 and 16, respectively.

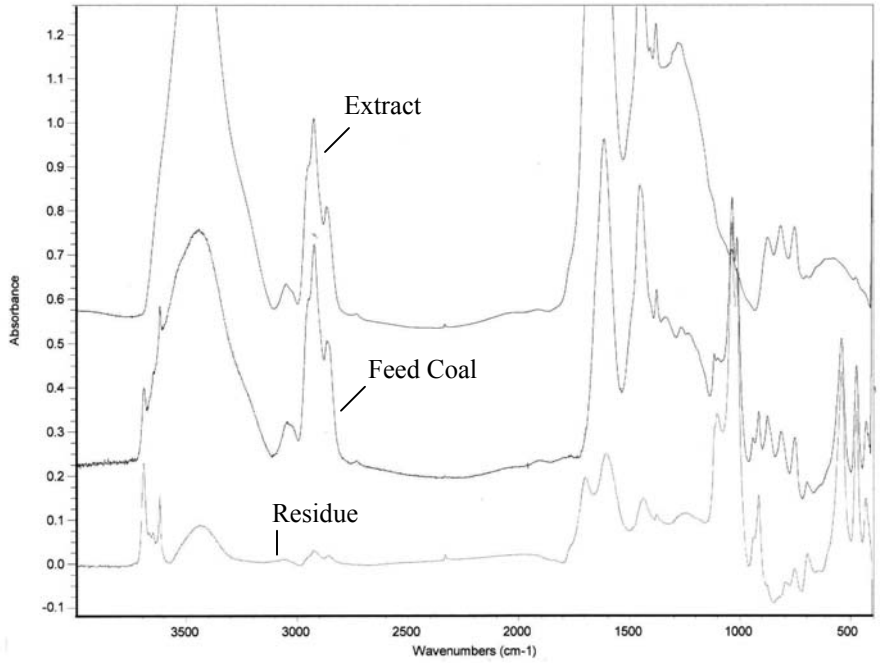

Figure 13. FTIR spectra of Kingwood coal, extract, and residue.

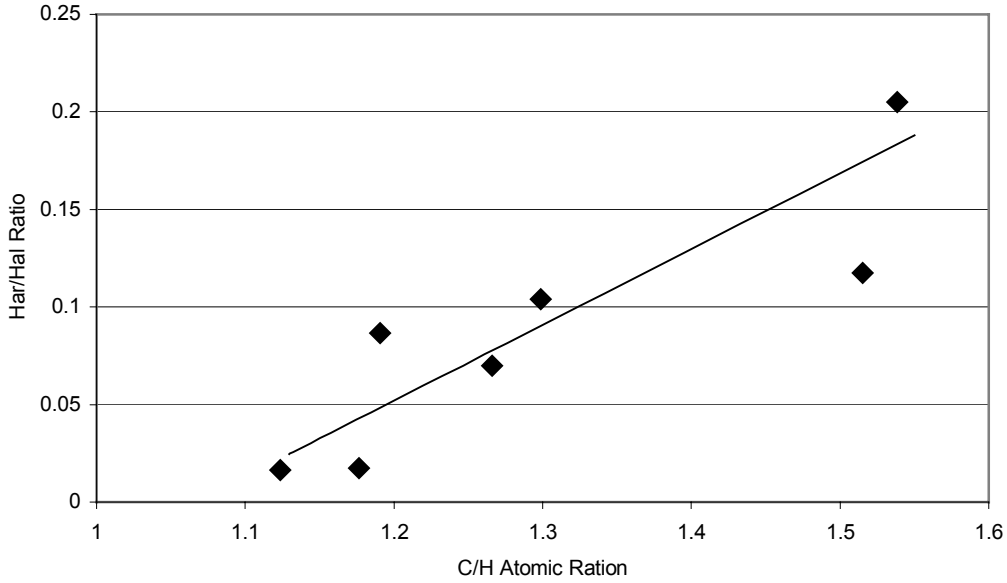

Figure 14. Atomic C/H ratio vs. H_{ar}/H_{al} ratio of feed coals.

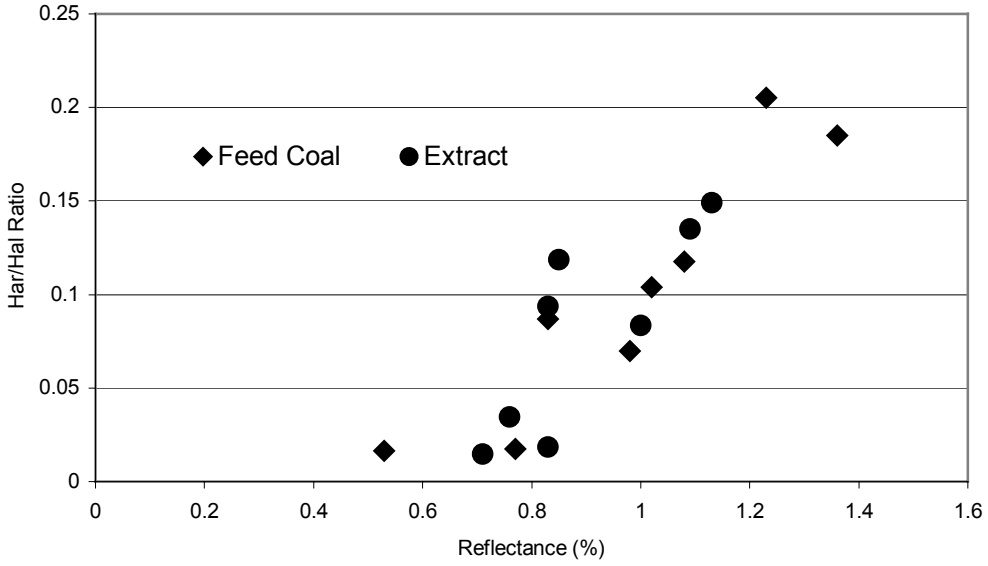

Figure 15. Reflectance vs. H_{ar}/H_{al} ratio of feed coals and extracts.

Figure 16 compares the thermogravimetric analysis of the feed coals, extracts, and residues. Weight change with temperature for the feed coals follows what would be expected with rank in that volatile material decreases as rank increased. The extracts lose more weight than either the feed coals or residues and did not follow weight changes associated with rank as closely as the feed coals. It is interesting that the insoluble residues still contain significant amounts of volatile material even after solvent extraction.

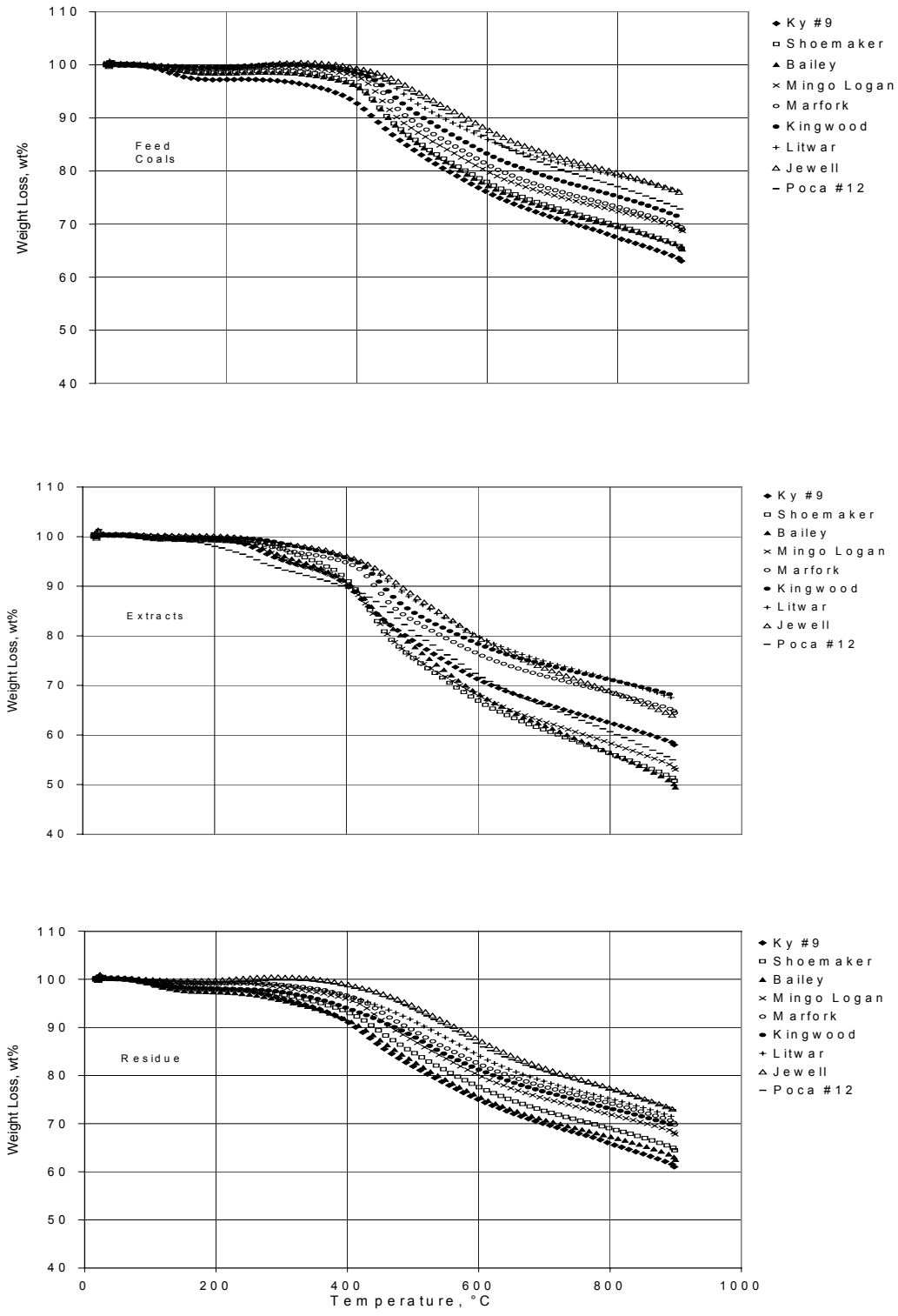

Figure 16. TGA analysis of feed coal, extract, and residue.

5.3 Optical Microscopy of Coal and Solvent Extracted Products: Observations and Comments

For this research project, the petrographic maceral and mineral classification terminology used in the descriptive and quantitative analysis of coal and insoluble residue is shown in Table 7. The vitrinite group as used in this report consists of several subgroup macerals. Telinite displays wood structure and collinite appears structureless together with attrital vitrinite. Pseudovitrinite is slightly higher in reflectance than collinite and exhibits distinct fracture patterns. Attrite vitrinite was divided into particulate and layered categories.

Collinite, appearing structureless, is homogeneous and is a major component of most coals. The collinite is commonly used in ranking coal by determining its reflectance. The reflectance values are reported as V-types, which represent reflectance categories. The distribution of V-types determined for the feed coals, extracts, and residues are provided in Appendices 8, 9, and 10, respectively. Telovitrinite consists of vitrinite that displays cellular plant structures. Pseudovitrinite is a variety of telinite that commonly is higher reflecting than other vitrinites and displays remnant cell structure, fusiform slits, and stepped particle edges. Attrital vitrinite frequently occurs as fine size bands (attrital banded) and/or particles (attrital fine) in attrital coal. Figure 17 shows some of the macerals identified in one of the bituminous coals used in this project.

Table 7. Petrographic maceral and mineral classification.

	Organic Macerals
Vitrinites	**Intermediate Reflecting Matrix Material**
Collinite	Does not display woody cell structure.
Telinite	Displays woody cell structure.
Attrital Fines	Particulate Vitrinite (<20 μm) in matrix.
Attrital Banded	Banded Vitrinite (<20 μm) in matrix.
Pseudovitrinite	Higher than normal Vitrinite reflectance with slitted fissures and stepped edges.
Liptinite	**Lowest Reflecting**
Sporinite	Spore and/or pollen outer coatings.
Cutinite	Leaf and stem coatings.
Resinite - Turpene	Probably exudation plant resins.
Resinite – Others	Probably plant transport ducts.
Inertinite	**Highest Reflecting**
Coarse	
Semifusinite	Thermally, chemically or biologically porous charcoal like (+20μm).
Fusinite	Like Semifusinite but higher reflecting (+3%) (+20μm).
Fine	
Micrinite	Granular (-5μm) decay products.
Macronite	Oval to rounded (+5μm)
Inertodetrinite	Mostly particulates (-20μm) Semifusinite and/or Fusinite.
Mineral Matter	**Inorganic Rocks and Minerals**
Coarse	
Shales	Fine granular sedimentary rock.
Bone	Mixture of organics with +30% minerals.
Others	Sandstone, siltstone, limestone etc.
Fine (Optional)	
Clay	Various minerals mostly illite and kaolinite.
Pyrite	FeS_2 in all forms both primary and secondary.
Carbonates	Calcite, siderite, ankerite and others.
Quartz	SiO_2
Others	Wide variety of most sedimentary and secondary precipitate minerals.

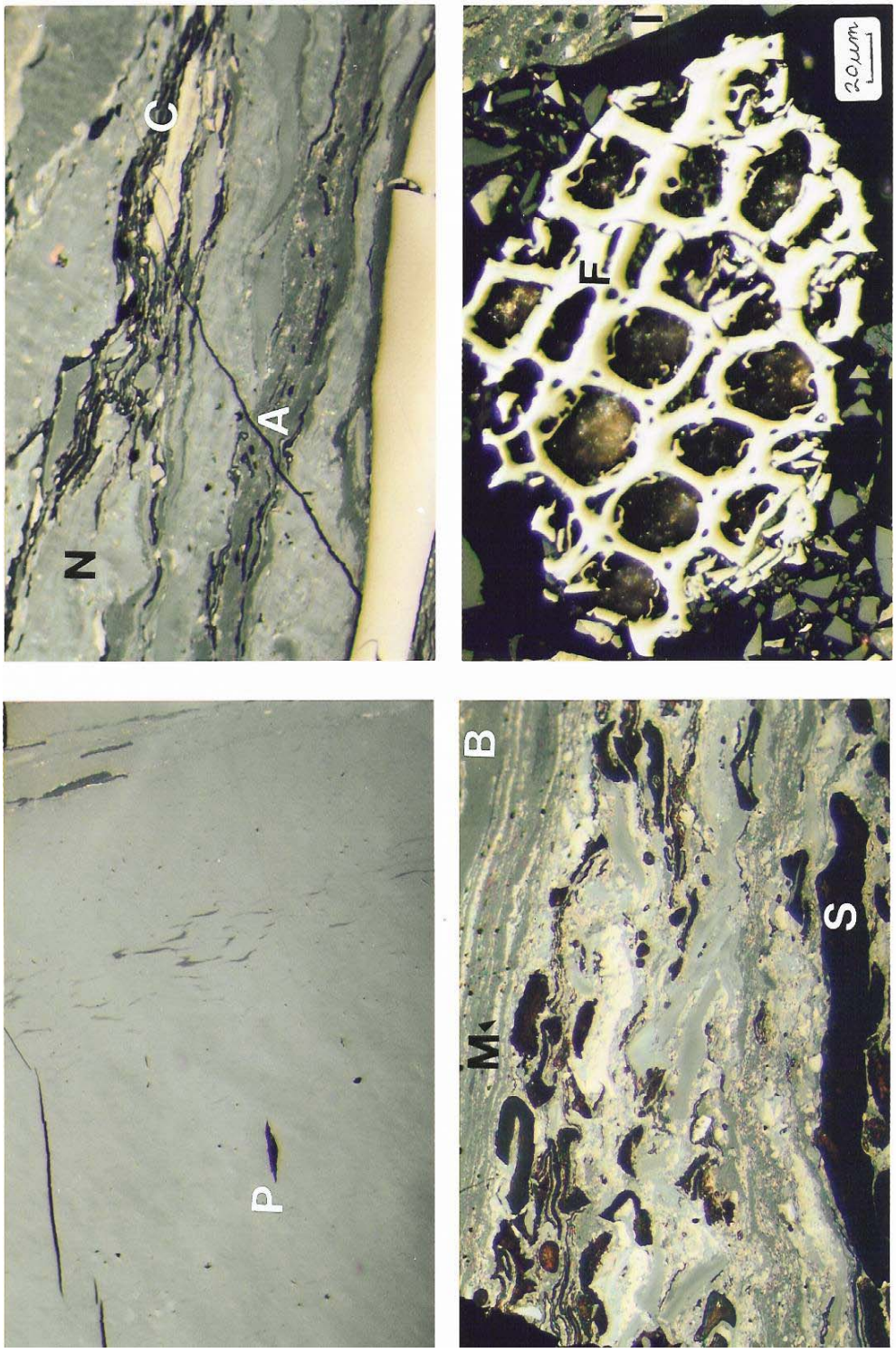

Photomicrographs of Macerals in Arch Minerals Mingo Logan Coal, West Virginia Showing; P=Pseudovitrininte, A=Fine Attrital Vitrinite, B=Banded Attrital Vitrinite, S=Sporinite, C=Cutinite, M=Micrinite, N=Macrinite, I=Inertodetrinite and F=Fusinite. Reflected Light In Oil, X600.

Figure 17. Features of maceral components in bituminous coal.

Liptinite in bituminous coals has lower reflectance than the other group macerals. It consists of sporinite, cutinite, and resinite (lights and darks). Sporinite is commonly derived from the protective coatings of the reproductive organs of plants. Cutinite is derived from the protective coatings on leaves and stems. Liptinite is high in hydrogen and volatile matter. Resinous materials may be excretion products and/or duct and cell filling.

The inertinite maceral group consists of high carbon and relatively high oxygen materials with low volatility. It generally has the highest reflectance of all the other macerals. Inertinite has limited plasticity when heated. It is hard and tends to exhibit relief in polished samples. The inertinite macerals consist of fusinite, semifusinite, inertodetrinite, micrinite, macrinite, secretinite and funginite. Fusinite selectively exhibits cell wall preservation like charcoal. Semifusinite also exhibits distinct charcoal-like wall structures but is lower in reflectance than fusinite but higher in reflectance than vitrinite. Inertodetrinite consists of less than 50μm fragments of the other inertinite macerals, such as semifusinite and fusinite fragments. Micrinite occurs as relatively amorphous <10μm specks in vitrinite. Macrinite may be round or irregular in shape and exceeds 10μm in size but seldom exceeds 50μm. Funginite is frequently rounded to oval and less than 30μm in size. It commonly contains a network of walls and windows that are evidence of its fungal origin. Secretinite is commonly rounded to oval but can also be rod-like in shape. Secretinite may be the products of oxidation of resinite ducts in plants.

5.3.1 Petrographic Analysis of Feed Coals and Insoluble Residues

The basic coal petrographic data can be broken down into reactives and inerts as shown in Table 8. The reactives are more sensitive to oxidation and thermal changes.

The reactives consist mostly of vitrinite, which determines most of the coal's characteristics. The liptinite portion of the reactives does not respond well to NMP extraction while the vitrinites are the most amenable to extraction. The inerts remain unchanged during NMP extraction and concentrate more in the insoluble residue.

Table 8. Summary of petrographic analysis of coal and insoluble residue.

	Coal		Residue		Extraction Yield, wt%	
Coals	Reactives	Inerts	Reactives	Inerts	Extract	Residue
Ky #9	78.2 (7.5)*	21.8 (5.6)**	76.6 (9.0)*	23.4 (7.6)**	30.3	67.7
Shoemaker	79.2 (7.0)	20.8 (4.2)	68.8 (7.2)	31.2 (7.4)	34.1	65.9
Bailey	80.2 (6.5)	19.8 (3.4)	74.5 (7.6)	25.5 (6.1)	30.9	69.1
Mingo-Lo.	67.1(13.5)	32.9 (2.9)	60.7 (72.9)	39.3 (4.3)	32.4	67.6
Marfork	71.7 (6.5)	28.3 (4.4)	52.0 (13.9)	48.0 (6.9)	45.3	54.7
Kingwood	79.6 (5.0)	19.4 (4.3)	63.1 (11.4)	36.9 (16.4)	66.7	33.3
Litwar	76.9 (6.3)	23.1 (2.6)	65.7 (4.3)	34.8 (5.1)	40.6	59.4
Jewell	79.4 (2.9)	20.6 (4.4)	74.3 (2.9)	25.1 (5.6)	30.0	70.0
Poca #12	80.6 (1.2)	19.4 (3.1)	80.0 (1.1)	20.0 (2.3)	5.0	95.0

* (0.0) Liptinite
**(0.0) Mineral Matter

The mineral portion of the inerts is determined by volume (area) in the petrographic analysis. Thus, it has a disproportionate impact on the residue weight since the mineral weight is about twice that of macerals per unit volume. The summary petrographic data in Table 8 shows the inerts, liptinite, and mineral matter are almost all higher in the insoluble residue than in the parent coal. The most NMP extractable coals show the greatest increase in inerts, liptinite, and mineral matter in the residues. From other data it is also evident that particulate attrital vitrinite is the least amenable vitrinite in NMP extraction. Thus vitrinite, with the partial exception of particulate attrital vitrinite, is the NMP extractable portion of bituminous coals.

The composition of the feed coals and insoluble residues were calculated petrographically and converted from a volume to a weight basis. The results of the

calculations are tabulated in Appendix 14 and 15, respectively. If in the solvent extraction only vitrinite is dissolved, then it is possible to estimate the amount of vitrinite remaining in the insoluble residue from mass balances. Comparison of the petrographic and mass balance estimations in Figure 18, shows a reasonable relationship. However, vitrinite content by mass balance underestimates that by petrography. This could because non-vitrinite material passed through the filter during product work-up and/or the assumptions associated with petrographic analysis.

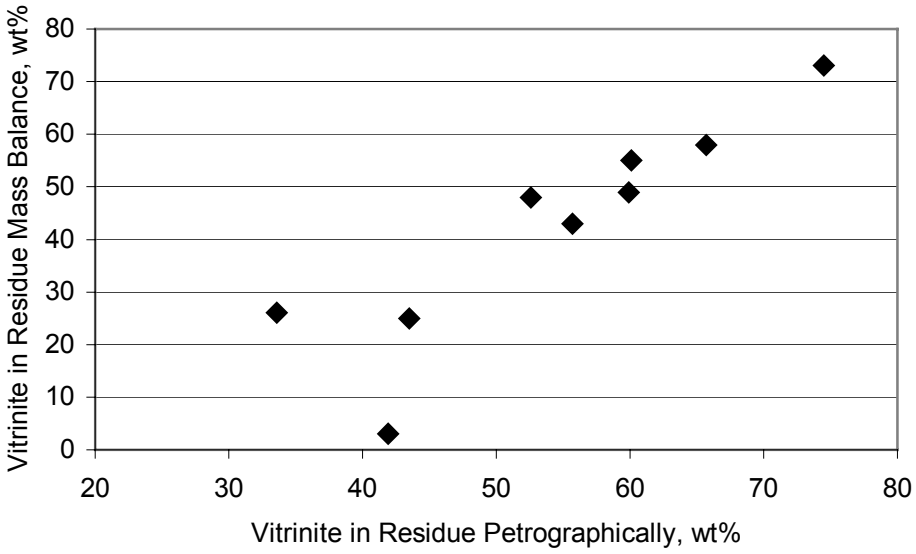

Figure 18. Estimated vitrinite content in insoluble residues.

Table 9. Classification of non-maceral microstructures.

Microstructure Categories	**Subdivisions of Microstructure Categories**
Normal Coal	Vitrinite coarse, +50µm Semifusinite coarse +50µ Fusinite coarse +50µm. Bright attrital >75% Vitrinite. Intermediate attrital <75% and <50% Vitrinite. Dull attrital <50% Vitrinite.
Fine Coal <5 microns	Angular Rounded Indistinct
Pseudovitrinite	All relatively high reflectance Slitted Remnant cellular texture Homogeneous Combinations of above
Microbrecciated	Fine Intermediate Coarse Faults or folds
Oxidized (Weathered)	Slight Moderate Bad
Oxidized (Thermal)	Rounded Bright rims Porous Semicoked Coked
Coarse Mineral Matter	Clay Shale Pyrite Carbonate Quartz Bone Others
Cenospheres	Semicoke Coked
Contamination	High-volatile coal Medium volatile Low volatile Others designated

5.3.2 Coal Types and Non-Maceral Microstructures

Some of the criteria used in the microscopic identification and counting of coal non-macerals and minerals are listed in Table 9. A normal coal is divided into bright, intermediate, and dull based on vitrinite content. This serves to separate coal into the rock types and is an indicator of the degree of homogeneity. Coarse vitrinite, pseudovitrinite, and fusinite are also counted.

There are many important coal characteristics that are not determined in a normal maceral analysis. Such features as oxidation are determined as well as brecciation faulting and folding and other occurrences such as cenospheres. Each of the determined microstructures has a specific significance. Non-maceral microstructure analysis is also useful in determining the extent to which a coal has or can be beneficiated based on mineral form and association. It is also very useful in determining contamination where coals of different ranks or other materials have been mixed either inadvertently or intentionally with the subject coal.

The non-maceral petrographic data show that there are only minor oxidation, contamination, or brecciation in the coals. The coarse mineral matter varied but is not unusually high in any of the coals. The sum of bright and intermediate attrital plus coarse vitrinite and pseudovitrinite, shown in Table 9, range from 61.9 o 83.3% by volume. None of the non-maceral data showed any correlation with NMP extractability.

5.3.3 Coal Etching in NMP

The nine coals were etched to determine if extract yield correlated with some microscopic feature of the etched coal. Dried polished coal pellets (ground and polished coal mounted in plastic) were used for etching. Following exposure to NMP and

treatment in the microwave oven for 30sec, the water rinse appeared to remove all of the NMP leaving coal particles that contained areas with various degrees of extraction (relief and fracturing). When an alcohol rinse was used, the relief and fracturing that differed for various coal macerals and coal types were retained but staining was added. Liptinite and inertinite did not show any evidence of change because of NMP etching. The vitrinite, particularly the coarser layers or bands, showed significant alteration. The Ky # 9 showed the greatest relief with the telinite cell walls showing less alteration than the cell fillings. Staining differences were also observed. The Shoemaker coal developed some distinct crack patterns in addition to relief changes. The staining consisted of a variety of colors, particularly blue with some green. A larger portion of what appeared to be collinite in the unetched coal developed a very distinct cellular pattern after etching: this was very prominent in the Shoemaker, Bailey, and Mingo Logan samples. The staining cellular structures became very distinct in the Marfork coal. The vitrinite staining appeared less intense in the Kingwood sample and distinct conchoidal fractures developed around the coal particles and many of the coal particles were reacted to the extent that they were plucked out of the etched Kingwood surface. The Litwar had less staining, the colors were more yellow to brown than blue, and the edges of particles had very distinct cracks. The etching caused the cellular structure of some vitrinite to become very distinct. The Jewell coal showed very little staining but the conchoidal cracks around particles became very distinct. The Poca #12 when etched did not develop stains but showed the most extensive fracturing around the coal particles.

The lower rank coals, including Ky #9, Shoemaker, and Bailey, showed greatest changes due to NMP etching. The Mingo Logan surface developed very distinct

conchoidal cracks. The Litwar sample had very little staining and the colors shifted from blue to yellow and brown, with pronounced particle cracking around the edges. The Jewell and Poca #12 had very little staining and were most unchanged except for conchoidal cracks. The coal staining might be because NMP remains on the surface after the alcohol rinse. The internal crack patterns are probably due to shrinkage while the conchoidal edge fractures may be due to a pressure difference between the coal and mounting media.

As expected, the liptinite, inertinite, and mineral matter did not change because of etching. The staining appears to be rank related. All of the vitrinites except particulate attrital vitrinite stained in all but the higher rank coals. The kind and amounts of fractures also appear to be related to vitrinite maturity. A quantitative relationship between etching characteristics and extractability was not established. Examples of the solvent-etch coal surfaces are shown in Figures 19, 20, and 21.

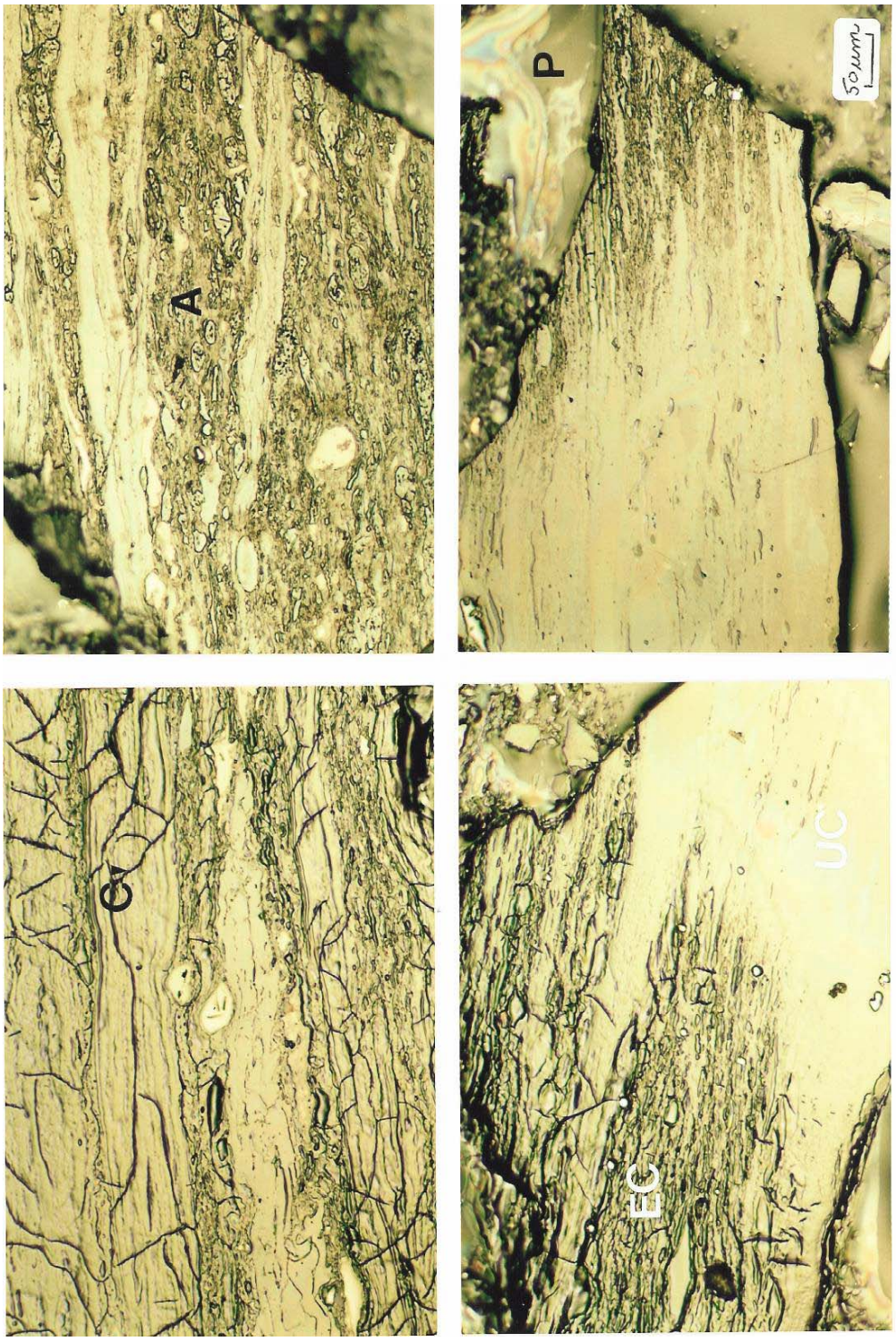

Photomicrographs of NMP Etched Pittsburgh Coal From Shoemaker Mine, Marshall County, West Virginia Showing; A=Etched Attrital Coal, EC=Etched Collinite and UE=Unetched Collinite, C=Cracks and P=Plastic. Reflected Light In Air, X160.

Figure 19. Optical microscopy of NMP-etched coal.

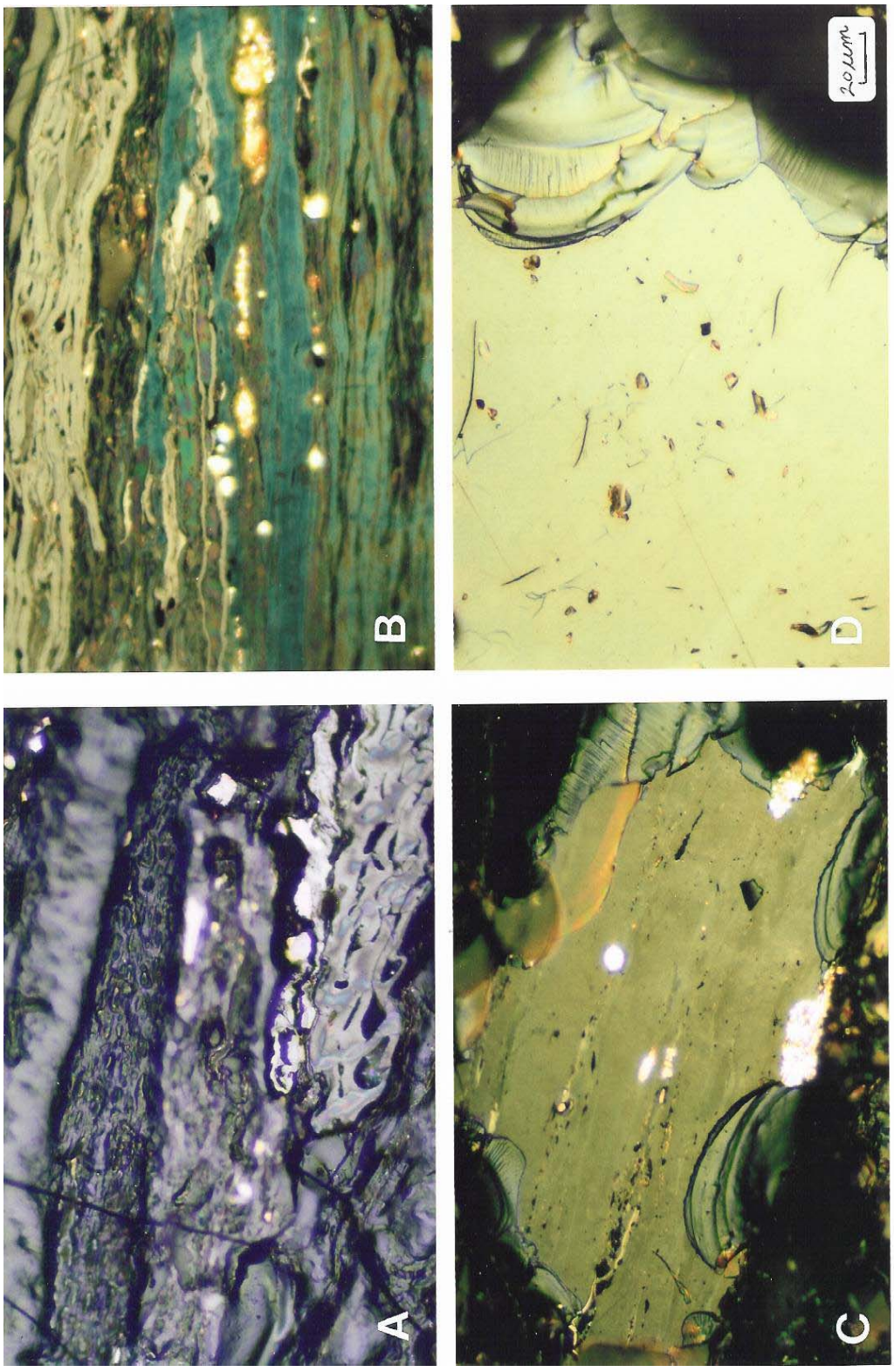

Photomicrographs of NMP Etched Coals Showing; A=Various Shades of Dark Blues Stains In Deeply Etched Kentucky No. 9; B=Bright Blue and Green Stains in Banded Bailey Coal; C=Olive Stains In Kingwood Coal and Concoidal Fractures an Particle Edges; and D=Unstained Poca 12 Coal With Concoidal Cracks. A Through D Arranged In Order of Inceasing Rank. Reflected Light In Oil, X600.

Figure 20. Optical microscopy of NMP-etched coal.

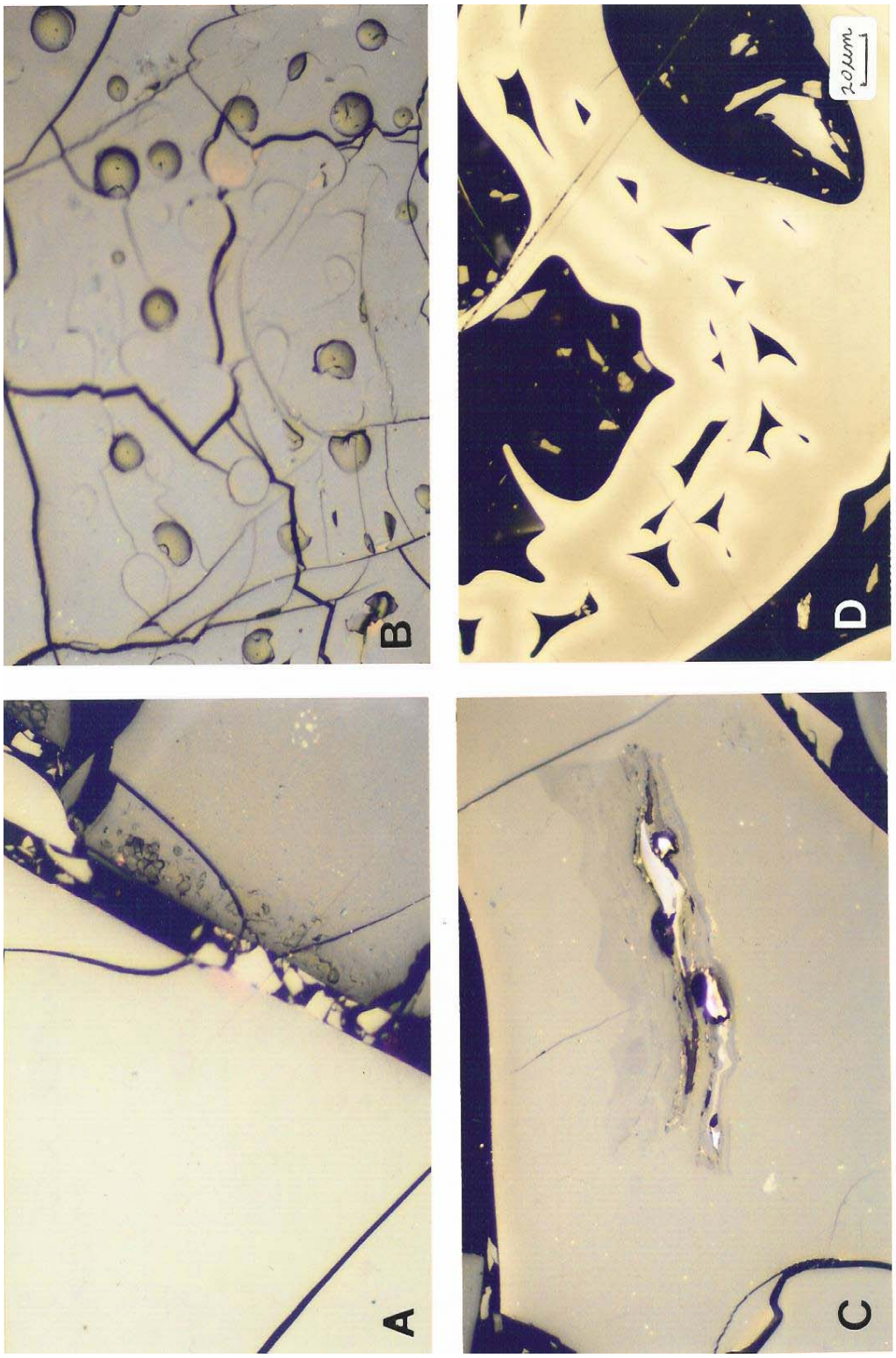

Photomicrographs of NMP Extracted Pitch Showing; A - Has White (most Altered) and Gray (Less Altered) Particles; B - Showing Circular Areas of NMP Entrapment; C - Shows Partially Altered Coal; and D - Shows Flow Patterns With Lighter (Oxidized) Surfaces. Reflected Light In Oil, X600.

Figure 21. Optical microscopy of NMP-etched coal.

5.3.4 Microscopic Properties of NMP-Soluble Extracts

The extracts were heterogeneous in terms of their degree of alteration and flow characteristics, and NMP, coal, and oxidized content, as shown in Table 10. The extracts contained areas that ranged from white (bright) to various shades of gray (dark). This indicated differences in treatment of the extract. There are flow shapes which are also related to how the extracts were processed. Several of the extracts have NMP inclusions. All of the extracts have traces of coal, with small amounts of coal in Shoemaker and Bailey, and a large amount in the Poca #12, as summarized in Table 10. All of the extracts have some oxidized material. It is most abundant in the Shoemaker, Bailey, Kingwood, and Litwar coals, which were prepared for microscopy at the same time.

Table 10. Microscopic properties of NMP-soluble extracts

Decreasing Reflectance →								
Coal	White	Light Gray	Darker Gray	Darkest Gray	Flow Shapes	NMP	Coal	Oxidized
Ky #9	81.7	14.0	--	--	3.3	0.3	--	0.7
Shoemaker	62.5	20.0	1.0	6.7	1.3	1.3	0.7	6.5
Bailey	50.5	34.6	4.3	--	1.0	T	0.3	9.3
Mingo Lo.	80.7	9.6	--	0.3	4.7	0.7	T	4.0
Marfork	87.6	3.7	--	--	7.7	--	T	1.0
Kingwood	62.7	18.0	2.7	--	4.3	0.3	T	12.1
Litwar	62.4	20.7	1.0	--	3.3	--	T	12.2
Jewell	73.5	3.3	1.3	--	17.6	1.3	T	3.1
Poca #12	6.0	57.5	3.0	0.3	2.7	2.7	26.5	1.4

T= Occurred in count area but not in count.

5.3.5 Microstructures in NMP-Insoluble Residues

The insoluble residues contained a variety of relatively distinct microstructures that range from unaltered or rounded particles to particles with altered edge surfaces. In addition, all of the samples had some fused agglomeration. Some particles showed

distinct pore development and all of the samples displayed oxidation, Figure 22 and Table 11.

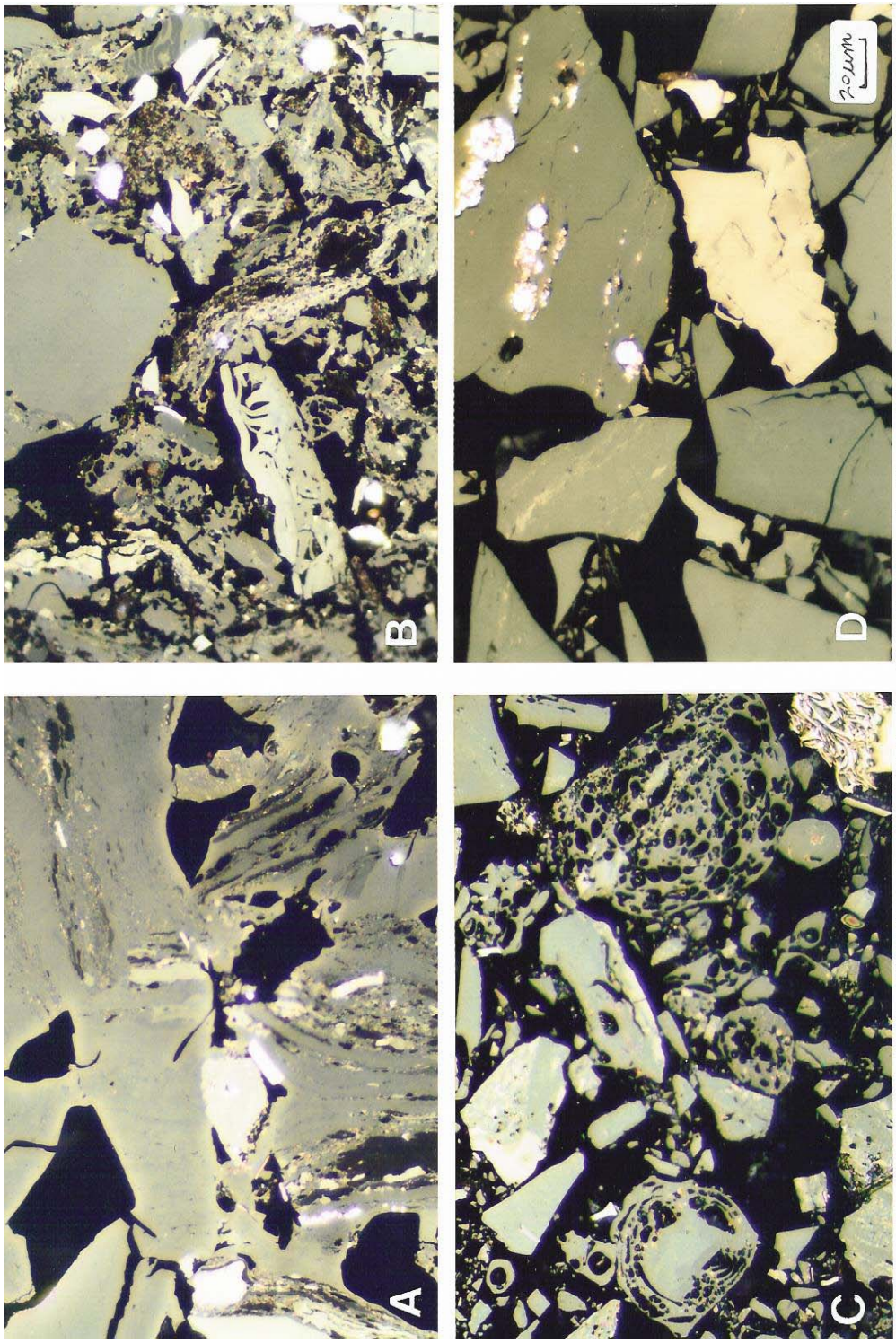

Photomicrographs of NMP Residue From Extraction Test Showing; A – Shows Coarse Coal Agglomerate With Oxidized Particle Borders From Extracted Bailey Coal; B- Shows Loose Aggregates of Fine Size High Inert Coal From Kingwood Residue; C – Shows Spherical Porous Coal Alteration Products in the Jewell Extraction Residue and D – Shows Unaltered Coal Particles From the Poca #12 Extraction Residue. Reflected Light In Oil, X600.

Figure 22. Insoluble residue from NMP extraction.

Table 11. Microstructures in NMP-insoluble residues.

			Reacted	Agglomerates			
Coal	Unaltered	Rounded	Edges	Coarse	Fine	Pores	Oxidized
Ky #9	14.8	6.8	13.6	56.4	7.6	0.0	0.8
Shoemaker	9.6	5.6	0.0	78.4	0.0	0.0	6.4
Bailey	12.8	6.4	0.0	72.8	0.0	0.0	8.0
Mingo Lo.	44.4	13.6	10.4	29.6	0.0	0.0	2.0
Marfork	17.6	4.0	9.2	60.4	8.0	0.0	0.8
Kingwood	11.8	15.6	4.8	28.4	23.6	14.4	1.4
Litwar	14.2	7.0	9.6	39.6	20.8	6.4	2.4
Jewell	30.0	18.8	17.6	1.2	2.0	26.8	3.6
Poca #12	61.6	20.4	14.0	1.2	0.0	0.0	2.8

The coal with the most liptinite and inerts, Mingo Logan, had a large amount of unaltered coal. The highest rank coals, Jewell and Poca #12, also had significant amounts of unaltered coal. All of the coals but the higher rank Jewell and Poca #12 had large amounts of fused agglomerates or aggregates. The Kingwood, Litwar, and Jewell had particles with distinct pore development. All of the residues had some oxidized coal particles particularly Bailey and Shoemaker. The Ky #9, Shoemaker, and Bailey had large amounts of aggregates which may cause filtering or separation problems. This effect was borne out in the laboratory extraction studies.

5.3.6 Reflectance Characteristics of Coal, Extract, Residue, FSI Coke

The vitrinite reflectance of coals increases with coal rank as shown in column one in Table 12. The reflectance of the vitrinite in the extracts and residues has a similar pattern but differs in the actual volumes. The Shoemaker, Bailey, Kingwood, and Litwar all have significant amounts of oxidized materials in the insoluble residues and extracts. The estimated R_o from the coal FSI coke parallels that of the coal reflectances, except for

the Kingwood estimated reflectances which are high. The estimated reflectances from the extract FSI show the same rank trends as that of the coal, but the Kingwood is higher in the FSI coke. The estimated reflectance from the insolubles shows no trends with the other reflectance data. This may be due to significant oxidation of the residue used to make the FSI button.

The vitrinite reflectances of the extracts were generally lower than the vitrinite reflectances of the feed coals. The Ky #9 extract sample appeared relatively uniform in reflectance (0.59% R_o). The Bailey extract is similar to Shoemaker, but contains less NMP and more evidence of oxidation. The Shoemaker extract appeared variable in reflectance averaging 0.71 %R_o . In addition to cracks, some particles had round cavities that appear to be due to entrapped NMP. Most of the samples also contained oxidized coal and a small amount of undissolved attrital coal.

Table 12. Reflectance of indicated samples in the order of increasing rank.

Coal	Coal Vitrinite Mean Max., $\%R_o$	Vitrinite In Extract, $\%R_o$	Vitrinite In Residue, $\%R_o$	Estimated $\%R_o$ From Coal FSI	Estimated $\%R_o$ From Residue FSI	Estimated $\%R_o$ From Extract FSI
Ky #9	0.53	1.59	0.57	1.60	0.60	0.66
Shoemaker	0.77	0.71	0.66	0.90	0.60	0.86
Bailey	0.83	0.76	0.73	0.90	0.60	0.89
Mingo Logan	0.98	0.83	0.86	0.99	0.79	1.07
Marfork	1.02	0.85	0.96	1.02	0.80	1.07
Kingwood	1.08	1.00	1.00	1.24	0.65	1.21
Litwar	1.23	1.09	1.14	1.25	0.68	1.26
Jewell	1.36	1.13	1.38	1.30	1.25	1.38
Poca #12	1.53	1.04	1.56	1.50	1.48	1.46

The Mingo Logan extract averages 0.83% R_o. In addition to cracks, some particles have traces of what appears to be NMP as well as partially dissolved coal. The Marfork extract has only slightly variable reflectance averaging 0.85% R_o . The Kingwood extract is homogeneous and has an average reflectance of 1.0% R_o and contains some normal cracks. In addition, this extract has a significant level of unusual features that appear to be due to plastic deformation and flow. There are traces of coal and a relatively large amount of oxidized surfaces. The Litwar extract has variable gray levels and an average reflectance of 1.09% R_o . It has some cracks and distinct plastic deformation features. It also has some thermal oxidation around the particles and cracks. The Jewell extract is relatively uniform in gray levels and has an average reflectance of 1.13% R_o . It contains the normal compression cracks in addition to some fusiform voids and a significant amount of flow structures and some oxidized coal. The Poca #12 extract has an unusually low reflectance of 1.04% R_o . The extract sample is different than all of the previous extracts. It consists of a continuous matrix binder phase with relatively distinct coal inclusions. Most of the coal inclusions are angular and consist of coal inerts and/or dull coal particles with attrital vitrinite, liptinite, and inertinite.

5.3.7 Petrographic Analysis of FSI Coke from Coal, Extract, Residue

The binder phase in cokes is produced from the reactive macerals and the filler phase is produced from incorporated inerts. During carbonization, the development of anisotropy increases upon moving up in rank from low rank bituminous to low volatile bituminous coals. The organic inerts are isotropic in all cokes while the binder phase carbon forms from the reactive macerals. A measure of anisotropy is expressed by an anisotropic index; the higher the index the more anisotropic the carbon. The feed coals,

extracts, and residues produced in the FSI determinations were analyzed petrographically Figures 23, 24, and 25, respectively, and the anisotropic index calculated, Table13 .

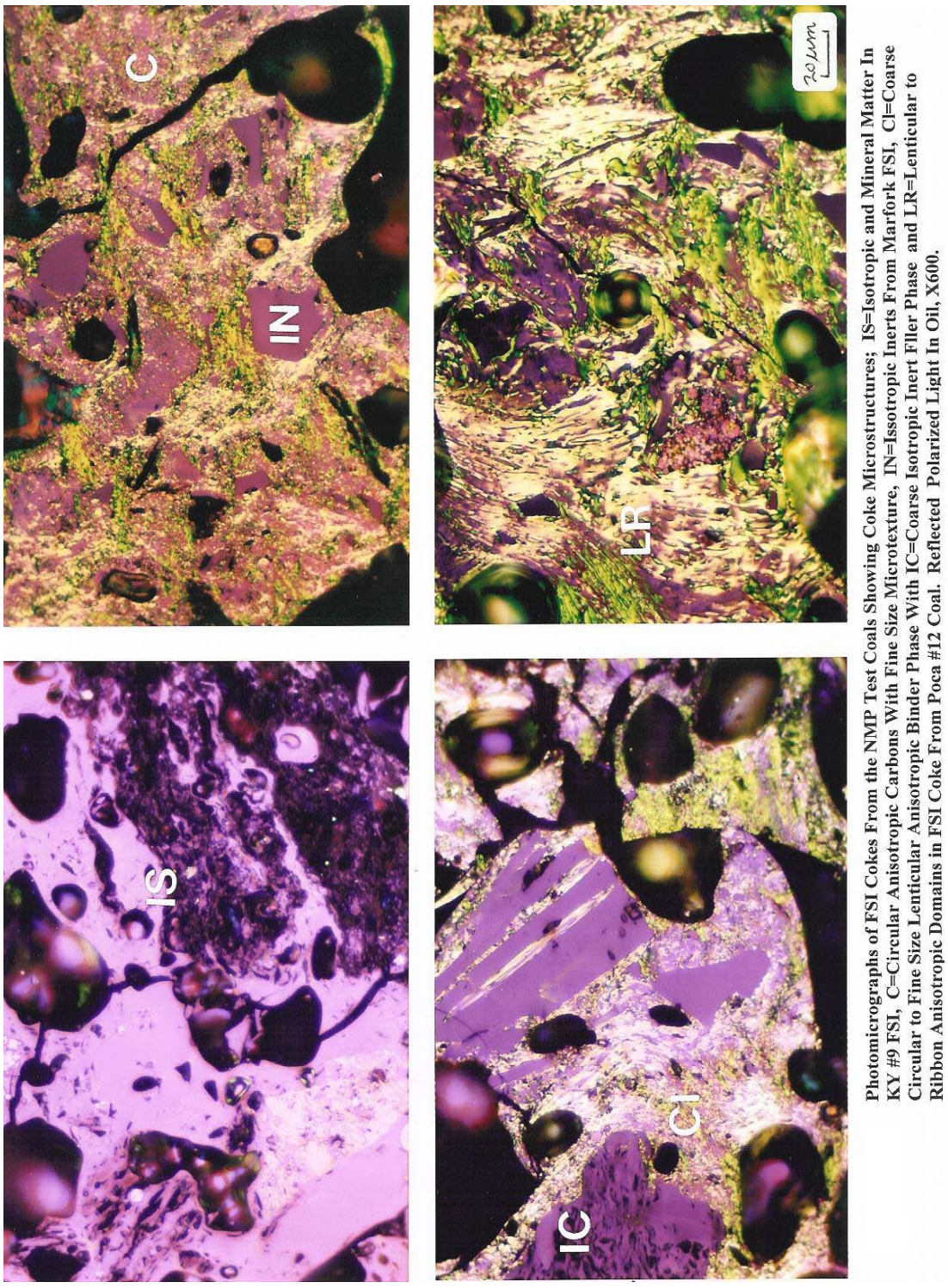

Photomicrographs of FSI Cokes From the NMP Test Coals Showing Coke Microstructures; IS=Isotropic and Mineral Matter In KY #9 FSI, C=Circular Anisotropic Carbons With Fine Size Microtexture, IN=Issotropic Inerts From Marfork FSI, CI=Coarse Circular to Fine Size Lenticular Anisotropic Binder Phase With IC=Coarse Isotropic Inert Filer Phase and LR=Lenticular to Ribbon Anisotropic Domains in FSI Coke From Poca #12 Coal. Reflected Polarized Light In Oil, X600.

Figure 23. Photomicrographs of FSI cokes from feed coals.

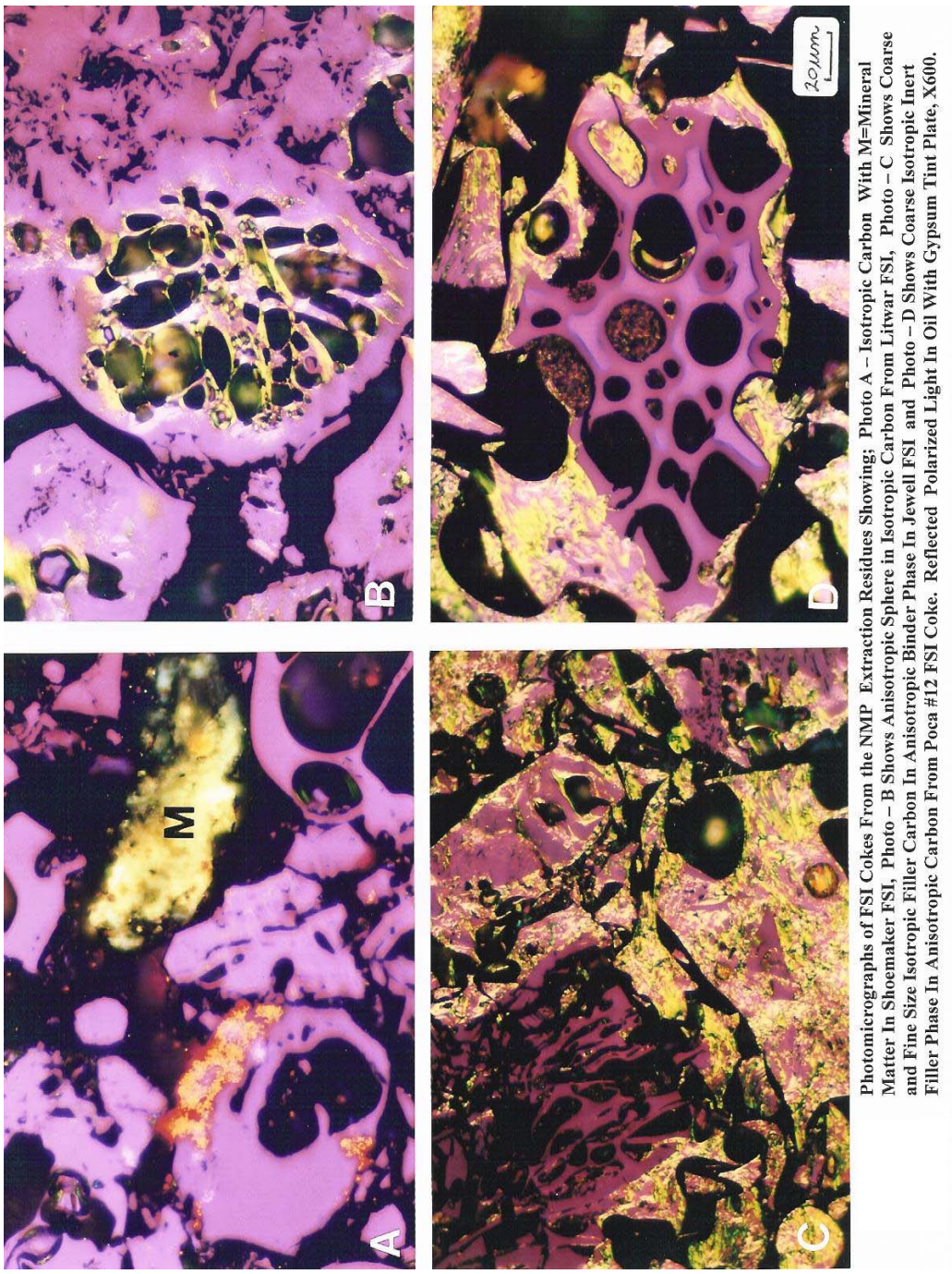

Photomicrographs of FSI Cokes From the NMP Extraction Residues Showing; Photo A – Isotropic Carbon With M=Mineral Matter In Shoemaker FSI, Photo – B Shows Anisotropic Sphere in Isotropic Carbon From Litwar FSI, Photo – C Shows Coarse and Fine Size Isotropic Filler Carbon In Anisotropic Binder Phase In Jewell FSI and Photo – D Shows Coarse Isotropic Inert Filler Phase In Anisotropic Carbon From Poca #12 FSI Coke. Reflected Polarized Light In Oil With Gypsum Tint Plate, X600.

Figure 24. Photomicrographs of FSI cokes from insoluble residues.

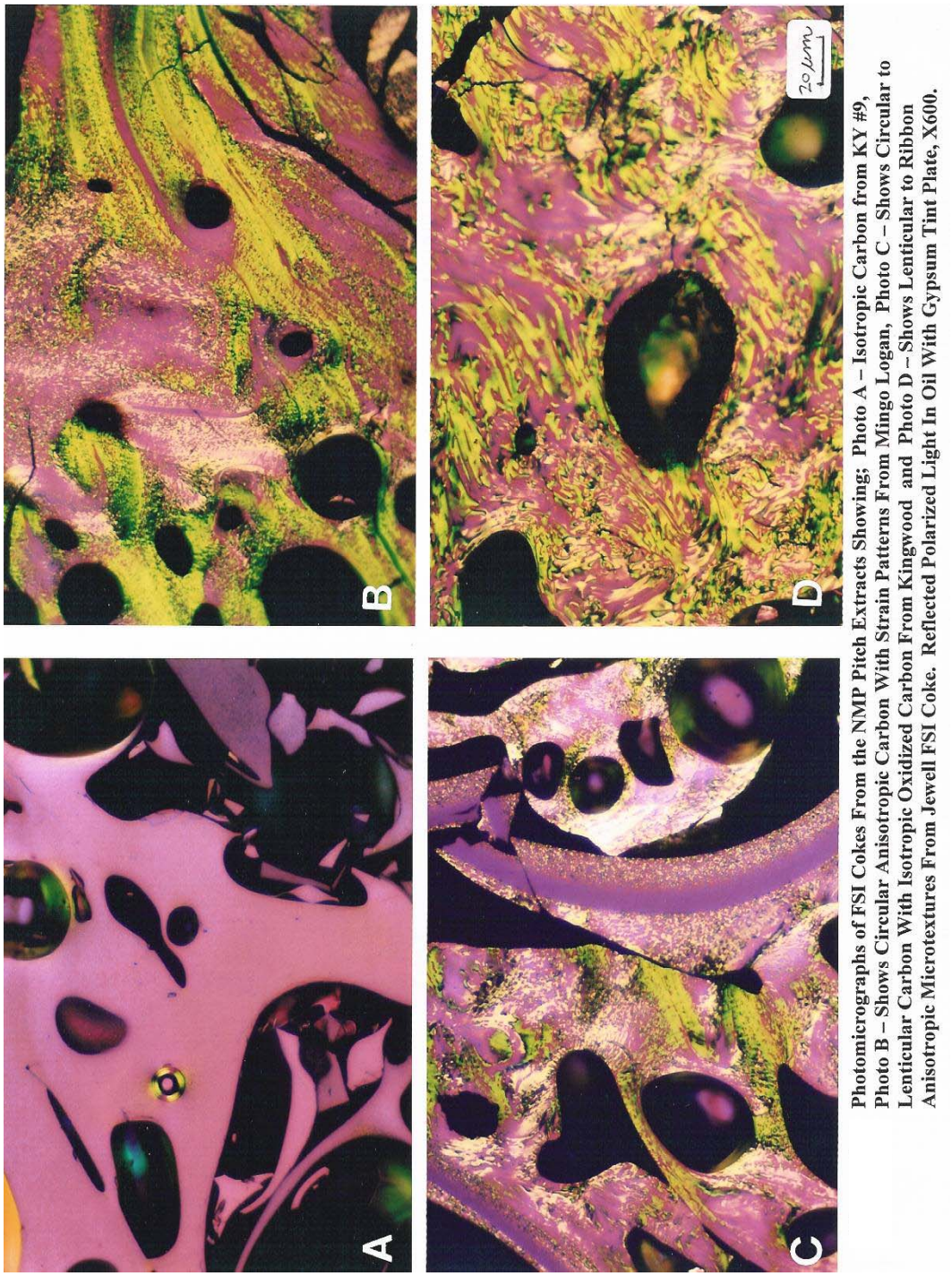

Photomicrographs of FSI Cokes From the NMP Pitch Extracts Showing; Photo A – Isotropic Carbon from KY #9, Photo B – Shows Circular Anisotropic Carbon With Strain Patterns From Mingo Logan, Photo C – Shows Circular to Lenticular Carbon With Isotropic Oxidized Carbon From Kingwood and Photo D – Shows Lenticular to Ribbon Anisotropic Microtextures From Jewell FSI Coke. Reflected Polarized Light In Oil With Gypsum Tint Plate, X600.

Figure 25. Photomicrographs of FSI cokes from extracts.

All of the FSI cokes from coals have relatively high amounts of binder phase from bright (high reactives) coals. The coke binder phase ranges from 67.2 to 78.4 percent by volume. FSI coke from extracts has only traces of coal inerts except the Poca #12 ,

which contain significant amounts of coal inerts. The anisotropic index ranges from 0.29 to 7.63 and increases with increased rank. The FSI coke from residues have anisotropic index values that range from 0.01 to 7.80, but also contain significantly more isotropic carbon than either the feed coal or extract.

Table 13. Summary petrographic analysis of FSI coke from coal, extract, and residue

Coal	Coal FSI Coke			Residue FSI Coke			Extract FSI Coke	
	Binder Phase	Filler Phase	AI	Binder Phase	Filler Phase	AI	Binder Phase	AI
Ky #9	73.3	26.7	0.02	54.2	45.8	0.01	100	0.29
Shoemaker	70.9	29.1	2.03	55.2	44.8	0.00	100	1.64
Bailey	78.4	21.6	2.05	62.8	37.2	0.01	100	1.86
Mingo Lo.	67.2	32.8	2.94	50.8	49.2	1.13	100	3.69
Marfork	71.2	28.8	3.87	33.9	66.1	1.16	100	3.74
Kingwood	78.0	22.0	5.41	24.6	75.4	0.33	100	5.06
Litwar	70.2	29.8	5.49	52.4	47.6	.054	100	5.63
Jewell	78.1	21.4	5.99	53.6	46.2	5.46	100	6.76
Poca #12	77.6	22.4	7.98	77.9	22.1	7.80	100	7.63

AI = anisotropic index

5.4 Results of WVU Coal Extraction Pilot Plant Runs

Based on the results of the research, the Kingwood coal was chosen for processing in the WVU coal extraction pilot plant. About 22lb of ¼ inch coal were added to 100L of NMP in the continuously stirred extractor. The coal was added slowly using a scoop while the reactor was stirring. The mixture was then heated to about 190°C and held at this temperature for 20 minutes. Experience with other coals showed that most of the coal is extracted at this temperature and time. A process flow diagram is shown in Figure 26. After the extraction was complete, the mixture was then pumped (Pump 1) through a basket filter to remove any large undissolved particles before being sent to the

centrifuge. The filter is a 15-gallon chrome plated vessel with a removable stainless steel 60 mesh screen filter basket.

The filtered mixture was then pumped (Pump 2) to the centrifuge to remove the remaining undissolved coal and mineral matter, and then sent to a holding tank before being sent to the Ross unit.

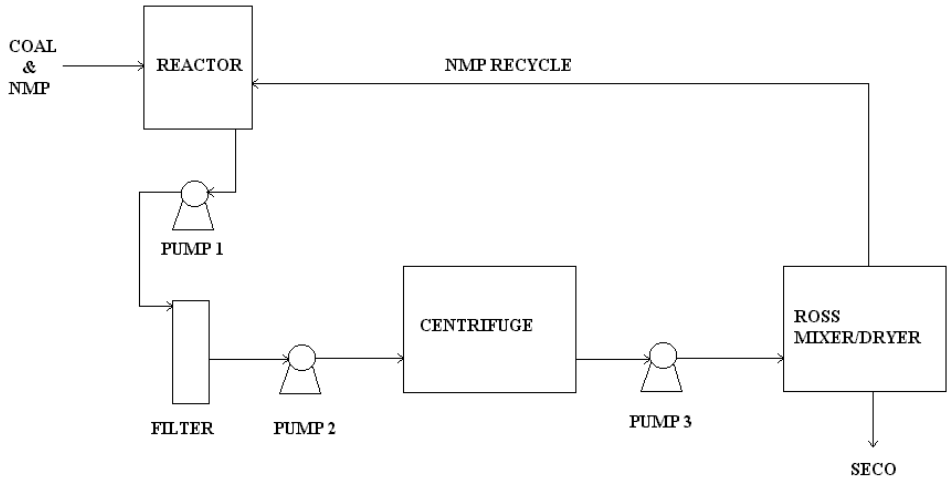

.

Figure 26 Flow diagram of the WVU coal extraction pilot plant

The liquid mixture is then pumped (Pump 3) into the Ross drier where the solvent is stripped and recycled leaving a dry, powdered coal extract. Mass balance showed that about 61wt% of the coal was extracted (about 67wt% in laboratory trials) but contained over 2wt% ash. It was felt that the system was contaminated from previous runs. Thus another attempted to extract the Kingwood coal was conducted under identical conditions. Again, extraction yields were over 60wt% but with an extract ash content of about 0.2wt%. The Kingwood coal underwent processing through the pilot scale system

without any difficulty whatsoever and as one of the engineers stated is a “joy” with which to work.

6 CONCLUSIONS

The results of this research show that several methods can be used to aid in the selection of bituminous coals for solvent extraction, particularly under mild conditions where coal composition is especially important. Some of the more effective tests involve the determination of thermoplasitc behavior in which Gieseler plasticity and Audibert-Arnu dilatometry are helpful. Proximate, FTIR, and elemental analyses are also useful in defining rank parameters and in predicting the chemical nature of the coal and extract. Petrographic examination and analysis are especially necessary to the successful operation of the process in determining the quantity, quality, and susceptibility of vitrinite to extraction.

7 REFERENCES

1) Lowry, H. H. *Chemistry of Coal Utilization*; John Wiley & Sons; New York, 1945; Volumes I & II.

2) Lowry, H. H. *Chemistry of Coal Utilization Supplementary Volume*; John Wiley & Sons; New York, 1963.

3) Elliot, M. A. *Chemistry of Coal Utilization Second Supplementary Volume;* John Wiley & Sons; New York, 1981.

4) Stach, E.; Mackowsky, M. Th.; Teichmuller, M.;Taylor, G. H.; Chandra, D.; Teichmuller, R. *Textbook of Coal Petrology 3rd Edition*; Borntraeger, Berlin, 1982.

5) Van Krevelen, D. W. *Coal: Typology, Physics, Chemistry, Constitution*; Elsevier, New York, 1993.

6) Dilo Paul, A. *The Solvent Extraction of Coal*; DOE; September 30, 2002.

7) Given, P. H.; Spackman, W.; Davis, A.; Jenkins, R. G. In *Coal Liquefaction Fundamentals*; Whitehurst, D. D., Ed.; American Chemical Society, Washington, D. C., 1980; Symposium Series 139.

8) Neavel, R. C. In *Chemistry of Coal Utilization Second Supplementary Volume*; John Wiley & Sons; New York, 1981; Chapter 3.

9) Derbyshire, F. *Fuel* **1991**, *70*, 276.

10) Murchison, D. G. *Fuel* **1991**, *70*, 296.

11) E.C.E., Coal Committee *International Codification System for Medium and High Rank Coals*; United Nations, New York, 1988.

12) Van Krevelen, D. W. *Coal: Typology, Physics, Chemistry, Constitution*; Elsevier, New York, 1993; pg. 553.

13) Given, P. H. In *Coal Science*; Gorbaty, M. L.; Larsen, J. W.; Wender, I., Eds.; Academic Press: New York, 1984; Vol. 3.

14) Van Krevelen, D. W. *Fuel* **1965**, *44*, 229.

15) Szeliga, J.; Marzec, A. *Fuel* **1983**, *62*, 1229.

16) Larsen, J. W.; Green, T. K.; Kovac, J. *J. Org. Chem.* **1985**, *50*, 4729.

17) Iino, M.; Takanohash, H; Ohsuga, H.; Toda, K. *Fuel* **1988**, *67*, 1639.

18) Nishioka, M.; Larsen, J. W. *Energy & Fuels* **1990**, *4*, 100.

19) Oele, , A. P.; Waterman, H. I.; Goedkoop, M. L.; van Krevelen, D. W. *Fuel* **1951**, *30*, 169.

20) Iino, M.; Takanohashi, T.; Gamble, V. *Fuel* **1988**, *67*, 1639.

21) Derbyshire, F. J.; Whitehurst, D. D. *Fuel* **1981**, *60*, 655.

22) Derbyshire, F. J.; Odoerfer, G. A..; Varghese, P.; Whitehurst, D. D. *Fuel* **1982**, *61*, 899.

23) Golumbic, C.; Anderson, J. B.; Orchin, M.; Storch, H. H. *U.S. Bur. Mines Rep. Invest. No. 4664*, 1950.

24) Heredy, L. A.; Fugass, P. In *Coal Science*; American Chemical Society, Washington, D. C., 1966; Advances in Chemistry Series No. 55.

25) Waters, P. L. *Fuel* **1962**, *41*, 3.

26) Van Krevelen, D. W.; Huntjens, F. J.; Dormans, H. N. M. *Fuel*, **1956**, *35*, 462.

27) Illingworth, S. R. *Fuel*, **1922**, *1*, 17.

28) Burgess, M. J.; Wheeler, R. V. *J. Chem. Soc.*, **1911**, *99*, 649.

29) Dryden, I. G. C.; Pankhurst, K. S. *Fuel*, **1955**, *34*, 363.

30) Neavel, R. C. In *Coal Science*; Gorbaty, M. L.; Larsen, J. W.; Wender, I., Eds.; Academic Press: New York, 1982; Vol. 1.

31) Derbyshire, F. J.; Davis, A.; Stansberry, P. G.; Terrer, M.-T. *Fuel Proc. Tech.*, **1986**, *12*, 127.

32) Stansberry, P. G.; Lin, L.; Terrer, M.-T.; Lee, C. W.; Davis, A.; Derbyshire, F. J. *J. Ener. Fuels*, **1987**, *1*, 89.

33) Brown, H. R.; Waters, P. L. *Fuel*, **1966**, *45*, 17.

34) Brown, H. R.; Waters, P. L. *Fuel*, **1966**, *45*, 41.

35) Van Krevelen, D. W. *Coal: Typology, Physics, Chemistry, Constitution*; Elsevier, New York, 1993; pg. 564.

36) Whitehurst, D. D.; Mitchell, T. O.; Farcasiu, M. *Coal Liquefaction*; Academic Press, New York, 1980; pg 179.

37) Stansberry, P. G. *A Study on the Molybdenum-Catalyzed Hydrogenation of Coals in the Absence of Solvent*; PhD Thesis; The Pennsylvania State University; 1988; pg 31.

38) American Society for Testing Materials; standard method D-2797.

39) American Society for Testing Materials; standard method D-2799.

40) American Society for Testing Materials; standard method D-2798.

41) American Society for Testing Materials; standard method D-2796-88.

42) Davis, A. In *Analytical Methods for Coal and Coal Products*; Karr, C., Ed.; Academic Press: New York, 1978; Vol. I, Chap. 2.

43) Gray, R. J. *Org. Geochem.* **1991**, *17*, 535.

44) Mahajan, O. P.; Walker, P. L In *Analytical Methods for Coal and Coal Products*; Karr, C., Ed.; Academic Press: New York, 1978; Vol. I, Chap. 4.

45) Supaluknari, S.; Larkins, F. P.; Redlich, P.; Jackson, W. R. *Fuel* **1988**, *18*, 147.

APPENDIX 1
Feed Coals
Basic Analyses

Coal Name	Ky #9	Shoemaker	Bailey	Mingo Logan	Marfork	Kingwood	Litwar	Jewell-Tiller	Poca #12
Seam	No. 9	Pittsburgh	Pittsburgh		70/30 Pow/CG	Kittanning	Litwar	Tiller	McDowell/WV
County/State	KY	Marshall/WV	PA	WV	WV	Preston/WV	WV	Buch./VA	WV
Mean Max Vitrinite Reflectance R_o, %	*0.53*	*0.77*	*0.83*	*0.98*	*1.02*	*1.08*	*1.23*	*1.36*	*1.53*
Sulfur, %dry	3.26	3.12	1.91	0.76	1.06	1.02	0.74	0.92	1.11
Proximate, %dry									
Volatile Matter	36.65	38.06	36.22	35.00	33.45	33.17	27.42	22.77	19.63
Fixed Carbon	53.52	51.92	56.11	59.27	60.05	57.91	68.09	70.63	76.63
Ash	9.83	10.02	7.67	5.73	6.50	8.92	4.49	6.60	3.83
Elemental Analysis, wt%									
C	68.94	72.37	74.74	78.08	80.52	77.44	82.57	84.6	85.96
H	5.13	5.1	5.25	5.16	5.21	4.95	5.02	4.76	4.68
N	1.34	1.22	1.18	1.12	1.13	1.18	1.32	0.93	1.06
S	2.72	2.59	1.56	0.66	0.72	1.58	0.6	0.7	0.99
O by difference	21.87	18.72	17.27	15.64	12.42	14.85	10.49	9.01	7.31
C/H atomic ratio	1.124	1.176	1.190	1.266	1.30	1.515	1.538	1.538	1.531

APPENDIX 2

Feed Coals and Residues

Surface and Bulk Properties

Coal Name	Ky #9	Shoemaker	Bailey	Mingo Logan	Marfork	Kingwood	Litwar	Jewell-Tiller	Poca #12
Seam	No. 9	Pittsburgh	Pittsburgh		70/30 Pow/CG	Kittanning	Litwar	Tiller	McDowell/WV
County/State	KY	Marshall/WV	PA	WV	WV	Preston/WV	WV	Buch./VA	WV
Real Density, g/cm^3									
Feed Coal	1.374	1.330	1.370	1.361	1.364	1.404	1.356	1.394	1.369
Insoluble Residue	1.432	1.426	1.402	1.365	1.992	1.649	1.417	1.398	1.359
BET Multipoint Surface Area, m^2/g									
Feed Coal	18.209	0.664	0.514	0.472	0.559	0.429	0.531	0.664	0.532
Insoluble Residue	0.243	0.538	0.451	0.481	0.484	0.992	0.959	0.655	0.291
Mercury Porosimetry									
Feed Coals									
Median Pore Diameter (Volume), μm	ND	14.149	11.820	ND	ND	12.383	10.982	ND	ND
Median Pore Diameter (Area), μm	ND	0.0052	0.0046	ND	ND	0.0033	0.0045	ND	ND
Apparent Density, g/cm^3	ND	1.320	1.343	ND	ND	1.267	1.315	ND	ND
Insoluble Residues									
Median Pore Diameter (V), μm	ND	32.216	24.290	ND	ND	24.099	17.579	ND	ND
Median Pore Diameter (A), μm	ND	0.0064	0.0050	ND	ND	0.0051	5.043	ND	ND
Apparent Density, g/cm^3	ND	1.408	1.427	ND	ND	1.697	1.186	ND	ND

ND = not determined

APPENDIX 3

Feed Coals

Thermoplastic Properties

Coal Name	Ky #9	Shoemaker	Bailey	Mingo Logan	Marfork	Kingwood	Litwar	Jewell-Tiller	Poca #12
Seam	No. 9	Pittsburgh	Pittsburgh		70/30 Pow/CG	Kittanning	Litwar	Tiller	McDowell/ WV
County/State	KY	Marshall/WV	PA	WV	WV	Preston/WV	WV	Buch./VA	WV
Mean Max Vitrinite Reflectance R_o, %	0.53	0.77	0.83	0.98	1.02	1.08	1.23	1.36	1.53
Yield NMP Solubles, wt%	30.3	34.1	30.9	32.4	45.3	66.7	40.6	30	5
Yield NMP Solubles, daf%	33.6	37.9	33.5	34.4	48.4	73.2	42.5	32.1	5.2
Free Swelling Index, FSI									
FSI	4.0	7.0	7.5	7.5	7.5	9.0	8.5	9.0	9.0
Gieseler Plastometry									
Max ddpm	9	12019	771	20246	29999	30000	11009	1914	551
Temp Max ddpm, °C	422	429	440	441	453	456	456	471	476
Temp Softening, °C	382	382	400	394	391	369	397	409	424
Temp Soldification, °C	443	465	471	483	489	500	499	509	506
Plastic Range, °C	61	83	71	89	98	121	102	100	82
Arnu Dilatometry									
Max Contraction, %	-22	-28	-30	-24	-29	-32	-30	-25	-29
Max Dilatation, %	-35	185	73	149	300	300	271	182	114
Init Softening Point, °C	356	347	360	354	349	346	362	393	399
Init Dilatation Temp, °C	403	390	400	406	395	382	403	418	434
Max Dilation Temp, °C	427	441	433	452	478	466	476	480	479

APPENDIX 4

Thermoplastic Properties

Feed Coals, Extracts, and Residues

Coal Name	Ky #9	Shoemaker	Bailey	Mingo Logan	Marfork	Kingwood	Litwar	Jewell-Tiller	Poca #12
Feed Coals									
Free Swelling Index, FSI									
FSI	4.0	7.0	7.5	7.5	7.5	9.0	8.5	9.0	9.0
Gieseler Plastometry									
Max ddpm	9	12019	771	20246	29999	30000	11009	1914	551
Temp Max ddpm, °C	422	429	440	441	453	456	456	471	476
Temp Softening, °C	382	382	400	394	391	369	397	409	424
Temp Soldification, °C	443	465	471	483	489	500	499	509	506
Plastic Range, °C	61	83	71	89	98	121	102	100	82
Arnu Dilatometry									
Max Contraction, %	-22	-28	-30	-24	-29	-32	-30	-25	-29
Max Dilatation, %	-35	185	73	149	300	300	271	182	114
Init Softening Point, °C	356	347	360	354	349	346	362	393	399
Init Dilatation Temp, °C	403	390	400	406	395	382	403	418	434
Max Dilation Temp, °C	427	441	433	452	478	466	476	480	479
Residues									
Free Swelling Index, FSI									
FSI	0.5	0.5	0.0	1.0	1.0	0.5	0.0	7.5	9
Gieseler Plastometry									
Max ddpm	0	0	0	12	4	0	0	3	95
Temp Max ddpm, °C	na	na	na	449	457	na	na	479	480
Temp Softening, °C	na	na	na	436	436	na	na	459	437
Temp Soldification, °C	na	na	na	470	475	na	na	499	511
Plastic Range, °C	na	na	na	34	39	na	na	40	74
Max ddpm	0	0	0	12	4	0	0	3	95
Extracts									
Free Swelling Index, FSI									
FSI	9.0	9.0	9.0	9.0	9.0	9.0	9.0	9.0	9.0
Gieseler Plastometry									
Max ddpm	2438	5500	6522	30000	29967	17782	11089	30000	30000
Temp Max ddpm, °C	408	428	429	422	431	445	444	435	350
Temp Softening, °C	333	333	351	318	337	354	342	308	<300
Temp Soldification, °C	454	474	474	490	489	494	495	512	507
Plastic Range, °C	121	141	123	172	152	140	153	204	>207
Max ddpm	2438	5500	6522	30000	29967	17782	11089	30000	30000

APPENDIX 5
Feed Coals, Residues, and Extracts
FTIR Analysis

Coal Name	Ky #9	Shoemaker	Bailey	Mingo Logan	Marfork	Kingwood	Litwar	Jewell-Tiller	Poca #12
Seam	No. 9	Pittsburgh	Pittsburgh		70/30 Pow/CG	Kittanning	Litwar	Tiller	McDowell/ WV
County/State	KY	Marshall/WV	PA	WV	WV	Preston/WV	WV	Buch./VA	WV
Mean Max Vitrinite Reflectance R_o, %	0.53	0.77	0.83	0.98	1.02	1.08	1.23	1.36	1.53
Yield NMP Solubles, wt%	30.3	34.1	30.9	32.4	45.3	66.7	40.6	30	5
Yield NMP Solubles, daf%	33.6	37.9	33.5	34.4	48.4	73.2	42.5	32.1	5.2
Feed Coal									
Hal[1]	29.856	39.236	42.948	36.229	53.396	46.604	30.325	40.8605	NA
Har[2]	0.487	0.684	3.724	2.5275	5.5495	5.481	6.219	7.5625	NA
Har/Hal	0.016311	0.017433	0.08671	0.069765	0.103931	0.117608	0.205078	0.185081	NA
Insoluble Residue									
Hal[1]	25.0845	NA	NA	22.9815	22.493	3.156	10.193	44.0625	NA
Har[2]	0.329	NA	NA	0.585	1.5365	0.599	1.34	8.888	NA
Har/Hal	0.013116	NA	NA	0.025455	0.06831	0.189797	0.131463	0.201713	NA
Extracts									
Hal[1]	53.0045	31.363	50.724	76.7235	59.316	40.686	58.32	52.7065	NA
Har[2]	0.978	0.465	1.748	7.191	7.0345	3.399	7.869	9.231	NA
Har/Hal	0.018451	0.014826	0.034461	0.093726	0.118594	0.083542	0.134928	0.149037	NA

1 Integrated IR intensity associated with aliphatic C-H stretching mode

2 Integrated IR intensity associated with aromatic C-H stretching mode
NA = not applicable or available

APPENDIX 6

Maceral Analysis-Feed Coal

Volume Percent

Coal Name	Ky #9	Shoemaker	Bailey	Mingo Logan	Marfork	Kingwood	Litwar	Jewell-Tiller	Poca #12
Mean Max Vitrinite Reflectance R_o, %	0.53	0.77	0.83	0.98	1.02	1.08	1.23	1.36	1.53
Vitrinite Group									
Collinite	41.1	37.8	38.3	24.6	28.1	39.8	31.0	39.5	53.9
Telinite	13.9	5.8	3.4	4.0	5.2	9.5	1.1	0.0	1.0
Attrital Fine	7.5	10.1	15.6	14.4	15.9	12.9	18.7	9.0	8.1
Attrital Band	6.8	15.3	10.0	7.6	12.5	10.3	16.5	9.4	7.2
Pseudovitrinite	1.4	3.2	6.4	3.0	3.5	2.1	3.3	18.6	9.2
Total Vitrinite Group	70.7	72.2	73.7	53.6	65.2	74.6	70.6	76.5	79.4
Liptinite Group									
Sporinite	4.7	5.0	5.1	9.6	4.5	2.8	4.8	2.3	0.7
Cutinite	0.5	0.2	0.1	0.8	0.4	0.7	0.2	0.2	0.1
Resinite-Light	2.1	1.4	1.1	2.8	0.8	1.3	1.3	0.4	0.3
Resinite-Dark	0.2	0.4	0.2	0.3	0.8	0.2	0.0	0.0	0.1
Total Liptinite Group	7.5	7.0	6.5	13.5	6.5	5.0	6.3	2.9	1.2
Inertinite Group									
Semifusinite	4.7	3.8	5.7	6.6	7.5	3.2	2.7	5.4	5.3
Micrinite-Granular	5.4	3.8	4.7	11.1	6.7	6.9	8.5	5.2	4.9
Micrinite-Macrinite	0.4	1.8	0.3	2.0	1.3	0.3	0.7	0.5	0.8
Micrinite-Inertodetrinite	2.8	3.8	2.3	6.4	3.1	2.4	4.5	2.5	3.3
Fusinite	2.9	3.4	3.4	3.9	5.3	2.3	4.1	2.6	2.0
Total Inertinite Group	16.2	16.6	16.4	30.0	23.9	16.1	20.5	16.2	16.3
Mineral Matter									
Pyrite	1.1	1.4	0.8	0.5	0.6	0.9	0.3	0.6	0.9
Clay	1.8	1.0	1.4	1.5	2.0	0.4	1.5	2.2	1.8
Carbonates	0.0	Trace	0.0	0.1	0.0	1.1	0.2	0.0	0.1
Calcite	0.4	0.2	0.0	0.0	0.0	1.2	0.1	0.2	0.0
Quartz	0.5	0.8	1.0	0.3	0.7	0.3	0.1	0.0	0.2
Shale	0.2	0.6	0.2	0.3	0.2	0.4	0.3	0.0	Trace
Bone	1.6	0.2	0.0	0.2	0.9	0.0	0.1	1.4	0.1
Rust	0.0	Trace	0.0	0.0	0.0	0.0	0.0	0.0	0.0
Total Mineral Matter	5.6	4.2	3.4	2.9	4.4	4.3	2.6	4.4	3.1
Total All Groups	100	100	100	100	100	100	100	100	100

APPENDIX 7

Maceral Analysis-Insoluble Residue

Volume Percent

Coal Name	Ky #9	Shoemaker	Bailey	Mingo Logan	Marfork	Kingwood	Litwar	Jewell-Tiller	Poca #12
Vitrinite Group									
Collinite	30.2	44.6	50.5	20.9	5.4	36.5	39.3	47.4	54.6
Telinite	2.9	2.0	0.8	2.2	0.5	0.0	0.0	0.7	0.6
Attrital Fine	14.6	5.1	3.4	14.2	18.6	6.3	10.8	12.6	8.0
Attrital Band	17.6	5.8	7.7	6.2	12.1	3.0	7.9	6.2	12.4
Pseudovitrinite	2.3	3.6	4.5	4.3	1.5	5.9	3.4	5.1	3.3
Total Vitrinite Group	67.6	61.1	66.9	47.8	38.1	51.7	61.4	72.0	78.9
Liptinite Group									
Sporinite	6.1	5.9	6.1	9.4	9.2	9.9	3.7	2.7	0.9
Cutinite	0.5	0.7	0.7	0.5	0.5	0.6	0.1	0.0	0.1
Resinite-Light	2.2	0.6	0.8	2.8	4.0	0.9	0.5	0.2	0.1
Resinite-Dark	0.2	0.0	0.0	0.2	0.2	0.0	0.0	0.0	0.0
Total Liptinite Group	9.0	7.2	7.6	12.9	13.9	11.4	4.3	2.9	1.1
Inertinite Group									
Semifusinite	3.6	6.1	4.6	8.6	12.2	6.5	7.2	4.7	6.6
Micrinite-Granular	3.5	4.8	4.1	13.1	13.6	2.8	9.3	5.9	4.0
Micrinite-Macrinite	0.9	1.6	0.5	1.6	1.7	1.5	1.6	0.9	0.9
Micrinite-Inertodetrinite	5.4	7.6	6.0	6.9	10.0	6.2	7.8	3.8	3.2
Fusinite	2.4	4.2	4.2	4.8	3.6	3.5	3.3	4.2	3.0
Total Inertinite Group	15.8	24.3	19.4	35.0	41.1	20.5	29.2	19.5	17.7
Mineral Matter									
Pyrite	1.7	2.7	1.2	0.6	0.7	2.1	0.5	0.4	0.5
Clay	4.3	2.3	2.4	2.2	4.3	8.9	2.9	2.3	1.0
Carbonates	0.0	0.0	0.0	0.0	0.1	0.0	0.0	0.0	0.0
Calcite	0.0	0.2	0.2	0.2	0.1	0.2	0.2	0.4	0.0
Quartz	0.6	0.3	0.2	0.3	0.3	0.7	0.2	0.5	0.1
Shale	0.1	1.1	0.7	0.2	0.1	0.9	0.5	0.4	0.2
Bone	0.9	0.8	1.4	0.8	1.3	3.6	0.8	1.6	0.5
Rust	0.0	0.0	0.0	0.0	0.0	0.0	0.0	0.0	0.0
Total Mineral Matter	7.6	7.4	6.1	4.3	6.9	16.4	5.1	5.6	2.3
Total Inertinite + MM	23.4	31.7	25.5	39.3	48.0	36.9	34.3	25.1	20.0
Total All Groups	100	100	100	100	100	100	100	100	100

APPENDIX 8
Feed Coals
Vitrinoid-Type Distribution
Reflectance Analysis

Coal Name	Ky #9	Shoemaker	Bailey	Mingo Logan	Marfork	Kingwood	Litwar	Jewell-Tiller	Poca #12
Seam	No. 9	Pittsburgh	Pittsburgh		70/30 Pow/CG	Kittanning	Litwar	Tiller	McDowell/ WV
County/State	KY	Marshall/WV	PA	WV	WV	Preston/WV	WV	Buch./VA	WV
Reflectance Analysis, %									
V4	37.0								
V5	51.0								
V6	12.0	4.0	1.0						
V7		74.0	21.0						
V8		22.0	72.0	6.0	8.5	1.0			
V9			6.0	56.0	33.0	13.0			
V10				38.0	36.5	46.0			
V11					20.5	38.0	33.0		
V12					1.5	2.0	57.0	9.5	
V13							10.0	75.5	1.0
V14								13.0	25.0
V15								2.0	67.5
V16									6.0
V17									0.5
Total	100	100	100	100	100	100	100	100	100

APPENDIX 9

NMP-Soluble Extract
Vitrinoid-Type Distribution
Reflectance Analysis

Coal Name	Ky #9	Shoemaker	Bailey	Mingo Logan	Marfork	Kingwood	Litwar	Jewell-Tiller	Poca #12
Seam	No. 9	Pittsburgh	Pittsburgh		70/30 Pow/CG	Kittanning	Litwar	Tiller	McDowell/ WV
County/State	KY	Marshall/WV	PA	WV	WV	Preston/WV	WV	Buch./VA	WV
Reflectance Analysis, %									
V5	64.0	4.0							
V6	36.0	36.0							
V7		56.0	90.0	24.0					
V8		4.0	10.	76.0	100.0				
V9						48.0			10.0
V10						52.0	64.0	18.0	88.0
V11							36.0	80.0	2.0
V12								2.0	
V13									
V14									
V15									
V16									
V17									
Total	100	100	100	100	100	100	100	100	100
Mean Max Reflec Ext.	0.59	0.71	0.76	0.83	0.85	1.00	1.09	1.13	1.04
Microscopic Observations									
White Binder Phase	81.7	62.5	50.5	80.7	87.6	62.7	62.4	73.5	6.0
Light Gray Binder Ph	14.0	20.0	34.6	9.6	3.7	18.0	20.7	3.3	57.5
Darker Gray Bind Ph	0.0	1.0	4.3	0.0	0.0	2.7	1.0	1.3	3.0
Darkest Gray Bind Ph	0.0	6.7	0.0	0.3	0.0	0.0	0.0	0.0	0.3
Flow Shapes	3.3	1.3	1.0	4.7	7.7	4.3	3.3	17.6	2.7
NMP	0.3	1.3	Trace	0.7	0.0	0.3	0.0	1.3	2.7
Coal	0.0	0.7	0.3	Trace	Trace	Trace	Trace	Trace	26.5
Oxidized	0.7	6.5	9.3	4.0	1.0	12.0	12.6	3.0	1.3
Total, %	100	100	100	100	100	100	100	100	100

APPENDIX 10
Insoluble Residue
Vitrinoid-Type Distribution
Reflectance Analysis

Coal Name	Ky #9	Shoemaker	Bailey	Mingo Logan	Marfork	Kingwood	Litwar	Jewell-Tiller	Poca #12
Seam	No. 9	Pittsburgh	Pittsburgh		70/30 Pow/CG	Kittanning	Litwar	Tiller	McDowell/ WV
County/State	KY	Marshall/WV	PA	WV	WV	Preston/WV	WV	Buch./VA	WV
Reflectance Analysis, %									
V4	2.0								
V5	78.0	10.0							
V6	20.0	74.0	32.0						
V7		12.0	58.0	12.0					
V8		4.0	10.0	66.0	26.0	2.0			
V9				22.0	42.0	46.0	2.0		
V10					26.0	50.0	16.0		
V11					6.0	2.0	70.0		
V12							12.0	6.0	
V13								62.0	
V14								30.0	8.0
V15								2.0	70.0
V16									22.0
V17									
Total	100	100	100	100	100	100	100	100	100
Mn Max Refl Residue	0.57	0.66	0.73	0.86	0.96	1.00	1.14	1.38	1.56

APPENDIX 11

Non-Maceral Microstructures-Feed Coal

Volume Percent

Coal Name	Ky #9	Shoemaker	Bailey	Mingo Logan	Marfork	Kingwood	Litwar	Jewell-Tiller	Poca #12
Normal-Bright	48.8	45.5	45.1	28.2	35.6	50.3	44.0	33.8	47.4
Normal-Intermediate	8.2	13.8	16.7	17.0	15.8	10.8	12.5	10.4	6.9
Normal-Dull	5.4	9.6	9.8	21.0	13.3	7.8	9.1	9.1	4.3
Normal-Coarse Pure Vitrinite	19.5	14.8	11.4	10.3	10.9	9.6	12.2	9.3	21.3
Normal-Semifusinite-Isolated or >50µm	2.8	2.4	1.6	5.8	6.0	0.9	2.4	2.2	2.5
Normal-Fusinite-Isolated or >50µm	2.3	2.2	2.3	2.2	3.1	1.6	3.9	2.7	1.7
Ultrafine Coal <5µm	4.0	3.1	5.4	5.2	5.6	5.2	7.5	8.0	4.5
Pseudovitrinite	1.7	2.9	3.8	6.4	5.4	7.3	4.7	17.5	7.7
Oxidized Slight	0.2	0.2	0.2	0.6	0.6	0.3	0.5	0.5	0.5
Oxidized Moderate	0.3	0.1	0.0	0.2	0.2	0.0	0.0	0.0	0.1
Oxidized Severe	0.1	0.0	0.0	0.0	0.0	0.0	0.0	0.0	0.0
Microbrecciation Fine	0.5	0.2	0.0	0.2	0.8	0.2	0.6	0.2	0.3
Microbrecciation Inter	0.2	0.3	0.4	0.4	0.0	0.3	0.5	0.2	0.2
Microbrecciation Coarse	0.2	0.0	0.2	0.0	0.0	0.2	0.0	0.0	0.0
Coarse Mineral Matter-Clay	1.8	0.6	0.9	0.5	0.4	0.9	0.6	2.4	0.5
Coarse Mineral Matter-Bone Coal	1.4	0.8	0.3	0.5	1.3	1.9	0.5	1.3	1.1
Coarse Mineral Mattter-Carbon Shale	0.3	0.0	0.0	0.2	0.0	0.1	0.2	0.0	0.1
Coarse Mineral Matter-Shale	0.0	1.3	0.3	0.0	0.2	0.8	0.3	0.5	0.1
Coarse Mineral Matter-Pyrite	1.3	1.9	1.3	0.2	0.6	0.9	0.2	0.8	0.5
Coarse Mineral Matter-Carbonates	0.7	0.1	0.1	0.2	0.0	0.9	0.1	0.2	0.0
Coarse Mineral Mattter-Quartz	0.3	0.2	0.0	0.2	0.2	0.0	0.1	0.0	0.3
Miscellaneous Features									
Contamination-Mill Scale	0.0	0.0	0.1	0.0	0.0	0.0	0.0	0.0	0.0
Contamination-rank	0.0	0.0	0.0	0.0	0.0	0.0	0.1	0.9	0.0
Contamination-Coke Dust	0.0	0.0	0.1	0.0	0.0	0.0	0.0	0.0	0.0
Cenosheres	0.0	0.0	0.0	0.0	0.0	0.0	0.0	0.0	0.0

APPENDIX 12
Feed Coal
Coke Petrography
FSI Button

Coal Name	Ky #9	Shoemaker	Bailey	Mingo Logan	Marfork	Kingwood	Litwar	Jewell-Tiller	Poca #12
Binder Phase Carbon									
Isotropic	71.7	0.6	1.5	0.3	0.0				
Incipient	1.5	9.5	10.3	0.5	0.7				
Circular Anisotropy-Fine	0.0	49.2	52.4	19.6	2.1		0.1		
Circular Anisotropy-Interm	0.1	10.4	12.1	34.2	17.4	0.5	0.1		
Circular Anisotropy-Coarse		1.0	1.0	9.9	37.1	7.3	0.4	1.1	
Lentcular Anisotrop-Fine		0.1	0.9	1.3	13.4	40.3	36.7	19.6	
Lenticular Anisotrop-Interm		0.1	0.2	0.9	0.3	22.6	30.7	41.9	1.9
Lenticular Anisotrop-Coarse				0.4	0.1	5.1	2.2	10.0	7.7
Ribbon Anisotrop-Fine				0.1	0.1	1.7		5.5	58.8
Ribbon Anisotrop-Intermediate						0.5			9.0
Ribbon Anisotrop-Coarse									0.2
Total Binder Phase	73.3	70.9	78.4	67.2	71.2	78.0	70.2	78.1	77.6
Filler Phase Carbon									
Organic Inerts <50µm	8.8	13.5	9.0	19.8	15.2	10.0	17.8	10.5	10.0
Organic Inerts ≥50µm	3.8	5.3	5.8	6.0	4.0	4.0	8.4	4.9	4.1
Inorganic Inerts-Fine	5.6	4.5	3.4	4.0	5.2	2.8	2.7	3.3	4.9
Inorganic Inerts-Coarse	5.6	3.4	2.0	1.8	2.6	4.0	0.6	2.1	1.7
Misc. Org. Inerts (Oxid.)	0.0	0.1	0.0	0.4	1.2	0.0	0.0	0.2	0.5
Pyrite	2.9	2.3	1.4	0.8	0.6	1.2	0.3	0.4	1.2
Total Filler Phase	26.7	29.1	21.6	32.8	28.8	22.0	29.8	21.4	22.4
Pyrolytic Carbon	0.0	0.0	0.0	0.0	0.0	0.0	0.0	0.4	0.0
Non-Coal Related MM	0.0	0.0	0.0	0.0	0.0		0.0	0.1	0.0
Binder Reflectance-Estimated	0.6	0.90	0.90	0.99	1.02	1.24	1.25	1.30	1.50
Feed Coal Reflectance	0.53	0.77	0.83	0.98	1.02	1.08	1.23	1.36	1.53
Anisotropic Index	0.02	2.03	2.05	2.94	3.87	5.41	5.49	5.99	7.98

APPENDIX 13
NMP-Soluble Extract
Coke Petrography
FSI Button

Coal Name	Ky #9	Shoemaker	Bailey	Mingo Logan	Marfork	Kingwood	Litwar	Jewell-Tiller	Poca #12
Binder Phase Carbon									
Isotropic	71.7	4.1		1.8	0.9			0.6	
Incipient	27.9	36.4	30.5	0.2	2.8		0.9		
Circular Anisotropy-Fine	0.4	52.6	59.8	7.2	10.6	3.9	1.9		
Circular Anisotropy-Interm		5.5	6.2	31.6	26.1	9.6	4.2		
Circular Anisotropy-Coarse		1.2	1.3	42.2	30.2	19.1	11.8	1.4	
Lentcular Anisotrop-Fine		0.2	1.4	14.4	25.5	40.6	19.1	4.8	2.9
Lenticular Anisotrop-Interm			0.8	0.8	3.9	10.3	39.6	31.6	10.2
Lenticular Anisotrop-Coarse				0.8		4.2	14.8	36.4	25.7
Ribbon Anisotrop-Fine				1.0		12.3	7.7	24.8	43.6
Ribbon Anisotrop-Intermediate								0.4	17.6
Ribbon Anisotrop-Coarse									
Total Binder Phase	100	100	100	100	100	100	100	100	100
Filler Phase Carbon									
Organic Inerts <50µm									
Organic Inerts ≥50µm									
Inorganic Inerts-Fine									
Inorganic Inerts-Coarse									
Misc. Org. Inerts (Oxid.)									
Pyrite									
Total Filler Phase	0	0	0	0	0	0	0	0	0
Oxidation Themal?	?	8.4	7.5	?	?	8.6	9.6	?	?
Non-Coal Related MM									
Binder Reflectance-Estimated	0.89	0.86	0.89	1.07	1.07	1.21	1.26	1.38	1.46
Feed Coal Reflectance	0.83	0.77	0.83	0.98	1.02	1.08	1.23	1.36	1.53
Anisotropic Index	1.86	1.64	1.86	3.69	3.74	5.06	5.63	6.76	7.63

APPENDIX 14
Feed Coal
Maceral Analysis
Weight Percent

Coal Name	Ky #9	Shoemaker	Bailey	Mingo Logan	Marfork	Kingwood	Litwar	Jewell-Tiller	Poca #12
Seam	No. 9	Pittsburgh	Pittsburgh		70/30 Pow/CG	Kittanning	Litwar	Tiller	McDowell/ WV
County/State	KY	Marshall/WV	PA	WV	WV	Preston/WV	WV	Buch./VA	WV
Mean Max Vitrinite Reflectance R_o, %	0.53	0.77	0.83	0.98	1.02	1.08	1.23	1.36	1.53
Maceral Analysis									
Total Vitrinite Group	64.3	66.1	68.7	49.8	59.7	67.5	66.4	70.9	74.1
Total Liptinite Group	6.4	6.0	5.7	11.8	5.6	4.2	5.6	2.5	1.0
Semifusinite	4.7	3.8	5.8	6.7	7.5	2.3	2.8	5.5	5.4
Total Micrinite	8.9	9.7	7.7	20.5	11.5	9.8	14.6	8.6	9.5
Fusinite	3.5	4.1	4.2	4.8	6.4	1.8	5.1	3.2	2.5
Mineral Matter									
Pyrite	3.9	5.0	2.9	1.8	2.1	3.2	1.1	2.2	3.3
Clay	3.3	1.9	2.7	2.8	3.7	5.7	2.9	4.1	3.4
Carbonates	0.0	0.0	0.0	0.2	0.0	2.0	0.4	0.0	0.2
Calcite	0.7	0.4	0.0	0.0	0.0	2.2	0.2	0.4	0.0
Quartz	0.9	1.5	1.9	0.6	1.3	0.6	0.2	0.0	0.4
Shale	0.4	1.1	0.4	0.6	0.4	0.7	0.6	0.0	0.0
Bone	3.0	0.4	0.0	0.4	1.7	0.0	0.2	2.6	0.2
Rust	0.0	0.0	0.0	0.0	0.0	0.0	0.0	0.0	0.0
Total All Groups	100	100	100	100	100	100	100	100	100

APPENDIX 15

Insoluble Residue
Maceral Analysis
Weight Percent

Coal Name	Ky #9	Shoemaker	Bailey	Mingo Logan	Marfork	Kingwood	Litwar	Jewell-Tiller	Poca #12
Seam	No. 9	Pittsburgh	Pittsburgh		70/30 Pow/CG	Kittanning	Litwar	Tiller	McDowell/ WV
County/State	KY	Marshall/WV	PA	WV	WV	Preston/WV	WV	Buch./VA	WV
Mean Max Vitrinite Reflectance R_o, %	0.53	0.77	0.83	0.98	1.02	1.08	1.23	1.36	1.53
Maceral Analysis									
Total Vitrinite Group	59.9	52.6	60.1	43.5	33.6	41.9	55.7	65.7	74.5
Total Liptinite Group	7.5	5.8	6.4	11.0	11.5	8.7	3.7	2.5	1.0
Semifusinite	3.5	5.7	4.5	8.6	11.8	5.8	7.1	4.7	6.8
Total Micrinite	9.8	13.7	10.8	22.2	25.3	9.6	19.2	11.0	8.7
Fusinite	2.8	4.8	5.0	5.8	4.2	3.8	4.0	5.1	3.8
Insol Residue Refle %	0.57	0.66	0.73	0.86	0.96	1.00	1.14	1.38	1.56
Mineral Matter									
Pyrite	5.9	9.1	4.2	2.1	2.4	6.7	1.8	1.4	1.8
Clay	7.7	4.0	4.4	4.1	7.7	14.7	5.3	4.3	1.9
Carbonates	0.0	0.0	0.0	0.0	0.2	0.0	0.0	0.0	0.0
Calcite	0.0	0.4	0.4	0.4	0.2	0.3	0.4	0.7	0.0
Quartz	1.1	0.5	0.4	0.6	0.5	1.2	0.4	0.9	0.2
Shale	0.2	1.9	1.3	0.4	0.2	1.5	0.9	0.7	0.4
Bone	1.6	1.4	2.6	1.5	2.3	5.9	1.5	3.0	1.0
Rust	0.0	0.0	0.0	0.0	0.0	0.0	0.0	0.0	0.0
Total All Groups	100	100	100	100	100	100	100	100	100

APPENDIX 16

Feed Coals, Residues, and Extracts

Elemental Analysis

Coal Name	Ky #9	Shoemaker	Bailey	Mingo Logan	Marfork	Kingwood	Litwar	Jewell-Tiller	Poca #12
Mean Max Vitrinite Reflectance R_o, %	0.53	0.77	0.83	0.98	1.02	1.08	1.23	1.36	1.53
Yield NMP Solubles, wt%	30.3	34.1	30.9	32.4	45.3	66.7	40.6	30	5
Feed Coal, wt%									
C	68.94	72.37	74.74	78.08	80.52	77.44	82.57	84.6	85.96
H	5.13	5.1	5.25	5.16	5.21	4.95	5.02	4.76	4.68
N	1.34	1.22	1.18	1.12	1.13	1.18	1.32	0.93	1.06
S	2.72	2.59	1.56	0.66	0.72	1.58	0.6	0.7	0.99
O by diff.	21.87	18.72	17.27	14.98	12.42	14.85	10.49	9.01	7.31
C/H atomic ratio	1.12	1.12	1.19	1.26	1.29	1.30	1.37	1.48	1.53
Insoluble Residue, wt%									
C	64.59	67.11	69.58	74.51	70.53	55.8	76.7	82.44	83.57
H	4.72	4.46	4.55	4.84	4.51	3.08	4.18	4.44	4.54
N	1.76	1.38	1.78	1.46	1.12	0.87	1.34	1.1	1.21
S	2.7	2.46	1.37	0.51	0.78	3.27	0.61	0.58	0.89
O by diff.	26.23	24.59	22.72	18.68	23.06	36.98	17.17	11.44	9.79
C/H atomic ratio	1.14	1.25	1.27	1.28	1.30	1.59	1.53	1.55	1.53
Extracts, wt%									
C	78.16	80.54	79.35	84.12	84.39	82.9	83.85	87.45	86.55
H	5.88	5.97	5.6	5.99	5.79	5.36	5.17	5.54	5.58
N	2.4	2.55	2.57	2.31	2.17	2.14	1.85	1.95	2.41
S	1.64	0.91	0.75	0.45	0.53	0.59	0.49	0.48	0.65
O by diff.	11.92	10.03	11.73	7.13	7.12	9.01	8.64	4.58	4.81
C/H atomic ratio	1.11	1.12	1.18	1.17	1.21	1.29	1.35	1.32	1.29